# PROPERTIES OF STRONGLY INTERACTING MATTER UNDER EXTREME CONDITIONS

*A thesis submitted in fulfillment of the requirements for the degree of*
***Doctor of Philosophy***

by
**Deepak KUMAR**
Roll No. 17330011

Under the supervision of
**Prof. Hiranmaya MISHRA**
Senior Professor
Theoretical Physics Division
Physical Research Laboratory
Ahmedabad 380009

Discipline of Physics
Indian Institute of Technology Gandhinagar - 382355
JULY 2022

# Declaration

I declare that this written submission represents my ideas in my own words and where other's ideas or words have been included, I have adequately cited and referenced the original sources. I also declare that I have adhered to all principles of academic honesty and integrity and have not misrepresented or fabricated or falsified any idea/data/fact/source in my submission. I understand that any violation of the above will be cause for disciplinary action by the Institute and can also evoke penal action from the sources which have thus not been properly cited or from whom proper permission has not been taken when needed.

Place : Ahmedabad
Date : 15 May 2023

**Deepak KUMAR**
(IITGn Roll No. 17330011)

**Discipline of Physics**
**Indian Institute of Technology Gandhinagar - 382355**

# Certificate

This has to certified that this thesis entitled "**Properties of Strongly Interacting Matter Under Extreme Conditions**" submitted by **Mr. Deepak KUMAR (Roll no: 17330011)**, to "**Indian Institute of Technology Gandhinagar**" is a record of bonafide research work carried out under my supervision and has not been submitted elsewhere for the degree.

I have read this thesis and in my opinion, it is fully adequate in scope and quality as a thesis for the degree of Doctor of Philosophy.

Hiranmaya Mishra

**Prof. Hiranmaya MISHRA**
Senior Professor
Theoretical Physics Division
Physical Research Laboratory
Ahmedabad 380009

Place : Ahmedabad
Date : 15 May 2023

# Acknowledgements

Words could not express the magnanimity of a person, only the feeling of gratitude can make the expression a bit justified.

I express my foremost thanks to the almighty for his grace and choicest blessings. I would like to convey my heartful thanks to my supervisor **Prof. Hiranmaya Mishra**, Theoretical Physics Division, PRL Ahmedabad for the continuous support during my PhD and for his patience, motivation, enthusiasm and immensce knowledge. It was his amicable behaviour and unpriced support due to which I could make my challenging work complete. His guidance helped me in all the time of research and writing this thesis. I could not have imagined having better advisor and mentor for my PhD.

Here with my advisor, I would like to thank the rest of my Doctoral Studies Committee (DSC) members **Prof. Jitesh R Bhatt**, **Prof. R P Singh** and **Prof. Namit Mahajan** for their encouragement, insightful comments and critical questions.

I would also like to thank my collaborators and seniors **Prof. Constança Providência**, **Dr. Arpan Das**, **Dr. Tuhin Malik**, **Dr. Aman Abhishek** and **Dr. Balbeer Singh** for their valuabe discussions and they helped me a lot during my PhD.

My appreciation and thank are also due to all the teaching and non-teaching staff of PRL. Also my sincere appreciation to all research scholars of PRL who had helped me in one way or the other during the course of my work.

Particularly, I would like to thank **Prof. Srubabati Goswami** for teaching me group theory and standard model, **Prof. Subhendra Mohanty** for teaching general theory of relativity, supersymmetry (SUSY) theory etc, **Prof. Partha Konar** for teaching particle physics, **Prof. Namit Mahajan** for teaching renormaluzation groups and path integrals, **Prof. Jitesh R Bhatt** for teaching me quantum field theory, **Prof. Dilip Angom** for teaching physics of complex system and topology, **Prof. Navinder Singh** for teaching superconductivity at low temperature.

I would like to thank every single person with whom I have been in contact. They all have played a crucial role in my career and life. Friends add humour, hascaination and beauty to life, my special thanks to *friend forever* for all the fun we have had in the last five years, the innumerable ways they have been there for me.

I would like to thank my brothers and sisters, who are miles away but have always had words of encouragement, advices and taken interests in my welfare.

Most of all, I would like to thank my father and my mother, who laid the foundation of the academic pursuit right from my childhood and for their sacrifice.

They have been a pillar of emotional support, encouraging me to no end.

**I would like to dedicate this thesis to my parents.**

**Deepak KUMAR**
(IITGn Roll No. 17330011)

# List of Publications

1. **Publications/Submitted**

   (a) **Chiral susceptibility in the Nambu–Jona-Lasinio model: A Wigner function approach**
   Arpan Das, **Deepak Kumar**, Hiranmaya Mishra
   Published PhysRevD.100.094030

   (b) **Thermoelectric transport coefficients of quark matter**
   Aman Abhishek, Arpan Das, **Deepak Kumar**, Hiranmaya Mishra
   Published Eur.Phys.J.C 82 (2022) 1, 71

   (c) **Non-radial oscillation modes in hybrid stars: consequences of a mixed phase**
   **Deepak Kumar**, Tuhin Malik, Hiranmaya Mishra
   Published JCAP 02 (2023) 015

   (d) **Robust universal relations in neutron star asteroseismology**
   **Deepak Kumar**, Tuhin Malik, Hiranmaya Mishra, Constança Providência
   Under Review in PRL

2. **Details of paper presented in conference**

   (a) Chiral Susceptibility in NJL model: A Wigenar Function Approach [PhysRevD.100.094030]

   (b) Non-radial oscillation modes in hybrid stars: consequences of a mixed phase

   (c) Robust universal relations in neutron star asteroseismology

3. **Details of proceeding**

   (a) **Recent progress in the "Dynamics of QCD Matter"**
   Published Int. J. Mod. Phys. E

# Abstract

Normal matter (protons, neutrons, mesons) are expected to undergo a phase transition at extremely high temperature ($\sim 10^{12}$ degree Kelvin) and/or extremely high density ($\sim 10^{14}$ gm/cc) to a state where the relevant degrees of freedom are their constituents described in terms of quarks, antiquarks and gluons called quark gluon plasma. Such kind of matter is believed to be there upto few tens of microseconds after the big bang. The cold quark matter is also expected to be present in the core of ultra compact astrophysical objects for example neutron stars, hybrid stars. In laboratory, quark gluon plasma can be produced at the collision center by colliding heavy ions at relativistic energies and it cools through the QCD phase diagram. In the off-central heavy ions collisions, extremely strong magnetic fields ($\sim 10^{18}$ Gauss) is produced by the current of the relativistically moving ions in opposite directions. It is very interesting to study the properties of matter under such extreme conditions of temperature, density and magnetic field.

We have worked on the two regions of the QCD phase diagram (in $T - \mu$ plane) - (i) zero temperature and non-zero chemical potential, and (ii) non-zero temperature and zero baryon chemical potential regions.-

In the first part, we estimate the chiral susceptibility at finite temperature within the framework of the Nambu–Jona-Lasinio (NJL) model using the Wigner function. We also estimate it in the presence of chiral chemical potential ($\mu_5$) as well as a non-vanishing magnetic field ($B$). We use a medium separation regularization scheme (MSS) in the presence of magnetic field and the chiral chemical potential to regularise the infinities present in the chiral condensate and corresponding susceptibility. It is observed that for a fixed value of chiral chemical potential ($\mu_5$), transition temperature increases with the magnetic field. While for the fixed value of the magnetic field, transition temperature decreases with chiral chemical potential. For a strong magnetic field, we observe non degeneracy in susceptibility for up and down type quarks.

We also estimate some of the transport properties of the strongly interacting medium produced in the heavy ion collisions. A thermal gradient and/or a chemical potential gradient in a conducting medium can lead to an electric field, an effect known as thermoelectric effect or Seebeck effect. In the context of heavy-ion collisions, we estimate the thermoelectric transport coefficients for quark matter within the ambit of the NJL model. We estimate the thermal conductivity, electrical conductivity and the Seebeck coefficient of the same. These coefficients are calculated using the relativistic Boltzmann transport equation within the relaxation time approximation. The relaxation times for the quarks are estimated from the quark-quark and quark-antiquark scattering through meson exchange within the NJL model. As a comparison to the NJL model estimation of the Seebeck coefficient, we also estimate the Seebeck coefficient within a quasi-particle approach.

In the second part, in the context of the cold quark matter, we study the possibility of existence of quark matter in the core of compact stars (hybrid stars) and non-radial oscillation modes in neutron and hybrid stars. The Walecka type relativistic mean field models - (i) NL3 parametrised and (ii) with density dependent coupling parametrised (DDB) are considered to describe the nuclear matter at low densities and zero temperature and the NJL model is considered to describe quark matter at high densities in the zero temperature limit. A Gibbs construct is used to describe the hadron-quark phase transition at large densities. Within the models, as the density increases, a mixed phase appears at density about $2.36\rho_0$ ($3.93\rho_0$) where $\rho_0$ is the nuclear matter saturation density and ends at density about $5.22\rho_0$ ($6.9\rho_0$) for NL3 (DDB) models and beyond which pure quark matter phase appears. It turns out that a stable hybrid star of maximum mass, $M = 2.27\ M_\odot$ with radius $R = 14$ km, can exist with the quark matter in the core in a mixed phase only. The hadron-quark phase transition in the core of maximum mass hybrid star occurs at radial distance, $r_c = 0.27R$ where the equilibrium speed of sound shows a discontinuity. Existence of quark matter in the core enhances the non-radial oscillation frequencies in hybrid stars compared to neutron stars of the same mass. This enhancement is more for the $g$ modes. The non-radial oscillation frequencies depend on the vector coupling in NJL model. The values of $g$ and $f$ mode frequencies decrease with increase the vector coupling in quark matter.

The non-radial oscillations of neutron stars have been suggested as an useful tool to probe the composition of neutron star matter. With this scope in mind, we consider a large number of equation of states (EOS) that are consistent with nuclear matter properties and pure neutron matter EOS based on a chiral effective field theory calculation for the low densities and perturbative QCD (pQCD) EOS at very high densities. This ensemble of EOSs is also consistent with astronomical observations, gravitational waves in GW170817, mass and radius measurements from Neutron star Interior Composition ExploreR (NICER). Apart from verifying the robustness of universal relations (URs) among the quadrupolar $f$ modes frequencies, masses and radii with such a large number of EOSs, we find a strong correlation between the $f$ mode frequencies and the radii of neutron stars. Such a correlation is very useful in accurately determining the radius from a measurement of $f$ mode frequencies in near future. We also show that the quadrupolar $f$ mode frequencies of neutron stars of masses 2.0 $M_\odot$ and above lie in the range 1.68 - 2.16 kHz in this ensemble of physically realistic EOSs. A two solar mass neutron stars with a low $f$ mode frequency may indicate the existence of non-nucleonic degrees of freedom.

# Contents

# Acronyms

**ABJ** Adler-Bell-Jackiw

**BCS** Bardeen-Cooper-Schrieffer

**BNL** Brookheaven National Laboratory

**BNS** binary neutron star

**BPS** Bethe-Pethick-Sutherland

**CEFT** chiral effective field theory

**CEP** critical end point

**CERN** European Council for Nuclear Research

**CFT** chiral effective field theory

**CME** chiral magnetic effect

**CPT** chiral perturbation theory

**CS** compact star

**CSB** chiral symmetry breaking

**CSR** chiral symmetry restored

**CVE** chiral vortical effect

**DCSB** dynamical chiral symmetry breaking

**DDB** a nucleonic $\beta-$ equilibrated EOS based on a relativistic description of hadrons through their density-dependent coupling with mesons constrained by the existing observational, theoretical and experimental data through Bayesian analysis

**DDB-Hyb** a hybrid set of EOSs which consists of the DDB EOS at low density ($\leq 2\rho_0$) and the deconfined quark matter at very high densities ($\geq 40\rho_0$) while the region ($2\rho_0$-$40\rho_0$) is interpolated by piecewise polytropes

**DHW** Dirac-Heisenberg-Wigner

**DIS** deep inelastic scattering

**DSE** Dyson-Schwinger equation

**EOS** equation of state

**FAIR** Facility for Antiproton and Ion Research

**GR** general relativistic

**GTR** general theory of relativity

**GW** gravitational wave

**GWs** gravitational waves

**HP** hadronic phase

**HQPT** hadron-quark phase transition

**HRG** hadron resonance gas

**HS** hybrid star

**HSM** hybrid star matter

**HTL** hard thermal loop

**KSS** Kovtun-Son-Starinet

**LHC** Large Hadron Collider

**LQCD** lattice quantum chromodynamics

**MP** mixed phase

**MSS** medium separation regularization scheme

**NICA** Nuclotron-based Ion Collider Facility

**NICER** Neutron star Interior Composition ExploreR

**NJL** Nambu–Jona-Lasinio

**NS** neutron star

**NSM** neutron star matter

**PNJL** Polyakov loop extended Nambu–Jona-Lasinio

**PNM** pure neutron matter

**PQ** Peccei–Quinn

**pQCD** perturbative quantum chromodynamics

**PVC** polarization vorticity coupling

**QCD** quantum chromodynamics

**QED** quantum electrodynamics

**QGP** quark-gluon plasma

**QHD** quantum hadrodynamics

**QNM** quasi-normal mode

**QP** quark phase

**RHIC** Relativistic Heavy-Ion Collider

**RMF** relativistic mean field

**RTA** relaxation time approximation

**SHE** spin Hall effect

**SNM** symmetric nuclear matter

**SUSY** supersymmetric

**TOV** Tolman-Oppenheimer-Volkoff

**UR** universal relation

# Chapter 1

# Introduction

## 1.1 Introduction

It has been a continuous endeavour over the years of a curious human mind to understand the basic constituents of matter and their interactions. As per our current understanding, all matter that we observe in nature and their interactions can be described by a few elementary particles and four types of fundamental forces or interactions. The four fundamental forces in nature are 1) gravitational force, 2) weak force, 3) electromagnetic force and 4) strong force. Among them two forces, gravitational force and electromagnetic force, are long range forces. We experience them in day to day life. The gravitational force is the first fundamental force that was discovered, it is the one which is least understood at the fundamental level. Such force is responsible for the fall of the fruits from the tree to the motion of planets orbiting the stars and stars orbiting the galaxies etc. The most understood and common force is the electromagnetic force which manifests itself in the macroscopic world and is used in modern technology. On the atomic level, it is the electromagnetic interaction of the electrons in the atoms that eventually gives rise to different chemical properties of elements. On the other hand, the weak and strong forces are the short range forces so they are limited to the field of nuclear and particle physics. An example of the weak force is the $\beta$ radiation of a neutron where a free neutron decays to a proton, an electron and an anti-neutrino. Finally the strong interaction which is the strongest force among all forces binds quarks to form nucleons and eventually nucleons to form nuclei. Apart from the gravitational interaction, the remaining fundamental interactions can be described by gauge theories. The fundamental particles constitute three generations of quarks ($u$, $d$; $c$, $s$ and $t$, $b$) which interact through strong, electromagnetic and weak interactions. The other set of fundamental particles, the three generation of leptons ($e$, $\mu$ and $\tau$) and corresponding neutrinos ($\nu_e$, $\nu_\mu$ and $\nu_\tau$, respectively) which interact through electromagnetic and weak interactions. Apart from this all of these particles interact with the Higgs field. This essentially describes the standard model of particle physics. The fundamental particles and their interactions in the standard model are described in Fig. 1.1.

In the present thesis we will focus on the study of strong interaction which is described at a fundamental level by the theory called quantum chromodynamics

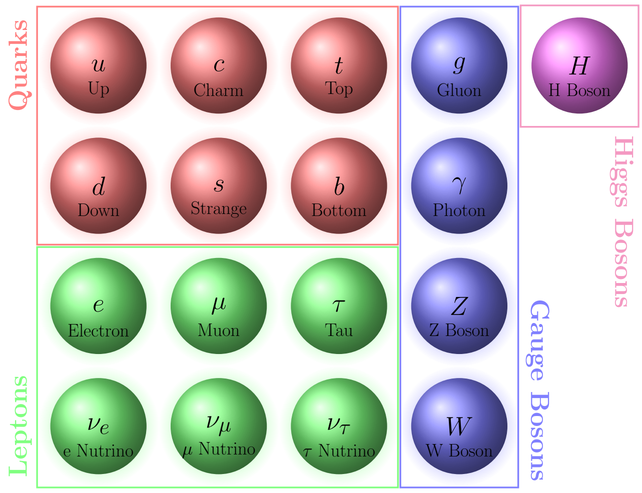


FIGURE 1.1: Elementary particles: the constituents of matter.

(QCD) in terms of quark and gluons as the fundamental fields with their interactions being described by a SU(3) gauge theory. It is similar to the best established theory of electromagnetic interactions, the quantum electrodynamics (QED). The difference is the quanta of the QCD (the gluon) interacts with another gluon but the quanta of QED (the photon) does not interact with other photons. The constituents of the atomic nuclei are the neutrons and protons, collectively nucleons, which are the vacuum states of QCD. Nucleons are the colourless bound states of the elementary particles, quarks, which are found with three colours: **red**, **blue** and **green**, the colour is a quantum number of quarks. For example protons and neutrons are the colour neutral bound states of up, $u$ and down, $d$ quarks, p(uud) and n(udd). An account of all the observed baryons requires six quark species of QCD namely, up ($u$), down ($d$), charm ($c$), strange ($s$), bottom ($b$) and top ($t$). In Fig. 1.1 we collect all the elementary particles and interaction quanta which are the fundamental building blocks of matter. The interactions between these quarks are mediated by the emission and absorption of gluons which are the colour states. In Table 1.1, we collect all the fundamental particles with their quantum numbers.

On the experimental side, the strong interactions at low energy can be understood in two ways. One is related to probing the hadronic structure by shooting a proton target with high energetic electron and muon beams [1–13]. The other approach is to study the QCD phase diagram in extreme conditions through the high energy heavy-ion collisions and inside the cores of compact star (CS)s. We will follow the second approach to study the strong interaction. There are several motivations to study QCD under extreme conditions. As we all believed, the universe passed through a state where the temperature was of the order of QCD scale after a few microseconds of the big bang. Later the matter condensed into stars. Some of the stars after exhausting their fuel collapsed and underwent a supernovae explosion. The remnant can be a neutron star (NS). The density at the center of a NS is not known precisely but it can be a few times the nuclear saturation density,

| Elementary Particles | Electric Charge | Spin | Mass ($\simeq$) | Baryon Number | Lapton Number |
|---|---|---|---|---|---|
| $u$ | 2/3 | 1/2 | 2.2 MeV | 1/3 | 0 |
| $d$ | -1/3 | 1/2 | 4.7 MeV | 1/3 | 0 |
| $s$ | -1/3 | 1/2 | 96.0 MeV | 1/3 | 0 |
| $c$ | 1/3 | 1/2 | 1.3 GeV | 1/3 | 0 |
| $t$ | 2/3 | 1/2 | 173 GeV | 1/3 | 0 |
| $b$ | -1/3 | 1/2 | 4.2 GeV | 1/3 | 0 |
| $e$ | -1 | 1/2 | 0.5 MeV | 0 | 1 |
| $\mu$ | -1 | 1/2 | 106 MeV | 0 | 1 |
| $\tau$ | -1 | 1/2 | 1.8 GeV | 0 | 1 |
| $\nu_e$ | 0 | 1/2 | 1.0 eV | 0 | 1 |
| $\nu_\mu$ | 0 | 1/2 | 0.2 MeV | 0 | 1 |
| $\nu_\tau$ | 0 | 1/2 | 18.0 MeV | 0 | 1 |
| $g$ | 0 | 1 | 0 | 0 | 0 |
| $\gamma$ | 0 | 1 | 0 | 0 | 0 |
| $Z$ | 0 | 1 | 91.2 GeV | 0 | 0 |
| $W$ | $\pm1$ | 1 | 80.4 GeV | 0 | 0 |
| $H$ | 0 | 0 | 125 GeV | 0 | 0 |

TABLE 1.1: Electric charge, spin, mass, baryon number and lepton number of the elementary particles.

($\rho_0 = 0.16$ fm$^{-3}$). At this extreme density, the quarks can be treated as a relevant degree of freedom. The NSs provide an opportunity to study the matter at ultra high density.

In this chapter, we will discuss the QCD theory in Sec. 1.2 and QCD phase diagram in Subsec. 1.2.1. In Sec. 1.4 we shall discuss heavy-ion collisions and in Sec. 1.6 we shall discuss the NS structure.

## 1.2 Strong interaction physics and QCD

In the present thesis, we will focus on the strong interaction under extreme conditions. At a fundamental level the strong interaction is described by the interaction of quarks and gluons with the interactions being dictated by a SU(3) gauge theory. This means the underlying QCD Lagrangian is invariant under local SU(3) gauge transformations with the quarks being in the fundamental and gluons being in the adjoint representation of the color SU(3) gauge group. Thus the Lagrangian is given by

$$\mathcal{L}_{\text{QCD}} = \sum_q \left(\bar{\psi}_q i\gamma^\mu \left[\partial_\mu + igA^a_\mu T_a\right] \psi_q - m_q \bar{\psi}_q \psi_q\right) - \frac{1}{4} G^a_{\mu\nu} G^{\mu\nu}_a, \tag{1.1}$$

where $G_a^{\mu\nu} = \partial^\mu A_a^\nu - \partial^\nu A_a^\mu - g f^{abc} A_b^\mu A_c^\nu$ is the colour field tensor and $A_a^\mu$ is the four-potential of the gluon field, $a = 1, \ldots, 8$, $T_a$ are the $3 \times 3$ Gell-Mann matrices. The Gell-Mann matrices $T_a$ (SU(3) generators) follow the Lie algebra $\left[T^a, T^b\right] = i f^{abc} T^c$ where $f^{abc}$ is the structure constant of the SU(3) gauge group, $\psi_q$ is the quark field and $g$ is the strong coupling constant. The Lagrangian, given in Eq. (1.1), is invariant under local gauge transformation $\psi_q(x) \rightarrow U(x)\psi_a(x)$ and $D_\mu \rightarrow U(x) D_\mu U^\dagger(x)$. The term $g f^{abc} A_b^\mu A_c^\nu$ in the field strength tensor distinguishes QCD from QED which gives the self interacting gauge bosons in this non-abelian gauge theory.

The non-abelian gauge group structure of QCD gives rise to a running coupling constant which is small at large momentum transfer processes. Fig. 1.2 shows the scale dependent QCD coupling $\alpha_s(Q) = g^2/4\pi$ as a function of momentum transfer inferred from various experiments. The smallness of QCD coupling at large momentum transfer processes is known as *asymptotic freedom*. Thus, the hard processes with large momentum transfer can be described using familiar perturbative methods as in deep inelastic scattering processes. Scaling behaviour as seen here arises naturally within a perturbative treatment of QCD. However, for the low energy sector, the QCD coupling becomes stronger leading to breakdown of the perturbative methods. This is indicative of the increased importance of the nonperturbative dynamics which binds the quarks to form hadrons and it requires infinite energy to have isolated quark or gluon. This phenomenon of not having colour charged objects in isolation is called *confinement*. The other manifestation of the non-perturbative feature of QCD is the *chiral symmetry breaking* through which quarks generate their constituent mass and is related to non-trivial structure of QCD vacuum with quark-antiquark condensates.

The Lagrangian Eq. (1.1) has space-time reflection symmetry. However, consistent with gauge and Lorentz symmetry one can also have $\mathcal{CP}$-violating terms, the so called $\theta$-term given as [14]

$$\mathcal{L}_\theta = \frac{\theta}{64\pi^2} g^2 G_{\mu\nu}^a \tilde{G}^{a\mu\nu} \tag{1.2}$$

where $\tilde{G}^{a\mu\nu} = \epsilon_{\mu\nu\alpha\beta} G^{a\alpha\beta}$ is the dual field strength tensor. Such a term violates charge conjugation and parity unless $\theta$ is 0 or mod $\pi$. However $\mathcal{CP}$ is almost conserved in vacuum. The current experimental limit on $\theta$ is $\theta < 0.7 \times 10^{-11}$ [15] from the neutron dipole moment measurement. The smallness of $\theta$ or its complete absence is not understood completely although a possible explanation is given in the spontaneous breaking of a new symmetry called Peccei–Quinn (PQ) symmetry [16] giving rise to axions. However, while $\theta$ is small for vacuum, it can be large in an out of equilibrium system leading to a non-zero value of the chiral chemical potential ($\mu_5$). We shall explore later the consequence of finite $\mu_5$ on the chiral transition in QCD.

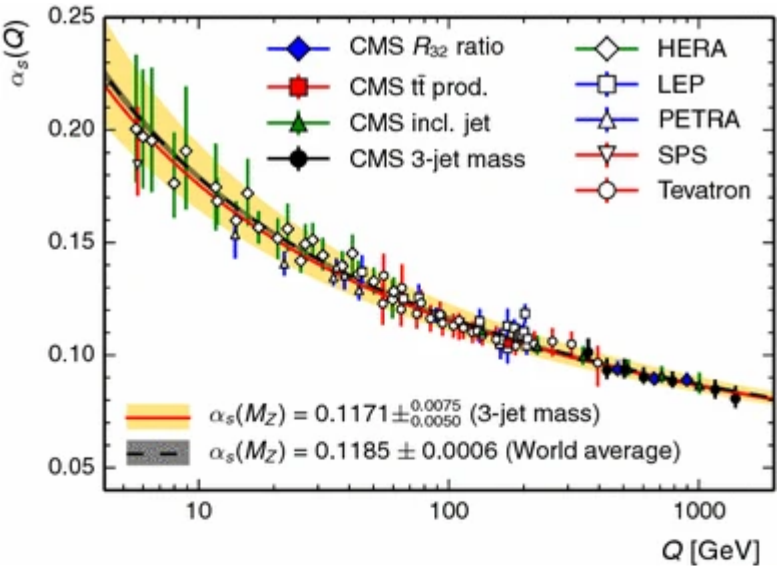


FIGURE 1.2: The strong running coupling constant, $\alpha_s(Q)$ (solid line) and its uncertainty (yellow band) as a function of the scale $Q$. This figure is taken from the Ref. [17]. All the credit of this figure goes to the Author(s) and publishing agency.

### 1.2.1 QCD phase diagram

As we discussed earlier, the strong interaction binds the atomic nuclei. Although the density in the center of heavy nuclei is extremely high ($\sim \rho_0$), the mean free path exceeds their diameter. Thus normal nuclear matter is the diluted many body system. If such system is compressed or heated in high-energy nuclear collisions to even higher densities or temperatures then one could expect quarks (the building blocks of nucleons) to be no longer confined in the nucleon rather they are able to move over the distances much larger than the size of the nucleon. Such deconfined state of matter is knowns as quark-gluon plasma (QGP). This state of matter is likely to have existed in the early universe within a few microseconds after the big bang. One of the challenging questions in nuclear physics is to identify the structure and the phases of such strongly interacting matter. In recent years extensive effort has been made to create and understand the strongly interacting matter in relativistic heavy-ion collision experiments e.g. at Relativistic Heavy-Ion Collider (RHIC) and at Large Hadron Collider (LHC). There are many evidences indicating the formation of a deconfined QGP phase of QCD in the initial stages and the formation of a confined hadronic phase (HP) in the subsequent evolution of QGP. The ground state of QCD exhibits two main non-perturbative features, (i) *color confinement* and (ii) *spontaneous breaking of chiral symmetry*. The deconfined phase and the chiral symmetric restoration phase both are defined as: in chiral symmetric restored phase, the effective mass of the quark becomes approximately zero or equal to bare quark mass due to the quark-antiquark condensate vanishes while vanishing of quark-antiquark condensate is not necessary in deconfined phase. The dynamical chiral symmetry breaking (DCSB) characterizes the non-perturbative nature of QCD vacuum at vanishing temperature and/or density. As we increase temperature and/or baryon density, the QCD vacuum undergoes a transition from a chiral symmetry breaking (CSB) phase to a chiral symmetry restored (CSR) phase. This transition is characterized by the quark-antiquark scalar condensate, the order parameter of chiral phase transition. Although in first order phase transition the order parameter varies discontinuously across the transition point, in second order phase transition or in a cross-over the order parameter across the transition point is rather smooth.

Keeping all of that in mind we can construct the phase diagram (Fig. 1.3) of QCD in terms of the net baryon number density (or chemical potential, $\mu_B$) and temperature ($T$). Following is the schematic phase diagram of QCD.

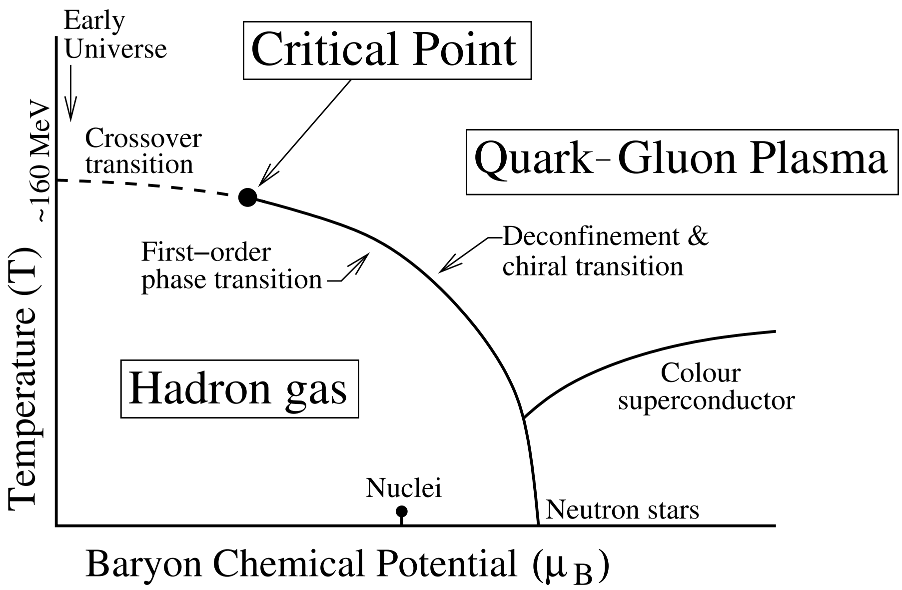


FIGURE 1.3: Schematice phase diagram of QCD. This figure is taken from the Ref. [18].

The horizontal axis defines net chemical potential ($\mu_B$) and the vertical axis defines temperature ($T$). The origin of the phase diagram i.e. $T = 0$ and $\mu_B = 0$ corresponds to the QCD vacuum. As temperature increases we find a cross-over nearly $T \sim (150 - 170)$ MeV ($\hbar = 1 = c = k_B$) from HP to QGP phase where the symmetries of the system become the symmetries of the Lagrangian, which is called the restoration of dynamical chiral symmetry. On the other hand as net chemical potential increases (net baryon density) we encounter the densities found in the core of NSs and even higher we find the colour superconducting phase of QCD. The black close circle in Fig. 1.3 is the critical end point (CEP). One can perform lattice simulations, where QCD equations are solved numerically by discretising QCD Lagrangian on the four-dimensional space-time lattice and evaluating them statistically via Monte-Carlo methods, at high temperature and zero chemical potential limits. The lattice simulations indicate that there is a cross-over at high temperature $T_c = 154 \pm 9$ MeV [19] and $T_c = 156 \pm 9$ MeV [20, 21] with different fermion actions. Recent lattice quantum chromodynamics (LQCD) calculations also quantify the small decrease of $T_c$ with increasing $\mu_B$ as long as $\mu_B < 3T_c$. Within this parameter range the transition is of cross-over type. The fundamental question is the possible existence of the CEP where a second order chiral phase transition is expected. This has been pointed out by both experiments and theory but remains one of the outstanding questions related to our understanding of the phase structure of hot and dense QCD matter.

On the other hand, at the low temperature and high density, many effective models predict the possibilities of various exotic phases of quark matter. These include pion superfluidity [22–24], various color superconducting phases like 2 flavor color superconductivity (2SC) [25–27], color flavor locked (CFL) phase [28], Larkin-Ovchinkov-Fulde-Ferrel (LOFF) [29, 30] phase, crystalline superconductivity (CSC) phase etc. However, the signature of such phases in quark matter from the study of NS have been rather challenging. We shall discuss hadron-quark phase transition (HQPT) at extremely high density in the context of NS in Chapter 4.

It is very difficult to study the strong interactions from QCD equations found from QCD Lagrangian Eq. (1.1). There are effective models which contain some features of QCD and are easy to handle. In the following sections we discuss some effective models relevant for the thesis.

## 1.3 Effective models

In this section we briefly summarize the relativistic mean field (RMF) model which is also known as quantum hadrodynamics (QHD) to describe the nuclear matter and the Nambu–Jona-Lasinio (NJL) model to analyze quark matter. Here the idea is to give a brief recapitulation of models that we shall be using in later chapters.

### 1.3.1 Mean field model for nuclear matter

In this model the nucleons are the quasi-particles with an effective medium dependent mass and chemical potential. They move in the background of the meson fields. The interactions between the nucleons are governed by the exchange of different mesons. The scalar meson exchange gives an attraction force while the vector meson exchange exerts repulsion. The isovector meson establishes the asymmetry in the nuclear matter. The scalar mesons couple to the baryon scalar density while vector mesons couple to the baryon vector four-current by contraction. The Lagrangian of the model is [31–33]

$$\mathcal{L} = \sum_b \mathcal{L}_b + \mathcal{L}_{\text{int}} \tag{1.3}$$

where

$$\mathcal{L}_b = \sum_b \bar{\Psi}_b (i\gamma_\mu \partial^\mu - m_b + g_\sigma \sigma - g_\omega \gamma_\mu \omega^\mu - g_\rho \gamma_\mu \vec{I}_b \vec{\rho}^\mu) \Psi_b \tag{1.4}$$

$$\begin{aligned}
\mathcal{L}_{\text{int}} = & \frac{1}{2}\partial_\mu \sigma \partial^\mu \sigma - \frac{1}{2} m_\sigma^2 \sigma^2 - \frac{\kappa}{3!}(g_{\sigma N}\sigma)^3 - \frac{\lambda}{4!}(g_{\sigma N}\sigma)^4 \\
& -\frac{1}{4}\Omega^{\mu\nu}\Omega_{\mu\nu} + \frac{1}{2} m_\omega^2 \omega_\mu \omega^\mu \\
& -\frac{1}{4}\vec{R}^{\mu\nu}\vec{R}_{\mu\nu} + \frac{1}{2} m_\rho^2 \vec{\rho}_\mu \vec{\rho}^\mu
\end{aligned} \tag{1.5}$$

where $\Omega_{\mu\nu} = \partial_\mu \omega_\nu - \partial_\nu \omega_\mu$ and $\vec{R}_{\mu\nu} = \partial_\mu \vec{\rho}_\nu - \partial_\nu \vec{\rho}_\mu$ are the mesonic field strength tensors. $\vec{I}_b$ denotes the isospin operator. The $\Psi_b$ is baryon field. The $\sigma$, $\omega$, $\rho$ meson fields are denoted by $\sigma$, $\omega$ and $\rho$, respectively. The $m_\sigma$, $m_\omega$ and $m_\rho$ denote the masses of mesons. The parameters $m_b$ denote the vacuum masses for baryons. The meson-baryon couplings $g_\sigma$, $g_\omega$ and $g_\rho$ are the scalar, vector and isovector coupling constants, respectively. In RMF approximation, one replaces the meson fields by their expectation values which then act as classical fields in which baryons move *i.e.* $\langle\sigma\rangle = \sigma_0$, $\langle\omega_\mu\rangle = \omega_0 \delta_{\mu 0}$, $\langle\rho_\mu^a\rangle = \delta_{\mu 0}\delta_3^a \rho_3^0$. Hence the effective mass of baryons get redefined as $m_b^* = m_b - g_\sigma \sigma_0$ and the effective chemical potential as $\mu_b^* = \mu_b - g_\omega \omega_0 - g_\rho I_{3b} \rho_3^0$. The mesonic equations of motion can be found by the Euler-Lagrange equations for the meson fields using the Lagrangian Eq. (4.1). We discuss more in the following chapters, Chapters 2, 3, 4 and 5.

### 1.3.2 Nambu–Jona-Lasinio model for quark matter

Historically it was inspired by the Bardeen-Cooper-Schrieffer (BCS) theory of electrical superconductivity when QCD and even quarks were unknown. In the original version, the NJL model was a model of interacting nucleons and confinement. In pre-QCD era, there were some indications of the existence of chiral symmetry. So the problem was to find the mechanism to define the large nucleon mass without disturbing the symmetry at the Lagerangian level. It was the poineer idea of Nambu and Jona-Lasinio that the mass gap in the Dirac spectrum can be generated as the energy gap in the BCS theory of superconductors. To that end they introduced a Lagrangian for the nucleon field $\psi$ with point like, chirally symmetric four-fermion interaction [34]

$$\mathcal{L}_{\text{NJL}} = \bar{\psi}\left(i\gamma_\mu \partial^\mu - m\right)\psi + G\left[(\bar{\psi}\psi)^2 + (\bar{\psi} i\gamma_5 \boldsymbol{\tau} \psi)^2\right] \tag{1.6}$$

where $m$ is the nucleon bare mass, $\boldsymbol{\tau}$ is the Pauli matrix and $G$ is a dimensionless coupling constant. After development of QCD, the NJL model was reinterpreted as a schematic quark model. Besides the lack of confinement, it explains the DCSB and the Goldstone nature of the pion which makes the NJL model superior over the MIT bag model of quarks. If we replace the nucleon field $\psi$ by the quark field $\psi_q$ then the Lagrangian for quarks becomes

$$\mathcal{L}_{\mathrm{NJL}} = \bar{\psi}_q \left(i\gamma_\mu \partial^\mu - m_q\right) \psi_q + G\left[(\bar{\psi}_q \psi_q)^2 + (\bar{\psi}_q i\gamma_5 \boldsymbol{\tau} \psi_q)^2\right] \tag{1.7}$$

where $m_q$ is the bare quark mass and $G$ becomes the quark coupling constant. The NJL model is a QCD inspired effective model which incorporates various aspects of the chiral symmetry of QCD. The NJL model Lagrangian as given in Eq. (1.7) is symmetric under the chiral symmetry group $SU(2)_V \times SU(2)_A \times U(1)_V$. In the mean field approximation Eq.(1.7) reduced to

$$\mathcal{L}_{\mathrm{NJL}} = \bar{\psi}_q \left(i\gamma_\mu \partial^\mu - M_q\right) \psi_q - \frac{\sigma^2}{G} \tag{1.8}$$

where the dynamic mass $M_q = m_q - 2\sigma$ and $\sigma = G\langle\bar{\psi}_q \psi_q\rangle$ is the chiral condensate.

The NJL model is non-renormalisable. It contains three parameters like $m_q$, $G$ and the three momentum cut-off $\Lambda$. These parameters are fitted from the QCD vacuum structure, pion mass, pion decay constant and the chiral condensate. We discuss it in more detail in Chapters 2, 3 and 4.

## 1.4 Heavy ion collisions

The nonperturbative scale of QCD, $\Lambda_{\mathrm{qcd}} \sim 200$ MeV emerges as a scale anomaly of QCD. Near this scale, QCD interactions become very strong and as a result quarks and gluons start confining inside the baryons or mesons. To probe this there are two ways as we discussed earlier. One way is to shoot the target with a high energy relativistic beam of electrons and see the structure of the target, (deep inelastic scattering (DIS)). Another way is to heat the chunk of QCD matter in heavy-ion collisions to a temperature of the order of QCD scale ($T \sim \Lambda_{\mathrm{QCD}}$). It was envisioned in the late 1970s that a new phase of matter could be possible, 'QGP' at these extreme temperatures. The first principle calculations confirm the idea and provide the full quantitative understanding of QCD thermodynamics. Heavy-ion collisions at RHIC in Brookheaven National Laboratory (BNL) and at LHC in European Council for Nuclear Research (CERN) offer an excellent opportunity to explore the properties of the strongly interacting medium at extreme conditions. In heavy-ion collision experiments one can reproduce the thermodynamic conditions of the early universe. Thus heavy-ion collisions are known to little bangs or mini universes. As two relativistically heavy ions (Au or Pb) in opposite directions collide with each other in off-centre position they deposit their kinetic energy at the center of the collision as a form of thermal energy, a fireball (mini universe) is created. The expansion of this fireball shows the possible stages of the collision starting from the energy deposition by the colliding ions followed by the QGP expansion, a hadronization phase, a kinetic freeze-out boundary and finally the particles landing on the detectors and observations being done.

The high temperature in the collisions liberates not only quarks and gluons but also restores the chiral symmetry. This implies that the quarks become very light in the QGP phase. To understand the medium produced in relativistic heavy-ion collision, generally thermodynamic and/or hydrodynamic models have been used, which assume local thermal equilibrium. However, the medium produced in the heavy-ion collision is rather dynamical in nature and lives for a very short time and non-equilibrium as well as quantum effects can affect the evolution of the medium significantly. These effects can be considered within the framework of non-equilibrium quantum transport theory. It is important to point out that in the case of interacting field theory of fermions and gauge bosons, transport theory should be invariant under local gauge transformation. Such a gauge covariant quantum transport theory for QCD has been developed in [35–37]. Classical kinetic theory is characterized by an ensemble of point-like particles with their single particle phase-space distribution function. The time evolution of the single particle phase-space distribution function governed by the transport equation encodes the evolution of the system. Similar to the single particle distribution in classical kinetic theory, the Wigner function, which is the quantum mechanical analogue of classical distribution function, encodes quantum corrections in the transport equation [38].

## 1.5 Chiral transition and chiral chemical potential

The compactness of the underlying non-abelian gauge group of strong interaction allows for non-trivial maps from gauge space to the euclidean space-time. This in Minkowski space describes tunnelling transitions between different topological sectors of vacuum characterized by different Chern-Simon numbers. These quantum transitions between different topological vacuum sectors of QCD lead to chirality violation. In non equilibrium condition this can lead to generation of chiral asymmetry i.e. the difference between the number of left and right handed quarks can be different. This is physically similar to baryogenesis in the electroweak theory. While such transitions are small in vacuum, at finite temperature one can have thermally assisted transitions through sphaleron configurations which, unlike instanton induced transitions, are not suppressed.

In the context of heavy ion collisions, in addition to temperature and baryon chemical potential, the effect of a strong magnetic field is also important. Indeed, in non-central collisions of relativistic heavy ions a strong transient magnetic field is produced whose strength could be a few times square of the pion mass ($\mathbf{B} \sim m_\pi^2$). How long this strong magnetic field stays is not clear at present as it depends upon the electrical conductivity of the medium which is poorly known. In the presence of strong magnetic field and with an asymmetry of the number densities of left and right handed quarks, this results in an electric current directed along or opposite to the direction of the magnetic field depending upon the sign of such an asymmetry and is given by

$$\mathbf{j} = \frac{e^2}{2\pi^2}\mu_5\mathbf{B} \tag{1.9}$$

In the above $\mathbf{j}, \mathbf{B}$ are the electric current and magnetic field respectively. The chiral chemical potential $\mu_5 = \mu_L - \mu_R$ characterizes the density difference between the left handed and right handed quarks. At a fundamental level $\mu_5$ is related to the time derivative of the $\theta$ parameter introduced in Eq. (1.2). Such a current induced by a chirality difference in/opposite to the direction of magnetic field is called the chiral magnetic effect.

In the presence of chiral chemical potential and magnetic field, it is interesting to look into the phase structure of quark matter. To get an insight one can use the NJL model for quark matter introduced earlier in Sec. 1.3.2. In the presence of magnetic field and $\mu_5$, the NJL Lagrangian is given as

$$\mathcal{L}_{NJL} = \bar{\psi}(i\gamma_\mu D^\mu + \mu_5\gamma_0\gamma^5)\psi + G\left[(\bar{\psi}\psi)^2 + (\bar{\psi}i\gamma^5\vec{\tau}\psi)^2\right] \tag{1.10}$$

where, $\psi$ is a quark doublet, the covariant derivative takes care of interaction with the external magnetic field and $\mu_5$ couples to the chiral density operator $N_5 = \psi^\dagger\gamma^5\psi = \psi_R^\dagger\psi_R - \psi_L^\dagger\psi_L$. One can calculate the thermodynamic potential in the standard way at the mean field level. The crucial ingredient is the single particle dispersion relation for the quarks in the presence of $\mathbf{B}$ and $\mu_5$. For constant magnetic field in the $z$ direction one can solve the Dirac equation to obtain the dispersion relation

$$\omega_k^2 = \left[|\mathbf{k}|^2 + s\mu_5 Sgn(k_z)\right] + M_f^2 \tag{1.11}$$

with $|\mathbf{k}|^2 = k_z^2 + 2nq_f B$ with Landau quantization and $q_f$ and $M_f$ are the flavor dependent mass of the quarks. Once the single particle energy is known, one can write down the thermodynamic potential $\Omega$ as,

$$\begin{aligned}\Omega = &-N_c\sum_f \frac{|q_f\mathbf{B}|}{(2\pi)}\sum_{s=\pm}\sum_n \alpha_{n,s}\int dp_z\omega_{p,s} + \frac{\sigma^2}{G}\\ &-TN_c\sum_f \frac{|q_f\mathbf{B}|}{(2\pi)}\sum_{s=\pm}\sum_n \alpha_{n,s}\int dp_z\log(1+e^{-\beta\omega_{p,s}}).\end{aligned} \tag{1.12}$$

In the above $\alpha_{n,s}$ is a spin degeneracy factor which is unity for nonzero values of landau level while it is $\delta_s, 1$ for $qB > 0$ and is $\delta_s, -1$ for $qB < 0$.

Once the thermodynamic potential is known, various thermodynamic quantities can be calculated. Indeed, the condensate behaviour in the presence of a nonvanishing chemical potential was considered in Ref. [39] in the Polyakov loop extended Nambu–Jona-Lasinio (PNJL) model. We shall use a different approach using Wigner function formalism to study the effect of nonvanishing chiral chemical potential on the chiral transition. We shall also use a different regularisation scheme to deal with divergences in the presence of magnetic fields in some detail.

### 1.5.1 Thermoelectric transport coefficient

We focus on the thermoelectric response of the strongly interacting system produced in a heavy-ion collision. It is well known from a condensed matter system that a temperature gradient can result in the generation of an electric current. This is known as the Seebeck effect. Due to temperature gradient, there is a non zero gradient of charge density leading to the generation of an electric field. A measure of the electric field produced in a conducting medium due to a temperature gradient is the Seebeck coefficient which is defined as the ratio of an electric field to the temperature gradient in the limit of vanishing electric current. Seebeck effect has been extensively studied in condensed matter systems such as superconductors, quantum dots, high-temperature cuprates, superconductor-ferromagnetic tunnel junctions, low dimensional organic metals, etc [40–48]. Such a phenomenon could also be present in the thermal medium created in heavy-ion collisions. In condensed matter systems only a temperature gradient is required for thermoelectric effect as there is only one type of dominant charge carriers in these systems. In the strongly interacting medium produced in heavy-ion collision both positive and negative charges contribute to transport phenomena. For vanishing baryon chemical potential (quark chemical potential) with equal numbers of particles and antiparticles there is no net thermoelectric effect. Thus a finite baryon chemical potential (quark chemical potential) is required for the thermoelectric effect to be observed. The strongly interacting matter at finite baryon density can be produced in low energy heavy-ion collisions at finite, e.g. at Facility for Antiproton and Ion Research (FAIR) and Nuclotron-based Ion Collider Facility (NICA). Along with the temperature gradient, we also consider a gradient in the baryon (quark) chemical potential to estimate the Seebeck coefficient of the partonic medium. The gradient in the chemical potential has effects similar to the temperature gradient. Using Gibbs Duhem relation for a static medium one can express gradient in the baryon (quark) chemical potential to a gradient in temperature. Effect of the chemical potential gradient significantly affects the thermoelectric coefficients as has been demonstrated in Ref.[49].

The Seebeck effect in the hadronic matter has been investigated previously by some of us within the framework of the Hadron resonance gas model [49, 50]. However, the Hadron resonance gas model can only describe the hadronic medium at chemical freezeout whereas one expects deconfined partonic medium at the early stages of the heavy-ion collisions. In this investigation, we estimate the thermoelectric behavior of the partonic medium within the framework of the NJL model. Seebeck coefficient has also been estimated for the partonic matter within relaxation time approximation in Ref.[51, 52]. However, this has been attempted with the relaxation time estimated within perturbative QCD which may be valid for asymptotically high temperatures. Further, it ought to be mentioned that, the vacuum structure of QCD remain nontrivial near the critical temperature region with nonvanishing values for the quark-antiquark condensates associated with chiral symmetry breaking as well as Polyakov loop condensates associated with the physics of statistical confinement [53–56]. Indeed, within the ambit of the NJL model, it was shown that the temperature dependence of viscosity coefficients exhibits interesting behavior of phase transition with the shear viscosity to entropy ratio showing a minimum while the coefficient of bulk viscosity showing a maximum at the phase transition [53, 54, 57]. The crucial reason for this behaviour was the estimation of relaxation time using medium dependent masses for the quarks as well as the exchanged mesons which reveal nontrivial dependence before and after the transition temperature. This motivates us to investigate the behavior of thermoelectric transport coefficients within the NJL model which takes into account the medium dependence of quark and meson masses. This model has been used to study different transport properties of quark matter at high temperatures [57–60] and high densities [61–68].

## 1.6 Neutron stars

NSs are the natural astrophysical laboratories emerge as the remnant of supernovae explosions that can be used to study the low temperature and high density (large chemical potential) region of QCD phase diagram, Fig. 1.3. They are the second densest kind of objects in the universe after the black holes. The density of matter in the core of a NS is a few times nuclear saturation density ($\rho_0 \sim 10^{14}$ gm cm$^3$). At this ultra-high density one could expect matter with rich phases in the core. The phase of matter in the core is still unknown. The core, in principle, can support various possible exotic phases of QCD. While perturbative quantum chromodynamics (pQCD) predicts deconfined quark matter at large densities, their applicability is rather limited in the sense that these conclusions are applicable only to very large baryon densities *i.e.* $\rho_B \geq 40\rho_0$ [69]. The most challenging region to study theoretically is, however, at intermediate densities *i.e.* a few times nuclear matter saturation density which is actually relevant for the matter in the core of NSs. First principle LQCD calculations under these conditions are also difficult due to sign problem that arises at finite densities. At present such calculations are limited to low baryon densities only i.e. $\mu_B/T \leq 3.5$ [70].

From an astrophysicist point of view, we observe the macroscopic properties of CSs like mass, radius, tidal deformability, rotating frequency, moment of inertia, temperature etc. These macroscopic properties can be described from the microscopic nature of matter inside the core of stars. It's a big question whether matter inside NSs is nuclear matter, or quark matter, or a mixture of nuclear and quark matter. Let's come to the fundamental questions about the phases of matter at high densities coined in the previous paragraph. If we increase the baryon number density by squeezing matter then after a level of squeezing the atoms or molecules into

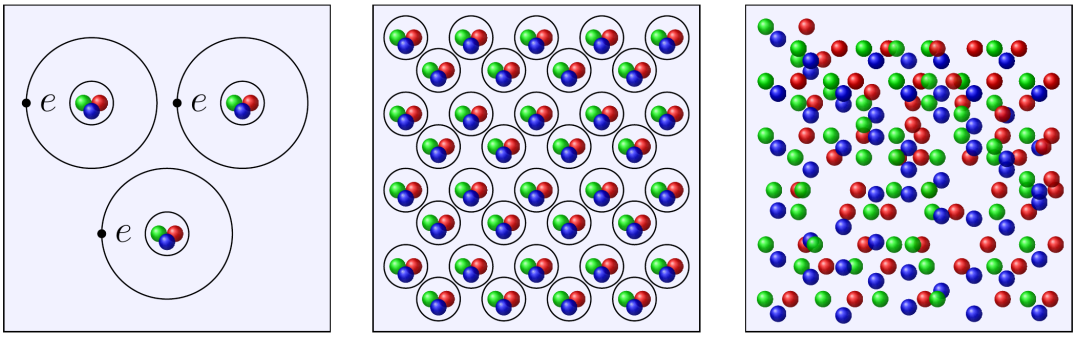


FIGURE 1.4: Schematic view of matter as increasing density from left to right (normal matter → nuclear matter → quark matter).

neutrons and protons where neutrons and protons emerge as the degrees of freedom of matter, we call it nuclear matter (see Fig. 1.4). If we continue the squeezing of matter further then we might reach another level where neutrons and protons lose their identity, matter becomes a soup of quarks, another degree of freedom of matter at this stage, we call it quark matter. As we introduce the many various exotic phases of quark matter at such high densities. However, the signature of such phases in quark matter from the study of NSs has been rather challenging. The GW170817 [71] event explored the constraints on the equation of state (EOS) using tidal deformability extracted from the phase of the gravitational waveforms during the late stage of inspiral merger [72–77]. Though not conclusive, it is quite possible that one or both the merging NSs could be hybrid star (HS)s *i.e.* with a core of quark matter or a mixed phase core of quark and hadronic matter [78, 79].

The typical mass of a canonical NS is about $1.3M_\odot$ ($M_\odot$ denotes the mass of the sun) and radius is about 10 km. The pressure, to support the high mass star with a small radius, should be large enough against gravitational collapse. The pressure increases as we go from the surface to the center of CSs. We may expect different phases of matter at different radial distances. In Fig. 1.5 we display the cross-section view of NS. The inner core of NS is still unknown. We discuss the possible hadron-quark phase transition at ultra-high density in chapter Chapter 4. We consider nuclear matter described by the Walecka type RMF model and quark matter described by the NJL model. We establish a HQPT using a Gibbs construction mechanism.

Before going to discuss the neutron star matter (NSM) in detail, let's discuss the structure of CSs. The structure of CSs can be found using EOS by solving the Tolman-Oppenheimer-Volkoff (TOV) equations,

$$p' = -(p+\epsilon)\left[\frac{m+4\pi r^3 p}{r(r-2m)}\right] \tag{1.13}$$

$$m' = 4\pi r^2 \epsilon \tag{1.14}$$

where 'prime' denotes the derivative with respect to $r$. Eq.(1.13) is the hydrostatic

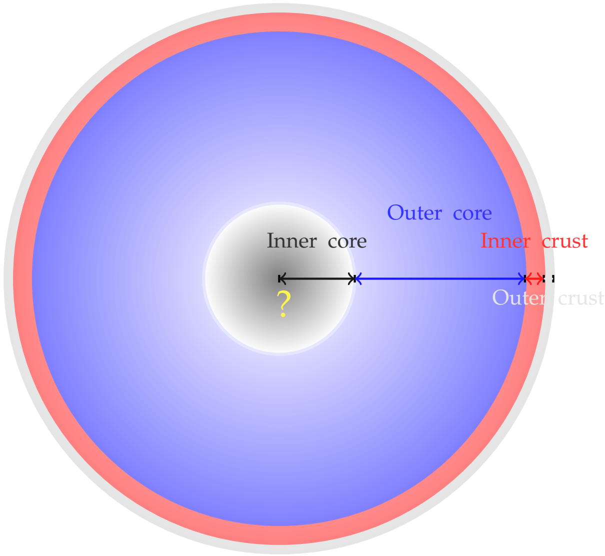


FIGURE 1.5: Schematic view of different layers in neutron stars.

equilibrium equation, where $\epsilon$ and $p$ are the energy density and pressure function of radial distance $r$ from the center of the star. Eq.(1.14) is the mass balance equation. $m$ is the total mass of the matter enclosed within the radius $r$. These equations are the coupled equations. These equations should be supplemented by EOS $p = p(\epsilon)$. These equations constitute a close system to be solved for a given EOS to obtain a mass-radius curve of CSs. To solve these equations we have taken the following initial conditions.

$$m(r = 0) = 0 \quad \text{and} \quad p(r = 0) = p_0$$

where $p_0$ is the central pressure inside CS.

Within the current observational status, it is difficult to distinguish between a canonical NS without a quark matter core from a HS with a core of pure quark matter or a core of quark matter in a mixed phase (MP) with hadronic matter. This calls for exploring other observational signatures to solve this “MASQUERADE" problem [80, 81]. In this context, it has been suggested that the study of the non-radial oscillation modes of NS can have the possibility of providing the compositional information regarding the matter in the interior of NS. This includes NS with a hyperon core [82–84], a quark core or a MP core with quark and hadronic matter components [81, 85–90]. The pulsating equations that describe oscillations can be obtained by the perturbed Einstein field equations $\delta G_{\alpha\beta} = 8\pi\delta T_{\alpha\beta}$ with $G_{\alpha\beta} = R_{\alpha\beta} - \frac{1}{2}g_{\alpha\beta}R$

being the Einstein tensor. Linearising these equations in the perturbation, the differential equations can be obtained as [91]

$$Q' - \frac{1}{c_s^2}\left[\omega^2 r^2 e^{\lambda-2\nu} Z + \nu' Q\right] + l(l+1)e^{\lambda} Z = 0 \tag{1.15}$$

$$Z' - 2\nu' Z + e^{\lambda}\frac{Q}{r^2} - \nu'\left(\frac{1}{c_e^2} - \frac{1}{c_s^2}\right)\left(Z + \nu' e^{-\lambda+2\nu}\frac{Q}{\omega^2 r^2}\right) = 0 \tag{1.16}$$

The two coupled first order differential equations for the perturbing functions $Q(r,t)$ and $Z(r,t)$, Eqs.(1.15) and (1.16), are to be solved with appropriate boundary conditions at the center and the surface. Near the center of CSs the behavior of the functions $Q(r)$ and $Z(r)$ are given by [85]

$$Q(r) = Cr^{l+1} \quad \text{and} \quad Z(r) = -Cr^{l}/l \tag{1.17}$$

where $C$ is an arbitrary constant and $l$ is the order of the oscillation. The other boundary condition is the vanishing of the Lagrangian perturbation pressure, *i.e.* $\Delta p = 0$ at the stellar surface, which gives

$$\left[\omega^2 r^2 e^{\lambda-2\nu} Z + \nu' Q\right]_{r=R} = 0. \tag{1.18}$$

where the field functions $\nu$ and $\lambda$ are defined as

$$e^{-2\lambda} = 1 - \frac{2m}{r} \tag{1.19}$$

$$\nu' = \frac{m + 4\pi r^3 p}{r(r-2m)} \tag{1.20}$$

The field function $\nu$ can be found by integrating Eq.(1.20) from the center of the star to radial distance $r$. The integration constant is determined by satisfying the following

$$e^{2\nu(R)} = 1 - \frac{2M}{R}. \tag{1.21}$$

We shall discuss these pulsating equations in more detail in chapters Chapter 4 and Chapter 5 and find the non-radial oscillations.

## 1.7 Thesis organization

This thesis is organized as follows-

- **Chapter 2:** In this chapter we shall discuss the chiral phase transition and chiral susceptibility of the strongly interacting matter produced in relativistic heavy-ion collision in the presence of strong external magnetic field using the Wigner function approach.

- **Chapter 3:** In this chapter we shall focus our attention to the thermoelectric transport coefficients of the strongly interacting matter in the context of electrical conductivity, thermal conductivity, Seebeck coefficient and the Lorenz number in the presence of magnetic field.

- **Chapter 4:** In this succinct chapter we deal with matter at high densities and zero temperature which is relevant for CSs. In this chapter we shall discuss the non-radial oscillation modes namely, $f$ and $g$ modes. They are interesting observations, depending on the composition of NSM. Such oscillation modes have the possibility of detection in the planed future detectors like advanced LIGO/VIRGO.

- **Chapter 5:** In this chapter we shall find the robust universal relations between $f$ mode oscillation frequency, mass and radius of NSs. They are insensitive to the equation of state of NSM.

- **Chapter 6:** In this chapter we give the summary and conclusion of the results and discuss future outcomes.

# Chapter 2

# Chiral symmetry breaking in the presence of a magnetic field

The DCSB is the manifestation of quark-antiquark condensation in the QCD vacuum. DCSB characterizes the non-perturbative nature of QCD vacuum at vanishing temperature and/or density. With increasing temperature and/or baryon density, the QCD vacuum undergoes a transition from a chiral symmetry broken phase to a chiral symmetric phase. This transition is characterized by the quark-antiquark scalar condensate, the order parameter of the chiral phase transition. Although for a first order phase transition the order parameter changes discontinuously across the transition point, for a second order phase transition or for a cross-over transition the variation of the order parameter across the transition point is rather smooth. In these cases the fluctuations of the order parameter and the associated susceptibilities are more relevant for the characterization of the thermodynamic properties of the system. In this chapter we shall discuss the effects of non-zero magnetic field (magnetic catalysis) and non-zero chiral chemical potential (chirogenesis) on QCD medium produced in heavy-ion collisions.

## 2.1 Introduction

The characteristics of fluctuations and correlations are intimately connected to the phase transition dynamics, *e.g*. fluctuations of all length scales are relevant at the QCD CEP where the first order quark-hadron phase transition line ends (see Fig. 1.3). The study of fluctuations and correlations are an essential phenomenological tool for the experimental point of view for the QCD phase diagram. In the context of heavy-ion collisions by studying the net electric charge fluctuation, it has been demonstrated that net electric charges are suppressed in the QGP phase as compared to the hadronic phase [92, 93]. It has also been pointed out that the correlation between baryon number and strangeness is stronger in the QGP phase as compared to the hadronic phase [94, 95]. The quantity of interest here is the chiral susceptibility which measures the response of the chiral condensate to the variation of the current quark mass. Chiral susceptibility has been calculated using first principle LQCD simulations [96–101]. These results show a pronounced peak in the variation of chiral susceptibility with temperature at the transition temperature, which essentially characterizes the chiral transition. Apart from these LQCD studies which incorporates the non perturbative effects of QCD vacuum, complementary approaches *e.g.* NJL model [102, 103], chiral perturbation theory (CPT) [104], Dyson-Schwinger equation (DSE) [105], hard thermal loop (HTL) approximation [106] etc. have been considered to study the chiral susceptibility.

An entirely new line of investigations have been initiated to understand the QCD phase diagram due to the possibility of generation of extremely large magnetic fields in non central relativistic heavy ion collision experiments. In the early stages the magnetic field in the QGP can be very large, at least of the order of few $m_\pi^2$ [107–115]. Such fields rapidly decay in the vacuum while in a conducting medium they can be sustained for a longer time due to induced currents [112–115]. It has been shown that the external magnetic field acts as a catalyst for chiral condensation. It enhances the chiral condensate and hence the constituent quark mass. It can affect the DCSB. Magnetic catalysis has been explored extensively in $(2+1)$ and $(3+1)$- dimensional models with local four fermion interactions [63, 64, 116–133], supersymmetric (SUSY) models [134], quark meson models [135, 136], CPT [137, 138] etc. Such a strong magnetic field can also introduce some exotic phenomenon, e.g. chiral magnetic effect (CME), chiral vortical effect (CVE) etc, in a chirally imbalanced medium [139]. Underlying physics of the chiral imbalance is the axial anomaly and topologically non trivial vacuum of QCD, which allows topological field configurations like instantons to exist. An asymmetry between the number of left- and right-handed quarks can be generated by these non trivial topological field configurations due to the Adler-Bell-Jackiw (ABJ) anomaly. Such an imbalance can lead to observable $\mathcal{P}$ and $\mathcal{CP}$ violating effects in heavy ion collisions. In the presence of a magnetic field chirally imbalanced quark matter can give rise CME where a charge separation can be produced. Effects of a chiral imbalance on the QCD phase diagram can be studied within the framework of grand canonical ensemble by introducing a chiral chemical potential $\mu_5$, which enters the QCD Lagrangian via a term $\mu_5\bar{\psi}\gamma^0\gamma^5\psi$.

To probe the medium produced in relativistic heavy-ion collisions, generally thermodynamic or hydrodynamic models have been used, which assume local thermal equilibrium. However, due to the short time scales associated with the strong interaction, the medium produced in the heavy-ion collisions is rather dynamical in nature and lives for a very short time and non-equilibrium as well as quantum effects can affect the evolution of the medium significantly. These effects can be considered within the framework of non-equilibrium quantum transport theory. It is important to point out that in the case of interacting field theory of fermions and gauge bosons, transport theory should be invariant under local gauge transformation. Such a gauge covariant quantum transport theory for the QCD has been developed in [35–37]. Classical kinetic theory is characterized by an ensemble of point-like particles with their single particle phase-space distribution function. The time evolution of the single particle phase-space distribution function governed by the transport equation encodes the evolution of the system.

Similar to the single particle distribution in classical kinetic theory, Wigner function which is the quantum analogue of classical distribution function, encodes quantum corrections in the transport equation [38]. An equation of motion for the Winger function, can be derived from the equation of motion for the associated field operators, *e.g*. for fermions, the evolution equation of Wigner functions can be derived using the Dirac equation [140, 141]. In the case of local gauge theories, the Wigner function has to be defined in a gauge invariant manner [142]. The covariant Wigner function method for spin-1/2 fermions has already been explored extensively in the context of heavy ion collisions to study various effects including CME, CVE, polarization vorticity coupling (PVC), hydrodynamics with spin, dynamical generation of magnetic moment etc. [143–155].

In this investigation, we study the chiral phase transition and chiral susceptibility in the presence of a magnetic field and chiral chemical potential in quantum kinetic theory framework using the NJL model [156–161]. Our work is based on the spinor decomposition of the Wigner function using the formalism of Refs. [150, 162] and we limit ourselves to the mean field or classical level of quantum kinetic theory, since the DCSB and generation of dynamical mass of fermions takes place at the mean field level [162]. In the present study, we limit ourselves to using the Wigner function for an extended system in global thermal equilibrium i.e. at constant temperature and chemical potentials to calculate chiral susceptibility.

In this context some comments regarding chiral transition in the presence of a chiral chemical potential ($\mu_5$) may be in order. In Ref. [39] this was investigated within PNJL model. It was observed that the chiral transition temperature decreases with chiral chemical potential. To eliminate artifacts of a sharp three momentum cutoff, in Ref. [39] a smooth cutoff for the three momentum models through a form factor was used. Further, it was observed that with increasing $\mu_5$ the chiral transition becomes a first order transition. In fact the phase diagram in the $\mu_5 - T$ plane for the chiral transition becomes similar to the same in the $\mu - T$ plane. This was also the conclusion in Ref. [39, 163, 164]. On the contrary a non local version of the NJL model was further analyzed in Ref. [165] with the result that the chiral transition temperature increases with chiral chemical potential and the chiral transition is second order. Similar conclusions were also drawn in Ref. [166, 167] using a Schwinger Dyson approach. Further, the NJL model with chiral chemical potential was analyzed in Ref. [168] with a novel medium separation regularization scheme (MSS) for regulating divergent integrals and the conclusion was that the chiral transition temperature increases with $\mu_5$ and such conclusions are also in accordance with some Lattice calculations [169, 170]. However, it ought to be mentioned here that the Lattice data has not been obtained in the chiral limit and some of the results are for $N_c = 2$ QCD, e.g [170]. A further careful analysis of NJL model was done in Ref. [171] to examine the dependence of chiral transition temperature on different regularization schemes. It was observed that chiral transition temperature decreases with chiral chemical potential with a smooth cutoff and shows a first order transition at large $\mu_5$. In the present investigation we use a MSS in the presence of magnetic field and chiral chemical potential. Such a scheme was introduced in Ref. [168, 172, 173]. As we will see later, we also do not see a first order transition at large chiral chemical potential as in the analysis in Ref. [165]. However, we observe that the chiral transition temperature decreases with chiral chemical potential as in Ref. [39, 171].

We organize this chapter as follows. In Sec. 2.2, we recapitulate the results of Ref. [162] to study the chiral condensate in the NJL model using the Wigner function approach. In Sec. 2.3 we discuss the Winger function in the presence of a magnetic field as well as a chiral chemical potential and find the chiral condensate for two flavour NJL model. In Sec. 2.4 we discuss the chiral susceptibility in presence of magnetic field as well as chiral chemical potential. In Sec. 3.5 we present the results and discussions. Finally in Sec. 2.6 we conclude the investigation with an outlook.

## 2.2 Wigner function and chiral condensate

In this section we first briefly discuss the salient features of the formalism of the Wigner function in the NJL model for single flavour fermion of vanishing current quark mass [162]. Once we get the representation of scalar condensate in terms of Wigner function, we generalize it to the more realistic situation with non vanishing current quark mass in following sections. For a single flavour the NJL model we start with the following Lagrangian [162],

$$\mathcal{L} = \bar{\psi} i \partial\!\!\!/ \psi + G\left( (\bar{\psi}\psi)^2 + (\bar{\psi} i\gamma_5 \psi)^2 \right), \tag{2.1}$$

where $\psi$ is the Dirac fermion field, $G$ is the scalar coupling. The first term in the RHS of Eq. (2.1) is the usual kinetic term and the second term represents the four Fermi interactions. One can define the composite field operators $\hat{\sigma}$ and $\hat{\pi}$ as,

$$\hat{\sigma} = -2G\bar{\psi}\psi, \quad \text{and} \quad \hat{\pi} = -2G\bar{\psi} i\gamma_5\psi. \tag{2.2}$$

Using Eq. (2.2), Eq. (2.1) can be recast as [162],

$$\mathcal{L} = \bar{\psi} i \partial\!\!\!/ \psi - \hat{\sigma}\bar{\psi}\psi - \hat{\pi}\bar{\psi} i\gamma_5\psi - \frac{\hat{\sigma}^2 + \hat{\pi}^2}{4G}. \tag{2.3}$$

In the mean field approximation the operators $\hat{\sigma}$ and $\hat{\pi}$ are replaced by their mean field values,

$$\hat{\sigma} \to \sigma = \langle \hat{\sigma} \rangle = \mathrm{Tr}(\hat{\rho}\hat{\sigma}), \quad \text{and} \quad \hat{\pi} \to \pi = \langle \hat{\pi} \rangle = \mathrm{Tr}(\hat{\rho}\hat{\pi}). \tag{2.4}$$

where $\hat{\rho}$ is the density matrix operator and "Tr" denotes trace over all the physical states of the system. In mean field approximation, for a non-equilibrium transport theory, the fundamental quantity is the Green function, which is defined as

$$G^{<}_{\alpha\beta}(x,y) = \langle \bar{\psi}_\beta(y)\psi_\alpha(x)\rangle. \tag{2.5}$$

The mean field values of the operators $\hat{\sigma}$ and $\hat{\pi}$, i.e. $\sigma(x)$ and $\pi(x)$ can be determined in terms of the Green function $G^{<}(x,y)$ as follows,

$$\sigma(x) = -2G\mathrm{Tr}\, G^{<}(x,x), \quad \text{and} \quad \pi(x) = -2G\mathrm{Tr}\, i\gamma_5 G^{<}(x,x). \tag{2.6}$$

The Wigner function is defined for the fermion as [162],

$$\begin{aligned} W_{\alpha\beta}(X,p) &= \int \frac{d^4X'}{(2\pi)^4} e^{-ip_\mu X'^\mu} \left\langle \bar{\psi}_\beta\left(X+\frac{X'}{2}\right)\psi_\alpha\left(X-\frac{X'}{2}\right)\right\rangle \\ &= \int \frac{d^4X'}{(2\pi)^4} e^{-ip_\mu X'^\mu} G^{<}_{\alpha\beta}\left(X+\frac{X'}{2}, X-\frac{X'}{2}\right) \end{aligned} \tag{2.7}$$

It is important to mention that there are no gluons in the NJL model, hence the $SU(3)_c$ gauge invariance of the Wigner function does not appear in the NJL model. Again in this case we are not considering the background magnetic field. So there is no $U(1)_{\text{em}}$ gauge field in the NJL model. However in the presence of a gauge field one has to introduce a gauge link in Wigner function for the gauge invariant description of Wigner function [174].

Since the Wigner function $W(X,p)$ as given in Eq. (2.7), is a composite operator made out of the Dirac field operators $\psi$ and $\bar{\psi}$, it can be decomposed in terms of the generators of the Clifford algebra as,

$$W = \frac{1}{4}\left[F + i\gamma_5 P + \gamma^\mu V_\mu + \gamma^\mu\gamma^5 A_\mu + \frac{1}{2}\sigma^{\mu\nu}S_{\mu\nu}\right]. \tag{2.8}$$

Where $\mathbb{1}$, $i\gamma_5$, $\gamma^\mu$, $\gamma^\mu\gamma_5$ and $\sigma^{\mu\nu}$ are the basis of the Clifford algebra and the coefficients $F$, $P$, $V_\mu$, $A_\mu$ and $S_{\mu\nu}$ are the scalar, pseudo scalar, vector, axial vector and tensor components of the Wigner function respectively, also known as Dirac-Heisenberg-Wigner (DHW) functions. These DHW functions can be expressed in terms of Wigner function as,

$$F(X,p) = \mathrm{Tr}W(X,p), \tag{2.9}$$
$$P(X,p) = -i\mathrm{Tr}\gamma_5 W(X,p), \tag{2.10}$$
$$V^\mu(X,p) = \mathrm{Tr}\gamma^\mu W(X,p), \tag{2.11}$$
$$A^\mu(X,p) = \mathrm{Tr}\gamma^5\gamma^\mu W(X,p), \tag{2.12}$$
$$S^{\mu\nu}(X,p) = \mathrm{Tr}\sigma^{\mu\nu} W(X,p). \tag{2.13}$$

Using Eq. (2.6) and Eq. (2.7), the scalar and pseudoscalar condensates as given in Eq. (2.9) and Eq. (2.10) can be written in terms of Wigner function as,

$$\sigma(X) = -2G \int \mathrm{d}^4 p \mathrm{Tr}\, W(X,p) = -2G \int \mathrm{d}^4 p F(X,p), \tag{2.14}$$

and,

$$\pi(X) = -2G \int \mathrm{d}^4 p \mathrm{Tr}\, i\gamma_5 W(X,p) = 2G \int \mathrm{d}^4 p P(X,p). \tag{2.15}$$

Using Eq. (2.2) and Eq. (2.14), the scalar condensate can be expressed as,

$$\langle \bar{\psi}\psi \rangle = \int d^4 p F(X,p). \tag{2.16}$$

In the above description we have briefly discussed the relations between the scalar and pseudoscalar condensates with the Wigner function, $W(X,p)$ and the scalar condensate in terms of the Wigner function. In this chapter we rather focus on the chiral condensate as given in Eq. (2.16) and associated chiral susceptibility in two flavour NJL model.

The expression of the Wigner function can be found by inserting the Dirac field operators in Eq. (2.7). The Dirac field operators in the absence of magnetic field can be written as [175],

$$\psi(x) = \frac{1}{\sqrt{V}} \sum_{\vec{k},s} \frac{1}{\sqrt{2\mathcal{E}_{0k}}} \left[ a(\vec{k},s) u(\vec{k},s) e^{-ik.x} + b^{\dagger}(\vec{k},s) v(\vec{k},s) e^{ik.x} \right], \tag{2.17}$$

$$\bar{\psi}(x) = \frac{1}{\sqrt{V}} \sum_{\vec{k},s} \frac{1}{\sqrt{2\mathcal{E}_{0k}}} \left[ a^{\dagger}(\vec{k},s) \bar{u}(\vec{k},s) e^{ik.x} + b(\vec{k},s) \bar{v}(\vec{k},s) e^{-ik.x} \right], \tag{2.18}$$

where $V$ is the volume and $s = \pm 1$ denotes the spin states. Using the field decomposition as given in Eqs. (2.17) and (2.18), the Wigner function of a fermion of mass $\mathcal{M}_0$ can be shown to be [175],

$$\begin{aligned} W_{\alpha\beta}(X,p) = \frac{1}{(2\pi)^3} \delta(p^2 - \mathcal{M}_0^2) \Big[ & \theta(p^0) \sum_s f_{\mathrm{FD}}(\mathcal{E}_{0p} - \mu_s) u_\alpha(\vec{p},s) \bar{u}_\beta(\vec{p},s) \\ & + \theta(-p^0) \sum_s (1 - f_{\mathrm{FD}}(\mathcal{E}_{0p} + \mu_s)) v_\alpha(-\vec{p},s) \bar{v}_\beta(-\vec{p},s) \Big], \end{aligned} \tag{2.19}$$

where the creation and the annihilation operators of the particle satisfy,

$$\langle a^{\dagger}(\vec{p},s) a(\vec{p},s) \rangle = f_{\mathrm{FD}}(\mathcal{E}_{0p} - \mu_s).$$

On the other hand the creation and the annihilation operators of the anti-particle satisfy,

$$\langle b^{\dagger}(-\vec{p},s) b(-\vec{p},s) \rangle = f_{\mathrm{FD}}(\mathcal{E}_{0p} + \mu_s).$$

Where $f_{\mathrm{FD}}(z) = 1/(1+\exp(z/T))$ is the Fermi Dirac distribution function at temperature $T$ and $\mu_s$ is the chemical potential for the spin state $s$. $\mathcal{E}_{0p} = \sqrt{p^2 + \mathcal{M}_0^2}$ is the single particle energy and $\mathcal{M}_0$ is the mass of the Dirac fermion. It is important to note that the space-time dependence in the Wigner function $W(X,p)$ is hidden in the space-time dependence of the temperature and chemical potential. However for a uniform temperature and chemical potential i.e. for a system in global equilibrium the Wigner function is independent of space-time. Hence from now onward we omit the space-time dependence in the Wigner function. Using Eqs. (2.9) and (2.19) the scalar DHW function can be expressed as [175],

$$\begin{aligned} F(p) = \mathcal{M}_0\delta(p^2-\mathcal{M}_0^2) \quad &\times \\ &\frac{2}{(2\pi)^3}\sum_s\Big(\theta(p^0)f_{\mathrm{FD}}(\mathcal{E}_{0p}-\mu_s)-\theta(-p^0)(1-f_{\mathrm{FD}}(\mathcal{E}_{0p}+\mu_s))\Big). \end{aligned} \tag{2.20}$$

Using Eq. (2.20), the scalar condensate for a single fermion of mass $\mathcal{M}_0$ given in Eq. (2.16) can be expressed as,

$$\begin{aligned} \langle\bar{\psi}\psi\rangle = \int \mathrm{d}^4p\mathcal{M}_0\delta(p^2-\mathcal{M}_0^2) \quad &\times \\ &\frac{2}{(2\pi)^3}\sum_s\Big(\theta(p^0)f_{\mathrm{FD}}(\mathcal{E}_{0p}-\mu_s)-\theta(-p^0)(1-f_{\mathrm{FD}}(\mathcal{E}_{0p}+\mu_s))\Big). \\ = -\sum_s\int\frac{\mathrm{d}^3p}{(2\pi)^3}\frac{\mathcal{M}_0}{\mathcal{E}_{0p}}&\Big[1-f_{\mathrm{FD}}(\mathcal{E}_{0p}-\mu_s)-f_{\mathrm{FD}}(\mathcal{E}_{0p}+\mu_s)\Big] \end{aligned} \tag{2.21}$$

In a situation where the chemical potential is independent of the spin of the state,

$$\langle\bar{\psi}\psi\rangle = -2N_c\int\frac{\mathrm{d}^3p}{(2\pi)^3}\frac{\mathcal{M}_0}{\mathcal{E}_{0p}}\Big[1-f_{\mathrm{FD}}(\mathcal{E}_{0p}-\mu)-f_{\mathrm{FD}}(\mathcal{E}_{0p}+\mu)\Big], \tag{2.22}$$

with $\mathcal{M}_0 = -2G\langle\bar{\psi}\psi\rangle$ is the mass gap equation. The factor of $N_c$ appears in Eq. (2.22) due to the "Tr" over all the degrees of freedom.

Next we shall consider two flavours ($u$, and $d$ quarks) NJL model for vanishing magnetic field and chiral chemical potential, with the Lagrangian given as [34],

$$\mathcal{L} = \mathcal{L}_0 + \mathcal{L}_1 + \mathcal{L}_2, \tag{2.23}$$

where the free part is,

$$\mathcal{L}_0 = \bar{\psi}(i\partial\!\!\!/ - m)\psi, \tag{2.24}$$

and the interaction parts are given as,

$$\mathcal{L}_1 = G_1\sum_{a=0}^{3}\Big[(\bar{\psi}\tau^a\psi)^2 + (\bar{\psi}i\gamma_5\tau^a\psi)^2\Big], \quad \text{and} \tag{2.25}$$

$$\mathcal{L}_2 = G_2\left[(\bar{\psi}\psi)^2 - (\bar{\psi}\vec{\tau}\psi)^2 - (\bar{\psi}i\gamma_5\psi)^2 + (\bar{\psi}i\gamma_5\vec{\tau}\psi)^2\right], \tag{2.26}$$

where $\psi = (\psi_u, \psi_d)^T$ is the quark doublet, $m = \mathrm{diag}(m_u, m_d)$ is the current quark mass metrix with $m_u = m_d$. $\tau^0 = I_{2\times 2}$ and $\vec{\tau}$ are the Pauli matrices. The above Lagrangian, Eq. (2.23), is invariant under $SU(2)_L \times SU(2)_R \times U(1)_V$ gauge transformations. $\mathcal{L}_1$ has an additional $U(1)_A$ symmetry and $\mathcal{L}_2$ is identical with t-Hooft determinant interaction term which breaks the $U(1)_A$ symmetry explicitly. $\mathcal{L}_2$ term introduces mixing between different flavours. The value of the coupling $G_2$ is fixed by fitting the masses of the pseudo scalar octet [34]. It is also important to emphasis that since we are considering only the scalar condensates of the form $\bar{\psi}_u\psi_u$ and $\bar{\psi}_d\psi_d$, so we can safely ignore the pseudo scalar condensate as well as the scalar condensates of the form $\bar{\psi}_u\psi_d$, $\bar{\psi}_d\psi_u$ etc. Using these approximations at the mean field level, the Lagrangian of the two flavour NJL model as given in Eq. (2.23) can be written as,

$$\begin{aligned}\mathcal{L} &= \bar{\psi}_u(i\partial\!\!\!/ - \mathcal{M}_{0_u})\psi_u + \bar{\psi}_d(i\partial\!\!\!/ - \mathcal{M}_{0_d})\psi_d \\ &-2G_1\left(\langle\bar{\psi}_u\psi_u\rangle^2 + \langle\bar{\psi}_d\psi_d\rangle^2\right) - 4G_2\langle\bar{\psi}_u\psi_u\rangle\langle\bar{\psi}_d\psi_d\rangle,\end{aligned} \tag{2.27}$$

where $\langle\bar{\psi}_u\psi_u\rangle$ and $\langle\bar{\psi}_d\psi_d\rangle$ are the $u$ and $d$ quark condensates respectively. The mass gap equations for $u$ and $d$ quarks are given as,

$$\mathcal{M}_{0_u} = m_u - 4G_1\langle\bar{\psi}_u\psi_u\rangle - 4G_2\langle\bar{\psi}_d\psi_d\rangle, \quad \mathcal{M}_{0_d} = m_d - 4G_1\langle\bar{\psi}_d\psi_d\rangle - 4G_2\langle\bar{\psi}_u\psi_u\rangle. \tag{2.28}$$

One can easily generalize the expression of the scalar condensate as given in Eq. (2.22) for a single flavour NJL model to two flavour NJL model. The chiral condensate in the NJL model of $N_f$ quark flavour and $N_c$ color can be written as,

$$\langle\bar{\psi}\psi\rangle^{\mu_5=0}_{B=0} = \sum_{f=1}^{N_f}\langle\bar{\psi}_f\psi_f\rangle^{\mu_5=0}_{B=0} \qquad \text{with,}$$

$$\langle\bar{\psi}_f\psi_f\rangle^{\mu_5=0}_{B=0} = -2N_c\int\frac{d^3p}{(2\pi)^3}\frac{\mathcal{M}_{0_f}}{\mathcal{E}_{0p,f}}\left[1 - f_{\mathrm{FD}}(\mathcal{E}_{0p,f}-\mu) - f_{\mathrm{FD}}(\mathcal{E}_{0p,f}+\mu)\right]. \tag{2.29}$$

The chiral condensate for $N_f$ flavour NJL model as given in Eq. (2.29) can also be obtained by first calculating the thermodynamic potential using the mean field Lagrangian as given in Eq. (2.27) and then calculating the gap equation using the minimization of thermodynamic potential.

## 2.3 Wigner function and chiral condensate in a nonvanishing magnetic field and chiral chemical potential

In the presence of a magnetic field ($B$) and chiral chemical potential ($\mu_5$), the Wigner function has been explicitly written down in Ref. [150]. They have used the solutions of the Dirac equation for fermions in presence of magnetic field and chiral chemical potential. We shall use it to obtain the chiral condensate. For the sake of completeness, we write the relevant expressions for the Wigner function. In the presence of a magnetic field, the Wigner function, given in Eq. (2.7), gets modified to a gauge invariant Wigner function as [150],

$$W_{\alpha\beta}(X,p) = \int \frac{d^4X'}{(2\pi)^4} e^{\left(-ip_\mu X'^\mu\right)} \quad \times \\ \left\langle \bar{\psi}_\beta \left(X + \frac{X'}{2}\right) U\left(A, X + \frac{X'}{2}, X - \frac{X'}{2}\right) \psi_\alpha \left(X - \frac{X'}{2}\right) \right\rangle, \tag{2.30}$$

where $U\left(A, X + \frac{X'}{2}, X - \frac{X'}{2}\right)$ is the gauge link between two space-time points $\left(X - \frac{X'}{2}\right)$ and $\left(X + \frac{X'}{2}\right)$ for the gauge field $A^\mu$. The gauge link has been introduced to make the Wigner function gauge invariant. In the presence of a homogeneous external magnetic field along the $z$ direction, the gauge link is just a phase. In this case the Wigner function simplifies to,

$$W_{\alpha\beta}(X,p) = \int \frac{d^4X'}{(2\pi)^4} e^{\left(-ip_\mu X'^\mu - iqByx'\right)} \left\langle \bar{\psi}_\beta \left(X + \frac{X'}{2}\right) \otimes \psi_\alpha \left(X - \frac{X'}{2}\right) \right\rangle, \tag{2.31}$$

where $A^\mu(X) = (0, -By, 0, 0)$ is a specific gauge choice of the external magnetic field. $q$ is the charge of the particle and it has been taken to be positive. Analogous to the case of a vanishing magnetic field, the Wigner function can be calculated for a non-vanishing magnetic field by using the Dirac field operator in a background magnetic field. The Wigner function in presence of magnetic field at finite temperature ($T$), chemical potential ($\mu$) and finite chiral chemical potential ($\mu_5$) has been shown to be [150],

$$W(p) = \sum_{n,s} \Big[ f_{\rm FD}(E^{(n)}_{p_z,s} - \mu)\delta(p_0 + \mu - E^{(n)}_{p_z,s}) W^{(n)}_{+,s}(\vec{p}) \\ + (1 - f_{\rm FD}(E^{(n)}_{p_z,s} + \mu))\delta(p_0 + \mu + E^{(n)}_{p_z,s}) W^{(n)}_{-,s}(\vec{p}) \Big], \quad n \geq 0 \tag{2.32}$$

where the functions $W^{(n)}_{\pm,s}(\vec{p})$ denote the contribution of fermion/antifermion in the $n$-th Landau level. The single particle energy at the lowest Landau level and higher

Landau levels are given as

$$E_{p_z}^{(0)} = \sqrt{M^2 + (p_z - \mu_5)^2}$$

and

$$E_{p_z,s}^{(n)} = \sqrt{M^2 + (\sqrt{p_z^2 + 2nqB} - s\mu_5)^2}$$

respectively. $+$ and $-$ in Eq. (2.32) denote contributions of positive and negative energy solutions respectively. In the lowest Landau level fermions can only be in a specific spin state. On the other hand for higher Landau levels ($n > 0$) both spin states contribute.

The functions $W_{\pm,s}^{(n)}(\vec{p})$ in Eq. (2.32) can be expressed in terms of Dirac spinors in the following manner [150],

$$W_{rs}^{(n)}(\vec{p}) \equiv \frac{1}{(2\pi)^3} \int dy' \exp(ip_y y') \times \\ \xi_{rs}^{(n)\dagger}\left(p_x, p_z, \frac{y'}{2}\right) \gamma^0 \otimes \xi_{rs}^{(n)}\left(p_x, p_z, -\frac{y'}{2}\right), \quad n \geq 0 \tag{2.33}$$

In Eq. (2.33), $r = \pm$ denotes positive energy and negative energy solutions respectively. The Dirac spinors $\xi_r^{(0)}$ and $\xi_{rs}^{(n)}$, where $r = \pm$ denotes positive and negative energy states and $s$ denotes the spin of the state, are defined as,

$$\xi_r^{(0)}(p_x, p_z, y) = \frac{1}{\sqrt{2E_{p_z}^{(0)}}} \begin{pmatrix} r\sqrt{E_{p_z}^{(0)} - r(p_z - \mu_5)} \\ \sqrt{E_{p_z}^{(0)} + r(p_z - \mu_5)} \end{pmatrix} \otimes \chi^{(0)}(p_x, y) \tag{2.34}$$

$$\xi_{rs}^{(n)}(p_x, p_z, y) = \frac{1}{\sqrt{2E_{p_z,s}^{(n)}}} \begin{pmatrix} r\sqrt{E_{p_z,s}^{(n)} + r\mu_5 - rs\sqrt{p_z^2 + 2nqB}} \\ \sqrt{E_{p_z,s}^{(n)} - r\mu_5 + rs\sqrt{p_z^2 + 2nqB}} \end{pmatrix} \otimes \chi^{(n)}(p_x, p_z, y), \tag{2.35}$$

for ($n > 0$). Where the normalized eigen spinors $\chi$ are

$$\chi^{(0)}(p_x, y) = \begin{pmatrix} 1 \\ 0 \end{pmatrix} \phi_0(p_x, y), \tag{2.36}$$

$$\chi_s^{(n)}(p_x, p_z, y) = \frac{1}{\sqrt{2\sqrt{p_z^2 + 2nqB}}} \begin{pmatrix} \sqrt{\sqrt{p_z^2 + 2nqB} + sp_z}\phi_n(p_x, y) \\ s\sqrt{\sqrt{p_z^2 + 2nqB} - sp_z}\phi_{n-1}(p_x, y) \end{pmatrix}, \tag{2.37}$$

for $n > 0$. Where,

$$\phi_n(p_x, y) = \left(\frac{qB}{\pi}\right)^{1/4} \frac{1}{\sqrt{2^n n!}} \exp\left[-\frac{qB}{2}\left(y + \frac{p_x}{qB}\right)^2\right] H_n\left[\sqrt{qB}\left(y + \frac{p_x}{qB}\right)\right]. \tag{2.38}$$

for $n > 0$. $H_n$ represents $n$-th Hermite polynomial. Inserting the explicit expression of the Dirac spinors as given in Eq. (2.36) and Eq. (2.37) into Eq. (2.33) one can get the explicit form of the function $W^{(n)}_{\pm,s}(\vec{p})$ [150].

For lowest Landau level,

$$\begin{aligned} W^{(0)}_r(\vec{p}) = &\frac{r}{4(2\pi)^3 E^{(0)}_{p_z}} \Lambda^{(0)}(p_T) \times \\ &\left[M(1 + \sigma^{12}) + rE^{(0)}_{p_z}(\gamma^0 - \gamma^5\gamma^3) - (p_z - \mu_5)(\gamma^3 - \gamma^5\gamma^0)\right], \end{aligned} \tag{2.39}$$

while for higher Landau levels ($n > 0$),

$$\begin{aligned} W^{(n)}_{rs}(\vec{p}) = & r\frac{1}{4(2\pi)^3 E^{(n)}_{p_z,s}} \left\{ \left(\Lambda^{(n)}_+(p_T) + X^{(n)}_s \Lambda^{(n)}_-(p_T)\right)\left(M + rE^{(n)}_{p_z,s}\gamma^0 + Y^{(n)}_s \gamma^5\gamma^0\right) \right. \\ & - \left(\Lambda^{(n)}_-(p_T) + X^{(n)}_s \Lambda^{(n)}_+(p_T)\right)\left(Y^{(n)}_s \gamma^3 + rE^{(n)}_{p_z,s}\gamma^5\gamma^3 - M\sigma^{12}\right) \\ & - \frac{2nqB}{p_T^2\sqrt{p_z^2 + 2nqB}} \Lambda^{(n)}_+(p_T) \times \\ & \left. \left(sY^{(n)}_s(p_x\gamma^1 + p_y\gamma^2) + rsE^{(n)}_{p_z,s}(p_x\gamma^5\gamma^1 + p_y\gamma^5\gamma^2) - sM(p_z\sigma^{23} - p_y\sigma^{13})\right) \right\} \end{aligned} \tag{2.40}$$

where we have defined

$$X^{(n)}_s = s\frac{p_z}{\sqrt{p_z^2 + 2nqB}}, \qquad Y^{(n)}_s = s\sqrt{p_z^2 + 2nqB} - \mu_5.$$

where,

$$\Lambda^{(0)}_\pm(p_T) = 2\exp\left(-\frac{p_T^2}{qB}\right), \tag{2.41}$$

$$\Lambda^{(n)}_\pm(p_T) = (-1)^n \left[L_n\left(\frac{2p_T^2}{qB}\right) \mp L_{n-1}\left(\frac{2p_T^2}{qB}\right)\right] \exp\left(-\frac{p_T^2}{qB}\right), \quad n > 0. \tag{2.42}$$

Here $L_n(x)$ are the Laguerre polynomials with $L_{-1}(x) = 0$. Using the Wigner function $W(p)$ as given in Eq. (2.32) it can be shown that the scalar DHW function is [150],

$$F(p) = M\left[\sum_{n=0}^{\infty} V_n(p_0, p_z)\Lambda_+^{(n)}(p_T) + \sum_{n=1}^{\infty} \frac{1}{\sqrt{p_z^2 + 2nqB}} A_n(p_0, p_z) p_z \Lambda_-^{(n)}(p_T)\right], \tag{2.43}$$

where,

$$\begin{aligned} V_0(p_0, p_z) = & \frac{2}{(2\pi)^3}\delta\{(p_0+\mu)^2 - |E_{p_z}^{(0)}|^2\}\times \\ & \{\theta(p_0+\mu)f_{\rm FD}(p_0) + \theta(-p_0-\mu)[f_{\rm FD}(-p_0) - 1]\} \end{aligned} \tag{2.44}$$

$$\begin{aligned} V_n(p_0, p_z) = & \frac{2}{(2\pi)^3}\sum_s \delta\{(p_0+\mu)^2 - |E_{p_z,s}^{(n)}|^2\}\times \\ & \{\theta(p_0+\mu)f_{\rm FD}(p_0) + \theta(-p_0-\mu)\left[f_{\rm FD}(-p_0) - 1\right]\}, \quad n > 0 \end{aligned} \tag{2.45}$$

$$\begin{aligned} A_n(p_0, p_z) = & \frac{2}{(2\pi)^3}\sum_s s\delta\{(p_0+\mu)^2 - |E_{p_z,s}^{(n)}|^2\}\times \\ & \{\theta(p_0+\mu)f_{\rm FD}(p_0) + \theta(-p_0-\mu)\left[f_{\rm FD}(-p_0) - 1\right]\}, \quad n > 0 \end{aligned} \tag{2.46}$$

Once the scalar DHW function is known explicitly as given in Eq. (2.43), the chiral condensate of single flavour fermion can be calculated using Eq. (2.16) and is given as,

$$\langle\bar{\psi}\psi\rangle = \int d^4p\, F(p) = \int 2\pi p_T\, dp_0\, dp_T\, dp_z\, F(p) \tag{2.47}$$

Using Eq. (2.43) and Eq. (2.47), it can be shown that (see Appendix A.1 for details),

$$\begin{aligned} \langle\bar{\psi}\psi\rangle_{B\neq0}^{\mu_5\neq0} = & -\frac{qB}{(2\pi)^2}\Bigg\{\int dp_z \frac{M}{E_{p_z}^{(0)}}\Big(1 - f_{\rm FD}(E_{p_z}^{(0)} - \mu) - f_{\rm FD}(E_{p_z}^{(0)} + \mu)\Big) \\ & + \sum_{n=1}^{\infty}\sum_s \int dp_z \frac{M}{E_{p_z,s}^{(n)}}\Big(1 - f_{\rm FD}(E_{p_z,s}^{(n)} - \mu) - f_{\rm FD}(E_{p_z,s}^{(n)} + \mu)\Big)\Bigg\}. \end{aligned} \tag{2.48}$$

For vanishing chiral chemical potential, $\mu_5 = 0$, scalar condensate get reduced to,

$$\langle\bar{\psi}\psi\rangle_{B\neq0}^{\mu_5=0} = -\frac{qB}{(2\pi)^2}\sum_{n=0}^{\infty}(2-\delta_{n,0})\int dp_z \frac{M_0}{\epsilon_{p_z}^{(n)}}\Big(1 - f_{\rm FD}(\epsilon_{p_z}^{(n)} - \mu) - f_{\rm FD}(\epsilon_{p_z}^{(n)} + \mu)\Big), \tag{2.49}$$

where we denote $M_0$ as the mass of fermion in the absence of chiral chemical potential and finite magnitude field. The single particle energy $\epsilon_{p_z}^{(n)}$, for vanishing chiral chemical potential can be written as,

$$\epsilon_{p_z}^{(n)} = \sqrt{M_0^2 + p_z^2 + 2nqB}, \;\; n \geq 0. \tag{2.50}$$

The chiral condensate for a single flavour as given in Eq. (2.48) can be easily extended to NJL model with two flavours. Most general Lagrangian for two flavour NJL model with $u$ and $d$ quarks in the magnetic field including chiral chemical potential is given as,

$$\begin{aligned}\mathcal{L} = \bar{\psi}(i\not{D} - m + \mu_5\gamma^0\gamma^5)\psi + G_1 \sum_{a=0}^{3} \left[ (\bar{\psi}\tau^a\psi)^2 + (\bar{\psi}i\gamma_5\tau^a\psi)^2 \right] \\ + G_2 \left[ (\bar{\psi}\psi)^2 - (\bar{\psi}\vec{\tau}\psi)^2 - (\bar{\psi}i\gamma_5\psi)^2 + (\bar{\psi}i\gamma_5\vec{\tau}\psi)^2 \right],\end{aligned} \tag{2.51}$$

where $\psi$ is the $U(2)$ quark doublet, given as $\psi = (\psi_u, \psi_d)^T$. The covariant derivative is given as $\not{D} = \not{\partial} + iq\not{A}$ and the current quark mass matrix is $m = \mathrm{diag}(m_u, m_d)$, with $m_u = m_d$. The first term in Eq. (2.51) is the free Dirac Lagrangian in the presence of a magnetic field. For the calculation we have considered the gauge choice of the background magnetic field as $A^\mu = (0, -By, 0, 0)$. The second term in Eq. (2.51) is the four Fermi interactions and the attractive part of the quark anti-quark channel of the Fierz transformed color current-current interaction. $\tau^a, a = 0, ..3$ are the $U(2)$ generators in the flavour space. Third term is the t-Hooft interaction terms which introduces flavour mixing as earlier in Eq. (2.26). Since the magnetic field couples to the electric charge of particles, in the presence of magnetic field $u$ quark and $d$ quarks couple differently with the magnetic field, hence the isospin symmetry is explicitly broken. In the mean field approximation, in the absence of any pseudo scalar condensate, Eq. (2.51) can be recast as,

$$\begin{aligned}\mathcal{L} = \bar{\psi}_u(i\not{D} - M_u + \mu_5\gamma^0\gamma^5)\psi_u + \bar{\psi}_d(i\not{D} - M_d + \mu_5\gamma^0\gamma^5)\psi_d \\ -2G_1\left(\langle\bar{\psi}_u\psi_u\rangle^2 + \langle\bar{\psi}_d\psi_d\rangle^2\right) - 4G_2\langle\bar{\psi}_u\psi_u\rangle\langle\bar{\psi}_d\psi_d\rangle,\end{aligned} \tag{2.52}$$

where $u, d$ quark condensates are given as $\langle\bar{\psi}_u\psi_u\rangle$ and $\langle\bar{\psi}_d\psi_d\rangle$ respectively. The constituent quark masses for $u$ and $d$ quarks in terms of the chiral condensates can be given as,

$$M_u = m_u - 4G_1\langle\bar{\psi}_u\psi_u\rangle - 4G_2\langle\bar{\psi}_d\psi_d\rangle, \qquad M_d = m_d - 4G_1\langle\bar{\psi}_d\psi_d\rangle - 4G_2\langle\bar{\psi}_u\psi_u\rangle. \tag{2.53}$$

Generalizing Eq. (2.48) for two flavour NJL model, the chiral condensate in the presence of magnetic field and chiral chemical potential can be written as,

$$\langle\bar{\psi}\psi\rangle_{B\neq0}^{\mu_5\neq0} = \sum_{f=u,d}\langle\bar{\psi}_f\psi_f\rangle_{B\neq0}^{\mu_5\neq0}, \tag{2.54}$$

where

$$\begin{aligned}\langle\bar{\psi}_f\psi_f\rangle_{B\neq0}^{\mu_5\neq0} = -\frac{N_c|q_f|B}{(2\pi)^2}\Bigg[\int \mathrm{d}p_z\frac{M_f}{E^{(0)}_{p_z,f}}\Big(1-f_{\mathrm{FD}}(E^{(0)}_{p_z,f}-\mu)-f_{\mathrm{FD}}(E^{(0)}_{p_z,f}+\mu)\Big)\\ +\sum_{n=1}^{\infty}\sum_s\int \mathrm{d}p_z\frac{M_f}{E^{(n)}_{p_z,s,f}}\Big(1-f_{\mathrm{FD}}(E^{(n)}_{p_z,s,f}-\mu)-f_{\mathrm{FD}}(E^{(n)}_{p_z,s,f}+\mu)\Big)\Bigg],\end{aligned} \tag{2.55}$$

and the single particle energy of flavour $f$ can be expressed as for $n=0$ and $n>0$ respectively,

$$E^{(0)}_{p_z,f} = \sqrt{M_f^2+(p_z-\mu_5)^2}, \quad E^{(n)}_{p_z,s,f} = \sqrt{M_f^2+\left(\sqrt{p_z^2+2n|q_f|B}-s\mu_5\right)^2}. \tag{2.56}$$

For vanishing chiral chemical potential $\mu_5=0$, the chiral condensate of single flavour can be expressed as,

$$\begin{aligned}\langle\bar{\psi}_f\psi_f\rangle_{B\neq0}^{\mu_5=0} = -\frac{N_c|q_f|B}{(2\pi)^2} \quad \times\\ \sum_{n=0}^{\infty}(2-\delta_{n,0})\int \mathrm{d}p_z\frac{M_{0_f}}{\epsilon^{(n)}_{p_z,f}}\left[1-f_{\mathrm{FD}}(\epsilon^{(n)}_{p_z,f}-\mu)-f_{\mathrm{FD}}(\epsilon^{(n)}_{p_z,f}+\mu)\right]\Bigg],\end{aligned} \tag{2.57}$$

and the single particle energies of flavour $f$ can be expressed as,

$$\epsilon^{(n)}_{p_z,f} = \sqrt{p_z^2+M_{0_f}^2+2n|q_f|B}. \tag{2.58}$$

The first term of Eq. (2.57) is UV divergent and it needs to be regularized to derive the meaningful chiral condensate. The effective models like the NJL model which are non-renormalizable are complemented with the regularization schemes with the constraint that the qualitative results should be independent of the regularization prescription. Generally in the NJL model at zero temperature and zero chemical potential such divergent integrals are regularized by either a sharp three momentum cutoff [34, 156] or a smooth cutoff [176–178]. In the presence of magnetic fields, continuous momentum dependence in two spatial dimensions transverse to the direction of magnetic field, are being replaced by a sum over discretized Landau levels. Hence a sharp three momentum cutoff in the presence of the magnetic field suffers from a cutoff artifact. Instead of a sharp cutoff a smooth momentum cutoff was used in Ref. [39] in the context of chiral magnetic effects in the PNJL model to avoid such sharp cutoff artifacts. To regularize the first term of Eq. (2.57), we follow here an elegant procedure calling MSS that was followed in Ref. [63, 130, 179] by adding and subtracting a vacuum term to the chiral condensate which is also divergent. This makes the first term of Eq. (2.57) neatly separated into a zero field vacuum term and a term that is only dependent on the field written in terms of the Gamma function which is finite. Thus the regularized chiral condensate in presence of magnetic field at vanishing quark chemical potential is (see Appendix A.2, Eq. (A.25)),

$$
\begin{aligned}
\langle \bar{\psi}_f \psi_f \rangle^{\mu_5=0}_{B\neq 0} = & -2N_c \int_{|\vec{p}|\leq\Lambda} \frac{\mathrm{d}^3 p}{(2\pi)^3} \frac{M_{0_f}}{\sqrt{p^2+M_{0_f}^2}} \\
& - \frac{N_c M_{0_f} |q_f| B}{2\pi^2} \left[ x_{0_f}(1-\ln x_{0_f}) + \ln\Gamma(x_{0_f}) + \frac{1}{2}\ln\left(\frac{x_{0_f}}{2\pi}\right)\right] \\
& + \frac{N_c |q_f| B}{2\pi^2} \sum_{n=0}^{\infty} (2-\delta_{n,0}) \int_{-\infty}^{\infty} \mathrm{d}p_z \frac{M_{0_f}}{\epsilon^{(n)}_{p_z,f}} f_{\mathrm{FD}}(\epsilon^{(n)}_{p_z,f}),
\end{aligned} \tag{2.59}
$$

where the dimensionless variable $x_{0_f} = M_{0_f}^2/2|q_f|B$. The scalar condensate given in Eq. (2.59) can also be obtained by minimizing the regularized thermodynamic potential which is obtained using the mean field Lagrangian as given in Eq. (2.52) in case of vanishing chiral chemical potential. By solving the equation Eq. (2.53) using Eq. (2.59) we get constituent quark masses of $u$ and $d$ quarks for vanishing chiral chemical potential with finite magnetic field. These constituent quark masses will be later used to estimate constituent quark masses at finite chiral chemical potential and finite magnetic field. We discuss it in the following subsection.

### 2.3.1 Regularization of chiral condensate in the presence of a magnetic field and a chiral chemical potential

The chiral condensate of the quark (flavour $f$), $\langle \bar{\psi}_f \psi_f \rangle$, in the presence of a magnetic field and a chiral chemical potential is given as,

$$
\begin{aligned}
\langle \bar{\psi}_f \psi_f \rangle^{\mu_5\neq 0}_{B\neq 0} = & -\frac{N_c |q_f| B}{(2\pi)^2} \Bigg[ \int \mathrm{d}p_z \frac{M_f}{E^{(0)}_{p_z,f}} \left(1 - f_{\mathrm{FD}}(E^{(0)}_{p_z,f}+\mu) - f_{\mathrm{FD}}(E^{(0)}_{p_z,f}-\mu)\right) \\
& + \sum_{n=1}^{\infty} \sum_{s} \int \mathrm{d}p_z \frac{M_f}{E^{(n)}_{p_z,s,f}} \left(1 - f_{\mathrm{FD}}(E^{(n)}_{p_z,s,f}+\mu) - f_{\mathrm{FD}}(E^{(n)}_{p_z,s,f}-\mu)\right)\Bigg] \\
= & \langle \bar{\psi}_f \psi_f \rangle^{\mu_5\neq 0}_{vac,B\neq 0} + \langle \bar{\psi}_f \psi_f \rangle^{\mu_5\neq 0}_{med,B\neq 0}
\end{aligned} \tag{2.60}
$$

where $\langle\bar{\psi}_f\psi_f\rangle^{\mu_5\neq 0}_{vac,B\neq 0}$ is the vanishing temperature and vanishing quark chemical potential part of the chiral condensate and $\langle\bar{\psi}_f\psi_f\rangle^{\mu_5\neq 0}_{med,B\neq 0}$ is the medium term at finite temperature and quark chemical potential. $\langle\bar{\psi}_f\psi_f\rangle^{\mu_5\neq 0}_{vac,B\neq 0}$ contains a divergent integral which has to be regularized to obtain meaningful physical results. To regularize the vacuum part of the chiral condensate for non vanishing magnetic field and chiral chemical potential we have not considered the naive regularization with finite cutoff (Traditional Regularization scheme-TRS) to remove cutoff artifacts, rather we have considered MSS outlined in Ref. [180]. By adding and subtracting the lowest Landau level term in the zero temperature and zero quark chemical potential part of the chiral condensate for non vanishing magnetic field and chiral chemical potential, we get (for details see Appendix A.3),

$$\begin{aligned}
\langle\bar{\psi}_f\psi_f\rangle^{\mu_5\neq 0}_{vac,B\neq 0} &= -\frac{N_c|q_f|B}{(2\pi)^2}\sum_{n=0}^{\infty}\sum_{s=\pm 1}\int \mathrm{d}p_z\frac{M_f}{E^{(n)}_{p_z,s,f}} + \frac{N_c|q_f|B}{(2\pi)^2}\int dp_z\frac{M_f}{E^{(0)}_{p_z,f}} \\
&= -\frac{N_c|q_f|B}{(2\pi)^2}\sum_{n=0}^{\infty}\sum_{s=\pm 1}\left(\frac{1}{\pi}\right)\int \mathrm{d}p_z\int_{-\infty}^{\infty}\mathrm{d}p_4\frac{M_f}{p_4^2+\left(E^{(n)}_{p_z,s,f}\right)^2} \\
&\quad +\frac{N_c|q_f|B}{(2\pi)^2}\int \mathrm{d}p_z\frac{M_f}{E^{(0)}_{p_z,f}} \\
&= I_1 + I_2,
\end{aligned} \tag{2.61}$$

where $E^{(0)}_{p_z,f} = \sqrt{M_f^2+(p_z-\mu_5)^2}$ and $E^{(n)}_{p_z,s,f} = \sqrt{M_f^2+(\sqrt{p_z^2+2n|q_f|B}-s\mu_5)^2}$. Both the integrals, $I_1$ and $I_2$, diverge at large momentum, these integrals need to be regularized. We use MSS to regularize these integrals. The MSS has been applied for the case of finite chiral chemical potential and vanishing magnetic field in Ref. [168]. In the present case we keep both the magnetic field $B\neq 0$ and the chiral chemical potential $\mu_5\neq 0$. The integral $I_1$ can be regularized by adding and subtracting the similar term with non-zero magnetic field ($B\neq 0$) and $\mu_5=0$,

$$\begin{aligned}
\frac{1}{p_4^2+\left\{E^{(n)}_{p_z,s,f}\right\}^2} &= \frac{1}{p_4^2+\left\{\epsilon^{(n)}_{p_z,f}\right\}^2} - \frac{1}{p_4^2+\left\{\epsilon^{(n)}_{p_z,f}\right\}^2} + \frac{1}{p_4^2+\left\{E^{(n)}_{p_z,s,f}\right\}^2} \\
&= \frac{1}{p_4^2+\left\{\epsilon^{(n)}_{p_z,f}\right\}^2} + \frac{A+2s\mu_5\sqrt{p_z^2+2n|q_f|B}}{\left(p_4^2+\left\{\epsilon^{(n)}_{p_z,f}\right\}^2\right)\left(p_4^2+\left\{E^{(n)}_{p_z,s,f}\right\}^2\right)},
\end{aligned} \tag{2.62}$$

where $\epsilon^{(n)}_{p_z,f} = \sqrt{M_{0_f}^2+p_z^2+2n|q_f|B}$ and $A = M_{0_f}^2 - M_f^2 - \mu_5^2$. Using the identity given in Eq. (2.62) twice we can write the integrand of the integral $I_1$, as given in

Eq. (2.61), in the following way,

$$\frac{1}{p_4^2+\left\{E^{(n)}_{p_z,s,f}\right\}^2}=\frac{1}{p_4^2+\left\{\epsilon^{(n)}_{p_z,f}\right\}^2}+\frac{A+2s\mu_5\sqrt{p_z^2+2n|q_f|B}}{\left(p_4^2+\left\{\epsilon^{(n)}_{p_z,f}\right\}^2\right)^2}$$
$$+\frac{\left(A+2s\mu_5\sqrt{p_z^2+2n|q_f|B}\right)^2}{\left(p_4^2+\left\{\epsilon^{(n)}_{p_z,f}\right\}^2\right)^3}+\frac{\left(A+2s\mu_5\sqrt{p_z^2+2n|q_f|B}\right)^3}{\left(p_4^2+\left\{\epsilon^{(n)}_{p_z,f}\right\}^2\right)^3\left(p_4^2+\left\{E^{(n)}_{p_z,s,f}\right\}^2\right)}. \tag{2.63}$$

Now, let's perform $p_4$ integration, we obtain (for details see Appendix A.2),

$$I_1=I_{1_{\text{quad}}}-\frac{M_f(M_{0_f}^2-M_f^2+2\mu_5^2)}{2}I_{1_{\log}}+I_{1_{\text{finite1}}}+I_{1_{\text{finite2}}}, \tag{2.64}$$

where

$$I_{1_{\text{quad}}}=-\frac{N_c|q_f|B}{(2\pi)^2}\sum_{n=0}^{\infty}\sum_s\int dp_z\frac{M_f}{\epsilon^{(n)}_{p_z,f}}, \tag{2.65}$$

$$I_{1_{\log}}=\frac{N_c|q_f|B}{(2\pi)^2}\sum_{n=0}^{\infty}\sum_s\int dp_z\frac{1}{\left(\epsilon^{(n)}_{p_z,f}\right)^3}, \tag{2.66}$$

$$I_{1_{\text{finite1}}}=-\frac{N_c|q_f|B}{(2\pi)^2}\sum_{n=0}^{\infty}\sum_s\int dp_z\left(\frac{3}{8}\right)\frac{\left(M_fA^2-4M_f\mu_5^2M_{0_f}^2\right)}{\left(\epsilon^{(n)}_{p_z,f}\right)^5}, \tag{2.67}$$

and

$$I_{1_{\text{finite2}}}=-\frac{N_c|q_f|B}{(2\pi)^2}\left(\frac{15}{16}\right)\sum_{n=0}^{\infty}\sum_s\int dp_z\int_0^1 dx \quad\times$$
$$\frac{(1-x)^2M_f\left(A+2s\mu_5\sqrt{p_z^2+2n|q_f|B}\right)^3}{\left[\left(\epsilon^{(n)}_{p_z,f}\right)^2-x(A+2s\mu_5\sqrt{p_z^2+2n|q_f|B})\right]^{7/2}}. \tag{2.68}$$

The integrals $I_{1_{\text{quad}}}$ and $I_{1_{\log}}$ are UV divergent. On the other hand $I_{1_{\text{finite1}}}$ and $I_{1_{\text{finite2}}}$ are finite.

Similarly, the integral $I_2$ given in Eq. (2.61) can be written as,

$$I_2 = I_{2_{\rm finite}} + I_{2_{\rm log}}, \tag{2.69}$$

where

$$I_{2_{\rm finite}} = \left(\frac{1}{2}\right)\frac{N_c|q_f|B}{(2\pi)^2}\int \mathrm{d}p_z \int_0^1 \mathrm{d}x \frac{M_f(A+2p_z\mu_5)}{\left[\left(\epsilon^{(0)}_{p_z,f}\right)^2 - x(A+2p_z\mu_5)\right]^{3/2}}, \tag{2.70}$$

and

$$I_{2_{\rm log}} = \frac{N_c|q_f|B}{(2\pi)^2}\int \mathrm{d}p_z \frac{M_f}{\epsilon^{(0)}_{p_z,f}}. \tag{2.71}$$

Using Eqs. (2.64) and (2.69), $\langle\bar\psi_f\psi_f\rangle^{\mu_5\neq0}_{vac,B\neq0}$ can be expressed as,

$$\langle\bar\psi_f\psi_f\rangle^{\mu_5\neq0}_{vac,B\neq0} = -\frac{M_f(M^2_{0_f}-M^2_f+2\mu_5^2)}{2} I_{1_{\rm log}} + I_{1_{\rm finite1}} + I_{1_{\rm finite2}} + I_{2_{\rm finite}} + I_{\rm quad},$$

where

$$\begin{aligned} I_{\rm quad} &= I_{1_{\rm quad}} + I_{2_{\rm log}} \\ &= \frac{M_f}{M_{0_f}}\left[-\frac{N_c|q_f|B}{(2\pi)^2}\sum_{n=0}^{\infty}\sum_s\int \mathrm{d}p_z\frac{M_{0_f}}{\epsilon^{(n)}_{p_z,f}} + \frac{N_c|q_f|B}{(2\pi)^2}\int \mathrm{d}p_z \frac{M_{0_f}}{\epsilon^{(0)}_{p_z,f}}\right] \end{aligned} \tag{2.72}$$

Each integral in $I_{\rm quad}$ is divergent. Using dimensional regularization, we get the regularized $I_{\rm quad}$ (see Appendix A.2, Eq. (A.14) and Eq. (A.25)),

$$\begin{aligned} I_{\rm quad} &= \frac{M_f}{M_{0_f}}\left[-\frac{N_c|q_f|B}{(2\pi)^2}\sum_{n=0}^{\infty}\sum_s\int \mathrm{d}p_z\frac{M_{0_f}}{\epsilon^{(n)}_{p_z,f}} + \frac{N_c|q_f|B}{(2\pi)^2}\int \mathrm{d}p_z \frac{M_{0_f}}{\epsilon^{(0)}_{p_z,f}}\right] \\ &= I^{field}_{\rm quad} + I^{vac}_{\rm quad}, \end{aligned} \tag{2.73}$$

where

$$I^{field}_{\rm quad} = -\frac{N_c M_f|q_f|B}{2\pi^2}\left[x_{0_f}(1-\ln x_{0_f}) + \ln\Gamma(x_{0_f}) + \frac{1}{2}\ln\left(\frac{x_{0_f}}{2\pi}\right)\right] \tag{2.74}$$

$$I^{vac}_{\rm quad} = -\frac{N_c M_f}{2\pi^2}\left[\Lambda\sqrt{M^2_{0_f}+\Lambda^2} - M^2_{0_f}\ln\left(\frac{\Lambda+\sqrt{\Lambda^2+M^2_{0_f}}}{M_{0_f}}\right)\right] \tag{2.75}$$

Similarly the term $I_{1_{\log}}$ has UV divergence. The regularization of it can be done using dimensional regularization. In the dimensional regularization scheme we get (see Appendix A.2, Eq. (A.28)),

$$I_{1_{\log}} = \frac{N_c|q_f|B}{(2\pi)^2}\sum_{n=0}^{\infty}\sum_{s}\int dp_z\frac{1}{\left(\epsilon^{(n)}_{p_z,f}\right)^3} = I^{field}_{1_{\log}} + I^{vac}_{1_{\log}}, \tag{2.76}$$

here

$$I^{field}_{1_{\log}} = -\frac{N_c}{2\pi^2}\left[-\ln x_{0_f} + \frac{\Gamma'(x_{0_f})}{\Gamma(x_{0_f})}\right], \tag{2.77}$$

$$I^{vac}_{1_{\log}} = \frac{N_c}{\pi^2}\left[\ln\left(\frac{\Lambda}{M_{0_f}} + \sqrt{1+\frac{\Lambda^2}{M^2_{0_f}}}\right) - \frac{\Lambda}{\sqrt{\Lambda^2+M^2_{0_f}}}\right]. \tag{2.78}$$

Hence the regularized chiral condensate of quark flavour $f$ with non-vanishing magnetic field and chiral chemical potential using MSS for vanishing quark chemical potential is given as,

$$\begin{aligned}\langle\bar{\psi}_f\psi_f\rangle^{\mu_5\neq0}_{B\neq0} = &-\frac{M_f(M^2_{0_f}-M_f^2+2\mu_5^2)}{2}I_{1_{\log}} + I_{1_{\text{finite1}}} + I_{1_{\text{finite2}}} + I_{2_{\text{finite}}} + I_{\text{quad}}\\ &+\frac{N_c|q_f|B}{2\pi^2}\left[\int_{-\infty}^{\infty}dp_z\frac{M_f}{E^{(0)}_{p_z,f}}f_{\text{FD}}(E^{(0)}_{p_z,f})\right.\\ &\left.+\sum_{n=1}^{\infty}\sum_{s}\int_{-\infty}^{\infty}dp_z\frac{M_f}{E^{(n)}_{p_z,s,f}}f_{\text{FD}}(E^{(n)}_{p_z,s,f})\right]\end{aligned} \tag{2.79}$$

where the regularized $I_{\text{quad}}$ and $I_{1_{\log}}$ are given in Eqs. (2.76) and (2.73) respectively. This makes the expression for $\langle\bar{\psi}_f\psi_f\rangle^{\mu_5\neq0}_{B\neq0}$ finite which we shall use later for the calculation of constituent quark mass $(M_f)$ for non-vanishing magnetic field and chiral chemical potential. Note that for the estimation of constituent quark mass $(M_f)$ for non-vanishing magnetic field and chiral chemical potential one requires constituent quark mass $M_{0_f}$ for non-vanishing magnetic field and vanishing chiral chemical potential which can be obtained from Eq. (2.59).

## 2.4 Chiral susceptibility

The fluctuations and the correlations are the important characteristics of any physical system. They provide the essential information about the effective degrees of freedom and their possible quasi-particle nature. These fluctuations and correlations are connected with susceptibility. Susceptibility is the response of the system to small external forces. The chiral susceptibility measures the response of the chiral condensate to the infinitesimal change of the current quark mass. Chiral susceptibility in two flavour NJL model can be defined as,

$$\begin{aligned}\chi_c &= \frac{\partial\langle\bar{\psi}\psi\rangle}{\partial m} \\ &= \frac{\partial\langle\bar{\psi}_u\psi_u\rangle}{\partial m} + \frac{\partial\langle\bar{\psi}_d\psi_d\rangle}{\partial m} = \chi_{cu} + \chi_{cd}\end{aligned} \tag{2.80}$$

Using Eq. (2.53), we get $\chi_{cu}$ and $\chi_{cd}$ as,

$$\chi_{cu} = \frac{\partial\langle\bar{\psi}_u\psi_u\rangle}{\partial m} = \frac{\partial\langle\bar{\psi}_u\psi_u\rangle}{\partial M_u}\left(1 - 4G_1\frac{\partial\langle\bar{\psi}_u\psi_u\rangle}{\partial m} - 4G_2\frac{\partial\langle\bar{\psi}_d\psi_d\rangle}{\partial m}\right), \tag{2.81}$$

$$\chi_{cd} = \frac{\partial\langle\bar{\psi}_d\psi_d\rangle}{\partial m} = \frac{\partial\langle\bar{\psi}_d\psi_d\rangle}{\partial M_d}\left(1 - 4G_1\frac{\partial\langle\bar{\psi}_d\psi_d\rangle}{\partial m} - 4G_2\frac{\partial\langle\bar{\psi}_u\psi_u\rangle}{\partial m}\right). \tag{2.82}$$

By solving Eqs. (2.81) and (2.82) for $\chi_{cu}$ and $\chi_{cd}$, we get,

$$\chi_{cu} = \frac{\partial\langle\bar{\psi}_u\psi_u\rangle}{\partial M_u}\frac{1 - 4G_2\chi_{cd}}{1 + 4G_1\frac{\partial\langle\bar{\psi}_u\psi_u\rangle}{\partial M_u}}, \tag{2.83}$$

$$\chi_{cd} = \frac{\partial\langle\bar{\psi}_d\psi_d\rangle}{\partial M_d}\frac{1 - 4G_2\chi_{cu}}{1 + 4G_1\frac{\partial\langle\bar{\psi}_d\psi_d\rangle}{\partial M_d}}. \tag{2.84}$$

and by solving Eqs. (2.83) and (2.84), we get,

$$\chi_{cu} = \frac{\partial\langle\bar{\psi}_u\psi_u\rangle}{\partial M_u}\left\{\frac{1 + 4(G_1 - G_2)\frac{\partial\langle\bar{\psi}_d\psi_d\rangle}{\partial M_d}}{\left(1 + 4G_1\frac{\partial\langle\bar{\psi}_u\psi_u\rangle}{\partial M_u}\right)\left(1 + 4G_1\frac{\partial\langle\bar{\psi}_d\psi_d\rangle}{\partial M_d}\right) - 16G_2^2\frac{\partial\langle\bar{\psi}_u\psi_u\rangle}{\partial M_u}\frac{\partial\langle\bar{\psi}_d\psi_d\rangle}{\partial M_d}}\right\}, \tag{2.85}$$

$$\chi_{cd} = \frac{\partial\langle\bar{\psi}_d\psi_d\rangle}{\partial M_d}\left\{\frac{1 + 4(G_1 - G_2)\frac{\partial\langle\bar{\psi}_u\psi_u\rangle}{\partial M_u}}{\left(1 + 4G_1\frac{\partial\langle\bar{\psi}_u\psi_u\rangle}{\partial M_u}\right)\left(1 + 4G_1\frac{\partial\langle\bar{\psi}_d\psi_d\rangle}{\partial M_d}\right) - 16G_2^2\frac{\partial\langle\bar{\psi}_u\psi_u\rangle}{\partial M_u}\frac{\partial\langle\bar{\psi}_d\psi_d\rangle}{\partial M_d}}\right\}. \tag{2.86}$$

Hence, to get the chiral susceptibilities for $u$ and $d$ quarks, we have to estimate $\frac{\partial\langle\bar{\psi}_f\psi_f\rangle}{\partial M_f}$. However, it is important to note that like chiral condensate, chiral susceptibility also contains a UV divergence. Hence the $\frac{\partial\langle\bar{\psi}_f\psi_f\rangle}{\partial M_f}$ term also has to be regularized. Using Eq. (2.59), for vanishing chemical potential ($\mu = 0$) and vanishing chiral chemical potential ($\mu_5 = 0$) in the presence of magnetic field we get,

$$\begin{aligned}
\frac{\partial\langle\bar{\psi}_f\psi_f\rangle^{\mu_5=0}_{B\neq0}}{\partial M_{0_f}} =& -\frac{2N_c}{(2\pi)^3}\int_{|\vec{p}|\leq\Lambda} d^3p\left[\frac{1}{\sqrt{p^2+M_{0_f}^2}}-\frac{M_{0_f}^2}{\sqrt{(p^2+M_{0_f}^2)^3}}\right] \\
&-\frac{N_c|q_f|B}{2\pi^2}\left[x_{0_f}(1-\ln x_{0_f})+\ln\Gamma(x_{0_f})+\frac{1}{2}\ln\left(\frac{x_{0_f}}{2\pi}\right)\right] \\
&-\frac{N_cM_{0_f}^2}{2\pi^2}\left[-\ln x_{0_f}+\frac{1}{2x_{0_f}}+\frac{\Gamma'(x_{0_f})}{\Gamma(x_{0_f})}\right] \\
&+\sum_{n=0}^{\infty}\frac{N_c|q_f|B}{\pi^2}(2-\delta_{n,0})\int_0^\infty dp_z\left[\frac{1}{\epsilon^{(n)}_{p_z,f}}f_{\text{FD}}\left(\epsilon^{(n)}_{p_z,f}\right)-\frac{M_{0_f}^2}{(\epsilon^{(n)}_{p_z,f})^3}f_{\text{FD}}\left(\epsilon^{(n)}_{p_z,f}\right)\right. \\
&\left.-\frac{1}{T}\left(\frac{M_{0_f}}{\epsilon^{(n)}_{p_z,f}}\right)^2 f_{\text{FD}}\left(\epsilon^{(n)}_{p_z,f}\right)\left(1-f_{\text{FD}}\left(\epsilon^{(n)}_{p_z,f}\right)\right)\right]
\end{aligned} \tag{2.87}$$

$\frac{\partial\langle\bar{\psi}_f\psi_f\rangle^{\mu_5=0}_{B\neq0}}{\partial M_{0_f}}$ as given in Eq. (2.87) is regularized and it can be used to calculate the individual chiral susceptibilities $\chi_{cu}$, $\chi_{cu}$ and the total chiral susceptibility $\chi_c$ in the presence of a finite magnetic field and vanishing chiral chemical potential. To estimate the chiral susceptibility at non-vanishing magnetic field and chiral chemical potential we have to estimate the regularized $\frac{\partial\langle\bar{\psi}_f\psi_f\rangle}{\partial M_f}$ at finite $B$ and $\mu_5$. This regularization has been done using the MSS regularization scheme.

### 2.4.1 Regularization of the chiral susceptibility in the presence of a magnetic field and a chiral chemical potential

For non-vanishing magnetic field ($B$) and chiral chemical potential ($\mu_5$) for $\mu = 0$, using Eq. (2.55) the variation of chiral condensate with constituent quark mass is written as,

$$\frac{\partial\langle\bar{\psi}_f\psi_f\rangle^{\mu_5\neq0}_{B\neq0}}{\partial M_f} = \frac{\partial\langle\bar{\psi}_f\psi_f\rangle^{\mu_5\neq0}_{vac,B\neq0}}{\partial M_f} + \frac{\partial\langle\bar{\psi}_f\psi_f\rangle^{\mu_5\neq0}_{med,B\neq0}}{\partial M_f}. \tag{2.88}$$

Here the first term (the "vacuum" term) is given as,

$$\begin{aligned}\frac{\partial\langle\bar{\psi}_f\psi_f\rangle^{\mu_5\neq0}_{vac,B\neq0}}{\partial M_f} &= -\frac{N_c|q_f|B}{(2\pi)^2}\sum_{n=0}^{\infty}\sum_{s=\pm1}\int dp_z\frac{1}{E^{(n)}_{p_z,s,f}}+\frac{N_c|q_f|B}{(2\pi)^2}\int dp_z\frac{1}{E^{(0)}_{p_z,f}}\\ &+\frac{N_c|q_f|B}{(2\pi)^2}\sum_{n=0}^{\infty}\sum_{s=\pm1}\int dp_z\frac{M_f^2}{\left(E^{(n)}_{p_z,s,f}\right)^3}-\frac{N_c|q_f|B}{(2\pi)^2}\int dp_z\frac{M_f^2}{\left(E^{(0)}_{p_z,f}\right)^3}\\ &= \mathbf{I}_1+\mathbf{I}_2+\mathbf{I}_3+\mathbf{I}_4,\end{aligned}\tag{2.89}$$

and the other term (the medium dependent term) is given as,

$$\begin{aligned}\frac{\partial\langle\bar{\psi}_f\psi_f\rangle^{\mu_5\neq0}_{med,B\neq0}}{\partial M_f} &= \frac{N_c|q_f|B}{(2\pi)^2}\int dp_z\frac{1}{E^{(0)}_{p_z,f}}\left(2f_{\mathrm{FD}}(E^{(0)}_{p_z,f})\right)-\frac{N_c|q_f|B}{(2\pi)^2}\int dp_z\frac{M_f^2}{(E^{(0)}_{p_z,f})^3}\left(2f_{\mathrm{FD}}(E^{(0)}_{p_z,f})\right)\\ &-\frac{N_c|q_f|B}{(2\pi)^2}\int dp_z\frac{M_f^2}{(E^{(0)}_{p_z,f})^2}\left(\frac{2}{T}\right)f_{\mathrm{FD}}(E^{(0)}_{p_z,f})\left(1-f_{\mathrm{FD}}(E^{(0)}_{p_z,f})\right)\\ &+\frac{N_c|q_f|B}{(2\pi)^2}\sum_{n=1}^{\infty}\sum_{s=\pm1}\int dp_z\frac{1}{E^{(n)}_{p_z,s,f}}\left(2f_{\mathrm{FD}}(E^{(n)}_{p_z,s,f})\right)\\ &-\frac{N_c|q_f|B}{(2\pi)^2}\sum_{n=1}^{\infty}\sum_{s=\pm1}\int dp_z\frac{M_f^2}{(E^{(n)}_{p_z,s,f})^3}\left(2f_{\mathrm{FD}}(E^{(n)}_{p_z,s,f})\right)\\ &-\frac{N_c|q_f|B}{(2\pi)^2}\sum_{n=1}^{\infty}\sum_{s=\pm1}\int dp_z\frac{M_f^2}{(E^{(n)}_{p_z,s,f})^2}\left(\frac{2}{T}\right)f_{\mathrm{FD}}(E^{(n)}_{p_z,s,f})\left(1-f_{\mathrm{FD}}(E^{(n)}_{p_z,s,f})\right)\end{aligned}\tag{2.90}$$

The medium dependent term is convergent and does not need any regularization. On the other hand the "vacuum" term is not convergent. The integrals, $\mathbf{I}_1$, $\mathbf{I}_2$, and $\mathbf{I}_3$ are divergent and need regularization. We perform the MSS as done for the chiral condensate. The regularized $\frac{\partial\langle\bar{\psi}_f\psi_f\rangle^{\mu_5\neq0}_{vac,B\neq0}}{\partial M_f}$ can be expressed as (see Appendix A.4, Eq. (A.59)),

$$\begin{aligned}\frac{\partial\langle\bar{\psi}_f\psi_f\rangle^{\mu_5\neq0}_{vac,B\neq0}}{\partial M_f} &= -\left(\frac{M_{0_f}^2-M_f^2+2\mu_5^2}{2}\right)\mathbf{I}_{1,\log}\\ &+\mathbf{I}_{1,\text{finite1}}+\mathbf{I}_{1,\text{finite2}}+\mathbf{I}_{2,\text{finite}}+\mathbf{I}_{3,\text{finite}}\\ &+\mathbf{I}_{\text{finite}}+\mathbf{I}_{\text{quad}}+\mathbf{I}_{\log},\end{aligned}\tag{2.91}$$

where regularized $\mathbf{I}_{\text{quad}}, \mathbf{I}_{\log}, \mathbf{I}_{1,\log}$ can be expressed as (see Appendix A.4, Eq. (A.61), Eq. (A.62), Eq. (A.63),

$$\begin{aligned}\mathbf{I}_{\text{quad}} &= -\frac{N_c|q_f|B}{(2\pi)^2}\sum_{n=0}^{\infty}\sum_{s=\pm1}\int dp_z \frac{1}{\epsilon^{(n)}_{p_z,f}} + \frac{N_c|q_f|B}{(2\pi)^2}\int dp_z \frac{1}{\epsilon^{(0)}_{p_z,f}}\\ &= -\frac{N_c|q_f|B}{2\pi^2}\left[x_{0_f}(1-\ln x_{0_f}) + \ln\Gamma(x_{0_f}) + \frac{1}{2}\ln\left(\frac{x_{0_f}}{2\pi}\right)\right]\\ &\quad -\frac{N_c}{2\pi^2}\left[\Lambda\sqrt{\Lambda^2+M_{0_f}^2} - M_{0_f}^2\ln\left(\frac{\Lambda+\sqrt{\Lambda^2+M_{0_f}}}{M_{0_f}}\right)\right],\end{aligned} \tag{2.92}$$

$$\begin{aligned}\mathbf{I}_{\log} &= \frac{N_c|q_f|B}{(2\pi)^2}\sum_{n=0}^{\infty}\sum_{s=\pm1}\int dp_z \frac{M_f^2}{(\epsilon^{(n)}_{p_z,f})^3} - \frac{N_c|q_f|B}{(2\pi)^2}\int dp_z \frac{M_f^2}{(\epsilon^{(0)}_{p_z,f})^3}\\ &= -\frac{N_c M_f^2}{2\pi^2}\left[-\ln x_{0_f} + \frac{1}{2x_{0_f}} + \frac{\Gamma'(x_{0_f})}{\Gamma(x_{0_f})}\right]\\ &\quad +\frac{N_c M_f^2}{\pi^2}\left[\ln\left(\frac{\Lambda+\sqrt{\Lambda^2+M_{0_f}^2}}{M_{0_f}}\right) - \frac{\Lambda}{\sqrt{\Lambda^2+M_{0_f}^2}}\right],\end{aligned} \tag{2.93}$$

$$\begin{aligned}\mathbf{I}_{1,\log} &= \frac{N_c|q_f|B}{(2\pi)^2}\sum_{n=0}^{\infty}\sum_{s=\pm1}\int dp_z \frac{1}{(\epsilon^{(n)}_{p_z,f})^3}\\ &= -\frac{N_c}{2\pi^2}\left[-\ln x_{0_f} + \frac{\Gamma'(x_{0_f})}{\Gamma(x_{0_f})}\right] + \frac{N_c}{\pi^2}\left[\ln\left(\frac{\Lambda+\sqrt{\Lambda^2+M_{0_f}^2}}{M_{0_f}}\right) - \frac{\Lambda}{\sqrt{\Lambda^2+M_{0_f}^2}}\right],\end{aligned} \tag{2.94}$$

and the convergent integrals $\mathbf{I}_{1,\text{finite1}}, \mathbf{I}_{1,\text{finite2}}, \mathbf{I}_{2,\text{finite}}, \mathbf{I}_{3,\text{finite}}$ and $\mathbf{I}_{\text{finite}}$ are given as

$$\mathbf{I}_{1,\text{finite1}} = -\frac{N_c|q_f|B}{(2\pi)^2}\sum_{n=0}^{\infty}\sum_{s=\pm1}\int dp_z \left(\frac{3}{8}\right)\frac{A^2 - 4\mu_5^2 M_f^2}{\left(\epsilon^{(n)}_{p_z,f}\right)^5}, \tag{2.95}$$

$$\begin{aligned}\mathbf{I}_{1,\text{finite2}} = -\frac{N_c|q_f|B}{(2\pi)^2}\left(\frac{15}{16}\right)\sum_{n=0}^{\infty}\sum_{s=\pm1}\int dp_z \int_0^1 dx \quad \times\\ \frac{(1-x)^2\left(A+2s\mu_5\sqrt{p_z^2+2n|q_f|B}\right)^3}{\left[(\epsilon^{(n)}_{p_z,f})^2 - x\left(A+2s\mu_5\sqrt{p_z^2+2n|q_f|B}\right)\right]^{7/2}}\end{aligned} \tag{2.96}$$

$$\mathbf{I}_{2,\text{finite}} = \left(\frac{1}{2}\right)\frac{N_c|q_f|B}{(2\pi)^2}\int dp_z \int_0^1 dx \frac{A+2p_z\mu_5}{\left[\left(\epsilon^{(0)}_{p_z,f}\right)^2 - x(A+2p_z\mu_5)\right]^{3/2}} \tag{2.97}$$

$$\mathbf{I}_{3,\text{finite}} = \frac{N_c|q_f|B}{(2\pi)^2}\sum_{n=0}^{\infty}\sum_{s=\pm 1}\int dp_z M_f^2\left(\frac{1}{(E^{(n)}_{p_z,s,f})^3} - \frac{1}{\left(\epsilon^{(n)}_{p_z,f}\right)^3}\right) \tag{2.98}$$

$$\mathbf{I}_{\text{finite}} = -\frac{N_c|q_f|B}{(2\pi)^2}\int dp_z M_f^2\left(\frac{1}{\left(E^{(0)}_{p_z,f}\right)^3} - \frac{1}{\left(\epsilon^{(0)}_{p_z,f}\right)^3}\right). \tag{2.99}$$

For non-vanishing magnetic field and chiral chemical potential Eqs. (2.90) and (2.91) along with Eqs. (2.85) and (2.86) can be used to calculate chiral susceptibility ($\chi_c$).

## 2.5 Results and discussion

Let us note that the Lagrangian as given in Eq. (2.51) has the following parameters, two couplings $G_1$, $G_2$, the three momentum cutoff $\Lambda$ and the current quark masses $m_u$ and $m_d$. To study the effects of flavour mixing, the couplings $G_1$ and $G_2$ are parametrized as $G_2 = \alpha g$, $G_1 = (1-\alpha)g$ [34]. The extent of flavour mixing is controlled by $\alpha$. For the numerical studies we take the parameters $m_u = m_d = 6$ MeV, the three momentum cut off : $\Lambda = 590$ MeV and the scalar coupling: $g = 2.435/\Lambda^2$. For these values of the parameters, pion vacuum mass is 140.2 MeV, pion decay constant is 92.6 MeV and the quark condensates are $\langle\bar{\psi}_u\psi_u\rangle = \langle\bar{\psi}_d\psi_d\rangle$ = $(-241.5)$ MeV$^3$. This parameter set also leads to a vacuum constituent quark mass 400 MeV. It may be relevant here to mention that in the absence of magnetic field the two condensates $\langle\bar{\psi}_u\psi_u\rangle = \langle\bar{\psi}_d\psi_d\rangle$ and therefore the gap equation (2.53) depends upon the sum of the two couplings $(G_1 + G_2)$ which is independent of $\alpha$. Thus the masses $M_u$ and $M_d$ are the same and do not depend upon $\alpha$, in the absence of magnetic field.

Next we discuss about choosing the parameter $\alpha$. One can fix the parameter $\alpha$ from the mass of the iso-scalar pseudo scalar particle that arises in the spectrum because of breaking of $U(1)_A$ symmetry. In a two flavour case, this meson can be identified with the $\eta$ meson. The mass of $\eta$ meson can be given approximately by [181],

$$m_\eta^2 = m_\pi^2 + \frac{G_2 M^2}{(G_1^2 - G_2^2)f_\pi^2}. \tag{2.100}$$

Clearly, for $\alpha = 0.5$, the $\eta$ meson disappear from the spectrum. With the physical mass of the $\eta$-meson ($m_\eta = 547.8$ MeV); the above equation lead to a value of $\alpha \simeq 0.09$. On the other hand, a description of $\eta$-meson without strange quarks is not realistic and therefore a better way to fix $\alpha$ is from the three flavour NJL model in which case the determinant interaction become a six fermion interaction and leads to $\eta - \eta'$ splitting. In such a case, e.g. the gap equation for $M_u$ become [34],

$$M_u = m_u - 4G\langle\bar{\psi}_u\psi_u\rangle + 2K\langle\bar{\psi}_s\psi_s\rangle\langle\bar{\psi}_d\psi_d\rangle. \tag{2.101}$$

Comparing the constituent quark mass as given in Eq. (2.53), we can identify $G_1 = G$ and $G_2 = -\frac{1}{2}K\phi_s$, where $\phi_s \equiv \langle\bar{\psi}_s\psi_s\rangle$ is the strange quark condensate. Thus using the strange quark condensate we can express $\alpha$ as [34],

$$\alpha = \frac{-\frac{1}{2}K\phi_s}{G - \frac{1}{2}K\phi_s}. \tag{2.102}$$

The parameters $G, K, \langle\bar{\psi}_s\psi_s\rangle$ are fixed from fitting the masses of the pseudo scalar octet. In particular, the determinant interaction parameter $K$ is fixed from the $\eta - \eta'$ mass difference. Even in such cases, the value of $\alpha$ can vary about 25% to 30 % (i.e.from $\alpha$=0.21 to $\alpha$=0.16) depending upon the parametrization chosen. This wide variation in $\alpha$ has to do with the different ways $\eta'$ is treated in the model. Since NJL model does not confine and $M_{\eta'}$ lies above the threshold for $q\bar{q}$ decay with an unphysical imaginary part of the corresponding polarization diagram. This is an unavoidable feature of NJL model and leaves an uncertainty that is reflected in difference in the parameters of the determinant interaction. Further, it may be mentioned here that, in a different context of spontaneous CP violation in strong interactions, in Ref. [182, 183] it has been argued that $0 \leq \alpha \leq 0.5$ so that spontaneous parity violation is not there for QCD at zero temperature and density for $\theta = 0$ in accordance with Vafa-Witten theorem. In the present work, we have considered the cases when $\alpha = 0$ i.e. no flavour mixing, $\alpha = 0.5$ when both the couplings are same and a value for $\alpha = 0.15$ between these two limits to examine the effects of instanton induced flavour mixing interaction in the presence of magnetic field that breaks the isospin symmetry.

In Fig. 2.1 we plot the constituent quark masses and the associated chiral susceptibility as a function of temperature ($T$) for different values of chiral chemical potential ($\mu_5$) at vanishing magnetic fields. At zero magnetic field $\langle\bar{\psi}_u\psi_u\rangle = \langle\bar{\psi}_d\psi_d\rangle$, hence the constituent quark masses of the $u$ and $d$ quarks remain same. From the left plot of Fig. 2.1 it is clear that the constituent mass decreases with increasing chiral chemical potential. One can understand this result in the following way, the chiral chemical potential is a conserved number of the associated chiral symmetry. Chiral symmetry is an exact symmetry when the fermions are massless. Chiral symmetry tries to protect the mass of the fermion from quantum corrections. Hence the chiral chemical potential which is the measure of the chiral symmetry tries to reduce the mass of the fermion. This decreasing behaviour of the

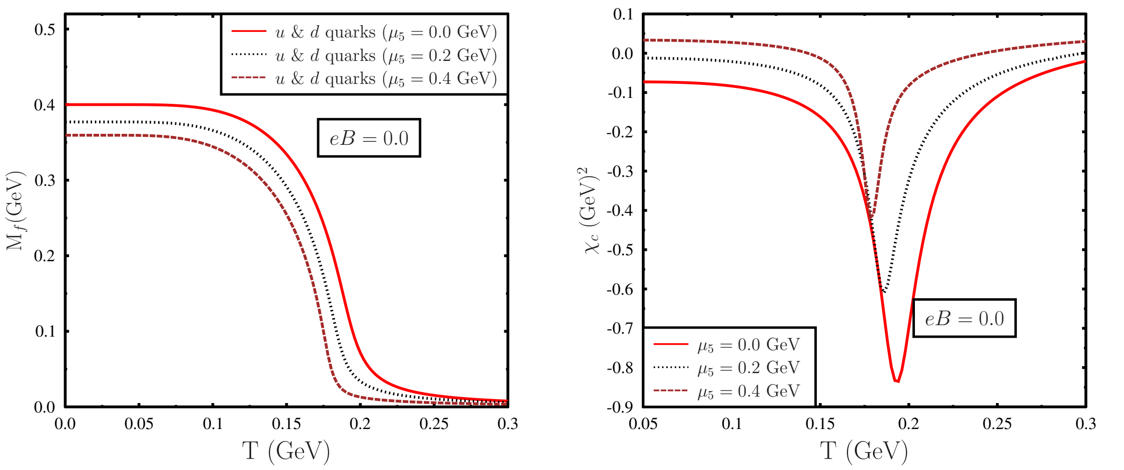


FIGURE 2.1: Constituent quark mass ($M_u = M_d$) as a function of temperature ($T$) at zero magnetic field and at different values of chiral chemical potential ($\mu_5$) (left plot). It is clear from the left plot, the constituent quark mass decreases with increasing temperature. Chiral susceptibility $\chi_c$ as a function of temperature ($T$) for zero magnetic field and with various values of chiral chemical potential ($\mu_5$) (right plot). The peaks in the $\chi_c$ plot define the chiral transition temperature. From the right plot, it is clear that the transition temperature decreases with increasing chiral chemical potential.

constituent quark mass with chiral chemical potential is in contrast with other calculations [165, 171]. Further, we also observe that the chiral transition is a smooth cross-over as in Ref. [165] and no first order phase transition is observed even for chiral chemical potential as large as 0.4 GeV unlike in Ref. [171]. It ought to be mentioned here that while the vacuum quark mass satisfies a gap equation with a cutoff in the three momentum, for the thermal contribution no such cutoff was used similar to the Ref. [171, 184], as the distribution functions make the corresponding contribution convergent.

In the right plot of Fig. 2.1 we show the chiral susceptibility as a function of temperature for vanishing quark chemical potential and magnetic field. The peak in the chiral susceptibility plot which defines the chiral transition temperature shifts towards the low temperature as we increase the chiral chemical potential. This decreasing chiral transition temperature behaviour with $\mu_5$ is similar to Ref. [39]. Using Eq. (2.85) and Eq. (2.86), it can be shown that $\chi_{cu} = \chi_{cd}$ for a vanishing magnetic field. Hence the chiral susceptibility has only one peak. Further the height of the peak decreases with $\mu_5$ and we do not observe any sharp peak which indicates the first order transition. It is also observed in Ref. [165]. However in the presence of magnetic fields $\chi_{cu}$ and $\chi_{cd}$ are different, so the variation of total chiral susceptibility $\chi_c$ with temperature can have multiple peaks. From the right plot we can say that the chiral transition temperature decreases with increasing chiral chemical potential. We would like to mention here that in Ref. [171] for vanishing magnetic field, an opposite behaviour regarding chiral transition temperature was observed i.e. $T_c$ increases with $\mu_5$. However, the parameters of the NJL model chosen there were different compared to the parameters taken here or in Ref. [34]. We have also verified that taking parameters of Ref. [171] $T_c$ increases with $\mu_5$.

It may be relevant here to compare this behaviour of $T_c$ with $\mu_5$, Such a decreasing behaviour of $T_c$ with $\mu_5$ was also observed in PNJL model, however, the nature of the transition was a first order transition at some critical value of chiral chemical potential [39]. On the other hand, a non local NJL analysis showed the critical temperature to increase with $\mu_5$ [165]. A careful analysis in Ref.[171] shows different behaviour of $T_c$ with $\mu_5$. In Ref.[171] it has been shown that if a cutoff is given to the thermal part also then $T_c$ increases with $\mu_5$ while not giving any cutoff decreases $T_c$ with $\mu_5$. On the other hand we have applied here a medium separation scheme to remove cutoff artefact as was done in Ref.[168, 172, 173]. However, our result for vanishing magnetic field showed a opposite behaviour i.e. $T_c$ decreases with $\mu_5$. It turns out that the behaviour of $T_c$ with $\mu_5$ depends upon the parameter chosen. A stronger scalar coupling as we have taken leads to $T_c$ decreasing with $\mu_5$ while a weaker scalar coupling shows a mild increase in $T_c$ with $\mu_5$ [168]. We therefore feel a deeper understanding is still required to understand the opposite behaviour of $T_c$ with $\mu_5$ with change in the scalar coupling. With the parameters considered here, while the behaviour of $T_c$ decreasing with $\mu_5$ is consistent with Ref. [171], the transition itself seems to be a smooth crossover leading to absence of a critical point in the $(\mu_5, T)$ plane of the phase diagram [165, 171].

In Fig. 2.2 we plot the variation of the constituent quark masses $M_u$ and $M_d$ with temperature for vanishing chiral chemical potential and with finite magnetic field for different values of $\alpha$. From this figure it is clear that at a non vanishing magnetic field constituent quark mass increases. At the vanishing magnetic field the constituent masses of $u$ and $d$ quarks are the same. Although in the presence of magnetic field, quark condensates $\langle\bar{\psi}_u\psi_u\rangle \neq \langle\bar{\psi}_d\psi_d\rangle$, but for $\alpha = 0.5$ the quark masses $M_u = M_d$. This is because for $\alpha = 0.5$ constituent quark mass is $M_f = m - 2g(\langle\bar{\psi}_u\psi_u\rangle + \langle\bar{\psi}_d\psi_d\rangle)$, as can be seen from Eq. (2.53). On the other hand, for $\alpha \neq 0.5$ quark masses $M_u$ and $M_d$ are not the same. The difference between $M_u$ and $M_d$ increases with decrease in the value of $\alpha$ and this difference is largest when $\alpha = 0.0$. $\alpha = 0.0$ corresponds to the case when there is no flavour mixing interaction, and $\alpha = 0.5$ corresponds to maximal flavour mixing. It is important to note that for vanishing magnetic field flavour mixing interaction does not affect the quark masses. Only in the presence of magnetic field when $\langle\bar{\psi}_u\psi_u\rangle \neq \langle\bar{\psi}_d\psi_d\rangle$, flavour mixing interaction affects the constituent quark masses $M_u$ and $M_d$ significantly.

In Fig.(2.3) we show the variation of constituent quark masses $M_u$ and $M_d$ and the associated total chiral susceptibility, with temperature for vanishing chiral chemical potential and with different values of magnetic field for $\alpha = 0.5$. It has been already mentioned that for $\alpha = 0.5$ even in the presence of magnetic field $M_u = M_d$. From the left plot in Fig.(2.3) it is clear that with increasing magnetic

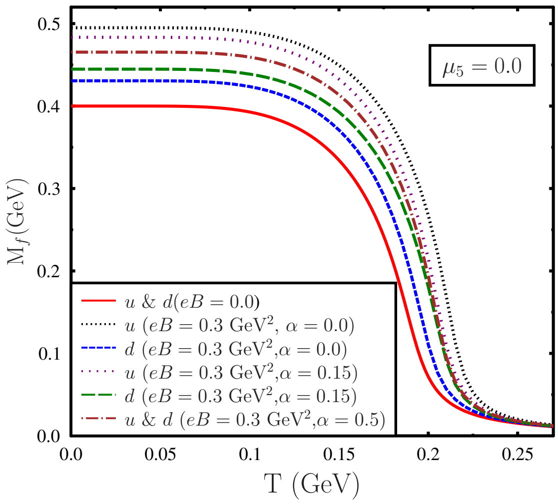


FIGURE 2.2: Constituent quark masses $M_u$ and $M_d$ as a function of temperature for vanishing chiral chemical potential ($\mu_5$) and finite magnetic field for different values of $\alpha$. Constituent quark masses $M_u$ and $M_d$ are the same for vanishing magnetic fields. In the presence of magnetic field and $\alpha = 0.5$, although $\langle\bar{\psi}_u\psi_u\rangle \neq \langle\bar{\psi}_d\psi_d\rangle$, the constituent quark masses $M_u = M_d$ and for $\alpha \neq 0.5$, the constituent quark masses $M_u \neq M_d$.

field constituent quark mass increases. On the other hand from the right plot in Fig.(2.3) it is clear that chiral transition temperature increases with increasing magnetic field.

In Fig.(2.4) we show the variation of constituent quark masses $M_u$ and $M_d$ and the associated total chiral susceptibility, with temperature for vanishing chiral chemical potential and with different values of magnetic field for $\alpha = 0.0$. For $\alpha = 0.0$ there is no flavour mixing. From the left plot it is clear that at finite magnetic field $M_u \neq M_d$. This is because in the presence of magnetic field $u$ and $d$ quark condensates are different and in the absence of flavour mixing for $\alpha = 0.0$, $M_u$ is independent of $\langle\bar{\psi}_d\psi_d\rangle$. Similarly $M_d$ is independent of $\langle\bar{\psi}_u\psi_u\rangle$ for $\alpha = 0.0$. From the right plot in Fig.(2.4) it is clear that chiral transition temperature increases with increasing magnetic field. However it is important to mention that unlike the case when $\alpha = 0.5$, in this case susceptibility plot shows two distinct peaks at relatively large magnetic field values. In fact these two peaks are associated with $u$ and $d$ quarks, which has been shown in Fig.(2.5). In the left plot of Fig.(2.5) we show $\chi_{cu}$, $\chi_{cd}$ and $\chi_c$ for $eB = 0.4\text{GeV}^2$ and $\alpha = 0.0$. On the other hand In the right plot of Fig.(2.5) we show $\chi_{cu}$, $\chi_{cd}$ and $\chi_c$ for $eB = 0.4\text{GeV}^2$ and $\alpha = 0.5$. From the left plot in Fig.(2.5) it is clear that for $\alpha = 0.0$, i.e. in the absence of flavour mixing, at relatively large magnetic field chiral susceptibility $\chi_c$ shows two distinct peaks.

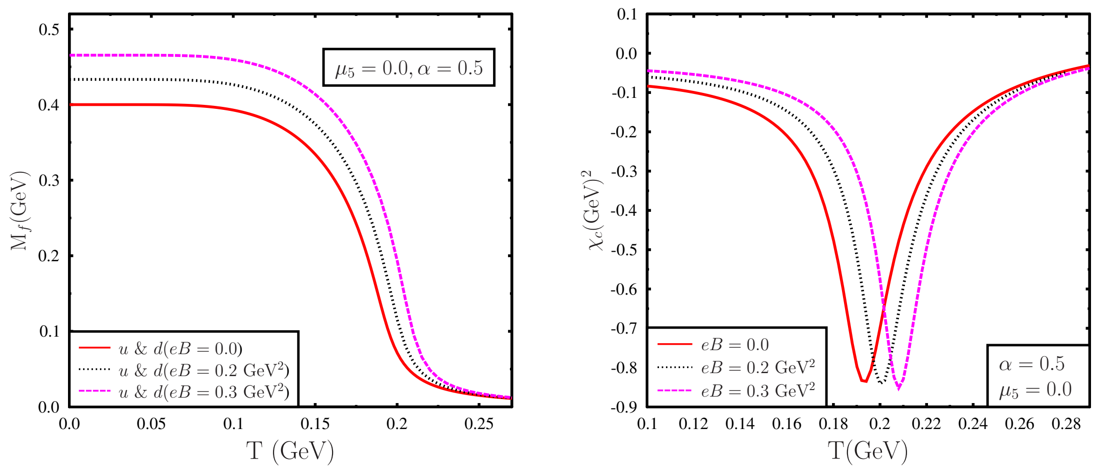


FIGURE 2.3: Constituent quark masses ($M_u$ and $M_d$) as the function of temperature ($T$) for vanishing chiral chemical potential ($\mu_5$) at different values of magnetic field for $\alpha = 0.5$. The constituent quark masses increase with increasing magnetic field (see left plot). The chiral susceptibility $\chi_c$ as a function of temperature ($T$) for the vanishing chiral chemical potential $\mu_5$ at different values of magnetic field for $\alpha = 0.5$ (right plot). It is clear from the right plot that the transition temperature increases with increasing magnetic field.

These two peaks are associated with $u$ and $d$ quarks. At relatively large magnetic field with $\alpha = 0.0$, chiral restoration of $d$ quark happens at relatively low temperature with respect to the $u$ quarks. This is due to the fact that at non zero magnetic field $M_u > M_d$, as can be seen in Fig.(2.4). On the other hand from the right plot in Fig.(2.5) we can see that, although $\langle\bar{\psi}_u\psi_u\rangle \neq \langle\bar{\psi}_d\psi_d\rangle$, $\chi_{cu}$ and $\chi_{cd}$ shows peak at same temperature. Hence for $\alpha = 0.5$, at finite magnetic field chiral transition temperature for $u$ and $d$ quarks are same.

In Fig. 2.5, we show the individual chiral susceptibilities $\chi_{cu}$, $\chi_{cd}$ and the total chiral susceptibility $\chi_c$ for $eB = 0.4\text{GeV}^2$ and $\alpha = 0.0$ (left plot) and $\alpha = 0.5$ (right plot) as a function of temperature. In the left plot, it is seen that the chiral susceptibility $\chi_c$ shows two distinct peaks, which are associated to the $u$ and $d$ quarks, for $\alpha = 0.0$ at a relatively large magnetic field. At a relatively large magnetic field with $\alpha = 0.0$, chiral restoration of $d$ quark happens at a relatively low temperature with respect to the $u$ quarks. This is because at a non-zero magnetic field $M_u > M_d$, as it can be seen in Fig. 2.4. On the other hand, in the right plot, we can see that although $\langle\bar{\psi}_u\psi_u\rangle \neq \langle\bar{\psi}_d\psi_d\rangle$, $\chi_{cu}$ and $\chi_{cd}$ show peak at same temperature, this is because $\alpha = 0.5$ gives the maximal mixing and hence at finite magnetic field chiral transition temperature for $u$ and $d$ quarks are the same.

Finally, in Fig. 2.6 we show the variation of constituent quark masses $M_u$ and

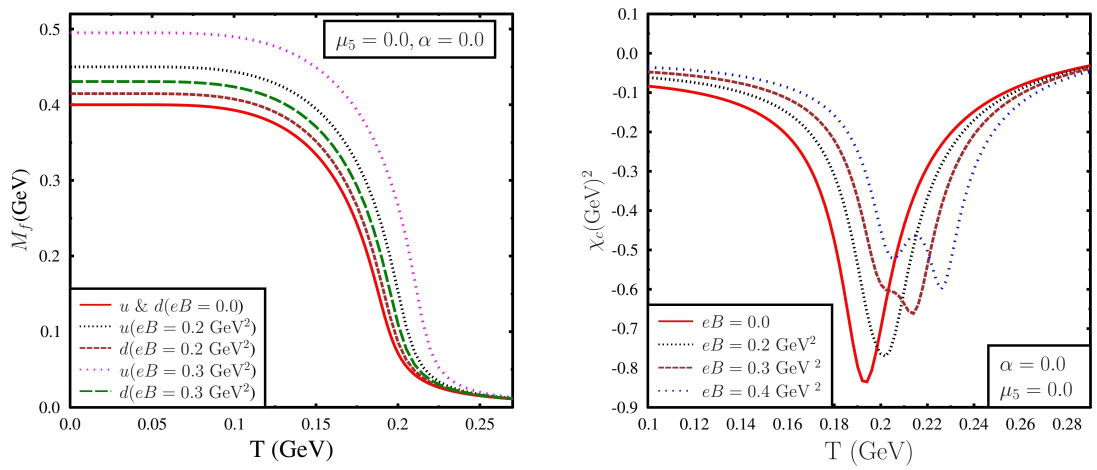


FIGURE 2.4: Constituent quark masses $M_u$ and $M_d$ as the functions with temperature $T$ for vanishing chiral chemical potential ($\mu_5$) at finite magnetic fields for $\alpha = 0.0$. The constituent quark mass increases with increasing magnetic field (left plot). The chiral susceptibility $\chi_c$ as a function of temperature ($T$) for vanishing chiral chemical potential ($\mu_5$) at a finite magnetic field for $\alpha = 0.5$. The transition temperature is different for different quarks at higher magnetic fields (right plot).

$M_d$ and the associated susceptibilities $\chi_{cu}$ and $\chi_{cd}$ with temperature at finite magnetic field and finite chiral chemical potential ($\mu_5$) while $\alpha = 0.5$. The variation of constituent quark masses and associated chiral susceptibilities with temperature are the same for different values of $\alpha$. Left plot of the Fig. 2.6 shows that the constituent quark mass decreases with increasing chiral chemical potential at finite magnetic fields. This behaviour is also manifested in the right plot of Fig. 2.6, which shows that the chiral transition temperature decreases with increasing chiral chemical potential.

## 2.6 Summary and conclusion

Some of the previous studies show the chiral transition temperature decreases with the chiral chemical potential [39] and some of them show it increases with chiral chemical potential [171]. The behaviour depends on the regularisation schemes used in the study. But the first principle calculation (Lattice QCD calculation) shows that the chiral transition temperature increases which is similar to our study where we investigated a brand new approach to study the chiral phase transition. In this study we have seen the chiral phase transition and the associated chiral susceptibility of the medium produced in the relativistic heavy-ion collisions at

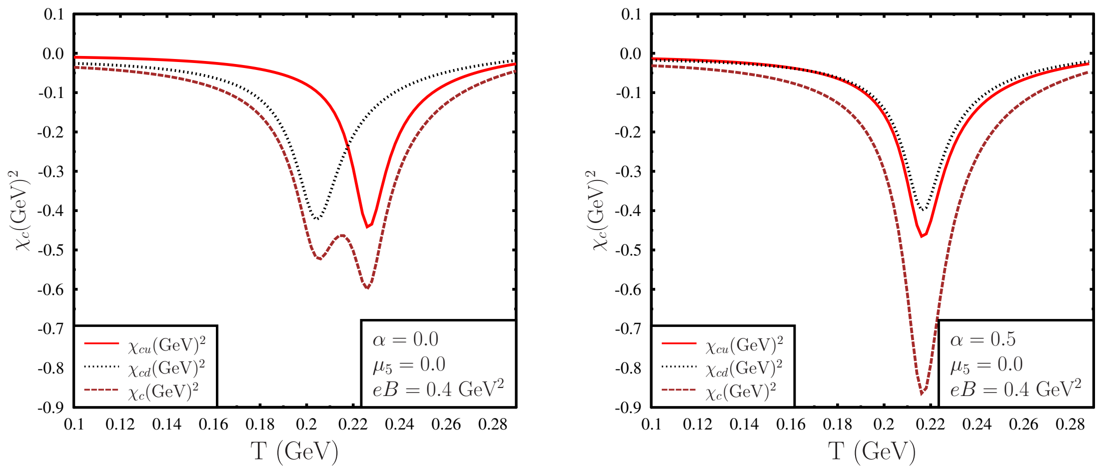


FIGURE 2.5: Individual chiral susceptibilities of $u$ and $d$ quarks $\chi_{cu}$, $\chi_{cd}$ and total chiral susceptibility $\chi_c$ as a function of temperature at vanishing chiral chemical potential ($\mu_5$) at $eB = 0.4\,\mathrm{GeV}^2$ and $\alpha = 0.0$ (left plot). Individual chiral susceptibilities of $u$ and $d$ quarks $\chi_{cu}$, $\chi_{cd}$ and the total chiral susceptibility $\chi_c$ as a function of temperature at vanishing chiral chemical potential ($\mu_5$) at $eB = 0.4\,\mathrm{GeV}^2$ and $\alpha = 0.5$. From the left plot it is clear that chiral susceptibility shows two distinct peaks at large magnetic fields. This is due to the large magnetic field difference between $M_u$ and $M_d$ is large. On the other hand right plot shows that, for $\alpha = 0.5$, $\langle\bar{\psi}_u\psi_u\rangle \neq \langle\bar{\psi}_d\psi_d\rangle$, $\chi_{cu}$ and $\chi_{cd}$ shows peak at same temperature. Hence for $\alpha = 0.5$, at finite magnetic field chiral transition temperature for $u$ and $d$ quarks are the same.

vanishing quark chemical potential using Wigner function within the framework of two flavour NJL model. For a dynamical system like the medium produced in relativistic heavy-ion collision, the quantum effects can be relevant. Hence the quantum kinetic equation is a suitable formalism to understand the evolution of these dynamical systems. The central quantity of the quantum kinetic description is the Wigner function. Each component of the Wigner function satisfies the quantum kinetic equation. However in this investigation we have constrained ourselves to the case of global equilibrium so that $T$ and $\mu_5$ are constant and we do not consider evolution of the Wigner function.

We have looked into the behaviour of the constituent quark masses and associated chiral susceptibilities within the two flavour NJL model with flavour mixing determinant interaction. At a vanishing magnetic field, $u$ and $d$ quark masses are degenerate because of isospin symmetry. However at a non-vanishing magnetic field, due to different electric charge of $u$ and $d$ quark, the constituent quark masses $M_u$ and $M_d$ can be different depending on the value of mixing parameter $\alpha$. For non-maximal flavour mixing ($\alpha \neq 0.5$) the constituent quark masses are

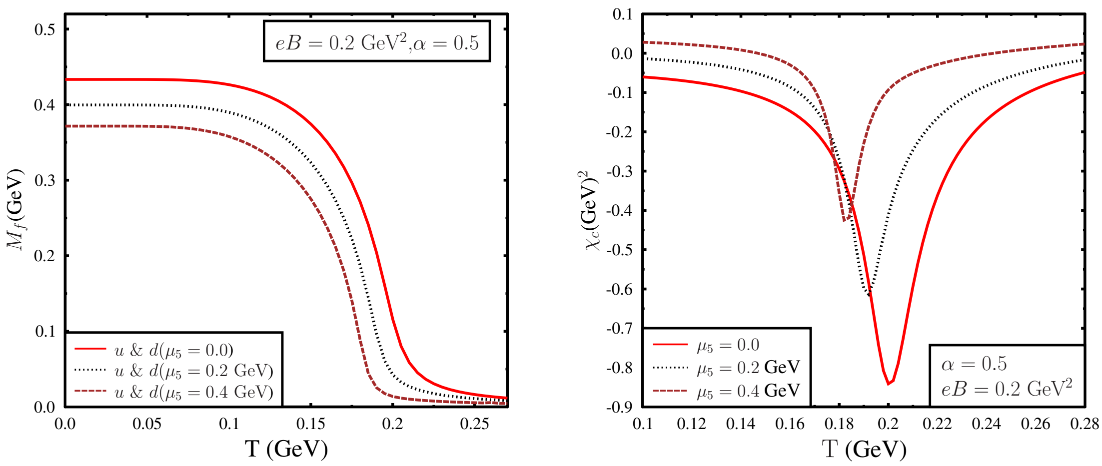


FIGURE 2.6: Constituent quark masses $M_u = M_d$ as the function of temperature $T$ at non-vanishing magnetic field and chiral chemical potential ($\mu_5$) (left plot). The chiral susceptibility $\chi_c$ as a function of temperature $T$ at non-vanishing magnetic field and chiral chemical potential $\mu_5$. It is clear that the chiral transition temperature and constituent quark mass decreases with increasing chiral chemical potential.

non-degenerate in the presence of magnetic field while for maximal mixing the magnetic field does not affect the constituent quark masses. The constituent quark masses $M_u$ and $M_d$ are larger for non-vanishing magnetic fields compared to their vanishing magnetic field counterpart. With increasing magnetic field constituent quark masses also increase. Apart from this, the chiral transition temperature is higher for non-vanishing magnetic fields compared to the vanishing magnetic field case. This is the manifestation of magnetic catalysis i.e. in the presence of magnetic field the formation of chiral condensate is more probable, also the magnitude of the chiral condensate is higher for larger magnetic fields. It is important to note that in the presence of non-maximal flavour mixing instanton interaction, the chiral transition temperatures of $u$ and $d$ quarks are the same for vanishing magnetic fields. But for larger magnetic fields, the transition temperatures of $u$ and $d$ quarks are different. The difference between the transition temperatures of $u$ and $d$ quarks also increases with increasing magnetic field. We have also shown that non-vanishing chiral chemical potential reduces constituent quark mass at vanishing as well as non-vanishing magnetic field. Unlike magnetic catalysis, the chiral transition temperature decreases with increasing the chiral chemical potential. Also note that in the presence of magnetic field, the chiral susceptibility shows a double peak structure because the isospin symmetry breaks down in presence of magnetic field.

# Chapter 3

# Transport properties and Seebeck coefficient

Heavy-ion collision experiments conducted at particle accelerators allow us to study the properties of fundamental constituents of nature, quarks and gluons. Experiments at RHIC and LHC indicate the formation of such a deconfined medium of quarks and gluons. The partonic medium produced in heavy-ion collision behaves like a strongly interacting liquid with a smallest value of shear viscosity ($\eta$) to entropy density ($s$) ratio $(\eta/s)$. It expands, cools down and undergoes a transition from the strongly interacting partonic medium (QGP) to the hadronic phase and finally free streams to the detector. One of the successful descriptions of the bulk evolution of such strongly interacting matter has been through relativistic hydrodynamics. Transport coefficients are the important inputs that enter in such a dissipative hydrodynamic description as well as in transport simulations that have been used to describe the evolution of such matter produced in a heavy-ion collision. In this chapter we shall study the transport properties of the strongly interacting partonic medium produced in heavy-ion collisions like electrical conductivity, thermal conductivity and Seebeck coefficient etc.

## 3.1 Introduction

Hydrodynamic studies of the heavy-ion collisions suggest that the medium produced in heavy-ion collisions has a very small ratio of shear viscosity to entropy density ($\eta/s$) [185–187]. It is amongst the smallest of known materials suggesting that the QGP is the most perfect fluid. The value of this ratio estimated from experiments is also found to be very close to the conjectured Kovtun-Son-Starinet (KSS) bound on the value of $\eta/s$ [187]. Just like shear viscosity determines the response to transverse momentum gradients, there are other transport coefficients such as bulk viscosity, electrical conductivity, etc. which determine the response of the system to other such perturbations. Bulk viscosity [60, 188–192] determines the response to bulk stresses. It scales with the conformal anomaly ($\frac{\epsilon-3P}{T^4}$) and is expected to be large near the phase transition as inferred from LQCD calculations [193, 194]. The effects of such a large bulk viscosity to entropy ratio have been investigated on the particle spectrum and flow coefficients [195, 196]. Electrical conductivity ($\sigma_{el}$) [58, 197–214] is also important as the heavy-ion collisions may be associated with large electromagnetic fields. The magnetic field produced in non-central collisions has been estimated to be of the order of $m_\pi^2$ ($\sim 10^{18}$ Gauss) at RHIC energy scales [107, 108, 215–220]. Such magnetic fields are amongst the strongest magnetic fields produced in nature and can affect various properties of the strongly interacting medium. They may also lead to interesting $\mathcal{CP}$ violating effects such as CME etc [221]. In a conducting medium the evolution of the magnetic field depends on the electrical conductivity. Electrical conductivity modifies the decay of the magnetic field substantially in comparison with the decay of the magnetic field in vacuum. Hence the estimation of the electrical conductivity of the strongly interacting medium is important regarding the decay of the magnetic field produced at the initial stages of heavy-ion collision. These transport coefficients have been estimated in pQCD and effective models [202, 222–241]. At finite baryon densities, the other transport coefficient that is relevant is the coefficient of thermal conductivity and has been studied in Refs. [242, 243] both in the hadronic matter as well as partonic matter.

In the present chapter, we investigate the thermoelectric response of the strongly interacting matter produced in a heavy-ion collision. It is well known from a condensed matter system that a temperature gradient can result in the generation of an electric current. This is known as the Seebeck effect. Due to temperature gradient, there is a non zero gradient of charge density leading to the generation of an electric field. A measure of the electric field produced in a conducting medium due to a temperature gradient is the Seebeck coefficient which is defined as the ratio of an electric field to the temperature gradient in the limit of vanishing electric current. Seebeck effect has been extensively studied in condensed matter systems such as superconductors, quantum dots, high-temperature cuprates, superconductor-ferromagnetic tunnel junctions, low dimensional organic metals, etc [40–48]. Such a phenomenon could also be present in the thermal medium created in relativistic heavy-ion collisions. In condensed matter systems, because of one type of dominant charge carriers, only a temperature gradient is required for thermoelectric effect in the systems while in the strongly interacting medium produced in heavy-ion collision both positive and negative charges contribute to transport phenomena. In case of vanishing baryon chemical potential with equal numbers of particles and antiparticles we do not see any thermoelectric effect. Thus a finite baryon chemical potential is required for the thermoelectric effect. The strongly interacting matter with finite baryon density can be produced in low energy heavy-ion collisions at e.g. FAIR and NICA. Along with the temperature gradient, we also consider a gradient in the baryon (quark) chemical potential to investigate the Seebeck coefficient. The gradient in quark chemical potential has effects similar to the temperature gradient. Using Gibbs-Duhem relation for a static medium one can express the gradient in the baryon (quark) chemical potential to a gradient in temperature. Effect of the gradient in chemical potential significantly affects the thermoelectric coefficients Ref. [49].

Seebeck effect in hadronic matter has been investigated within the framework of the hadron resonance gas (HRG) model [49, 50]. However, the HRG model describes only the hadronic medium at chemical freezeout whereas one expects a deconfined partonic medium at the early stages of the heavy-ion collisions. In this chapter, we investigate the thermoelectric behavior of the deconfined partonic medium within the framework of the NJL model. The Seebeck coefficient has also been estimated for the partonic matter within relaxation time approximation (RTA) in Refs. [51, 52]. However, this has been attempted with the relaxation time estimated within pQCD which may only be valid for asymptotically high temperatures. Further, it ought to be mentioned that, the vacuum structure of QCD remains nontrivial near the critical temperature region with nonvanishing values for the quark-antiquark condensates associated with DCSB as well as Polyakov loop condensates associated with the physics of statistical confinement [53–56]. Indeed, within the NJL model, it was shown that the temperature dependence of viscosity coefficients exhibits interesting behavior of phase transition with the shear viscosity to entropy ratio showing a minimum while the coefficient of bulk viscosity showing a maximum at the phase transition [53, 54, 57]. The crucial reason for this behavior was the estimation of relaxation time using medium dependent masses for the quarks as well as the exchanged mesons which reveal nontrivial dependence before and after the transition temperature. This motivates to investigate the behavior of thermoelectric transport coefficients within the NJL model which takes into account the medium dependence of quark and meson masses. This model has been used to study different transport properties of quark matter at high temperatures [57–60] and high densities [61–68]. Apart from the NJL model, we also use use quasi-particle model [244–246] which provides a reasonable thermodynamic and transport behavior of the deconfined phase.

We organize this chapter in the following manner. In Sec. 3.2, we discuss the Boltzmann equation within RTA and find the expressions for the different thermoelectric transport coefficients. In Sec. 3.3 we estimate the relaxation time within the two flavor NJL model. In Sec. 3.4 we discuss the quasi-particle model approach for the same in the absence of any quark-antiquark condensate. In Sec. 3.5 we present the results of different transport coefficients. Finally, in Sec. 3.6 we conclude our investigation.

## 3.2 Boltzmann equation in the relaxation time approximation and the transport coefficients

Within a quasi-particle approximation, a kinetic theory treatment for the calculation of transport coefficient can be a reasonable approximation therefore we shall be following similar to that in Refs. [60, 189, 225, 226, 247, 248]. The plasma can be described by a phase space density for each species of particle. Near the equilibrium, the distribution function can be expanded about a local equilibrium distribution function, $f^{(0)}$ for the quarks as,

$$f(\vec{x},\vec{p},t) = f^{(0)}(\vec{x},\vec{p}) + \delta f(\vec{x},\vec{p},t),$$

where $\delta f(\vec{x},\vec{p},t)$ is the deviation from the local equilibrium distribution function and

$$f^{(0)}(\vec{x},\vec{p}) = \left[\exp\left(\beta(\vec{x})\left(u_\nu p^\nu \mp \mu(\vec{x})\right)\right) + 1\right]^{-1}. \tag{3.1}$$

Here, $u^\mu = \gamma_u(1,\vec{u})$, is the flow four-velocity, where, $\gamma_u = (1-\vec{u}^2)^{1/2}$ and $\mu$ is the quark chemical potential associated with a conserved charge, $\beta = 1/T$ is the inverse of temperature. Further, $p^\mu = (E,\vec{p})$ is the particle four-momenta and the single particle energy $E = \sqrt{p^2+M^2}$ with $p = |\vec{p}|$. $M$ is the mass of the particle which, in general, is medium dependent. The departure of the system from its equilibrium is described by the Boltzmann equation,

$$\frac{df_a(\vec{x},\vec{p},t)}{dt} = \frac{\partial f_a}{\partial t} + \frac{dx^i}{dt}\frac{\partial f_a}{\partial x^i} + \frac{dp^i}{dt}\frac{\partial f_a}{\partial p^i} = C^a[f], \tag{3.2}$$

where the index '$a$' on the distribution function denotes the different species in the system. The term on the right-hand side of Eq.(3.2) is the collision term $C^a[f]$ which we shall discuss later. The left-hand side of the Eq.(3.2) involves the trajectory $\vec{x}(t)$ and the momentum $\vec{p}(t)$. In general, this trajectory is not a straight line as the particle is moving in a mean-field, it can be space-time dependent. The velocity of the particle '$a$' is defined as

$$\frac{dx^i}{dt} = \frac{\partial E_a}{\partial p_a^i} = \frac{p_a^i}{E_a} = v_a^i.$$

Next, the time derivative of momentum in presence of an electric field $(\vec{\mathcal{E}})$, in presence of magnetic field $(\vec{B})$ of a mean field dependent mass can be defined as

$$\frac{dp^i}{dt} = -\frac{\partial E_a}{\partial x^i} + q_a(\mathcal{E}^i + \epsilon^{ijk}v_j B_k).$$

After the substitution of the time derivatives of $\vec{x}$ and $\vec{p}$, the Boltzmann equation Eq.(3.2) reduces to

$$\frac{\partial f_a}{\partial t} + v^i\frac{\partial f_a}{\partial x^i} + \frac{\partial f_a}{\partial p^i}\left(-\frac{M_a}{E_a}\frac{\partial M_a}{\partial x^i} + q_a(\mathcal{E}^i + \epsilon^{ijk}v_j B_k)\right) = C^a[f]. \tag{3.3}$$

For the collision, we shall restrict ourselves to $2 \to 2$ scatterings only. In RTA, the collision term for the species $a$ is calculated by assuming that all the distribution functions are given by the equilibrium distribution function except the distribution function for particle $a$. The collision term, to first order in the deviation from the equilibrium function, will then be proportional to $\delta f_a$, given the fact that $C^a[f^{(0)}] = 0$ by the principle of local detailed balance. In that case, the collision term is given by

$$C[f] = -\frac{\delta f_a}{\tau_a}, \tag{3.4}$$

where, $\tau_a$ is the relaxation time for particle '$a$'. In general relaxation time is a function of energy. The left-hand side of the Boltzmann equation Eq.(3.3) is explicitly small because of the gradients and we, therefore, may replace $f_a$ by $f_a^{(0)}$. While the spatial derivative of the distribution function is given by,

$$\begin{aligned}\frac{\partial f_a^{(0)}}{\partial x^i} &= -f_a^{(0)}(1-f_a^{(0)})\partial_i(\beta E_a - \beta\mu_a)\\ &= -f_a^{(0)}(1-f_a^{(0)})\Big(-\frac{E_a}{T^2}\partial_i T + \beta\frac{M_a}{E_a}\frac{\partial M_a}{\partial x^i} - \partial_i(\beta\mu_a)\Big),\end{aligned} \tag{3.5}$$

here $\mu_a = b_a\mu$, $b_a$ being the quark number i.e. $b_a = 1$ for quarks and $b_a = -1$ for antiquarks. The momentum derivative of the equilibrium distribution function is given by,

$$\frac{\partial f_a^{(0)}}{\partial p^i} = -\frac{1}{T}f_a^{(0)}(1-f_a^{(0)})v_a^i. \tag{3.6}$$

Substituting Eqs.(3.6) and (3.5) in the Boltzmann equation Eq.(3.3) for the static case in the absence of magnetic field, we have

$$-f_a^{(0)}(1-f_a^{(0)})\left[v_a^i\left(-\frac{1}{T^2}\partial_i T E_a - \partial_i(\beta\mu_a)\right) + q_a\beta v_a^i\mathcal{E}^i\right] = -\frac{\delta f_a}{\tau_a}. \tag{3.7}$$

The spatial gradients of temperature and chemical potential can be related using momentum conservation in the system and Gibbs-Duhem relation. Momentum conservation in a steady-state leads to $\partial_i P = 0$ ( $P$, being the pressure) [249]. Using Gibbs-Duhem relation, the pressure gradient can be written as,

$$\partial_i P = \frac{\omega}{T}\partial_i T + T n_q \partial_i(\mu/T) \tag{3.8}$$

which vanishes in steady-state. Where $\omega = \epsilon + P$ denotes the enthalpy, $n_q$ denotes the net quark number density and $\epsilon$ is the energy density. The above equation gives the relation between the spatial gradient in temperature and the spatial gradients in chemical potential and it is

$$\partial_i\mu = \left(\mu - \frac{\omega}{n_q}\right)\frac{\partial_i T}{T}. \tag{3.9}$$

Using Eqs.(3.9) and (3.7), one can find the deviation of the distribution function from the equilibrium $\delta f_a$ as,

$$\delta f_a = \frac{\tau_a f_a^0(1-f_a^0)}{T}\left[q_a\vec{v}_a\cdot\vec{\mathcal{E}} - \left(E_a - b_a\frac{\omega}{n_q}\right)\frac{\vec{v}_a\cdot\vec{\nabla}T}{T}\right]. \tag{3.10}$$

The non-equilibrium part of the distribution function gives rise to transport coefficients. The electric current ($\vec{J}$) is given as,

$$\begin{aligned}\vec{J} &= \sum_a g_a\int\frac{d^3p_a}{(2\pi)^3}\,q_a\vec{v}_a\,\delta f_a\\ &= \sum_a\frac{g_a q_a^2}{3T}\int\frac{d^3p_a}{(2\pi)^3}\,v_a^2\tau_a f_a^0(1-f_a^0)\,\vec{\mathcal{E}}\\ &\quad-\sum_a\frac{g_a q_a}{3T^2}\int\frac{d^3p_a}{(2\pi)^3}\,\tau_a\left(E_a-b_a\frac{\omega}{n_q}\right)f_a^0(1-f_a^0)v_a^2\,\vec{\nabla}T. \end{aligned}\tag{3.11}$$

Where $b_a=\pm1$ for quarks and antiquarks respectively. In Eq.(3.11), we have used $v_a^i v_a^j = \frac{1}{3}v_a^2\delta^{ij}$ as because the integrand only depends on the magnitude of momenta. Further, the sum is over all flavors including antiparticles. The degeneracy factor $g_a = 6$ corresponds to color and spin degrees of freedom.

Next, we write down the heat current $\vec{\mathcal{I}}$ associated with the conserved quark number. For a relativistic system, a thermal current arises corresponding to conserved particle number. The thermal conduction due to quarks arises when there is energy flow relative to enthalpy [249]. Therefore the heat current is defined as [249],

$$\mathcal{I}^i = \sum_a T_a^{0i} - \frac{\omega}{n_q}\sum_a b_a J_{qa}^i. \tag{3.12}$$

Here, $n_q$ is the net quark number density. The energy flux is given by $T^{0i}$, the spatio-temporal component of energy-momentum tensor ($T^{\mu\nu}$) [249],

$$T_a^{0i} = g_a\int\frac{d^3p_a}{(2\pi)^3}p_a^i f_a. \tag{3.13}$$

While the quark current is given $\vec{J}_q$ is given by

$$J_{qa}^i = g_a\int\frac{d^3p_a}{(2\pi)^3}\frac{p_a^i}{E_a}f_a b_a, \tag{3.14}$$

The contribution to the energy flux and quark current vanishes, arising from the equilibrium distribution function $f_a^{(0)}$ due to symmetry consideration and it is the only non-equilibrium part $\delta f_a$ which contributes to the energy flux and quark current. Substituting the expression for $\delta f_a$ from Eq.(3.10) in Eq.(3.12), the heat current

$\vec{\mathcal{I}}$ is given as,

$$\vec{\mathcal{I}} = \sum_a \frac{g_a}{3T} \int \frac{d^3p_a}{(2\pi)^3} f_a^0(1-f_a^0)\, v_a^2 \tau_a \quad \times \\ \left[q_a\left(E_a - b_a\frac{\omega}{n_q}\right)\vec{\mathcal{E}} - \left(E_a - b_a\frac{\omega}{n_q}\right)^2 \frac{\vec{\nabla}T}{T}\right] \tag{3.15}$$

The Seebeck coefficient $S$ is defined by setting the electric current $\vec{J} = 0$ in Eq.(3.11) so that the electric field becomes proportional to the temperature gradient i.e.

$$\vec{\mathcal{E}} = S\vec{\nabla}T. \tag{3.16}$$

Therefore, the Seebeck coefficient for the quark matter in the presence of a gradient in temperature and chemical potential can be expressed as,

$$S = \frac{\sum_a \frac{g_a q_a}{3T} \int \frac{d^3p_a}{(2\pi)^3} \tau_a v^2 \left(E_a - b_a\frac{\omega}{n_q}\right) f_a^{(0)}(1-f_a^{(0)})}{T\sum_a \frac{g_a}{3T} q_a^2 \int \frac{d^3p_a}{(2\pi)^3} v^2 \tau_a f_a^{(0)}(1-f_a^{(0)})} \tag{3.17}$$

The denominator of the Seebeck coefficient in the above may be identified as $T\sigma_{el}$, where the electrical conductivity $\sigma_{el}$ is given by [204, 250],

$$\sigma_{el} = \sum_a \frac{g_a}{3T} q_a^2 \int \frac{d^3p_a}{(2\pi)^3} \left(\frac{p_a}{E_a}\right)^2 \tau_a f_a^{(0)}(1-f_a^{(0)}) \tag{3.18}$$

which may be identified from Eq.(3.11). Let us note that, while the denominator of the Seebeck coefficient is positive definite, the numerator is not so as it is linearly dependent on the electric charge of the species as well as on the difference $(E_a - b_a\frac{\omega}{n_q})$. This makes the Seebeck coefficient not always positive definite. This is also observed in different condensed matter systems [251].

In terms of the electrical conductivity and the Seebeck coefficient, the electric current Eq. (3.11) can be written as

$$\vec{J} = \sigma_{el}\vec{\mathcal{E}} - \sigma_{el}S\vec{\nabla}T. \tag{3.19}$$

In a similar manner, the heat current as given in Eq.(3.15) can be written as,

$$\vec{\mathcal{I}} = T\sigma_{el}S\vec{\mathcal{E}} - \kappa_0\vec{\nabla}T, \tag{3.20}$$

where, $\kappa_0$, the thermal conductivity can be written as [249]

$$\kappa_0 = \sum_a \frac{g_a}{3T^2} \int \frac{d^3p_a}{(2\pi)^3} \tau_a \left(\frac{p_a}{E_a}\right)^2 \left(E_a - b_a\frac{\omega}{n_q}\right)^2 f_a^{(0)}(1-f_a^{(0)}). \tag{3.21}$$

Using Eqs.(3.19) and (3.20), we can express the heat current ($\vec{\mathcal{I}}$) in terms of electric current ($\vec{J}$) in the following way,

$$\vec{\mathcal{I}} = TS\vec{J} - \left(\kappa_0 - T\sigma_{el}S^2\right)\vec{\nabla}T. \tag{3.22}$$

From Eq.(3.22) we can identify the Peltier coefficient ($\Pi$) and thermal conductivity ($\kappa$) in the presence of nonvanishing Seebeck coefficient as,

$$\Pi = TS, \quad \kappa = \kappa_0 - T\sigma_{el}S^2. \tag{3.23}$$

Note that the relation between the Peltier coefficient ($\Pi$) and the Seebeck coefficient as given in Eq.(3.23) can be considered as the consistency relation. Also, note that the thermal conductivity in the absence of any thermoelectric effect as given in Eq. (3.21) matches with the expression of the thermal conductivity as reported in Ref. [249]. The Seebeck coefficient ($S$), thermal conductivity ($\kappa_0$), and the electrical conductivity ($\sigma_{el}$) depend upon, the relaxation time as well as the quark masses that goes into the distribution functions through the single-particle energies and are medium dependent. We estimate these quantities in the NJL model which is described in the next section.

## 3.3 Estimation of the relaxation time in the NJL model

We use the two flavor NJL model to estimate the thermodynamic quantities, the quasi particle masses in the medium and the relaxation time. The two flavour NJL Lagrangian is given below, as discussed in Sec. 1.3.2 [34],

$$\mathcal{L} = \bar{\psi}(i\partial\!\!\!/ - m_q)\psi + G\left[(\bar{\psi}\psi)^2 + (\bar{\psi}i\gamma^5\vec{\tau}\psi)^2\right]. \tag{3.24}$$

Where $\psi$ is the doublet of $u$ and $d$ quarks, $m_q$ is the current quark mass matrix which is diagonal with elements $m_u$ and $m_d$ and we assume the isospin symmetry i.e. $m_u = m_d$, $\vec{\tau}$ are the Pauli matrices in the flavor space and $G$ is the scalar coupling. The thermodynamic quantities e.g. pressure ($P$), energy density ($\epsilon$) and the number density ($n_q$) can be obtained once we know the thermodynamic potential of the NJL model. In a grand canonical ensemble, the thermodynamic potential ($\Omega$) or equivalently the pressure ($P$) can be expressed as,

$$P = -\Omega(\beta,\mu)$$

and

$$\Omega(\beta,\mu) = -\frac{2N_cN_f}{(2\pi)^3\beta}\int d\vec{k}\left[\log\left(1+e^{-\beta(E-\mu)}\right) + \log\left(1+e^{-\beta(E+\mu)}\right)\right] \\ -\frac{2N_cN_f}{(2\pi)^3}\int d\vec{k}\sqrt{\vec{k}^2+M^2} + \frac{(M-m_0)^2}{4G}.$$

In the above, $N_c = 3$ is the number of colors and $N_f = 2$ is the number of flavors, $E = \sqrt{\vec{k}^2 + M^2}$ is the single particle energy with constituent quark mass $M$ which satisfies the self consistent gap equation

$$M = m_0 + \frac{2N_cN_f}{(2\pi)^3}\int d\vec{k}\frac{M}{\sqrt{k^2+M^2}}(1 - f^{(0)} - \bar{f}^{(0)}). \tag{3.25}$$

In the above equations $f^{(0)} = (1+\exp(\beta\omega_-))^{-1}$ and $\bar{f}^{(0)} = (1+\exp(\beta\omega_+))^{-1}$ are the equilibrium distribution functions for quarks and antiquarks respectively and we have written $\omega_\pm(k) = E(\vec{k}) \pm \mu$ with $k \equiv |\vec{k}|$. The energy density $\epsilon$ is given by,

$$\epsilon = -\frac{2N_cN_f}{(2\pi)^3}\int d\vec{k}E(k)(1 - f^{(0)} - \bar{f}^{(0)}) + \frac{(M-m_0)^2}{4G}, \tag{3.26}$$

so that enthalpy $\omega = \epsilon + P$ is also defined once the solution to the mass gap equation, Eq.(3.25) is known. In these calculations, we have taken a three momentum cutoff $\Lambda$ to regularize the UV divergence. The net quark number density $n_q$ is given as

$$n_q = \frac{2N_cN_f}{(2\pi)^3}\int d\vec{k}(f^{(0)} - \bar{f}^{(0)}). \tag{3.27}$$

This completes the discussion on all the bulk thermodynamic quantities defined in NJL model which enters in the definitions for Seebeck coefficient, electrical conductivity and thermal conductivity.

Next we estimate relaxation time. For a process $a + b \to c + d$, the relaxation time for the particle $a$ i.e. $\tau_a(E_a)$ is given by [57],

$$\tau_a^{-1}(E_a) \equiv \tilde{\omega}(E_a) = \frac{1}{2E_a}\sum_b \int d\vec{\pi}_b W_{ab} f_b^{(0)}(E_b), \tag{3.28}$$

where the sum runs over all species other than "$a$". Further, in Eq.(3.28), we have introduced the notation $d\vec{\pi}_i = \frac{d^3p_i}{(2\pi)^3 2E_i}$ and $W_{ab}$ is the dimensionless transition rate for the processes with $a,\ b$ as the initial states. $W_{ab}$ which is Lorentz invariant and a function of the Mandelstam variable ($s$) can be written by,

$$\begin{aligned} W_{ab}(s) = \frac{1}{1+\delta_{ab}}\int d\vec{\pi}_c d\vec{\pi}_d (2\pi)^4 \delta(p_a + p_b - p_c - p_d) \quad \times \\ |\mathcal{M}|^2_{ab\to cd}\left(1 - f_c^{(0)}(p_c)\right)\left(1 - f_d^{(0)}(p_d)\right). \end{aligned} \tag{3.29}$$

In the expression of $W_{ab}$, the Pauli blocking factors have been considered. The quantity $W_{ab}$ can be related to the cross sections of various scattering processes. In the present case within the NJL model, the quark-quark, quark-antiquark and antiquark-antiquark scattering cross sections are calculated to order $1/N_c$ which occur through the $\pi$ and $\sigma$ meson exchanges in "$s$" and "$t$" channels. The meson propagator that enters into the scattering amplitude is calculated within the random phase approximation and includes their masses and the widths. The mass of the meson is estimated from the pole of the meson propagator at vanishing three momentum i.e.,

$$1 - 2G\,\mathrm{Re}\Pi_{\tilde{m}}(M_{\tilde{m}}, 0) = 0. \tag{3.30}$$

where $\tilde{m}$ denotes $\sigma, \pi$ for scalar and pseudoscalar channel mesons, respectively. Polarization function in the corresponding mesonic channel is expressed as $\Pi_{\tilde{m}}$. The explicit expressions for $\mathrm{Re}\Pi_{\tilde{m}}$ and the imaginary part $\mathrm{Im}\Pi_{\tilde{m}}$ is given in Ref. [57] and we do not repeat it here.

While the relaxation time is energy dependent, one can also define an energy independent mean relaxation time by taking a thermal average as,

$$\bar{\omega}_a \equiv \bar{\tau}_a^{-1} = \frac{1}{n_a}\int \frac{d^3p_a}{(2\pi)^3} f_a^{(0)}(E_a)\tilde{\omega}_a(E_a) \equiv \sum_b n_b \bar{W}_{ab}, \tag{3.31}$$

to get an estimate of the average relaxation time. In the above equation, the sum is over all the particles other than 'a';

$$n_a = \int \frac{d^3p_a}{(2\pi)^3} f_a^{(0)}(E_a),$$

is the number density of the species "$a$" apart from the degeneracy factor. Here, $\bar{W}_{ab}$ is the thermal-averaged transition rate given as

$$\bar{W}_{ab} = \frac{1}{n_a n_b}\int d\vec{\pi}_a d\vec{\pi}_b f(E_a) f(E_b) W_{ab}. \tag{3.32}$$

For the case of two flavors, there are 12 different processes but the corresponding matrix elements can be related using isospin symmetry, charge conjugation and crossing symmetries with only two independent matrix elements. We have chosen them to be the processes $u\bar{u} \to u\bar{u}$ and $u\bar{d} \to u\bar{d}$. The explicit expressions for the matrix elements are given in Refs. [57, 248]. It is important to mention that while the matrix elements of different scattering processes are related, the thermal-averaged rates are not. This is because the thermal averaged rates involve the thermal distribution functions for the initial states along with the Pauli blocking factors for the final states.

## 3.4 Quasiparticle picture of the partonic medium

In the quasiparticle description, all the quarks (anti quarks) have both the thermal mass $m_{\mathrm{th}}$ arising due to the interaction with the constituents of the medium and the bare mass $m_0$. Therefore, in the quasiparticle picture the total effective mass of the quark flavor $i$ can be expressed as [244–246, 252],

$$m_i^2 = (m_0 + m_+(T,\mu))^2 + m_+(T,\mu)^2, \tag{3.33}$$

with

$$2m_+^2(T,\mu) = \frac{g^2(T,\mu)T^2}{3}\left(1 + \frac{\mu^2}{\pi^2 T^2}\right). \tag{3.34}$$

which is related to the asymptotic form of the gauge independent hard thermal (dense) loop self energies. The temperature and the chemical potential dependent strong coupling constant up to two loop order is [253, 254],

$$\begin{aligned}\alpha_S(T,\mu) &= \frac{g^2(T,\mu)}{4\pi} \\ &= \frac{6\pi}{(33-2N_f)\ln\left(\frac{T}{\Lambda_T}\sqrt{1+\frac{\mu^2}{\pi^2T^2}}\right)} \times \\ &\quad \left(1 - \frac{3(153-19N_f)}{(33-2N_f)^2}\frac{\ln\left(2\ln\frac{T}{\Lambda_T}\sqrt{1+\frac{\mu^2}{\pi^2T^2}}\right)}{\ln\left(\frac{T}{\Lambda_T}\sqrt{1+\frac{\mu^2}{\pi^2T^2}}\right)}\right),\end{aligned} \tag{3.35}$$

where $\Lambda_T$ is the QCD scale parameter which we consider as $\Lambda_T = 0.35T_c$ with $T_c =$ 200 MeV [254]. The effective mass of the gluon, which depends on the temperature and the chemical potential is given as [245, 255],

$$m_g^2(T) = \frac{N_c}{6}g^2(T,\mu)T^2\left[1 + \frac{1}{6}\left(N_f + \frac{3}{\pi^2}\sum_f \frac{\mu_f^2}{T^2}\right)\right], \tag{3.36}$$

where $N_c$ and $N_f$ represents the number of colors and flavors respectively. The relaxation time for the quarks and antiquarks for the massless case is given by [256],

$$\tau_{q(\bar{q})} = \frac{1}{5.1T\alpha_S^2 \log\left(\frac{1}{\alpha_S}\right)(1 + 0.12(2N_f+1))}. \tag{3.37}$$

Note that for simplicity we have used the relaxation time which is applicable for the massless case only. However, following Ref. [257] it can be argued that the effect of the massive quark is small in the estimation of the scattering cross sections and relaxation time. Therefore, we use the expressions of the relaxation time as given in Eq. (3.37) even for the massive quarks. To compare our results as obtained in the NJL model we consider two light flavors with bare mass $m_0 = 0.008$ GeV

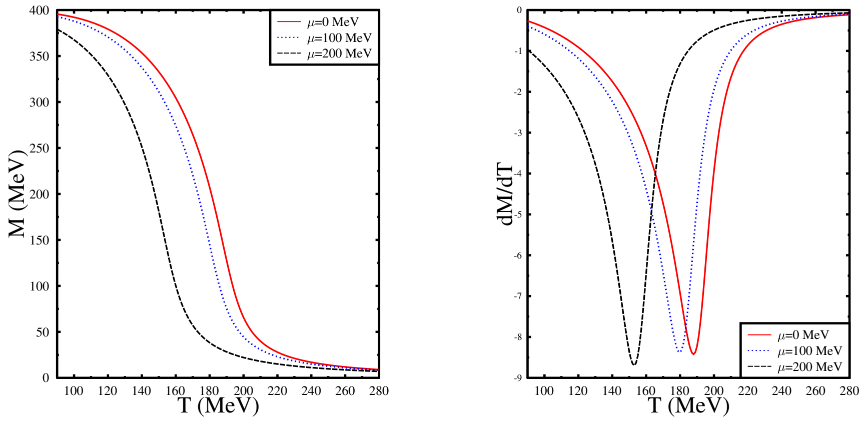


FIGURE 3.1: Constituent quarks mass ($M$) as a function of temperature at different chemical potentials (Left panel). The variation of $dM/dT$ with temperature for different chemical potentials (Right panel). The nonmonotonic variation of $dM/dT$ with a peak structure indicates the pseudo critical temperature for the chiral transition.

[245]. The relaxation time for the gluons is given by [252, 256, 258]

$$\tau_g = \frac{1}{22.5\alpha_s^2 \ln\left(\frac{1}{\alpha_s}\right)\left(1 + 0.06 n_f\right)} \tag{3.38}$$

## 3.5 Results and discussion

The two flavor NJL model as given in Eq.(3.24) has three parameters: the current quark mass $m_0$, the four fermions coupling constant $G$ and the three momenta cut off ($\Lambda$). The values of parameters are adjusted to fit the vacuum structure of QCD like the pion decay constant ($f_\pi$=94 MeV), the pion mass ($m_\pi$=135 MeV) and the vacuum quark condensate $\langle \bar{u}u \rangle = \langle \bar{d}d \rangle = (-241 \text{ MeV})^3$. Various sets of combinations of $G$, $\Lambda$, $m_0$ can be used to fix the vacuum structure of QCD but qualitatively all these different parameterizations are equivalent. Without going into such detailed parameter dependence we work with a single set of parameters. We consider here a parameter set $m_0 = 5.6$ MeV, $\Lambda = 587.9$ MeV and $G\Lambda^2 = 2.44$ [34] which gives rise the constituent quark mass of $u$ and $d$ quarks, $M = 397$ MeV in vacuum ($T = 0, \mu = 0$).

To analyze the variation of different transport coefficients with temperature and quark chemical potential, we have first plotted in the left panel of Fig. 3.1, the constituent quark masses ($M$) as a function of temperature ($T$) for different values of the quark chemical potential ($\mu$). The constituent quark masses of $u$ and $d$ quarks are the same and are related to the quark-antiquark condensate $\langle \bar{\psi}\psi \rangle$. In the right panel of Fig. 3.1, we have plotted variation of $dM/dT$ with temperature for different values of the quark chemical potential. For the range of temperature and quark chemical potential considered here the chiral transition is a smooth crossover. The chiral crossover temperature may be defined by the position of the peak in the variation of $dM/dT$ with temperature. For $\mu = 0$, 100 and 200 MeV, the corresponding chiral crossover temperatures turns out to be $\sim$ 188 MeV, 180 MeV and 153 MeV respectively. It is known that with an increase in chemical potential the crossover temperature decreases.

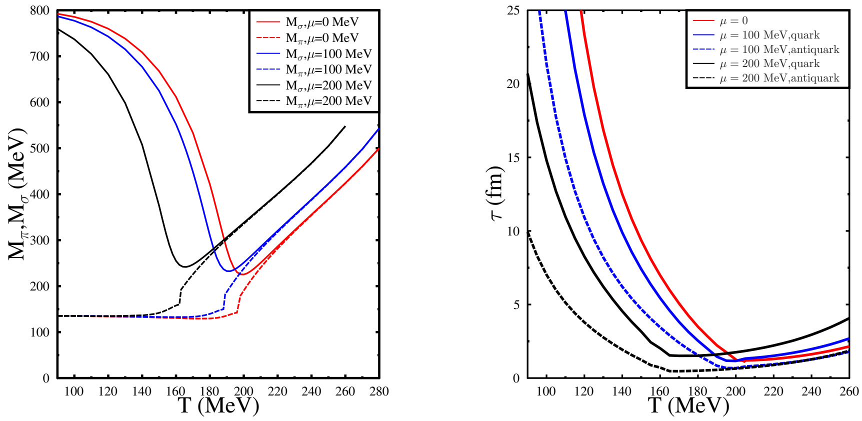


FIGURE 3.2: (Left plot) Variation of $\sigma$ and $\pi$ meson masses with temperature for different values of the quark chemical potentials. The solid lines correspond to $M_\sigma$ while the dashed lines correspond to $M_\pi$. (Right plot) Variation of thermal averaged relaxation times for quarks and antiquarks with temperature for different chemical potentials. Solid lines correspond to the relaxation time for quarks while the dotted lines correspond to relaxation time for antiquarks. For $\mu = 0$ the thermal averaged relaxation times for the quarks and antiquarks are the same. Difference between the relaxation times of quarks and antiquarks appears only at finite chemical potential.

In Fig. 3.2 (left plot) We have plotted the meson masses $M_\sigma$ and $M_\pi$ as a function of temperature for different values of quark chemical potential. Note that pions are pseudo-Goldstone modes, therefore in the chiral symmetry broken phase pion mass varies weakly. But $M_\sigma$ decreases rapidly near the crossover temperature. At higher temperatures, $M_\sigma$ and $M_\pi$, being chiral partners, become approximately degenerate and increase with temperature. Further one can define a characteristic temperature, the "Mott temperature" ($T_M$) where the pion mass becomes twice that of quark mass i.e. at Mott temperature $M_\pi(T_M) = 2M(T_M)$. The Mott temperatures for $\mu$= 0, 100 and 200 MeV turn out to be $\sim$ 198, 192 and 166 MeV respectively. As we shall see later it is the Mott temperature that becomes relevant while estimating the relaxation times of the quarks using thermal scattering rates of the quarks through meson exchange.

In Fig. 3.2 (right plot), we show the variation of average relaxation time as defined in Eq.(3.31), for quarks (solid lines) and antiquarks (dashed lines) with temperature for different values of the quark chemical potential. Let us note that the relaxation time of given particle $'a'$, as shown in Eq.(3.31), depends both on the scattering rates $\bar{W}_{ab}$ as well as on the number density $n_b$ of the particles other than $'a'$ in the initial state *i.e.* number density of scatterers. It turns out that, for the scattering processes considered here, the process $u\bar{d} \to u\bar{d}$ [57], through charged pion exchange in the s-channel gives the largest contribution as compared to other channels. As mentioned earlier, by crossing symmetry arguments, this also means that the $ud \to ud$ scattering rate also contribute dominantly to the thermally averaged scattering rate. Let us note that, below the the Mott temperature $T < T_M$, the averaged scattering rate decreases mostly due to the thermal distribution with large constituent quark masses apart from the suppression from the meson propagators in the scattering amplitudes arising from sigma mesons. As one approaches $T_M$ from lower temperature, the scattering rates become larger as the constituent quark mass decreases as well as the s-channel propagator develop a pole in the meson propagator for temperatures beyond $T_M$. However, at large temperatures there will be a suppression due to the large meson masses which increase with temperature. This results in a maximum scattering rate at $T_M$ or a minimum in the average relaxation time as generically seen in Fig. 3.2 (right plot).

At finite quark chemical potentials, beyond the Mott temperature, the quark-antiquark scattering still contributes dominantly to the scattering processes. However, at finite densities, there are few antiquarks as compared to quarks so that the quarks have fewer antiquarks to scatter off. This leads to a smaller cross-section giving rise to a larger relaxation time for quarks compared to the $\mu = 0$ case. Due to the enhancement of quark densities at finite $\mu$, the cross-section for quark-quark scattering becomes larger resulting in a smaller relaxation time for the quarks compared to the case at vanishing chemical potential below the Mott temperature. The antiquark relaxation time, on the other hand, is always smaller compared to the $\mu = 0$ case as there are more quarks to scatter off at finite chemical potential.

Some discussions on the estimation of the average relaxation time are in order here. Note that one of the initial calculations in the mid-1990s was done in Ref. [259], as well as a relatively recent calculation as done in Ref. [58], where the transport coefficients for QGP has been estimated within the framework of QCD inspired effective models, do not incorporate the full field theoretical methods to estimate the relaxation time. In these studies to estimate the average scattering rates or the relaxation time, one considers "integrated cross sections", by integrating the elastic cross section over the invariant energy squared with the help of a probability function (see Refs. [58] for a detailed discussion). Such an estimation of the relaxation time does not incorporate a possible nonmonotonic variation across the transition temperature/Mott temperature. On the other hand, the formalism that we have adopted here does not consider any adhoc probability function, rather we use basic definitions of scattering cross section and the thermal average of relaxation time. Also, the estimated relaxation time as obtained here and also in Ref. [57] clearly shows a nonmonotonic variation of the relaxation time across the transition temperature/Mott temperature. Such nonmonotonic variation of the relaxation time is also reflected in the expected nonmonotonic behavior of $\eta/s$ across the transition temperature [57].

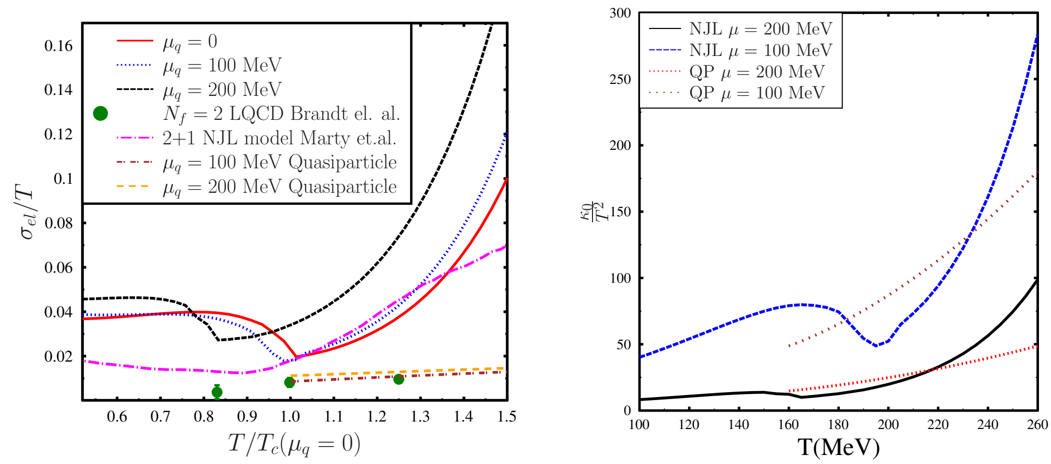


FIGURE 3.3: The variation of normalized electrical conductivity, $\sigma_{el}/T$ (left panel) and normalized thermal conductivity, $\kappa_0/T^2$ (right panel) as a function of temperature for different values of the chemical potential for two flavor NJL model and the quasi particle model for the partonic matter as considered here. For comparison, we also present the two flavor LQCD data Refs. [260, 261] and 2+1 flavour NJL model results Ref. [58].

Further as a validity of the Boltzmann kinetic approach within the RTA one may look into the value of the the mean free path $\lambda_f = v_f \tau_f$ for a given flavor $f$, here the mean velocity $v_f$ can be expressed as,

$$v_f = \frac{2N_c}{(2\pi)^3 n_f} \int d^3p \frac{|\vec{p}|}{E_p} f(E_p). \tag{3.39}$$

It can be argued that at the Mott transition temperature $\lambda_f = 1.2$ fm [57]. At the same temperature, the mass of the pion and sigma meson are of the order of 200 MeV with the corresponding Compton wavelength ($\lambda_C$) to be of the order of a Fermi. Therefore the value of the ratio $\lambda_f/\lambda_C$ is about 1.2 at the Mott transition temperature and its value increases rapidly both below and above the Mott temperature. Therefore except at the Mott transition temperature $\lambda_f$ can be significantly larger than $\lambda_C$. Thus, within the NJL model, it may not be too unreliable to use the Boltzmann equation within the RTA except at the Mott transition temperature. Therefore we believe our analysis is not unjustified given the fact that similar approaches have been well explored by various authors also. The novelty that we are addressing is the thermoelectric properties of the QCD matter across the chiral transition scale.

In the left panel of Fig. 3.3 we present the variation of normalized electrical conductivity, $\sigma_{el}/T$ as a function of temperature at different values of quark chemical potential in 2 flavour NJL model as well as in the quasi particle model. For the comparison, we also present the results obtained using LQCD for two light flavors in Refs. [260, 261] and the results obtained by studying 2+1 flavors NJL model in Ref. [58]. Further, for the sake of comparison, we have taken the temperature in units of $T_c$ of the corresponding models. For the 2 flavor NJL model we have taken the Mott transition temperature $T_c = T_M$=198 MeV as estimated in this study.

The left panel of the Fig. 3.3 reflects the variation of electrical conductivity which is having a minimum at Mott transition temperature for the two flavor NJL model shown by the solid red curve in Fig. 3.3. Apart from this, it is also observed that $\sigma_{el}/T$ increases with quark chemical potential which we have presented with the blue dotted ( $\mu = 100$ MeV) and black dashed ($\mu = 200$ MeV) curves. This is because the contribution to the $\sigma_{el}$ arises dominantly from quarks rather than antiquarks at finite chemical potential, as the antiquark contribution gets suppressed due to the distribution function. This apart, there is an enhancement of the relaxation time at finite $\mu$ beyond the Mott transition. The dominant contribution to the scattering process is $u\bar{d} \rightarrow u\bar{d}$. As the $\bar{d}$ density decreases with $\mu$, this scattering process gets suppressed as compared to the case of $\mu = 0$ and leads to an enhancement of relaxation time at finite chemical potential. Thus both the increase of charge carriers and an increase in relaxation time with $\mu$ lead to enhancement of electrical conductivity beyond the Mott temperature. On the other hand, below the Mott temperature, although the relaxation time decreases with chemical potential, the increase in quark number density makes the coefficient of electrical conductivity increasing with chemical potential. Further, in the high-temperature range $T >> M$, one can assume the quarks and antiquarks to be massless. In this high temperature or massless limit in the two flavor NJL model $\sigma_{el}/T$ can be shown to be $\sigma_{el}/T \sim T\tau \exp(\mu/T)$ (by considering only quark contribution as they are dominant at finite $\mu$). Therefore for a temperature range higher than the Mott transition temperature predominantly due to the increasing behavior of $\tau$ with temperature $\sigma_{el}/T$ increases. Again at a very high temperature due to the factor of $\exp(\mu/T)$, $\sigma_{el}/T$ increases with chemical potential. It is clear that the order of magnitude value of the normalized electrical conductivity as obtained in the present investigation is similar to the LQCD results. However, it should be emphasized that LQCD calculations take into account the full dynamical nature of the QCD gauge fields. On the other hand, gluons are not present in the NJL model. Therefore, quantitative variation of the relaxation time and $\sigma_{el}/T$ is not expected to be the same in NJL and LQCD calculations. Further, as compared to results of Marty etal

[58] shown by magenta dot dashed curve, the 2 flavor NJL model values are of similar values near the transition temperature and at high temperature ($T/T_c$>1.4) the two flavor NJL results are higher where as the 2+1 flavor values flatten out. This is because of two reasons: firstly, with 2+1 flavors, the relaxation time decreases as there are extra channels for scatterings available that reduces the relaxation time. Further, there is a difference in the definition of relaxation time given in Ref. [58] and the present definition for the estimation of the same [57].

We have also plotted the results for the electrical conductivity estimated from the quasi particle model which remains almost constant compared to the NJL model results. The reason is, in the quasi-particle models, the quasi-particle masses are increasing functions of temperature and hence the thermal distribution functions get suppressed at high temperature in contrast to the NJL model. Further, the magnitude of the velocity $|\mathbf{p}|/E$ also becomes smaller at high temperature in the quasi-particle model as compared to the NJL model.

Furthermore, in Ref. [262] various transport coefficients of deconfined quark matter have been studied within a different quasi-particle model, namely the effective fugacity quasi-particle model. The crucial difference between the quasi-particle model considered here and that in Ref. [262] lies in a different dispersion relation between the quasi particles. This is manifested in the estimation of relaxation time as well as in estimation of various transport coefficients. It should be noted that normalized electrical conductivity $\sigma_{el}/T$ as obtained in the present investigation is quantitatively as well as qualitatively different from the same as obtained in Ref. [262]. The presence of a background scalar condensate is the fundamental difference between the NJL model and the effective fugacity quasi-particle model as discussed in Ref. [262]. Further, relaxation time plays an important role in determining the variation of any transport coefficient with temperature and chemical potential. The thermal averaged relaxation time as obtained in the effective fugacity quasi-particle model as discussed in the Ref. [262] is different (quantitatively and quantitatively) from the relaxation time obtained in the NJL model as well as the quasi-particle model considered here. For a more detailed analysis of the estimation of electrical conductivity in the quasi-particle model as considered here and that of the effective fugacity quasi-particle model, we refer the interested reader to Ref. [258]. The difference stems from the difference in the single particle energy dispersion relation as compared to NJL model or the quasi-particle model considered here.

In the right panel of Fig. 3.3 we show the variation of the normalized thermal conductivity ($\kappa_0/T^2$) with temperature both for the NJL model and for the quasi-particle model. For the NJL model, the ratio shows a nonmonotonic variation with temperature. The origin of such behavior again lies with the variation of relaxation time with temperature. Beyond the Mott temperature, the thermal conductivity increases sharply with temperature. This can be understood as follows. For large temperatures, when quark masses can be neglected, it can be easily shown that the enthalpy to the net quark number density ratio goes as $\omega/n_q \sim T\coth(\mu/T)$. Also note that in the expression of the thermal conductivity $(E - \frac{\omega}{n_q})^2 \sim (\frac{\omega}{n_q})^2$, due to the fact that single-particle energy ($E$) is negligible as compared to the enthalpy per particle- $\omega/n_q$. Therefore, the variation of the normalized thermal conductivity with temperature and chemical potential will be determined by the variation of relaxation time, $\omega/n_q$, and the distribution function. It can be shown that in the high-temperature limit or the massless limit the normalized thermal conductivity, $\kappa_0/T^2$ can be approximately expressed as, $\kappa_0/T^2 \sim T\tau\exp(\mu/T)(\coth(\mu/T))^2$. Beyond the Mott transition temperature, the increasing behavior of $\tau$ essentially determines the increasing behavior of $\kappa_0/T^2$. On the other hand, for $\mu << T$, $\coth(\mu/T) \sim T/\mu$ in the leading order. Therefore in the high-temperature limit, $\kappa_0/T^2$ decreases with chemical potential. For the quasi particle model, on the other hand, the ratio $\kappa_0/T^2$ is of the same order near the transition temperature but rises slowly with temperature compared to the NJL model which again is a reflection of increasing behaviour in the masses of the quasi-particle with temperature which reduces the thermal distribution functions. Similar to $\sigma_{el}/T$, the qualitative nature of the normalized thermal conductivity ($\kappa_0/T^2$) as presented here is also different from the same as obtained in the Ref. [262]. This difference is again due to the different nature of the dispersion relation for the single particle energies of the quasi-particles in the effective fugacity quasi-particle model and the NJL or the quasi particle model considered here.

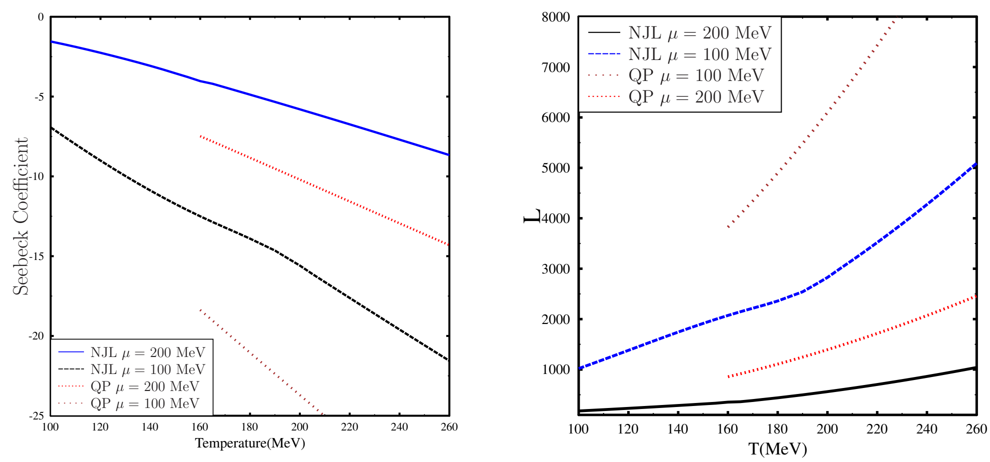


FIGURE 3.4: The variation of the Seebeck coefficient (left panel) and the Lorenz number, $L = \kappa_0/(\sigma_{el}T)$ (right panel) with temperature for different values of the chemical potential for NJL model and for quasi particle model.

We next show the behavior of the Seebeck coefficient as a function of temperature for different values of quark chemical potential in the left panel of Fig. 3.4 for both in NJL model and in quasi particle model. This coefficient, which is dimensionless, decreases monotonically with temperature. The variation of the Seebeck coefficient with temperature can be understood as follows. Note that this coefficient is a ratio of two quantities each of which is proportional to the relaxation time. When we consider the relaxation time as the average relaxation time, the ratio becomes independent of the average relaxation time. Note that at finite chemical potential quark contribution to the Seebeck coefficient is dominant with respect to the antiquark contribution. Therefore, contrary to the nonmonotonic variation of $\sigma_{el}/T$ and $\kappa_0/T^2$ with temperature for NJL model, where the nonmonotonic variation has its origin stemming from the behavior of relaxation time with temperature, the variation of the Seebeck coefficient is not expected to be nonmonotonic. Further unlike other transport coefficients, the positivity of the Seebeck coefficient is not guaranteed. This is because in the expression of the Seebeck coefficient as given in Eq. (3.17), the integrand in the numerator has the factor which is linear in $(E_a - b_a\omega/n_q)$. Therefore for the quarks, this factor becomes $(E - \omega/n_q)$, and the single-particle energy $E$ is much smaller than $\omega/n_q$. Therefore the term $(E - \omega/n_q)$ is negative which makes the Seebeck coefficient negative. However it is important to note that the expression of thermal conductivity also contains a term $(E - \omega/n_q)$, but it comes as a square. Therefore positivity of the thermal conductivity is guaranteed. In the condensed matter system the Seebeck coefficient can be both positive and negative, e.g. if for electron and holes the Seebeck coefficients are opposite to each other. Further for a bipolar medium with multiple charge carriers the sign of the Seebeck coefficient depends on the range of temperature considered [251]. Similar to the case of thermal conductivity, one can do an analysis regarding the behavior of the Seebeck coefficient in the massless limit. In the massless limit, it can be shown that $S \sim -\coth(\mu/T)$. Therefore in the high-temperature limit, the leading order contribution to the Seebeck coefficient is $S \sim -T/\mu$. Hence with increasing temperature the Seebeck coefficient decreases, on the other hand with an increase in chemical potential Seebeck coefficient increases. In the simple analysis, we have assumed that the dominant contributions in the sum over species arise from quarks as the antiquark contributions are suppressed due to finite chemical potential in the thermal distribution function. A comment regarding SU(2) flavor symmetry of the NJL Lagrangian may be relevant here. The thermalisation of the medium is decided by strong interaction. Thus, the relaxation time for up anda down quarks will be same. On the otherhand, the contribution of the up quark and down quark to the Seebeck coefficient will be different as the Seebeck coefficient depends linearly on the electrical charge of the relevant species (See e.g. the numerator of the expression for Seebeck coefficient in Eq. (3.17)). Thus, the contribution of the Seebeck coefficient of up quark will be twice in magnitude and opposite in sign of the down quark.

Compared to the NJL model, the behaviour of the Seebeck coefficient in the quasi particle model is qualitatively similar but quantitatively different. This can be understood from the behaviour of the electrical conductivity in the model as shown in Fig. 3.3. The smaller value for the electrical conductivity in quasi particle model leads to larger magnitude for the Seebeck coefficient. Further, in the quasi partcle models the gluons also contribute to the enthalpy which affects the Seebeck coefficient.

In the right panel of Fig. 3.4 we have plotted the ratio $L = \kappa_0/(\sigma_{el}T)$, as a function of temperature for the NJL model as well as for the quasi particle model. In condensed matter systems this ratio is a constant and is known as the Lorenz number. In the present case, however, it is observed that the ratio increases monotonically with temperature. Similar to the Seebeck coefficient, in the leading order for average relaxation time the ratio $L$, is independent of relaxation time. Further, in the high temperature limit or in the massless limit $\kappa_0/(\sigma T) \sim (\coth(\mu/T))^2$. Therefore, in the leading order for $\mu << T$, $\kappa_0/(\sigma T) \sim T^2/\mu^2$. Hence in the high temperature limit the ratio $L$ increases with temperature but decreases with quark chemical potential. In quasi-particle model this ratio is higher compared to the NJL model as the electrical conductivity in the quasi-particle description is smaller compared to that in the NJL model. This ratio is also estimated within an effective fugacity quasi particle model in Ref. [262] where this ratio approachs a constant at high temperature. This different behaviour has its origin in the different behaviour of the quasi particles in the effective fugacity quasi particle model as discussed earlier.

## 3.6 Summary and conclusion

In the present investigation, we have estimated the Seebeck coefficient in a hot and dense partonic medium modeled by the 2 flavor NJL model. For comparison, the NJL model results for the Seebeck coefficient, we have also estimated the same within a quasiparticle model of the deconfined matter. We have considered the thermoelectric effect arising due to the gradient in temperature as well as the gradient in chemical potential. In addition to the Seebeck coefficient, we have also estimated electrical conductivity ($\sigma_{el}$), thermal conductivity ($\kappa_0$), and Lorenz number (L) associated with the Wiedemann–Franz law. Note that $\sigma_{el}$ is the response of the medium in the presence of an external electric field and it also decides the time evolution of a magnetic field in the conducting medium. In the context of relativistic non-central heavy-ion collisions where the high magnetic field produced, the electrical conductivity plays a crucial role. It should be emphasized that in the presence of a magnetic field, simple Ohm's law gets modified and one needs to consider the anisotropic structure of the electrical conductivity tensor. All such investigations in the presence of a magnetic field should reproduce the electrical conductivity in the absence of any magnetic field, *i.e.* the electrical conductivity tensor should be isotropic in the absence of any magnetic field. Therefore, the estimation of electrical conductivity without any effect of the magnetic field should serve as a baseline for the studies that include the effect of magnetic field in a conducting medium.

Although electrical and thermal conductivities always remain positive and the Seebeck coefficient is negative for the range of temperature and quark chemical potential considered in our study. The variations of electrical and thermal conductivities with temperature and quark chemical potential are intimately related to the variation of the relaxation time with temperature and chemical potential. While the variations of Seebeck coefficient and the Lorenz number are insensitive to the variation of relaxation time.

In the presence of thermoelectric effects in a conducting medium, the temperature gradient can be converted into an electrical current and vice versa. Seebeck coefficient physically represents the efficiency of any conducting medium to convert a temperature gradient into an electrical current. Therefore for a nonvanishing Seebeck coefficient, electrical current as well as heat current gets modified. In presence of Seebeck effect, the electrical current becomes, $\vec{J} = \sigma_{el}\vec{\mathcal{E}} - \sigma_{el}S\vec{\nabla}T$. It is important to note that the electrical conductivity is always positive due to the constructive contributions of particles and antiparticles to the electric current. Positivity of the electrical conductivity can be shown using entropy production i.e. second law of thermodynamics. By demanding that in the presence of electromagnetic field $T\partial_\mu s^\mu \geq 0$, here $s^\mu$ is the entropy current, it can be shown that the electrical conductivity is positive [263]. For a negative Seebeck coefficient in the presence of a positive temperature gradient the electric current enhances. Therefore the net electric current increases if the electric current due to the thermoelectric effect and the electric current due to the external electric field contributes constructively. On the other hand, the thermal conductivity in the presence of the thermoelectric effect gets modified. In the presence of a nonvanishing Seebeck coefficient, the net thermal conductivity which can be given as $\kappa = \kappa_0 - T\sigma_{el}S^2$ indicates that the nonvanishing value of the Seebeck coefficient reduces the thermal conductivity. It is important to note that the thermal conductivity is required to be positive for the theory to be consistent with the second law of thermodynamics i.e. $T\partial_\mu s^\mu \geq 0$. Using the formalism of viscous hydrodynamics and viscous magnetohydrodynamics positivity of the electrical conductivity and the thermal conductivity has been shown explicitly [249, 263]. But the contributions to the entropy current coming from the thermoelectric effects are not considered in these investigations. Therefore in the context of entropy production in the viscous hydrodynamics and magnetohydrodynamics, it will be interesting to study the effects of thermoelectric coefficients.

Thermoelectric coefficients could also be important in the context of the spin Hall effect (SHE). SHE is an important ingredient for the generation of spin current and it is a key concept in spintronics. In SHE, an electric field induces a transverse spin current perpendicular to the direction of the electric field. SHE has recently been investigated in a hot and dense nuclear matter in the context of relativistic heavy-ion collisions [264]. It has been argued that due to SHE, a spin current will be produced proportional to the electric field. This also means that an external electric field $\vec{\mathcal{E}}$ will induce a local spin polarization and the spin polarization distribution function of fermions (anti fermions) in momentum space will feature the dipole distribution. Therefore there will be a spin flow in the plane transverse to the direction of the electric field. Observation of SHE may open a new direction in the exploration of the many body quantum effects in hot and dense nuclear matter.

However, the life-time of the electric field generated in heavy-ion collisions could be small of the order 1 fm/c. Therefore, the idea of the observation of the SHE becomes speculative. However, in the presence of nonvanishing thermoelectric coefficients, a temperature gradient and/or a gradient in the chemical potential can give rise to an effective electric field which may contribute to the SHE. Therefore a detailed analysis of the thermoelectric property of the hot and dense matter produced in a heavy-ion collision experiment could be relevant for SHE and needs further investigation.

# Chapter 4

# Hadron-quark phase transition and non-radial oscillations in neutron stars

In the previous chapters, chapter 2 and chapter 3, we have discussed the QCD phase diagram in the high temperature and zero baryon density. We studied the chiral phase transition in the context of relativistic heavy ion collisions. In the following two chapters we will study the other region of the phase diagram where the temperature is zero and the non-zero baryon chemical potential in the context of NSs and/or HSs.

Our main focus is to unveil the structure of matter inside the CSs. The radial oscillation modes do not couple with the gravitational waves (GWs) and give information about the stability of a star. For example, the fundamental radial mode gives the allowed minimum oscillation frequency for a stable star [265, 266] and determines the maximum allowed baryon density at the center of maximum mass star. They are also useful to determine the rotation frequency of a NS [266, 267]. While in the case of non-radial oscillation, they couple with the GWs and damp in the GWs. So they are more suitable observable to get insight of the NSM [266, 268, 269].

NSs are exciting astrophysical laboratories to study the behaviour of matter at extreme densities. The properties of NSs not only open up many possibilities related to composition, structure and dynamics of cold matter in the observable universe but also throw light on the interaction of matter at a fundamental level [270]. Such CSs, observed as pulsars, are believed to contain matter of densities few times nuclear saturation density ($\rho_0$) in their core. To explain and understand the properties of such stars, one needs to connect different branches of physics like low energy nuclear physics, QCD under extreme conditions, general theory of relativity (GTR) etc [271–275]. In this chapter we study matter at extreme densities in the zero temperature limit in the context of NSs. We study HQPT and discuss some of the quasi-normal mode (QNM)s in NSs and HSs. By HS, we mean CSs with a core of quark matter or a MP core of quark and hadronic matter [78, 79].

## 4.1 Introduction

The macroscopic properties of such a CS like its mass, radius, moment of inertia, tidal deformability in a binary merging system and different modes of oscillations etc. depend crucially on its composition that affect the variation of pressure with energy density or EOS. The GW170817 [71] event explored the constraints on the EOS using tidal deformability extracted from the phase of the gravitational waveforms during the late stage of inspiral merger [72–77]. Though not conclusive, it is quite possible that one or both the merging NSs could be HSs. Within the current observational status, it is difficult to distinguish between a canonical NS without a quark matter core from a HS with a core of pure quark matter or a core of quark matter in a MP with hadronic matter. This calls for exploring other observational signatures to solve this “masquerade" problem [80, 81].

In this context, it has been suggested that the study of QNM of NSs can have the possibility of providing compositional information regarding matter in the interior. This includes NSs with a hyperon core [82–84], a quark core or a MP core with quark and hadronic matter components [81, 85–90]. This is because QNMs not only depend upon the EOS *i.e.* $p(\epsilon)$ but also on the derivatives $\frac{dp}{d\epsilon}$ and $\frac{\partial p}{\partial \epsilon}$ [276]. Since the appearance of hyperons does not involve a first order phase transition, their effects on QNMs can be milder compared to a HQPT at finite densities whose effect can be more pronounced. These modes can be studied within the framework of GTR [277, 278] where the fluid perturbation equations (pulsating equations) can be decomposed into spherical harmonics leading to two classes of oscillations depending upon the parity of the harmonics. The even parity oscillations produce polar(spheroidal) deformation while the odd parity produce toroidal one. The polar QNMs can further be classified into different kinds of non-radial oscillation modes depending upon the restoring force that acts on the fluid element when it gets displaced from its equilibrium position [279]. These oscillations couple to the gravitational wave and can be diagnostic tools for studying the phase structure of the matter inside the CSs. The important modes for this are the pressure $(p)$ modes, fundamental $(f)$ modes and gravity $(g)$ modes. The frequency of the $g$ modes is lower than that of $p$ modes while the frequency of $f$ modes lies in between. These are the fluid modes to be distinguished from $w$ modes which are associated with the perturbation of the space-time metric itself.

In the present work, we focus on $g$ and $f$ modes oscillations arising from dense matter from both NSM and hybrid star matter (HSM). For nuclear matter the existence of such low frequency $g$ modes was shown earlier in Refs. [280, 281]. The origin of $g$ mode is related to the convective stability *i.e.* stable stratification of the star. When a parcel of the fluid is displaced, the pressure equilibrium is restored rapidly through sound waves while compositional equilibrium, decided by the weak interaction, takes a longer time causing the buoyancy force to oppose the displacement. This sets in the oscillations. The $g$ mode oscillation frequencies are related to the Brunt-Väisäla frequency ($\omega_{\rm BV}$) which depends on the difference between the equilibrium sound speed ($c_e^2$) and adiabatic or the constant composition sound speed ($c_s^2$) *i.e.* $\omega_{\mathrm{BV}}^2 \propto (1/c_e^2 - 1/c_s^2)$ as well as on the local metric. Such $g$ modes without any phase transition have been studied earlier for the nuclear matter, hyperonic matter, superfluidity [82, 83, 282–290].

In the present investigation, for the nuclear matter sector, we use a RMF theory (see Sec. 1.3.1) involving nucleons interacting with scalar and vector mean fields along with self-interactions of the mesons leading to reasonable saturation properties of nuclear matter. For the description of quark matter we use two flavor NJL model (see Sec. 1.3.2) where the parameters of the model are fixed from the physical variables like pion mass, pion decay constant and light quark condensates that encodes the physics of the chiral symmetry breaking. The phase transition from hadronic matter to quark matter can be considered either through a Maxwell construct or a Gibbs construct leading to a MP [291]. It ought to be noted that the kind of phase transition depends crucially on the surface tension [292–298] of the quark matter which, however, is poorly known. If the surface tension is large (small) then there will be sharp (smooth) interface and one can have a Maxwell (Gibbs) construct for HQPT, where there is a MP of nuclear and quark matter [299, 300]. We use a Gibbs construction mechanism for the construction of MP (see Sec. 4.2.3).

We organize this chapter as follows. In section 4.2.1, we discuss salient features of the RMF model describing the nuclear matter and in section, 4.2.2 we discuss NJL model and write down the equation of state for the quark matter. Section 4.2.3 details HQPT and MP structure using Gibbs construct with multiple chemical potentials. In section 4.3, we discuss the stellar structure as well as the non-radial oscillations of CSs. We give, here, in some detail, the derivation of the pulsation equations. In section 4.4, we discuss the estimation of the equilibrium and adiabatic speed of sound in different phases. In section 4.5, we discuss results of the present investigation regarding thermodynamics of the dense matter, MP structure, HS structure and non-radial oscillations. Finally in section 4.6, we summarize results and give an outlook for the further investigation.

## 4.2 Formalism

### 4.2.1 Equation of state of nuclear matter

We restrict our analysis for NSM consisting of baryons (neutron and proton) and leptons (electron and muon). The relevant mesons for this purpose are $\sigma$, $\omega$ and $\rho$ mesons [32, 301–303]. The scalar $\sigma$ meson creates strong attractive interactions, the vector $\omega$ meson on the other hand is responsible for the repulsive short range interactions. The neutron and proton do only differ in terms of their isospin projections with respect to the strong force. The isovector $\rho$ meson is included to distinguish baryons. The Lagrangian including baryons as the constituents of the nuclear matter and mesons as the carriers of the interactions is given as [304, 305]

$$\mathcal{L} = \sum_b \mathcal{L}_b + \mathcal{L}_l + \mathcal{L}_{\text{int}}, \tag{4.1}$$

where,

$$\mathcal{L}_b = \bar{\Psi}_b(i\gamma_\mu\partial^\mu - q_b\gamma_\mu A^\mu - m_b + g_\sigma\sigma - g_\omega\gamma_\mu\omega^\mu - g_\rho\gamma_\mu\vec{I}_b\vec{\rho}^\mu)\Psi_b, \tag{4.2}$$

$$\mathcal{L}_l = \bar{\psi}_l(i\gamma_\mu\partial^\mu - q_l\gamma_\mu A^\mu - m_l)\psi_l, \tag{4.3}$$

$$\begin{aligned}\mathcal{L}_{\text{int}} = &\frac{1}{2}\partial_\mu\sigma\partial^\mu\sigma - \frac{1}{2}m_\sigma^2\sigma^2 - V(\sigma) - \frac{1}{4}\Omega^{\mu\nu}\Omega_{\mu\nu} + \frac{1}{2}m_\omega^2\omega_\mu\omega^\mu,\\ &-\frac{1}{4}\vec{R}^{\mu\nu}\vec{R}_{\mu\nu} + \frac{1}{2}m_\rho^2\vec{\rho}_\mu\vec{\rho}^\mu - \frac{1}{4}F^{\mu\nu}F_{\mu\nu},\end{aligned} \tag{4.4}$$

and,

$$V(\sigma) = \frac{\kappa}{3!}(g_{\sigma N}\sigma)^3 + \frac{\lambda}{4!}(g_{\sigma N}\sigma)^4. \tag{4.5}$$

Where $\Omega_{\mu\nu} = \partial_\mu\omega_\nu - \partial_\nu\omega_\mu$, $\vec{R}_{\mu\nu} = \partial_\mu\vec{\rho}_\nu - \partial_\nu\vec{\rho}_\mu$ and $F_{\mu\nu} = \partial_\mu A_\nu - \partial_\nu A_\mu$ are the mesonic and electromagnetic field strength tensors. $\vec{I}_b$ denotes the isospin operator. The $\Psi_b$ and $\psi_l$ are baryon and lepton doublets. The $\sigma$, $\omega$ and $\rho$ meson fields are denoted by $\sigma$, $\omega$ and $\rho$ and their masses are $m_\sigma$, $m_\omega$ and $m_\rho$, respectively. The parameters $m_b$ and $m_l$ denote the vacuum masses for baryons and leptons. The meson-baryon couplings $g_\sigma$, $g_\omega$ and $g_\rho$ are scalar, vector and isovector coupling constants, respectively. In RMF approximation, one replaces the meson fields by their expectation values which then act as classical fields in which baryons move *i.e.* $\langle\sigma\rangle = \sigma_0$, $\langle\omega_\mu\rangle = \omega_0\delta_{\mu 0}$, $\langle\rho_\mu^a\rangle = \delta_{\mu 0}\delta_3^a\rho_3^0$. The mesonic equations of motion can be found by Euler-Lagrange equations for meson fields using Eq. (4.1)

$$m_\sigma^2\sigma_0 + V'(\sigma_0) = \sum_{i=n,p} g_\sigma n_i^s, \tag{4.6}$$

$$m_\omega^2\omega_0 = \sum_{i=n,p} g_\omega n_i, \tag{4.7}$$

$$m_\rho^2\rho_3^0 = \sum_{i=n,p} g_\rho I_{3i} n_i, \tag{4.8}$$

where, $I_{3i}$ is the third component of the isospin of a given baryon. We have taken $I_{3(n,p)} = \left(-\frac{1}{2}, \frac{1}{2}\right)$. The baryon density, $n_B$, lepton density, $n_l$, and scalar density, $n^s$, at zero temperature are given by

$$n_B = \sum_{i=n,p} \frac{\gamma k_{Fi}^3}{6\pi^2} \equiv \sum_{i=n,p} n_i, \tag{4.9}$$

$$n_l = \frac{k_{Fl}^3}{3\pi^2}, \tag{4.10}$$

and

$$n^s = \frac{\gamma}{(2\pi)^3} \sum_{i=n,p} \int_0^{k_{Fi}} \frac{m^*}{E(k)} d^3k \equiv \sum_{i=n,p} n_i^s, \tag{4.11}$$

where, $E(k) = \sqrt{m^{*2} + k^2}$ being the single particle energy for nucleons with a medium dependent mass given as

$$m^* = m_b - g_\sigma \sigma_0. \tag{4.12}$$

Further, $k_{Fi} = \sqrt{\tilde{\mu}_i^2 - m^{*2}}$ is the Fermi momenta of the nucleons defined through an effective baryonic chemical potential, $\tilde{\mu}_i$ given as

$$\tilde{\mu}_i = \mu_i - g_\omega \omega_0 - g_\rho I_{3i} \rho_3^0. \tag{4.13}$$

Similarly, $k_{Fl}$ is the leptonic Fermi momenta i.e. $k_{Fl} = \sqrt{\mu_l^2 - m_l^2}$. Further $\gamma = 2$ corresponds to the spin degeneracy factor for nucleons and leptons and $\mu_l$ denotes the chemical potential for leptons.

The total energy density, $\epsilon_{\rm HP}$, within the RMF model is given by

$$\begin{aligned} \epsilon_{\rm HP} = & \frac{m^{*4}}{\pi^2} \sum_{i=n,p} H(k_{Fi}/m^*) + \sum_{l=e,\mu} \frac{m_l^4}{\pi^2} H(k_{Fl}/m_l) \\ & + \frac{1}{2} m_\sigma^2 \sigma_0^2 + V(\sigma_0) + \frac{1}{2} m_\omega^2 \omega_0^2 + \frac{1}{2} m_\rho^2 \rho_3^{02}. \end{aligned} \tag{4.14}$$

The pressure, $p_{\rm HP}$, can be found using the thermodynamic relation as

$$p_{\rm HP} = \sum_{i=n,p,l} \mu_i n_i - \epsilon_{\rm HP}. \tag{4.15}$$

In Eq. (4.14) we have introduced the function $H(z)$ which is given as

$$H(z) = \frac{1}{8} \left[ z\sqrt{1+z^2}(1+2z^2) - \sinh^{-1} z \right], \tag{4.16}$$

In the present investigation, we consider two different parameterisation for the nucleonic EOS - (i) the NL3 parameterisation of RMF model as discussed in Ref. [306].

TABLE 4.1: The nucleon masses ($m_b$), $\sigma$ meson mass ($m_\sigma$), $\omega$ meson mass ($m_\omega$), $\rho$ meson mass ($m_\rho$) and couplings $g_\sigma$, $g_\omega$, $g_\rho$, $\kappa$, $\lambda$ in NL3 parameterisation [306].

| Parameters | Values |
|---|---|
| $m_b$ (MeV) | 939 |
| $m_\sigma$ (MeV) | 508.194 |
| $m_\omega$ (MeV) | 782.501 |
| $m_\rho$ (MeV) | 763.000 |
| $g_\sigma^2$ | 104.3871 |
| $g_\omega^2$ | 165.5854 |
| $g_\rho^2$ | 79.6 |
| $\kappa$ (fm$^{-1}$) | 3.8599 |
| $\lambda$ | -0.015905 |

TABLE 4.2: The nucleon masses ($m_b$), meson masses, $m_i$ ($i = \sigma, \omega, \rho$) and coupling constants $g_{i0}$, $a_i$ ($i = \sigma, \omega, \rho$) and the saturation nuclear density $n_0$ in DDB model [307, 308].

| Parameters | Values |
|---|---|
| $m_b$ (MeV) | 939 |
| $m_\sigma$ (MeV) | 508.194 |
| $m_\omega$ (MeV) | 782.501 |
| $m_\rho$ (MeV) | 763.000 |
| $a_\sigma$ | 0.071467 |
| $a_\omega$ | 0.04641 |
| $a_\rho$ | 0.665711 |
| $g_{\sigma 0}$ | 9.690022 |
| $g_{\omega 0}$ | 11.755566 |
| $g_{\rho 0}$ | 8.280652 |
| $n_0$ (fm$^{-3}$) | 0.147 |

The corresponding parameters are listed in Table 4.1. The other parameterisation of the RMF model is a nucleonic $\beta-$ equilibrated EOS based on a relativistic description of hadrons through their density-dependent coupling with mesons constrained by the existing observational, theoretical and experimental data through Bayesian analysis (DDB) [307, 308] consistent with the phenomenology of the saturation properties of nuclear matter as well as the gravitational wave data regarding tidal deformation [71]. In case of DDB, the couplings are density dependent and defined as

$$g_\sigma = g_{\sigma 0}\, e^{-(x^{a_\sigma}-1)}, \tag{4.17}$$

$$g_\omega = g_{\omega 0}\, e^{-(x^{a_\omega}-1)}, \tag{4.18}$$

$$g_\rho = g_{\rho 0}\, e^{-a_\rho(x-1)}, \tag{4.19}$$

where, $x = n_{\rm B}/n_0$. The DDB parameters $g_{i0}$, $a_i$, ($i = \sigma,\ \omega,\ \rho$) and $n_0$ are given in Table 4.2. In DDB parameterisation, the cubic and quartic terms in Eq. (4.1) are taken to be zero so that $V(\sigma) = 0$. Due to the density dependent couplings, the effective baryon chemical potential as in Eq. (4.13) gets redefined as

$$\tilde{\mu}_i = \mu_i - g_\omega \omega_0 - g_\rho I_{3i} \rho_3^0 - \Sigma^r, \tag{4.20}$$

where, $\Sigma^r$ is the "rearrangement term" which is given as [309]

$$\Sigma^r = \sum_{i=n,p} \left\{ -\frac{\partial g_\sigma}{\partial n_{\rm B}} \sigma_0 n_i^s + \frac{\partial g_\omega}{\partial n_{\rm B}} \omega_0 n_i + \frac{\partial g_\rho}{\partial n_{\rm B}} \rho_3^0 I_{3i} n_i \right\}. \tag{4.21}$$

NSs are globally charge neutral as well as the matter inside the core is under $\beta$-equilibrium. So the chemical potentials and the number densities of the constituents of NSM are related by the following equations,

$$\mu_i = \mu_B + q_i\mu_E, \tag{4.22}$$
$$\sum_{i=n,p,l} n_i q_i = 0, \tag{4.23}$$

where, $\mu_B$ and $\mu_E$ are the baryon and electric chemical potentials and $q_i$ is the charge of the $i^{th}$ particle.

### 4.2.2 Equation of state of quark matter

We note down here, for the sake of completeness, the salient features of the thermodynamics of NJL model with two flavours that we use to describe the EOS of the quark matter. The Lagrangian of the model with four point interactions is given by

$$\begin{aligned}\mathcal{L} = \bar{\psi}_q(i\gamma^\mu\partial_\mu - m_q)\psi_q + G_s\left[(\bar{\psi}_q\psi_q)^2 + (\bar{\psi}_q i\gamma^5 \boldsymbol{\o}\psi_q)^2\right] \\ +G_v\left[(\bar{\psi}_q\gamma^\mu\psi_q)^2 + (\bar{\psi}_q i\gamma^\mu\gamma^5\boldsymbol{\o}\psi_q)^2\right].\end{aligned} \tag{4.24}$$

Here, $\psi_q$ is the doublet of $u$ and $d$ quarks and $\tau$ is the Pauli matrices. We have also taken here a current quark mass, $m_q$ which is same for $u$ and $d$ quarks. The second term describes the four point interactions in the scalar and pseudoscalar channel. The third term is a phenomenological vector interaction giving rise to repulsive interaction for $G_v > 0$ which can make the EOS stiffer. Except for the explicit symmetry breaking term proportional to current quark mass, the Lagrangian is chirally symmetric. Using the standard method of thermal field theory one can write down the the thermodynamic potential $\Omega$ within a mean field approximation as a given temperature, ($T = \beta^{-1}$) and quark chemical potential, ($\mu_q = \mu_B/3$) [34] as

$$\begin{aligned}\Omega(M,T,\mu) = -2N_c\sum_{i=u,d}\int\frac{d\mathbf{k}}{(2\pi)^3}\times\Big\{E_k + \frac{1}{\beta}\log\big(1+\exp\big(-\beta(E_k-\tilde{\mu}_i)\big)\big) \\ +\frac{1}{\beta}\log\big(1+\exp\big(-\beta(E_k+\tilde{\mu}_i)\big)\big)\Big\} + G_s\rho_s^2 - G_v\rho_v^2.\end{aligned} \tag{4.25}$$

Where, $N_c = 3$ is the colour degrees of freedom and $E_k = \sqrt{\mathbf{k}^2 + M^2}$ is the on shell single particle energy of the quark with constituent quark mass $M$ and $\tilde{\mu}_i$ being an effective quark chemical potential in the presence of the vector interaction. The constituent quark mass, $M$, satisfies the mass gap equation

$$M = m_q - 2G_s\rho_s, \tag{4.26}$$

and the effective quark chemical potential satisfies

$$\tilde{\mu}_i = \mu_i - 2G_v\rho_v. \tag{4.27}$$

Here, we focus our attention to $T = 0$ which is applicable to the cold NSs. Using the relation $\lim_{\beta\to\infty} \frac{1}{\beta} \log\left(e^{-\beta x} + 1\right) = -x\Theta(-x)$, the thermal factors in Eq. (4.25) go over into step functions and the mean field thermodynamic potential Eq. (4.25) becomes in the limit $T \to 0$

$$\Omega(M, 0, \mu) = -2N_c \sum_{i=u,d} \int \frac{d\mathbf{k}}{(2\pi)^3} \Big\{ E_k + (\tilde{\mu}_i - E_k)\ \Theta\left(\tilde{\mu}_i - E_k\right) \Big\} + G_s\rho_s^2 - G_v\rho_v^2. \tag{4.28}$$

The scalar density, $\rho_s$, and vector density, $\rho_v$, are given as

$$\begin{aligned} \rho_s &= -2N_c \sum_{i=u,d} \int \frac{d\mathbf{k}}{(2\pi)^3} \frac{M}{E_k} \Big(1 - \Theta\left(\tilde{\mu}_i - E_k\right)\Big) \\ &= -\frac{N_c M^3}{\pi^2} \sum_{i=u,d} \Big[G(\Lambda/M) - G(k_{Fi}/M)\Big], \end{aligned} \tag{4.29}$$

and

$$\rho_v = 2N_c \sum_{i=u,d} \int \frac{d\mathbf{k}}{(2\pi)^3} \Theta\left(\tilde{\mu}_i - E_k\right) = 2N_c \sum_{i=u,d} \frac{k_{Fi}^3}{6\pi^2}. \tag{4.30}$$

In Eq. (4.29), we have introduced the function $G(z)$ which is defined as

$$G(z) = \frac{1}{2}\left[z\sqrt{1+z^2} - \tanh^{-1}\left(\frac{z}{\sqrt{1+z^2}}\right)\right]. \tag{4.31}$$

The difference of the vacuum energy densities between the non-perturbative vacuum (characterized by the constituent quark mass, $M$) and energy density of the perturbative vacuum (characterized by current quark mass, $m_q$) is the bag constant, $B$, i.e.

$$B = \Omega(M, T = 0, \mu = 0) - \Omega(m_q, T = 0, \mu = 0). \tag{4.32}$$

This bag constant is to be subtracted from Eq. (4.28) so that the thermodynamic potential vanishes at vanishing temperature and density. The pressure, $p_{\mathrm{NJL}}$, i.e. the negative of the thermodynamic potential of the quark matter in the NJL model is given as

$$p_{\mathrm{NJL}} = p_{\mathrm{vac}} + p_{\mathrm{med}} + B, \tag{4.33}$$

where the vacuum, $p_{\rm vac}$, and the medium, $p_{\rm med}$, contributions to the pressure are given by

$$p_{\rm vac} = \frac{4N_c}{(2\pi)^3}\int_{|k|\leq\Lambda} d\mathbf{k}\sqrt{\mathbf{k}^2+M^2} \equiv \frac{2N_c}{\pi^2}M^4\, H(\Lambda/M), \tag{4.34}$$

and,

$$\begin{aligned} p_{\rm med} &= \frac{2N_c}{(2\pi)^3}\sum_{i=u,d}\int_0^{k_{Fi}} d\mathbf{k}\left[\sqrt{\mathbf{k}^2+M^2}-\tilde{\mu}_i\right] + G_s\rho_s^2 - G_v\rho_v^2 \\ &= \frac{N_c}{\pi^2}\sum_{i=u,d}\left[M^4 H(k_{Fi}/M) - \tilde{\mu}_i\rho_i\right] + G_s\rho_s^2 - G_v\rho_v^2, \end{aligned} \tag{4.35}$$

where, $k_{Fi} = \Theta(\tilde{\mu}_i - M)\sqrt{\tilde{\mu}_i^2 - M^2}$ is the Fermi-momenta of $i = u, d$ quark and $\Lambda$ is the three momentum cut-off. The function $H(z)$ is already defined in Eq. (4.16). From the thermodynamic relation, the energy density, $\epsilon_{\rm NJL}$, is given as

$$\epsilon_{\rm NJL} = \sum_{i=u,d}\mu_i\rho_i - p_{\rm NJL}. \tag{4.36}$$

where, $\rho_i = \frac{\gamma k_{Fi}^3}{6\pi^2}$, $(i = u, d, e)$ with the degeneracy factor $\gamma = 6$ for quarks and $\gamma = 2$ for electron. NSM is charge neutral as well as $\beta$-equilibrated. So the chemical potentials of the $u$ and $d$ quarks can be expressed in terms of quark chemical potential, $\mu_q$, and electric chemical potential, $\mu_E$, as $\mu_i = \mu_q + q_i\mu_E$ $(i = u, d)$. $q_i$'s are the electric charges of $u$ and $d$ quarks. The condition of charge neutrality is

$$\frac{2}{3}\rho_u - \frac{1}{3}\rho_d - \rho_e = 0. \tag{4.37}$$

Since the typical electric charge chemical potential is of the order of MeV, one can neglect the electron mass so that $k_{Fe} = |\mu_e|$. The total pressure and the energy density for the charge neutral quark matter are then given by

$$p_{\rm QP} = p_{\rm NJL} + p_e, \tag{4.38}$$
$$\epsilon_{\rm QP} = \epsilon_{\rm NJL} + \epsilon_e, \tag{4.39}$$

where, $\epsilon_e \simeq \frac{\mu_e^4}{4\pi^2}$ and $p_e \simeq \epsilon_e/3$.

We may note that the NJL model has four parameters − namely, the current quark mass, $m_q$, the three momentum cutoff, $\Lambda$, and the two coupling constants, $G_s$ and $G_v$. The values of the parameters are usually chosen by fitting the pion decay constant, $f_\pi = 92.4$ MeV, the chiral condensate, $\langle -\bar{\psi}_q\psi_q\rangle_u = \langle -\bar{\psi}_q\psi_q\rangle_d = (240.8\ \text{MeV})^3$ and the pion mass, $m_\pi = 135$ MeV. This fixes $m_q = 5.6$ MeV, $G_s\Lambda^2 = 2.44$ and $\Lambda = 587.9$ MeV. As mentioned $G_v$ is not fitted from any other physical constraint and we take it as a free parameter. We shall show our results for the two values of $G_v$ namely $G_v = 0$ and $G_v = 0.2G_s$. With this parameterisation, the constituent quark mass, $M$, comes 400 MeV, the critical chemical potential, $\mu_c$ for the chiral transition turns out to be $\mu_c = 1168$ MeV for the vector coupling constant $G_v = 0$ in NJL model.

### 4.2.3 Hadron-quark phase transition and a mixed phase

The number density or the quark chemical potential at which HQPT occurs is not known precisely from the first principle calculations in QCD but it is expected from various model calculations to occur at a density which is few times the nuclear saturation density. In the context of NSs, two types of phase transitions can be possible depending upon the surface tension [292–298] of the quark matter depending on the value of the surface tension for quark matter. It ought to be mentioned, however, the estimated values of the surface tension for quark matter vary over a wide range and is very much model dependent. As the value of the surface tension is not precisely known yet both the scenarios, (Maxwell and Gibbs) are plausible. In summary, we see the both scenarios as

1. Maxwell construction [310]
   (a) The surface tension of the quark matter is large.
   (b) Based on the assumption that nuclear matter EOS and quark matter EOS both are locally charge neutral.
   (c) The transition takes place at constant pressure *i.e.* $p_{\rm NM}(\mu_B) = p_{\rm QM}(\mu_B)$.
   (d) As a result, both phases are separated by a sharp interface.
2. Gibbs construction [311, 312]
   (a) The surface tension is small.
   (b) Charged nuclear matter and quark matter may share a common leptonic background. Negatively (positively) charged quark matter may be neutralized by a positively (negatively) charged nuclear matter.
   (c) The transition takes place at constant pressure *i.e.* $p_{\rm NM}(\mu_B, \mu_E) = p_{\rm QM}(\mu_B, \mu_E)$.
   (d) As a consequence, we do not have a sharp interface. We have a MP, where both phases coexist and global charge neutral hybrid matter phase or mixed phase.

In the present study, we adopt the Gibbs construction for HQPT as nicely outlined in Ref. [311]. One can achieve charge neutrality with a positively charged hadronic matter mixed with a negatively charged quark matter in necessary amounts leading to a global charge neutrality where the pressures of the both phases are the functions of two independent chemical potentials $\mu_B$ and $\mu_E$. The Gibbs condition for the equilibrium at the zero temperature between the two phases for such a two component system is given by [291]

$$p_{\mathrm{HP}}(\mu_B, \mu_E) = p_{\mathrm{QP}}(\mu_B, \mu_E) = p_{\mathrm{MP}}(\mu_B, \mu_E), \tag{4.40}$$

where, the pressure for HP, $p_{\mathrm{HP}}$, is given in Eq. (4.15) and the pressure for the quark phase (QP), $p_{\mathrm{QP}}$, is written down in Eq. (4.38). In Fig. 4.1 we illustrate this calculation where the pressure is plotted as a function of baryon chemical potential, $\mu_B(=\mu_n)$, and electric chemical potential, $-\mu_E(=\mu_e)$. The green surface denotes the pressure in the HP estimated from the RMF model using NL3 parameters. The purple surface denotes the pressure in the QP estimated in NJL model. The two surfaces intersect along the curve $AB$ satisfying the global charge neutrality condition,

$$\chi\, \rho_c^{\mathrm{QP}} + (1-\chi)\, \rho_c^{\mathrm{HP}} = 0, \tag{4.41}$$

where, $\rho_c^{\mathrm{HP}}$ and $\rho_c^{\mathrm{QP}}$ denote the total charge densities in HP and QP respectively and $\chi$ defines the volume fraction of the quark matter in MP defined as,

$$\chi = \frac{V_{\mathrm{QP}}}{V_{\mathrm{QP}} + V_{\mathrm{HP}}}. \tag{4.42}$$

Explicitly, for a given $\mu_B$, we calculate the electric charge chemical potential, $\mu_E$, such that the pressure in both the phases are equal, satisfying the Gibbs condition, Eq. (4.40). This gives the intersection line ($AB$) of the two surfaces as shown in Fig. 4.1. Further imposing the global charge neutrality condition, Eq. (4.41), one obtains the volume fraction $\chi$ occupied by quark matter in MP. Thus along the line $AB$ in Fig. 4.1, the volume fraction occupied by quark matter increases monotonically from $\chi = 0$ (at point $A$) to $\chi = 1$ (at point $B$). This gives pressure for the globally charged neutral matter in MP. Below $\chi < 0$, EOS corresponds to the local charge neutral hadronic matter EOS shown as the red dashed curve while for $\chi > 1$ EOS corresponds to the local charge neutral quark matter EOS shown as the purple dashed curve in Fig. 4.1. With NL3 parametrization of the RMF model for hadronic matter and NJL model for quark matter, MP starts at

$$(\mu_B, \mu_e, p) = (1423\mathrm{MeV}, 289.26\mathrm{MeV}, 144.56\mathrm{MeV/fm}^3)$$

and ends at

$$(\mu_B, \mu_e, p) = (1597\mathrm{MeV}, 102.40\mathrm{MeV}, 266.23\mathrm{MeV/fm}^3).$$

This corresponds to starting of MP at baryon density $\rho_B = 2.75\rho_0$ and ending of MP at baryon density $\rho_B = 5.72\rho_0$. For NJL model we have taken, here, $G_v = 0.2G_s$. For $G_v = 0$, MP starts a little earlier *i.e.* $\rho_B = 2.36\rho_0$ and ends at $\rho_B = 5.22\rho_0$. After MP, as baryon density increases the matter is in pure charge neutral QP. We find

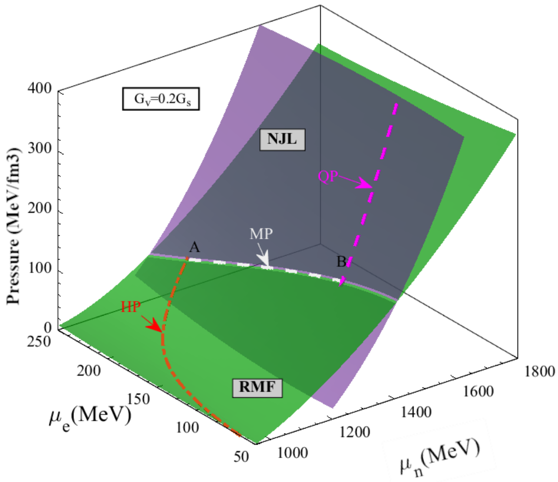


FIGURE 4.1: Pressure is plotted as a function of $\mu_n(\mu_B)$ and $\mu_e(-\mu_E)$ for HP and QP. The green surface is for HP and the purple surface is for QP. The two surfaces intersect along the curve $AB$. Along the dashed portion on this curve, global charge neutrality is maintained. Red and magenta dashed lines show the local charge neutrality in HP and QP, respectively. The quark matter fraction $\chi$ increases monotonically from $\chi = 0$ (at point $A$) to $\chi = 1$ (at point $B$) along the curve $AB$. Here, we have considered the NL3 parameterisation of RMF for the description of hadronic matter and NJL model for the description of quark matter.

energy density in the MP as follows,

$$\epsilon_{\rm MP} = \chi\epsilon_{\rm QP} + (1-\chi)\epsilon_{\rm HP}. \tag{4.43}$$

We also see the fraction of particles normalized with respect to the baryon number density in different phases which we have plotted in Fig. 4.2 for $G_v = 0.2G_s$. Similar to Eq. (4.43) the baryon number density in MP

$$\rho^B_{\rm MP} = \chi\rho^B_{\rm QP} + (1-\chi)\rho^B_{\rm HP}. \tag{4.44}$$

In MP region, nuclear matter fraction decreases while quark matter fraction increases with increasing $\rho_B$. As $\rho_B$ increases further the nuclear matter melts completely to quark matter which occurs for densities beyond $\rho_B = 5.72\rho_0$.

MP construction using the DDB parameterisation of the hadronic EOS is also similar. MP, in this case, starts at

$$(\mu_B, \mu_e, p) = (1416.5\text{MeV}, 204.58\text{MeV}, 181.76\text{MeV/fm}^3)$$

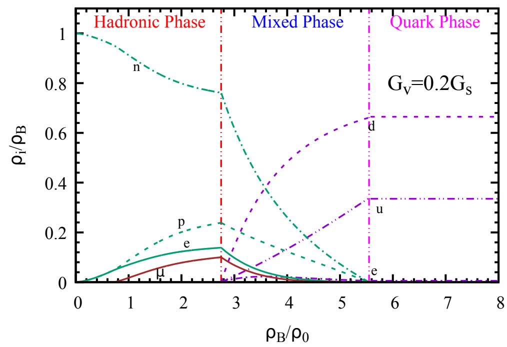


FIGURE 4.2: The particle fractions normalized with respect to baryon density for the charge neutral matter are plotted as a function of the baryon number density. At $\rho_B = 2.75\rho_0$, quark matter starts to appear and at $\rho_B = 5.72\rho_0$ hadronic matter melts completely in quark matter. HP is described by RMF model with NL3 parameterisation and QP is described in NJL model where we took the vector interaction $G_v = 0.2G_s$.

where the baryon number density is $\rho_B = 3.93\rho_0$ and ends at

$$(\mu_B, \mu_e, p) = (1504\text{MeV}, 108.42\text{MeV}, 245.51\text{MeV/fm}^3)$$

where the baryon number density is $\rho_B = 6.98\rho_0$ beyond which we find stable QP.

## 4.3 Non-radial oscillation modes in compact stars

In this section, we outline the equations governing the oscillation modes of the fluid comprising NSM. The most general metric for a spherically symmetric space-time is given by

$$\begin{aligned} ds^2 &= g_{\alpha\beta} dx^\alpha dx^\beta \\ &= e^{2\nu} dt^2 - e^{2\lambda} dr^2 - r^2(d\theta^2 + \sin^2\theta d\phi^2), \end{aligned} \tag{4.45}$$

where, $\nu$ and $\lambda$ are the metric functions. It is convenient to define the mass function, $m(r)$ in the favour of $\lambda$ as

$$e^{2\lambda} = \left(1 - \frac{2m}{r}\right)^{-1}. \tag{4.46}$$

Starting from the line element Eq. (4.45) one can obtain the equations governing the structure of spherical compact objects, the TOV equations, as

$$\frac{dp}{dr} = -(\epsilon + p)\frac{d\nu}{dr}, \tag{4.47}$$
$$\frac{dm}{dr} = 4\pi r^2 \epsilon, \tag{4.48}$$
$$\frac{d\nu}{dr} = \frac{m + 4\pi r^3 p}{r(r-2m)}. \tag{4.49}$$

In the above set of equations $\epsilon$, $p$ are the energy density and the pressure respectively. $m(r)$ is the mass of CS enclosed within a radius $r$. To solve these equations, one has to supplement these equations with an equation relating pressure and energy density *i.e.* an EOS. Further, one has to set the boundary conditions at the center and surface as

$$m(0) = 0 \qquad \text{and} \qquad p(0) = p_c, \tag{4.50}$$
$$p(R) = 0, \tag{4.51}$$
$$e^{2\nu(R)} = 1 - \frac{2M}{R}, \tag{4.52}$$

where, the total mass of the compact object is given by $M = m(R)$ [1], $R$ being it's radius which is defined as the radial distance where the pressure vanishes while integrating out Eqs. (4.47, 4.48 and 4.49) from the center to the surface of the star. One can solve these equations along with boundary conditions Eqs. (4.50, 4.51 and 4.52) for a set of central densities $\epsilon_c$ or corresponding pressure $p_c$ to obtain the mass-radius, $(M-R)$ curve.

For the sake of completeness, we give below a succinct derivation of pulsating equations in the context of NS within a relativistic setting [280, 313]. The Einstein field equation that relates the curvature of space time to the energy momentum tensor is given as

$$R_{\alpha\beta} - \frac{1}{2} g_{\alpha\beta} R = 8\pi T_{\alpha\beta}, \tag{4.53}$$

with $T_{\alpha\beta}$ being the stress energy tensor, which for a perfect fluid is given by

$$T^{\mu\nu} = (p+\epsilon) u^\mu u^\nu - p g^{\mu\nu}, \tag{4.54}$$

with $p$ and $\epsilon$ being the pressure and energy density respectively and $u^\mu$ is the four-velocity. Taking (covariant) divergence of the Einstein equation, Eq. (4.53), the left hand side of Eq. (4.53) vanishes using Bianchi identity leading to covariant conservation equation of the energy momentum tensor i.e. $T^{\mu\nu}_{;\mu} = 0$. With $T^{\mu\nu}$

[1] In this section, $M$ denotes the mass of CSs to be distinguished from the constituent quark mass defined in Sec 4.2.2.

given in Eq. (4.54), this reduces to

$$(p+\epsilon)u^{\mu}u_{\nu;\mu} = \partial_{\nu}p - u_{\nu}u^{\mu}\partial_{\mu}p \tag{4.55}$$

which is the relativistic Euler equation [313]. Next, to derive the equation of motion, we use the conservation of baryon number. This is similar to using continuity equation in non-relativistic case which follows from mass conservation. The baryon number conservation equation is given by

$$\frac{dn}{d\tau} = -nu^{\mu}_{;\mu}, \tag{4.56}$$

where, $n$ is the baryon number density.

We shall derive the equations in spherical coordinates and the perturbations will be expanded in terms of vector spherical harmonics. The position $(t, r, \theta, \phi)$ of a fluid element in space time as a function of proper time $\tau$ is given by the position four-vector $\xi(\tau)$ as

$$\xi(\tau) = \begin{pmatrix} \xi^t \\ \xi^r \\ \xi^{\theta} \\ \xi^{\phi} \end{pmatrix}. \tag{4.57}$$

Consider a fluid element located at $\xi_0$ as its equilibrium position is displaced to $\xi(\xi_0,\tau) = \xi_0 + \zeta(\xi_0,\tau)$. This results perturbation in pressure $p$, in energy density $\epsilon$ and in baryon number density $n$ as

$$p = p_0 + \delta p, \tag{4.58}$$
$$\epsilon = \epsilon_0 + \delta\epsilon, \tag{4.59}$$
$$n = n_0 + \delta n, \tag{4.60}$$

where, the subscript '0' refers to the corresponding quantities in equilibrium. To derive the equations of motion for the perturbation, one has to linearize the Euler equation, Eq. (4.55) in the perturbation. For this we need the four velocities of the fluid elements $u^{\mu} = \frac{d\xi^{\mu}}{d\tau} = \frac{d\zeta^{\mu}}{d\tau}$. Further, we shall confine ourselves to performing the analysis for a spherical harmonic component with the azimuthal index $m = 0$. For the displacement vector $\zeta^{\mu}$ we take the ansatz

$$\begin{pmatrix} \zeta^t \\ \zeta^r \\ \zeta^{\theta} \\ \zeta^{\phi} \end{pmatrix} = \begin{pmatrix} t \\ \dfrac{e^{-\lambda}Q(r,t)}{r^2}P_l(\cos\theta) \\ -\dfrac{Z(r,t)}{r^2}\partial_{\theta}P_l(\cos\theta) \\ 0 \end{pmatrix}, \tag{4.61}$$

where, $Q(r,t)$ and $Z(r,t)$ are the perturbing functions. We choose a harmonic time dependence for the perturbation *i.e.* $\propto e^{i\omega t}$ with frequency $\omega$. Further, we do not consider toroidal deformations here. From the normalisation condition for the velocity $u_\mu u^\mu = 1$, and keeping upto linear terms in the perturbation, we have $u^t = d\zeta^t/d\tau = e^{-\nu}$. The other components of the four-velocity are given as

$$\begin{pmatrix} u^t \\ u^r \\ u^\theta \\ u^\phi \end{pmatrix} = \begin{pmatrix} e^{-\nu} \\ e^{-\nu}\dot{\zeta}^r \\ e^{-\nu}\dot{\zeta}^\theta \\ 0 \end{pmatrix}, \tag{4.62}$$

where, the dot on the perturbed coordinate denotes the derivative with respect to time '$t$'. Similarly, the contravariant velocity components are given using the metric given in Eq. (4.45) and Eq. (4.62) as

$$\begin{pmatrix} u_t \\ u_r \\ u_\theta \\ u_\phi \end{pmatrix} = \begin{pmatrix} e^{\nu} \\ -e^{2\lambda-\nu}\dot{\zeta}^r \\ -r^2 e^{-\nu}\dot{\zeta}^\theta \\ 0 \end{pmatrix}. \tag{4.63}$$

Now we simplify the Euler equation *i.e.* Eq. (4.55) by substituting the expressions for pressure, energy density and the fluid four-velocity and linearizing in terms of the perturbing functions. The $\nu = t$ component of the Euler equation, Eq. (4.55), reduces to

$$(p_0 + \epsilon_0)\nu'(r) = -p_0'(r), \tag{4.64}$$

where, the superscript 'prime' corresponds to the derivative with respect to '$r$'. To obtain Eq. (4.64), we have used in the LHS of Eq. (4.55), with $\nu = t$, $u^\mu u_{t;\mu} = \nu'\dot{\zeta}^r$ and in RHS we have used the fact that $p_0$ is isotropic so that $\dot{p}_0 - u_t u^\mu \partial_\mu p \sim -\dot{\zeta}^r p_0'(r)$. Let us recognise that the Eq. (4.64) is essentially a part of the TOV equations (Eq. (4.47)) relating pressure gradient and the metric function gradient. Next, the $\nu = r$ component of the Euler equation, Eq. (4.55), reduces to

$$\omega^2(\epsilon_0 + p_0)e^{2(\lambda-\nu)}\zeta^r - (\delta\epsilon + \delta p)\nu'(r) - \frac{d}{dr}(\delta p) = 0. \tag{4.65}$$

Similarly, the $\nu = \theta$ component of the Euler equation, Eq. (4.55), by using $u^\mu u_{\theta;\mu} = u^t \partial_t u_\theta = -e^{-2\nu} r^2 \ddot{\zeta}^\theta$, is given as

$$\omega^2(\epsilon_0 + p_0)e^{-2\nu} r^2 \zeta^\theta - \partial_\theta \delta p = 0. \tag{4.66}$$

Having written down the Euler equation to linear order in the perturbation, let us next consider the baryon number conservation equation i.e. Eq. (4.56). With the velocity components given in Eqs. (4.62, 4.63) and Eq. (4.61) for the perturbation,the number conservation equation, Eq. (4.56) can be written in terms of the radial and azimuthal perturbing functions $Q(r)$ and $Z(r)$ as

$$\frac{dn}{d\tau} = -\frac{n}{r^2}\left[e^{-(\lambda+\nu)}\frac{\partial^2 Q(r,t)}{\partial r\partial t} + e^{-\nu}l(l+1)\dot{Z}\right]P_l(\cos\theta). \tag{4.67}$$

We might note here that, since the proper time derivative is taken along the world line of the fluid parcel, we can write $\frac{dn}{d\tau} = \frac{d\Delta n}{d\tau}$, where, $\Delta n$ is the Lagrangian perturbation. Further, using the relation $\partial/\partial t = e^{-\nu}\partial/\partial\tau$, we can integrate Eq. (4.67) over $d\tau$ to obtain the Lagrangian perturbation in number density $\Delta n$ in terms of the perturbing functions $Q$ and $Z$ as

$$\frac{\Delta n}{n_0} = -\frac{1}{r^2}\left[e^{-\lambda}Q' + l(l+1)Z\right]P_l(\cos\theta). \tag{4.68}$$

To write down the equations in terms of the perturbing functions $Q(r)$ and $Z(r)$, we need to express the energy density perturbation $\delta\epsilon$ and pressure perturbation $\delta p$ occurring in Eqs. (4.64, 4.65) in terms of the functions $Q(r)$ and $Z(r)$. The strategy is to use the Euler equation Eq. (4.55) to write $\delta\epsilon$ in terms of $\delta n$ and use definition of bulk modulus ($\kappa = n\frac{\Delta p}{\Delta n}$) to write $\delta p$ in terms of $\delta n$. One can then use the baryon number conservation equation Eq. (4.67) to write $\delta\epsilon$ and $\delta p$ in terms of the perturbing functions.

Thus, using the Euler equation Eq. (4.55) to eliminate $u^\mu_{;\mu}$ in the baryon number conservation Eq. (4.56), we have

$$\frac{dn}{d\tau} = \frac{n}{p+\epsilon}\frac{\partial\epsilon}{\partial\tau}, \tag{4.69}$$

which leads to

$$\Delta\epsilon \simeq \frac{\epsilon_0 + p_0}{n_0}\Delta n. \tag{4.70}$$

Further, using the relation between the Lagrangian perturbation and the Eulerian perturbation i.e. $\Delta\epsilon = \delta\epsilon + \zeta^r\frac{d\epsilon_0}{dr}$ and using Eq. (4.68), we have

$$\delta\epsilon = -\left[\frac{\epsilon_0 + p_0}{r^2}\left\{e^{-\lambda}Q' + l(l+1)Z\right\} + \frac{e^{-\lambda}}{r^2}Q\frac{d\epsilon_0}{dr}\right]P_l(\cos\theta). \tag{4.71}$$

Next, let us find out the relation between $\delta p$ and $\Delta n$. The Eulerian variation $\delta p$ and the Lagrangian variation $\Delta p$ are related as

$$\delta p = \Delta p - \zeta^r\frac{dp_0}{dr}. \tag{4.72}$$

Thus, using Eq. (4.61) and Eq. (4.68), we have

$$\delta p = -\left[\frac{\kappa}{r^2}(e^{-\lambda}Q' + l(l+1)Z) + \frac{e^{-\lambda}}{r^2}\frac{dp_0}{dr}Q\right] P_l(\cos\theta). \tag{4.73}$$

Further, $\Delta p$ is related to $\Delta n$, through bulk modulus $\kappa$ i.e.

$$\kappa = n\frac{\Delta p}{\Delta n}.$$

In the relativistic Cowling approximation, the metric perturbations are neglected. This will mean the energy and pressure perturbations should also vanish. In the relativistic Cowling approximation, the energy density perturbation $\delta\epsilon$ is set to zero but pressure perturbation is not set to zero. As shown in Ref.[280], such an approximation leads to qualitatively correct results which we shall also follow. Setting $\delta\epsilon = 0$ in Eq. (4.65), and using Eq. (4.73), we have

$$\nu'\delta p + \frac{d\delta p}{dr} = -\nu'\kappa X - \frac{d(\kappa X)}{dr} - \nu'(p_0+\epsilon_0)l(l+1)\frac{Z}{r^2} + (p_0+\epsilon_0)Q\frac{d}{dr}\left(\frac{e^{-\lambda}\nu'}{r^2}\right), \tag{4.74}$$

where, we have defined for the sake of brevity $X = (e^{-\lambda}Q' + l(l+1)Z)/r^2$.Using this, the radial Euler equation, Eq. (4.65) becomes

$$\omega^2(\epsilon_0+p_0)e^{\lambda-2\nu}\frac{Q}{r^2} + \frac{d\,[\kappa X]}{dr} + \nu'\kappa X + \nu'(\epsilon_0+p_0)l(l+1)\frac{Z}{r^2} - (\epsilon_0+p_0)\frac{d}{dr}\left(\frac{e^{-\lambda}\nu'}{r^2}\right) = 0. \tag{4.75}$$

Similarly, the azimuthal component of the Euler equation Eq. (4.66) becomes

$$\omega^2(p_0+\epsilon_0)e^{-2\nu}Z - \kappa X - p_0'\frac{e^{-\lambda}Q}{r^2} = 0. \tag{4.76}$$

It can be shown that the Eq. (4.75) through a rearrangement of terms is identical to that obtained earlier by McDermott et. al. [280] with an appropriate change of factor 2 in the metric functions $\nu(r)$ and $\lambda(r)$. Few more comments here may be in order. In literature, sometimes the adiabatic index $\gamma$ is used instead of $\kappa$ and is defined as [85]

$$\gamma = \left(\frac{\partial \ln p_0}{\partial \ln n_0}\right)_s = \frac{n_0\Delta p}{p_0\Delta n} \tag{4.77}$$

so that $\kappa = \gamma p_0$. Further, the same can be related to adiabatic speed of sound as follows. By using the definition of Jacobian and standard thermodynamic relation

$$\left(\frac{\partial \ln p_0}{\partial \ln n_0}\right)_s = \frac{n_0^2}{p_0\chi_{\mu\mu}} \tag{4.78}$$

in the zero temperature limit. The adiabatic speed of sound at zero temperature is defined as [314]

$$c_s^2 = \left(\frac{\partial p_0}{\partial \epsilon_0}\right)_s = \frac{n}{\mu \chi_{\mu\mu}}$$

so that

$$\gamma = \frac{p_0 + \epsilon_0}{p_0} c_s^2. \tag{4.79}$$

Let us note that Eq. (4.75) is a second order differential equation for the perturbing function $Q(r)$. We now use Eq. (4.76) to write down two coupled first order equations for the perturbing functions. Using Eq. (4.76) and Eq. (4.79), we have the equation for perturbation as

$$Q' - \frac{1}{c_s^2}\left[\omega^2 r^2 e^{\lambda - 2\nu} Z + \nu' Q\right] + l(l+1)e^{\lambda} Z = 0. \tag{4.80}$$

Next one can calculate the combination $d[Eq.(4.76)]/dr + [Eq.(4.75)]$ and substitute Eq. (4.76) again which leads to the first order differential equation for $Z'$ as

$$Z' - 2\nu' Z + e^{\lambda}\frac{Q}{r^2} - \nu'\left(\frac{1}{c_e^2} - \frac{1}{c_s^2}\right)\left(Z + \nu' e^{-\lambda + 2\nu}\frac{Q}{\omega^2 r^2}\right) = 0. \tag{4.81}$$

In the above equation $c_e^2 = \frac{dp_0}{d\epsilon_0} = \frac{p_0'}{\epsilon_0'}$ is the equilibrium speed of sound. It may be noted that Eq. (4.84) can be rewritten as

$$\omega^2 e^{\lambda}\frac{Q}{r^2} + \omega^2 Z' + A_- e^{\lambda}\omega^2 Z - A_+ e^{2\nu}\frac{p_0'}{p_0 + \rho_0}\frac{q}{r^2} = 0. \tag{4.82}$$

where, $A_+ = e^{-\lambda}(\epsilon_0'/(p_0 + \epsilon_0) + \nu'/c_s^2)$ and $A_- = A_+ - 2\nu' e^{-\lambda}$. It is reassuring to see that the Eq. (4.80) and Eq. (4.82) are identical to the corresponding equations Eq.(3b) and Eq.(4a) given in Ref. [280]. The gravity mode ($g$ mode) oscillation frequencies are closely related to the Brunt-Väisäla frequency, $\omega_{BV}$ [280]. The relativistic generalisation of $\omega_{BV}$ is given by

$$\omega_{BV}^2 = \nu'^2 e^{2\nu}\left(1 - \frac{2m}{r}\right)\left(\frac{1}{c_e^2} - \frac{1}{c_s^2}\right). \tag{4.83}$$

This also reduces to the expression for the $\omega_{BV}$ in Newtonian limit [281].

The equation for the perturbation function $Z(r)$ can be rewritten in terms of the Brunt-Väisäla frequencies as

$$Z' - 2\nu' Z + e^{\lambda}\frac{Q}{r^2} - \frac{\omega_{BV}^2 e^{-2\nu}}{\nu'\left(1 - \frac{2m}{r}\right)}\left(Z + \nu' e^{-\lambda + 2\nu}\frac{Q}{\omega^2 r^2}\right) = 0. \tag{4.84}$$

The two coupled first order differential equations for the perturbing functions $Q(r,t)$ and $Z(r,t)$, Eqs. (4.80),(4.84), are to be solved with appropriate boundary conditions at the center and the surface. Near the center of CSs the behavior of the functions $Q(r)$ and $Z(r)$ are given by [85]

$$Q(r) = Cr^{l+1} \qquad \text{and} \qquad Z(r) = -Cr^l/l \tag{4.85}$$

where, $C$ is an arbitrary constant and $l$ is the order of the oscillation. The other boundary condition is the vanishing of the Lagrangian perturbation pressure, i.e. $\Delta p = 0$ at the stellar surface. Using equations Eqs. (4.72, 4.73 and 4.80), we have the Lagrangian perturbation pressure $\Delta p$ given as

$$\Delta p = -\frac{(p_0 + \epsilon_0)}{r^2}\left[\omega^2 r^2 e^{\lambda - 2\nu} Z + \nu' Q\right] e^{-\lambda}. \tag{4.86}$$

Thus the vanishing of $\Delta p$ at the surface of the star ($r = R$) leads to the boundary condition [315]

$$\omega^2 r^2 e^{\lambda-2\nu} Z + \nu' Q\Big|_{r=R} = 0. \tag{4.87}$$

Further, in case one considers stellar models with a discontinuity in the energy density, one has to supplement additional condition at the surface of discontinuity demanding $\Delta p$ to be continuous *i.e.* $\Delta p(r = r_{c-}) = \Delta p(r = r_{c+})$. Where, $r_c$ is the radial distance of the surface of energy density discontinuity from the center. This leads to [85, 315]

$$Q_+ = Q_-, \tag{4.88}$$

$$Z_+ = \frac{e^{2\nu}}{\omega^2 r_c}\left\{\frac{\epsilon_{0-} + p_0}{\epsilon_{0+} + p_0}\left(\omega^2 r_c^2 e^{-2\nu} Z_- + e^{-\lambda}\nu' Q_-\right) - e^{-\lambda}\nu' Q_+\right\}, \tag{4.89}$$

where, the $-(+)$ subscript corresponds to the quantities before (after) the surface of discontinuity. In case of a Maxwell construct for phase transition, there is a discontinuity in energy density while in Gibbs construct of phase transition the energy density is continuous at the phase boundary as considered here.

With these boundary conditions the problem becomes an eigen-value problem for '$\omega$'. To calculate the eigen frequencies $\omega$, we proceed as follows. For a given central density $\epsilon_c$, we first solve the TOV equations, Eqs. (4.47 - 4.49), to get the profile of the unperturbed metric functions $\lambda(r)$, $\nu(r)$ and also mass $M$ and radius $R$ of a spherically symmetric CS. For a given $\omega$, we solve the pulsating equations, Eqs. (4.80 and 4.84), to determine the fluid perturbing functions $Q(r)$ and $Z(r)$ as a function of $r$. To solve these equations, we take the initial values for $Q$ and $Z$ consistent with Eq. (4.85). Specifically, we took C of the order 1. The solutions of $Q$ and $Z$ are independent of this choice, ($C = 1$). We then calculate the LHS of Eq. (4.87). The value of $\omega$ is then varied such that the boundary condition, Eq. (4.87), is satisfied. This gives the frequency, $\omega$ as function of mass and radius. It may be noted that there can be multiple solutions of $\omega$ satisfying pulsating equations and boundary conditions corresponding to different initial trail values for $\omega$. These different solutions for $\omega$ correspond to frequencies of different modes of oscillations of CS.

## 4.4 Equilibrium and adiabatic speeds of sound

In this section we discuss both equilibrium and adiabatic sound speeds which are needed to solve the pulsating equations Eqs. (4.80) and (4.84). We present the expressions of both sound speeds for matter in HP, QP and MP. The equilibrium speed of sound is given by

$$c_e^2 = \frac{dp}{d\epsilon} = \frac{dp/dr}{d\epsilon/dr}. \tag{4.90}$$

where, $p$ and $\epsilon$ are total pressure and energy density. The equilibrium sound speed in NS can be evaluated numerically as a function of radial distance from the center of the star while keeping the NSM in $\beta$-equilibrium. Using the above definition (4.90), we find the equilibrium speed of sound in HP, QP and MP.

The characteristic time scale of QNM is about $10^{-3}$sec which is much smaller than the $\beta$-equilibrium time scale. Therefore, during the oscillations the composition of the matter can be assumed to be constant. Such adiabatic approximation means the adiabatic speed of sound corresponds to the constant composition i.e.

$$c_s^2 = \left(\frac{\partial p}{\partial \epsilon}\right)_{y_i} = \frac{(\partial p/\partial n_B)_{y_i}}{(\partial p/\partial n_B)_{y_i}}, \tag{4.91}$$

where, $y_i = (n_i/n_B)$'s are the fractions of the constituents of the matter which need to be held fixed while taking the derivatives. Once the derivatives are taken, we apply the $\beta$-equilibrium condition and get the adiabatic speed of sound in different phases. In the following subsections we present the analytical expressions for the adiabatic speeds of sound in HP, QP and MP.

### 4.4.1 Speed of sound in hadronic phase

In the following we estimate the adiabatic speed of sound of hadronic matter within the RMF model as

$$c_{s,\mathrm{HP}}^2 = \frac{\left(\frac{\partial p_{\mathrm{HP}}}{\partial n_B}\right)_{y_i}}{\left(\frac{\partial \epsilon_{\mathrm{HP}}}{\partial n_B}\right)_{y_i}}. \tag{4.92}$$

The total energy density and total pressure of matter in HP are given in Eqs. (4.14) and (4.15). Using these equations we find the partial derivative of pressure and energy density with respect to baryon number density at constant composition (fixed $y_i$) as

$$\left(\frac{\partial p_{\rm HP}}{\partial n_B}\right)_{yi} = \sum_{i=n,p,l}\left[\mu_i y_i + \left(\frac{\partial \mu_i}{\partial n_B}\right)_{y_i} n_B\right] - \left(\frac{\partial \epsilon_{\rm HP}}{\partial n_B}\right)_{y_i}, \tag{4.93}$$

and,

$$\begin{aligned}\left(\frac{\partial \epsilon_{\rm HP}}{\partial n_B}\right)_{y_i} &= \frac{1}{2\pi^2}\sum_{i=n,p,e,\mu}\left[E_{Fi}k_{Fi}^2\left(\frac{\partial k_{Fi}}{\partial n_B}\right)_{y_i} + m^*\left(E_{Fi}k_{Fi} - m^{*2}\log x_i\right)\left(\frac{\partial m^*}{\partial n_B}\right)_{y_i}\right] \\ &+ (m_\sigma^2\sigma_0 + V'(\sigma_0))\left(\frac{\partial \sigma_0}{\partial n_B}\right)_{y_i} + m_\omega^2\omega_0\left(\frac{\partial \omega_0}{\partial n_B}\right)_{y_i} + m_\rho^2\rho_3^0\left(\frac{\partial \rho_3^0}{\partial n_B}\right)_{y_i}\end{aligned} \tag{4.94}$$

Here, $x_i = \dfrac{E_{Fi} + k_{Fi}}{m^*}$. The derivatives of the meson fields at constant composition, using Eqs. (4.6-4.8) are given as

$$\left(\frac{\partial \sigma_0}{\partial n_B}\right)_{y_i} = \frac{g_\sigma(a_p + a_n)}{m_\sigma^2 + V''(\sigma_0) - g_\sigma(b_p + b_n)}, \tag{4.95}$$

$$\left(\frac{\partial \omega_0}{\partial n_B}\right)_{y_i} = \frac{g_\omega(y_p + y_n)}{m_\omega^2}, \tag{4.96}$$

$$\left(\frac{\partial \rho_3^0}{\partial n_B}\right)_{y_i} = \frac{g_\rho(y_p - y_n)}{2m_\rho^2}, \tag{4.97}$$

where, $V''(\sigma_0)$ is the second derivative of Eq. (4.5) with respect to $\sigma_0$. The quantities $a_i$ and $b_i$, $(i = n, p)$ are given by

$$a_i = \frac{m^* y_i}{E_{Fi}}, \tag{4.98}$$

$$b_i = \frac{g_\sigma}{2\pi^2}\left[3m^{*2}\log x_i - E_{Fi}k_{Fi} - \frac{2m^{*2}k_{Fi}}{E_{Fi}}\right]. \tag{4.99}$$

Eqs. (4.93 and 4.94) lead, inturn, to the derivatives of the medium dependent mass ($m^*$) and the chemical potential ($\mu_i$) with respect to baryon number density at constant composition is given as

$$\left(\frac{\partial m^*}{\partial n_B}\right)_{y_i} = -g_\sigma\left(\frac{\partial \sigma_0}{\partial n_B}\right)_{y_i}, \tag{4.100}$$

$$\left(\frac{\partial \mu_i}{\partial n_B}\right)_{y_i} = \left(\frac{\partial \tilde{\mu}_i}{\partial n_B}\right)_{y_i} + g_\omega\left(\frac{\partial \omega_0}{\partial n_B}\right)_{y_i} + g_\rho I_{3i}\left(\frac{\partial \rho_{30}}{\partial n_B}\right)_{y_i}, \tag{4.101}$$

where, $\tilde{\mu}_i = \sqrt{k_{Fi}^2 + m^{*2}}$. Further, we have on direct evaluation, using $n_B = \sum_{i=n,p} \frac{k_{Fi}^3}{3\pi^2}$,

$$\left(\frac{\partial k_{Fi}}{\partial n_B}\right)_{y_i} = \frac{k_{Fi}}{3n_B}. \tag{4.102}$$

Thus the partial derivatives of pressure, Eq. (4.93) and energy density Eq. (4.94) gets completely defined. This gives the adiabatic speed of sound in hadronic matter in the RMF model.

Similarly, one can determine the sound speeds in DDB model. The expressions of the partial derivatives of pressure and energy density in DDB model are similar to Eq. (4.93) and Eq. (4.94) except that there are additional terms due to the density dependent couplings. Here we give the expressions with the incorporation of corresponding changes arising from the density dependent couplings. The derivatives of the meson fields in DDB model is given as follows

$$\left(\frac{\partial \sigma_0}{\partial n_B}\right)_{y_i} = \frac{1}{m_\sigma^2 - g_\sigma(b_p + b_n)} \left(g_\sigma(a_p' + a_n') + \left(\frac{\partial g_\sigma}{\partial n_B}\right)_{y_i} (n_p^s + n_n^s)\right), \tag{4.103}$$

$$\left(\frac{\partial \omega_0}{\partial n_B}\right)_{y_i} = \frac{1}{m_\omega^2} \left(g_\omega(y_p + y_n) + \left(\frac{\partial g_\omega}{\partial n_B}\right)_{y_i} (n_p + n_n)\right), \tag{4.104}$$

$$\left(\frac{\partial \rho_3^0}{\partial n_B}\right)_{y_i} = \frac{1}{2m_\rho^2} \left(g_\rho(y_p - y_n) + \left(\frac{\partial g_\rho}{\partial n_B}\right)_{y_i} (n_p - n_n)\right), \tag{4.105}$$

where, with $a_i$ and $b_i$ as given in Eqs. (4.98 and 4.99),

$$a_i' = a_i + \frac{b_i \sigma_0}{g_\sigma} \left(\frac{\partial g_\sigma}{\partial n_B}\right)_{y_i}, \tag{4.106}$$

and, the derivatives of the density dependent couplings are given as

$$\left(\frac{\partial g_\sigma}{\partial n_B}\right)_{y_i} = -\frac{g_\sigma a_\sigma}{\rho_0} x^{a_\sigma - 1}, \tag{4.107}$$

$$\left(\frac{\partial g_\omega}{\partial n_B}\right)_{y_i} = -\frac{g_\omega a_\omega}{\rho_0} x^{a_\omega - 1}, \tag{4.108}$$

$$\left(\frac{\partial g_\rho}{\partial n_B}\right)_{y_i} = -\frac{g_\rho a_\rho}{\rho_0}. \tag{4.109}$$

The derivatives of the medium dependent mass and the effective chemical potential at constant composition is defined as

$$\left(\frac{\partial m^*}{\partial n_B}\right)_{y_i} = -g_\sigma \left(\frac{\partial \sigma_0}{\partial n_B}\right)_{y_i} - \left(\frac{\partial g_\sigma}{\partial n_B}\right)_{y_i} \sigma_0, \tag{4.110}$$

and,

$$\left(\frac{\partial \mu_i}{\partial n_B}\right)_{y_i} = \left(\frac{\partial \mu_i^*}{\partial n_B}\right)_{y_i} + \left(\frac{\partial g_\omega}{\partial n_B}\right)_{y_i} \omega_0 + g_\omega \left(\frac{\partial \omega_0}{\partial n_B}\right)_{y_i} + \left(\frac{\partial g_\rho}{\partial n_B}\right)_{y_i} I_{3i}\rho_3^0 + g_\rho I_{3i} \left(\frac{\partial \rho_3^0}{\partial n_B}\right)_{y_i} + \left(\frac{\partial \Sigma^r}{\partial n_B}\right)_{y_i}. \tag{4.111}$$

The last term on the RHS above is due to the extra 're-arrangement term' in the effective baryon chemical potential, $\tilde{\mu}_i$, given in Eq. (4.21) and can be written as

$$\left(\frac{\partial \Sigma^r}{\partial n_B}\right)_{y_i} = \sum_{i=p,n} \left[ -\sigma_0 n_i^s \left(\frac{\partial^2 g_\sigma}{\partial n_B^2}\right)_{y_i} - \sigma_0 \left(\frac{\partial n_i^s}{\partial n_B}\right)_{y_i} \left(\frac{\partial g_\sigma}{\partial n_B}\right)_{y_i} - \left(\frac{\partial \sigma_0}{\partial n_B}\right)_{y_i} n_i^s \left(\frac{\partial g_\sigma}{\partial n_B}\right)_{y_i} + \omega_0 n_i \left(\frac{\partial^2 g_\omega}{\partial n_B^2}\right)_{y_i} + \omega_0 \left(\frac{\partial n_i}{\partial n_B}\right)_{y_i} \left(\frac{\partial g_\omega}{\partial n_B}\right)_{y_i} + \left(\frac{\partial \omega_0}{\partial n_B}\right)_{y_i} n_i \left(\frac{\partial g_\omega}{\partial n_B}\right)_{y_i} + \rho_3^0 I_{3i} n_i \left(\frac{\partial^2 g_\rho}{\partial n_B^2}\right)_{y_i} + \rho_3^0 I_{3i} \left(\frac{\partial n_i}{\partial n_B}\right)_{y_i} \left(\frac{\partial g_\rho}{\partial n_B}\right)_{y_i} + \left(\frac{\partial \rho_3^0}{\partial n_B}\right)_{y_i} I_{3i} n_i \left(\frac{\partial g_\rho}{\partial n_B}\right)_{y_i} \right]. \tag{4.112}$$

In the above, using Eqs. (4.107-4.109) the second derivatives of the couplings are directly given as

$$\left(\frac{\partial^2 g_\sigma}{\partial n_B^2}\right)_{y_i} = -\left(\frac{\partial g_\sigma}{\partial n_B}\right)_{y_i} \frac{a_\sigma x^{a_\sigma} - a_\sigma + 1}{x\,\rho_0}, \tag{4.113}$$

$$\left(\frac{\partial^2 g_\omega}{\partial n_B^2}\right)_{y_i} = -\left(\frac{\partial g_\omega}{\partial n_B}\right)_{y_i} \frac{a_\omega x^{a_\omega} - a_\omega + 1}{x\,\rho_0}, \tag{4.114}$$

$$\left(\frac{\partial^2 g_\rho}{\partial n_B^2}\right)_{y_i} = -\left(\frac{\partial g_\rho}{\partial n_B}\right)_{y_i} \frac{a_\rho}{\rho_0}. \tag{4.115}$$

Finally the derivative of the scalar condensate in Eq. (4.112) is given by, using Eq. (4.11)

$$\left(\frac{\partial n_i^s}{\partial n_B}\right)_{y_i} = a_i' + b_i \left(\frac{\partial \sigma_0}{\partial n_B}\right)_{y_i}. \tag{4.116}$$

Thus, the speed of sound in DDB is found using Eqs. (4.93-4.94) with the relevant derivatives in the DDB model defined in Eqs. (4.103-4.116).

### 4.4.2 Speed of sound in quark phase

In an identical manner one can estimate the adiabatic speed of sound in QP by taking the partial derivatives of total pressure and total energy density which are collected in Eqs. (4.38) and (4.39). In this subsection we present the analytic expression for the adiabatic speed of sound for the quark matter in NJL model. The partial derivatives of the pressure with respect to baryon number density using the Eq. (4.33) is given by

$$\left(\frac{\partial p_{\rm NJL}}{\partial n_q}\right)_{y_i} = \left(\frac{\partial p_{\rm vac}}{\partial n_q}\right)_{y_i} + \left(\frac{\partial p_{\rm med}}{\partial n_q}\right)_{y_i}, \tag{4.117}$$

where,

$$\left(\frac{\partial p_{\rm vac}}{\partial n_q}\right)_{y_i} = -\frac{N_c M^4}{\pi^2}\sum_{i=u,d}\left[H(z_\Lambda)\frac{4}{M}\left(\frac{\partial M}{\partial n_q}\right)_{y_i} + H'(z_\Lambda)\left(\frac{\partial z_\Lambda}{\partial n_q}\right)_{y_i}\right], \tag{4.118}$$

and,

$$\begin{aligned}\left(\frac{\partial p_{\rm med}}{\partial n_q}\right)_{y_i} &= \frac{N_c M^4}{\pi^2}\sum_{i=u,d}\left[H(z_i)\frac{4}{M}\left(\frac{\partial M}{\partial n_q}\right)_{y_i} + H'(z_i)\left(\frac{\partial z_i}{\partial n_q}\right)_{y_i}\right] \\ &\quad -\frac{N_c}{3}\sum_{i=u,d}\left[y_i\tilde{\mu}_i + n_i\left(\frac{\partial \tilde{\mu}_i}{\partial n_q}\right)_{y_i}\right] - 2g_v n_q + 2g_s\rho_s\left(\frac{\partial \rho_s}{\partial n_q}\right)_{y_i}\end{aligned} \tag{4.119}$$

The partial derivative of the energy density using Eq. (4.36) with respect to the baryon number density is given as

$$\left(\frac{\partial \epsilon_{\rm NJL}}{\partial n_q}\right)_{y_i} = \sum_{i=u,d}\left[y_i\mu_i + n_i\left(\frac{\partial \mu_i}{\partial n_q}\right)_{y_i}\right] - \left(\frac{\partial p_{\rm NJL}}{\partial n_q}\right)_{y_i}, \tag{4.120}$$

where, $z_i = k_{Fi}/M$ and $z_\Lambda = \Lambda/M$. The function $H(z)$ is given in Eq. (4.16) and $H'(z)$ is its derivative with respect to $z$. The derivative of the constituent mass is given by

$$\left(\frac{\partial M}{\partial n_q}\right)_{y_i} = -\frac{\dfrac{2N_c g_s}{\pi^2}M^2(B_u + B_d)}{1 + \dfrac{2N_c g_s}{\pi^2}M^2(A_u + A_d)} \tag{4.121}$$

where

$$A_i = 3G(z_i) - 3G(z_\Lambda) - G'(z_i)z_i + G'(z_\Lambda)z_\Lambda \tag{4.122}$$

$$B_i = G'(z_i)\frac{\partial k_{Fi}}{\partial n_q} \tag{4.123}$$

Here $i = u, d$. The function $G(z)$ is given in Eq. (4.31) and $G'(z)$ is its derivative with respect to $z$. Using these relations we can find the adiabatic speed of sound of quark matter in QP as

$$c^2_{s,\mathrm{QP}} = \frac{\left(\frac{\partial p_{\mathrm{QP}}}{\partial n_q}\right)_{y_i}}{\left(\frac{\partial \epsilon_{\mathrm{QP}}}{\partial n_q}\right)_{y_i}}. \tag{4.124}$$

### 4.4.3 Speed of sound in mixed phase

Once we have the expressions for the different sound speeds in HP and QP then it is state forward to get the sound speeds in MP by using the quark matter fraction $\chi$ as given in Eq. (4.42) in MP. In case of equilibrium sound speed, the total pressure and the total energy density of the MP are calculated by using Eqs. (4.40) and (4.43). We take the numerical derivative of pressure with respect to energy density and get the equilibrium sound speed in MP. To estimate the adiabatic sound speed in MP we take the corresponding quantities in HP and QP and hence $c^2_{s,\mathrm{MP}}$ is given as [276]

$$\frac{1}{c^2_{s,\mathrm{MP}}} = \frac{\chi}{c^2_{s,\mathrm{HP}}} + \frac{1-\chi}{c^2_{s,\mathrm{QP}}} \tag{4.125}$$

## 4.5 Results and discussion

In this section, we present the structural properties and non-radial oscillations of NSs and HSs. We consider two RMF models, one with NL3 [306] parameterized and other is DDB [307, 308] for nucleonic matter EOS (see sec. 4.2.1) and a two flavour NJL model for the quark matter EOS (see sec. 4.2.2) with parameters, $(G_s\Lambda^2, \Lambda, m) = (2.24, 587.6\mathrm{MeV}, 5.6\mathrm{MeV})$ [34]. The MP is calculated using Gibbs construction, as outlined in sec. 4.2.3.

### 4.5.1 Equation of state and properties of neutron/hybrid star

We display the particle content as a function of density for charge neutral matter for $G_v = 0.2G_s$ in Fig. 4.2. In HP, neutron density dominates with small fractions of proton. A small fraction of electron and muon (if available in the system) also appear(s) to get charge neutral HP. MP starts at $\rho_B \sim 2.76\rho_0$ from where the nucleon fraction decreases while the quark fraction starts to increase. Finally, at densities

$\rho_B \sim 5.56\rho_0$ and above, the pure QP takes over with $d$ quark densities roughly becoming twice that of the $u$ quarks to maintain the charge neutrality in QP. The smaller value of the vector coupling in the NJL model decreases the critical density at which the MP starts. In case of $G_v = 0$, the MP starts at density $\rho_B \sim 2.36\rho_0$ and ends at densities $\rho_B \sim 5.22\rho_0$. The resulting EOSs with the MP are shown in the Fig. 4.3 (left) for the two different values of vector coupling $G_v = [0, 0.2]\, G_s$ in the NJL model. As $G_v$ increases, the EOS becomes stiffer. Further, higher $G_v$ corresponds to a larger critical energy density at which HQPT occurs. In Fig. 4.3 (right), we show the EOS where the nuclear matter is described by the DDB model and the quark matter is described by the NJL model with no vector coupling i.e. $G_v = 0$. We have chosen zero vector coupling because the non-zero vector coupling makes EOS stiffer In this case, MP starts at $\rho_B \sim 3.93\rho_0$ and ends at $\rho_B \sim 6.98\rho_0$. Open and filled circles in Fig. 4.3 denote the central energy densities of the maximum mass stars for different $G_v$s and nuclear matter EOSs. These circles lie in MP indicating no pure quark matter core is realized. It can also be seen in Fig. 4.4, where we show the quark matter fraction $\chi$ in MP as a function of density for different $G_v$s and nuclear matter EOSs. The open (filled) circle in Fig. 4.3(left) corresponds to a maximum mass star denotes $\chi = 0.482$ $(0.438)$ which means 48.2% (43.8%) of the energy density is coming from quark matter and rest from nuclear matter at the center of a maximum mass HS of NL3+NJL type with $G_v = 0$ $(0.2G_s)$. While in Fig. 4.3 (right), the open circle corresponds to a maximum mass star indicating $\chi = 0.506$ which means 50.6% of the energy density is coming from quark matter and rest from nuclear matter at the center of a maximum mass HS of DDB+NJL type with $G_v = 0$. It realises that there is no pure quark core available in this study.

In Fig. 4.5 (left) we show the variation of square of the both speeds of sound $c_e^2$ and $c_s^2$ for the hybrid matter of NL3+NJL type and in Fig. 4.5 (right) same for the hybrid matter of DDB+NJL type, where we have taken zero vector coupling i.e. $G_v = 0$. As density increases in HP, the squares of both speeds of sound increase monotonically in both cases. The maximum value of the speeds of sound (square of them) are 0.608 in NL3+NJL model and 0.564 in DDB+NJL at the critical density after which MP starts. In both cases, both square of the sound speeds become very different in the MP. The square of the equilibrium sound speed, $c_e^2$, decreases discontinuously at the onset of MP to a value 0.08 $(0.09)$ beyond which it shows a continuous behaviour till the end of MP where it again discontinuously increases from 0.06 $(0.08)$ to 0.33 $(0.33)$ for NL3+NJL (DDB+NJL) case. The square of the adiabatic sound speed, on the other hand, does not show similar discontinuous behaviour. It has an important consequence for the $g$ modes as we shall see later. While the difference between both $c_s^2$ and $c_e^2$ is small in HP, at the onset of MP, this difference become large leading to large Brunt-Väisäla frequency giving rise to an enhancement of $g$ mode frequency. We may note here that the difference turns out to be vanishing for the present case of two flavor NJL model. This is similar to the case of bag model EOS [81]. For massless two flavors NJL model, the charge neutrality and $\beta$-equilibrium renders the electron density to be constant which makes the difference between the two speeds (squares) to be vanishing. On

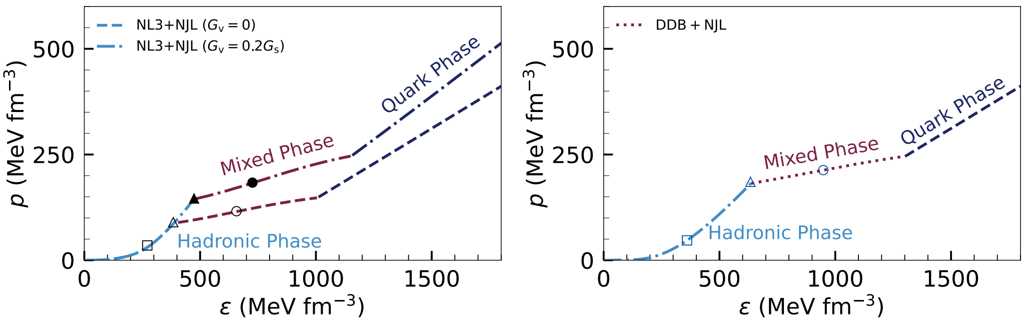


FIGURE 4.3: The EOSs of the charge neutral matter including the MP for both nuclear models in HP and the NJL model in QP. The left figure corresponds to the EOS with NL3 parameterized hadronic matter while the right figure corresponds to DDB parameterized hadronic matter. At high density, the NJL model is considered for the quark matter EOS with different vector couplings. In the left figure, the EOSs correspond to the vector couplings $G_v = 0$ (up) and $G_v = 0.2G_s$ (down) in the quark sector. In the right figure, the EOS corresponds to the vector coupling $G_v = 0$. In both figures, the sky blue portion refers to HP and the dark blue portion refers to QP while the dark red portion corresponds to MP. The open square corresponds to the central energy density of a NS of mass $1.4M_\odot$. The triangles denote the starting of the MP and correspond to NSs of mass $2.17M_\odot$ ($G_v = 0$) and $2.50M_\odot(G_v = 0.2G_s)$ for NL3+NJL and $2.18M_\odot$ ($G_v = 0$) for the DDB+NJL. The circles represent the maximum masses $2.27M_\odot(G_v = 0)$ and $2.55M_\odot(G_v = 0.2G_s)$ for NL3+NJL and $2.20M_\odot(G_v = 0)$ for the DDB+NJL HSs.

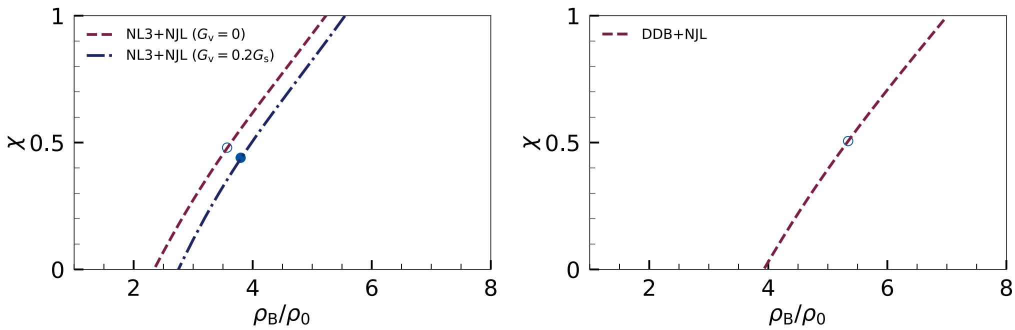


FIGURE 4.4: In the left figure, the quark fraction as a function of baryon density for the Nl3 parameterized EOSs in HP and NJL model in QP while in the right figure, the quark fraction as a function of baryon density for the DDB parameterized EOS in HP and NJL model in QP as shown in Fig. 4.3. In the left figure, the open (dark) circle indicates the central density of the maximum mass star i.e. $\rho_{B,\max} \simeq 3.5\rho_0(3.8\rho_0)$ corresponding to $M_{\max} = 2.27M_\odot(2.55M_\odot)$ for $G_v = 0$ ($G_v = 0.2G_s$). In the right figure, the open circle indicates the central density of the maximum mass star i.e. $\rho_{B,\max} \simeq 5.5\rho_0$

.

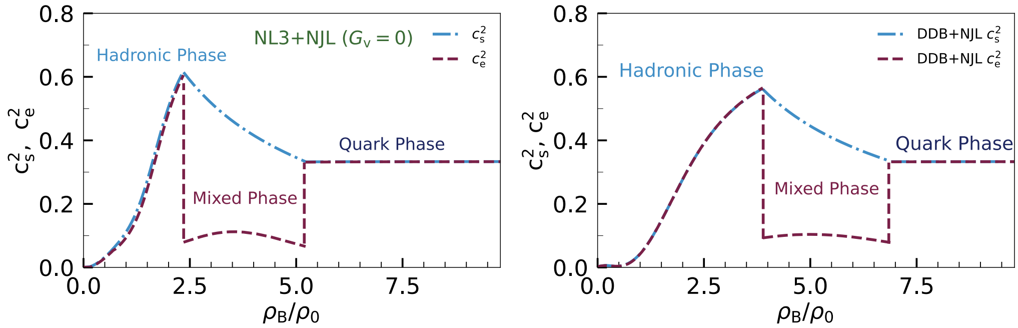


FIGURE 4.5: The variation of the square of sound speeds, (equilibrium, $c_e^2$ and adiabatic, $c_s^2$) as a function of baryon number density for the charge neutral matter. The brown dashed (blue dot-dashed) curve corresponds to the equilibrium (adiabatic) sound speed in the different phases like HP, QP and MP for the hybrid EOSs described by NL3+NJL in the left figure and DDB+NJL in the right figure. The vector coupling strength in NJL model is $G_v = 0$ in the case of both hybrid models.

the other hand, this need not be the same for 3 quark flavors as the electron chemical potential $\mu_e \sim m_s^2/(4\mu_q)$ leading to electron density depending on quark mass and quark chemical potential leading to a non-vanishing value for the difference between the two speeds of sound (squares).

Apart from enhancing the $g$ mode frequency, the existence of the sudden rise of equilibrium sound speed has also important consequences regarding the mass and radius relation in NS. One actually needs a rise in speed of sound in a narrow region of densities, for an explanation of CSs to have large mass and small radius [316]. To achieve this possibility, a quarkyonic phase [316] or a vector condensate phase along with pion superfluidity [317] have been proposed recently. On the other hand, such a steep rise in the speed of sound can also arise in a MP construct within the model for hadronic matter and quark matter as used here.

In Fig. 4.6, we show the mass-radius relations for NSs. For pure nucleonic matter EOS, the maximum mass turns out to be $2.77M_\odot$ ($2.35M_\odot$) and radius turns out to be 13.26 km (11.87 km) when the nuclear matter is described in NL3 (DDB) parameterisation of RMF model. If one uses MP EOS, the maximum mass of CS reduces to $2.27M_\odot$ with radius 14.39 km for $G_v = 0$ and to $2.55M_\odot$ with radius 14.17km for $G_v = 0.2G_s$ in NL3+NJL while the same decreases to $2.20M_\odot$ with radius 12.71 km for $G_v = 0$ in DDB+NJL. This is essentially due to the fact that the quark matter EOS is softer compared to the nuclear matter EOS. The central energy densities for the maximum mass HSs are $\epsilon_c^{\max} = 656$ MeV/fm$^3$ ($G_v = 0$) and $\epsilon_c^{\max} = 738$ MeV/fm$^3$ ($G_v = 0.2G_s$) in NL3+NJL while $\epsilon_c^{\max} = 948$ MeV/fm$^3$ ($G_v = 0$) in DDB+NJL. As central energy density is increased further, HSs become unstable i.e. $dM/d\epsilon < 0$. Thus, within the present models, we do not find stable HSs with pure quark matter core. The quark matter, if it is present in the core, is always in MP. As $G_v$ increases in NL3+NJL case, the MP starts at higher energy

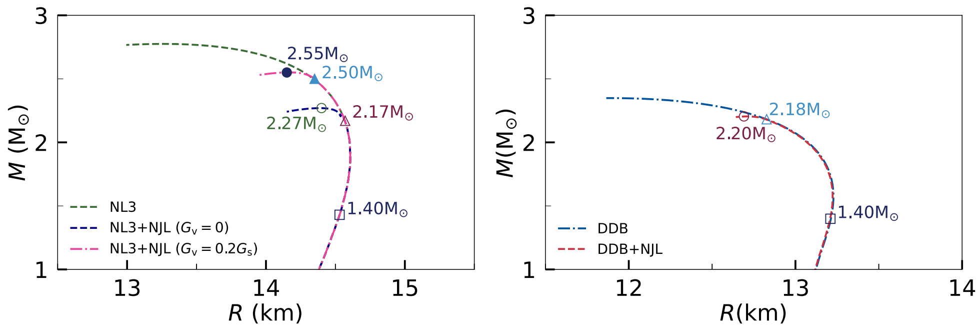


FIGURE 4.6: The mass-radius curves are plotted for CSs described by the models NL3, NL3+NJL in left figure and by the models DDB and DDB+NJL in right figure for the different values of the vector coupling, $G_v$ in NJL model. In the case of DDB and DDB+NJL models, the vector coupling is taken to be zero. The circles denote the maximum mass HSs having quark matter within the cores for different values of the $G_v$ in NJL model. While the triangles represent the maximum mass NSs having hadronic matter inside the core. In the left figure, the maximum mass of HSs, described by NL3+NJL hybrid model, are $2.27M_\odot$ for $G_v = 0$ and $2.55M_\odot$ for $G_v = 0.2G_s$. In the right figure, the maximum mass HS, described by DDB+NJL hybrid model, is $2.20M_\odot$.

density and hence a larger fraction of hadronic matter contributes to the total mass of the star as we see in Fig. 4.4 (left). This leads to an increase of the maximum mass of HS. With increasing $G_v$ further, we expect NSs without any quark matter in their cores. The radius $R_{1.4}$ for the canonical mass of $1.4M_\odot$ NSs turns out to be 14.52 km in NL3+NJL case while same turns out to be 13.21 km in DDB+NJL case. It may be noted that the x-ray pulse analysis of Neutron star Interior Composition ExploreR (NICER) data from PSR $J0030+0451$ by Miller et.al. found $R = 13.02^{+1.14}_{-1.19}$ km for $M = 1.44 \pm 0.15M_\odot$ [318]. Such a star will not have a quark core within these present models for the EOS of dense matter. Such a conclusion, however, should be taken with caution as this is very much dependent upon the EOSs both in hadronic and quark phase. In particular, more exotic phases of quark matter could also be possible including various color superconducting phases, and various inhomogeneous phases for dense quark matter which have not been considered here.

In Fig. 4.7, we show the energy density and pressure profiles i.e. energy density and pressure as the functions of the radial distance from the center of the maximum mass HSs described by NL3+NJL (left) and DDB+NJL (right) models. As mentioned earlier, the cores of such stars contain MP with about the 50% of quark matter and 50% of nuclear matter (see Fig. 4.4). The radius of MP core is about 3.8 km (2.7 km) with the total radius of 14.17 km (12.71 km) for HS described in NL3+NJL (DDB+NJL). We have taken here the vector coupling $G_v = 0.2G_s0$ ($G_v = 0$) in NL3+NJL (DDB+NJL) model. For $G_v = 0$, in NL3+NJL, MP core radius slightly larger i.e. 4.2 km while the star's radius being about 14.39 km. At $r = r_c$, the critical radial distance, where the matter goes from a MP to a HP or vice-versa,

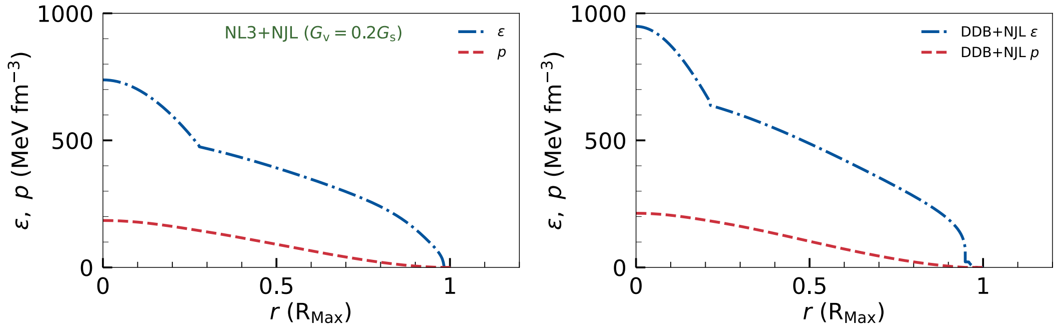


FIGURE 4.7: The energy density, $\epsilon$ (blue dot-dashed) and pressure, $p$ (red dashed) profiles as a function of radial distance from the center of the maximum mass HSs described by the hybrid models NL3+NJL (left) and DDB+NJL (right). In case of NL3+NJL hybrid model, the vector coupling is none-zero i.e. $G_v = 0.2G_s$ while in case of DDB+NJL hybrid model, the vector coupling is zero i.e. $G_v = 0$. The transition from MP to HP happens at $\rho_B = 2.75\rho_0$ ($\rho_B = 3.95\rho_0$) corresponding with the radial distance $r_c = 0.27R_{\rm Max}$ ($r_c = 0.21R_{\rm Max}$) in the NL3+NJL (DDB+NJL) model.

the energy density becomes non-differentiable while pressure shows smooth behaviour as may be observed in Fig. 4.7.

The behavior of both the square of the sound speeds, $c_e^2$ and $c_s^2$, are shown in Fig. 4.8 as a function of radial distance from the center of the stars for both HS as well as NS. In Fig. 4.8 (left) we show the square of the both sound speed profiles for the maximum mass stars described in NL3 and NL3+NJL models while in Fig. 4.8 (right) we show the same for the maximum mass stars described in DDB and DDB+acnjl models. We choose here the zero vector coupling i.e. $G_v = 0$ for the said models. The HQPT in HSs is reflected in the variation of the square of the equilibrium sound speed, $c_e^2$, which changes abruptly from $c_e^2 = 0.08$ to $c_e^2 = 0.608$ in NL3+NJL model and from $c_e^2 = 0.06$ to $c_e^2 = 0.564$ at the critical radius $r_c$. As motioned it plays an important role in the enhancement of non-radial oscillation frequencies which we discuss in the next subsection.

In Fig. 4.9 (left), we show the profile of Brunt-Väisäla frequency, $\omega_{\rm BV}$, in the stars of maximum masses described in NL3 and NL3+NJL while in Fig. 4.9 (right), we show the same described in DDB and DDB+NJL where the vector coupling $G_v = 0$ in NJL model. The steep rise of $\omega_{\rm BV}$ at the onset of MP may be noted. The Brunt-Väisäla frequency, $\omega_{\rm BV}$, depends on both the speeds of sound, see Eq. (4.83). In the core of maximum mass HS, the variation of the both sound speeds are different which is reflected in the $\omega_{\rm BV}$ profile. The onset of muons is shown by a little kink in the figure with a slight increase in $\omega_{\rm BV}$.

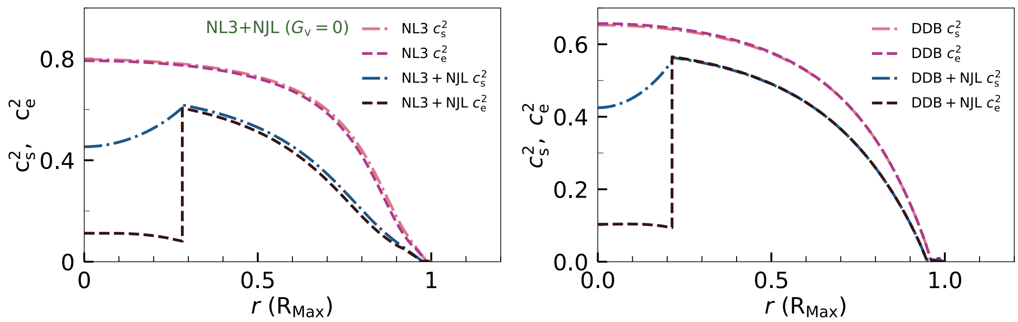


FIGURE 4.8: The equilibrium $c_e^2$ and the adiabatic $c_s^2$ sound speeds profiles inside the maximum mass stars as a function of radial distance from the center of the stars. In the left figure, the $c_e^2$ and $c_s^2$ profiles is shown as a function of the radial distance in the stars described by the NL3 and NL3+NJL models while in the right figure same in the stars described by the DDB and DDB+NJL models. The black dashed (dark blue dot-dashed) curve correspond to the $c_e^2$ ($c_s^2$) profile for the HS described by NL3+NJL (DDB+NJL) model while brown dashed (magenta dot-dashed) curve corresponds to the $c_e^2(c_s^2)$ profile in the NS described by NL3(DDB) model. The discontinuity in the profile of $c_s^2$ in the case of HSs at $r_c = 0.27R_{\rm Max}$ ($r_c = 0.21R_{\rm Max}$) shows the appearance of quark matter in the hybrid model NL3+NJL(DDB+NJL).

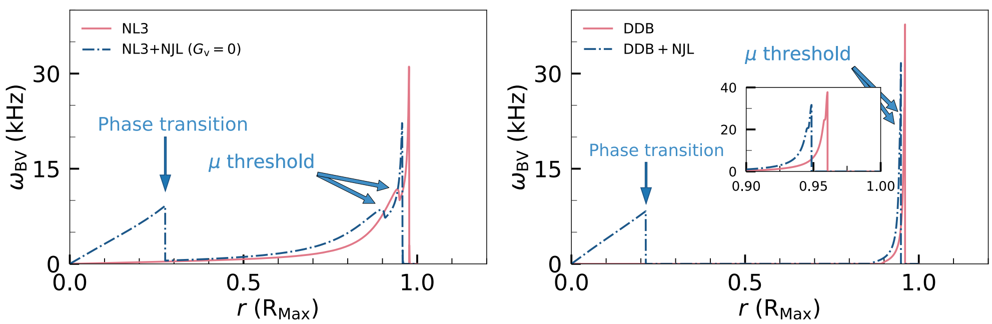


FIGURE 4.9: The Brunt-Väisäla frequency ($\omega_{\rm BV}$) profile in the maximum mass stars as a function of the radial distance from the center of the star. In the left figure, the $\omega_{\rm BV}$ profile is plotted as a function of radial distance in the stars described by the NL3 and NL3+NJL model while in the right we plot same in the stars described by the DDB and DDB+NJL models. Red solid (blue dot-dashed) curve shows the $\omega_{\rm BV}$ profile in the NS (HS where the vector coupling is considered to be zero i.e. $G_v = 0$). The little kink in the profiles near the surface of the stars shows the threshold for the appearance of muons in all the models.

### 4.5.2 Tidal deformability

The tidal distortion of NSs in a binary system links the EOS to the gravitational wave emissions during the inspiral [319]. Next we discuss the results for the tidal deformability with EOS considered here. In Fig. 4.10 (left) shows the dimensionless tidal deformability parameters $\Lambda_1$ and $\Lambda_2$ of the NSs involved in the binary neutron star (BNS) with masses $m_1$ and $m_2$, respectively, for the hadronic EOSs DDB, NL3 and corresponding mixed phase EOS with NJL model DDB+NJL, NL3+NJL. In the GW170817 event, the chirp mass, $\mathcal{M}_{\text{chirp}} = (m_1 m_2)^{3/5}(m_1 + m_2)^{-1/5}$, was measured as $1.186 M_{\odot}$ [71] and these curves were calculated based on the masses involved in the BNS merger by varying $m_1$ in the observed range $1.365 < m_1 < 1.60$. We may note here that the quark matter core occurs for NSs of masses at around $2M_{\odot}$. Thus the tidal deformability $\Lambda_1$ and $\Lambda_2$ as shown in the Fig. 4.10 (left) will correspond to hadronic phase only. We also show the constraint imposed on the $\Lambda_1 - \Lambda_2$ plane from the GW170817 event in the same plot. Based on a marginalized posterior for the tidal deformability of the two binary components of GW170817, the gray solid (dot-dashed) line represents the 90%(50%) confidence interval for the tidal deformability of these two components. There are magenta solid (blue dashed) lines representing 90%(50%) confidence intervals for the constraints from GW170817: marginalized posterior using a parametrized EOS with a maximum mass requirement of at least $1.97 M_{\odot}$. In this regard, it is important to note that the NL3 model disfavors the constraints imposed by GW170817. The DDB, however, is less stiff than NL3, so it satisfies those constraints well. The stiffness of the EOS may be attributed to either its symmetric nuclear part or its density-dependent symmetry energy. While NL3 and DDB exhibit similar symmetric nuclear matter (SNM), DDB has a softer symmetry energy than NL3. For the models NL3 and DDB, the nuclear matter incompressibility $K_0$ is 271 MeV, and 269 MeV and the slope of the symmetry energy $L_0$ is 118 MeV, 32 MeV, at saturation density respectively. Fig. 4.10 (right) shows the dimensionless tidal deformability as a function of NS mass of our EOS model adopted here. The blue horizontal bar indicates the 90% CI obtained for the tidal deformability of a $1.36 M_{\odot}$ or the combined tidal deformability in the BNS for $q = m_1/m_2 = 1$ [71]. It is clear that the NL3 is outside of the 90% CI constraint whereas DDB is within the acceptable range. As discussed above the NSs masses below $2.18 M_{\odot}$ and $2.17 M_{\odot}$ correspond to the only hadronic phase EOSs for DDB and NL3 mixed phases EOSs, respectively. It can be seen from the figure that the tidal deformability $\Lambda$ bifurcates from the same NS masses for those EOSs.

### 4.5.3 Oscillation modes in hybrid stars

We next show, here, the results for $f$ and $g$ modes for NSs and HSs in different models presented in this study. We shall focus our attention to the quadruple mode ($l = 2$) only because the quadrupolar oscillations are significant enough to observe. One can study the higher mode as well but their frequencies are very large and difficult to observe. It may be expected from the coupled Eqs. (4.80 and

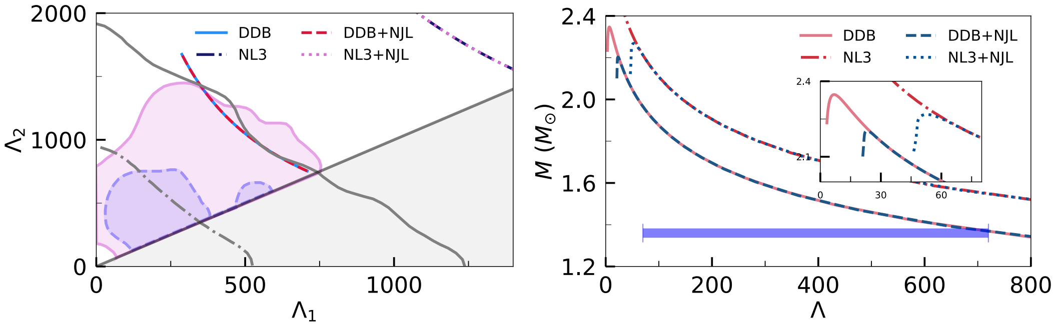


FIGURE 4.10: Based on the hadronic NL3, DDB and their hybrid EOS with NJL quark matter model for a mixed phase. (left) we show the dimensionless tidal deformability parameters $\Lambda_1$ and $\Lambda_2$ of the GW170817 BNS merger, for the fixed measured chirp mass of $\mathcal{M}_{\text{chirp}} = 1.186 M_\odot$. A gray solid (dot-dashed) line indicates a 90%(50%) confidence interval for the tidal deformability of GW170817's two binary components based on their marginalized posteriors. In this figure, magenta solid (blue dashed) lines represent 90%(50%) confidence intervals for the constraints from GW170817 : marginalized posterior using a parametrized EOS and a maximum mass requirement of $1.97 M_\odot$. (right) The dimensionless tidal deformability as a function of the NS mass. The tidal deformability constraint of a $1.36 M_\odot$ star is represented by the blue bar in the right panel.

4.84) for the fluid perturbation functions $Q(r)$ and $Z(r)$ that $c_s^2$ and $c_e^2$ play an important role in the determination of different solutions of these functions and hence on the frequencies of the oscillation modes. The typical frequencies of $g$ modes lie in the range from a few 100 Hz up to 1 kHz while that of $f$ modes lie in the range $1-3$ kHz. As mentioned in Sec. 4.3, we solve Eqs. (4.80 and 4.84) in a variational method to determine the oscillation frequencies. As this is computed using a variational method, the final solutions depend upon the initial guesses for the frequencies. To get a solution of the $f$ mode oscillation, we give the initial guess for the frequency $(f = \omega/2\pi)$ of the order of a few kHz. On the other hand, to look for a $g$ mode we give the initial guess for the same in the range of a few hundred Hz. In Fig. 4.11, we show the $f$ mode frequencies as a function of mass of CSs for the both NS and HS described by NL3 and NL3+NJL (DDB and DDB+NJL) models in the left (right) figure. In the left figure, the blue curves refer to the $f$ mode frequencies for HSs with $G_v = 0$ (blue dotted) and with $G_v = 0.2G_s$ (blue dot-dashed) while the magenta curve refers to the $f$ mode frequencies for NSs described by NL3+NJL and NL3, respectively. In the right figure, we show the same as the left figure but for the DDB+NJL and DDB models, respectively while considering $G_v = 0$. We may observe here that there is a mild rise in the frequencies for the $f$ modes for stars with a quark matter core. Such a rise of non-radial oscillation frequencies due to the quark matter core was also observed in Ref. [81, 276]. However for $f$ modes, the rise due to the quark matter in the core, is very small. Eg. for a HS star of mass $M = 2.27M_\odot$, described by NL3+NJL where $G_v = 0$, the $f$ mode frequency becomes 2 kHz from a value of 1.97 kHz of a NS of same mass.

In Fig. 4.12, we plot the $g$ mode frequencies as a function of the mass of CSs for the both NS and HS described by NL3 and NL3+NJL models in the left figure while same as described by DDB and DDB+NJL model in the right figure. For NSs, CSs without any quark matter core, the $g$ mode frequencies lie in the range of $(322-341)$ Hz $(139-148)$ Hz for the stars of masses larger than 2 $M_\odot$ described by NL3 (DDB) model. On the other hand, in the presence of quark matter in MP, the frequencies rise sharply to about 589 Hz ($G_v = 0$) and 589 Hz ($G_v = 0.2G_s$) in the case of NL3+NJL model while same rises sharply to about 303 Hz ($G_v = 0$) in the case of DDB+NJL. Let's note that at the onset of the MP in case of NSs, $c_e^2$ decreases abruptly. This is due to the fact that the electron chemical potential falls at the onset of the MP. This is due to the fact that the charge neutral nuclear matter undergoes a phase transition to one component of HP which is positively charged and the other component of QP which is negatively charged. This sudden change in the lepton number density at MP threshold leads to sudden drop of $c_e^2$ as shown in Fig. 4.8. This leads to an abrupt rise of the $\omega_{\rm BV}$ which enhances the $g$ mode frequency. With increasing the vector coupling $G_v$, MP core decreases and hence its contribution to the $g$ mode enhancement also decreases.

We note that the $g$ modes that we obtained for NSs or HSs are driven by the Brunt-Väisäla frequency which quantifies the mismatch between the mechanical and chemical equilibrium rates of a displaced fluid parcel and is expressed by the local equilibrium and adiabatic speeds of sound. Such core $g$ mode solutions in

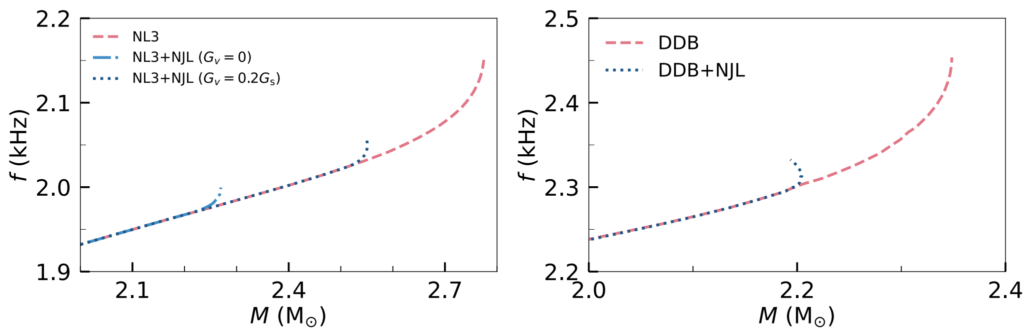


FIGURE 4.11: The oscillation frequencies of $f$ mode $f = \omega/2\pi$ in kHz as a function of the star's masses which are described by NL3 and NL3+NJL models in the left figure and same as a function of the star's masses which are described by DDB and DDB+NJL models in the right figure. The magenta dashed curve corresponds to NSs i.e. without any quark matter core. (left) The blue dot-dashed (blue dotted) curves correspond to the $f$ mode frequencies of the HSs which are described by NL3+NJL hybrid model for $G_v = 0 (G_v = 0.2G_s)$. (right) The blue dotted curve corresponds to the $f$ mode frequencies of the HSs which are described by DDB+NJL hybrid model for $G_v = 0$. The appearance of the quark matter in the core enhances the oscillation frequencies.

sub-kHz frequency range can also arise due to a sharp discontinuity in energy density in a first order phase transition [320, 321]. Such low frequency $g$ modes due to quark-hadron discontinuity has also been shown to be a feature of HSs that distinguish hadronic stars or strange quark stars based on non-radial oscillation modes [86]. On the other hand non-radial oscillation modes with a MP of quark-hadron matter was explored by Sotani etal [85]. It was shown here that including finite size effects in the mixed phase it is possible to distinguish between the existence or absence of density discontinuity in NS interior from gravitational waves of the $f$ mode [85]. In an interesting later work of Ranea-Sandoval etal explored different non-radial oscillation modes ($f$, $p$ and $g$ modes) with an interpolating function relating hadron and quark phases unlike a Gibbs construct as has been attempted here [88]. We might note that for the phase transition considered here with NJL model, a Gibbs construct is consistent as the recent calculation using effective models like linear sigma model [294]; Polyakov quark meson model [296] as well as NJL model [295] suggest a lower value of surface tension $\sim 5 - 20\text{MeV/fm}^2$ justifying the use of a Gibbs construct.

Next, we discuss the solution of the perturbing functions $Q(r)$ and $Z(r)$. In Fig. 4.13, we have plotted the functions $Q(r)$ and $Z(r)$ as a function of radial distance from the center for both $g$ and $f$ modes. Let us first discuss the solutions of perturbing functions $Q(r)$ and $Z(r)$ for NSs. The angular function $Z(r)$ is plotted as a solid red line ($Z_f$) for $f$ mode and as a solid blue line ($Z_g$) for $g$ mode. For $f$ modes, $Z(r)$ decreases monotonically starting from a vanishing value at $r = 0$ consistent

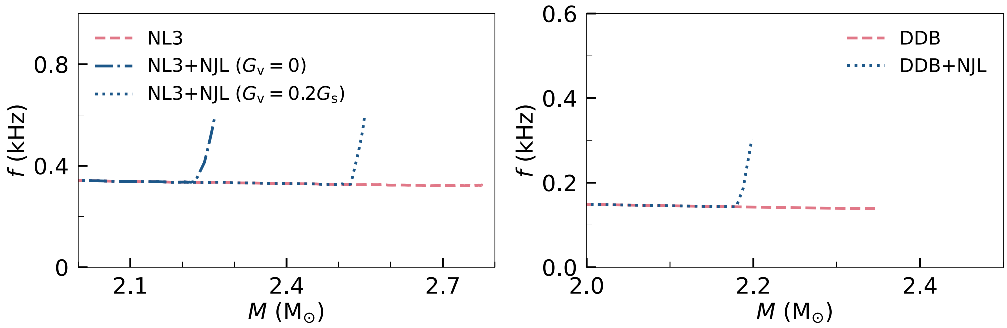


FIGURE 4.12: The oscillation frequencies of $g$ mode $f = \omega/2\pi$ in kHz as a function of the star's masses which are described by NL3 and NL3+NJL models in the left figure and same as a function of the star's masses which are described by DDB and DDB+NJL models in the right figure. The magenta dashed curve corresponds to NSs i.e. without any quark matter core. (left) The blue dot-dashed (blue dotted) curves correspond to the $g$ mode frequencies of the HSs which are described by NL3+NJL hybrid model for $G_v = 0(G_v = 0.2G_s)$. (right) The blue dotted curve corresponds to the $g$ mode frequencies of the HSs which are described by DDB+NJL hybrid model for $G_v = 0$. The appearance of the quark matter in the core enhances the oscillation frequencies.

with the initial condition given in Eq. (4.85). As may be clear from Eq. (4.84), for vanishing $\omega_{\rm BV}$, $Z'(r)$ is negative and therefore $Z(r)$ decreases as $r$ increases. When the Brünt-Väisala frequency, $\omega_{\rm BV}$ becomes significant, the forth term in Eq. (4.84) starts to become important. However, if $\omega$ is large (as in the case with $f$ modes) the contribution of the second term in the parenthesis of Eq. (4.84) is suppressed so that $Z(r)$ decreases monotonically as seen (red solid line) in Fig 4.13. On the other hand, for the $g$ mode with the lower $\omega$, the second term in the parenthesis becomes dominant. This makes the forth term in Eq. (4.84) negative and significant near the surface as $\omega_{\rm BV}$ becomes significant here. It turns out that the overall sign of $Z'(r)$ becomes positive near the surface resulting eventually in the change of sign of $Z(r)$ as shown (blue solid line) in Fig. 4.13. Thus the $f$ mode shows no node for $Z(r)$, the $g$ mode solution shows a node. We have taken throughout $l = 2$. The dashed lines show the behaviour of the perturbing function $Q(r)$ as $Q_{\rm f}$ and $Q_{\rm g}$ for $f$ and $g$ modes respectively. Both these functions start from vanishing values and start to increase with $r$. $Q(r)$ for $f$ mode ($Q_{\rm f}$) increases monotonically while $Q(r)$ for $g$ mode ($Q_{\rm g}$) starts to decrease when $Z(r)$ changes sign and eventually become negative near the surface consistent with the boundary condition given in Eq. (4.87). Thus similar to $Z(r)$, $Q(r)$ also does not show any node for $f$ modes while the solutions of the $Q(r)$ for the $g$ modes, ($Q_{\rm g}$) has a node near the surface.

Next, we display the perturbing functions $Q(r)$ and $Z(r)$ for HSs in Fig. 4.14. In the top panel, we have plotted the functions $Q(r)$ and $Z(r)$ for $g$ modes and in the bottom panel the same for $f$ modes. Let us first discuss the $g$ mode perturbing

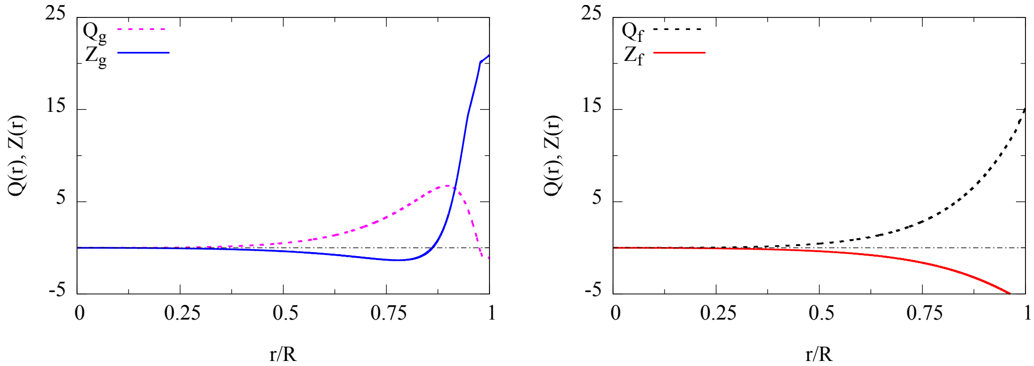


FIGURE 4.13: The solutions of the fluid perturbation functions $Q(r)$ and $Z(r)$ as a function of the radial distance for the maximum mass ($M = 2.77M_\odot$) NS obtained from the NL3 parameterized EOS. The solid (dashed) line corresponds to the angular function, $Z(r)$ (radial function, $Q(r)$). Both perturbing functions for $f$ modes ($Q_f$ and $Z_f$) show monotonic behavior while for $g$ modes these function do not and have nodes near the surface of the NS.

functions. We first observe that the Brunt-Väisäla frequency, $\omega_{BV}$ is also significant near the center as well as at the surface as may be seen in Fig. 4.9 in contrast to the hadronic matter (relevant for NSs) which becomes significant only near the surface. Thus there are additional nodes for $Z_g$ in the case of HSs in comparison to NSs. This is also reflected in the behaviour of the functions $Q(r)$ and $Z(r)$ as shown in the top panel of the Fig. 4.14. As was the case with NS, for $g$ mode the dominating contribution arises from the second term of the parenthesis of equation Eq. (4.84). The quantity in the parenthesis has a cancelling effect on the other two terms in the Eq. (4.84). This leads to a slight oscillatory behaviour for the functions $Z(r)$ depending upon whether $Z'(r)$ is positive or negative upto $r_c$. Beyond it, $\omega_{BV}$ becomes significant only near the surface and the behaviour of $Z(r)$ and $Q(r)$ are similar to that of NS. In the bottom panel of the Fig. 4.14, we have shown the same functions for the $f$ mode. The behaviour of these functions $Q(r)$ and $Z(r)$ are essentially similar to NSs.

## 4.6 Summary and conclusion

Some previous works [86, 297] also show similar results as in the current investigation where the non-radial oscillation, (QNM), frequencies enhance as quark matter appears in the core of neutron star. They investigated (QNM) of NSs and HSs by considering RMF models to describe nuclear matter and modified bag model to describe quark matter. While in our studies, we also found similar results where we have taken more realistic EOSs for nuclear matter and quark matter. Let us summarize the salient features of the present investigation. We have looked into

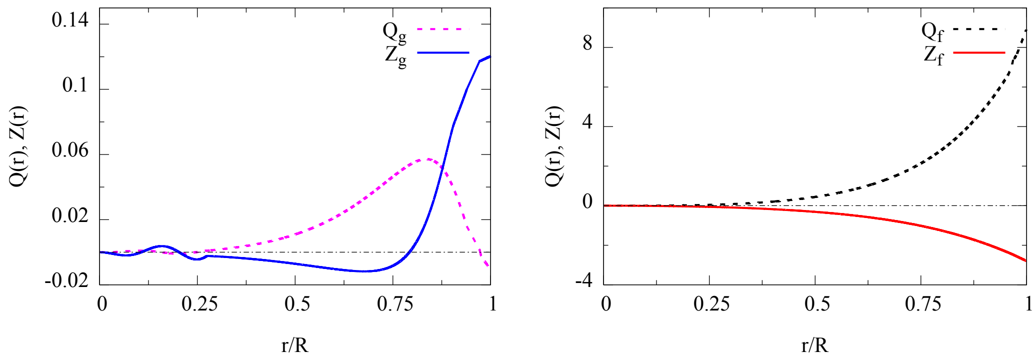


FIGURE 4.14: The solutions for the fluid perturbation functions $Q(r)$ and $Z(r)$, for the hybrid star of mass $M = 2.27M_\odot$ as a function of radial distance. The NL3 parameterized EOS is taken for hadronic matter while NJL model is taken for the quark matter EOS and Gibbs construction to find the mixed EOS. (left) figure shows the $g$ mode solutions and (right) figure shows the $f$ mode solutions. The oscillatory behaviour of $Z(r)$, ($Z_g$) near the core may be noted in the contrast to the Fig. 4.13

possible distinct features of HSs with quark matter and NSs without quark matter in their cores. This is investigated by looking into non-radial oscillations of CSs. The EOS for HS is constructed using a RMF theory for nuclear matter and the NJL model for quark matter. The Gibbs criterion for MP is used to construct MP with two chemical potentials ($\mu_B$ and $\mu_E$) imposing global charge neutrality conditions. It is observed that the core of HSs can accommodate a mixture of nucleonic and quark matter, the pure quark matter phase being never achieved. In comparison to a NS without quark matter, the inclusion of MP of matter softens EOS, resulting in lower values for the maximum masses and bigger corresponding radii. Determining the composition of NS through observables it is necessary to break the degeneracy between normal and hybrid stars. To this end, we looked into non-radial oscillation modes of such CSs for this purpose. Unlike M-R curves for which EOS is sufficient, the analysis of oscillation modes requires the speed of sound of the charge neutral matter. Using a MP structure, it is observed that the equilibrium speed of sound shoots up at the transition point between MP and HP in such a construct. It may be noted that such a steep rise in the speed of sound in a narrow region of density as one comes from the core towards the surface was also seen in a quarkyonic to hadronic matter transition [316] as well as in an EOS with $\omega$ condensate and fluctuations in pion condensate [317]. Such a steep rise in sound speed is generated here naturally through MP construct. This EOS is used to determine the frequencies of non-radial oscillations in NS within a relativistic Cowling approximation that neglects the fluctuation of the space time metric and results in a much simpler equations to solve and analyse. While this is not strictly consistent with the fully relativistic treatment, the impact of such simplified approximation is not severe, typically affecting the $g$ modes at the $5-10\%$ level while $f$ modes are more sensitive to Cowling approximation [313]. Within the RMF model for nuclear matter, we estimated the $f$ and $g$ modes frequencies. The $g$ mode solution for NS arises due to $\omega_{\mathrm{BV}}$ when it becomes significant towards the surface of NS. On the other hand for HSs the $\omega_{\mathrm{BV}}$ become significant near the core where the quark-hadron phase transition occurs. Due to the quark matter core both the $\omega_{\mathrm{BV}}$ and $g$ mode frequency get enhanced as compared to a normal NS.

We have focussed our attention in the present investigation to non-radial oscillation modes corresponding to quadrupole fundamental modes and the gravity modes. In the presence of a quark matter in a mixed phase with charge neutral nuclear matter, both these modes are enhanced with the effect being more for the $g$ modes as compared to the high frequency $f$ modes. The $g$ modes that we have considered here are driven by nonvanishing Brunt-Väisäla frequency resulting from a chemical stratification and depends upon the compositional characteristics rather than a density discontinuity. This enhancement is due to the sharp drop of the equilibrium speed of sound at the onset of the MP and is a distinct feature of HS as compared to a NS. In the context of gravitational wave from BNS merger, it is known that $g$ modes can couple to tidal forces and can draw energy and angular momentum from the binary to the NS and cause an associated phase shift in gravitational wave signal. With distinct enhancement of this mode for HS as compared to NS, one might expect a distinguishing signal from GW observations. However, the resulting phase shifts for NSs and HSs turns out to be similar order due to the longer merger times for the NSs [276]. Such conclusions are of course limited by the uncertainties arising from the value of tidal coupling. When these uncertainties are reduced through improved theoretical estimations, the high frequency $g$ modes of HS can possibly be distinguished from those of NSs. To observe the enhancement in the non-radial oscillation frequencies the highly sensitive detectors are required. The future advanced LIGO/VIRGO detector may observe these frequencies. There is also a possibility that in future NICER observation may observe these frequencies too. While the detection of $g$ mode frequencies in BNS merger observation by current detectors is challenging. One hopes that with the third generation detectors like Einstein telescope or Cosmic explorer, one can possibly have direct detection of these modes and have conclusive signatures regarding the composition of the NS interior.

One of the novel feature of the present investigation has been the use of hadronic EOS modeled through RMF models with their parameters determined from the nuclear matter properties at saturation density with the NL3 parameterisation as well DDB parameterisation.

Unlike meta models [276], mean field model EOS are derived from a microscopic model described in terms of nucleons and mesons and quite successful in describing various properties of finite nuclei as well as NSs. The derivation for $\omega_{\mathrm{BV}}$ as described here is rather general and can be used for any mean field model for nuclear/hyperonic matter. Similarly for quark matter NJL model is used which captures the important features of chiral symmetry breaking in strong interactions.

It may be noted that these models can be extended to include strange quark matter. The calculational method developed here can be applied to the various other sophisticated models like 3 flavour NJL model, quark-meson model or Polyakov loop extension of such model describing the quark matter.

We have given in some detail the derivation of the relativistic pulsating equations involving Brunt-Väisäla frequency in which such a MP EOS as derived here. In addition we have discussed the behaviour of the fluid perturbing functions in some details both with and without the hadron-quark phase transition which adds an understanding of the enhancement of oscillation frequencies for HSs. In future we would like to include the effects of the strange quarks in the quark matter sector and correspondingly hyperons in the hadronic sector. It will also be interesting and important to include the effects of strong magnetic field for the structure of NSs [319] and its effect on the non-radial oscillation modes. We have focused our attention for NSM which is at zero temperature and vanishing a neutrino chemical potential. However, to study the proto-NSs we should take into account the thermal effects on the oscillations including the effects of neutrino trapping on the phase structure of matter. This will be relevant for studying the oscillation modes from merging NS and detecting in future experimental facilities like advanced LIGO/Virgo and Einstein telescope.

# Chapter 5

# Universal relations with non-radial oscillation modes

In this chapter we discuss some relations, so called universal relation (UR)s, among non-radial frequency (specifically $f$ mode frequency), radius and mass of CSs. These relations are to some extent insensitive to the EOS. In the case of radial oscillation modes ($r$-modes), $r$-modes do not couple with the gravitational wave (GW)s and do give the information about the stability of a star. For example, the fundamental radial mode gives the allowed minimum oscillation frequency for a stable star [265, 266] and determines the maximum allowed baryon density at the center of maximum mass star. They are also useful to determine the rotation frequency of a NS [266, 267]. While in the case of non-radial oscillation, they couple with the GWs and dump energy in the GWs. So they are more suitable observable to get an insight of NSM [266, 268, 269]. Here in this chapter, we consider hadronic and hybrid EOSs sets, verify the robustness of the previously studied URs and find a new relation.

## 5.1 Introduction.

In this chapter we propose two major points of interest. Firstly we estimate, within the Cowling approximation, the $f$ mode oscillation frequencies for NSs using a large number of EOSs and demonstrate that the observation of $f$ mode frequencies, apart from causality $c_s^2 \leq 1$ and maximum mass constraints, further restrict the EOSs. Secondly we verify the robustness of few UR among the quadrupolar $f$ mode frequencies, masses and radii studied earlier with limited EOSs. We consider here a large number of EOSs and show that some of them are almost insensitive to the EOSs. It has been earlier found that the other URs between NS properties are strongly violated by hybrid hadron-quark EOSs [322–325] and certain exotic phases [326]. An ensemble of EOSs that we consider here are constructed by stitching together EOSs valid for different segments in baryon densities. For the outer crust the Bethe-Pethick-Sutherland (BPS) EOS is chosen [327]. The outer crust and the core are joined using a polytropic form $p(\varepsilon) = a_1 + a_2\varepsilon^{\gamma}$ in order to construct the inner crust, where the parameters $a_1$ and $a_2$ are determined in such a way that the EOS for the inner crust matches with the outer crust at one end ($\rho = 10^{-4}\ \text{fm}^{-3}$)

and with the core at the other end ($\rho = 0.04$ fm$^{-3}$). The polytropic index $\gamma$ is taken to be $4/3$ [328]. It is important to note that the differences in NSs radii between this treatment of the inner crust EOS and the unified inner crust description including the pasta phases have been found to be less than 0.5 km, as discussed in [329]. The core EOSs are considered within the two different approaches:

1. the nucleonic $\beta$-equilibrated EOSs, named DDB, obtained in [329], which satisfies pure neutron matter (PNM) constraints at low densities obtained from next-to-next-to-next-to leading order (N$^3$LO) calculations in the chiral effective field theory (CFT) [330, 331].

2. a hybrid set of EOSs which consists of the DDB EOS at low density ($\leq 2\rho_0$) and the deconfined quark matter at very high densities ($\geq 40\rho_0$) while the region ($2\rho_0$-$40\rho_0$) is interpolated by piecewise polytropes (DDB-Hyb).

In the present chapter we will discuss the formalism of both ensembles of EOSs in Sec. 5.2 subsequently. In Sec. 5.3 we discuss the non-radial oscillations as we already discussed it in the previous chapter, Chapter 4, where we found the pulsating equations in detail. To estimate the different modes in NS with both ensembles of EOSs, we use pulsating equations Eqs. (4.80 and 4.84). In Sec. 5.4 we discuss the results and future aspects.

## 5.2 Formalism

### 5.2.1 Equation of state of nuclear matter

In the previous chapter, (chapter 4), we have taken one set of parameters of DDB type. Here, in this chapter, we discuss how the parameters of DDB model are found using the Bayesian approach (see Ref. [329]). Bayesian approach enables one to carry out a detailed statistical analysis of the parameters of a model for a given set of fit data [332–335]. To a good approximation, the EOS of nuclear matter can be decomposed into two parts (i) the EOS for symmetric nuclear matter $\epsilon(\rho, 0)$ and (ii) a term involving the symmetry energy coefficient $S(\rho)$ and isospin asymmetry parameter $\delta$ ( $\delta = (\rho_n - \rho_p)/\rho$),

$$\epsilon(\rho, \delta) \simeq \epsilon(\rho, 0) + S(\rho)\delta^2, \tag{5.1}$$

where $\epsilon$ is the energy per nucleon at a given density $\rho$. We can recast the EOS in terms of various bulk nuclear matter properties of order $n$ at saturation density, $\rho_0$: (i) for the symmetric nuclear matter, the energy per nucleon $\epsilon_0 = \epsilon(\rho_0, 0)$ ($n = 0$), the incompressibility coefficient $K_0$ ($n = 2$), the skewness $Q_0$ ($n = 3$), and the kurtosis $Z_0$ ($n = 4$), respectively, given by [329]

$$X_0^{(n)} = 3^n \rho_0^n \left( \frac{\partial^n \epsilon(\rho, 0)}{\partial \rho^n} \right)_{\rho_0}, \qquad n = 2, 3, 4; \tag{5.2}$$

(ii) for the symmetry energy, the symmetry energy at saturation density $J_{\mathrm{sym},0}$ ($n = 0$),

$$J_{\mathrm{sym},0} = S(\rho_0), \quad S(\rho) = \frac{1}{2}\left(\frac{\partial^2 \epsilon(\rho,\delta)}{\partial \delta^2}\right)_{\delta=0}, \tag{5.3}$$

the slope $L_{\mathrm{sym},0}$ ($n = 1$), the curvature $K_{\mathrm{sym},0}$ ($n = 2$), the skewness $Q_{\mathrm{sym},0}$ ($n = 3$) and the kurtosis $Z_{\mathrm{sym},0}$ ($n = 4$) are defined as

$$X^{(n)}_{\mathrm{sym},0} = 3^n \rho_0^n \left(\frac{\partial^n S(\rho)}{\partial \rho^n}\right)_{\rho_0} \qquad n = 1,2,3,4. \tag{5.4}$$

In the Bayesian analysis the basic rules of probabilistic inference are used to update the probability for a hypothesis under the available evidence according to Bayes theorem. The posterior distributions of the model parameters $\theta$ in Bayes theorem can be written as [329]

$$P(\boldsymbol{\theta}|D) = \frac{\mathcal{L}(D|\boldsymbol{\theta})P(\boldsymbol{\theta})}{\mathcal{Z}}, \tag{5.5}$$

where $\boldsymbol{\theta}$ and $D$ denote the set of model parameters and the fit data. $P(\boldsymbol{\theta})$ in Eq. (5.5) is the prior for the model parameters and $\mathcal{Z}$ is the evidence. The type of prior can be chosen with the preliminary knowledge of the model parameters. The $P(\boldsymbol{\theta}|D)$ is the joint posterior distribution of the parameters, $\mathcal{L}(D|\boldsymbol{\theta})$ is the likelihood function.

### 5.2.2 Equations of state of quark matter

In the previous section Sec. 5.2.1, we introduced the nuclear matter EOS, DDB which is consistent with nuclear saturation properties very well but in this set of EOS there is no control at the higher densities. At asymptotically high densities, quarks are the degrees of freedom and the relevant theory is pQCD. We use pQCD theory to further constrain DDB EOS. In this section, for completeness, we collect here the previous study [336–338]. The pQCD EOS which can be casted as a simple fitting function for the pressure as a function of chemical potential ($\mu$) given as [338]

$$P_{pQCD}(\mu) = \frac{\mu^4}{108\pi^2}\left(c_1 - \frac{d_1 X^{-\nu_1}}{(\mu/GeV) - d_2 X^{-\nu_2}}\right) \tag{5.6}$$

where the parameters are $c_1 = 0.9008$, $d_1 = 0.5034$, $d_2 = 1.452$, $\nu_1 = 0.3553$ and $\nu_2 = 0.9101$ [338]. Here $X$ is a dimensionless renormalization scale parameter, $X = 3\bar{\Lambda}/\mu$ which is allowed to vary $X \in [1,4]$. We use this pQCD EOS for densities beyond $\rho \simeq 40\rho_0$ which corresponds to $\mu_{\mathrm{pQCD}} = 2.6$ GeV [338]. Between the region of the validity of pQCD and DDB i.e. $\mu_{\mathrm{DDB}} \leq \mu \leq \mu_{\mathrm{pQCD}}$, where $\mu_{\mathrm{DDB}}$ is the chemical potential of DDB EOS at $\rho = 2\rho_0$, we divide the interval into two segments, ($\mu_{\mathrm{DDB}}$-$\mu_c$) and ($\mu_c$-$\mu_{\mathrm{pQCD}}$), and assume EOS has a polytropic form in each segment i.e. $P_i(\rho_i) = \kappa_i \rho_i^{\gamma_i}$ for the $i$-th segment [337]. The segments can be connected to each other by requiring that pressure and energy density are continuous at $\mu_c$ as well as pressure shoud be an increasing function of energy density and EOS must be subluminal. We also ensure that there is no jump in baryon number density. This corresponds to assuming no first order phase transition between hadronic matter and quark matter. If one wishes to include a first order phase transition, an extra term to the number density at $\mu_c$ can be added [337].

To obtain EOS of the core, we proceed as follows. Below $\rho = 2\rho_0$ till the inner crust, we use a soft (stiff) DDB EOS as obtained in Ref. [329] within 90% CI. The corresponding value of chemical potential at $\rho = 2\rho_0$ is $\mu_{\rm DDB} = 1.036$ (1.097) GeV for a soft (stiff) DDB EOS. We interpolate the region from $\mu = \mu_{\rm DDB}$ to $\mu = \mu_c$ and from $\mu = \mu_c$ to $\mu = \mu_{\rm pQCD}$ with a piecewise polytrope. We select all those EOSs which (i) match with pQCD at $\mu = \mu_{\rm pQCD}$ (i.e. $X \in [1, 4]$) (ii) have pressure as an increasing function of energy density, and (iii) are subluminal. We refer this EOS as DDB-Hyb. The chemical potential $\mu_c$ is here chosen in such a way that it satisfies pQCD at $\mu = \mu_{\rm pQCD}$. We take $\mu_c \in [1.04, 2.2]$ GeV and the corresponding pressure $P_c \in [20, 1260]$ MeV.fm$^{-3}$. For an ensemble of DDB-Hyb EOSs we choose $\mu_c, P_c$ randomly in the prescribe domain by Latin-Hypercube-Sampling method [339] for an uniform distribution. For a given $\mu_c, P_c$ and $P_{\rm DDB}$, the parameters of the first polytrope, $(\kappa_1, \gamma_1)$ get determined. Similarly for a given $\mu_c, P_c$ and $P_2$ (where $P_2$ is the pQCD pressure for a given value of $X$ at $\mu = \mu_{\rm pQCD}$), the parameters of the second polytrope $(\kappa_2, \gamma_2)$ get determined. The domains for pressure ($P_c$) and chemical potential ($\mu_c$) become $P_c \in [45, 1255]$ MeV$\cdot$fm$^{-3}$ and $\mu_c \in [1.07, 2.09]$ GeV after constrained by pQCD. These domains further squeeze to $P_c \in [53, 680]$ MeV.fm$^{-3}$ and $\mu_c \in [1.15, 1.88]$ GeV after putting constraint of $M_{\rm max} \geq 2M_\odot$ and so we find 0.38 million EOSs out of 54 million sampled EOSs satisfying these constraints. It may be mentioned here that for an interpolation between ($\mu_{\rm DDB}$-$\mu_{\rm pQCD}$), we have used two polytropes. There have been different interpolation functions like spectral decomposition [340, 341] and speed of sound method [342, 343].

## 5.3 Non-radial oscillation modes in compact stars

We study non-radial oscillations in both scenarios with and without pQCD constraint. For the case of without pQCD constraint we use the full DDB ensemble of EOSs while for the case of with pQCD constraint we use the ensemble of EOSs which is found as for densities below $2\rho_0$ the 90% CI of DDB EOSs set which satisfies pure neutron matter constraints at low densities obtained from next-to-next-to next-to leading order (N$^3$ LO) calculations in chiral effective field theory (CEFT) [330, 331] and for the high densities the NNLO pQCD ensemble of EOSs as discussed in Refs. [336, 337] and intermediate density reason is interpolated using the two polytropes.

In this study, we find the non-radial oscillations within the Cowling approximation. The pulsating equations, which we use to get the non-radial oscillations

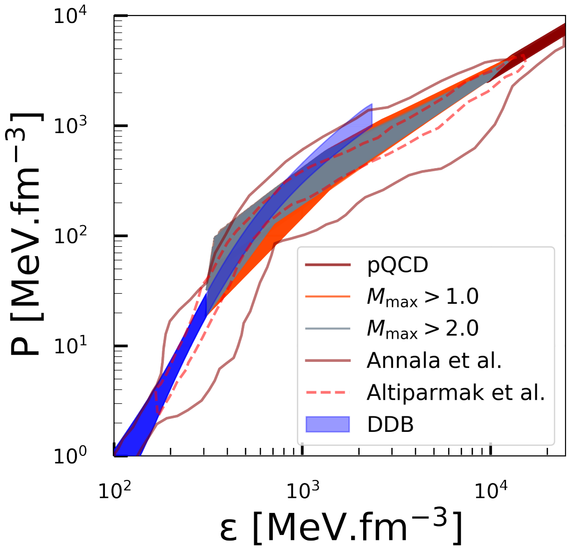


FIGURE 5.1: We show pressure and energy density regions in MeV.fm$^{-3}$ of our sampled EOSs (DDB and DDB-Hyb). We consider nucleonic $\beta$-equilibrated EOS of the 90% CIs for DDB (lightblue) as a full range and (darkblue) upto $2\rho_0$ [329] and at very high density $\sim 40\rho_0$ the NNLO pQCD (dark red). In the intermediate region, EOS is evolved in thermodynamically consistent way with two polytropic segments (see text for details).

in NS using both ensembles of EOSs (DDB and DDB-Hyb), are given in Eqs. (4.80) and (4.84). The perturbing functions $Q(r)$ and $Z(r)$ in the vicinity of the stellar center are given in Eq. (4.85) where $C$ is an arbitrary constant. We have taken $C = 1$ in our study (since it is arbitrary, so its value does not affect the result). The other boundary condition that needs to be satisfied is the Lagrange perturbation of pressure to vanish as pressure vanishes at the surface of the star i.e. $\Delta p|_{r=R} = 0$, $R$ is the radius of the star. This boundary condition at the stellar surface is given in Eq. (4.87). Apart from this, Eqs. (4.80) and (4.84) have to be supplemented by extra junction conditions which are given in Eqs. (4.88 and 4.89) at the surface of the discontinuity (where the speed of sound shows discontinuous behaviour).

With these boundary conditions the problem becomes an eigenvalue problem for the parameter $\omega$ which can be estimated numerically. We confine ourselves to $l = 2$ quadrupolar modes.

## 5.4 Results and discussion

We now proceed to analyze the ensembles of EOSs that are consistent with nuclear matter properties or PNM EOS based on theoretically robust CFT at low densities and pQCD at very high densities. As mentioned earlier, we started with 54 million

EOSs. We discarded those EOS which do not match the two end points or are superluminal (square of speed of sound $c_s^2 > 1$) as well as the condition of positive speed of sound. This leaves us with an ensemble of 0.38 million DDB-Hyb EOSs. This ensemble of EOSs is represented in Fig. 5.1 by the orange band. We next enforce the $M_{\max} \geq 2.0 M_\odot$ constraint resulting from solving the TOV equations with this ensemble. This constraint further reduces the number of EOSs to 55,000 which are displayed in Fig. 5.1 as the gray band, named here after DDB-Hyb set. The polytrope indices $\gamma_1$ and $\gamma_2$ are seen to vary over an intervals $\gamma_1 \in [1.67, 13.76]$ and $\gamma_2 \in [1.0, 1.51]$. The tight constraint on $\gamma_2$ has its origin on the matching to the pQCD pressure. In Fig. 5.1, the light blue band is the $\beta$-equilibrated nuclear matter $\approx$ 10K EOSs (DDB 90% CI) while the dark red band corresponds to pQCD EOS. For comparison, we also plot the domain of EOSs obtained in Ref. [344] (red solid curve) compatible with recent NICER and GWs observations. The red dashed lines refers to the dense PDF ($\geq 0.08$) obtained in Ref. [343] with continuous sound speed and consistent not only with nuclear theory and pQCD, but also with astronomical observations. It is to be noted that both of DDB and DDB-Hyb sets are compatible with them.

In Fig.5.2, we plot NS mass-radii and $f$ mode frequency-mass regions obtained for 90% CI for the conditional probabilities $P(R|M)$ (left) and $P(f|M)$ (right) from the mass-radius clouds arising from the ensembles of EOSs of DDB-Hyb (black dotted) and DDB (dark red). The blue horizontal bar on the left panel indicates the 90% CI radius for a $2.08 M_\odot$ star determined in Ref. [345] combining observational data from GW170817 and NICER as well as nuclear data. The top and bottom gray regions indicate, the 90% (solid) and 50% (dashed) CI of the LIGO/Virgo analysis for each binary component from the GW170817 event [346] respectively. The $1\sigma$ (68%) credible zone of the 2-D posterior distribution in mass-radii domain from millisecond pulsar PSR J0030+0451 (cyan and yellow) [318, 347] as well as PSR J0740 + 6620 (violet) [345, 348] are shown for the NICER x-rays data. The horizontal (radius) and vertical (mass) error bars reflect the $1\sigma$ credible interval derived for the same NICER data's 1-D marginalized posterior distribution. The mass-radius domain for the DDB-Hyb set sweeps a wider range than the DDB set, restricted to nucleonic degrees of freedom. The DDB-Hyb set constrained by pQCD at high density leads to larger radii for high mass NS. We conclude that the present observational constraints either obtained from GW170817 or NICER cannot rule out the existence of exotic degrees of freedom. In the right panel, we see that the 90% CI for $P(f|M)$ $f$ mode frequency $f \in [1.95, 2.7]$ kHz for both the DDB and DDB-Hyb sets. The range is smaller for low NS mass and as the mass increases the 90% CI for $f$ mode frequency increases. The $f$ mode frequency of a NS above $2M_\odot$ mass is in the range (2.1-2.7) kHz and (2.3-2.65) kHz for the DDB-Hyb and DDB sets, respectively. As mentioned in the earlier sections, the solutions for $f$ mode obtained in this work are within the Cowling approximation (neglecting perturbations of the background metric). It was shown that the Cowling approximation can overestimate the quadrupolar $f$ mode frequency of NSs by up to 30 to 10 % for NS masses

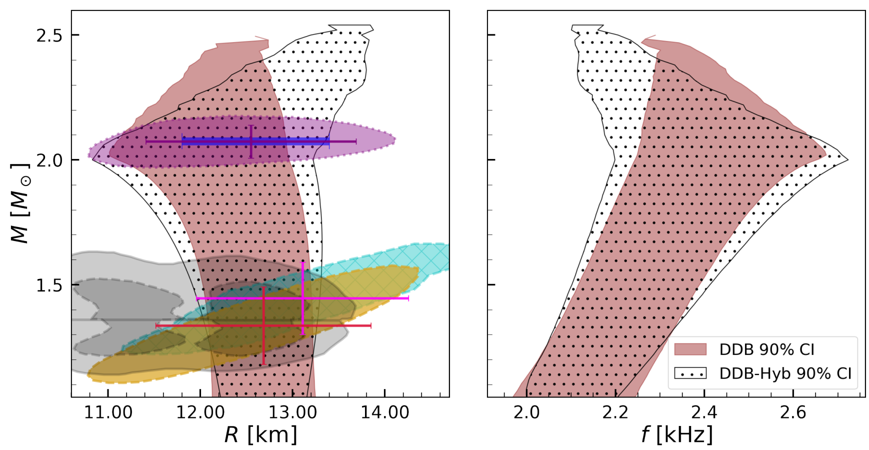


FIGURE 5.2: We plot NS mass ($M$)-radii ($R$) and $f$ mode frequency-mass ($M$) region obtained from the 90% CI for the conditional probabilities $P(R|M)$ (left) and $P(f|M)$ (right) for DDB-Hyb (black dotted) and DDB (dark red). The blue horizontal bar on the left panel indicates the 90% CI radius for a $2.08M_{\odot}$ star determined in [345] combining observational data from GW170817 and NICER as well as nuclear saturation properties. The top and bottom gray regions indicate, respectively, the 90% (solid) and 50% (dashed) CI of the LIGO/Virgo analysis for each binary component from the GW170817 event [346]. The $1\sigma$ (68%) credible zone of the 2-D posterior distribution in mass-radii domain from millisecond pulsar PSR J0030+0451 (cyan and yellow) [318, 347] as well as PSR J0740 + 6620 (violet) [345, 348] are shown for the NICER x-rays data. The horizontal (radius) and vertical (mass) error bars reflect the $1\sigma$ credible interval derived for the same NICER data's 1-D marginalized posterior distribution.

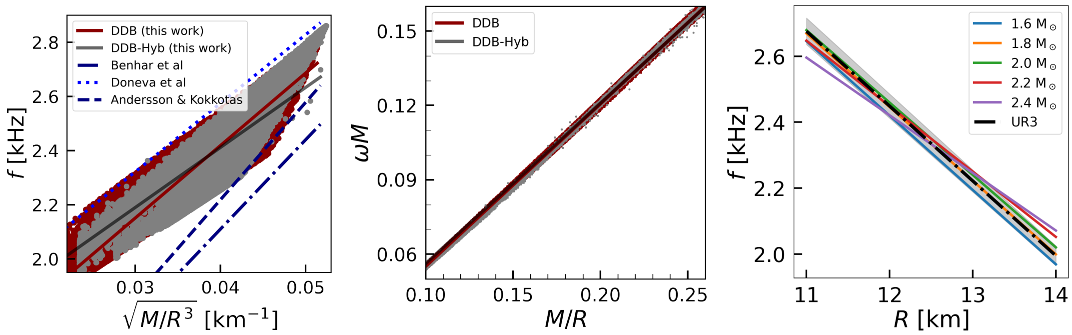


FIGURE 5.3: We plot URs obtained with our sets of EOSs, namely DDB-Hyb and DDB. UR1 (left): The frequency of the $f$ mode is plotted as a function of the square root of the average density, UR2a (center): The universality among $\omega M$ and $M/R$ and UR3 (right) the universal linear relations among $f$ mode frequency and radii of NS with masses ranged from 1.6 to 2.4 $M_\odot$ in a step of 0.2$M_\odot$.

in the range (1.0-2.5) $M_\odot$ compared to the frequency obtained in the linearized general relativistic (GR) formalism [349–351]. The accurate measurement of $f$ modes may further constrain EOS to a narrower range. Besides, a star of $2M_\odot$ with a low $f$ mode frequency may indicate an existence of non-nucleonic degrees of freedom.

In Fig. 5.3, we have studied two known URs involving the $f$ mode frequency with global properties of NS, often studied in literature with a limited EOSs. In particular, we have named UR1 for the $f$ mode frequency as a function of square root of the average star density $\sqrt{M/R^3}$, and UR2a for the $\omega M$ versus the compactness $M/R$, where $\omega = 2\pi f$. We have verified their robustness with our EOS sets, DDB-Hyb and DDB. We have also obtained a new and direct relation between the $f$ modes frequency, $f$ and radius, $R$ with the help of the existing strong correlation between them. In the left panel of the figure we show UR1:

$$f = a\sqrt{(M/R^3)} + b. \tag{5.7}$$

It has been shown in Refs. [352, 353] that the average density can be well parameterized via the $f$ mode frequency. The following values of $a$ and $b$ have been obtained: $a = 22.27 \pm 0.023$ $(26.76 \pm 0.01)$ kHz.km, $b = 1.520 \pm 0.001$ $(1.348 \pm 0.001)$ kHz for DDB-Hyb (DDB). The maximum relative percentage error obtained for UR1 within 90% CI is 6.0%(4.5%) for DDB-Hyb (DDB). In fact, the UR1 depends on EOS, therefore the dispersion, is obtained with a 90%CI. We can note that these uncertainties will remain for the entire valid domain of EOSs even if one solves full the linearized GR equations. For example, at 0.4 km$^{-1}$ mass density the frequency can vary by 400 Hz.

In Andersson & Kokkotas (Benhar et al) the authors have obtained the following parameters $a = 35.9(33.0)$kHz.km and $b = 0.78$ $(0.79)$ kHz [349, 352, 353], the difference between both works being the EOS considered in the study. In those studies the linearized GR equations were solved, and, as expected, lower frequencies have been determined. In Ref. [350], the oscillations of non-rotating and fast rotating NSs have been explored with a different set of EOSs based on microscopic theories within the Cowling approximation. The values of the coefficients of the UR1 obtained were $a = 25.32$ kHz.km and $b = 1.562$ kHz, which are at the 90% CI upper limit of the relations we have obtained.

In center panel of the Fig. 5.3 we display UR2a:

$$\omega M = a\left(\frac{M}{R}\right) + b \tag{5.8}$$

obtained for both DDB-Hyb and DDB sets, with $a = 0.6474 \pm 4.6 \times 10^{-5}$ ($a = 0.6549 \pm 2.6 \times 10^{-5}$) and $b = -0.0085 \pm 1.05 \times 10^{-5}$ ($b = -0.0103 \pm 6.18 \times 10^{-6}$) for DDB-Hyb (DDB) set. Both the coefficients are in dimensionless. The maximum relative percentage error obtained for UR2a within 90% CI is 3.78% (2.20%) for DDB-Hyb (DDB) set. The values of the slope and intercept for UR2a are also compatible with the ones obtained in Ref. [84] within Cowling approximation with a few nucleonic and hyperonic EOSs as $a = 0.65765$ and $b = 0.0127866$, respectively. We have also obtained a relation as UR2b for $\omega R$ as $\omega R = a\left(\frac{M}{R}\right)^2 + b\left(\frac{M}{R}\right) + c$. The coefficients are found to be $a = -3.0369 \pm 0.0013(-3.1844 \pm 0.0020)$, $b = 1.5829 \pm 0.0005(1.6288 \pm 0.0008)$ and $c = 0.4095 \pm 5 \times 10^{-5}(0.4087 \pm 7 \times 10^{-5})$ for DDB-Hyb (DDB) set, all the coefficients are dimensionless. In this case the maximum relative percentage error is 2.6% (1.6%) in the set DDB-Hyb (DDB). Compared with UR1, the relative maximum uncertainty is smaller for UR2a and UR2b for both DDB-Hyb and DDB sets. Using these relations we predict $f$ mode frequencies for the PSR J0740+6620. For this pulsar, the mass and radius are determined as $2.08 \pm 0.7$ $M_\odot$ and $12.35 \pm 0.75$ km in [345] combining observational data from GW170817 and NICER as well as nuclear data. The corresponding mean values of $f$ mode frequency is calculated as 2.35 kHz and 2.36 kHz for UR2a and UR2b, respectively, with a $\sim 1-4\%$ intrinsic error in the URs and additional $\sim 10-12\%$ error due to uncertainty present in mass and radius.

In chapter 4 we have discussed $f$ and $g$ modes in NSs and HSs with a number of realistic equations of states. We can see in Fig 5.4, all the equations of states follow the universal relations derived in this chapter. The maximum absolute error, $\left(\frac{|f_{\rm UR}-f_{\rm Num}|}{f_{\rm Num}}\right)$, is less than 11% (2.5%) for the case of NL3+NJL (DDB+NJL) model.

We have identified a strong linear correlation between the $f$ mode frequency and NS radius $R$ and are naming it as UR3. The values $r \in [0.98, 0.99]$ of the Pearson correlation coefficient were obtained between $f$ and $R$ for NS with a mass $M \in [1.6, 2.4]$ with our two sets of EOSs. These results can also be traced back from UR1 by keeping fixed NS mass while noting that the correlation is stronger for the larger mass NS. In the right panel of Fig. 5.3, we plot the linear relations between $f$ and $R$. The values of slope $m \in [-0.2256, -0.2233, -0.2196, -0.1984, -0.1748]$ and intercept are $c \in [5.1271, 5.1256, 5.0952, 4.8305, 4.5191]$ for NS of masses $M \in$

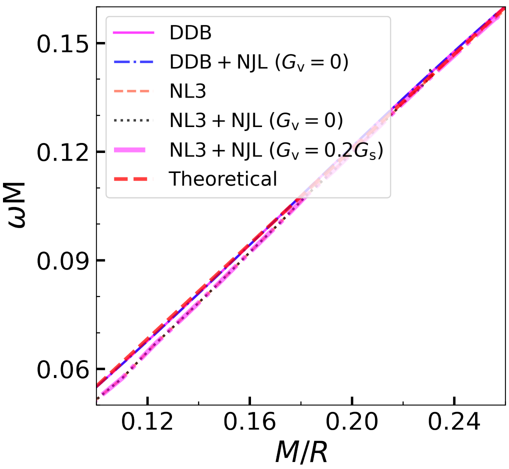


FIGURE 5.4: $\omega M$ as a function of $\frac{M}{R}$ for the different equation of state along with the universal relation UR2a.

$[1.6, 1.8, 2.0, 2.2, 2.4]$. We also plot a marginalized UR3 obtained with NS masses in the range of 1.6 to 2.4 $M_\odot$ with a slope, ($m = -0.227$) and an intercept, ($c = 5.173$). This gives $\approx$ 1.5% relative residual within 90% CI. We expect that the correlation is also present if the full GR solutions are considered. Taking this correction factor into account, the new relation (UR3) will be very useful for the upcoming future detection in order to constrain NS radius of massive NS precisely. For example, in order to measure a radius of a NS with $\sim$ 0.2 km uncertainty, the $f$ mode frequency needs to be measured within $\sim$ 2% uncertainty.

## 5.5 Summary and conclusion

The QNMs are related with the viscous properties of matter. In the future, precise measurements of them can put constraints on EOS of dense matter. We have studied the $f$ mode frequency among the QNMs, which is in the sensitivity band of the future gravitational waves networks [354]. We have calculated the $f$ mode frequency within the Cowling approximation with a nucleonic set of 14,000 EOSs (DDB set), obtained in Ref. [329] based on the RMF theory, constrained by existing observational, theoretical and experimental data through Bayesian analysis. We have also generated an ensemble of EOSs using DDB below twice saturation density ($\rho \leq 2\rho_0$) and pQCD at high densities ($\rho \geq 40\rho_0$) as in Ref.[342]. Piecewise polytropes have been used to interpolate region from $2\rho_0$ to $40\rho_0$. Implementing the constraints of causality and maximum mass $M_{\max} \geq 2.0 M_\odot$ a set of 55000 DDB-Hyb typed EOSs has obtained. The mass-radius cloud that we obtain from the ensembles of these EOSs is consistent with the GW170817 joint probability distribution as well as the recent NICER observations of mass and radius. We have analyzed the robustness of a few previously known universal relations and confirmed their dispersion with our large number of EOSs. We also found a novel strong correlation between the $f$ mode frequency, ($f$) and the radius, ($R$) for a NS of mass in the range (1.6-2.4) $M_\odot$. These new direct relations between $f$ and $R$ will allow an accurate determination of radius of NS using future $f$ mode detection.

We show that the quadrupolar $f$ mode frequencies obtained in Cowling approximation of NS of masses $2.0M_\odot$ and above lie in the range (2.1-2.7) kHz and (2.3-2.65) kHz for DDB-Hyb and DDB sets, respectively. We use these URs to predict the $f$ mode frequencies of the NICER observations and obtain $\sim$2.35 (1.88) kHz in Cowling approximation (renormalized to full GR solutions) for the PSR J0740+6620 which interestingly lies within the sensitivity band of the future gravitational wave detector networks [354] for the detection of gravitational waves. It was shown that a two solar mass star with a low $f$ mode frequency may indicate the existence of non-nucleonic degrees of freedom. In the future, a detailed investigation of how this frequency is correlated with the individual component of the EOS or different particle compositions in NS core will be carried out.

# Chapter 6

# Conclusions and future directions

In the thesis we studied the strongly interacting matter under extreme conditions, extreme density, extreme temperature, and extreme magnetic field. In the context of extreme temperature and extreme field, we study the matter created in relativistic heavy-ion collisions in RHIC and LHC. In the context of extreme density, we study the strongly interacting matter found in the core of CSs like NSs and HSs.

To understand the effects of the external magnetic field, chemical potential, chiral chemical potential etc. we have used the Wigner function within the framework of isospin symmetric 2 flavour NJL model with flavour mixing determinant interaction. We have looked at the chiral phase transition and the associated chiral susceptibilities of the medium created in relativistic heavy-ion collisions at vanishing quark chemical potential. We have seen that the chiral phase transition occurs at extreme temperature (150-170) MeV. The external magnetic field, non-zero chemical potential, chiral chemical potential affect the chiral phase transition. The chiral transition temperature is decided by the chiral susceptibility. The chiral susceptibility shows a peak at the chiral phase transition temperature. In the presence of magnetic field, the constituent masses of $u$ and $d$ quarks can be different because they couple differently with magnetic field due to different electric charges while in the vanishing magnetic field the constituent masses of $u$ and $d$ quarks are degenerate. In our study we have seen that the flavour mixing instanton induced interaction does not affect the quark masses in zero magnetic field while in non-zero magnetic field it affects the quark mass. For maximal flavour mixing, the $u$ and $d$ quark masses are degenerate even with nonvanishing magnetic field while other than maximal flavour mixing, $u$ and $d$ quark masses are non-degenerate. The constituent quark masses of $u$ and $d$ quarks become larger for nonvanishing magnetic fields compared to vanishing magnetic fields. This is the sign of magnetic catalysis which means magnetic field enhances the chiral condensate and hence the chiral phase transition temperature increases with magnetic field.

We have also investigated the thermoelectric effects on the strongly interacting system produced in heavy ion collision arising due to the temperature gradient as well as the chemical potential gradient in the medium and estimated the transport coefficients like electric conductivity, thermal conductivity, Seebeck coefficient and Lorenz number associated with the Wiedemann–Franz law in the NJL model. We estimate the same transport quantities in a quasi-particle model of the deconfined matter. We have seen that the electrical conductivity is almost constant in a quasi-particle model while it has increasing behaviour in NJL model. This is because the constituent quark mass increases with temperature and suppress the relaxation time while in the NJL model the constituent quark mass decreases with temperature. We have discussed the Seebeck effect and found the Seebeck coefficient for the system produced in heavy ion collisions. We have seen a temperature gradient can be converted into an electric current and vice-versa in a conducting medium. The electric and heat currents gets modified in the presence of non-vanishing Seebeck coefficient. In the presence of temperature gradient, an electric current becomes $\vec{J} = \sigma_{el}\vec{\mathcal{E}} - \sigma_{el}S\vec{\nabla}T$, where $S$ is the Seebeck coefficient. The electric conductivity, $\sigma_{el}$, always positive due to the constructive contributions of particles and antiparticles to the electric current. In the presence of a temperature gradient, the electric current enhances and hence the net electric current. On the other hand in the presence of non-vanishing Seebeck coefficient, the net thermal conductivity, $\kappa = \kappa_0 - T\sigma_{el}S^2$, reduces.

In the context of NSs, we have looked into the non-radial oscillation modes of CSs. We have studied CSs with and without quark matter in their cores. We have considered realistic models to describe the nuclear matter and quark matter. For nuclear matter we have considered a Walecka type models like NL3 parametrized RMF model and DDB model and for quark matter we have considered the NJL model with the vector interaction that incorporates the important feature of chiral symmetry breaking of the strong interaction. The parameters in the NJL model are taken in such a way that it defines low energy hadronic matter like pion mass, pion decay constant and the vacuum expectation value of chiral condensate. To establish the HQPT in the core of NSs we have used a Gibbs mechanism. All the EOSs considered in this study follow the tidal deformability constraint estimated in LIGO observation. We have found the HQPT occurs at $\rho \sim 2.36\rho_0$ ($\rho \sim 2.76\rho_0$) for the vector coupling $G_v = 0$ ($G_{\mathrm{v}} = 0.2G_s$). It is observed that the non-vanishing vector coupling makes EOS stiffer with respect to vanishing vector coupling. In case of DDB model we found the HQPT at $\rho \sim 3.93\rho_0$. It is observed that the core of HS can accommodate quark matter in a MP and we do not find HSs (first generation) to possess the pure quark matter core. We also have found that the HQPT softens the EOS with respect to without HQPT which reduces the maximum masses as compared to a NS without quark matter. To determine the composition of CSs through observable, it is necessary to break the degeneracy between NSs and HSs. To this end we also looked non-radial oscillation modes with different EOSs within the Cowling approximation. We found that the presence of quark matter in the core of HSs changes sound speed dramatically. This feature is also seen in case of HQPT [316] as well as in EOS with $\omega$ condensate and fluctuations in pion condensate [317]. Such dramatic decrease of the speed of sound is generated naturally here through MP construction which enhances the non-radial oscillation ($g$ and $f$ modes) frequencies as compare to without quark matter in the core of NSs.

Along with this study, we have checked the robustness of the previously studied URs, the EOS insensitive relations in masses, radii and $f$ mode oscillation frequencies of the NSs and found a new UR for the $f$ mode frequency and radius of a NS. To this end we have considered two sets of ensembles of EOSs - (i) DDB and (ii) DDB-Hyb. In a set of DDB, we took around 14000 EOS which are consistent with the nuclear matter at saturation density and CFT at low densities. In a set of DDB-Hyb, we have taken DDB EOS upto $2\rho_0$, pQCD at $40\rho_0$ and beyond and the region $2\rho_0 \leq \rho \leq 40\rho_0$ is interpolated with the piece wise polytropes. We have selected those DDB-Hyb type EOSs which are thermodynamically consistent and satisfy in NSs observations. With these relations we found the $f$ mode oscillation frequency $\sim$2.35 (1.88) kHz in Cowling approximation for the PSR J0740+6620 which interestingly lies within the sensitivity band of the future GWs detector networks [354] for the detection of GWs. It was shown that a two solar mass star with a low $f$ mode frequency may indicate the existence of non-nucleonic degrees of freedom. A novel strong correlation between the $f$ mode frequency and radius for a NS mass in the range 1.6-2.4 $M_\odot$ will allow an accurate determination of the radius of NS using future $f$ mode detection. In the future a detailed investigation of how this frequency is correlated with the individual component of the EOS or different particle composition in NS core will be carried out.

In future works, we would like to study the effects of thermoelectric coefficients. It is important to note that the thermal conductivity is required to be positive for the theory to be consistent with the second law of thermodynamics, i.e., $T\partial_\mu s^\mu \geq 0$. Using the formalism of viscous hydrodynamics and viscous magnetohydrodynamics positivity of the electrical conductivity and the thermal conductivity has been shown explicitly [249, 263]. But the contributions to the entropy current coming from the thermoelectric effects are not considered in these investigations. Therefore in the context of entropy production in the viscous hydrodynamics and magnetohydrodynamics, it will be interesting to study the effects of thermoelectric coefficients. Thermoelectric coefficients could also be relevant in the context of the SHE. SHE is an important ingredient for the generation of spin current and it is a key concept in spintronics. In the generation of spin current SHE plays an important role. In SHE an electric field induces a transverse spin current perpendicular to the direction of the electric field. SHE has been investigated recently in a hot and dense nuclear matter in the context of heavy-ion collisions [264]. It has been argued that due to SHE, a spin current will be produced proportional to the electric field. This also means that the external electric field $\vec{\mathcal{E}}$ will induce a local spin polarization and the spin polarization distribution function of fermions (anti-fermions) in momentum space will feature a dipole distribution. Therefore there will be a spin flow in the plane transverse to the direction of the electric field. Observation of SHE may open a new direction in the exploration of the many body quantum effects in hot and dense nuclear matter. However, the life-time of the electric field originated in heavy-ion collisions could be small of the order 1 fm/c. Therefore, the idea of the observation of the spin Hall effect becomes speculative. However, in the presence of non-vanishing thermoelectric coefficients any temperature gradient and/or a gradient in the chemical potential can give rise to an effective electric field which may contribute to the spin Hall effect. Therefore a detailed analysis of the thermoelectric property of the hot and dense matter produced in a heavy ion collision experiment could be relevant for SHE and needs further investigation.

In the context of CSs, we would like to include effects of the strange quarks in the quark matter sector and correspondingly hyperons in the hadronic sector. It will also be interesting and important to include effects of a strong magnetic field for the structure of NSs [319] and its effect on the non-radial oscillation modes. We have focused our attention for NSM which is at zero temperature and vanishing a neutrino chemical potential. However, to study proto-NSs we should take into account thermal effects on oscillations including effects of neutrino trapping on the phase structure of matter. As we have discussed in the first chapter that strongly interacting matter at high density is rich in different phases like pion superfluidity [22–24], various color superconducting phases like 2 flavor color superconductivity [25–27], color flavor locked phase (CFL) [28], Larkin-Ovchinkov-Fulde-Ferrel (LOFF) [29, 30] phase, crystalline superconductivity phase etc. In the future we would like to include the effect of these to the non-radial oscillations. It gives us more understanding about matter in the inner core of a NS. Some studies also show the possibility of dark matter, the study of dark matter in the core of a NS in the context of non-radial oscillations may unveil the NS core. We are sure, the future detection of $g$ and/or $f$ modes in NSs will boost our current understanding.

# Appendix A

# Regularization of scalar condensate

## A.1 Scalar condensate with a nonvanishing magnetic field and chiral chemical potential

Scalar condensate in the terms of the scalar DHW function can be written as,

$$\langle \bar{\psi}\psi \rangle = \int d^4 p F(p) \tag{A.1}$$

Using the explicit form of scalar DHW function ($F(p)$) as given in Eq.(2.43), scalar condensate in the presence of magnetic field as given in Eq.(A.1) can be expressed as,

$$\begin{aligned}
\langle \bar{\psi}\psi \rangle &= \int 2\pi p_T \mathrm{d}p_0 \mathrm{d}p_T \mathrm{d}p_z M \quad \times \\
&\left[ \sum_{n=0}^{\infty} V_n(p_0, p_z)\Lambda_+^{(n)}(p_T) + \sum_{n=1}^{\infty} \frac{1}{\sqrt{p_z^2 + 2nqB}} A_n(p_0, p_z) p_z \Lambda_-^{(n)}(p_T) \right] \\
&= \int 2\pi p_T \mathrm{d}p_0 \mathrm{d}p_T \mathrm{d}p_z M \Big[ V_0(p_0, p_z)\Lambda_+^{(0)}(p_T) + \sum_{n=1}^{\infty} V_n(p_0, p_z)\Lambda_+^{(n)}(p_T) \\
&+ \sum_{n=1}^{\infty} \frac{1}{\sqrt{p_z^2 + 2nqB}} A_n(p_0, p_z) p_z \Lambda_-^{(n)}(p_T) \Big] \\
&= \mathbb{I}_1 + \mathbb{I}_2 + \mathbb{I}_3
\end{aligned} \tag{A.2}$$

Now the first term in Eq.(A.2)

$$\mathbb{I}_1 = 2\pi \iint \mathrm{d}p_0 \mathrm{d}p_z M V_0(p_0, p_z) \int \mathrm{d}p_T p_T \Lambda_+^{(0)}(p_T). \tag{A.3}$$

Using the explicit form of $V_0(p_0, p_z)$ and $\Lambda_+^{(0)}(p_T)$, Eq.(A.3) can be expressed as,

$$\begin{aligned}
\mathbb{I}_1 &= 2\pi \iint \mathrm{d}p_0 \mathrm{d}p_z \frac{2}{(2\pi)^3} M\delta\Big( (p_0+\mu)^2 - |E_{p_z}^{(0)}|^2 \Big) \quad \times \\
&\Big[ \theta(p_0+\mu) f_{FD}(p_0) + \theta(-p_0-\mu)[f_{FD}(-p_0) - 1] \Big] \quad \times \\
&\int \mathrm{d}p_T p_T 2\exp\left[ -p_T^2/qB \right] \\
&= \frac{qB}{(2\pi)^2} \int \mathrm{d}p_z \frac{M}{E_{p_z}^{(0)}} \left[ f_{FD}(E_{p_z}^{(0)} - \mu) + f_{FD}(E_{p_z}^{(0)} + \mu) - 1 \right]
\end{aligned} \tag{A.4}$$

The second term in Eq.(A.2),

$$\mathbb{I}_2 = 2\pi \sum_{n=1}^{\infty} \iint \mathrm{d}p_0 \mathrm{d}p_z M V_n(p_0, p_z) \int \mathrm{d}p_T p_T \Lambda_+^{(n)}(p_T). \tag{A.5}$$

Using the explicit form of $\Lambda_{+}^{(n)}(p_T)$ one can calculate the following integral,

$$\int dp_T p_T \Lambda_{+}^{(n)}(p_T) = (-1)^n \int_0^\infty \mathrm{d}p_T p_T \exp(-p_T^2/qB) \quad \times$$
$$\Big[L_n(2p_T^2/qB) - L_{n-1}(2p_T^2/qB)\Big] = qB \tag{A.6}$$

To get the Eq.(A.6) we use the following identity[355],

$$\int_0^\infty \mathrm{d}x \exp(-bx) L_n(x) = (b-1)^n b^{-n-1}. \tag{A.7}$$

Using Eq.(A.6) and the explicit form of $V_n(p_0, p_z)$, $\mathbb{I}_2$ can be written as,

$$\begin{aligned}\mathbb{I}_2 = 2\pi(qB) \iint \mathrm{d}p_0 \mathrm{d}p_z \frac{2}{(2\pi)^3} M \sum_s \delta\left((p_0+\mu)^2 - |E_{p_z,s}^{(n)}|^2\right) \quad \times \\ [\theta(p_0+\mu) f_{FD}(p_0) + \theta(-p_0-\mu)(f_{FD}(-p_0) - 1)] \\ = -\frac{qB}{(2\pi)^2} \sum_{n=1}^{\infty} \sum_s \int \mathrm{d}p_z \frac{M}{E_{p_z,s}^{(n)}} \Big[1 - f_{FD}(E_{p_z,s}^{(n)} - \mu) - f_{FD}(E_{p_z,s}^{(n)} + \mu)\Big]\end{aligned} \tag{A.8}$$

Now let us consider the third term of Eq.(A.2)

$$\mathbb{I}_3 = 2\pi \iint \mathrm{d}p_0 \mathrm{d}p_z M \sum_{n=1}^{\infty} \frac{1}{\sqrt{p_z^2 + 2nqB}} A_n(p_0, p_z) p_z \int \mathrm{d}p_T p_T \Lambda_{-}^{(n)}(p_T). \tag{A.9}$$

Using the explicit form of $\Lambda_{-}^{(n)}(p_T)$, it can be shown that

$$\int \mathrm{d}p_T \mathrm{p}_T \Lambda_{-}^{(n)}(p_T) \quad = 0 \tag{A.10}$$

Hence the third term of the Eq.(A.2),

$$\mathbb{I}_3 = 0. \tag{A.11}$$

Hence using Eqs.(A.4), (A.8) and (A.11) the scalar condensate is

$$\begin{aligned}\langle\bar{\psi}\psi\rangle = -\frac{qB}{(2\pi)^2} \int \mathrm{d}p_z \frac{M}{E_{p_z}^{(0)}} \Big[1 - f_{FD}(E_{p_z}^{(0)} - \mu) - f_{FD}(E_{p_z}^{(0)} + \mu)\Big] \\ -\frac{qB}{(2\pi)^2} \sum_{n=1}^{\infty} \sum_s \int \mathrm{d}p_z \frac{M}{E_{p_z,s}^{(n)}} \Big[1 - f_{FD}(E_{p_z,s}^{(n)} - \mu) - f_{FD}(E_{p_z,s}^{(n)} + \mu)\Big].\end{aligned} \tag{A.12}$$

# A.2 Chiral condensate in the background magnetic field

The scalar condensate of a quark of flavour $f$, with $N_c$ color degrees of freedom at finite temperature $(T)$, chemical potential $(\mu)$ can be expressed as,

$$\begin{aligned}\langle\bar{\psi}_f\psi_f\rangle_{B\neq 0}^{\mu_5=0} = -\frac{N_c|q_f|B}{(2\pi)^2} \sum_{n=0}^{\infty} (2-\delta_{n,0}) \int \mathrm{d}p_z \frac{M_{0_f}}{\epsilon_{p_z,f}^{(n)}} \quad \times \\ \Big[1 - f_{FD}(\epsilon_{p_z,f}^{(n)} - \mu) - f_{FD}(\epsilon_{p_z,f}^{(n)} + \mu)\Big]\Big] \\ = \langle\bar{\psi}_f\psi_f\rangle_{vac,B\neq 0}^{\mu_5=0} + \langle\bar{\psi}_f\psi_f\rangle_{med,B\neq 0}^{\mu_5=0},\end{aligned} \tag{A.13}$$

where $\langle\bar{\psi}_f\psi_f\rangle_{vac,B\neq 0}^{\mu_5=0}$ is the $T = 0, \mu = 0$ part or the vacuum part of the scalar condensate and $\langle\bar{\psi}_f\psi_f\rangle_{med,B\neq 0}^{\mu_5=0}$ is the finite temperature and finite chemical potential part or the medium part of the scalar condensate in the presence of magnetic field. It is clear from the Eq.(A.13) the vacuum term is divergent for large momenta and however because of the distribution functions the medium part in Eq.(A.13) is not. Hence it is important to regulate the vacuum part in Eq.(A.13).

Let us consider the vacuum part $\langle\bar{\psi}_f\psi_f\rangle^{\mu_5=0}_{vac,B\neq0}$ which is given as,

$$\begin{aligned}\langle\bar{\psi}_f\psi_f\rangle^{\mu_5=0}_{vac,B\neq0} &= -\frac{N_c}{2\pi}\sum_{n=0}^{\infty}(2-\delta_{n,0})|q_f|B\int_{-\infty}^{\infty}\frac{\mathrm{d}p_z}{(2\pi)}\frac{M_{0_f}}{\epsilon^{(n)}_{p_z,f}}\\ &= -\frac{N_c}{2\pi}\sum_{n=0}^{\infty}2|q_f|B\int_{-\infty}^{\infty}\frac{\mathrm{d}p_z}{(2\pi)}\frac{M_{0_f}}{\epsilon^{(n)}_{p_z,f}}+\frac{N_c}{2\pi}|q_f|B\int_{-\infty}^{\infty}\frac{\mathrm{d}p_z}{(2\pi)}\frac{M_{0_f}}{\epsilon^{(0)}_{p_z,f}}\\ &= \mathcal{I}_1+\mathcal{I}_2\end{aligned}\tag{A.14}$$

Both integrals $\mathcal{I}_1$ and $\mathcal{I}_2$ are divergent at large momentum. These integrals can be regularized using dimensional regularization scheme. In this regularization scheme integral $\mathcal{I}_1$ can be expressed as,

$$\begin{aligned}\mathcal{I}_1 &= -\frac{N_c}{2\pi}\sum_{n=0}^{\infty}2|q_f|B\int_{-\infty}^{\infty}\frac{\mathrm{d}p_z}{(2\pi)}\frac{M_{0_f}}{\epsilon^{(n)}_{p_z,f}}\\ &= -\frac{N_c}{2\pi}\sum_{n=0}^{\infty}2|q_f|B\frac{M_{0_f}\Gamma(\epsilon/2)}{(4\pi)^{(1-\epsilon)/2}\Gamma(1/2)(x_{0_f}+n)^{\epsilon/2}},\end{aligned}\tag{A.15}$$

where the dimensionless variable $x_{0_f}\equiv M^2_{0_f}/2|q_f|B$. Similarly the integral $\mathcal{I}_2$ can be expressed as,

$$\begin{aligned}\mathcal{I}_2 &= \frac{N_c}{2\pi}|q_f|B\int\frac{\mathrm{d}p_z}{(2\pi)}\frac{M_{0_f}}{\sqrt{M^2_{0_f}+p_z^2}}\\ &= \frac{N_cM_{0_f}|q_f|B}{(2\pi)}\frac{\Gamma(\epsilon/2)}{(4\pi)^{(1-\epsilon)/2}\Gamma(1/2)x_{0_f}^{\epsilon/2}}\end{aligned}\tag{A.16}$$

Using Eq.(A.15) and Eq.(A.16), vacuum part of the scalar condensate in the presence of magnetic field as given in Eq.(A.14), can be recasted as,

$$\begin{aligned}\mathcal{I}_1+\mathcal{I}_2 &= -\frac{N_c}{2\pi}2|q_f|BM_{0_f}\frac{\Gamma(\epsilon/2)}{(4\pi)^{(1-\epsilon)/2}\Gamma(1/2)}\left[\sum_{n=0}^{\infty}\frac{1}{(x_{0_f}+n)^{\epsilon/2}}-\frac{1}{2x_{0_f}^{\epsilon/2}}\right]\\ &= -\frac{N_c}{2\pi}2|q_f|BM_{0_f}\frac{\Gamma(\epsilon/2)}{(4\pi)^{1/2}\Gamma(1/2)}\left[\zeta(\epsilon/2,x_{0_f})-\frac{1}{2x_{0_f}^{\epsilon/2}}\right].\end{aligned}\tag{A.17}$$

Expanding the right hand side of Eq.(A.17) around $\epsilon\to0$ and keeping only the leading order terms, we get,

$$\mathcal{I}_1+\mathcal{I}_2 = -\frac{N_c}{2\pi^2}|q_f|BM_{0_f}\left[-\frac{2x_{0_f}}{\epsilon}+\gamma_E x_{0_f}+\frac{1}{2}\ln x_{0_f}+\ln\Gamma(x_{0_f})-\frac{1}{2}\ln(2\pi)\right]\tag{A.18}$$

In Eq.(A.17), we have used the representation of Zeta function, which is given as [356],

$$\zeta(a,x)=\sum_{n=0}^{\infty}\frac{1}{(x+n)^a},\tag{A.19}$$

also, we have used the following identities to get Eq.(A.18),

$$\left.\begin{aligned} &\zeta(0,x)=\left(\tfrac{1}{2}-x\right),\\ \text{and}\qquad &\zeta'(0,x)=\ln\Gamma(x)-\tfrac{1}{2}\ln(2\pi),\\ \text{where}\qquad &\zeta'(0,x)=\left.\frac{d\zeta(a,x)}{da}\right|_{a=0}\end{aligned}\right\}\tag{A.20}$$

It is clear from Eq.(A.18), that the vacuum part has $1/\epsilon$ divergent part. To remove this $1/\epsilon$ divergence we use the following integral,

$$\mathcal{I}_3 = -2N_c \int \frac{\mathrm{d}^3 p}{(2\pi)^3} \frac{M_{0_f}}{\sqrt{p^2 + M_{0_f}^2}} \tag{A.21}$$

Using dimensional regularization method the integral in Eq.(A.21) can be recasted as,

$$\mathcal{I}_3 = \frac{-2N_c M_{0_f}}{(4\pi)^{3/2}\Gamma(1/2)} \frac{\Gamma(-1+\epsilon/2)}{(2x_{0_f}|q_f|B)^{-1+\epsilon/2}} \tag{A.22}$$

Expand the right hand side of Eq.(A.22) around $\epsilon \to 0$ and keeping only the leading order terms we get,

$$\mathcal{I}_3 = \frac{-N_c M_{0_f}|q_f|B}{2\pi^2}\left[-\frac{2x_{0_f}}{\epsilon} - x_{0_f} + x_{0_f}\gamma_E + x_{0_f}\ln x_{0_f}\right] \tag{A.23}$$

Using Eq.(A.18) and Eq.(A.23) we get,

$$\mathcal{I}_1 + \mathcal{I}_2 - \mathcal{I}_3 = -\frac{N_c M_{0_f}|q_f|B}{2\pi^2}\left[x_{0_f}(1-\ln x_{0_f}) + \ln\Gamma(x_{0_f}) + \frac{1}{2}\ln\left(\frac{x_{0_f}}{2\pi}\right)\right] \tag{A.24}$$

Using Eq.(A.14) and Eq.(A.24), we have the regularized vacuum part of the scalar condensate in the presence of magnetic field and is given as,

$$\begin{aligned}\langle\overline{\Psi}_f\Psi_f\rangle^{\mu_5=0}_{vac,B\neq 0} &= \mathcal{I}_1 + \mathcal{I}_2 - \mathcal{I}_3 + \mathcal{I}_3 \\ &= -\frac{N_c M_{0_f}|q_f|B}{2\pi^2}\left[x_{0_f}(1-\ln x_{0_f}) + \ln\Gamma(x_{0_f}) + \frac{1}{2}\ln\left(\frac{x_{0_f}}{2\pi}\right)\right] \\ &\quad -2N_c\int_{|\vec{p}|\leq\Lambda}\frac{\mathrm{d}^3 p}{(2\pi)^3}\frac{M_{0_f}}{\sqrt{p^2+M_{0_f}^2}}.\end{aligned} \tag{A.25}$$

Again

$$\begin{aligned}\mathcal{I}_1 &= \mathcal{I}_1 - \mathcal{I}_3 + \mathcal{I}_3 \\ &= -\frac{N_c|q_f|BM_{0_f}}{2\pi^2}\left[\frac{1}{\epsilon} - \frac{\gamma_E}{2} + x_{0_f}(1-\ln x_{0_f}) + \ln\Gamma(x_{0_f}) - \frac{1}{2}\ln(2\pi)\right] \\ &\quad -2N_c\int\frac{\mathrm{d}^3 p}{(2\pi)^3}\frac{M_{0_f}}{\sqrt{p^2+M_{0_f}^2}}.\end{aligned} \tag{A.26}$$

Hence

$$\begin{aligned}\mathcal{I} &\equiv -\frac{N_c|q_f|B}{(2\pi)^2}\sum_{s=\pm1}\sum_{n=0}^{\infty}\int \mathrm{d}p_z \frac{1}{\sqrt{p_z^2+M_{0_f}^2+2n|q_f|B}} \\ &= -\frac{N_c}{2\pi^2}|q_f|B\left[\frac{1}{\epsilon} - \frac{\gamma_E}{2} + x_{0_f}(1-\ln x_{0_f}) + \ln\Gamma(x_{0_f}) - \frac{1}{2}\ln(2\pi)\right] \\ &\quad -2N_c\int\frac{\mathrm{d}^3 p}{(2\pi)^3}\frac{1}{\sqrt{p^2+M_{0_f}^2}}\end{aligned} \tag{A.27}$$

Using Eq.(A.27) we get

$$\frac{N_c|q_f|B}{(2\pi)^2}\sum_{s=\pm1}\sum_{n=0}^{\infty}\int \mathrm{d}p_z \frac{1}{(p_z^2+M_{0_f}^2+2n|q_f|B)^{3/2}}$$
$$\equiv \frac{1}{M_{0_f}}\frac{\partial \mathcal{I}}{\partial M_{0_f}}$$
$$= -\frac{N_c}{2\pi^2}\left[-\ln x_{0_f}+\frac{\Gamma'(x_{0_f})}{\Gamma(x_{0_f})}\right]+2N_c\int_{|\vec{p}|\leq\Lambda}\frac{\mathrm{d}^3p}{(2\pi)^3}\frac{1}{(p^2+M_{0_f}^2)^{3/2}} \tag{A.28}$$

## A.3 Regularization of the chiral condensate in a background magnetic field and a chiral chemical potential

The scalar condensate of a quark of flavour $f$ with $N_c$ color degrees of freedom at finite temperature $(T)$, quark chemical potential $(\mu)$, chiral chemical potential $(\mu_5)$, electric charge $(q_f)$ and magnetic field $(B)$ can be expressed as,

$$\begin{aligned}\langle\bar{\psi}_f\psi_f\rangle^{\mu_5\neq0}_{B\neq0} &= -\frac{N_c|q_f|B}{(2\pi)^2}\Bigg[\int \mathrm{d}p_z\frac{M_f}{E^{(0)}_{p_z,f}}\left[1-f_{FD}(E^{(0)}_{p_z,f}-\mu)-f_{FD}(E^{(0)}_{p_z,f}+\mu)\right]\\ &+\sum_{n=1}^{\infty}\sum_{s}\int \mathrm{d}p_z\frac{M_f}{E^{(n)}_{p_z,s,f}}\left[1-f_{FD}(E^{(n)}_{p_z,s,f}-\mu)-f_{FD}(E^{(n)}_{p_z,s,f}+\mu)\right]\Bigg]\\ &= \langle\bar{\psi}_f\psi_f\rangle^{\mu_5\neq0}_{vac,B\neq0}+\langle\bar{\psi}_f\psi_f\rangle^{\mu_5\neq0}_{med,B\neq0},\end{aligned} \tag{A.29}$$

where $\langle\bar{\psi}_f\psi_f\rangle^{\mu_5\neq0}_{vac,B\neq0}$ is the $T=0,\mu=0$ part or the vacuum part of the scalar condensate and $\langle\bar{\psi}_f\psi_f\rangle^{\mu_5\neq0}_{med,B\neq0}$ is the finite temperature and finite chemical potential part or the medium part of the scalar condensate in the presence of magnetic field and chiral chemical potential $(\mu_5)$. It is clear from the Eq.(A.29) that the vacuum term is divergent at large momenta and however because of the distribution functions the medium part in Eq.(A.29) is not. Hence the vacuum term has to be regularized.

The vacuum term in the presence of magnetic field and chiral chemical potential can be expressed as,

$$\begin{aligned}\langle\bar{\psi}_f\psi_f\rangle^{\mu_5\neq0}_{vac,B\neq0} &= -N_c\frac{|q_f|B}{(2\pi)^2}\int \mathrm{d}p_z\frac{M_f}{\sqrt{M_f^2+(p_z-\mu_5)^2}}\\ &-N_c\frac{|q_f|B}{(2\pi)^2}\sum_{n=1}^{\infty}\sum_{s=\pm1}\int \mathrm{d}p_z\frac{M_f}{\sqrt{M_f^2+(\sqrt{p_z^2+2n|q_f|B}-s\mu_5)^2}}\end{aligned} \tag{A.30}$$

This can also be written as

$$\begin{aligned}\langle\bar{\psi}_f\psi_f\rangle^{\mu_5\neq0}_{vac,B\neq0} &= -N_c\frac{|q_f|B}{(2\pi)^2}\sum_{n=0}^{\infty}\sum_{s=\pm1}\int \mathrm{d}p_z\frac{M_f}{\sqrt{M_f^2+(\sqrt{p_z^2+2n|q_f|B}-s\mu_5)^2}}\\ &+N_c\frac{|q_f|B}{(2\pi)^2}\int \mathrm{d}p_z\frac{M_f}{\sqrt{M_f^2+(p_z-\mu_5)^2}}\\ &= -N_c\frac{|q_f|B}{(2\pi)^2}\sum_{n=0}^{\infty}\sum_{s=\pm1}\int \mathrm{d}p_z\frac{1}{\pi}\int_{-\infty}^{\infty}\mathrm{d}p_4\frac{M_f}{p_4^2+\left(M_f^2+(\sqrt{p_z^2+2n|q_f|B}-s\mu_5)^2\right)}\\ &+N_c\frac{|q_f|B}{(2\pi)^2}\int \mathrm{d}p_z\frac{1}{\pi}\int_{-\infty}^{\infty}\mathrm{d}p_4\frac{M_f}{p_4^2+M_f^2+(p_z-\mu_5)^2}\\ &= I_1+I_2\end{aligned} \tag{A.31}$$

Using the regularization method discussed in Ref. [168] we can write the integrand of the integral $I_1$ as given in the Eq.(A.31) as following

$$\begin{aligned}
&\frac{1}{p_4^2 + M_f^2 + (\sqrt{p_z^2 + 2n|q_f|B} - s\mu_5)^2} \\
&= \frac{1}{p_4^2 + p_z^2 + M_{0_f}^2 + 2n|q_f|B} - \frac{1}{p_4^2 + p_z^2 + M_{0_f}^2 + 2n|q_f|B} \\
&+ \frac{1}{p_4^2 + M_f^2 + (\sqrt{p_z^2 + 2n|q_f|B} - s\mu_5)^2} \\
&= \frac{1}{p_4^2 + p_z^2 + M_{0_f}^2 + 2n|q_f|B} \\
&+ \frac{M_{0_f}^2 - M_f^2 - \mu_5^2 + 2s\mu_5\sqrt{p_z^2 + 2n|q_f|B}}{\left(p_4^2 + p_z^2 + M_{0_f}^2 + 2n|q_f|B\right)\left(p_4^2 + M_f^2 + (\sqrt{p_z^2 + 2n|q_f|B} - s\mu_5)^2\right)}
\end{aligned} \tag{A.32}$$

Using Eq.(A.32) twice we can write the integrand of the integral $I_1$ in the following way

$$\begin{aligned}
\frac{1}{p_4^2 + M_f^2 + (\sqrt{p_z^2 + 2n|q_f|B} - s\mu_5)^2} &= \frac{1}{p_4^2 + p_z^2 + M_{0_f}^2 + 2n|q_f|B} \\
&+ \frac{A + 2s\mu_5\sqrt{p_z^2 + 2n|q_f|B}}{\left(p_4^2 + p_z^2 + M_{0_f}^2 + 2n|q_f|B\right)^2} + \frac{(A + 2s\mu_5\sqrt{p_z^2 + 2n|q_f|B})^2}{\left(p_4^2 + p_z^2 + M_{0_f}^2 + 2n|q_f|B\right)^3} \\
&+ \frac{(A + 2s\mu_5\sqrt{p_z^2 + 2n|q_f|B})^3}{\left(p_4^2 + p_z^2 + M_{0_f}^2 + 2n|q_f|B\right)^3\left(p_4^2 + M_f^2 + (\sqrt{p_z^2 + 2n|q_f|B} - s\mu_5)^2\right)},
\end{aligned} \tag{A.33}$$

where $A = M_{0_f}^2 - M_f^2 - \mu_5^2$. Performing $p_4$ integration in each term of Eq.(A.33) we get

$$\frac{1}{\pi}\sum_s \int \mathrm{d}p_4 \frac{1}{p_4^2 + p_z^2 + M_{0_f}^2 + 2n|q_f|B} = \sum_s \frac{1}{\sqrt{p_z^2 + M_{0_f}^2 + 2n|q_f|B}} \tag{A.34}$$

$$\frac{1}{\pi}\sum_s \int \mathrm{d}p_4 \frac{A + 2s\mu_5\sqrt{p_z^2 + 2n|q_f|B}}{\left(p_4^2 + p_z^2 + M_{0_f}^2 + 2n|q_f|B\right)^2} = \sum_s \frac{1}{2}\frac{A}{\left(p_z^2 + M_{0_f}^2 + 2n|q_f|B\right)^{3/2}} \tag{A.35}$$

$$\begin{aligned}
&\frac{1}{\pi}\sum_s \int \mathrm{d}p_4 \frac{(A + 2s\mu_5\sqrt{p_z^2 + 2n|q_f|B})^2}{\left(p_4^2 + p_z^2 + M_{0_f}^2 + 2n|q_f|B\right)^3} \\
&= \sum_s \left[\frac{3}{8}\frac{A^2}{(p_z^2 + M_{0_f}^2 + 2n|q_f|B)^{5/2}} - \frac{3}{2}\frac{\mu_5^2 M_{0_f}^2}{(p_z^2 + M_{0_f}^2 + 2n|q_f|B)^{5/2}} \right. \\
&\left. + \frac{3}{2}\frac{\mu_5^2}{(p_z^2 + M_{0_f}^2 + 2n|q_f|B)^{3/2}}\right]
\end{aligned} \tag{A.36}$$

$$\frac{1}{\pi}\sum_s \int \mathrm{d}p_4 \frac{(A+2s\mu_5\sqrt{p_z^2+2n|q_f|B})^3}{\left(p_4^2+p_z^2+M_{0_f}^2+2n|q_f|B\right)^3\left(p_4^2+M_f^2+(\sqrt{p_z^2+2n|q_f|B}-s\mu_5)^2\right)}$$
$$= \frac{1}{\pi}\sum_s \int \mathrm{d}p_4 \int_0^1 dx \times$$
$$\frac{3(1-x)^2(A+2s\mu_5\sqrt{p_z^2+2n|q_f|B})^3}{\left[x\left(p_4^2+M_f^2+(\sqrt{p_z^2+2n|q_f|B}-s\mu_5)^2\right)+(1-x)\left(p_4^2+p_z^2+M_{0_f}^2+2n|q_f|B\right)\right]^4}$$
$$= \sum_s \frac{15}{16}\int_0^1 \mathrm{d}x \frac{(1-x)^2(A+2s\mu_5\sqrt{p_z^2+2n|q_f|B})^3}{\left[p_z^2+M_{0_f}^2+2n|q_f|B-x(A+2s\mu_5\sqrt{p_z^2+2n|q_f|B})\right]^{7/2}} \tag{A.37}$$

Using Eq.(A.34), Eq.(A.35), Eq.(A.36) and Eq.(A.37), integral $I_1$ in Eq.(A.31) can be expressed as,

$$I_1 = -N_c\frac{|q_f|B}{(2\pi)^2}\sum_{n=0}^{\infty}\sum_{s=\pm1}\int \mathrm{d}p_z \frac{M_f}{\sqrt{M_f^2+(\sqrt{p_z^2+2n|q_f|B}-s\mu_5)^2}}$$
$$= I_{1_{\text{quad}}} - \frac{M_f(M_{0_f}^2-M_f^2+2\mu_5^2)}{2} I_{1_{\log}} + I_{1_{\text{finite1}}} + I_{1_{\text{finite2}}}, \tag{A.38}$$

where

$$I_{1_{\text{quad}}} = -N_c\frac{|q_f|B}{(2\pi)^2}\sum_{n=0}^{\infty}\sum_{s=\pm1}\int \mathrm{d}p_z \frac{M_f}{\sqrt{p_z^2+M_{0_f}^2+2n|q_f|B}}, \tag{A.39}$$

$$I_{1_{\log}} = N_c\frac{|q_f|B}{(2\pi)^2}\sum_{n=0}^{\infty}\sum_{s=\pm1}\int \mathrm{d}p_z \frac{1}{(p_z^2+M_{0_f}^2+2n|q_f|B)^{3/2}}, \tag{A.40}$$

$$I_{1_{\text{finite1}}} = -N_c\frac{|q_f|B}{(2\pi)^2}\sum_{n=0}^{\infty}\sum_{s=\pm1}\int \mathrm{d}p_z \left(\frac{3}{8}\right)\left[\frac{M_fA^2-4M_fM_{0_f}^2\mu_5^2}{(p_z^2+M_{0_f}^2+2n|q_f|B)^{5/2}}\right], \tag{A.41}$$

$$I_{1_{\text{finite2}}} = -N_c\frac{|q_f|B}{(2\pi)^2}\left(\frac{15}{16}\right)\sum_{n=0}^{\infty}\sum_{s=\pm1}\int dp_z \quad \times$$
$$\int_0^1 \mathrm{d}x \frac{(1-x)^2M_f(A+2s\mu_5\sqrt{p_z^2+2n|q_f|B})^3}{\left[p_z^2+M_{0_f}^2+2n|q_f|B-x(A+2s\mu_5\sqrt{p_z^2+2n|q_f|B})\right]^{7/2}}. \tag{A.42}$$

$$
\begin{aligned}
I_2 &= N_c \frac{|q_f|B}{(2\pi)^2} \int \mathrm{d}p_z \frac{M_f}{\sqrt{M_f^2 + (p_z - \mu_5)^2}} \\
&= N_c \frac{|q_f|B}{(2\pi)^2} \int \mathrm{d}p_z \frac{M_f}{\sqrt{M_f^2 + (p_z - \mu_5)^2}} \\
&\quad - N_c \frac{|q_f|B}{(2\pi)^2} \int \mathrm{d}p_z \frac{M_f}{\sqrt{p_z^2 + M_{0_f}^2}} + N_c \frac{|q_f|B}{(2\pi)^2} \int dp_z \frac{M_f}{\sqrt{p_z^2 + M_{0_f}^2}} \\
&= \left(\frac{1}{2}\right) N_c \frac{|q_f|B}{(2\pi)^2} \int \mathrm{d}p_z \int_0^1 dx \frac{M_f\,(A + 2p_z\mu_5)}{\left[p_z^2 + M_{0_f}^2 - x\,(A + 2p_z\mu_5)\right]^{3/2}} \\
&\quad + N_c \frac{|q_f|B}{(2\pi)^2} \int \mathrm{d}p_z \frac{M_f}{\sqrt{p_z^2 + M_{0_f}^2}} \\
&= I_{2_{\text{finite}}} + I_{2_{\log}}
\end{aligned}
\tag{A.43}
$$

Using Eq.(A.38) and Eq.(A.43), Eq.(A.31) can be recasted as,

$$
\begin{aligned}
\langle \bar{\psi}_f \psi_f \rangle^{\mu_5 \neq 0}_{vac, B \neq 0} = &- \frac{M_f(M_{0_f}^2 - M_f^2 + 2\mu_5^2)}{2} I_{1_{\log}} \\
&+ I_{1_{\text{finite1}}} + I_{1_{\text{finite2}}} + I_{2_{\text{finite}}} + I_{1_{\text{quad}}} + I_{2_{\log}},
\end{aligned}
\tag{A.44}
$$

where

$$
I_{1_{\log}} = -\frac{N_c}{2\pi^2}\left[-\ln x_{0_f} + \frac{\Gamma'(x_{0_f})}{\Gamma(x_{0_f})}\right] + 2N_c \int_{|\vec{p}| \leq \Lambda} \frac{d^3p}{(2\pi)^3} \frac{1}{(p^2 + M_{0_f}^2)^{3/2}},
\tag{A.45}
$$

and

$$
\begin{aligned}
I_{1_{\text{quad}}} + I_{2_{\log}} = &- \frac{N_c M_f |q_f| B}{2\pi^2}\left[x_{0_f}(1 - \ln x_{0_f}) + \ln \Gamma(x_{0_f}) + \frac{1}{2}\ln\left(\frac{x_{0_f}}{2\pi}\right)\right] \\
&- 2N_c \int_{|\vec{p}| \leq \Lambda} \frac{\mathrm{d}^3 p}{(2\pi)^3} \frac{M_f}{\sqrt{p^2 + M_{0_f}^2}}.
\end{aligned}
\tag{A.46}
$$

In Eq.(A.45) and (A.46) we have used (A.28) and (A.25) respectively.

## A.4 Chiral susceptibility and its regularization in the presence of a background magnetic field and chiral chemical potential

Using Eq.(A.31), we get,

$$\begin{aligned}
\frac{\partial\langle\bar{\psi}_f\psi_f\rangle^{\mu_5\neq 0}_{vac,B\neq 0}}{\partial M_f} &= -\frac{N_c|q_f|B}{(2\pi)^2}\sum_{n=0}^{\infty}\sum_{s=\pm 1}\int \mathrm{d}p_z\frac{1}{\sqrt{M_f^2+(\sqrt{p_z^2+2n|q_f|B}-s\mu_5)^2}} \\
&+\frac{N_c|q_f|B}{(2\pi)^2}\int \mathrm{d}p_z\frac{1}{\sqrt{M_f^2+(p_z-\mu_5)^2}} \\
&+\frac{N_c|q_f|B}{(2\pi)^2}\sum_{n=0}^{\infty}\sum_{s=\pm 1}\int \mathrm{d}p_z\frac{M_f^2}{\left(M_f^2+(\sqrt{p_z^2+2n|q_f|B}-s\mu_5)^2\right)^{3/2}} \\
&-\frac{N_c|q_f|B}{(2\pi)^2}\int \mathrm{d}p_z\frac{M_f^2}{\left(M_f^2+(p_z-\mu_5)^2\right)^{3/2}} \\
&= \mathbf{I}_1+\mathbf{I}_2+\mathbf{I}_3+\mathbf{I}_4
\end{aligned} \tag{A.47}$$

Using Eq.(A.38), we can write,

$$\begin{aligned}
\mathbf{I}_1 &= -N_c\frac{|q_f|B}{(2\pi)^2}\sum_{n=0}^{\infty}\sum_{s=\pm 1}\int \mathrm{d}p_z\frac{1}{\sqrt{M_f^2+(\sqrt{p_z^2+2n|q_f|B}-s\mu_5)^2}} \\
&= \mathbf{I}_{1,\text{quad}}-\frac{(M_{0_f}^2-M_f^2+2\mu_5^2)}{2}\mathbf{I}_{1,\log}+\mathbf{I}_{1,\text{finite1}}+\mathbf{I}_{1,\text{finite2}},
\end{aligned} \tag{A.48}$$

where

$$\mathbf{I}_{1,\text{quad}} = -N_c\frac{|q_f|B}{(2\pi)^2}\sum_{n=0}^{\infty}\sum_{s=\pm 1}\int \mathrm{d}p_z\frac{1}{\sqrt{p_z^2+M_{0_f}^2+2n|q_f|B}}, \tag{A.49}$$

$$\mathbf{I}_{1,\log} = N_c\frac{|q_f|B}{(2\pi)^2}\sum_{n=0}^{\infty}\sum_{s=\pm 1}\int \mathrm{d}p_z\frac{1}{(p_z^2+M_{0_f}^2+2n|q_f|B)^{3/2}}, \tag{A.50}$$

$$\mathbf{I}_{1,\text{finite1}} = -N_c\frac{|q_f|B}{(2\pi)^2}\sum_{n=0}^{\infty}\sum_{s=\pm 1}\int \mathrm{d}p_z\left(\frac{3}{8}\right)\left[\frac{A^2-4M_{0_f}^2\mu_5^2}{(p_z^2+M_{0_f}^2+2n|q_f|B)^{5/2}}\right], \tag{A.51}$$

$$\begin{aligned}
\mathbf{I}_{1,\text{finite2}} &= -N_c\frac{|q_f|B}{(2\pi)^2}\left(\frac{15}{16}\right)\sum_{n=0}^{\infty}\sum_{s=\pm 1}\int \mathrm{d}p_z\int_0^1 \mathrm{d}x \quad\times \\
&\frac{(1-x)^2(A+2s\mu_5\sqrt{p_z^2+2n|q_f|B})^3}{\left[p_z^2+M_{0_f}^2+2n|q_f|B-x(A+2s\mu_5\sqrt{p_z^2+2n|q_f|B})\right]^{7/2}}.
\end{aligned} \tag{A.52}$$

The integral $\mathbf{I}_2$ in Eq.(A.47) can be expressed as

$$\begin{aligned}
\mathbf{I}_2 &= N_c\frac{|q_f|B}{(2\pi)^2}\int \mathrm{d}p_z\frac{1}{\sqrt{M_f^2+(p_z-\mu_5)^2}} \\
&= \mathbf{I}_{2,\text{finite}}+\mathbf{I}_{2,\log},
\end{aligned} \tag{A.53}$$

where divergence free $\mathbf{I}_{2,\text{finite}}$ is,

$$\mathbf{I}_{2,\text{finite}} = \frac{N_c}{2}\frac{|q_f|B}{(2\pi)^2}\int \mathrm{d}p_z \int_0^1 \mathrm{d}x \frac{(A+2p_z\mu_5)}{\left[p_z^2+M_{0_f}^2 - x\,(A+2p_z\mu_5)\right]^{3/2}}, \tag{A.54}$$

and the divergence term $\mathbf{I}_{2,\log}$ is,

$$\mathbf{I}_{2,\log} = \frac{N_c|q_f|B}{(2\pi)^2}\int \mathrm{d}p_z \frac{1}{\sqrt{p_z^2+M_{0_f}^2}}. \tag{A.55}$$

Similarly, the integral $\mathbf{I}_3$ can be separated into a divergent and a convergent terms as

$$\begin{aligned}\mathbf{I}_3 &= \frac{N_c|q_f|B}{(2\pi)^2}\sum_{n=0}^{\infty}\sum_{s=\pm1}\int \mathrm{d}p_z \frac{M_f^2}{\left(M_f^2+(\sqrt{p_z^2+2n|q_f|B}-s\mu_5)^2\right)^{3/2}}\\ &= \mathbf{I}_{3,\text{finite}}+\mathbf{I}_{3,\log},\end{aligned} \tag{A.56}$$

where

$$\begin{aligned}\mathbf{I}_{3,\text{finite}} = &\frac{N_c|q_f|B}{(2\pi)^2}\sum_{n=0}^{\infty}\sum_{s=\pm1}\int \mathrm{d}p_z M_f^2 \quad\times\\ &\left(\frac{1}{\left(M_f^2+(\sqrt{p_z^2+2n|q_f|B}-s\mu_5)^2\right)^{3/2}} - \frac{1}{\left(M_{0_f}^2+p_z^2+2n|q_f|B\right)^{3/2}}\right),\end{aligned} \tag{A.57}$$

and

$$\mathbf{I}_{3,\log} = \frac{N_c|q_f|B}{(2\pi)^2}\sum_{n=0}^{\infty}\sum_{s=\pm1}\int \mathrm{d}p_z \frac{M_f^2}{\left(M_{0_f}^2+p_z^2+2n|q_f|B\right)^{3/2}}. \tag{A.58}$$

It can be shown that the term $\mathbf{I}_{3,\text{finite}}$ is finite. On the other hand the term $\mathbf{I}_{3,\log}$ is not convergent at large momenta. Using Eq.(A.48), Eq.(A.53) and Eq.(A.56), Eq.(A.47) can be rearranged in the following way,

$$\begin{aligned}\frac{\partial\langle\bar\psi_f\psi_f\rangle^{\mu_5\neq0}_{vac,B\neq0}}{\partial M_f} &= \mathbf{I}_{1,\text{quad}} - \frac{M_{0_f}^2-M_f^2+2\mu_5^2}{2}\mathbf{I}_{1,\log}+\mathbf{I}_{1,\text{finite1}}+\mathbf{I}_{1,\text{finite2}}+\mathbf{I}_{2,\text{finite}}\\ &\quad+\mathbf{I}_{3,\text{finite}}+\mathbf{I}_4+\mathbf{I}_{2,\log}+\mathbf{I}_{3,\log}\\ &= -\frac{M_{0_f}^2-M_f^2+2\mu_5^2}{2}\mathbf{I}_{1,\log}+\mathbf{I}_{1,\text{finite1}}+\mathbf{I}_{1,\text{finite2}}+\mathbf{I}_{2,\text{finite}}+\mathbf{I}_{3,\text{finite}}\\ &\quad+\left(\mathbf{I}_4+\frac{N_c|q_f|B}{(2\pi)^2}\int dp_z\frac{M_f^2}{(M_{0_f}^2+p_z^2)^{3/2}}\right)+\mathbf{I}_{1,\text{quad}}+\mathbf{I}_{2,\log}\\ &\quad+\left(\mathbf{I}_{3,\log}-\frac{N_c|q_f|B}{(2\pi)^2}\int dp_z\frac{M_f^2}{(M_{0_f}^2+p_z^2)^{3/2}}\right)\\ &= -\frac{M_{0_f}^2-M_f^2+2\mu_5^2}{2}\mathbf{I}_{1,\log}+\mathbf{I}_{1,\text{finite1}}+\mathbf{I}_{1,\text{finite2}}+\mathbf{I}_{2,\text{finite}}+\mathbf{I}_{3,\text{finite}}\\ &\quad+\mathbf{I}_{\text{finite}}+\mathbf{I}_{\text{quad}}+\mathbf{I}_{\log},\end{aligned} \tag{A.59}$$

where $\mathbf{I}_{\text{finite}}$ is,

$$\mathbf{I}_{\text{finite}} = \mathbf{I}_4+\frac{N_c|q_f|B}{(2\pi)^2}\int dp_z\frac{M_f^2}{(p^2+M_{0_f}^2)^{3/2}}, \tag{A.60}$$

and

$$\begin{aligned}
\mathbf{I}_{\text{quad}} &= \mathbf{I}_{1,\text{quad}} + \mathbf{I}_{2,\log} \\
&= -\frac{N_c|q_f|B}{2\pi^2}\left[x_{0_f}(1-\ln x_{0_f}) + \ln\Gamma(x_{0_f}) + \frac{1}{2}\ln\left(\frac{x_{0_f}}{2\pi}\right)\right] \\
&\quad - \frac{2N_c}{(2\pi)^3}\int_{|\vec{p}|\leq\Lambda} \mathrm{d}^3p \frac{1}{\sqrt{p^2+M_{0_f}^2}}.
\end{aligned} \tag{A.61}$$

$$\begin{aligned}
\mathbf{I}_{\log} &= \mathbf{I}_{3,\log} - \frac{N_c|q_f|B}{(2\pi)^2}\int dp_z \frac{M_f^2}{(p^2+M_{0_f}^2)^{3/2}}, \\
&= -\frac{N_c M_f^2}{2\pi^2}\left[-\ln x_{0_f} + \frac{1}{2x_{0_f}} + \frac{\Gamma'(x_{0_f})}{\Gamma(x_{0_f})}\right] + \frac{2N_c}{(2\pi)^3}\int_{|\vec{p}|\leq\Lambda} \mathrm{d}^3p \frac{M_f^2}{\left(p^2+M_{0_f}\right)^{3/2}},
\end{aligned} \tag{A.62}$$

with,

$$\begin{aligned}
\mathbf{I}_{1,\log} &= \frac{N_c|q_f|B}{(2\pi)^2}\sum_{s=\pm1}\sum_{n=0}^{\infty}\int \mathrm{d}p_z \frac{1}{(p_z^2+M_{0_f}^2+2n|q_f|B)^{3/2}} \\
&= -\frac{N_c}{2\pi^2}\left[-\ln x_{0_f} + \frac{\Gamma'(x_{0_f})}{\Gamma(x_{0_f})}\right] + 2N_c\int_{|\vec{p}|\leq\Lambda} \frac{\mathrm{d}^3p}{(2\pi)^3}\frac{1}{(p^2+M_{0_f}^2)^{3/2}}.
\end{aligned} \tag{A.63}$$

# Bibliography

[1] Caroline Riedl. “Probing nucleon spin structure in deep-inelastic scattering, proton-proton collisions and Drell-Yan processes”. In: *61 Cracow School of Theoretical Physics: Physics of the EIC*. Apr. 2022. DOI: 10.5506/APhysPolB.53.5-A2. arXiv: 2204.03684 [hep-ex].

[2] G. Beuf, T. Lappi, and R. Paatelainen. “Massive quarks at one loop in the dipole picture of Deep Inelastic Scattering”. In: (Dec. 2021). arXiv: 2112.03158 [hep-ph].

[3] Marco Cè et al. “Deep inelastic scattering off quark-gluon plasma and its photon emissivity”. In: (Dec. 2021). arXiv: 2112.00450 [hep-lat].

[4] Ignazio Scimemi and Alexey Vladimirov. “Non-perturbative structure of semi-inclusive deep-inelastic and Drell-Yan scattering at small transverse momentum”. In: *JHEP* 06 (2020), p. 137. DOI: 10.1007/JHEP06(2020)137. arXiv: 1912.06532 [hep-ph].

[5] Henning Schnurbusch. “Measurement of the proton structure from high-$Q^2$ neutral current events in $e^+p$ deep inelastic scattering at HERA”. PhD thesis. Bonn U., 2002.

[6] D. de Florian and R. Sassot. “QCD analysis of diffractive and leading proton DIS structure functions in the framework of fracture functions”. In: *Phys. Rev. D* 58 (1998), p. 054003. DOI: 10.1103/PhysRevD.58.054003. arXiv: hep-ph/9804240.

[7] D. Adams et al. “Spin structure of the proton from polarized inclusive deep inelastic muon - proton scattering”. In: *Phys. Rev. D* 56 (1997), pp. 5330–5358. DOI: 10.1103/PhysRevD.56.5330. arXiv: hep-ex/9702005.

[8] S. Liuti and Franz Gross. “Extraction of the ratio of the neutron to proton structure functions from deep inelastic scattering”. In: *Phys. Lett. B* 356 (1995), pp. 157–162. DOI: 10.1016/0370-2693(95)00843-A. arXiv: hep-ph/9506240.

[9] L. W. Whitlow et al. “Precise measurements of the proton and deuteron structure functions from a global analysis of the SLAC deep inelastic electron scattering cross-sections”. In: *Phys. Lett. B* 282 (1992), pp. 475–482. DOI: 10.1016/0370-2693(92)90672-Q.

[10] R. G. Roberts. *The Structure of the proton: Deep inelastic scattering*. Cambridge Monographs on Mathematical Physics. Cambridge University Press, Feb. 1994. ISBN: 978-0-521-44944-1, 978-1-139-24244-8. DOI: 10.1017/CBO9780511564062.

[11] A. C. Benvenuti et al. “A High Statistics Measurement of the Proton Structure Functions F(2) (x, Q**2) and R from Deep Inelastic Muon Scattering at High Q**2”. In: *Phys. Lett. B* 223 (1989), pp. 485–489. DOI: 10.1016/0370-2693(89)91637-7.

[12] J. Ashman et al. “A Measurement of the Spin Asymmetry and Determination of the Structure Function g(1) in Deep Inelastic Muon-Proton Scattering”. In: *Phys. Lett. B* 206 (1988). Ed. by V. W. Hughes and C. Cavata, p. 364. DOI: 10.1016/0370-2693(88)91523-7.

[13] N. S. Craigie and G. Schierholz. “On Extracting the Deep Inelastic Structure of Reggeons from High-Energy Muon-Proton Experiments”. In: *Nucl. Phys. B* 100 (1975), pp. 125–156. DOI: 10.1016/0550-3213(75)90229-1.

[14] Bhaswar Chatterjee, Hiranmaya Mishra, and Amruta Mishra. “Strong CP violation and chiral symmetry breaking in hot and dense quark matter”. In: *Phys. Rev. D* 85 (2012), p. 114008. DOI: 10.1103/PhysRevD.85.114008. arXiv: 1111.4061 [hep-ph].

[15] C. A. Baker et al. "An Improved experimental limit on the electric dipole moment of the neutron". In: *Phys. Rev. Lett.* 97 (2006), p. 131801. DOI: 10.1103/PhysRevLett.97.131801. arXiv: hep-ex/0602020.

[16] R. D. Peccei and Helen R. Quinn. "CP Conservation in the Presence of Instantons". In: *Phys. Rev. Lett.* 38 (1977), pp. 1440–1443. DOI: 10.1103/PhysRevLett.38.1440.

[17] Vardan Khachatryan et al. "Measurement of the inclusive 3-jet production differential cross section in proton–proton collisions at 7 TeV and determination of the strong coupling constant in the TeV range". In: *Eur. Phys. J. C* 75.5 (2015), p. 186. DOI: 10.1140/epjc/s10052-015-3376-y. arXiv: 1412.1633 [hep-ex].

[18] Rajeev S. Bhalerao. "Relativistic heavy-ion collisions". In: *1st Asia-Europe-Pacific School of High-Energy Physics*. 2014, pp. 219–239. DOI: 10.5170/CERN-2014-001.219. arXiv: 1404.3294 [nucl-th].

[19] A. Bazavov et al. "Equation of state in $(2+1)$-flavor QCD". In: *Phys. Rev. D* 90 (9 2014), p. 094503. DOI: 10.1103/PhysRevD.90.094503. URL: https://link.aps.org/doi/10.1103/PhysRevD.90.094503.

[20] Szabolcs Borsanyi et al. "Is there still any $T_c$ mystery in lattice QCD? Results with physical masses in the continuum limit III". In: *JHEP* 09 (2010), p. 073. DOI: 10.1007/JHEP09(2010)073. arXiv: 1005.3508 [hep-lat].

[21] Szabolcs Borsányi et al. "Full result for the QCD equation of state with 2+1 flavors". In: *Physics Letters B* 730 (2014), pp. 99–104. ISSN: 0370-2693. DOI: https://doi.org/10.1016/j.physletb.2014.01.007. URL: https://www.sciencedirect.com/science/article/pii/S0370269314000197.

[22] D. T. Son and M. A. Stephanov. "QCD at Finite Isospin Density". In: *Phys. Rev. Lett.* 86 (4 2001), pp. 592–595. DOI: 10.1103/PhysRevLett.86.592. URL: https://link.aps.org/doi/10.1103/PhysRevLett.86.592.

[23] D. Ebert and K. G. Klimenko. "Pion condensation in electrically neutral cold matter with finite baryon density". In: *Eur. Phys. J. C* 46 (2006), pp. 771–776. DOI: 10.1140/epjc/s2006-02527-5. arXiv: hep-ph/0510222.

[24] A. Barducci et al. "A Calculation of the QCD phase diagram at finite temperature, and baryon and isospin chemical potentials". In: *Phys. Rev. D* 69 (2004), p. 096004. DOI: 10.1103/PhysRevD.69.096004. arXiv: hep-ph/0402104.

[25] Mark G. Alford, Krishna Rajagopal, and Frank Wilczek. "QCD at finite baryon density: Nucleon droplets and color superconductivity". In: *Phys. Lett. B* 422 (1998), pp. 247–256. DOI: 10.1016/S0370-2693(98)00051-3. arXiv: hep-ph/9711395.

[26] Amruta Mishra and Hiranmaya Mishra. "Chiral symmetry breaking, color superconductivity and color neutral quark matter: A Variational approach". In: *Phys. Rev. D* 69 (2004), p. 014014. DOI: 10.1103/PhysRevD.69.014014. arXiv: hep-ph/0306105.

[27] Aman Abhishek and Hiranmaya Mishra. "Chiral Symmetry Breaking, Color Superconductivity, and Equation of State for Magnetized Strange Quark Matter". In: *Springer Proc. Phys.* 261 (2021). Ed. by Prafulla Kumar Behera et al., pp. 593–598. DOI: 10.1007/978-981-33-4408-2_82.

[28] Mark G. Alford, Krishna Rajagopal, and Frank Wilczek. "Color flavor locking and chiral symmetry breaking in high density QCD". In: *Nucl. Phys. B* 537 (1999), pp. 443–458. DOI: 10.1016/S0550-3213(98)00668-3. arXiv: hep-ph/9804403.

[29] Massimo Mannarelli, Krishna Rajagopal, and Rishi Sharma. "Testing the Ginzburg-Landau approximation for three-flavor crystalline color superconductivity". In: *Phys. Rev. D* 73 (2006), p. 114012. DOI: 10.1103/PhysRevD.73.114012. arXiv: hep-ph/0603076.

[30] Krishna Rajagopal and Rishi Sharma. "The Crystallography of Three-Flavor Quark Matter". In: *Phys. Rev. D* 74 (2006), p. 094019. DOI: 10.1103/PhysRevD.74.094019. arXiv: hep-ph/0605316.

[31] J. D. Walecka. "A Theory of highly condensed matter". In: *Annals Phys.* 83 (1974), pp. 491–529. DOI: 10.1016/0003-4916(74)90208-5.

[32] Brian D. Serot and John Dirk Walecka. "Recent progress in quantum hadrodynamics". In: *Int. J. Mod. Phys.* E6 (1997), pp. 515–631. DOI: 10.1142/S0218301397000299. arXiv: nucl-th/9701058 [nucl-th].

[33] H. C. Jean, J. Piekarewicz, and Anthony G. Williams. "Medium modification to the omega meson mass in the Walecka model". In: *Phys. Rev. C* 49 (1994), pp. 1981–1988. DOI: 10.1103/PhysRevC.49.1981. arXiv: nucl-th/9311005.

[34] Michael Buballa. "NJL-model analysis of dense quark matter". In: *Physics Reports* 407.4 (2005), pp. 205–376. ISSN: 0370-1573. DOI: https://doi.org/10.1016/j.physrep.2004.11.004.

[35] H. T. Elze, M. Gyulassy, and D. Vasak. "Transport Equations for the QCD Quark Wigner Operator". In: *Nucl. Phys. B* 276 (1986), pp. 706–728. DOI: 10.1016/0550-3213(86)90072-6.

[36] H. T. Elze, M. Gyulassy, and D. Vasak. "Transport Equations for the QCD Gluon Wigner Operator". In: *Phys. Lett. B* 177 (1986), pp. 402–408. DOI: 10.1016/0370-2693(86)90778-1.

[37] Ulrich W. Heinz. "Kinetic Theory for Nonabelian Plasmas". In: *Phys. Rev. Lett.* 51 (1983), p. 351. DOI: 10.1103/PhysRevLett.51.351.

[38] Eugene P. Wigner. "On the quantum correction for thermodynamic equilibrium". In: *Phys. Rev.* 40 (1932), pp. 749–760. DOI: 10.1103/PhysRev.40.749.

[39] Kenji Fukushima, Marco Ruggieri, and Raoul Gatto. "Chiral magnetic effect in the PNJL model". In: *Phys. Rev. D* 81 (2010), p. 114031. DOI: 10.1103/PhysRevD.81.114031. arXiv: 1003.0047 [hep-ph].

[40] P. Ao. "Nernst Effect, Seebeck Effect, and Vortex Dynamics in the Mixed State of Superconductors". In: *arXiv: cond-mat/9505002* ().

[41] Marcin Matusiak, Krzysztof Rogacki, and Thomas Wolf. "Thermoelectric anisotropy in the iron-based superconductor $\mathrm{Ba(Fe_{1-x}Co_x)_2As_2}$". In: *Phys. Rev. B* 97 (22 2018), p. 220501.

[42] C. S. Yadav M. K. Hooda. "Electronic transport properties of intermediately coupled superconductors: PdTe2 and Cu0.04PdTe2". In: *arXiv:1704.07194* ().

[43] O. Cyr-Choinière et al. "Anisotropy of the Seebeck Coefficient in the Cuprate Superconductor $\mathrm{YBa_2Cu_3O}_y$: Fermi-Surface Reconstruction by Bidirectional Charge Order". In: *Phys. Rev. X* 7 (3 2017), p. 031042.

[44] Sergeenkov Sergei. "Nonlinear Seebeck Effect in a Model Granular Superconductor". In: *JETP Letters* 67 (1998), pp. 680–684.

[45] Marcin M. Wysokinski and Jozef Spalek. "Seebeck effect in the graphene-superconductor junction". In: *Journal of Applied Physics* 113 (2013), p. 163905.

[46] Krzysztof P. Wójcik and Ireneusz Weymann. "Proximity effect on spin-dependent conductance and thermopower of correlated quantum dots". In: *Phys. Rev. B* 89 (16 2014), p. 165303.

[47] Kangjun Seo and Sumanta Tewari. "Fermi-surface reconstruction and transport coefficients from a mean-field bidirectional charge-density wave state in the high-$T_c$ cuprates". In: *Phys. Rev. B* 90 (17 2014), p. 174503.

[48] Paramita Dutta, Arijit Saha, and A. M. Jayannavar. "Thermoelectric properties of a ferromagnet-superconductor hybrid junction: Role of interfacial Rashba spin-orbit interaction". In: *Phys. Rev. B* 96 (11 2017), p. 115404.

[49] Arpan Das, Hiranmaya Mishra, and Ranjita K. Mohapatra. "Magneto-Seebeck coefficient and Nernst coefficient of hot and dense hadron gas". In: *arXiv: 2004.04665* ().

[50] Jitesh R. Bhatt, Arpan Das, and Hiranmaya Mishra. "Thermoelectric effect and Seebeck coefficient for hot and dense hadronic matter". In: *Phys. Rev. D* 99.1 (2019), p. 014015. DOI: 10.1103/PhysRevD.99.014015.

[51] Debarshi Dey and Binoy Krishna Patra. "Seebeck effect in a thermal QCD medium in the presence of strong magnetic field". In: *arXiv: 2004.03149* ().

[52] He-Xia Zhang. "Thermoelectric properties of (an-)isotropic QGP in magnetic fields". In: *arXiv:2004.08767* ().

[53] Pracheta Singha et al. "Calculations of shear, bulk viscosities and electrical conductivity in the Polyakov-quark–meson model". In: *J. Phys. G* 46.1 (2019), p. 015201. DOI: 10.1088/1361-6471/aaf256.

[54] Aman Abhishek, Hiranmaya Mishra, and Sabyasachi Ghosh. "Transport coefficients in the Polyakov quark meson coupling model: A relaxation time approximation". In: *Phys. Rev. D* 97.1 (2018), p. 014005. DOI: 10.1103/PhysRevD.97.014005.

[55] Balbeer Singh et al. "Heavy quark diffusion in a Polyakov loop plasma". In: *Phys. Rev. D* 100.11 (2019), p. 114019. DOI: 10.1103/PhysRevD.100.114019.

[56] Claudia Ratti, Michael A. Thaler, and Wolfram Weise. "Phases of QCD: Lattice thermodynamics and a field theoretical model". In: *Phys. Rev. D* 73 (2006), p. 014019. DOI: 10.1103/PhysRevD.73.014019.

[57] Paramita Deb, Guru Prakash Kadam, and Hiranmaya Mishra. "Estimating transport coefficients in hot and dense quark matter". In: *Phys. Rev.* D94.9 (2016), p. 094002. DOI: 10.1103/PhysRevD.94.094002. arXiv: 1603.01952 [hep-ph].

[58] Rudy Marty et al. "Transport coefficients from the Nambu-Jona-Lasinio model for $SU(3)_f$". In: *Phys. Rev.* C88 (2013), p. 045204. DOI: 10.1103/PhysRevC.88.045204. arXiv: 1305.7180 [hep-ph].

[59] P. Rehberg, S. P. Klevansky, and J. Hufner. "Hadronization in the SU(3) Nambu-Jona-Lasinio model". In: *Phys. Rev.* C53 (1996), pp. 410–429. DOI: 10.1103/PhysRevC.53.410. arXiv: hep-ph/9506436 [hep-ph].

[60] Chihiro Sasaki and Krzysztof Redlich. "Transport coefficients near chiral phase transition". In: *Nucl. Phys.* A832 (2010), pp. 62–75. DOI: 10.1016/j.nuclphysa.2009.11.005. arXiv: 0811.4708 [hep-ph].

[61] Yasuhiko Tsue et al. "Effective Potential Approach to Quark Ferromagnetization in High Density Quark Matter". In: *Prog. Theor. Phys.* 128 (2012), pp. 507–522. DOI: 10.1143/PTP.128.507. arXiv: 1205.2409 [nucl-th].

[62] T. Maruyama, E. Nakano, and T. Tatsumi. "Horizons in World Physics (Nova Science, NY, 2011),Vol.276, Chap.7". In: (2011).

[63] D. P. Menezes et al. "Quark matter under strong magnetic fields in the Nambu-Jona-Lasinio Model". In: *Phys. Rev.* C79 (2009), p. 035807. DOI: 10.1103/PhysRevC.79.035807. arXiv: 0811.3361 [nucl-th].

[64] Bhaswar Chatterjee, Hiranmaya Mishra, and Amruta Mishra. "Vacuum structure and chiral symmetry breaking in strong magnetic fields for hot and dense quark matter". In: *Phys. Rev.* D84 (2011), p. 014016. DOI: 10.1103/PhysRevD.84.014016. arXiv: 1101.0498 [hep-ph].

[65] Tanumoy Mandal, Prashanth Jaikumar, and Sanatan Digal. "Chiral and Diquark condensates at large magnetic field in two-flavor superconducting quark matter". In: (2009). arXiv: 0912.1413 [nucl-th].

[66] Tanumoy Mandal and Prashanth Jaikumar. "Neutrality of a magnetized two-flavor quark superconductor". In: *Phys. Rev.* C87 (2013), p. 045208. DOI: 10.1103/PhysRevC.87.045208. arXiv: 1209.2432 [nucl-th].

[67] Tanumoy Mandal and Prashanth Jaikumar. "Effect of temperature and magnetic field on two-flavor superconducting quark matter". In: *Phys. Rev.* D94.7 (2016), p. 074016. DOI: 10.1103/PhysRevD.94.074016. arXiv: 1608.00882 [hep-ph].

[68] M. Coppola et al. "Magnetized color superconducting quark matter under compact star conditions: Phase structure within the SU(2)f NJL model". In: *Phys. Rev.* D96.5 (2017), p. 056013. DOI: 10.1103/PhysRevD.96.056013. arXiv: 1707.03795 [hep-ph].

[69] Tyler Gorda et al. "Next-to-Next-to-Next-to-Leading Order Pressure of Cold Quark Matter: Leading Logarithm". In: *Phys. Rev. Lett.* 121.20 (2018), p. 202701. DOI: 10.1103/PhysRevLett.121.202701. arXiv: 1807.04120 [hep-ph].

[70] S. Borsányi et al. "Lattice QCD equation of state at finite chemical potential from an alternative expansion scheme". In: *Phys. Rev. Lett.* 126.23 (2021), p. 232001. DOI: 10.1103/PhysRevLett.126.232001. arXiv: 2102.06660 [hep-lat].

[71] B. P. Abbott et al. "GW170817: Measurements of neutron star radii and equation of state". In: *Phys. Rev. Lett.* 121.16 (2018), p. 161101. DOI: 10.1103/PhysRevLett.121.161101. arXiv: 1805.11581 [gr-qc].

[72] David Radice et al. "GW170817: Joint Constraint on the Neutron Star Equation of State from Multimessenger Observations". In: *The Astrophysical Journal* 852.2 (2018), p. L29. DOI: 10.3847/2041-8213/aaa402. URL: https://doi.org/10.3847/2041-8213/aaa402.

[73] Tuhin Malik et al. "GW170817: constraining the nuclear matter equation of state from the neutron star tidal deformability". In: *Phys. Rev. C* 98.3 (2018), p. 035804. DOI: 10.1103/PhysRevC.98.035804. arXiv: 1805.11963 [nucl-th].

[74] Cheng-Ming Li et al. "Constraints on the hybrid equation of state with a crossover hadron-quark phase transition in the light of GW170817". In: *Phys. Rev. D* 98.8 (2018), p. 083013. DOI: 10.1103/PhysRevD.98.083013. arXiv: 1808.02601 [nucl-th].

[75] Jinniu Hu et al. "Effects of symmetry energy on the radius and tidal deformability of neutron stars in the relativistic mean-field model". In: *PTEP* 2020.4 (2020), p. 043D01. DOI: 10.1093/ptep/ptaa016. arXiv: 2002.00562 [nucl-th].

[76] Soumi De et al. "Tidal Deformabilities and Radii of Neutron Stars from the Observation of GW170817". In: *Phys. Rev. Lett.* 121.9 (2018). [Erratum: Phys.Rev.Lett. 121, 259902 (2018)], p. 091102. DOI: 10.1103/PhysRevLett.121.091102. arXiv: 1804.08583 [astro-ph.HE].

[77] Katerina Chatziioannou, Carl-Johan Haster, and Aaron Zimmerman. "Measuring the neutron star tidal deformability with equation-of-state-independent relations and gravitational waves". In: *Phys. Rev. D* 97.10 (2018), p. 104036. DOI: 10.1103/PhysRevD.97.104036. arXiv: 1804.03221 [gr-qc].

[78] Vasileios Paschalidis et al. "Implications from GW170817 and I-Love-Q relations for relativistic hybrid stars". In: *Phys. Rev. D* 97.8 (2018), p. 084038. DOI: 10.1103/PhysRevD.97.084038. arXiv: 1712.00451 [astro-ph.HE].

[79] Rana Nandi and Prasanta Char. "Hybrid stars in the light of GW170817". In: *Astrophys. J.* 857.1 (2018), p. 12. DOI: 10.3847/1538-4357/aab78c. arXiv: 1712.08094 [astro-ph.HE].

[80] Mark Alford et al. "Hybrid stars that masquerade as neutron stars". In: *Astrophys. J.* 629 (2005), pp. 969–978. DOI: 10.1086/430902. arXiv: nucl-th/0411016.

[81] Wei Wei et al. "Lifting the Veil on Quark Matter in Compact Stars with Core $g$-mode Oscillations". In: *Astrophys. J.* 904.2 (2020), p. 187. DOI: 10.3847/1538-4357/abbe02. arXiv: 1811.11377 [nucl-th].

[82] V. A. Dommes and M. E. Gusakov. "Oscillations of superfluid hyperon stars: decoupling scheme and g-modes". In: *Mon. Not. Roy. Astron. Soc.* 455.3 (2016), pp. 2852–2870. DOI: 10.1093/mnras/stv2408. arXiv: 1512.04900 [astro-ph.SR].

[83] Hang Yu and Nevin N. Weinberg. "Resonant tidal excitation of superfluid neutron stars in coalescing binaries". In: *Mon. Not. Roy. Astron. Soc.* 464.3 (2017), pp. 2622–2637. DOI: 10.1093/mnras/stw2552. arXiv: 1610.00745 [astro-ph.HE].

[84] Bikram Keshari Pradhan and Debarati Chatterjee. "Effect of hyperons on f-mode oscillations in Neutron Stars". In: *Phys. Rev. C* 103.3 (2021), p. 035810. DOI: 10.1103/PhysRevC.103.035810. arXiv: 2011.02204 [astro-ph.HE].

[85] Hajime Sotani et al. "Signatures of hadron-quark mixed phase in gravitational waves". In: *Phys. Rev. D* 83 (2011), p. 024014. DOI: 10.1103/PhysRevD.83.024014. arXiv: 1012.4042 [astro-ph.HE].

[86] C. V. Flores and G. Lugones. "Discriminating hadronic and quark stars through gravitational waves of fluid pulsation modes". In: *Class. Quant. Grav.* 31 (2014), p. 155002. DOI: 10.1088/0264-9381/31/15/155002. arXiv: 1310.0554 [astro-ph.HE].

[87] Alessandro Brillante and Igor N. Mishustin. "Radial oscillations of neutral and charged hybrid stars". In: *EPL* 105.3 (2014), p. 39001. DOI: 10.1209/0295-5075/105/39001. arXiv: 1401.7915 [astro-ph.SR].

[88] Ignacio F. Ranea-Sandoval et al. "Oscillation modes of hybrid stars within the relativistic Cowling approximation". In: *JCAP* 12 (2018), p. 031. DOI: 10.1088/1475-7516/2018/12/031. arXiv: 1807.02166 [astro-ph.HE].

[89] M. C. Rodriguez et al. "Hybrid stars with sequential phase transitions: the emergence of the $g_2$ mode". In: *JCAP* 02 (2021), p. 009. DOI: 10.1088/1475-7516/2021/02/009. arXiv: 2009.03769 [astro-ph.HE].

[90] Shu Yan Lau and Kent Yagi. "Probing hybrid stars with gravitational waves via interfacial modes". In: *Phys. Rev. D* 103.6 (2021), p. 063015. DOI: 10.1103/PhysRevD.103.063015. arXiv: 2012.13000 [astro-ph.HE].

[91] Hajime Sotani. "Neutron star asteroseismology and nuclear saturation parameter". In: *Phys. Rev. D* 103.12 (2021), p. 123015. DOI: 10.1103/PhysRevD.103.123015. arXiv: 2105.13212 [astro-ph.HE].

[92] S. Jeon and V. Koch. "Fluctuations of particle ratios and the abundance of hadronic resonances". In: *Phys. Rev. Lett.* 83 (1999), pp. 5435–5438. DOI: 10.1103/PhysRevLett.83.5435. arXiv: nucl-th/9906074.

[93] Masayuki Asakawa, Ulrich W. Heinz, and Berndt Muller. "Fluctuation probes of quark deconfinement". In: *Phys. Rev. Lett.* 85 (2000), pp. 2072–2075. DOI: 10.1103/PhysRevLett.85.2072. arXiv: hep-ph/0003169.

[94] Johann Rafelski and Berndt Muller. "Strangeness Production in the Quark - Gluon Plasma". In: *Phys. Rev. Lett.* 48 (1982). [Erratum: Phys.Rev.Lett. 56, 2334 (1986)], p. 1066. DOI: 10.1103/PhysRevLett.48.1066.

[95] P. Koch, Berndt Muller, and Johann Rafelski. "Strangeness in Relativistic Heavy Ion Collisions". In: *Phys. Rept.* 142 (1986), pp. 167–262. DOI: 10.1016/0370-1573(86)90096-7.

[96] Frithjof Karsch and Edwin Laermann. "Susceptibilities, the specific heat and a cumulant in two flavor QCD". In: *Phys. Rev. D* 50 (1994), pp. 6954–6962. DOI: 10.1103/PhysRevD.50.6954. arXiv: hep-lat/9406008.

[97] C. Bernard et al. "QCD thermodynamics with three flavors of improved staggered quarks". In: *Phys. Rev. D* 71 (2005), p. 034504. DOI: 10.1103/PhysRevD.71.034504. arXiv: hep-lat/0405029.

[98] M. Cheng et al. "The Transition temperature in QCD". In: *Phys. Rev. D* 74 (2006), p. 054507. DOI: 10.1103/PhysRevD.74.054507. arXiv: hep-lat/0608013.

[99] Y. Aoki et al. "The QCD transition temperature: Results with physical masses in the continuum limit". In: *Phys. Lett. B* 643 (2006), pp. 46–54. DOI: 10.1016/j.physletb.2006.10.021. arXiv: hep-lat/0609068.

[100] M. Cheng et al. "Study of the finite temperature transition in 3-flavor QCD using the R and RHMC algorithms". In: *Phys. Rev. D* 75 (2007), p. 034506. DOI: 10.1103/PhysRevD.75.034506. arXiv: hep-lat/0612001.

[101] Liang-Kai Wu, Xiang-Qian Luo, and He-Sheng Chen. "Phase structure of lattice QCD with two flavors of Wilson quarks at finite temperature and chemical potential". In: *Phys. Rev. D* 76 (2007), p. 034505. DOI: 10.1103/PhysRevD.76.034505. arXiv: hep-lat/0611035.

[102] P. Zhuang, J. Hufner, and S. P. Klevansky. "Thermodynamics of a quark - meson plasma in the Nambu-Jona-Lasinio model". In: *Nucl. Phys. A* 576 (1994), pp. 525–552. DOI: 10.1016/0375-9474(94)90743-9.

[103] C. Sasaki, B. Friman, and K. Redlich. "Susceptibilities and the Phase Structure of a Chiral Model with Polyakov Loops". In: *Phys. Rev. D* 75 (2007), p. 074013. DOI: 10.1103/PhysRevD.75.074013. arXiv: hep-ph/0611147.

[104] Andrei V. Smilga and J. J. M. Verbaarschot. "Scalar susceptibility in QCD and the multiflavor Schwinger model". In: *Phys. Rev. D* 54 (1996), pp. 1087–1093. DOI: 10.1103/PhysRevD.54.1087. arXiv: hep-ph/9511471.

[105] D. Blaschke et al. "Analysis of chiral and thermal susceptibilities". In: *Phys. Rev. C* 58 (1998), pp. 1758–1766. DOI: 10.1103/PhysRevC.58.1758. arXiv: nucl-th/9803030.

[106] Purnendu Chakraborty, Munshi G. Mustafa, and Markus H. Thoma. "Chiral susceptibility in hard thermal loop approximation". In: *Phys. Rev. D* 67 (2003), p. 114004. DOI: 10.1103/PhysRevD.67.114004. arXiv: hep-ph/0210159.

[107] Dmitri E. Kharzeev, Larry D. McLerran, and Harmen J. Warringa. "The Effects of topological charge change in heavy ion collisions: 'Event by event P and CP violation'". In: *Nucl. Phys. A* 803 (2008), pp. 227–253. DOI: 10.1016/j.nuclphysa.2008.02.298. arXiv: 0711.0950 [hep-ph].

[108] V. Skokov, A.Yu. Illarionov, and V. Toneev. "Estimate of the magnetic field strength in heavy-ion collisions". In: *Int. J. Mod. Phys. A* 24 (2009), pp. 5925–5932. DOI: 10.1142/S0217751X09047570. arXiv: 0907.1396 [nucl-th].

[109] V. Voronyuk et al. "(Electro-)Magnetic field evolution in relativistic heavy-ion collisions". In: *Phys. Rev. C* 83 (2011), p. 054911. DOI: 10.1103/PhysRevC.83.054911. arXiv: 1103.4239 [nucl-th].

[110] Wei-Tian Deng and Xu-Guang Huang. "Event-by-event generation of electromagnetic fields in heavy-ion collisions". In: *Phys. Rev. C* 85 (2012), p. 044907. DOI: 10.1103/PhysRevC.85.044907. arXiv: 1201.5108 [nucl-th].

[111] John Bloczynski et al. "Azimuthally fluctuating magnetic field and its impacts on observables in heavy-ion collisions". In: *Phys. Lett. B* 718 (2013), pp. 1529–1535. DOI: 10.1016/j.physletb.2012.12.030. arXiv: 1209.6594 [nucl-th].

[112] L. McLerran and V. Skokov. "Comments About the Electromagnetic Field in Heavy-Ion Collisions". In: *Nucl. Phys. A* 929 (2014), pp. 184–190. DOI: 10.1016/j.nuclphysa.2014.05.008. arXiv: 1305.0774 [hep-ph].

[113] Umut Gursoy, Dmitri Kharzeev, and Krishna Rajagopal. "Magnetohydrodynamics, charged currents and directed flow in heavy ion collisions". In: *Phys. Rev. C* 89.5 (2014), p. 054905. DOI: 10.1103/PhysRevC.89.054905. arXiv: 1401.3805 [hep-ph].

[114] Victor Roy and Shi Pu. "Event-by-event distribution of magnetic field energy over initial fluid energy density in $\sqrt{s_{\rm NN}}$= 200 GeV Au-Au collisions". In: *Phys. Rev. C* 92 (2015), p. 064902. DOI: 10.1103/PhysRevC.92.064902. arXiv: 1508.03761 [nucl-th].

[115] Kirill Tuchin. "Electromagnetic field and the chiral magnetic effect in the quark-gluon plasma". In: *Phys. Rev. C* 91.6 (2015), p. 064902. DOI: 10.1103/PhysRevC.91.064902. arXiv: 1411.1363 [hep-ph].

[116] V. P. Gusynin, V. A. Miransky, and I. A. Shovkovy. "Dimensional reduction and dynamical chiral symmetry breaking by a magnetic field in (3+1)-dimensions". In: *Phys. Lett. B* 349 (1995), pp. 477–483. DOI: 10.1016/0370-2693(95)00232-A. arXiv: hep-ph/9412257.

[117] V. P. Gusynin, V. A. Miransky, and I. A. Shovkovy. "Dynamical chiral symmetry breaking by a magnetic field in QED". In: *Phys. Rev. D* 52 (1995), pp. 4747–4751. DOI: 10.1103/PhysRevD.52.4747. arXiv: hep-ph/9501304.

[118] V. P. Gusynin, V. A. Miransky, and I. A. Shovkovy. "Dynamical flavor symmetry breaking by a magnetic field in (2+1)-dimensions". In: *Phys. Rev. D* 52 (1995), pp. 4718–4735. DOI: 10.1103/PhysRevD.52.4718. arXiv: hep-th/9407168.

[119] A. Yu. Babansky, E. V. Gorbar, and G. V. Shchepanyuk. "Chiral symmetry breaking in the Nambu-Jona-Lasinio model in external constant electromagnetic field". In: *Phys. Lett. B* 419 (1998), pp. 272–278. DOI: 10.1016/S0370-2693(97)01445-7. arXiv: hep-th/9705218.

[120] K. G. Klimenko. "Magnetic catalysis and oscillating effects in Nambu-Jona-Lasinio model at nonzero chemical potential". In: *5th International Workshop on Thermal Field Theories and Their Applications*. Aug. 1998. arXiv: hep-ph/9809218.

[121] D. Ebert et al. "Magnetic oscillations in dense cold quark matter with four fermion interactions". In: *Phys. Rev. D* 61 (2000), p. 025005. DOI: 10.1103/PhysRevD.61.025005. arXiv: hep-ph/9905253.

[122] M. A. Vdovichenko, A. S. Vshivtsev, and K. G. Klimenko. "Magnetic catalysis and magnetic oscillations in the Nambu-Jona-Lasinio model". In: *Phys. Atom. Nucl.* 63 (2000), pp. 470–479. DOI: 10.1134/1.855661.

[123] V. Ch. Zhukovsky, K. G. Klimenko, and V. V. Khudyakov. "Magnetic catalysis in a P-even, chiral invariant three-dimensional model with four-fermion interaction". In: *Theor. Math. Phys.* 124 (2000), p. 1132. DOI: 10.1007/BF02551083. arXiv: hep-ph/0010123.

[124] Tomohiro Inagaki, Daiji Kimura, and Tsukasa Murata. "Four fermion interaction model in a constant magnetic field at finite temperature and chemical potential". In: *Prog. Theor. Phys.* 111 (2004), pp. 371–386. DOI: 10.1143/PTP.111.371. arXiv: hep-ph/0312005.

[125] Tomohiro Inagaki, Daiji Kimura, and Tsukasa Murata. "NJL model at finite chemical potential in a constant magnetic field". In: *Prog. Theor. Phys. Suppl.* 153 (2004). Ed. by A. Nakamura et al., pp. 321–324. DOI: 10.1143/PTPS.153.321. arXiv: hep-ph/0404219.

[126] Sutapa Ghosh, Soma Mandal, and Somenath Chakrabarty. "Chiral properties of QCD vacuum in magnetars- A Nambu-Jona-Lasinio model with semi-classical approximation". In: *Phys. Rev. C* 75 (2007), p. 015805. DOI: 10.1103/PhysRevC.75.015805. arXiv: astro-ph/0507127.

[127] A. A. Osipov et al. "Dynamical chiral symmetry breaking by a magnetic field and multiquark interactions". In: *Phys. Lett. B* 650 (2007), pp. 262–267. DOI: 10.1016/j.physletb.2007.05.033. arXiv: hep-ph/0701090.

[128] Brigitte Hiller et al. "Effects of quark interactions on dynamical chiral symmetry breaking by a magnetic field". In: *SIGMA* 4 (2008). Ed. by Anatoly Nikitin, p. 024. DOI: 10.3842/SIGMA.2008.024. arXiv: 0802.3193 [hep-ph].

[129] K. G. Klimenko and V. Ch. Zhukovsky. “Does there arise a significant enhancement of the dynamical quark mass in a strong magnetic field?” In: *Phys. Lett. B* 665 (2008), pp. 352–355. DOI: 10.1016/j.physletb.2008.06.033. arXiv: 0803.2191 [hep-ph].

[130] D. P. Menezes et al. “Quark matter under strong magnetic fields in the su(3) Nambu-Jona-Lasinio Model”. In: *Phys. Rev. C* 80 (2009), p. 065805. DOI: 10.1103/PhysRevC.80.065805. arXiv: 0907.2607 [nucl-th].

[131] Sh. Fayazbakhsh and N. Sadooghi. “Phase diagram of hot magnetized two-flavor color superconducting quark matter”. In: *Phys. Rev. D* 83 (2011), p. 025026. DOI: 10.1103/PhysRevD.83.025026. arXiv: 1009.6125 [hep-ph].

[132] Sidney S. Avancini et al. “The QCD Critical End Point Under Strong Magnetic Fields”. In: *Phys. Rev. D* 85 (2012), p. 091901. DOI: 10.1103/PhysRevD.85.091901. arXiv: 1202.5641 [hep-ph].

[133] Gabriel N. Ferrari, Andre F. Garcia, and Marcus B. Pinto. “Chiral Transition Within Effective Quark Models Under Magnetic Fields”. In: *Phys. Rev. D* 86 (2012), p. 096005. DOI: 10.1103/PhysRevD.86.096005. arXiv: 1207.3714 [hep-ph].

[134] V. Elias et al. “The Gross-Neveu model and the supersymmetric and nonsupersymmetric Nambu-Jona-Lasinio model in a magnetic field”. In: *Phys. Rev. D* 54 (1996), pp. 7884–7893. DOI: 10.1103/PhysRevD.54.7884. arXiv: hep-th/9605027.

[135] Jens O. Andersen and Rashid Khan. “Chiral transition in a magnetic field and at finite baryon density”. In: *Phys. Rev. D* 85 (2012), p. 065026. DOI: 10.1103/PhysRevD.85.065026. arXiv: 1105.1290 [hep-ph].

[136] Jens O. Andersen and Anders Tranberg. “The Chiral transition in a magnetic background: Finite density effects and the functional renormalization group”. In: *JHEP* 08 (2012), p. 002. DOI: 10.1007/JHEP08(2012)002. arXiv: 1204.3360 [hep-ph].

[137] Thomas D. Cohen, David A. McGady, and Elizabeth S. Werbos. “The Chiral condensate in a constant electromagnetic field”. In: *Phys. Rev. C* 76 (2007), p. 055201. DOI: 10.1103/PhysRevC.76.055201. arXiv: 0706.3208 [hep-ph].

[138] Thomas D. Cohen and Elizabeth S. Werbos. “Magnetization of the QCD vacuum at large fields”. In: *Phys. Rev. C* 80 (2009), p. 015203. DOI: 10.1103/PhysRevC.80.015203. arXiv: 0810.5103 [hep-ph].

[139] Dmitri E. Kharzeev. “The Chiral Magnetic Effect and Anomaly-Induced Transport”. In: *Prog. Part. Nucl. Phys.* 75 (2014), pp. 133–151. DOI: 10.1016/j.ppnp.2014.01.002. arXiv: 1312.3348 [hep-ph].

[140] S. R. De Groot. *Relativistic Kinetic Theory. Principles and Applications*. Ed. by W. A. Van Leeuwen and C. G. Van Weert. 1980.

[141] P. Carruthers and F. Zachariasen. “Quantum Collision Theory with Phase Space Distribution Functions”. In: *Rev. Mod. Phys.* 55 (1983), p. 245. DOI: 10.1103/RevModPhys.55.245.

[142] I. Bialynicki-Birula. “Classical Limit of Quantum Electrodynamics”. In: *Acta Phys. Austriaca Suppl.* 18 (1977), pp. 111–151.

[143] Nora Weickgenannt et al. “Kinetic theory for massive spin-1/2 particles from the Wigner-function formalism”. In: *Phys. Rev. D* 100.5 (2019), p. 056018. DOI: 10.1103/PhysRevD.100.056018. arXiv: 1902.06513 [hep-ph].

[144] Nestor Armesto et al. “The Color Glass Condensate density matrix: Lindblad evolution, entanglement entropy and Wigner functional”. In: *JHEP* 05 (2019), p. 025. DOI: 10.1007/JHEP05(2019)025. arXiv: 1901.08080 [hep-ph].

[145] Shijun Mao and Dirk H. Rischke. “Dynamically generated magnetic moment in the Wigner-function formalism”. In: *Phys. Lett. B* 792 (2019), pp. 149–155. DOI: 10.1016/j.physletb.2019.03.034. arXiv: 1812.06684 [hep-th].

[146] Xin-Li Sheng et al. "Wigner function and pair production in parallel electric and magnetic fields". In: *Phys. Rev. D* 99.5 (2019), p. 056004. DOI: 10.1103/PhysRevD.99.056004. arXiv: 1812.01146 [hep-ph].

[147] Jian-hua Gao, Jin-Yi Pang, and Qun Wang. "Chiral vortical effect in Wigner function approach". In: *Phys. Rev. D* 100.1 (2019), p. 016008. DOI: 10.1103/PhysRevD.100.016008. arXiv: 1810.02028 [nucl-th].

[148] Jian-Hua Gao et al. "Disentangling covariant Wigner functions for chiral fermions". In: *Phys. Rev. D* 98.3 (2018), p. 036019. DOI: 10.1103/PhysRevD.98.036019. arXiv: 1802.06216 [hep-ph].

[149] George Prokhorov and Oleg Teryaev. "Anomalous current from the covariant Wigner function". In: *Phys. Rev. D* 97.7 (2018), p. 076013. DOI: 10.1103/PhysRevD.97.076013. arXiv: 1707.02491 [hep-th].

[150] Xin-li Sheng et al. "Wigner functions for fermions in strong magnetic fields". In: *Eur. Phys. J. A* 54.2 (2018), p. 21. DOI: 10.1140/epja/i2018-12414-9. arXiv: 1707.01388 [hep-ph].

[151] E. V. Gorbar et al. "Wigner function and kinetic phenomena for chiral plasma in a strong magnetic field". In: *JHEP* 08 (2017), p. 103. DOI: 10.1007/JHEP08(2017)103. arXiv: 1707.01105 [hep-ph].

[152] Jian-hua Gao, Shi Pu, and Qun Wang. "Covariant chiral kinetic equation in the Wigner function approach". In: *Phys. Rev. D* 96.1 (2017), p. 016002. DOI: 10.1103/PhysRevD.96.016002. arXiv: 1704.00244 [nucl-th].

[153] Yan Wu, Defu Hou, and Hai-cang Ren. "Field theoretic perspectives of the Wigner function formulation of the chiral magnetic effect". In: *Phys. Rev. D* 96.9 (2017), p. 096015. DOI: 10.1103/PhysRevD.96.096015. arXiv: 1601.06520 [hep-ph].

[154] Yoshimasa Hidaka, Shi Pu, and Di-Lun Yang. "Relativistic Chiral Kinetic Theory from Quantum Field Theories". In: *Phys. Rev. D* 95.9 (2017), p. 091901. DOI: 10.1103/PhysRevD.95.091901. arXiv: 1612.04630 [hep-th].

[155] Koichi Hattori, Yoshimasa Hidaka, and Di-Lun Yang. "Axial Kinetic Theory and Spin Transport for Fermions with Arbitrary Mass". In: *Phys. Rev. D* 100.9 (2019), p. 096011. DOI: 10.1103/PhysRevD.100.096011. arXiv: 1903.01653 [hep-ph].

[156] T. Hatsuda and T. Kunihiro. "Fluctuation Effects in Hot Quark Matter: Precursors of Chiral Transition at Finite Temperature". In: *Phys. Rev. Lett.* 55 (1985), pp. 158–161. DOI: 10.1103/PhysRevLett.55.158.

[157] Wojciech Florkowski and Bengt L. Friman. "Screening of the meson fields in the Nambu-Jona-Lasinio model". In: *Acta Phys. Polon. B* 25 (1994), pp. 49–71.

[158] J. Hufner et al. "Thermodynamics of a quark plasma beyond the mean field: A generalized Beth-Uhlenbeck approach". In: *Annals Phys.* 234 (1994), pp. 225–244. DOI: 10.1006/aphy.1994.1080.

[159] S. P. Klevansky. "The Nambu-Jona-Lasinio model of quantum chromodynamics". In: *Rev. Mod. Phys.* 64 (1992), pp. 649–708. DOI: 10.1103/RevModPhys.64.649.

[160] M. K. Volkov. "Effective chiral Lagrangians and the Nambu-Jona-Lasinio model". In: *Phys. Part. Nucl.* 24 (1993), pp. 35–58.

[161] Tetsuo Hatsuda and Teiji Kunihiro. "QCD phenomenology based on a chiral effective Lagrangian". In: *Phys. Rept.* 247 (1994), pp. 221–367. DOI: 10.1016/0370-1573(94)90022-1. arXiv: hep-ph/9401310.

[162] W. Florkowski et al. "Chirally invariant transport equations for quark matter". In: *Annals Phys.* 245 (1996), pp. 445–463. DOI: 10.1006/aphy.1996.0016. arXiv: hep-ph/9505407.

[163] M. N. Chernodub and A. S. Nedelin. "Phase diagram of chirally imbalanced QCD matter". In: *Phys. Rev. D* 83 (2011), p. 105008. DOI: 10.1103/PhysRevD.83.105008. arXiv: 1102.0188 [hep-ph].

[164] Raoul Gatto and Marco Ruggieri. "Hot Quark Matter with an Axial Chemical Potential". In: *Phys. Rev. D* 85 (2012), p. 054013. DOI: 10.1103/PhysRevD.85.054013. arXiv: 1110.4904 [hep-ph].

[165] M. Ruggieri and G. X. Peng. "Critical Temperature of Chiral Symmetry Restoration for Quark Matter with a Chiral Chemical Potential". In: *J. Phys. G* 43.12 (2016), p. 125101. DOI: 10.1088/0954-3899/43/12/125101. arXiv: 1602.05250 [hep-ph].

[166] Shu-Sheng Xu et al. "Chiral phase transition with a chiral chemical potential in the framework of Dyson-Schwinger equations". In: *Phys. Rev. D* 91.5 (2015), p. 056003. DOI: 10.1103/PhysRevD.91.056003. arXiv: 1505.00316 [hep-ph].

[167] Bin Wang et al. "Effect of the chiral chemical potential on the position of the critical endpoint". In: *Phys. Rev. D* 91.3 (2015), p. 034017. DOI: 10.1103/PhysRevD.91.034017.

[168] R. L. S. Farias et al. "Thermodynamics of quark matter with a chiral imbalance". In: *Phys. Rev. D* 94.7 (2016), p. 074011. DOI: 10.1103/PhysRevD.94.074011. arXiv: 1604.04518 [hep-ph].

[169] V. V. Braguta et al. "Study of QCD Phase Diagram with Non-Zero Chiral Chemical Potential". In: *Phys. Rev. D* 93.3 (2016), p. 034509. DOI: 10.1103/PhysRevD.93.034509. arXiv: 1512.05873 [hep-lat].

[170] V. V. Braguta et al. "Two-Color QCD with Non-zero Chiral Chemical Potential". In: *JHEP* 06 (2015), p. 094. DOI: 10.1007/JHEP06(2015)094. arXiv: 1503.06670 [hep-lat].

[171] Lang Yu, Hao Liu, and Mei Huang. "Effect of the chiral chemical potential on the chiral phase transition in the NJL model with different regularization schemes". In: *Phys. Rev. D* 94.1 (2016), p. 014026. DOI: 10.1103/PhysRevD.94.014026. arXiv: 1511.03073 [hep-ph].

[172] R. L. S. Farias et al. "Cutoff-independent regularization of four-fermion interactions for color superconductivity". In: *Phys. Rev. C* 73 (2006), p. 018201. DOI: 10.1103/PhysRevC.73.018201. arXiv: hep-ph/0510145.

[173] Sidney S. Avancini et al. "Cold QCD at finite isospin density: confronting effective models with recent lattice data". In: *Phys. Rev. D* 100.11 (2019), p. 116002. DOI: 10.1103/PhysRevD.100.116002. arXiv: 1907.09880 [hep-ph].

[174] D. Vasak, M. Gyulassy, and H. T. Elze. "Quantum Transport Theory for Abelian Plasmas". In: *Annals Phys.* 173 (1987), pp. 462–492. DOI: 10.1016/0003-4916(87)90169-2.

[175] Ren-hong Fang et al. "Polarization of massive fermions in a vortical fluid". In: *Phys. Rev. C* 94.2 (2016), p. 024904. DOI: 10.1103/PhysRevC.94.024904. arXiv: 1604.04036 [nucl-th].

[176] W. Vincent Liu and Frank Wilczek. "Interior gap superfluidity". In: *Phys. Rev. Lett.* 90 (2003), p. 047002. DOI: 10.1103/PhysRevLett.90.047002. arXiv: cond-mat/0208052.

[177] Juergen Berges and Krishna Rajagopal. "Color superconductivity and chiral symmetry restoration at nonzero baryon density and temperature". In: *Nucl. Phys. B* 538 (1999), pp. 215–232. DOI: 10.1016/S0550-3213(98)00620-8. arXiv: hep-ph/9804233.

[178] Jorge L. Noronha and Igor A. Shovkovy. "Color-flavor locked superconductor in a magnetic field". In: *Phys. Rev. D* 76 (2007). [Erratum: Phys.Rev.D 86, 049901 (2012)], p. 105030. DOI: 10.1103/PhysRevD.76.105030. arXiv: 0708.0307 [hep-ph].

[179] G. Endrödi. "QCD equation of state at nonzero magnetic fields in the Hadron Resonance Gas model". In: *JHEP* 04 (2013), p. 023. DOI: 10.1007/JHEP04(2013)023. arXiv: 1301.1307 [hep-ph].

[180] Dyana C. Duarte, Ricardo L. S. Farias, and Rudnei O. Ramos. “Regularization issues for a cold and dense quark matter model in $\beta-$equilibrium”. In: *Phys. Rev. D* 99.1 (2019), p. 016005. DOI: 10.1103/PhysRevD.99.016005. arXiv: 1811.10598 [hep-ph].

[181] Veljko Dmitrasinovic. “U-A(1) breaking and scalar mesons in the Nambu-Jona-Lasinio model”. In: *Phys. Rev. C* 53 (1996), pp. 1383–1396. DOI: 10.1103/PhysRevC.53.1383.

[182] Jorn K. Boomsma and Daniel Boer. “The High temperature CP-restoring phase transition at theta = pi”. In: *Phys. Rev. D* 80 (2009), p. 034019. DOI: 10.1103/PhysRevD.80.034019. arXiv: 0905.4660 [hep-ph].

[183] Daniel Boer and Jorn K. Boomsma. “Spontaneous CP-violation in the strong interaction at theta = pi”. In: *Phys. Rev. D* 78 (2008), p. 054027. DOI: 10.1103/PhysRevD.78.054027. arXiv: 0806.1669 [hep-ph].

[184] R. L. S. Farias et al. “Thermo-magnetic effects in quark matter: Nambu–Jona-Lasinio model constrained by lattice QCD”. In: *Eur. Phys. J. A* 53.5 (2017), p. 101. DOI: 10.1140/epja/i2017-12320-8. arXiv: 1603.03847 [hep-ph].

[185] Ulrich Heinz and Raimond Snellings. “Collective flow and viscosity in relativistic heavy-ion collisions”. In: *Ann. Rev. Nucl. Part. Sci.* 63 (2013), pp. 123–151. DOI: 10.1146/annurev-nucl-102212-170540. arXiv: 1301.2826 [nucl-th].

[186] Paul Romatschke and Ulrike Romatschke. “Viscosity Information from Relativistic Nuclear Collisions: How Perfect is the Fluid Observed at RHIC?” In: *Phys. Rev. Lett.* 99 (2007), p. 172301. DOI: 10.1103/PhysRevLett.99.172301.

[187] P. Kovtun, Dan T. Son, and Andrei O. Starinets. “Viscosity in strongly interacting quantum field theories from black hole physics”. In: *Phys. Rev. Lett.* 94 (2005), p. 111601. DOI: 10.1103/PhysRevLett.94.111601.

[188] Antonio Dobado and Juan M. Torres-Rincon. “Bulk viscosity and the phase transition of the linear sigma model”. In: *Phys. Rev. D* 86 (2012), p. 074021. DOI: 10.1103/PhysRevD.86.074021. arXiv: 1206.1261 [hep-ph].

[189] C. Sasaki and K. Redlich. “Bulk viscosity in quasi particle models”. In: *Phys. Rev. C* 79 (2009), p. 055207. DOI: 10.1103/PhysRevC.79.055207. arXiv: 0806.4745 [hep-ph].

[190] Frithjof Karsch, Dmitri Kharzeev, and Kirill Tuchin. “Universal properties of bulk viscosity near the QCD phase transition”. In: *Phys. Lett. B* 663 (2008), pp. 217–221. DOI: 10.1016/j.physletb.2008.01.080. arXiv: 0711.0914 [hep-ph].

[191] Stefano I. Finazzo et al. “Hydrodynamic transport coefficients for the non-conformal quark-gluon plasma from holography”. In: *JHEP* 02 (2015), p. 051. DOI: 10.1007/JHEP02(2015)051. arXiv: 1412.2968 [hep-ph].

[192] Sangyong Jeon and Laurence G. Yaffe. “From quantum field theory to hydrodynamics: Transport coefficients and effective kinetic theory”. In: *Phys. Rev. D* 53 (1996), pp. 5799–5809. DOI: 10.1103/PhysRevD.53.5799. arXiv: hep-ph/9512263.

[193] A. Bazavov et al. “Equation of state and QCD transition at finite temperature”. In: *Phys. Rev. D* 80 (2009), p. 014504. DOI: 10.1103/PhysRevD.80.014504. arXiv: 0903.4379 [hep-lat].

[194] Alexei Bazavov and Peter Petreczky. “Taste symmetry and QCD thermodynamics with improved staggered fermions”. In: *PoS* LATTICE2010 (2010). Ed. by Giancarlo Rossi, p. 169. DOI: 10.22323/1.105.0169. arXiv: 1012.1257 [hep-lat].

[195] Piotr Bozek. “Bulk and shear viscosities of matter created in relativistic heavy-ion collisions”. In: *Phys. Rev. C* 81 (2010), p. 034909. DOI: 10.1103/PhysRevC.81.034909. arXiv: 0911.2397 [nucl-th].

[196] Jean-Bernard Rose et al. “Extracting the bulk viscosity of the quark–gluon plasma”. In: *Nucl. Phys. A* 931 (2014). Ed. by Peter Braun-Munzinger, Bengt Friman, and Johanna Stachel, pp. 926–930. DOI: 10.1016/j.nuclphysa.2014.09.044. arXiv: 1408.0024 [nucl-th].

[197] Kirill Tuchin. “Photon decay in strong magnetic field in heavy-ion collisions”. In: *Phys. Rev. C* 83 (2011), p. 017901. DOI: 10.1103/PhysRevC.83.017901. arXiv: 1008.1604 [nucl-th].

[198] Kirill Tuchin. “Synchrotron radiation by fast fermions in heavy-ion collisions”. In: *Phys. Rev.* C82 (2010). [Erratum: Phys. Rev.C83,039903(2011)], p. 034904. DOI: 10.1103/PhysRevC.83.039903,10.1103/PhysRevC.82.034904. arXiv: 1006.3051 [nucl-th].

[199] Gabriele Inghirami et al. “Numerical magneto-hydrodynamics for relativistic nuclear collisions”. In: *Eur. Phys. J. C* 76.12 (2016), p. 659. DOI: 10.1140/epjc/s10052-016-4516-8. arXiv: 1609.03042 [hep-ph].

[200] Arpan Das et al. “Effects of magnetic field on plasma evolution in relativistic heavy-ion collisions”. In: *Phys. Rev. C* 96.3 (2017), p. 034902. DOI: 10.1103/PhysRevC.96.034902. arXiv: 1703.08162 [hep-ph].

[201] Moritz Greif, Carsten Greiner, and Gabriel S. Denicol. “Electric conductivity of a hot hadron gas from a kinetic approach”. In: *Phys. Rev. D* 93.9 (2016). [Erratum: Phys.Rev.D 96, 059902 (2017)], p. 096012. DOI: 10.1103/PhysRevD.93.096012. arXiv: 1602.05085 [nucl-th].

[202] Moritz Greif et al. “Electric conductivity of the quark-gluon plasma investigated using a perturbative QCD based parton cascade”. In: *Phys. Rev. D* 90.9 (2014), p. 094014. DOI: 10.1103/PhysRevD.90.094014. arXiv: 1408.7049 [nucl-th].

[203] Armando Puglisi, Salvatore Plumari, and Vincenzo Greco. “Shear viscosity $\eta$ to electric conductivity $\sigma_{el}$ ratio for the quark–gluon plasma”. In: *Phys. Lett.* B751 (2015), pp. 326–330. DOI: 10.1016/j.physletb.2015.10.070. arXiv: 1407.2559 [hep-ph].

[204] A. Puglisi, S. Plumari, and V. Greco. “Electric Conductivity from the solution of the Relativistic Boltzmann Equation”. In: *Phys. Rev. D* 90 (2014), p. 114009. DOI: 10.1103/PhysRevD.90.114009. arXiv: 1408.7043 [hep-ph].

[205] W. Cassing et al. “Electrical Conductivity of Hot QCD Matter”. In: *Phys. Rev. Lett.* 110.18 (2013), p. 182301. DOI: 10.1103/PhysRevLett.110.182301. arXiv: 1302.0906 [hep-ph].

[206] T. Steinert and W. Cassing. “Electric and magnetic response of hot QCD matter”. In: *Phys. Rev. C* 89.3 (2014), p. 035203. DOI: 10.1103/PhysRevC.89.035203. arXiv: 1312.3189 [hep-ph].

[207] Gert Aarts et al. “Electrical conductivity and charge diffusion in thermal QCD from the lattice”. In: *JHEP* 02 (2015), p. 186. DOI: 10.1007/JHEP02(2015)186. arXiv: 1412.6411 [hep-lat].

[208] Gert Aarts et al. “Spectral functions at small energies and the electrical conductivity in hot, quenched lattice QCD”. In: *Phys. Rev. Lett.* 99 (2007), p. 022002. DOI: 10.1103/PhysRevLett.99.022002. arXiv: hep-lat/0703008.

[209] Alessandro Amato et al. “Electrical conductivity of the quark-gluon plasma across the deconfinement transition”. In: *Phys. Rev. Lett.* 111.17 (2013), p. 172001. DOI: 10.1103/PhysRevLett.111.172001. arXiv: 1307.6763 [hep-lat].

[210] Sourendu Gupta. “The Electrical conductivity and soft photon emissivity of the QCD plasma”. In: *Phys. Lett. B* 597 (2004), pp. 57–62. DOI: 10.1016/j.physletb.2004.05.079. arXiv: hep-lat/0301006.

[211] H.-T. Ding et al. “Thermal dilepton rate and electrical conductivity: An analysis of vector current correlation functions in quenched lattice QCD”. In: *Phys. Rev. D* 83 (2011), p. 034504. DOI: 10.1103/PhysRevD.83.034504. arXiv: 1012.4963 [hep-lat].

[212] Olaf Kaczmarek and Marcel Müller. “Temperature dependence of electrical conductivity and dilepton rates from hot quenched lattice QCD”. In: *PoS* LATTICE2013 (2014), p. 175. DOI: 10.22323/1.187.0175. arXiv: 1312.5609 [hep-lat].

[213] Si-xue Qin. “A divergence-free method to extract observables from correlation functions”. In: *Phys. Lett. B* 742 (2015), pp. 358–362. DOI: 10.1016/j.physletb.2015.02.009. arXiv: 1307.4587 [nucl-th].

[214] D. Fernandez-Fraile and A. Gomez Nicola. “The Electrical conductivity of a pion gas”. In: *Phys. Rev. D* 73 (2006), p. 045025. DOI: 10.1103/PhysRevD.73.045025. arXiv: hep-ph/0512283.

[215] Hui Li, Xin-li Sheng, and Qun Wang. “Electromagnetic fields with electric and chiral magnetic conductivities in heavy ion collisions”. In: *Phys. Rev. C* 94.4 (2016), p. 044903. DOI: 10.1103/PhysRevC.94.044903. arXiv: 1602.02223 [nucl-th].

[216] Gabriele Inghirami et al. “Magnetic fields in heavy ion collisions: flow and charge transport”. In: *Eur. Phys. J. C* 80.3 (2020), p. 293. DOI: 10.1140/epjc/s10052-020-7847-4. arXiv: 1908.07605 [hep-ph].

[217] G. Inghirami et al. “Magneto-hydrodynamic simulations of Heavy Ion Collisions with ECHO-QGP”. In: *J. Phys. Conf. Ser.* 1024.1 (2018). Ed. by Marco Destefanis et al., p. 012043. DOI: 10.1088/1742-6596/1024/1/012043.

[218] M. Shokri and N. Sadooghi. “Novel self-similar rotating solutions of nonideal transverse magnetohydrodynamics”. In: *Phys. Rev. D* 96.11 (2017), p. 116008. DOI: 10.1103/PhysRevD.96.116008. arXiv: 1705.00536 [nucl-th].

[219] M. Shokri and N. Sadooghi. “Evolution of magnetic fields from the 3 + 1 dimensional self-similar and Gubser flows in ideal relativistic magnetohydrodynamics”. In: *JHEP* 11 (2018), p. 181. DOI: 10.1007/JHEP11(2018)181. arXiv: 1807.09487 [nucl-th].

[220] S.M.A. Tabatabaee and N. Sadooghi. “Wigner function formalism and the evolution of thermodynamic quantities in an expanding magnetized plasma”. In: *Phys. Rev. D* 101.7 (2020), p. 076022. DOI: 10.1103/PhysRevD.101.076022. arXiv: 2003.01686 [hep-ph].

[221] Dmitri E. Kharzeev et al. “‘Strongly interacting matter in magnetic fields’: an overview”. In: vol. 871. 2013, pp. 1–11. DOI: 10.1007/978-3-642-37305-3_1. arXiv: 1211.6245 [hep-ph].

[222] Moritz Greif et al. “Diffusion of conserved charges in relativistic heavy ion collisions”. In: *Phys. Rev. Lett.* 120.24 (2018), p. 242301. DOI: 10.1103/PhysRevLett.120.242301. arXiv: 1711.08680 [hep-ph].

[223] Madappa Prakash et al. “Nonequilibrium properties of hadronic mixtures”. In: *Phys. Rept.* 227 (1993), pp. 321–366. DOI: 10.1016/0370-1573(93)90092-R.

[224] Anton Wiranata and Madappa Prakash. “Shear Viscosities from the Chapman-Enskog and the Relaxation Time Approaches”. In: *Phys. Rev. C* 85 (2012), p. 054908. DOI: 10.1103/PhysRevC.85.054908. arXiv: 1203.0281 [nucl-th].

[225] P. Chakraborty and J.I. Kapusta. “Quasi-Particle Theory of Shear and Bulk Viscosities of Hadronic Matter”. In: *Phys. Rev. C* 83 (2011), p. 014906. DOI: 10.1103/PhysRevC.83.014906. arXiv: 1006.0257 [nucl-th].

[226] A.S. Khvorostukhin, V.D. Toneev, and D.N. Voskresensky. “Viscosity Coefficients for Hadron and Quark-Gluon Phases”. In: *Nucl. Phys. A* 845 (2010), pp. 106–146. DOI: 10.1016/j.nuclphysa.2010.05.058. arXiv: 1003.3531 [nucl-th].

[227] S. Plumari et al. “Shear Viscosity of a strongly interacting system: Green-Kubo vs. Chapman-Enskog and Relaxation Time Approximation”. In: *Phys. Rev. C* 86 (2012), p. 054902. DOI: 10.1103/PhysRevC.86.054902. arXiv: 1208.0481 [nucl-th].

[228] M.I. Gorenstein, M. Hauer, and O.N. Moroz. “Viscosity in the excluded volume hadron gas model”. In: (Aug. 2007), pp. 214–220. DOI: 10.1103/PhysRevC.77.024911. arXiv: 0708.0137 [nucl-th].

[229] Jacquelyn Noronha-Hostler, Jorge Noronha, and Carsten Greiner. “Hadron Mass Spectrum and the Shear Viscosity to Entropy Density Ratio of Hot Hadronic Matter”. In: *Phys. Rev. C* 86 (2012), p. 024913. DOI: 10.1103/PhysRevC.86.024913. arXiv: 1206.5138 [nucl-th].

[230] S.K. Tiwari, P.K. Srivastava, and C.P. Singh. “Description of Hot and Dense Hadron Gas Properties in a New Excluded-Volume model”. In: *Phys. Rev. C* 85 (2012), p. 014908. DOI: 10.1103/PhysRevC.85.014908. arXiv: 1111.2406 [hep-ph].

[231] Sabyasachi Ghosh et al. “Shear viscosity due to Landau damping from the quark-pion interaction”. In: *Phys. Rev. C* 88.6 (2013), p. 068201. DOI: 10.1103/PhysRevC.88.068201. arXiv: 1311.4070 [nucl-th].

[232] Robert Lang, Norbert Kaiser, and Wolfram Weise. “Shear viscosities from Kubo formalism in a large-$N_c$ Nambu-Jona-Lasinio model”. In: *Eur. Phys. J. A* 51.10 (2015), p. 127. DOI: 10.1140/epja/i2015-15127-7. arXiv: 1506.02459 [hep-ph].

[233] Sabyasachi Ghosh, Gastão Krein, and Sourav Sarkar. “Shear viscosity of a pion gas resulting from $\rho\pi\pi$ and $\sigma\pi\pi$ interactions”. In: *Phys. Rev. C* 89.4 (2014), p. 045201. DOI: 10.1103/PhysRevC.89.045201. arXiv: 1401.5392 [nucl-th].

[234] A. Wiranata et al. “Shear viscosity of a multi-component hadronic system”. In: *J. Phys. Conf. Ser.* 509 (2014), p. 012049. DOI: 10.1088/1742-6596/509/1/012049.

[235] Anton Wiranata, Madappa Prakash, and Purnendu Chakraborty. “Comparison of Viscosities from the Chapman-Enskog and Relaxation Time Methods”. In: *Central Eur. J. Phys.* 10 (2012), pp. 1349–1351. DOI: 10.2478/s11534-012-0082-3. arXiv: 1201.3104 [nucl-th].

[236] Jacquelyn Noronha-Hostler, Jorge Noronha, and Carsten Greiner. “Transport Coefficients of Hadronic Matter near T(c)”. In: *Phys. Rev. Lett.* 103 (2009), p. 172302. DOI: 10.1103/PhysRevLett.103.172302. arXiv: 0811.1571 [nucl-th].

[237] Guru Prakash Kadam and Hiranmaya Mishra. “Bulk and shear viscosities of hot and dense hadron gas”. In: *Nucl. Phys. A* 934 (2014), pp. 133–147. DOI: 10.1016/j.nuclphysa.2014.12.004. arXiv: 1408.6329 [hep-ph].

[238] Guru Kadam. “Transport properties of hadronic matter in magnetic field”. In: *Mod. Phys. Lett. A* 30.10 (2015), p. 1550031. DOI: 10.1142/S0217732315500315. arXiv: 1412.5303 [hep-ph].

[239] Sabyasachi Ghosh. “A real-time thermal field theoretical analysis of Kubo-type shear viscosity: Numerical understanding with simple examples”. In: *Int. J. Mod. Phys. A* 29 (2014), p. 1450054. DOI: 10.1142/S0217751X14500547. arXiv: 1404.4788 [nucl-th].

[240] J. B. Rose et al. “Shear viscosity of a hadron gas and influence of resonance lifetimes on relaxation time”. In: *Phys. Rev. C* 97.5 (2018), p. 055204. DOI: 10.1103/PhysRevC.97.055204. arXiv: 1709.03826 [nucl-th].

[241] C. Wesp et al. “Calculation of shear viscosity using Green-Kubo relations within a parton cascade”. In: *Phys. Rev. C* 84 (2011), p. 054911. DOI: 10.1103/PhysRevC.84.054911. arXiv: 1106.4306 [hep-ph].

[242] G.S. Denicol et al. “Solving the heat-flow problem with transient relativistic fluid dynamics”. In: *Phys. Rev. D* 89.7 (2014), p. 074005. DOI: 10.1103/PhysRevD.89.074005. arXiv: 1207.6811 [nucl-th].

[243] Joseph I. Kapusta and Juan M. Torres-Rincon. “Thermal Conductivity and Chiral Critical Point in Heavy Ion Collisions”. In: *Phys. Rev. C* 86 (2012), p. 054911. DOI: 10.1103/PhysRevC.86.054911. arXiv: 1209.0675 [nucl-th].

[244] A. Peshier, Burkhard Kampfer, and G. Soff. “From QCD lattice calculations to the equation of state of quark matter”. In: *Phys. Rev. D* 66 (2002), p. 094003. DOI: 10.1103/PhysRevD.66.094003. arXiv: hep-ph/0206229.

[245] P. K. Srivastava, S. K. Tiwari, and C. P. Singh. “QCD Critical Point in a Quasiparticle Model”. In: *Phys. Rev. D* 82 (2010), p. 014023. DOI: 10.1103/PhysRevD.82.014023. arXiv: 1002.4780 [hep-ph].

[246] Vishnu M. Bannur. “Quasi-particle model for QGP with nonzero densities”. In: *JHEP* 09 (2007), p. 046. DOI: 10.1088/1126-6708/2007/09/046. arXiv: hep-ph/0604158.

[247] A.S. Khvorostukhin, V.D. Toneev, and D.N. Voskresensky. “Remarks concerning bulk viscosity of hadron matter in relaxation time ansatz”. In: *Nucl. Phys. A* 915 (2013), pp. 158–169. DOI: 10.1016/j.nuclphysa.2013.07.008.

[248] P. Zhuang et al. “Transport properties of a quark plasma and critical scattering at the chiral phase transition”. In: *Phys. Rev. D* 51 (1995), pp. 3728–3738. DOI: 10.1103/PhysRevD.51.3728.

[249] S. Gavin. “TRANSPORT COEFFICIENTS IN ULTRARELATIVISTIC HEAVY ION COLLISIONS”. In: *Nucl. Phys. A* 435 (1985), pp. 826–843. DOI: 10.1016/0375-9474(85)90190-3.

[250] Guru Prakash Kadam, Hiranmaya Mishra, and Lata Thakur. “Electrical and thermal conductivities of hot and dense hadronic matter”. In: *Phys. Rev.* D98.11 (2018), p. 114001. DOI: 10.1103/PhysRevD.98.114001. arXiv: 1712.03805 [hep-ph].

[251] Li-Yan Zhou et al. “Bipolar Thermoelectrical Transport of SnSe Nanoplate in Low Temperature”. In: *Chinese Physics Letters* 37 (2020), p. 017301. DOI: 10.1088/0256-307x/37/1/017301.

[252] Lata Thakur et al. “Shear viscosity $\eta$ to electrical conductivity $\sigma_{el}$ ratio for an anisotropic QGP”. In: *Phys. Rev. D* 95.9 (2017), p. 096009. DOI: 10.1103/PhysRevD.95.096009. arXiv: 1703.03142 [hep-ph].

[253] Vishnu M. Bannur. “Self-consistent quasiparticle model for quark-gluon plasma”. In: *Phys. Rev. C* 75 (2007), p. 044905. DOI: 10.1103/PhysRevC.75.044905. arXiv: hep-ph/0609188.

[254] L. L. Zhu and C. B. Yang. “A self-consistent thermodynamical quasiparticle description of QGP”. In: *Nucl. Phys. A* 831 (2009), pp. 49–58. DOI: 10.1016/j.nuclphysa.2009.09.001.

[255] Mark I. Gorenstein and Shin-Nan Yang. “Gluon plasma with a medium dependent dispersion relation”. In: *Phys. Rev. D* 52 (1995), pp. 5206–5212. DOI: 10.1103/PhysRevD.52.5206.

[256] A. Hosoya and K. Kajantie. “Transport Coefficients of QCD Matter”. In: *Nucl. Phys. B* 250 (1985), pp. 666–688. DOI: 10.1016/0550-3213(85)90499-7.

[257] H. Berrehrah et al. “Collisional processes of on-shell and off-shell heavy quarks in vacuum and in the Quark-Gluon-Plasma”. In: *Phys. Rev. C* 89.5 (2014), p. 054901. DOI: 10.1103/PhysRevC.89.054901. arXiv: 1308.5148 [hep-ph].

[258] Arpan Das, Hiranmaya Mishra, and Ranjita K. Mohapatra. “Electrical conductivity and Hall conductivity of a hot and dense quark gluon plasma in a magnetic field: A quasiparticle approach”. In: *Phys. Rev. D* 101.3 (2020), p. 034027. DOI: 10.1103/PhysRevD.101.034027. arXiv: 1907.05298 [hep-ph].

[259] P. Rehberg, S. P. Klevansky, and J. Hufner. “Elastic scattering and transport coefficients for a quark plasma in SU-f(3) at finite temperatures”. In: *Nucl. Phys. A* 608 (1996), pp. 356–388. DOI: 10.1016/0375-9474(96)00247-3. arXiv: hep-ph/9607263.

[260] Bastian B. Brandt et al. “Charge transport and vector meson dissociation across the thermal phase transition in lattice QCD with two light quark flavors”. In: *Phys. Rev. D* 93.5 (2016), p. 054510. DOI: 10.1103/PhysRevD.93.054510. arXiv: 1512.07249 [hep-lat].

[261] Gert Aarts and Aleksandr Nikolaev. “Electrical conductivity of the quark-gluon plasma: perspective from lattice QCD”. In: *Eur. Phys. J. A* 57.4 (2021), p. 118. DOI: 10.1140/epja/s10050-021-00436-5. arXiv: 2008.12326 [hep-lat].

[262] Sukanya Mitra and Vinod Chandra. "Transport coefficients of a hot QCD medium and their relative significance in heavy-ion collisions". In: *Phys. Rev. D* 96.9 (2017), p. 094003. DOI: 10.1103/PhysRevD.96.094003. arXiv: 1702.05728 [nucl-th].

[263] Xu-Guang Huang et al. "Anisotropic hydrodynamics, bulk viscosities, and $r$-modes of strange quark stars with strong magnetic fields". In: *Phys. Rev. D* 81 (4 2010), p. 045015.

[264] Shuai Y.F. Liu and Yi Yin. "Baryonic spin Hall effect in heavy ion collisions". In: (June 2020). arXiv: 2006.12421 [nucl-th].

[265] Kostas. D. Kokkotas and Johannes Ruoff. "Radial oscillations of relativistic stars". In: *Astron. Astrophys.* 366 (2001), p. 565. DOI: 10.1051/0004-6361:20000216. arXiv: gr-qc/0011093.

[266] P. Haensel, A. Y. Potekhin, and D. G. Yakovlev. *Neutron stars 1: Equation of state and structure*. Vol. 326. New York, USA: Springer, 2007. DOI: 10.1007/978-0-387-47301-7.

[267] R. C. Baral et al. "Radial oscillation of compact stars in the presence of magnetic field". In: *Int. J. Mod. Phys. E* 25.06 (2016), p. 1650037. DOI: 10.1142/S0218301316500373.

[268] Vinh Tran et al. "g-mode Oscillations in Neutron Stars with Hyperons". In: (Dec. 2022). arXiv: 2212.09875 [nucl-th].

[269] G. Miniutti et al. "Non-radial oscillation modes as a probe of density discontinuities in neutron stars". In: *Mon. Not. Roy. Astron. Soc.* 338 (2003), p. 389. DOI: 10.1046/j.1365-8711.2003.06057.x. arXiv: astro-ph/0206142.

[270] Luciano Rezzolla et al., eds. *The Physics and Astrophysics of Neutron Stars*. Vol. 457. Springer, 2018. DOI: 10.1007/978-3-319-97616-7.

[271] P. Haensel, A. Y. Potekhin, and D. G. Yakovlev. *Neutron stars 1: Equation of state and structure*. Vol. 326. New York, USA: Springer, 2007. DOI: 10.1007/978-0-387-47301-7.

[272] James M. Lattimer. "The nuclear equation of state and neutron star masses". In: *Ann. Rev. Nucl. Part. Sci.* 62 (2012), pp. 485–515. DOI: 10.1146/annurev-nucl-102711-095018. arXiv: 1305.3510 [nucl-th].

[273] James M. Lattimer and Madappa Prakash. "The Equation of State of Hot, Dense Matter and Neutron Stars". In: *Phys. Rept.* 621 (2016), pp. 127–164. DOI: 10.1016/j.physrep.2015.12.005. arXiv: 1512.07820 [astro-ph.SR].

[274] M. Oertel et al. "Equations of state for supernovae and compact stars". In: *Rev. Mod. Phys.* 89.1 (2017), p. 015007. DOI: 10.1103/RevModPhys.89.015007. arXiv: 1610.03361 [astro-ph.HE].

[275] Gordon Baym et al. "From hadrons to quarks in neutron stars: a review". In: *Rept. Prog. Phys.* 81.5 (2018), p. 056902. DOI: 10.1088/1361-6633/aaae14. arXiv: 1707.04966 [astro-ph.HE].

[276] Prashanth Jaikumar et al. "$g$-mode oscillations in hybrid stars: A tale of two sounds". In: *Phys. Rev. D* 103.12 (2021), p. 123009. DOI: 10.1103/PhysRevD.103.123009. arXiv: 2101.06349 [nucl-th].

[277] Kip S. Thorne and Alfonso Campolattaro. "Non-Radial Pulsation of General-Relativistic Stellar Models. I. Analytic Analysis for L >= 2". In: *ApJ* 149 (Sept. 1967), p. 591. DOI: 10.1086/149288.

[278] Steven L. Detweiler and L. Lindblom. "On the nonradial pulsations of general relativistic stellar models". In: *Astrophys. J.* 292 (1985), pp. 12–15. DOI: 10.1086/163127.

[279] Kostas D. Kokkotas and Bernd G. Schmidt. "Quasinormal modes of stars and black holes". In: *Living Rev. Rel.* 2 (1999), p. 2. DOI: 10.12942/lrr-1999-2. arXiv: gr-qc/9909058.

[280] P. N. McDermott, H. M. van Horn, and J. F. Scholl. "Nonradial g-mode oscillations of warm neutron stars". In: *ApJ* 268 (May 1983), pp. 837–848. DOI: 10.1086/161006.

[281] Andreas Reisenegger and Peter Goldreich. "Excitation of Neutron Star Normal Modes during Binary Inspiral". In: *ApJ* 426 (May 1994), p. 688. DOI: 10.1086/174105.

[282] Umin Lee and Tod E. Strohmayer. "Nonradial oscillations of rotating neutron stars: The Effects of the Coriolis force". In: (Feb. 1996).

[283] Reinhard Prix and Michel L. E. Rieutord. "Adiabatic oscillations of non-rotating superfluid neutron stars". In: *Astron. Astrophys.* 393 (2002), pp. 949–964. DOI: 10.1051/0004-6361:20021049. arXiv: astro-ph/0204520.

[284] N. Andersson and G. L. Comer. "On the dynamics of superfluid neutron star cores". In: *Mon. Not. Roy. Astron. Soc.* 328 (2001), p. 1129. DOI: 10.1046/j.1365-8711.2001.04923.x. arXiv: astro-ph/0101193.

[285] Mikhail E. Gusakov and Elena M. Kantor. "Thermal $g$-modes and unexpected convection in superfluid neutron stars". In: *Phys. Rev. D* 88.10 (2013), p. 101302. DOI: 10.1103/PhysRevD.88.101302.

[286] L. Gualtieri et al. "Quasinormal modes of superfluid neutron stars". In: *Phys. Rev. D* 90.2 (2014), p. 024010. DOI: 10.1103/PhysRevD.90.024010. arXiv: 1404.7512 [gr-qc].

[287] E. M. Kantor and M. E. Gusakov. "Composition temperature-dependent g-modes in superfluid neutron stars". In: *Mon. Not. Roy. Astron. Soc.* 442 (2014), p. 90. DOI: 10.1093/mnrasl/slu061. arXiv: 1404.6768 [astro-ph.SR].

[288] A. Passamonti, N. Andersson, and W. C. G. Ho. "Buoyancy and g-modes in young superfluid neutron stars". In: *Mon. Not. Roy. Astron. Soc.* 455.2 (2016), pp. 1489–1511. DOI: 10.1093/mnras/stv2149. arXiv: 1504.07470 [astro-ph.SR].

[289] Hang Yu and Nevin N. Weinberg. "Dynamical tides in coalescing superfluid neutron star binaries with hyperon cores and their detectability with third generation gravitational-wave detectors". In: *Mon. Not. Roy. Astron. Soc.* 470.1 (2017), pp. 350–360. DOI: 10.1093/mnras/stx1188. arXiv: 1705.04700 [astro-ph.HE].

[290] P. B. Rau and I. Wasserman. "Compressional modes in two-superfluid neutron stars with leptonic buoyancy". In: *Mon. Not. Roy. Astron. Soc.* 481.4 (2018), pp. 4427–4444. DOI: 10.1093/mnras/sty2458. arXiv: 1802.08741 [astro-ph.HE].

[291] Norman K. Glendenning. "First-order phase transitions with more than one conserved charge: Consequences for neutron stars". In: *Phys. Rev. D* 46.4 (Aug. 1992), pp. 1274–1287. DOI: 10.1103/PhysRevD.46.1274.

[292] Mark G. Alford et al. "The Minimal CFL nuclear interface". In: *Phys. Rev. D* 64 (2001), p. 074017. DOI: 10.1103/PhysRevD.64.074017. arXiv: hep-ph/0105009.

[293] D. N. Voskresensky, M. Yasuhira, and T. Tatsumi. "Charge screening at first order phase transitions and hadron quark mixed phase". In: *Nucl. Phys. A* 723 (2003), pp. 291–339. DOI: 10.1016/S0375-9474(03)01313-7. arXiv: nucl-th/0208067.

[294] Leticia F. Palhares and Eduardo S. Fraga. "Droplets in the cold and dense linear sigma model with quarks". In: *Phys. Rev. D* 82 (2010), p. 125018. DOI: 10.1103/PhysRevD.82.125018. arXiv: 1006.2357 [hep-ph].

[295] Marcus B. Pinto, Volker Koch, and Jorgen Randrup. "The Surface Tension of Quark Matter in a Geometrical Approach". In: *Phys. Rev. C* 86 (2012), p. 025203. DOI: 10.1103/PhysRevC.86.025203. arXiv: 1207.5186 [hep-ph].

[296] Bruno W. Mintz et al. "Phase diagram and surface tension in the three-flavor Polyakov-quark-meson model". In: *Phys. Rev. D* 87.3 (2013), p. 036004. DOI: 10.1103/PhysRevD.87.036004. arXiv: 1212.1184 [hep-ph].

[297] G. Lugones, A. G. Grunfeld, and M. Al Ajmi. "Surface tension and curvature energy of quark matter in the Nambu-Jona-Lasinio model". In: *Phys. Rev. C* 88.4, 045803 (Oct. 2013), p. 045803. DOI: 10.1103/PhysRevC.88.045803. arXiv: 1308.1452 [hep-ph].

[298] N. Yasutake et al. "Finite-size effects at the hadron-quark transition and heavy hybrid stars". In: *Phys. Rev. C* 89 (2014), p. 065803. DOI: 10.1103/PhysRevC.89.065803. arXiv: 1403.7492 [astro-ph.HE].

[299] D. N. Voskresensky, M. Yasuhira, and T. Tatsumi. "Charge screening at first order phase transitions". In: *Phys. Lett. B* 541 (2002), pp. 93–100. DOI: 10.1016/S0370-2693(02)02186-X. arXiv: nucl-th/0109009.

[300] Toshiki Maruyama et al. "Hadron-quark mixed phase in hyperon stars". In: *Phys. Rev. D* 76 (2007), p. 123015. DOI: 10.1103/PhysRevD.76.123015. arXiv: 0708.3277 [nucl-th].

[301] J. D. Walecka. "A Theory of highly condensed matter". In: *Annals Phys.* 83 (1974), pp. 491–529. DOI: 10.1016/0003-4916(74)90208-5.

[302] J. Boguta and A. R. Bodmer. "Relativistic Calculation of Nuclear Matter and the Nuclear Surface". In: *Nucl. Phys.* A292 (1977), pp. 413–428. DOI: 10.1016/0375-9474(77)90626-1.

[303] J. Boguta and Horst Stoecker. "Systematics of Nuclear Matter Properties in a Nonlinear Relativistic Field Theory". In: *Phys. Lett.* 120B (1983), pp. 289–293. DOI: 10.1016/0370-2693(83)90446-X.

[304] Amruta Mishra, P. K. Panda, and W. Greiner. "Vacuum polarization effects in hyperon rich dense matter: A Nonperturbative treatment". In: *J. Phys. G* 28 (2002), pp. 67–83. DOI: 10.1088/0954-3899/28/1/305. arXiv: nucl-th/0101006.

[305] Laura Tolos, Mario Centelles, and Angels Ramos. "The Equation of State for the Nucleonic and Hyperonic Core of Neutron Stars". In: *Publications of the Astronomical Society of Australia* 34 (2017), e065. DOI: 10.1017/pasa.2017.60.

[306] Laura Tolos, Mario Centelles, and Angels Ramos. "EQUATION OF STATE FOR NUCLEONIC AND HYPERONIC NEUTRON STARS WITH MASS AND RADIUS CONSTRAINTS". In: *The Astrophysical Journal* 834.1 (2016), p. 3. DOI: 10.3847/1538-4357/834/1/3. URL: https://doi.org/10.3847/1538-4357/834/1/3.

[307] Tuhin Malik and Constança Providência. "Bayesian inference of signatures of hyperons inside neutron stars". In: *Phys. Rev. D* 106.6 (2022), p. 063024. DOI: 10.1103/PhysRevD.106.063024. arXiv: 2205.15843 [nucl-th].

[308] Tuhin Malik et al. "Relativistic Description of Dense Matter Equation of State and Compatibility with Neutron Star Observables: A Bayesian Approach". In: *Astrophys. J.* 930.1 (2022), p. 17. DOI: 10.3847/1538-4357/ac5d3c. arXiv: 2201.12552 [nucl-th].

[309] S. Typel and H. H. Wolter. "Relativistic mean field calculations with density dependent meson nucleon coupling". In: *Nucl. Phys. A* 656 (1999), pp. 331–364. DOI: 10.1016/S0375-9474(99)00310-3.

[310] O Benhar and A Cipollone. "Implementation of the Nambu Jona-Lasinio model in hybrid stars". In: *Astronomy & Astrophysics* 525 (2011), p. L1.

[311] Klaus Schertler, Stefan Leupold, and Jurgen Schaffner-Bielich. "Neutron stars and quark phases in the NJL model". In: *Phys. Rev. C* 60 (1999), p. 025801. DOI: 10.1103/PhysRevC.60.025801. arXiv: astro-ph/9901152.

[312] I. N. Mishustin et al. "Catastrophic rearrangement of a compact star due to the quark core formation". In: *Phys. Lett. B* 552 (2003), pp. 1–8. DOI: 10.1016/S0370-2693(02)03108-8. arXiv: hep-ph/0210422.

[313] Pablo Gregorian. "Nonradial neutron star oscillations". In: *A Master Thesis* (Nov. 2014), Universiteit Utrecht, Institute for theoretical physics. URL: https://dspace.library.uu.nl/bitstream/handle/1874/306758/Master%20Thesis%20Theoretical%20Physics%2C%20Pablo%20Gregorian.pdf?sequence=2.

[314] M. Albright and J. I. Kapusta. “Quasiparticle Theory of Transport Coefficients for Hadronic Matter at Finite Temperature and Baryon Density”. In: *Phys. Rev. C* 93.1 (2016), p. 014903. DOI: 10.1103/PhysRevC.93.014903. arXiv: 1508.02696 [nucl-th].

[315] Hajime Sotani, Kazuhiro Tominaga, and Kei-ichi Maeda. “Density discontinuity of a neutron star and gravitational waves”. In: *Phys. Rev. D* 65 (2002), p. 024010. DOI: 10.1103/PhysRevD.65.024010. arXiv: gr-qc/0108060.

[316] Larry McLerran and Sanjay Reddy. “Quarkyonic Matter and Neutron Stars”. In: *Phys. Rev. Lett.* 122.12 (2019), p. 122701. DOI: 10.1103/PhysRevLett.122.122701. arXiv: 1811.12503 [nucl-th].

[317] Robert D. Pisarski. “Remarks on nuclear matter: How an $\omega_0$ condensate can spike the speed of sound, and a model of $Z(3)$ baryons”. In: *Phys. Rev. D* 103.7 (2021), p. L071504. DOI: 10.1103/PhysRevD.103.L071504. arXiv: 2101.05813 [nucl-th].

[318] M. C. Miller et al. “PSR J0030+0451 Mass and Radius from *NICER* Data and Implications for the Properties of Neutron Star Matter”. In: *Astrophys. J. Lett.* 887.1 (2019), p. L24. DOI: 10.3847/2041-8213/ab50c5. arXiv: 1912.05705 [astro-ph.HE].

[319] N. K. Patra et al. “An Equation of State for Magnetized Neutron Star Matter and Tidal Deformation in Neutron Star Mergers”. In: *Astrophys. J.* 900.1 (2020), p. 49. DOI: 10.3847/1538-4357/aba8fc.

[320] G. Miniutti et al. “Non-radial oscillation modes as a probe of density discontinuities in neutron stars”. In: *MNRAS* 338.2 (Jan. 2003), pp. 389–400. DOI: 10.1046/j.1365-8711.2003.06057.x. arXiv: astro-ph/0206142 [astro-ph].

[321] C. J. Krüger, W. C. G. Ho, and N. Andersson. “Seismology of adolescent neutron stars: Accounting for thermal effects and crust elasticity”. In: *Phys. Rev. D* 92 (6 2015), p. 063009. DOI: 10.1103/PhysRevD.92.063009. URL: https://link.aps.org/doi/10.1103/PhysRevD.92.063009.

[322] S. Y. Lau, P. T. Leung, and L. M. Lin. “Two-layer compact stars with crystalline quark matter: Screening effect on the tidal deformability”. In: *Phys. Rev. D* 99.2 (2019), p. 023018. DOI: 10.1103/PhysRevD.99.023018. arXiv: 1808.08107 [astro-ph.HE].

[323] Debades Bandyopadhyay et al. “Moment of inertia, quadrupole moment, Love number of neutron star and their relations with strange matter equations of state”. In: *Eur. Phys. J. A* 54.2 (2018), p. 26. DOI: 10.1140/epja/i2018-12456-y. arXiv: 1712.01715 [astro-ph.HE].

[324] Sophia Han and Andrew W. Steiner. “Tidal deformability with sharp phase transitions in (binary) neutron stars”. In: *Phys. Rev. D* 99.8 (2019), p. 083014. DOI: 10.1103/PhysRevD.99.083014. arXiv: 1810.10967 [nucl-th].

[325] P. Belli et al. “Experimental searches for rare alpha and beta decays”. In: *Eur. Phys. J. A* 55.8 (2019), p. 140. DOI: 10.1140/epja/i2019-12823-2. arXiv: 1908.11458 [nucl-ex].

[326] P. von Doetinchem et al. “Cosmic-ray antinuclei as messengers of new physics: status and outlook for the new decade”. In: *JCAP* 08 (2020), p. 035. DOI: 10.1088/1475-7516/2020/08/035. arXiv: 2002.04163 [astro-ph.HE].

[327] Gordon Baym, Christopher Pethick, and Peter Sutherland. “The Ground state of matter at high densities: Equation of state and stellar models”. In: *Astrophys. J.* 170 (1971), pp. 299–317. DOI: 10.1086/151216.

[328] J. Carriere, C. J. Horowitz, and J. Piekarewicz. “Low mass neutron stars and the equation of state of dense matter”. In: *Astrophys. J.* 593 (2003), pp. 463–471. DOI: 10.1086/376515. arXiv: nucl-th/0211015.

[329] Tuhin Malik et al. “Relativistic description of dense matter equation of state and compatibility with neutron star observables: a Bayesian approach”. In: (Jan. 2022). arXiv: 2201.12552 [nucl-th].

[330] I. Tews et al. “Neutron matter at next-to-next-to-next-to-leading order in chiral effective field theory”. In: *Phys. Rev. Lett.* 110.3 (2013), p. 032504. DOI: 10.1103/PhysRevLett.110.032504. arXiv: 1206.0025 [nucl-th].

[331] K. Hebeler et al. “Equation of state and neutron star properties constrained by nuclear physics and observation”. In: *Astrophys. J.* 773 (2013), p. 11. DOI: 10.1088/0004-637X/773/1/11. arXiv: 1303.4662 [astro-ph.SR].

[332] S. Wesolowski et al. “Bayesian parameter estimation for effective field theories”. In: *J. Phys. G* 43.7 (2016), p. 074001. DOI: 10.1088/0954-3899/43/7/074001. arXiv: 1511.03618 [nucl-th].

[333] R. J. Furnstahl et al. “Quantifying truncation errors in effective field theory”. In: *Phys. Rev. C* 92.2 (2015), p. 024005. DOI: 10.1103/PhysRevC.92.024005. arXiv: 1506.01343 [nucl-th].

[334] Gregory Ashton et al. “BILBY: A user-friendly Bayesian inference library for gravitational-wave astronomy”. In: *Astrophys. J. Suppl.* 241.2 (2019), p. 27. DOI: 10.3847/1538-4365/ab06fc. arXiv: 1811.02042 [astro-ph.IM].

[335] Philippe Landry, Reed Essick, and Katerina Chatziioannou. “Nonparametric constraints on neutron star matter with existing and upcoming gravitational wave and pulsar observations”. In: *Phys. Rev. D* 101.12 (2020), p. 123007. DOI: 10.1103/PhysRevD.101.123007. arXiv: 2003.04880 [astro-ph.HE].

[336] Aleksi Kurkela et al. “Constraining neutron star matter with Quantum Chromodynamics”. In: *Astrophys. J.* 789 (2014), p. 127. DOI: 10.1088/0004-637X/789/2/127. arXiv: 1402.6618 [astro-ph.HE].

[337] Aleksi Kurkela, Paul Romatschke, and Aleksi Vuorinen. “Cold Quark Matter”. In: *Phys. Rev. D* 81 (2010), p. 105021. DOI: 10.1103/PhysRevD.81.105021. arXiv: 0912.1856 [hep-ph].

[338] Eduardo S. Fraga, Aleksi Kurkela, and Aleksi Vuorinen. “Interacting quark matter equation of state for compact stars”. In: *Astrophys. J. Lett.* 781.2 (2014), p. L25. DOI: 10.1088/2041-8205/781/2/L25. arXiv: 1311.5154 [nucl-th].

[339] Aleš Florian. “An efficient sampling scheme: Updated Latin Hypercube Sampling”. In: *Probabilistic Engineering Mechanics* 7.2 (1992), pp. 123–130. ISSN: 0266-8920. DOI: https://doi.org/10.1016/0266-8920(92)90015-A. URL: https://www.sciencedirect.com/science/article/pii/026689209290015A.

[340] Lee Lindblom. “Spectral Representations of Neutron-Star Equations of State”. In: *Phys. Rev. D* 82 (2010), p. 103011. DOI: 10.1103/PhysRevD.82.103011. arXiv: 1009.0738 [astro-ph.HE].

[341] Lee Lindblom. “Causal Representations of Neutron-Star Equations of State”. In: *Phys. Rev. D* 97.12 (2018), p. 123019. DOI: 10.1103/PhysRevD.97.123019. arXiv: 1804.04072 [astro-ph.HE].

[342] Eemeli Annala et al. “Evidence for quark-matter cores in massive neutron stars”. In: *Nature Phys.* 16.9 (2020), pp. 907–910. DOI: 10.1038/s41567-020-0914-9. arXiv: 1903.09121 [astro-ph.HE].

[343] Sinan Altiparmak, Christian Ecker, and Luciano Rezzolla. “On the Sound Speed in Neutron Stars”. In: (Mar. 2022). arXiv: 2203.14974 [astro-ph.HE].

[344] Eemeli Annala et al. “Multimessenger Constraints for Ultradense Matter”. In: *Phys. Rev. X* 12.1 (2022), p. 011058. DOI: 10.1103/PhysRevX.12.011058. arXiv: 2105.05132 [astro-ph.HE].

[345] M. C. Miller et al. “The Radius of PSR J0740+6620 from NICER and XMM-Newton Data”. In: *Astrophys. J. Lett.* 918.2 (2021), p. L28. DOI: 10.3847/2041-8213/ac089b. arXiv: 2105.06979 [astro-ph.HE].

[346] B. P. Abbott et al. “Properties of the binary neutron star merger GW170817”. In: *Phys. Rev. X* 9.1 (2019), p. 011001. DOI: 10.1103/PhysRevX.9.011001. arXiv: 1805.11579 [gr-qc].

[347] Thomas E. Riley et al. "A *NICER* View of PSR J0030+0451: Millisecond Pulsar Parameter Estimation". In: *Astrophys. J. Lett.* 887.1 (2019), p. L21. DOI: 10.3847/2041-8213/ab481c. arXiv: 1912.05702 [astro-ph.HE].

[348] Thomas E. Riley et al. "A NICER View of the Massive Pulsar PSR J0740+6620 Informed by Radio Timing and XMM-Newton Spectroscopy". In: *Astrophys. J. Lett.* 918.2 (2021), p. L27. DOI: 10.3847/2041-8213/ac0a81. arXiv: 2105.06980 [astro-ph.HE].

[349] Omar Benhar, Valeria Ferrari, and Leonardo Gualtieri. "Gravitational wave asteroseismology revisited". In: *Phys. Rev. D* 70 (2004), p. 124015. DOI: 10.1103/PhysRevD.70.124015. arXiv: astro-ph/0407529.

[350] Daniela D. Doneva et al. "Gravitational wave asteroseismology of fast rotating neutron stars with realistic equations of state". In: *Phys. Rev. D* 88.4 (2013), p. 044052. DOI: 10.1103/PhysRevD.88.044052. arXiv: 1305.7197 [astro-ph.SR].

[351] Bikram Keshari Pradhan et al. "General relativistic treatment of $f$-mode oscillations of hyperonic stars". In: (Mar. 2022). arXiv: 2203.03141 [astro-ph.HE].

[352] Nils Andersson and Kostas D. Kokkotas. "Towards gravitational wave asteroseismology". In: *Mon. Not. Roy. Astron. Soc.* 299 (1998), pp. 1059–1068. DOI: 10.1046/j.1365-8711.1998.01840.x. arXiv: gr-qc/9711088.

[353] K. D. Kokkotas, T. A. Apostolatos, and N. Andersson. "The Inverse problem for pulsating neutron stars: A 'Fingerprint analysis' for the supranuclear equation of state". In: *Mon. Not. Roy. Astron. Soc.* 320 (2001), pp. 307–315. DOI: 10.1046/j.1365-8711.2001.03945.x. arXiv: gr-qc/9901072.

[354] Geraint Pratten, Patricia Schmidt, and Tanja Hinderer. "Gravitational-Wave Asteroseismology with Fundamental Modes from Compact Binary Inspirals". In: *Nature Commun.* 11.1 (2020), p. 2553. DOI: 10.1038/s41467-020-15984-5. arXiv: 1905.00817 [gr-qc].

[355] I. S. Gradshteyn et al. *Table of Integrals, Series and Products*. Elsevier Academic Press Publication, 2007. ISBN: 13:978-0-12-373637-6, 10:0-12-373637-4. URL: https://www.elsevier.com/books/table-of-integrals-series-and-products/zwillinger/978-0-08-047111-2.

[356] URL: http://mathworld.wolfram.com/HurwitzZetaFunction.html.

# Chiral susceptibility in the Nambu–Jona-Lasinio model: A Wigner function approach

Arpan Das,[1,*] Deepak Kumar,[1,2,†] and Hiranmaya Mishra[1,‡]

[1]*Theory Division, Physical Research Laboratory, Navrangpura, Ahmedabad 380 009, India*
[2]*Indian Institute of Technology Gandhinagar, Gandhinagar 382 355, Gujarat, India*

(Received 9 August 2019; published 26 November 2019)

We estimate here chiral susceptibility at finite temperature within the framework of the Nambu–Jona-Lasinio model (NJL) using the Wigner function approach. We also estimate it in the presence of chiral chemical potential ($\mu_5$) as well as a nonvanishing magnetic field ($B$). We use a medium separation regularization scheme (MSS) in the precence of magnetic field to calculate the chiral condensate and corresponding susceptibility. It is observed that for a fixed value of chiral chemical potential ($\mu_5$), transition temperature increases with the magnetic field. While for the fixed value of the magnetic field, transition temperature decreases with chiral chemical potential. For a strong magnetic field, we observe non-degeneracy in susceptibility for up and down type quarks.

DOI: 10.1103/PhysRevD.100.094030

## I. INTRODUCTION

In recent years, extensive efforts have been made to create and understand strongly interacting matter in relativistic heavy ion collision experiments, e.g., at the relativistic heavy-ion collider and the large hadron collider. There are mounting evidences which indicate formation of deconfined quark gluon plasma (QGP) phase of QCD in the initial stages of these experiments as well as the formation of confined hadron phase in the subsequent evolution of QGP. Ground state of QCD exhibits two main nonperturbative features, color confinement and spontaneous breaking of chiral symmetry. The dynamical breaking of chiral symmetry is the manifestation of the quark-antiquark condensation in the QCD vacuum. Dynamical chiral symmetry breaking characterizes the nonperturbative nature of QCD vacuum at vanishing temperature and/or density. With increase in temperature and/or baryon density, the QCD vacuum undergoes a transition from a chiral symmetry broken phase to a chiral symmetric phase. This transition is characterized by the quark-antiquark scalar condensate, the order parameter of the chiral phase transition. Although for first order phase transition order parameter changes discontinuously across the transition point, for second order phase transition or for a crossover transition the variation of order parameter across the transition point is rather smooth. In these cases, the fluctuation of this order parameter and the associated susceptibilities are more relevant for the characterization of the thermodynamic properties of the system.

The characteristics of fluctuations and correlations are intimately connected to the phase transition dynamics, e.g., fluctuations of all length scales are relevant at QCD critical point where the first order quark-hadron phase transition line ends. The study of fluctuations and correlations are essential phenomenological tool for the experimental exploration of the QCD phase diagram. In the context of heavy-ion collisions by studying the net electric charge fluctuation, it has been demonstrated that net electric charges are suppressed in the QGP phase as compared to the hadronic phase [1,2]. It has also been pointed out that the correlation between baryon number and strangeness is stronger in the QGP phase as compared to the hadronic phase [3,4]. The quantity of interest here is the chiral susceptibility which measures the response of the chiral condensate to the variation of the current quark mass. Chiral susceptibility has been calculated using first principle lattice QCD (LQCD) simulations [5–10]. All these lattice results show a pronounced peak in the variation of chiral susceptibility with temperature at the transition temperature, which essentially characterizes the chiral transition. Apart from these LQCD studies which incorporate the nonperturbative effects of QCD vacuum, complementary approaches, e.g., Nambu–Jona-Lasinio (NJL) model [11,12], chiral perturbation theory [13], Dyson-Schwinger equation [14], hard thermal loop approximation [15], etc. have been considered to study the chiral susceptibility.

*arpan@prl.res.in
†deepakk@prl.res.in
‡hm@prl.res.in

An entirely new line of investigations has been initiated to understand the QCD phase diagram due to the possibility of generation of extremely large magnetic field in noncentral relativistic heavy ion collision experiments. In the early stages, the magnetic field in QGP can be very large, at least of the order of few $m_\pi^2$ [16–24]. While such fields rapidly decay in the vacuum, in a conducting medium they can be sustained for a longer time due to induced current [21–24]. Strong magnetic field can affect dynamical chiral symmetry breaking. It has been shown that external magnetic field acts as catalysis for chiral condensation; the value of chiral condensation or the constituent mass of quarks is larger than vanishing magnetic field case. It is important to mention that the effect of magnetic field on the order parameter is not unique to QCD medium. In fact, in condensed matter systems, e.g., superconductors magnetic field can play a significant role. A striking contrast of the effect of magnetic field on the chiral condensate contrary to superconductors is that the magnetic field helps to strengthen the chiral condensate. Naively one can understand this in the following way. Unlike the electrically charged superconducting condensate, chiral condensate is an electrically neutral spin zero condensate. Hence, for the chiral condensate, the magnetic moment of the fermion and the antifermion point in the same direction. Hence, in the presence of magnetic field, both magnetic moments can align themselves along the direction of the magnetic field without any frustration in the pair [25]. It has also been pointed out that in the presence of magnetic field dimensional reduction can play an essential role in the pairing of fermions [26].

Magnetic catalysis has been explored extensively in $(2+1)$ and $(3+1)$-dimensional models with local four fermion interactions [27–46], supersymmetric models [47], quark meson models [48,49], chiral perturbation theory [50,51], etc. Such a strong magnetic field can also introduce some exotic phenomenon, e.g., chiral magnetic effect (CME), chiral vortical effect (CVE), etc. in a chirally imbalanced medium [52]. Underlying physics of the chiral imbalance is the axial anomaly and topologically nontrivial vacuum of QCD, which allows topological field configurations like instantons to exist. An asymmetry between the number of left- and right-handed quarks can be generated by these nontrivial topological field configurations due to Adler-Bell-Jackiw anomaly. Such an imbalance can lead to observable $P$ and $CP$ violating effects in heavy ion collisions. In the presence of magnetic field, chirally imbalance quark matter can give rise to chiral magnetic effect where a charge separation can be produced. Effects of a chiral imbalance on the QCD phase diagram can be studied within the framework of grand canonical ensemble by introducing a chiral chemical potential $\mu_5$, which enters the QCD Lagrangian via a term $\mu_5\bar{\psi}\gamma^0\gamma^5\psi$. Chiral phase transition has been discussed extensively. These studies include NJL type models [53–59], quark linear sigma model [53,60], lattice QCD studies [61,62], etc. Although the effect of chiral chemical potential has been explored extensively, contradicting results have been reported in various literature, e.g., Refs. [53–58] predict that chiral transition temperature decreases with chiral chemical potential. On the other hand, in Ref. [59], it has been argued that with a specific regularization method chiral transition temperature increases with chiral chemical potential, which is in agreement with lattice results in Refs. [61,62]. In this context, in a recent interesting work, the Winger function in the presence of nonvanishing magnetic field and chiral chemical potential has been evaluated in a nonperturbative manner using explicit solutions of the Dirac equation in a magnetic field and chiral chemical potential [63]. This has been later used for pair production in the presence of electromagnetic field [64].

To probe the medium produced in relativistic heavy ion collisions, generally thermodynamic or hydrodynamic model has been used, which assumes local thermal equilibrium. However, due to the short timescales associated with the strong interaction, the medium produced in the heavy ion collision is rather dynamical in nature and lives for a very short time and nonequilibrium as well as quantum effects can affect the evolution of the medium significantly. These effects can be considered within the framework of nonequilibrium quantum transport theory. It is important to point out that in the case of interacting field theory of fermions and gauge bosons, transport theory should be invariant under local gauge transformation. Such a gauge covariant quantum transport theory for QCD has been developed in [65–67]. Classical kinetic theory is characterized by an ensemble of pointlike particles with their single particle phase-space distribution function. The time evolution of single particle phase-space distribution function governed by the transport equation encodes the evolution of the system. Similar to the single particle distribution in classical kinetic theory, Wigner function, which is the quantum mechanical analogue of classical distribution function, encodes quantum corrections in the transport equation [68]. Equation of motion of Winger function can be derived from the equation of motion for the associated field operators, e.g., for fermions, evolution equation of Wigner functions can be derived using the Dirac equation [69,70]. In the case of local gauge theories, the Wigner function has to be defined in a gauge invariant manner [71]. The covariant Wigner function method for spin-1/2 fermions has already been explored extensively in the context of heavy ion collisions to study various effects including the CME, CVE, polarization-vorticity coupling, hydrodynamics with spin, dynamical generation of magnetic moment, etc. [63,72–83].

In this investigation, we study the chiral phase transition and chiral susceptibility in the presence of magnetic field and chiral chemical potential in quantum kinetic theory framework using NJL model [84–89]. Our work is based on the spinor decomposition of the Wigner function using formalism of Refs. [63,90]. In this investigation, we limit ourselves to mean field or classical level of the quantum kinetic theory, since the chiral symmetry breaking and generation of dynamical mass of fermions take place at mean field level [90]. The formulation of transport theory of NJL model has been studied in Refs. [90–93]. In this work, we have used the formalism given in Ref. [90] to calculate the chiral condensate and the chiral susceptibility using the Wigner function. Wigner function in general is used for deriving dynamical equations for the out of equilibrium system [90]. In the present study, we limit ourselves to use the Wigner function for an extended system in global thermal equilibrium, i.e., at constant temperature and chemical potentials to calculate chiral susceptibility.

In this context, some comments regarding chiral transition in the presence of a of chiral chemical potential ($\mu_5$) may be in order. In Ref. [54], this was investigated within Polyakov loop extended NJL (PNJL) model. It was observed that the chiral transition temperature decreases with chiral chemical potential. To eliminate artifacts of a sharp three momentum cutoff, in Ref. [54] a smooth cutoff for the three momentum modeled through a form factor was used. Further, it was observed that with increasing $\mu_5$ the chiral transition becomes a first order transition. In fact, the phase diagram in $\mu_5 - T$ plane for the chiral transition becomes similar to the same in $\mu - T$ plane. This was also the conclusion in Refs. [54,60,94]. On the contrary, nonlocal version of the NJL model was further analyzed in Ref. [95] with the result that the chiral transition temperature increases with chiral chemical potential and the chiral transition is second order. Similar conclusion was also drawn in Refs. [96,97] using a Schwinger Dyson approach. Further, NJL model with chiral chemical potential was analyzed in Ref. [59] with a novel "medium separation scheme" (MSS) for regulating divergent integrals, and the conclusion was that the chiral transition temperature increases with $\mu_5$ and such conclusions are also in accordance with some lattice calculations [61,62]. However, it ought to be mentioned here that the lattice data have not been obtained in the chiral limit and some of the results are for $N_c = 2$ QCD, e.g., [62]. A further careful analysis of NJL model was done in Ref. [57] to examine dependence of chiral transition temperature on different regularization scheme. It was observed that chiral transition temperature decreases with chiral chemical potential with a smooth cutoff and shows a first order transition at large $\mu_5$. In the present investigation, we use a medium separation scheme in the presence of magnetic field and chiral chemical potential. Such a scheme was introduced in Refs. [59,98,99]. As we will see later, we also do not see a first order transition at large chiral chemical potential as in the analysis in Ref. [95]. However, we observe that chiral transition temperature decreases with chiral chemical potential as in Refs. [54,57].

We organize the paper in the following manner. In Sec. II, for the sake of completeness, we recapitulate the results of Ref. [90] to study chiral condensate in NJL model using Wigner function approach. Then in Sec. III we introduce the Winger function in the presence of magnetic field as well as chiral chemical potential and calculate the chiral condensate for two flavor NJL model. In Sec. IV, we discuss the chiral susceptibility for two flavor NJL model in the presence of magnetic field ($B$) as well as chiral chemical potential ($\mu_5$). In Sec. V, we present the results and discussions. Finally, in Sec. VI, we conclude our results with an outlook on it.

## II. WARM UP: WIGNER FUNCTION AND CHIRAL CONDENSATE IN NJL MODEL

In this section we first briefly discuss the salient features of the formalism of Wigner function in NJL model for single flavor fermion having vanishing current quark mass as given in Ref. [90]. Once we get the representation of scalar condensate in terms of Wigner function, we can generalize it to a more realistic situation with nonvanishing current quark mass. For a single flavor NJL model, we start with the following Lagrangian [90]:

$$\mathcal{L} = \bar{\psi} i \partial\!\!\!/ \psi + G((\bar{\psi}\psi)^2 + (\bar{\psi} i\gamma_5\psi)^2), \tag{1}$$

where $\psi$ is the Dirac field, $G$ is the scalar coupling. The first term is the usual kinetic term, and the second term represents the four Fermi interaction. One can define composite field operators $\hat{\sigma}$ and $\hat{\pi}$ as

$$\hat{\sigma} = -2G\bar{\psi}\psi, \qquad \hat{\pi} = -2G\bar{\psi} i\gamma_5\psi. \tag{2}$$

Using Eq. (2), the Lagrangian given in Eq. (1) can be recasted as [90]

$$\mathcal{L} = \bar{\psi} i \partial\!\!\!/ \psi - \hat{\sigma}\bar{\psi}\psi - \hat{\pi}\bar{\psi}\, i\gamma_5\psi - \frac{\hat{\sigma}^2 + \hat{\pi}^2}{4G}. \tag{3}$$

In the mean field approximation, the operators $\hat{\sigma}$ and $\hat{\pi}$ are replaced by their mean field values

$$\hat{\sigma} \to \sigma = \langle\hat{\sigma}\rangle = \mathrm{Tr}(\hat{\rho}\,\hat{\sigma}), \quad \hat{\pi} \to \pi = \langle\hat{\pi}\rangle = \mathrm{Tr}(\hat{\rho}\,\hat{\pi}), \tag{4}$$

where $\hat{\rho}$ is the density matrix operator and "Tr" denotes trace over all physical states of the system. For a nonequilibrium transport theory, in mean field approximation, the fundamental quantity is the Green function, which is defined as

$$G^{<}_{\alpha\beta}(x, y) = \langle\bar{\psi}_\beta(y)\psi_\alpha(x)\rangle. \tag{5}$$

The mean field values of the operators $\hat{\sigma}$ and $\hat{\pi}$, i.e., $\sigma(x)$ and $\pi(x)$ can be determined in terms of the Green function $G^{<}(x,y)$ as follows:

$$\sigma(x) = -2G\mathrm{Tr}G^{<}(x,x), \qquad \pi(x) = -2G\mathrm{Tr}i\gamma_5 G^{<}(x,x). \tag{6}$$

The Wigner function for fermion is defined as [90]

$$W_{\alpha\beta}(X,p) = \int \frac{d^4X'}{(2\pi)^4} e^{-ip_\mu X'^\mu} \left\langle \bar{\psi}_\beta\left(X+\frac{X'}{2}\right)\psi_\alpha\left(X-\frac{X'}{2}\right)\right\rangle = \int \frac{d^4X'}{(2\pi)^4} e^{-ip_\mu X'^\mu} G^{<}_{\alpha\beta}\left(X+\frac{X'}{2}, X-\frac{X'}{2}\right). \tag{7}$$

It is important to mention that in NJL model there are no gluons; hence, the $SU(3)_c$ gauge invariance of the Wigner function does not appear in NJL model. Again, in this case, we are not considering background magnetic field. Hence, there is no $U(1)_{em}$ gauge field associated with the NJL model. However, in the presence of gauge field, one has to introduce a gauge link in Wigner function for a gauge invariant description [100].

Since the Wigner function ($W(X,p)$), as given in Eq. (7), is a composite operator made out of the Dirac field operators $\psi$ and $\bar{\psi}$, it is convenient to decompose $W(X,p)$ in terms of the generators of the Clifford algebra. The Wigner function $W(X,p)$, in terms of the conventional basis of Clifford algebra $\mathbb{1}, i\gamma_5, \gamma^\mu, \gamma^\mu\gamma_5$, and $\sigma^{\mu\nu}$, can be written as

$$W = \frac{1}{4}\left[F + i\gamma_5 P + \gamma^\mu V_\mu + \gamma^\mu\gamma^5 A_\mu + \frac{1}{2}\sigma^{\mu\nu}S_{\mu\nu}\right]. \tag{8}$$

Here the coefficients $F, P, V_\mu, A_\mu$, and $S_{\mu\nu}$ are the scalar, pseudoscalar, vector, axial vector, and tensor components of the Wigner function, respectively, also known as Dirac-Heisenberg-Wigner (DHW) functions. The scalar, pseudoscalar, vector, axial vector, and tensor Dirac-Heisenberg-Wigner functions can be, respectively, expressed as

$$F(X,p) = \mathrm{Tr}W(X,p), \tag{9}$$

$$P(X,p) = -i\mathrm{Tr}\gamma_5 W(X,p), \tag{10}$$

$$V^\mu(X,p) = \mathrm{Tr}\gamma^\mu W(X,p), \tag{11}$$

$$A^\mu(X,p) = \mathrm{Tr}\gamma^5\gamma^\mu W(X,p), \tag{12}$$

$$S^{\mu\nu}(X,p) = \mathrm{Tr}\sigma^{\mu\nu} W(X,p). \tag{13}$$

Using Eqs. (6) and (7), the scalar and pseudoscalar condensates as given in Eqs. (9) and (10) can be written in terms of Wigner function in the following manner:

$$\sigma(X) = -2G\int d^4p\mathrm{Tr}W(X,p) = -2G\int d^4pF(X,p), \tag{14}$$

and

$$\pi(X) = -2G\int d^4p\mathrm{Tr}i\gamma_5 W(X,p) = 2G\int d^4pP(X,p). \tag{15}$$

Using Eqs. (2) and (14), one can express the scalar condensate as

$$\langle\bar{\psi}\psi\rangle = \int d^4pF(X,p). \tag{16}$$

In the above description, we have briefly mentioned the relation between the different mean fields with the Wigner function. It is important to mention that by the virtue of the Dirac equation for the field operator $\psi$ and $\bar{\psi}$ the Wigner function, $W(X,p)$, also satisfies a quantum kinetic equation. However, in this investigation, we have not focused on the kinetic equation of the Wigner function. For a detailed discussion on the kinetic equation for the components of Wigner function, kinetic equation for quark distribution function, and related topic, see Ref. [90]. In this investigation, we rather focus on the estimation of chiral condensate, as given in Eq. (16), and associated chiral susceptibility in two flavor NJL model.

The Wigner function can be calculated by inserting the Dirac field operators in Eq. (7). The Dirac field operators in the absence of magnetic field can be written as [101]

$$\psi(x) = \frac{1}{\sqrt{\Omega}}\sum_{\vec{k},s}\frac{1}{\sqrt{2\mathcal{E}_{0k}}}\left[a(\vec{k},s)u(\vec{k},s)e^{-ik.x} + b^\dagger(\vec{k},s)v(\vec{k},s)e^{ik.x}\right], \tag{17}$$

$$\bar{\psi}(x) = \frac{1}{\sqrt{\Omega}}\sum_{\vec{k},s}\frac{1}{\sqrt{2\mathcal{E}_{0k}}}\left[a^\dagger(\vec{k},s)\bar{u}(\vec{k},s)e^{ik.x} + b(\vec{k},s)\bar{v}(\vec{k},s)e^{-ik.x}\right], \tag{18}$$

where $\Omega$ is the volume and $s = \pm 1$ denotes the spin states. Using the field decomposition as given in Eqs. (17) and (18), the Wigner function of a fermion with mass $\mathcal{M}_0$ can be shown to be [101]

$$W_{\alpha\beta}(X,p) = \frac{1}{(2\pi)^3}\delta(p^2 - \mathcal{M}_0^2)\Big[\theta(p^0)\sum_s f_{FD}(\mathcal{E}_{0p} - \mu_s)u_\alpha(\vec{p},s)\bar{u}_\beta(\vec{p},s) + \theta(-p^0)\sum_s (1 - f_{FD}(\mathcal{E}_{0p} + \mu_s))v_\alpha(-\vec{p},s)\bar{v}_\beta(-\vec{p},s)\Big], \tag{19}$$

where the creation and the annihilation operators of the particle satisfy $\langle a^\dagger(\vec{p},s)a(\vec{p},s)\rangle = f_{FD}(\mathcal{E}_{0p} - \mu_s)$. On the other hand, the creation and the annihilation operators of the antiparticle satisfy $\langle b^\dagger(-\vec{p},s)b(-\vec{p},s)\rangle = f_{FD}(\mathcal{E}_{0p} + \mu_s)$. Here $f_{FD}(z) = 1/(1+\exp(z/T))$ is the Fermi Dirac distribution function at temperature $T$, and $\mu_s$ is the chemical potential for the spin state $s$. $\mathcal{E}_{0p} = \sqrt{p^2 + \mathcal{M}_0^2}$ is the single particle energy, and $\mathcal{M}_0$ is the mass of the Dirac fermion. It is important to note that the space time dependence in the Wigner function $W(X,p)$ is hidden in the space time dependence of the temperature and chemical potential. However, for a uniform temperature and chemical potential, i.e., for a system in global equilibrium the Wigner function is independent of space time. In this investigation, we considered a global thermal equilibrium. Hence, from now onward, we will omit the space time dependence in the Wigner function. Using Eqs. (9) and (19), the scalar DHW function can be expressed as [101]

$$F(p) = \mathcal{M}_0\delta(p^2 - \mathcal{M}_0^2)\left[\frac{2}{(2\pi)^3}\sum_s (\theta(p^0)f_{FD}(\mathcal{E}_{0p} - \mu_s) - \theta(-p^0)(1 - f_{FD}(\mathcal{E}_{0p} + \mu_s)))\right]. \tag{20}$$

Using the scalar DHW function as given in Eq. (20), the scalar condensate for a single fermion species of mass $\mathcal{M}_0$ given in Eq. (16) can be recasted as

$$\begin{aligned}\langle\bar{\psi}\psi\rangle &= \int d^4p\mathcal{M}_0\delta(p^2 - \mathcal{M}_0^2)\left[\frac{2}{(2\pi)^3}\sum_s (\theta(p^0)f_{FD}(\mathcal{E}_{0p} - \mu_s) - \theta(-p^0)(1 - f_{FD}(\mathcal{E}_{0p} + \mu_s)))\right] \\ &= -\sum_s \int \frac{d^3p}{(2\pi)^3}\frac{\mathcal{M}_0}{\mathcal{E}_{0p}}[1 - f_{FD}(\mathcal{E}_{0p} - \mu_s) - f_{FD}(\mathcal{E}_{0p} + \mu_s)].\end{aligned} \tag{21}$$

In a situation where the chemical potential is independent of the spin of the state,

$$\langle\bar{\psi}\psi\rangle = -2N_c\int \frac{d^3p}{(2\pi)^3}\frac{\mathcal{M}_0}{\mathcal{E}_{0p}}[1 - f_{FD}(\mathcal{E}_{0p} - \mu) - f_{FD}(\mathcal{E}_{0p} + \mu)], \quad \text{with} \quad \mathcal{M}_0 = -2G\langle\bar{\psi}\psi\rangle. \tag{22}$$

The factor of $N_c$ appears in Eq. (22) due to the "Tr" over all the degrees of freedom (d.o.f.).

Next, we shall consider two flavor ($u$, $d$ quarks) NJL model for vanishing magnetic field and chiral chemical potential, with the Lagrangian given as [102–104], along with a 't Hooft determinant interaction

$$\mathcal{L} = \mathcal{L}_0 + \mathcal{L}_1 + \mathcal{L}_2, \tag{23}$$

where the free part is

$$\mathcal{L}_0 = \bar{\psi}(i\partial\!\!\!/ - m)\psi, \tag{24}$$

and the interaction parts are given as

$$\mathcal{L}_1 = G_1\sum_{a=0}^{3}[(\bar{\psi}\tau^a\psi)^2 + (\bar{\psi}i\gamma_5\tau^a\psi)^2] \tag{25}$$

and

$$\mathcal{L}_2 = G_2[(\bar{\psi}\psi)^2 - (\bar{\psi}\,\vec{\tau}\,\psi)^2 - (\bar{\psi}i\gamma_5\psi)^2 + (\bar{\psi}i\gamma_5\vec{\tau}\psi)^2], \tag{26}$$

where $\psi = (\psi_u, \psi_d)^T$ is the quark doublet, $m = \mathrm{diag}(m_u, m_d)$ is the current quark mass with $m_u = m_d$. $\tau^0 = I_{2\times2}$ and $\vec{\tau}$ are the Pauli matrices. The above Lagrangian as given in Eq. (23) is invariant under $SU(2)_L \times SU(2)_R \times U(1)_V$ transformations. $\mathcal{L}_1$ has an additional $U(1)_A$ symmetry. $\mathcal{L}_2$ is identical with 't Hooft determinant interaction term which breaks the $U(1)_A$ symmetry explicitly. $\mathcal{L}_2$ interaction term introduces mixing between different flavors. It is also important to emphasize that since we are considering only the scalar condensates of the form $\langle\bar{\psi}_u\psi_u\rangle$ and $\langle\bar{\psi}_d\psi_d\rangle$, so we can safely ignore the pseudoscalar condensate as well as the scalar condensates of the form $\langle\bar{\psi}_u\psi_d\rangle$, $\langle\bar{\psi}_d\psi_u\rangle$ etc. Using these approximations at the mean field level, the Lagrangian of the two flavor NJL model as given in Eq. (23) can be expressed as

$$\mathcal{L} = \bar{\psi}_u(i\partial\!\!\!/ - \mathcal{M}_{0_u})\psi_u + \bar{\psi}_d(i\partial\!\!\!/ - \mathcal{M}_{0_d})\psi_d - 2G_1(\langle\bar{\psi}_u\psi_u\rangle^2 + \langle\bar{\psi}_d\psi_d\rangle^2) - 4G_2\langle\bar{\psi}_u\psi_u\rangle\langle\bar{\psi}_d\psi_d\rangle, \tag{27}$$

where $u$ and $d$ quark condensates are given as $\langle\bar{\psi}_u\psi_u\rangle$ and $\langle\bar{\psi}_d\psi_d\rangle$, respectively. The constituent quark masses of $u$ and $d$ quarks in terms of the chiral condensates are given as

$$\begin{aligned}\mathcal{M}_{0_u} &= m_u - 4G_1\langle\bar{\psi}_u\psi_u\rangle - 4G_2\langle\bar{\psi}_d\psi_d\rangle,\\ \mathcal{M}_{0_d} &= m_d - 4G_1\langle\bar{\psi}_d\psi_d\rangle - 4G_2\langle\bar{\psi}_u\psi_u\rangle.\end{aligned} \tag{28}$$

One can easily generalize the scalar condensate as given in Eq. (22) for single flavor NJL model to multiflavor NJL model. Hence, for NJL model of $N_f$ quark flavor and $N_c$ color, the chiral condensate can be written as

$$\langle\bar{\psi}\psi\rangle^{\mu_5=0}_{B=0} = \sum_{f=1}^{N_f}\langle\bar{\psi}_f\psi_f\rangle^{\mu_5=0}_{B=0},$$

with

$$\langle\bar{\psi}_f\psi_f\rangle^{\mu_5=0}_{B=0} = -2N_c\int\frac{d^3p}{(2\pi)^3}\frac{\mathcal{M}_{0_f}}{\mathcal{E}_{0p,f}}[1 - f_{FD}(\mathcal{E}_{0p,f} - \mu) - f_{FD}(\mathcal{E}_{0p,f} + \mu)]. \tag{29}$$

The chiral condensate for $N_f$ flavor NJL model as given in Eq. (29) can also be obtained by first calculating the thermodynamic potential using the mean field Lagrangian as given in Eq. (27) and then calculating the gap equation using the minimization of thermodynamic potential.

## III. WIGNER FUNCTION AND CHIRAL CONDENSATE IN NJL MODEL FOR NONVANISHING MAGNETIC FIELD AND CHIRAL CHEMICAL POTENTIAL

In the presence of magnetic field ($B$) and chiral chemical potential ($\mu_5$), the Wigner function has been explicitly written down in Ref. [63], using solutions of the Dirac equation for fermions in magnetic field and finite chiral chemical potential. We shall use them to calculate chiral condensate. For the sake of completeness, we write down the relevant expressions for the Wigner function. In the presence of background magnetic field, the Wigner function given in Eq. (7) gets modified to a gauge invariant Wigner function as [63]

$$W_{\alpha\beta}(X,p) = \int\frac{d^4X'}{(2\pi)^4}e^{(-ip_\mu X'^\mu)}\left\langle\bar{\psi}_\beta\left(X+\frac{X'}{2}\right)\times U\left(A,X+\frac{X'}{2},X-\frac{X'}{2}\right)\psi_\alpha\left(X-\frac{X'}{2}\right)\right\rangle, \tag{30}$$

where $U(A, X+\frac{X'}{2}, X-\frac{X'}{2})$ is the gauge link between two space time points $(X-\frac{X'}{2})$ and $(X+\frac{X'}{2})$ for the gauge field $A^\mu$. The gauge link has been introduced to make the Wigner function gauge invariant. In the presence of homogeneous external magnetic field along the $z$ direction, the gauge link is just a phase. In this case, the Wigner function simplifies to

$$W_{\alpha\beta}(X,p) = \int\frac{d^4X'}{(2\pi)^4}e^{(-ip_\mu X'^\mu - iqByx')}\left\langle\bar{\psi}_\beta\left(X+\frac{X'}{2}\right)\otimes\psi_\alpha\left(X-\frac{X'}{2}\right)\right\rangle, \tag{31}$$

where $A^\mu(X) = (0, -By, 0, 0)$ is a specific gauge choice of the external magnetic field. $q$ is the charge of the particle, and it has been taken to be positive. Analogous to the case of vanishing magnetic field, Wigner function can be calculated for nonvanishing magnetic field by using the Dirac field operator in a background magnetic field. The Wigner function in a background magnetic field at finite temperature ($T$), chemical potential ($\mu$), and finite chiral chemical potential ($\mu_5$) has been shown to be [63]

$$W(p) = \sum_{n,s}\Big[f_{FD}(E^{(n)}_{p_z,s} - \mu)\delta(p_0 + \mu - E^{(n)}_{p_z,s})W^{(n)}_{+,s}(\vec{p}) + (1 - f_{FD}(E^{(n)}_{p_z,s} + \mu))\delta(p_0 + \mu + E^{(n)}_{p_z,s})W^{(n)}_{-,s}(\vec{p})\Big], \quad n \geq 0, \tag{32}$$

where the functions $W^{(n)}_{\pm,s}(\vec{p})$ denote the contribution of fermion/antifermion in the $n$th Landau level. The single particle energy at the lowest Landau level and higher Landau level is given as $E^{(0)}_{p_z} = \sqrt{M^2 + (p_z - \mu_5)^2}$ and $E^{(n)}_{p_z,s} = \sqrt{M^2 + (\sqrt{p_z^2 + 2nqB} - s\mu_5)^2}$, respectively. $+$ and $-$ in Eq. (32) denote contributions of positive and negative energy solutions, respectively. In the lowest Landau level, fermions can only be in a specific spin state. On the other hand, for higher Landau levels ($n > 0$), both spin states contribute.

The functions $W^{(n)}_{\pm,s}(\vec{p})$ in Eq. (32) can be expressed in terms of Dirac spinors in the following manner [63]:

$$W^{(n)}_{rs}(\vec{p}) \equiv \frac{1}{(2\pi)^3}\int dy'\exp(ip_y y')\xi^{(n)\dagger}_{rs}\left(p_x, p_z, \frac{y'}{2}\right)\gamma^0 \otimes \xi^{(n)}_{rs}\left(p_x, p_z, -\frac{y'}{2}\right), \quad n \geq 0. \tag{33}$$

In Eq. (33), $r = \pm$ denotes positive energy and negative energy solutions, respectively. The Dirac spinors $\xi_r^{(0)}$ and $\xi_{rs}^{(n)}$, where $r = \pm$ denotes positive and negative energy states and $s$ denotes the spin of the state, are defined as

$$\xi_r^{(0)}(p_x, p_z, y) = \frac{1}{\sqrt{2E_{p_z}^{(0)}}} \begin{pmatrix} r\sqrt{E_{p_z}^{(0)} - r(p_z - \mu_5)} \\ \sqrt{E_{p_z}^{(0)} + r(p_z - \mu_5)} \end{pmatrix} \otimes \chi^{(0)}(p_x, y), \tag{34}$$

$$\xi_{rs}^{(n)}(p_x, p_z, y) = \frac{1}{\sqrt{2E_{p_z,s}^{(n)}}} \begin{pmatrix} r\sqrt{E_{p_z,s}^{(n)} + r\mu_5 - rs\sqrt{p_z^2 + 2nqB}} \\ \sqrt{E_{p_z,s}^{(n)} - r\mu_5 + rs\sqrt{p_z^2 + 2nqB}} \end{pmatrix} \otimes \chi^{(n)}(p_x, p_z, y), \quad n > 0, \tag{35}$$

where the normalized eigen spinors $\chi$ are

$$\chi^{(0)}(p_x, y) = \begin{pmatrix} 1 \\ 0 \end{pmatrix} \phi_0(p_x, y), \tag{36}$$

and

$$\chi_s^{(n)}(p_x, p_z, y) = \frac{1}{\sqrt{2\sqrt{p_z^2 + 2nqB}}} \begin{pmatrix} \sqrt{\sqrt{p_z^2 + 2nqB} + sp_z}\,\phi_n(p_x, y) \\ s\sqrt{\sqrt{p_z^2 + 2nqB} - sp_z}\,\phi_{n-1}(p_x, y) \end{pmatrix}, \quad n > 0, \tag{37}$$

where

$$\phi_n(p_x, y) = \left(\frac{qB}{\pi}\right)^{1/4} \frac{1}{\sqrt{2^n n!}} \exp\left[-\frac{qB}{2}\left(y + \frac{p_x}{qB}\right)^2\right] H_n\left[\sqrt{qB}\left(y + \frac{p_x}{qB}\right)\right], \quad n \geq 0. \tag{38}$$

$H_n$ represents $n$th Hermite polynomial. Inserting the explicit expression of the Dirac spinors as given in Eqs. (36) and (37) into Eq. (33), one can get the explicit form of the function $W_{\pm,s}^{(n)}(\vec{p})$[63]. For lowest Landau level,

$$W_r^{(0)}(\vec{p}) = \frac{r}{4(2\pi)^3 E_{p_z}^{(0)}} \Lambda^{(0)}(p_T)[M(1 + \sigma^{12}) + rE_{p_z}^{(0)}(\gamma^0 - \gamma^5\gamma^3) - (p_z - \mu_5)(\gamma^3 - \gamma^5\gamma^0)], \tag{39}$$

while for higher Landau levels,

$$\begin{aligned} W_{rs}^{(n)}(\vec{p}) = r\frac{1}{4(2\pi)^3 E_{p_z,s}^{(n)}} \Bigg\{ & \left[\Lambda_+^{(n)}(p_T) + s\frac{p_z}{\sqrt{p_z^2 + 2nqB}}\Lambda_-^{(n)}(p_T)\right]\left[M + rE_{p_z,s}^{(n)}\gamma^0 + \left(s\sqrt{p_z^2 + 2nqB} - \mu_5\right)\gamma^5\gamma^0\right] \\ & - \left[\Lambda_-^{(n)}(p_T) + s\frac{p_z}{\sqrt{p_z^2 + 2nqB}}\Lambda_+^{(n)}(p_T)\right]\left[\left(s\sqrt{p_z^2 + 2nqB} - \mu_5\right)\gamma^3 + rE_{p_z,s}^{(n)}\gamma^5\gamma^3 - M\sigma^{12}\right] \\ & - \frac{2nqB}{p_T^2\sqrt{p_z^2 + 2nqB}}\Lambda_+^{(n)}(p_T)\Bigg[\left(\sqrt{p_z^2 + 2nqB} - s\mu_5\right)(p_x\gamma^1 + p_y\gamma^2) \\ & + rsE_{p_z,s}^{(n)}(p_x\gamma^5\gamma^1 + p_y\gamma^5\gamma^2) - sM(p_z\sigma^{23} - p_y\sigma^{13})\Bigg]\Bigg\}, \quad n > 0, \end{aligned} \tag{40}$$

where

$$\Lambda_\pm^{(0)}(p_T) = 2\exp\left(-\frac{p_T^2}{qB}\right), \tag{41}$$

$$\Lambda_{\pm}^{(n)}(p_T) = (-1)^n \left[L_n\left(\frac{2p_T^2}{qB}\right) \mp L_{n-1}\left(\frac{2p_T^2}{qB}\right)\right] \exp\left(-\frac{p_T^2}{qB}\right), \quad n > 0. \tag{42}$$

Here $L_n(x)$ are the Laguerre polynomials with $L_{-1}(x) = 0$. Using the Wigner function $W(p)$, as given in Eq. (32), it can be shown that the scalar DWH function is [63]

$$F(p) = M\left[\sum_{n=0}^{\infty} V_n(p_0, p_z)\Lambda_+^{(n)}(p_T) + \sum_{n=1}^{\infty} \frac{1}{\sqrt{p_z^2 + 2nqB}} A_n(p_0, p_z) p_z \Lambda_-^{(n)}(p_T)\right], \tag{43}$$

where

$$V_0(p_0, p_z) = \frac{2}{(2\pi)^3}\delta\{(p_0+\mu)^2 - |E_{p_z}^{(0)}|^2\}\{\theta(p_0+\mu) f_{FD}(p_0) + \theta(-p_0-\mu)[f_{FD}(-p_0) - 1]\} \tag{44}$$

$$V_n(p_0, p_z) = \frac{2}{(2\pi)^3}\sum_s \delta\{(p_0+\mu)^2 - |E_{p_z,s}^{(n)}|^2\}\{\theta(p_0+\mu) f_{FD}(p_0) + \theta(-p_0-\mu)[f_{FD}(-p_0) - 1]\}, \quad n > 0 \tag{45}$$

$$A_n(p_0, p_z) = \frac{2}{(2\pi)^3}\sum_s s\delta\{(p_0+\mu)^2 - |E_{p_z,s}^{(n)}|^2\}\{\theta(p_0+\mu) f_{FD}(p_0) + \theta(-p_0-\mu)[f_{FD}(-p_0) - 1]\}, \quad n > 0. \tag{46}$$

Once the scalar DWH function is known explicitly as given in Eq. (43), the chiral condensate of single flavor fermion can be calculated using Eq. (16) and is given as

$$\langle\bar{\psi}\psi\rangle = \int d^4p F(p) = \int 2\pi p_T \, dp_0 \, dp_T \, dp_z \, F(p). \tag{47}$$

Using Eqs. (43) and (47), it can be shown that (see Appendix A for details)

$$\begin{aligned}\langle\bar{\psi}\psi\rangle_{B\neq 0}^{\mu_5\neq 0} = -\frac{qB}{(2\pi)^2}\Bigg[\int dp_z \frac{M}{E_{p_z}^{(0)}}\left[1 - f_{FD}(E_{p_z}^{(0)} - \mu) - f_{FD}(E_{p_z}^{(0)} + \mu)\right] \\ + \sum_{n=1}^{\infty}\sum_s \int dp_z \frac{M}{E_{p_z,s}^{(n)}}\left[1 - f_{FD}(E_{p_z,s}^{(n)} - \mu) - f_{FD}(E_{p_z,s}^{(n)} + \mu)\right]\Bigg].\end{aligned} \tag{48}$$

For vanishing chiral chemical potential, $\mu_5 = 0$, scalar condensate gets reduced to

$$\langle\bar{\psi}\psi\rangle_{B\neq 0}^{\mu_5=0} = -\frac{qB}{(2\pi)^2}\sum_{n=0}^{\infty}(2 - \delta_{n,0})\int dp_z \frac{M_0}{\epsilon_{p_z}^{(n)}}\left[1 - f_{FD}(\epsilon_{p_z}^{(n)} - \mu) - f_{FD}(\epsilon_{p_z}^{(n)} + \mu)\right], \tag{49}$$

where we denote $M_0$ as the mass of fermion in the absence of chiral chemical potential and finite magnitude field. The single particle energy $\epsilon_{p_z}^{(n)}$ for vanishing chiral chemical potential can be written as

$$\epsilon_{p_z}^{(n)} = \sqrt{M_0^2 + p_z^2 + 2nqB}, \quad n \geq 0. \tag{50}$$

The chiral condensate for a single flavor as given in Eq. (48) can be easily extended to NJL model with two flavors. Most general Lagrangian for two flavor NJL model with $u$ and $d$ quarks in the magnetic field including chiral chemical potential is given as

$$\mathcal{L} = \bar{\psi}(i\not{D} - m + \mu_5\gamma^0\gamma^5)\psi + G_1\sum_{a=0}^{3}[(\bar{\psi}\tau^a\psi)^2 + (\bar{\psi}i\gamma_5\tau^a\psi)^2] + G_2[(\bar{\psi}\psi)^2 - (\bar{\psi}\,\vec{\tau}\psi)^2 - (\bar{\psi}i\gamma_5\psi)^2 + (\bar{\psi}i\gamma_5\vec{\tau}\psi)^2], \tag{51}$$

where $\psi$ is the $U(2)$ quark doublet, given as $\psi = (\psi_u, \psi_d)^T$. The covariant derivative is given as $\not{D} = \not{\partial} + iq\not{A}$, and the current quark mass matrix is $m = \mathrm{diag}(m_u, m_d)$, with $m_u = m_d$. The first term in Eq. (51) is the free Dirac Lagrangian in the presence of magnetic field. For the calculation, we have considered the gauge choice of the background magnetic field as $A^\mu = (0, -By, 0, 0)$. The second term in Eq. (51) is the four Fermi interaction and the attractive part of the quark-antiquark channel of the Fierz transformed color current-current interaction. $\tau^a$, $a = 0, \ldots 3$ are the $U(2)$ generators in the flavor space. The third term is the 't Hooft interaction term which introduces flavor mixing, as in Eq. (26). Since the magnetic field couples to the electric charge of particles, in the presence of magnetic field, $u$ quark and $d$ quarks couple differently with the magnetic field; hence, the isospin symmetry is explicitly broken. In the mean field approximation, in the absence of any pseudoscalar condensate, Eq. (51) can be recasted as

$$\mathcal{L} = \bar{\psi}_u(i\not{D} - M_u + \mu_5\gamma^0\gamma^5)\psi_u + \bar{\psi}_d(i\not{D} - M_d + \mu_5\gamma^0\gamma^5)\psi_d - 2G_1(\langle\bar{\psi}_u\psi_u\rangle^2 + \langle\bar{\psi}_d\psi_d\rangle^2) - 4G_2\langle\bar{\psi}_u\psi_u\rangle\langle\bar{\psi}_d\psi_d\rangle, \tag{52}$$

where $u$, $d$ quark condensates are given as $\langle\bar{\psi}_u\psi_u\rangle$ and $\langle\bar{\psi}_d\psi_d\rangle$, respectively. The constituent quark masses for $u$ and $d$ quarks in terms of the chiral condensates can be given as

$$M_u = m_u - 4G_1\langle\bar{\psi}_u\psi_u\rangle - 4G_2\langle\bar{\psi}_d\psi_d\rangle,$$
$$M_d = m_d - 4G_1\langle\bar{\psi}_d\psi_d\rangle - 4G_2\langle\bar{\psi}_u\psi_u\rangle. \tag{53}$$

Generalizing Eq. (48) for two flavor NJL model, the chiral condensate in the presence of magnetic field and chiral chemical potential can be written as

$$\langle\bar{\psi}\psi\rangle^{\mu_5\neq0}_{B\neq0} = \sum_{f=u,d}\langle\bar{\psi}_f\psi_f\rangle^{\mu_5\neq0}_{B\neq0}, \tag{54}$$

where

$$\langle\bar{\psi}_f\psi_f\rangle^{\mu_5\neq0}_{B\neq0} = -\frac{N_c|q_f|B}{(2\pi)^2}\Bigg[\int dp_z \frac{M_f}{E^{(0)}_{p_z,f}}\left[1 - f_{FD}(E^{(0)}_{p_z,f} - \mu) - f_{FD}\left(E^{(0)}_{p_z,f} + \mu\right)\right] + \sum_{n=1}^{\infty}\sum_{s}\int dp_z \frac{M_f}{E^{(n)}_{p_z,s,f}}\left[1 - f_{FD}\left(E^{(n)}_{p_z,s,f} - \mu\right) - f_{FD}\left(E^{(n)}_{p_z,s,f} + \mu\right)\right]\Bigg], \tag{55}$$

and the single particle energy of flavor $f$ can be expressed as

$$E^{(0)}_{p_z,f} = \sqrt{M_f^2 + (p_z - \mu_5)^2} \quad \text{for } n = 0,$$
$$E^{(n)}_{p_z,s,f} = \sqrt{M_f^2 + \left(\sqrt{p_z^2 + 2n|q_f|B} - s\mu_5\right)^2} \quad \text{for } n > 0. \tag{56}$$

For vanishing chiral chemical potential $\mu_5 = 0$, the chiral condensate of single flavor can be expressed as

$$\langle\bar{\psi}_f\psi_f\rangle^{\mu_5=0}_{B\neq0} = -\frac{N_c|q_f|B}{(2\pi)^2}\sum_{n=0}^{\infty}(2 - \delta_{n,0}) \times \int dp_z \frac{M_{0_f}}{\epsilon^{(n)}_{p_z,f}}\left[1 - f_{FD}\left(\epsilon^{(n)}_{p_z,f} - \mu\right) - f_{FD}\left(\epsilon^{(n)}_{p_z,f} + \mu\right)\right], \tag{57}$$

and the single particle energies of flavor $f$ can be expressed as

$$\epsilon^{(n)}_{p_z,f} = \sqrt{p_z^2 + M_{0_f}^2 + 2n|q_f|B}. \tag{58}$$

The first term of the quark condensate as given in Eq. (57) contains divergence and needs to be regularized to derive meaningful results. Usually, in NJL model at vanishing temperature and chemical potential, such integrals are regularized either by a sharp three momentum cutoff [84,102] or a smooth cutoff [105–107]. Effective models like NJL model which are nonrenormalizable have to be complemented with a regularization scheme with the constraint that the physically meaningful results should be eventually independent of the regularization prescription. In the presence of magnetic field, continuous momentum dependence in two spatial dimensions transverse to the direction of magnetic field is replaced by a sum over discretized Landau levels. Hence, a sharp three momentum cutoff in the presence of the magnetic field can suffer from the cutoff artifacts. Instead, of a sharp cutoff, a smooth momentum cutoff was used in Ref. [54] in the context of chiral magnetic effects in the PNJL model to avoid such sharp cutoff artifacts. To regularize the first term in Eq. (57), we follow an elegant procedure that was followed in Refs. [41,42,44,108–110] by adding and subtracting a vacuum (zero field) term to the chiral condensate which is also divergent. This makes the first term of Eq. (57) neatly separated into a zero field vacuum term and a term that is only dependent on the field written in terms of gamma function which is finite. Thus, the regularized chiral condensate in the presence of magnetic field at vanishing quark chiral chemical potential is [see Appendix B, Eq. (B13)]

$$\langle\bar{\psi}_f\psi_f\rangle^{\mu_5=0}_{B\neq 0} = -2N_c\int_{|\vec{p}|\leq\Lambda}\frac{d^3p}{(2\pi)^3}\frac{M_{0_f}}{\sqrt{p^2+M_{0_f}^2}} - \frac{N_c M_{0_f}|q_f|B}{2\pi^2}\left[x_{0_f}(1-\ln x_{0_f})+\ln\Gamma(x_{0_f})+\frac{1}{2}\ln\left(\frac{x_{0_f}}{2\pi}\right)\right]$$
$$+\frac{N_c|q_f|B}{2\pi^2}\sum_{n=0}^{\infty}(2-\delta_{n,0})\int_{-\infty}^{\infty}dp_z\frac{M_{0_f}}{\epsilon^{(n)}_{p_z,f}}f_{FD}(\epsilon^{(n)}_{p_z,f}), \tag{59}$$

where the dimensionless variable $x_{0_f} = M_{0_f}^2/2|q_f|B$. Scalar condensate as given in Eq. (59) can also be obtained by minimizing the regularized thermodynamic potential using the mean field Lagrangian as given in Eq. (52) in the case of vanishing chiral chemical potential. Solving Eq. (53) using Eq. (59), we get quark masses for vanishing chiral chemical potential with finite magnetic field. This constituent mass will be later used to estimate quark masses at finite chiral chemical potential and finite magnetic field, as discussed in the following subsection.

### A. Regularization of chiral condensate in the presence of magnetic field and chiral chemical potential

Chiral condensate $\langle\bar{\psi}_f\psi_f\rangle$ of quark flavor $f$ in the presence of magnetic field and nonzero chiral chemical potential is given as

$$\langle\bar{\psi}_f\psi_f\rangle^{\mu_5\neq 0}_{B\neq 0} = -\frac{N_c|q_f|B}{(2\pi)^2}\left[\int dp_z\frac{M_f}{E^{(0)}_{p_z,f}}\left[1-f_{FD}(E^{(0)}_{p_z,f}-\mu)-f_{FD}(E^{(0)}_{p_z,f}+\mu)\right]\right.$$
$$\left.+\sum_{n=1}^{\infty}\sum_{s}\int dp_z\frac{M_f}{E^{(n)}_{p_z,s,f}}\left[1-f_{FD}(E^{(n)}_{p_z,s,f}-\mu)-f_{FD}(E^{(n)}_{p_z,s,f}+\mu)\right]\right]$$
$$=\langle\bar{\psi}_f\psi_f\rangle^{\mu_5\neq 0}_{\mathrm{vac,B}\neq 0}+\langle\bar{\psi}_f\psi_f\rangle^{\mu_5\neq 0}_{\mathrm{med,B}\neq 0}, \tag{60}$$

where $\langle\bar{\psi}_f\psi_f\rangle^{\mu_5\neq 0}_{\mathrm{vac,B}\neq 0}$ is zero temperature and zero quark chemical potential part of the chiral condensate, and $\langle\bar{\psi}_f\psi_f\rangle^{\mu_5\neq 0}_{\mathrm{med,B}\neq 0}$ is the medium term at finite temperature and quark chemical potential. $\langle\bar{\psi}_f\psi_f\rangle^{\mu_5\neq 0}_{\mathrm{vac,B}\neq 0}$ contains divergent integral which has to be regularized to obtain meaningful physical result. To regularize the vacuum part of the chiral condensate for nonvanishing magnetic field and chiral chemical potential, we have not considered the naive regularization with finite cutoff (Traditional Regularization Scheme (TRS)) to remove cutoff artifacts, rather we have considered MSS outlined in Ref. [111]. By adding and subtracting the lowest Landau level term in the zero temperature and zero quark chemical potential part of the chiral condensate for nonvanishing magnetic field and chiral chemical potential, we get (for details, see Appendix C)

$$\langle\bar{\psi}_f\psi_f\rangle^{\mu_5\neq 0}_{\mathrm{vac,B}\neq 0} = -\frac{N_c|q_f|B}{(2\pi)^2}\sum_{n=0}^{\infty}\sum_{s=\pm 1}\int dp_z\frac{M_f}{E^{(n)}_{p_z,s,f}}+\frac{N_c|q_f|B}{(2\pi)^2}\int dp_z\frac{M_f}{E^{(0)}_{p_z,f}}$$
$$=-\frac{N_c|q_f|B}{(2\pi)^2}\sum_{n=0}^{\infty}\sum_{s=\pm 1}\int dp_z\left(\frac{1}{\pi}\right)\int_{-\infty}^{\infty}dp_4\frac{M_f}{p_4^2+(E^{(n)}_{p_z,s,f})^2}+\frac{N_c|q_f|B}{(2\pi)^2}\int dp_z\frac{M_f}{E^{(0)}_{p_z,f}}$$
$$=I_1+I_2, \tag{61}$$

where $E^{(n)}_{p_z,s,f}=\sqrt{M_f^2+(\sqrt{p_z^2+2n|q_f|B}-s\mu_5)^2}$ and $E^{(0)}_{p_z,f}=\sqrt{M_f^2+(p_z-\mu_5)^2}$. Both integrals $I_1$ and $I_2$ are not convergent at large momentum; hence, these integrals have to be regularized to get physically meaningful results. In the present investigation, we are using MSS to regularize the integrals $I_1$ and $I_2$. MSS method has also been applied in the case of finite chiral chemical potential but vanishing magnetic field in Ref. [59]. In the present case, we keep both $B\neq 0$ and $\mu_5\neq 0$ and use the same scheme in the following. Integral $I_1$ can be regularized by adding and subtracting the similar term with magnetic field ($B$) but $\mu_5=0$,

$$\frac{1}{p_4^2+(E^{(n)}_{p_z,s,f})^2} = \frac{1}{p_4^2+(\epsilon^{(n)}_{p_z,f})^2} - \frac{1}{p_4^2+(\epsilon^{(n)}_{p_z,f})^2} + \frac{1}{p_4^2+(E^{(n)}_{p_z,s,f})^2} = \frac{1}{p_4^2+(\epsilon^{(n)}_{p_z,f})^2} + \frac{A+2s\mu_5\sqrt{p_z^2+2n|q_f|B}}{[p_4^2+(\epsilon^{(n)}_{p_z,f})^2][p_4^2+(E^{(n)}_{p_z,s,f})^2]}, \tag{62}$$

where $A=M_{0_f}^2-M_f^2-\mu_5^2$ and $\epsilon^{(n)}_{p_z,f}=\sqrt{M_{0_f}^2+p_z^2+2n|q_f|B}$. Using the identity given in Eq. (62) twice, we can write the integrand of the integral $I_1$, as given in Eq. (61), in the following way:

$$\frac{1}{p_4^2+(E^{(n)}_{p_z,s,f})^2} = \frac{1}{p_4^2+(\epsilon^{(n)}_{p_z,f})^2} + \frac{A+2s\mu_5\sqrt{p_z^2+2n|q_f|B}}{(p_4^2+(\epsilon^{(n)}_{p_z,f})^2)^2} + \frac{\left(A+2s\mu_5\sqrt{p_z^2+2n|q_f|B}\right)^2}{\left(p_4^2+\left(\epsilon^{(n)}_{p_z,f}\right)^2\right)^3} + \frac{\left(A+2s\mu_5\sqrt{p_z^2+2n|q_f|B}\right)^3}{\left(p_4^2+\left(\epsilon^{(n)}_{p_z,f}\right)^2\right)^3\left(p_4^2+\left(E^{(n)}_{p_z,s,f}\right)^2\right)}. \tag{63}$$

Performing $p_4$ integration, we obtain (for details, see Appendix B)

$$I_1 = I_{1_{\text{quad}}} - \frac{M_f(M_{0_f}^2-M_f^2+2\mu_5^2)}{2} I_{1_{\text{log}}} + I_{1_{\text{finite1}}} + I_{1_{\text{finite2}}}, \tag{64}$$

where

$$I_{1_{\text{quad}}} = -\frac{N_c|q_f|B}{(2\pi)^2}\sum_{n=0}^{\infty}\sum_s \int dp_z \frac{M_f}{\epsilon^{(n)}_{p_z,f}}, \tag{65}$$

$$I_{1_{\text{log}}} = \frac{N_c|q_f|B}{(2\pi)^2}\sum_{n=0}^{\infty}\sum_s \int dp_z \frac{1}{(\epsilon^{(n)}_{p_z,f})^3}, \tag{66}$$

$$I_{1_{\text{finite1}}} = -\frac{N_c|q_f|B}{(2\pi)^2}\sum_{n=0}^{\infty}\sum_s \int dp_z \left(\frac{3}{8}\right)\frac{(M_fA^2-4M_f\mu_5^2M_{0_f}^2)}{(\epsilon^{(n)}_{p_z,f})^5}, \tag{67}$$

and

$$I_{1_{\text{finite2}}} = -\frac{N_c|q_f|B}{(2\pi)^2}\left(\frac{15}{16}\right)\sum_{n=0}^{\infty}\sum_s \int dp_z \times \int_0^1 dx \frac{(1-x)^2M_f\left(A+2s\mu_5\sqrt{p_z^2+2n|q_f|B}\right)^3}{\left[(\epsilon^{(n)}_{p_z,f})^2 - x\left(A+2s\mu_5\sqrt{p_z^2+2n|q_f|B}\right)\right]^{7/2}}. \tag{68}$$

The integrals $I_{1_{\text{quad}}}$ and $I_{1_{\text{log}}}$ are divergent at large momentum. On the other hand, $I_{1_{\text{finite1}}}$ and $I_{1_{\text{finite2}}}$ are finite. In a similar manner, the integral $I_2$ in Eq. (61), we obtain

$$I_2 = I_{2_{\text{finite}}} + I_{2_{\text{log}}}, \tag{69}$$

where

$$I_{2_{\text{finite}}} = \left(\frac{1}{2}\right)\frac{N_c|q_f|B}{(2\pi)^2}\int dp_z \times \int_0^1 dx \frac{M_f(A+2p_z\mu_5)}{\left[(\epsilon^{(0)}_{p_z,f})^2 - x(A+2p_z\mu_5)\right]^{3/2}}, \tag{70}$$

and

$$I_{2_{\text{log}}} = \frac{N_c|q_f|B}{(2\pi)^2}\int dp_z \frac{M_f}{\epsilon^{(0)}_{p_z,f}}. \tag{71}$$

Using Eqs. (64) and (69), $\langle\bar{\psi}_f\psi_f\rangle^{\mu_5\neq0}_{\text{vac},B\neq0}$ can be expressed as

$$\langle\bar{\psi}_f\psi_f\rangle^{\mu_5\neq0}_{\text{vac},B\neq0} = -\frac{M_f(M_{0_f}^2-M_f^2+2\mu_5^2)}{2} I_{1_{\text{log}}} + I_{1_{\text{finite1}}} + I_{1_{\text{finite2}}} + I_{2_{\text{finite}}} + I_{\text{quad}}, \tag{72}$$

where

$$I_{\text{quad}} = I_{1_{\text{quad}}} + I_{2_{\text{log}}} = \frac{M_f}{M_{0_f}}\left[-\frac{N_c|q_f|B}{(2\pi)^2}\sum_{n=0}^{\infty}\sum_s\int dp_z \frac{M_{0_f}}{\epsilon^{(n)}_{p_z,f}} + \frac{N_c|q_f|B}{(2\pi)^2}\int dp_z \frac{M_{0_f}}{\epsilon^{(0)}_{p_z,f}}\right]. \tag{73}$$

Each integral in $I_{\text{quad}}$ is divergent. Using dimensional regularization, it can be regularized to get [see Appendix B, Eqs. (B2) and (B13)]

$$I_{\mathrm{quad}} = \frac{M_f}{M_{0_f}}\left[-\frac{N_c|q_f|B}{(2\pi)^2}\sum_{n=0}^{\infty}\sum_s\int dp_z\frac{M_{0_f}}{\epsilon^{(n)}_{p_z,f}} + \frac{N_c|q_f|B}{(2\pi)^2}\int dp_z\frac{M_{0_f}}{\epsilon^{(0)}_{p_z,f}}\right] = I^{\mathrm{field}}_{\mathrm{quad}} + I^{\mathrm{vac}}_{\mathrm{quad}}, \tag{74}$$

where

$$I^{\mathrm{field}}_{\mathrm{quad}} = -\frac{N_c M_f|q_f|B}{2\pi^2}\left[x_{0_f}(1-\ln x_{0_f}) + \ln\Gamma(x_{0_f}) + \frac{1}{2}\ln\left(\frac{x_{0_f}}{2\pi}\right)\right] \tag{75}$$

and,

$$I^{\mathrm{vac}}_{\mathrm{quad}} = -\frac{N_c M_f}{2\pi^2}\left[\Lambda\sqrt{M^2_{0_f}+\Lambda^2} - M^2_{0_f}\ln\left(\frac{\Lambda+\sqrt{\Lambda^2+M^2_{0_f}}}{M_{0_f}}\right)\right]. \tag{76}$$

Similarly, the term $I_{1_{\mathrm{log}}}$ is divergent at large momentum, hence it has to be regularized. Regularization of $I_{1_{\mathrm{log}}}$ can be done using dimensional regularization. In the dimensional regularization scheme [see Appendix B, Eq. (B16)],

$$I_{1_{\mathrm{log}}} = \frac{N_c|q_f|B}{(2\pi)^2}\sum_{n=0}^{\infty}\sum_s\int dp_z\frac{1}{\left(\epsilon^{(n)}_{p_z,f}\right)^3} = I^{\mathrm{field}}_{1_{\mathrm{log}}} + I^{\mathrm{vac}}_{1_{\mathrm{log}}}. \tag{77}$$

Here,

$$I^{\mathrm{field}}_{1_{\mathrm{log}}} = -\frac{N_c}{2\pi^2}\left[-\ln x_{0_f} + \frac{\Gamma'(x_{0_f})}{\Gamma(x_{0_f})}\right], \tag{78}$$

and

$$I^{\mathrm{vac}}_{1_{\mathrm{log}}} = \frac{N_c}{\pi^2}\left(\ln\left(\frac{\Lambda}{M_{0_f}} + \sqrt{1+\frac{\Lambda^2}{M^2_{0_f}}}\right) - \frac{\Lambda}{\sqrt{\Lambda^2+M^2_{0_f}}}\right). \tag{79}$$

Hence, the regularized chiral condensate of quark flavor $f$ for finite magnetic field and chiral chemical potential in MSS for vanishing quark chemical potential can be expressed as

$$\langle\bar\psi_f\psi_f\rangle^{\mu_5\neq0}_{B\neq0} = -\frac{M_f(M^2_{0_f}-M^2_f+2\mu_5^2)}{2}I_{1_{\mathrm{log}}} + I_{1_{\mathrm{finite1}}} + I_{1_{\mathrm{finite2}}} + I_{2_{\mathrm{finite}}} + I_{\mathrm{quad}} + \frac{N_c|q_f|B}{2\pi^2}\left[\int_{-\infty}^{\infty}dp_z\frac{M_f}{E^{(0)}_{p_z,f}}f_{FD}(E^{(0)}_{p_z,f}) + \sum_{n=1}^{\infty}\sum_s\int_{-\infty}^{\infty}dp_z\frac{M_f}{E^{(n)}_{p_z,s,f}}f_{FD}(E^{(n)}_{p_z,s,f})\right], \tag{80}$$

where regularized $I_{1_{\mathrm{log}}}$ and $I_{\mathrm{quad}}$ are given in Eqs. (77) and (74), respectively. This makes the expression for $\langle\bar\psi_f\psi_f\rangle^{\mu_5\neq0}_{B\neq0}$ finite which we shall use later for the calculation of constituent mass ($M_f$) for nonvanishing magnetic field and chiral chemical potential. Note that for the estimation of constituent mass ($M_f$) for nonvanishing magnetic field and chiral chemical potential, one requires constituent mass $M_{0_f}$ for nonvanishing magnetic field and vanishing chiral chemical potential, which can be obtained from Eq. (59).

## IV. CHIRAL SUSCEPTIBILITY

The fluctuations and correlations are an important characteristics of any physical system. They provide essential information about the effective d.o.f. and their possible quasiparticle nature. These fluctuations and correlations are connected with susceptibility. Susceptibility is the response of the system to small external force. The chiral susceptibility measures the response of the chiral condensate to the infinitesimal change of the current quark mass. Chiral susceptibility in two flavor NJL model can be defined as

$$\chi_c = \frac{\partial\langle\bar\psi\psi\rangle}{\partial m} = \frac{\partial\langle\bar\psi_u\psi_u\rangle}{\partial m} + \frac{\partial\langle\bar\psi_d\psi_d\rangle}{\partial m} = \chi_{cu} + \chi_{cd}. \tag{81}$$

Using Eq. (53), we get

$$\chi_{cu} = \frac{\partial\langle\bar\psi_u\psi_u\rangle}{\partial m} = \frac{\partial\langle\bar\psi_u\psi_u\rangle}{\partial M_u}\left(1-4G_1\frac{\partial\langle\bar\psi_u\psi_u\rangle}{\partial m}-4G_2\frac{\partial\langle\bar\psi_d\psi_d\rangle}{\partial m}\right) \tag{82}$$

and

$$\chi_{cd} = \frac{\partial\langle\bar\psi_d\psi_d\rangle}{\partial m} = \frac{\partial\langle\bar\psi_d\psi_d\rangle}{\partial M_d}\left(1-4G_1\frac{\partial\langle\bar\psi_d\psi_d\rangle}{\partial m}-4G_2\frac{\partial\langle\bar\psi_u\psi_u\rangle}{\partial m}\right). \tag{83}$$

Using Eq. (82), Eq. (83) solving for $\chi_{cu}$ and $\chi_{cd}$, we get

$$\chi_{cu} = \frac{\partial\langle\bar{\psi}_u\psi_u\rangle}{\partial M_u}\frac{1-4G_2\chi_{cd}}{1+4G_1\frac{\partial\langle\bar{\psi}_u\psi_u\rangle}{\partial M_u}} \tag{84}$$

and

$$\chi_{cd} = \frac{\partial\langle\bar{\psi}_d\psi_d\rangle}{\partial M_d}\frac{1-4G_2\chi_{cu}}{1+4G_1\frac{\partial\langle\bar{\psi}_d\psi_d\rangle}{\partial M_d}}. \tag{85}$$

Solving Eqs. (84) and (85), we get

$$\chi_{cu} = \frac{\partial\langle\bar{\psi}_u\psi_u\rangle}{\partial M_u}\left(\frac{1+4(G_1-G_2)\frac{\partial\langle\bar{\psi}_d\psi_d\rangle}{\partial M_d}}{(1+4G_1\frac{\partial\langle\bar{\psi}_u\psi_u\rangle}{\partial M_u})(1+4G_1\frac{\partial\langle\bar{\psi}_d\psi_d\rangle}{\partial M_d})-16G_2^2\frac{\partial\langle\bar{\psi}_u\psi_u\rangle}{\partial M_u}\frac{\partial\langle\bar{\psi}_d\psi_d\rangle}{\partial M_d}}\right), \tag{86}$$

$$\chi_{cd} = \frac{\partial\langle\bar{\psi}_d\psi_d\rangle}{\partial M_d}\left(\frac{1+4(G_1-G_2)\frac{\partial\langle\bar{\psi}_u\psi_u\rangle}{\partial M_u}}{(1+4G_1\frac{\partial\langle\bar{\psi}_u\psi_u\rangle}{\partial M_u})(1+4G_1\frac{\partial\langle\bar{\psi}_d\psi_d\rangle}{\partial M_d})-16G_2^2\frac{\partial\langle\bar{\psi}_u\psi_u\rangle}{\partial M_u}\frac{\partial\langle\bar{\psi}_d\psi_d\rangle}{\partial M_d}}\right). \tag{87}$$

It is clear from Eqs. (86) and (87) that to calculate chiral susceptibility for $u$ and $d$ quarks, we have to estimate $\frac{\partial\langle\bar{\psi}_f\psi_f\rangle}{\partial M_f}$. However, it is important to note that like chiral condensate, chiral susceptibility also contains ultraviolet divergence. Hence, $\frac{\partial\langle\bar{\psi}_f\psi_f\rangle}{\partial M_f}$ term also has to be regularized to get meaningful results. Using Eq. (59), for vanishing chemical potential ($\mu = 0$) and vanishing chiral chemical potential ($\mu_5 = 0$), in the presence of magnetic field, we get

$$\begin{aligned}\frac{\partial\langle\bar{\psi}_f\psi_f\rangle_{B\neq0}^{\mu_5=0}}{\partial M_{0_f}} =& -\frac{2N_c}{(2\pi)^3}\int_{|\vec{p}|\leq\Lambda}d^3p\left[\frac{1}{\sqrt{p^2+M_{0_f}^2}}-\frac{M_{0_f}^2}{\sqrt{(p^2+M_{0_f}^2)^3}}\right]\\ &-\frac{N_c|q_f|B}{2\pi^2}\left[x_{0_f}(1-\ln x_{0_f})+\ln\Gamma(x_{0_f})+\frac{1}{2}\ln\left(\frac{x_{0_f}}{2\pi}\right)\right]-\frac{N_cM_{0_f}^2}{2\pi^2}\left[-\ln x_{0_f}+\frac{1}{2x_{0_f}}+\frac{\Gamma'(x_{0_f})}{\Gamma(x_{0_f})}\right]\\ &+\sum_{n=0}^{\infty}\frac{N_c|q_f|B}{\pi^2}(2-\delta_{n,0})\int_0^\infty dp_z\left[\frac{1}{\epsilon_{p_z,f}^{(n)}}f_{FD}(\epsilon_{p_z,f}^{(n)})-\frac{M_{0_f}^2}{(\epsilon_{p_z,f}^{(n)})^3}f_{FD}(\epsilon_{p_z,f}^{(n)})\right.\\ &\left.-\frac{1}{T}\left(\frac{M_{0_f}}{\epsilon_{p_z,f}^{(n)}}\right)^2f_{FD}\left(\epsilon_{p_z,f}^{(n)}\right)(1-f_{FD}(\epsilon_{p_z,f}^{(n)}))\right].\end{aligned} \tag{88}$$

$\frac{\partial\langle\bar{\psi}_f\psi_f\rangle_{B\neq0}^{\mu_5=0}}{\partial M_{0_f}}$ as given in Eq. (88) is regularized and it can be used to calculate $\chi_{cu}$, $\chi_{cu}$ and chiral susceptibility $\chi_c$ for finite magnetic field, but vanishing chiral chemical potential. To estimate chiral susceptibility at finite magnetic field as well as nonvanishing chiral chemical potential, we have to estimate regularized $\frac{\partial\langle\bar{\psi}_f\psi_f\rangle}{\partial M_f}$ at finite $B$ and $\mu_5$. This regularization has been done using the MSS regularization scheme.

### A. Regularization of chiral susceptibility in the presence of magnetic field and chiral chemical potential

For nonvanishing magnetic field ($B$) and chiral chemical potential ($\mu_5$) for $\mu = 0$, using Eq. (55), the variation of chiral condensate with constituent quark mass can be written as

$$\frac{\partial\langle\bar{\psi}_f\psi_f\rangle_{B\neq0}^{\mu_5\neq0}}{\partial M_f} = \frac{\partial\langle\bar{\psi}_f\psi_f\rangle_{\mathrm{vac,B\neq0}}^{\mu_5\neq0}}{\partial M_f}+\frac{\partial\langle\bar{\psi}_f\psi_f\rangle_{\mathrm{med,B\neq0}}^{\mu_5\neq0}}{\partial M_f}. \tag{89}$$

Here, the first term is the "vacuum" term given as

$$\frac{\partial\langle\bar{\psi}_f\psi_f\rangle^{\mu_5\neq 0}_{\mathrm{vac,B}\neq 0}}{\partial M_f} = -\frac{N_c|q_f|B}{(2\pi)^2}\sum_{n=0}^{\infty}\sum_{s=\pm 1}\int dp_z\frac{1}{E^{(n)}_{p_z,s,f}} + \frac{N_c|q_f|B}{(2\pi)^2}\int dp_z\frac{1}{E^{(0)}_{p_z,f}} + \frac{N_c|q_f|B}{(2\pi)^2}\sum_{n=0}^{\infty}\sum_{s=\pm 1}\int dp_z\frac{M_f^2}{(E^{(n)}_{p_z,s,f})^3} - \frac{N_c|q_f|B}{(2\pi)^2}\int dp_z\frac{M_f^2}{(E^{(0)}_{p_z,f})^3} = \mathbf{I}_1+\mathbf{I}_2+\mathbf{I}_3+\mathbf{I}_4, \tag{90}$$

and the medium dependent term is given as

$$\begin{aligned}\frac{\partial\langle\bar{\psi}_f\psi_f\rangle^{\mu_5\neq 0}_{\mathrm{med,B}\neq 0}}{\partial M_f} &= \frac{N_c|q_f|B}{(2\pi)^2}\int dp_z\frac{1}{E^{(0)}_{p_z,f}}\left(2f_{FD}(E^{(0)}_{p_z,f})\right) - \frac{N_c|q_f|B}{(2\pi)^2}\int dp_z\frac{M_f^2}{(E^{(0)}_{p_z,f})^3}\left(2f_{FD}(E^{(0)}_{p_z,f})\right)\\
&- \frac{N_c|q_f|B}{(2\pi)^2}\int dp_z\frac{M_f^2}{(E^{(0)}_{p_z,f})^2}\left(\frac{2}{T}\right)f_{FD}\left(E^{(0)}_{p_z,f})(1-f_{FD}(E^{(0)}_{p_z,f})\right)\\
&+ \frac{N_c|q_f|B}{(2\pi)^2}\sum_{n=1}^{\infty}\sum_{s=\pm 1}\int dp_z\frac{1}{E^{(n)}_{p_z,s,f}}\left(2f_{FD}(E^{(n)}_{p_z,s,f})\right) - \frac{N_c|q_f|B}{(2\pi)^2}\sum_{n=1}^{\infty}\sum_{s=\pm 1}\int dp_z\frac{M_f^2}{(E^{(n)}_{p_z,s,f})^3}\left(2f_{FD}(E^{(n)}_{p_z,s,f})\right)\\
&- \frac{N_c|q_f|B}{(2\pi)^2}\sum_{n=1}^{\infty}\sum_{s=\pm 1}\int dp_z\frac{M_f^2}{(E^{(n)}_{p_z,s,f})^2}\left(\frac{2}{T}\right)f_{FD}(E^{(n)}_{p_z,s,f})\left(1-f_{FD}(E^{(n)}_{p_z,s,f})\right).\end{aligned} \tag{91}$$

The medium dependent term is convergent and does not need any regularization. The "vacuum" term, on the other hand, the integrals, $\mathbf{I}_1$, $\mathbf{I}_2$, and $\mathbf{I}_3$ are divergent and need regularization. We perform the MSS scheme as was done for the chiral condensate. The regularized $\frac{\partial\langle\bar{\psi}_f\psi_f\rangle^{\mu_5\neq 0}_{\mathrm{vac,B}\neq 0}}{\partial M_f}$ can be expressed as [see Appendix D, Eq. (D13)]

$$\frac{\partial\langle\bar{\psi}_f\psi_f\rangle^{\mu_5\neq 0}_{\mathrm{vac,B}\neq 0}}{\partial M_f} = -\left(\frac{M_{0_f}^2 - M_f^2 + 2\mu_5^2}{2}\right)\mathbf{I}_{1,\log} + \mathbf{I}_{1,\mathrm{finite1}} + \mathbf{I}_{1,\mathrm{finite2}} + \mathbf{I}_{2,\mathrm{finite}} + \mathbf{I}_{3,\mathrm{finite}} + \mathbf{I}_{\mathrm{finite}} + \mathbf{I}_{\mathrm{quad}} + \mathbf{I}_{\log}, \tag{92}$$

where regularized $\mathbf{I}_{\mathrm{quad}}, \mathbf{I}_{\log}, \mathbf{I}_{1,\log}$ can be expressed as (see Appendix D, Eqs. (D15)–(D17)]

$$\begin{aligned}\mathbf{I}_{\mathrm{quad}} &= -\frac{N_c|q_f|B}{(2\pi)^2}\sum_{n=0}^{\infty}\sum_{s=\pm 1}\int dp_z\frac{1}{\epsilon^{(n)}_{p_z,f}} + \frac{N_c|q_f|B}{(2\pi)^2}\int dp_z\frac{1}{\epsilon^{(0)}_{p_z,f}}\\
&= -\frac{N_c|q_f|B}{2\pi^2}\left[x_{0_f}(1-\ln x_{0_f}) + \ln\Gamma(x_{0_f}) + \frac{1}{2}\ln\left(\frac{x_{0_f}}{2\pi}\right)\right] - \frac{N_c}{2\pi^2}\left[\Lambda\sqrt{\Lambda^2+M_{0_f}^2} - M_{0_f}^2\ln\left(\frac{\Lambda+\sqrt{\Lambda^2+M_{0_f}}}{M_{0_f}}\right)\right],\end{aligned} \tag{93}$$

$$\begin{aligned}\mathbf{I}_{\log} &= \frac{N_c|q_f|B}{(2\pi)^2}\sum_{n=0}^{\infty}\sum_{s=\pm 1}\int dp_z\frac{M_f^2}{(\epsilon^{(n)}_{p_z,f})^3} - \frac{N_c|q_f|B}{(2\pi)^2}\int dp_z\frac{M_f^2}{(\epsilon^{(0)}_{p_z,f})^3}\\
&= -\frac{N_cM_f^2}{2\pi^2}\left[-\ln x_{0_f} + \frac{1}{2x_{0_f}} + \frac{\Gamma'(x_{0_f})}{\Gamma(x_{0_f})}\right] + \frac{N_cM_f^2}{\pi^2}\left[\ln\left(\frac{\Lambda+\sqrt{\Lambda^2+M_{0_f}^2}}{M_{0_f}}\right) - \frac{\Lambda}{\sqrt{\Lambda^2+M_{0_f}^2}}\right],\end{aligned} \tag{94}$$

$$\mathbf{I}_{1,\log} = \frac{N_c|q_f|B}{(2\pi)^2}\sum_{n=0}^{\infty}\sum_{s=\pm1}\int dp_z \frac{1}{(\epsilon^{(n)}_{p_z,f})^3}$$
$$= -\frac{N_c}{2\pi^2}\left[-\ln x_{0_f} + \frac{\Gamma'(x_{0_f})}{\Gamma(x_{0_f})}\right] + \frac{N_c}{\pi^2}\left[\ln\left(\frac{\Lambda + \sqrt{\Lambda^2 + M_{0_f}^2}}{M_{0_f}}\right) - \frac{\Lambda}{\sqrt{\Lambda^2 + M_{0_f}^2}}\right], \quad (95)$$

and the convergent integrals $\mathbf{I}_{1,\mathrm{finite1}}$, $\mathbf{I}_{1,\mathrm{finite2}}$, $\mathbf{I}_{2,\mathrm{finite}}$, $\mathbf{I}_{3,\mathrm{finite}}$, and $\mathbf{I}_{\mathrm{finite}}$ are given as

$$\mathbf{I}_{1,\mathrm{finite1}} = -\frac{N_c|q_f|B}{(2\pi)^2}\sum_{n=0}^{\infty}\sum_{s=\pm1}\int dp_z\left(\frac{3}{8}\right)\frac{A^2 - 4\mu_5^2 M_f^2}{(\epsilon^{(n)}_{p_z,f})^5}, \quad (96)$$

$$\mathbf{I}_{1,\mathrm{finite2}} = -\frac{N_c|q_f|B}{(2\pi)^2}\left(\frac{15}{16}\right)\sum_{n=0}^{\infty}\sum_{s=\pm1}\int dp_z\int_0^1 dx \frac{(1-x)^2\left(A + 2s\mu_5\sqrt{p_z^2 + 2n|q_f|B}\right)^3}{\left[\left(\epsilon^{(n)}_{p_z,f}\right)^2 - x\left(A + 2s\mu_5\sqrt{p_z^2 + 2n|q_f|B}\right)\right]^{7/2}} \quad (97)$$

$$\mathbf{I}_{2,\mathrm{finite}} = \left(\frac{1}{2}\right)\frac{N_c|q_f|B}{(2\pi)^2}\int dp_z\int_0^1 dx \frac{A + 2p_z\mu_5}{[(\epsilon^{(0)}_{p_z,f})^2 - x(A + 2p_z\mu_5)]^{3/2}}, \quad (98)$$

$$\mathbf{I}_{3,\mathrm{finite}} = \frac{N_c|q_f|B}{(2\pi)^2}\sum_{n=0}^{\infty}\sum_{s=\pm1}\int dp_z M_f^2\left(\frac{1}{(E^{(n)}_{p_z,s,f})^3} - \frac{1}{(\epsilon^{(n)}_{p_z,f})^3}\right), \quad (99)$$

$$\mathbf{I}_{\mathrm{finite}} = -\frac{N_c|q_f|B}{(2\pi)^2}\int dp_z M_f^2\left(\frac{1}{(E^{(0)}_{p_z,f})^3} - \frac{1}{(\epsilon^{(0)}_{p_z,f})^3}\right). \quad (100)$$

For nonvanishing magnetic field and chiral chemical potential Eq. (91), Eq. (92) along with Eqs. (86) and (87), can be used to calculate chiral susceptibility ($\chi_c$).

## V. RESULTS

Let us note that the Lagrangian as given in Eq. (51) has the following parameters, two couplings $G_1$, $G_2$, the three momentum cutoff $\Lambda$, and the current quark masses $m_u$ and $m_d$. To study the effects of flavor mixing, the couplings $G_1$ and $G_2$ are parametrized as $G_2 = \alpha g$, $G_1 = (1-\alpha)g$ [102]. The extent of flavor mixing is controlled by $\alpha$. For the numerical studies, we take the parameters $m_u = m_d = 6$ MeV, the three momentum cutoff $\Lambda = 590$ MeV, and the scalar coupling $g = 2.435/\Lambda^2$. For these values of the parameters, pion vacuum mass is 140.2 MeV, pion decay constant is 92.6 MeV, and the quark condensates are $\langle\bar{\psi}_u\psi_u\rangle = \langle\bar{\psi}_d\psi_d\rangle = (-241.5)$ MeV$^3$. This parameter set also leads to a vacuum constituent quark mass 400 MeV. It may be relevant here to mention that in the absence of magnetic field the two condensates $\langle\bar{\psi}_u\psi_u\rangle = \langle\bar{\psi}_d\psi_d\rangle$ and therefore the gap equation (53) depends upon the sum of the two couplings $(G_1 + G_2)$ which is independent of $\alpha$. Thus, the masses $M_u$ and $M_d$ are the same and do not depend upon $\alpha$ in the absence of magnetic field.

Next, we discuss about choosing the parameter $\alpha$. One can fix the parameter $\alpha$ from the mass of the isoscalar pseudoscalar particle that arises in the spectrum because of breaking of $U(1)_A$ symmetry. In a two flavor case, this meson can be identified with the $\eta$ meson. The mass of $\eta$ meson can be given approximately by [103]

$$m_\eta^2 = m_\pi^2 + \frac{G_2 M^2}{(G_1^2 - G_2^2)f_\pi^2}. \quad (101)$$

Clearly, for $\alpha = 0.5$, the $\eta$ meson disappears from the spectrum. With the physical mass of the $\eta$ meson ($m_\eta = 547.8$ MeV), the above equation leads to a value of $\alpha \simeq 0.09$. On the other hand, a description of $\eta$ meson without strange quarks is not realistic and therefore a better way to fix $\alpha$ is from the three flavor NJL model in which case the determinant interaction becomes a six fermion interaction and leads to $\eta - \eta'$ splitting. In such a case, e.g., the gap equation for $M_u$ becomes [102]

$$M_u = m_u - 4G\langle\bar{\psi}_u\psi_u\rangle + 2K\langle\bar{\psi}_s\psi_s\rangle\langle\bar{\psi}_d\psi_d\rangle. \quad (102)$$

Comparing the constituent quark mass as given in Eq. (53), we can identify $G_1 = G$ and $G_2 = -\frac{1}{2}K\phi_s$, where $\phi_s \equiv \langle \bar{\psi}_s \psi_s \rangle$ is the strange quark condensate. Thus, using the strange quark condensate, we can express $\alpha$ as [102]

$$\alpha = \frac{-\frac{1}{2} K \phi_s}{G - \frac{1}{2} K \phi_s}. \tag{103}$$

The parameters $G, K, \langle \bar{\psi}_s \psi_s \rangle$ are fixed from fitting the masses of the pseudoscalar octet. In particular, the determinant interaction parameter $K$ is fixed from the $\eta - \eta'$ mass difference. Even in such cases, the value of $\alpha$ can vary about 25%–30% (i.e., from $\alpha = 0.21$ to $\alpha = 0.16$) depending upon the parametrization chosen. This wide variation in $\alpha$ has to do with the different ways $\eta'$ is treated in the model. Since NJL model does not confine and $M_{\eta'}$ lies above, the threshold for $q\bar{q}$ decays with an unphysical imaginary part of the corresponding polarization diagram. This is an unavoidable feature of NJL model and leaves an uncertainty that is reflected in difference in the parameters of the determinant interaction. Further, it may be mentioned here that, in a different context of spontaneous $CP$ violation in strong interactions, in Ref. [112] it has been argued that $0 \leq \alpha \leq 0.5$ so that spontaneous parity violation is not there for QCD at zero temperature and density for $\theta = 0$ in accordance with Vafa-Witten theorem. In the present work, we have considered the cases when $\alpha = 0$, i.e., no flavor mixing, $\alpha = 0.5$ when both the couplings are same and a value for $\alpha = 0.15$ between these two limits to examine the effects of instanton induced flavor mixing interaction in the presence of magnetic field that breaks the isospin symmetry.

In Fig. 1, we show the variation of constituent quark masses and the associated chiral susceptibility as a function of temperature ($T$) for different values of chiral chemical potential ($\mu_5$) and for vanishing magnetic field. For zero magnetic field $\langle \bar{\psi}_u \psi_u \rangle = \langle \bar{\psi}_d \psi_d \rangle$, hence the masses of the $u$ and $d$ quarks remain same. From the left plot in Fig. 1, we can see that the constituent mass decreases with increasing chiral chemical potential. This decreasing behavior of the constituent quark mass with $\mu_5$ is in contrast with other calculations [57,95]. In contrast to Ref. [57], where the condensates increase with $\mu_5$ at lower temperature and decrease with $\mu_5$ at a higher temperature, we find the scalar condensate always decreases with $\mu_5$. Further, we also observe that the chiral transition is a smooth crossover as in Ref. [95] and no first order phase transition is seen even for $\mu_5$ as large as 0.4 GeV unlike in Ref. [57]. It ought to be mentioned here that while the vacuum mass satisfies a gap equation with a cutoff in the three momentum, for the thermal contribution no such cutoff was used, similar to Refs. [57,113], as the distribution functions make the corresponding contribution convergent.

The right plot in Fig. 1 shows the chiral susceptibility for vanishing quark chemical potential and magnetic field. Peak in the chiral susceptibility plot shows the chiral transition temperature. Using Eqs. (86) and (87), it can be shown that $\chi_{cu} = \chi_{cd}$ for vanishing magnetic field. Hence, the variation of total chiral susceptibility ($\chi_c$) with temperature shows only one peak. This behavior of chiral transition temperature decreasing with $\mu_5$ is similar to Ref. [54]. Further the height of the peak decreases with $\mu_5$ and we do not observe any sharp peak indicative of a first order transition. Absence of a first order transition with

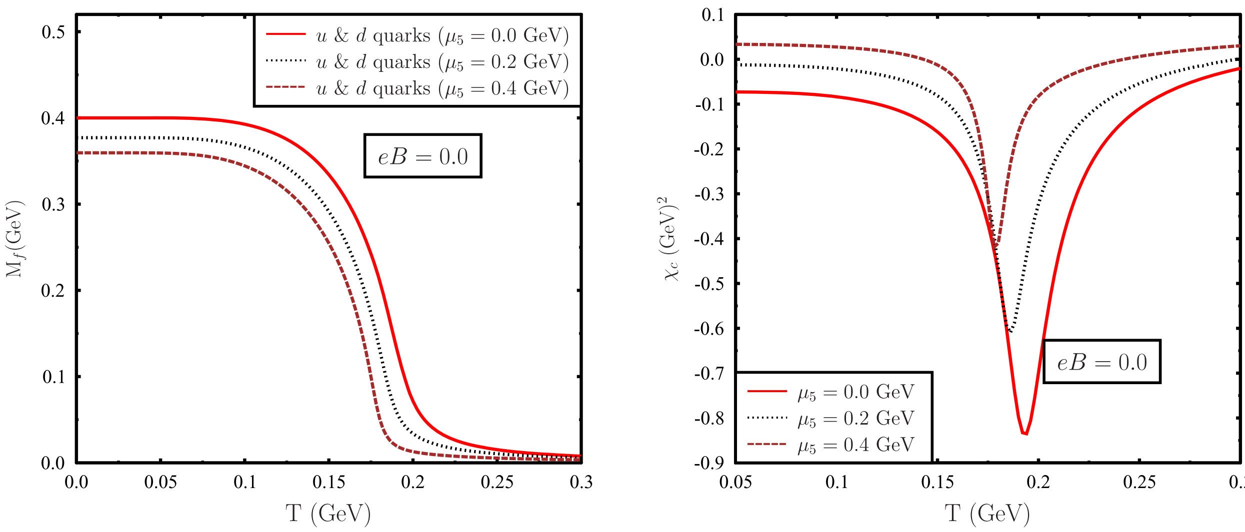


FIG. 1. Left plot: variation of constituent quark mass $M_u = M_d$ with temperature ($T$) for zero magnetic field but for various values of chiral chemical potential. Right plot: variation of chiral susceptibility $\chi_c$ with temperature ($T$) for zero magnetic field but with different values of chiral chemical potential. Prominent peak in the chiral susceptibility plot shows the chiral transition temperature. From the left plot, it is clear that with increasing chiral chemical potential ($\mu_5$) constituent mass decreases. From the susceptibility plot, it is clear that transition temperature decreases with chiral chemical potential.

large $\mu_5$ was also observed in Ref. [95]. However, in the presence of magnetic field, in general $\chi_{cu}$ can be different from $\chi_{cd}$ and variation of total chiral susceptibility $\chi_c$ with temperature can show multiple peaks. Results for non-vanishing magnetic field will be shown later. From the right plot in Fig. 1, it is clear that with increasing chiral chemical potential ($\mu_5$) chiral transition temperature decreases. We would like to mention here that in Ref. [57] for vanishing magnetic field, an opposite behavior regarding chiral transition temperature was observed, i.e., $T_c$ increases with $\mu_5$. However, the parameters of the NJL model chosen were different compared to the parameters taken here or in Ref. [102]. We have also verified that taking parameters of Ref. [57] $T_c$ increases with $\mu_5$.

It may be relevant here to compare this behavior of $T_c$ with $\mu_5$. Such a decreasing behavior of $T_c$ with $\mu_5$ was also observed in PNJL model; however, the nature of the transition was a first order transition at some critical value of chiral chemical potential [54]. On the other hand, a nonlocal NJL analysis showed the critical temperature to increase with $\mu_5$ [95]. A careful analysis in Ref. [57] shows different behavior of $T_c$ with $\mu_5$. In Ref. [57], it has been shown that if a cutoff is given to the thermal part also then $T_c$ increases with $\mu_5$ while not giving any cutoff decreases $T_c$ with $\mu_5$. On the other hand, we have applied here a medium separation scheme to remove cutoff artifact as was done in Refs. [59,98,99]. However, our result for vanishing magnetic field showed a opposite behavior, i.e., $T_c$ decreases with $\mu_5$. It turns out that the behavior of $T_c$ with $\mu_5$ depends upon the parameter chosen. A stronger scalar coupling as we have taken leads to $T_c$ decreasing with $\mu_5$, while a weaker scalar coupling shows a mild increase in $T_c$ with $\mu_5$ [59]. We therefore feel a deeper understanding is still required to understand the opposite behavior of $T_c$ with $\mu_5$ with change in the scalar coupling. With the parameters considered here, while the behavior of $T_c$ decreasing with $\mu_5$ is consistent with Ref. [57], the transition itself seems to be a smooth crossover leading to the absence of a critical point in the ($\mu_5$, $T$) plane of the phase diagram [57,95].

In Fig. 2, we show the variation of constituent quark masses $M_u$ and $M_d$ with temperature for vanishing chiral chemical potential and with finite magnetic field for different values of $\alpha$. From this figure, it is clear that at nonvanishing magnetic field constituent quark mass increases. At vanishing magnetic field, constituent mass of $u$ and $d$ quarks is the same. Although in the presence of magnetic field, quark condensates $\langle\bar{\psi}_u\psi_u\rangle \neq \langle\bar{\psi}_d\psi_d\rangle$, but for $\alpha = 0.5$ the quark masses $M_u = M_d$. This is because for $\alpha = 0.5$, constituent quark mass is $M_f = m - 2g(\langle\bar{\psi}_u\psi_u\rangle + \langle\bar{\psi}_d\psi_d\rangle)$, as can be seen from Eq. (53). On the other hand, for $\alpha \neq 0.5$ quark masses, $M_u$ and $M_d$ are not the same. The difference between $M_u$ and $M_d$ increases with decrease in the value of $\alpha$ and this difference is largest when $\alpha = 0.0$. $\alpha = 0.0$corresponds to the case when there is no flavor

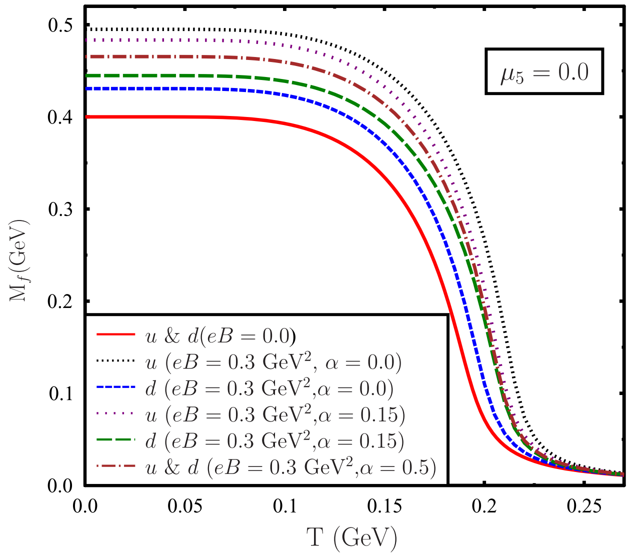


FIG. 2. Variation of constituent quark masses $M_u$ and $M_d$ with temperature for vanishing chiral chemical potential but with finite magnetic field for different values of $\alpha$. For vanishing magnetic field, $M_u$ and $M_d$ are same. Note that in the presence of magnetic field, for $\alpha = 0.5$, although $\langle\bar{\psi}_u\psi_u\rangle \neq \langle\bar{\psi}_d\psi_d\rangle$, but the constituent quark masses $M_u = M_d$. However, for $\alpha \neq 0.5$, the constituent quark masses $M_u \neq M_d$ in the presence of magnetic field. $\alpha = 0.0$ corresponds to the case when there is no flavor mixing interaction, and $\alpha = 0.5$ corresponds to maximal flavor mixing.

mixing interaction, and $\alpha = 0.5$ corresponds to maximal flavor mixing. It is important to note that for vanishing magnetic field, flavor mixing interaction does not affect the quark masses. Only in the presence of magnetic field when $\langle\bar{\psi}_u\psi_u\rangle \neq \langle\bar{\psi}_d\psi_d\rangle$, flavor mixing interaction affects the constituent quark masses $M_u$ and $M_d$ significantly.

In Fig. 3, we show the variation of constituent quark masses $M_u$ and $M_d$ and the associated total chiral susceptibility, with temperature for vanishing chiral chemical potential and with different values of magnetic field for $\alpha = 0.5$. It has been already mentioned that for $\alpha = 0.5$ even in the presence of magnetic field $M_u = M_d$. From the left plot in Fig. 3, it is clear that with increasing magnetic field constituent quark mass increases. On the other hand, from the right plot in Fig. 3, it is clear that chiral transition temperature increases with increasing magnetic field.

In Fig. 4, we show the variation of constituent quark masses $M_u$ and $M_d$ and the associated total chiral susceptibility, with temperature for vanishing chiral chemical potential and with different values of magnetic field for $\alpha = 0.0$. For $\alpha = 0.0$, there is no flavor mixing. From the left plot, it is clear that at finite magnetic field $M_u \neq M_d$. This is because in the presence of magnetic field $u$ and $d$ quark condensates are different and in the absence of flavor mixing for $\alpha = 0.0$, $M_u$ is independent of $\langle\bar{\psi}_d\psi_d\rangle$. Similarly, $M_d$ is independent of $\langle\bar{\psi}_u\psi_u\rangle$ for $\alpha = 0.0$. From the right plot in Fig. 4, it is clear that chiral transition

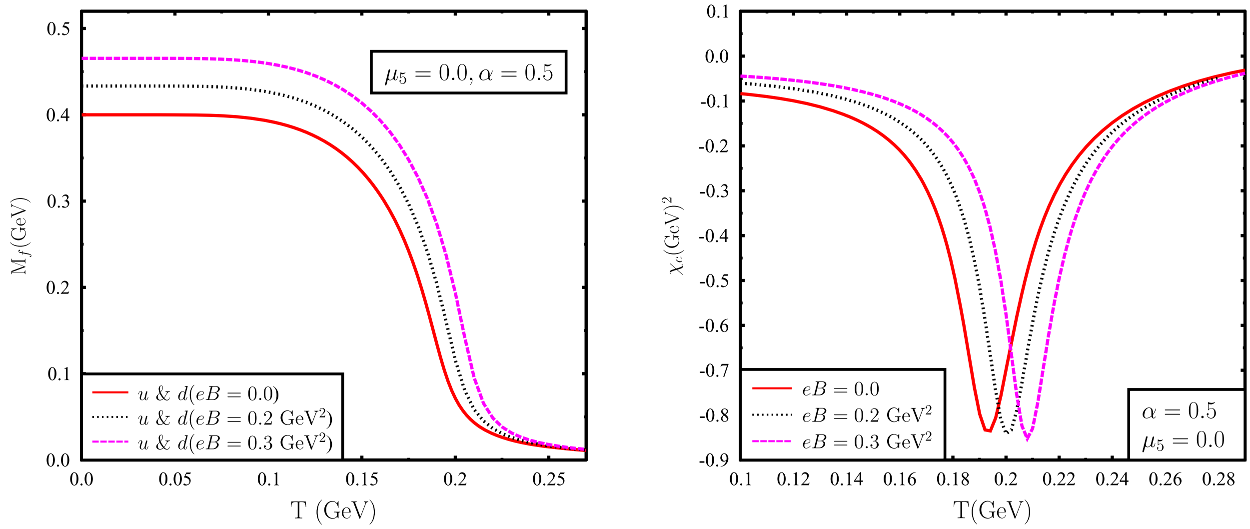


FIG. 3. Left plot: variation of constituent quark mass $M_u$ and $M_d$, with temperature for vanishing chiral chemical potential, but with different values of magnetic field for $\alpha = 0.5$. Right plot: variation of chiral susceptibility $\chi_c$ with temperature ($T$) for vanishing chiral chemical potential, but with different values of magnetic field for $\alpha = 0.5$. From the left plot, it is clear that with increasing magnetic field constituent mass $M_u = M_d$ increases. From the susceptibility plot, it is clear that transition temperature increases with magnetic field.

temperature increases with increasing magnetic field. However, it is important to mention that unlike the case when $\alpha = 0.5$, in this case the susceptibility plot shows two distinct peaks at relatively large magnetic field values. In fact, these two peaks are associated with $u$ and $d$ quarks, which have been shown in Fig. 5. In the left plot of Fig. 5, we show $\chi_{cu}$, $\chi_{cd}$, and $\chi_c$ for $eB = 0.4$ GeV$^2$ and $\alpha = 0.0$. On the other hand, in the right plot of Fig. 5, we show $\chi_{cu}$, $\chi_{cd}$, and $\chi_c$ for $eB = 0.4$ GeV$^2$ and $\alpha = 0.5$. From the left plot in Fig. 5, it is clear that for $\alpha = 0.0$, i.e., in the absence of flavor mixing, at relatively large magnetic field, chiral susceptibility $\chi_c$ shows two distinct peaks. These two peaks are associated with $u$ and $d$ quarks. At relatively large magnetic field with $\alpha = 0.0$, chiral restoration of $d$ quark happens at relatively low temperature with respect to the $u$ quarks. This is due to the fact that at nonzero magnetic field

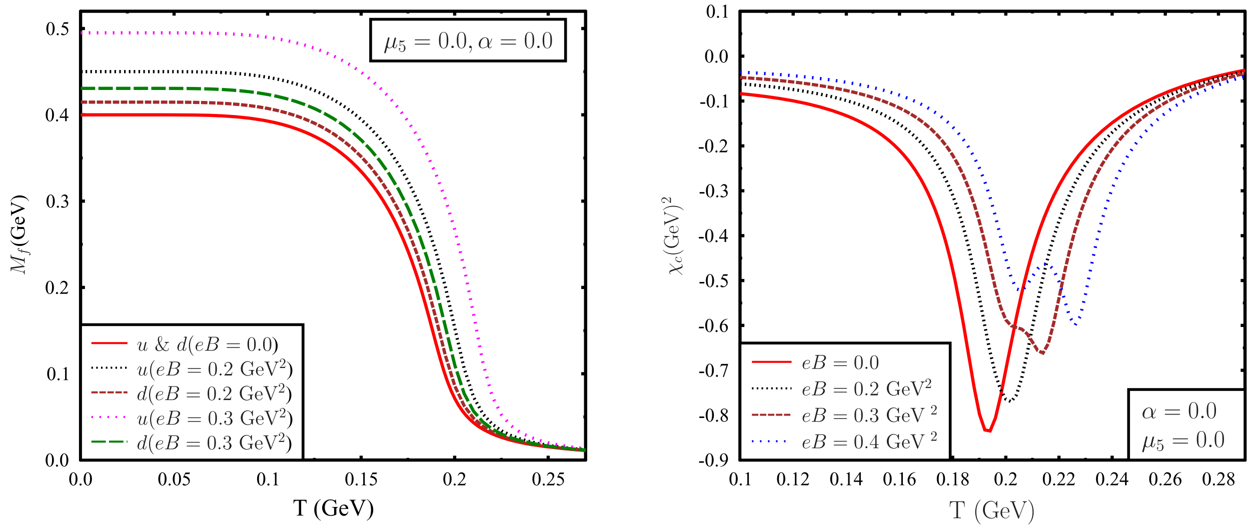


FIG. 4. Left plot: variation of constituent quark mass $M_u$ and $M_d$, with temperature for vanishing chiral chemical potential, but with different values of magnetic field for $\alpha = 0.0$. Right plot: variation of chiral susceptibility $\chi_c$ with temperature ($T$) for vanishing chiral chemical potential, but with different values of magnetic field for $\alpha = 0.0$. From the left plot, it is clear that with increasing magnetic field constituent mass increases. From the susceptibility plot, it is clear that transition temperature increases with magnetic field. In the right plot, we can observe two distinct peaks at relatively large magnetic fields.

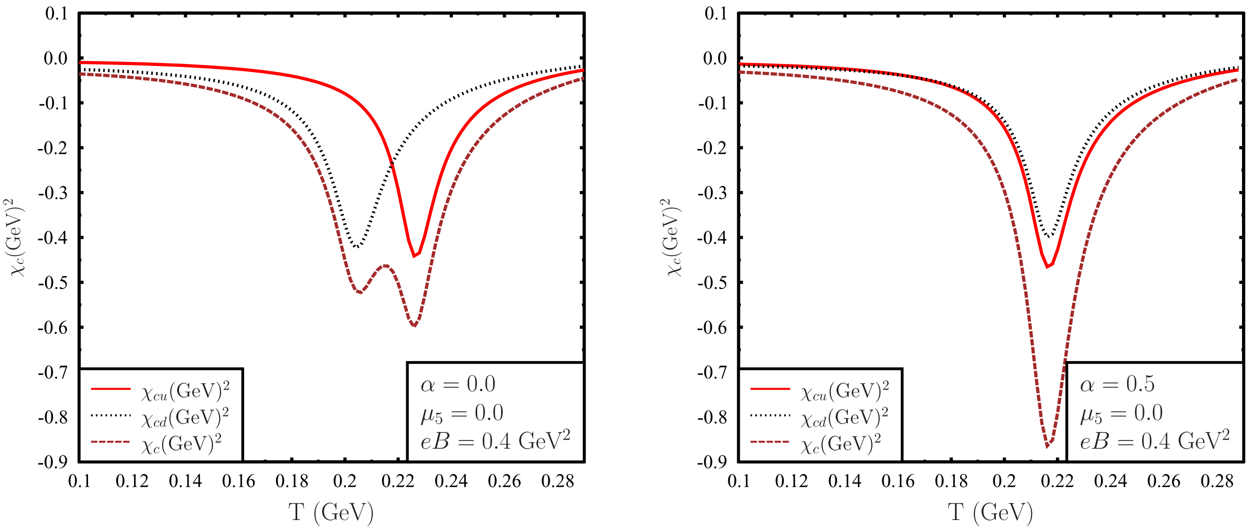


FIG. 5. Left plot: variation of $\chi_{cu}, \chi_{cd}$, and $\chi_c$ with temperature at vanishing chiral chemical potential for $eB = 0.4$ GeV$^2$ and $\alpha = 0.0$. Right plot: variation of $\chi_{cu}, \chi_{cd}$, and $\chi_c$ with temperature at vanishing chiral chemical potential for $eB = 0.4$ GeV$^2$ and $\alpha = 0.5$. From the left plot, it is clear that chiral susceptibility shows two distinct peaks at large magnetic field. This is due to the fact that at large magnetic field, difference between $M_u$ and $M_d$ is large. On the other hand, the right plot shows that for $\alpha = 0.5$, $\langle\bar{\psi}_u\psi_u\rangle \neq \langle\bar{\psi}_d\psi_d\rangle, \chi_{cu}$ and $\chi_{cd}$ show peak at same temperature. Hence, for $\alpha = 0.5$, at finite magnetic field, chiral transition temperature for $u$ and $d$ quarks is the same.

$M_u > M_d$, as can be seen in Fig. 4. On the other hand, from the right plot in Fig. 5, we can see that, although $\langle\bar{\psi}_u\psi_u\rangle \neq \langle\bar{\psi}_d\psi_d\rangle, \chi_{cu}$ and $\chi_{cd}$ show peak at same temperature. Hence, for $\alpha = 0.5$, at finite magnetic field, chiral transition temperature for $u$ and $d$ quarks is the same.

Finally, in Fig. 6, we show the variation of quark constituent masses $M_u$ and $M_d$ and the associated susceptibilities with temperature for finite magnetic field and finite chiral chemical potential for $\alpha = 0.5$. Behavior of quark constituent masses and the chiral susceptibilities with temperature are similar for other values of $\alpha$. The left plot in Fig. 6 shows that with increasing value of chiral chemical potential and for finite magnetic field constituent quark mass decreases.

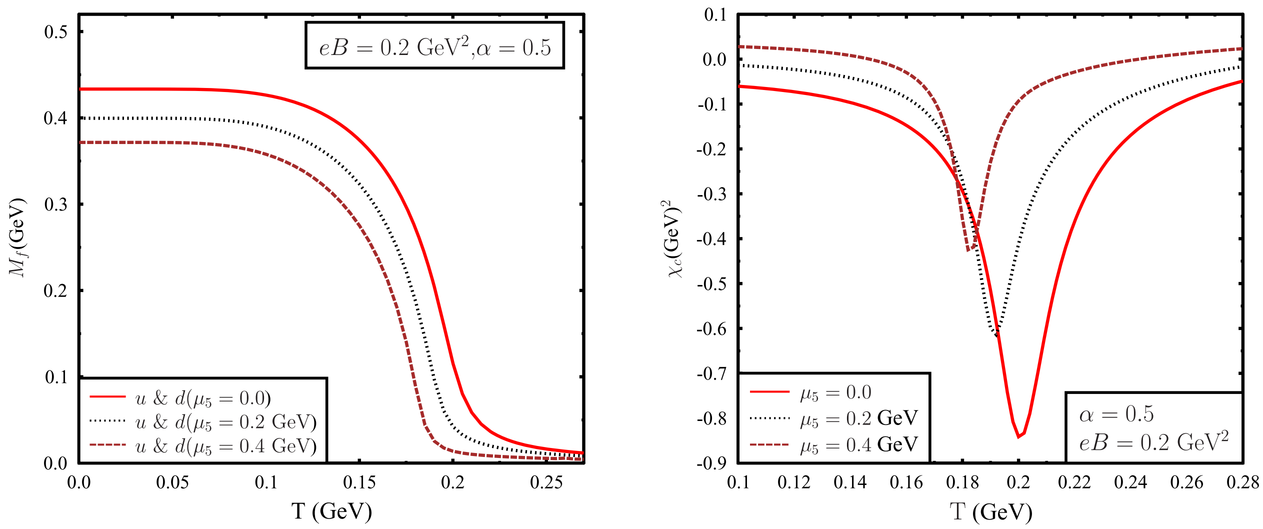


FIG. 6. Left plot: variation of constituent quark mass $M_u = M_d$, with temperature for finite magnetic field and finite chiral chemical potential. Right plot: variation of chiral susceptibility $\chi_c$ with temperature for finite magnetic field and finite chiral chemical potential. From this figure, it is clear that with increasing chiral chemical potential quark mass as well as the chiral transition temperature decreases.

This decrease in mass with increasing chiral chemical potential has also manifested in the right plot of Fig. 6, which shows that with increasing chiral chemical potential chiral transition temperature decreases.

## VI. CONCLUSION

In this investigation, we have studied chiral phase transition and the associated chiral susceptibility of the medium produced in ultrarelativistic heavy ion collisions at vanishing quark chemical potential using Wigner function approach within the framework of two flavor NJL model. For a dynamical system, like the medium produced in heavy ion collision, quantum effects can be relevant. Hence, the quantum kinetic equation is a suitable formalism to understand the evolution of these dynamical system. The central quantity of the quantum kinetic description is the Wigner function. Wigner function is the quantum mechanical analog of classical distribution function. Different components of Wigner function satisfies quantum kinetic equation. However, in this investigation, we have restricted ourselves to the case of global equilibrium so that $T$, $\mu_5$ are constant and we do not consider evolution of Wigner function. In fact, we could have done the analysis by estimating the mean field thermodynamic potential and minimizing the same to get the quark masses as well as the susceptibility.

We have looked into the behavior of quark masses and chiral susceptibility within a two flavor NJL model with flavor mixing determinant interaction. In the absence of magnetic field, $u$ and $d$ quark masses are degenerate, due to the isospin symmetry. However, in the presence of magnetic field, due to different electric charge of $u$ and $d$ quark, constituent mass of $u$ and $d$ quark can be different. Our results show that while flavor mixing instanton induced interaction does not affect the quark masses in the absence of magnetic field; however, in the presence of magnetic field, this interaction can affect quark masses. For maximal flavor mixing, i.e., $\alpha = 0.5$ in NJL model for a nonvanishing magnetic field, $u$ and $d$ quark masses are degenerate as the mass gap equation for $M_u$ and $M_d$ depend upon the sum of two condensates $(\langle\bar{\psi}_u\psi_u\rangle + \langle\bar{\psi}_d\psi_d\rangle)$. However, one has to keep in mind that this limiting case is not consistent with large $N_c$ limit of $G_1$ and $G_2$ as $G_1/G_2 \sim N_c$ at large $N_c$. For nonmaximal flavor mixing, quark masses are nondegenerate in the presence of magnetic field. Constituent mass of $u$ and $d$ quark is larger for nonvanishing magnetic field compared to $B = 0$ counterpart. With increasing magnetic field, constituent mass of $u$ and $d$ quark also increases. This apart the chiral transition temperature is higher for nonvanishing magnetic field as compared to the case of vanishing magnetic field. This is the manifestation of magnetic catalysis, i.e., in the presence of magnetic field the formation of chiral condensate is preferred even if the four Fermi coupling is below the critical coupling [25]. Further, the magnitude of the chiral condensate is higher for larger magnetic field. It is interesting to note that in the presence of nonmaximal flavor mixing instanton interaction, for vanishing magnetic field as well as for relatively small magnetic field, the chiral transition temperatures of $u$ and $d$ quark are the same. This is due to the fact that the mass difference between $u$ and $d$ quark arises due to the magnetic field and for weak magnetic field this difference is negligible and leads to the similar transition temperature. Only when this mass difference is large (due to strong enough magnetic field), one can have different transition temperature for two flavors. The difference between the transition temperature of $u$ and $d$ quark also increases with magnetic field. We have also shown that nonvanishing chiral chemical potential ($\mu_5$) reduces quark mass in the absence as well as in the presence of magnetic field. Unlike magnetic catalysis, with increasing chiral chemical potential ($\mu_5$), chiral transition temperature decreases. It is further observed that in the presence of magnetic field, the chiral susceptibility shows a double peak structure due to isospin breaking in the presence of magnetic field.

## ACKNOWLEDGMENTS

We thank Aman Abhishek for useful discussions on MSS used in this work and also thank Jitesh R. Bhatt for useful discussions on Wigner function formalism. We would also like to thank M. Ruggieri and R. L. S. Farias for their valuable comments.

## APPENDIX A: DERIVATION OF SCALAR CONDENSATE IN A BACKGROUND MAGNETIC FIELD AND CHIRAL CHEMICAL POTENTIAL

Scalar condensate in the terms of the scalar DHW function can be written as

$$\langle\bar{\psi}\psi\rangle = \int d^4pF(p). \tag{A1}$$

Using the explicit form of scalar DHW function ($F(p)$), as given in Eq. (43), scalar condensate in the presence of magnetic field, as given in Eq. (A1), can be expressed as

$$
\begin{aligned}
\langle\bar{\psi}\psi\rangle &= \int 2\pi p_T dp_0 dp_T dp_z M\left[\sum_{n=0}^{\infty} V_n(p_0,p_z)\Lambda_+^{(n)}(p_T) + \sum_{n=1}^{\infty}\frac{1}{\sqrt{p_z^2+2nqB}}A_n(p_0,p_z)p_z\Lambda_-^{(n)}(p_T)\right] \\
&= \int 2\pi p_T dp_0 dp_T dp_z M\Bigg[V_0(p_0,p_z)\Lambda_+^{(0)}(p_T) + \sum_{n=1}^{\infty} V_n(p_0,p_z)\Lambda_+^{(n)}(p_T) \\
&\quad + \sum_{n=1}^{\infty}\frac{1}{\sqrt{p_z^2+2nqB}}A_n(p_0,p_z)p_z\Lambda_-^{(n)}(p_T)\Bigg] \\
&= \mathbb{I}_1+\mathbb{I}_2+\mathbb{I}_3.
\end{aligned} \tag{A2}
$$

Now, the first term in Eq. (A2),

$$
\mathbb{I}_1 = 2\pi\iint dp_0 dp_z M V_0(p_0,p_z)\int dp_T p_T \Lambda_+^{(0)}(p_T). \tag{A3}
$$

Using the explicit form of $V_0(p_0,p_z)$ and $\Lambda_+^{(0)}(p_T)$, Eq. (A3) can be expressed as

$$
\begin{aligned}
\mathbb{I}_1 &= 2\pi\iint dp_0 dp_z \frac{2}{(2\pi)^3} M\delta\Big((p_0+\mu)^2-|E_{p_z}^{(0)}|^2\Big)[\theta(p_0+\mu)f_{FD}(p_0) \\
&\quad +\theta(-p_0-\mu)[f_{FD}(-p_0)-1]]\int dp_T p_T 2\exp[-p_T^2/qB] \\
&= \frac{qB}{(2\pi)^2}\int dp_z\frac{M}{E_{p_z}^{(0)}}\Big[f_{FD}(E_{p_z}^{(0)}-\mu)+f_{FD}(E_{p_z}^{(0)}+\mu)-1\Big].
\end{aligned} \tag{A4}
$$

The second term in Eq. (A2),

$$
\mathbb{I}_2 = 2\pi\sum_{n=1}^{\infty}\iint dp_0 dp_z M V_n(p_0,p_z)\int dp_T p_T\Lambda_+^{(n)}(p_T). \tag{A5}
$$

Using the explicit form of $\Lambda_+^{(n)}(p_T)$, one can calculate the following integral:

$$
\int dp_T p_T\Lambda_+^{(n)}(p_T) = (-1)^n\int_0^{\infty} dp_T p_T[L_n(2p_T^2/qB)-L_{n-1}(2p_T^2/qB)]\exp(-p_T^2/qB) = qB. \tag{A6}
$$

To get Eq. (A6), we use the following identity [114]:

$$
\int_0^{\infty} dx\,\exp(-bx)L_n(x) = (b-1)^n b^{-n-1}. \tag{A7}
$$

Using Eq. (A6) and the explicit form of $V_n(p_0,p_z)$, $\mathbb{I}_2$ can be written as

$$
\begin{aligned}
\mathbb{I}_2 &= 2\pi(qB)\iint dp_0 dp_z\frac{2}{(2\pi)^3}M\sum_s\delta((p_0+\mu)^2-|E_{p_z,s}^{(n)}|^2)[\theta(p_0+\mu)f_{FD}(p_0)+\theta(-p_0-\mu)(f_{FD}(-p_0)-1)] \\
&= -\frac{qB}{(2\pi)^2}\sum_{n=1}^{\infty}\sum_s\int dp_z\frac{M}{E_{pz,s}^{(n)}}\Big[1-f_{FD}(E_{p_z,s}^{(n)}-\mu)-f_{FD}(E_{p_z,s}^{(n)}+\mu)\Big].
\end{aligned} \tag{A8}
$$

Now let us consider the third term of Eq. (A2),

$$
\mathbb{I}_3 = 2\pi\iint dp_0 dp_z M\sum_{n=1}^{\infty}\frac{1}{\sqrt{p_z^2+2nqB}}A_n(p_0,p_z)p_z\int dp_T p_T\Lambda_-^{(n)}(p_T). \tag{A9}
$$

Using the explicit form of $\Lambda_{-}^{(n)}(p_T)$, it can be shown that

$$\int dp_T p_T \Lambda_{-}^{(n)}(p_T) = 0. \tag{A10}$$

Hence, the third term of Eq. (A2),

$$\mathbb{I}_3 = 0. \tag{A11}$$

Hence, using Eqs. (A4), (A8), and (A11), the scalar condensate is

$$\begin{aligned}\langle\bar{\psi}\psi\rangle = &-\frac{qB}{(2\pi)^2}\int dp_z \frac{M}{E_{p_z}^{(0)}}\left[1 - f_{FD}(E_{p_z}^{(0)} - \mu) - f_{FD}(E_{p_z}^{(0)} + \mu)\right] \\ &-\frac{qB}{(2\pi)^2}\sum_{n=1}^{\infty}\sum_{s}\int dp_z \frac{M}{E_{p_z,s}^{(n)}}\left[1 - f_{FD}(E_{p_z,s}^{(n)} - \mu) - f_{FD}(E_{p_z,s}^{(n)} + \mu)\right].\end{aligned} \tag{A12}$$

## APPENDIX B: REGULARIZATION OF CHIRAL CONDENSATE IN A BACKGROUND MAGNETIC FIELD

The scalar condensate of a quark of flavor $f$, with $N_c$ color d.o.f. at finite temperature ($T$), chemical potential ($\mu$) can be expressed as

$$\begin{aligned}\langle\bar{\psi}_f\psi_f\rangle_{B\neq 0}^{\mu_5=0} &= -\frac{N_c|q_f|B}{(2\pi)^2}\sum_{n=0}^{\infty}(2-\delta_{n,0})\int dp_z \frac{M_{0_f}}{\epsilon_{p_z,f}^{(n)}}\left[1 - f_{FD}\left(\epsilon_{p_z,f}^{(n)} - \mu\right) - f_{FD}\left(\epsilon_{p_z,f}^{(n)} + \mu\right)\right] \\ &= \langle\bar{\psi}_f\psi_f\rangle_{\mathrm{vac,B\neq 0}}^{\mu_5=0} + \langle\bar{\psi}_f\psi_f\rangle_{\mathrm{med,B\neq 0}}^{\mu_5=0},\end{aligned} \tag{B1}$$

where $\langle\bar{\psi}_f\psi_f\rangle_{\mathrm{vac,B\neq 0}}^{\mu_5=0}$ is the $T = 0$, $\mu = 0$ part, or the vacuum part of the scalar condensate, and $\langle\bar{\psi}_f\psi_f\rangle_{\mathrm{med,B\neq 0}}^{\mu_5=0}$ is the finite temperature and finite chemical potential part or the medium part of the scalar condensate in the presence of magnetic field. It is clear from Eq. (B1) the vacuum term is divergent for large momenta and however because of the distribution functions the medium part in Eq. (B1) is not. Hence, it is important to regulate the vacuum part in Eq. (B1).

Let us consider the vacuum part $\langle\bar{\psi}_f\psi_f\rangle_{\mathrm{vac,B\neq 0}}^{\mu_5=0}$, which is given as

$$\begin{aligned}\langle\bar{\psi}_f\psi_f\rangle_{\mathrm{vac,B\neq 0}}^{\mu_5=0} &= -\frac{N_c}{2\pi}\sum_{n=0}^{\infty}(2-\delta_{n,0})|q_f|B\int_{-\infty}^{\infty}\frac{dp_z}{(2\pi)}\frac{M_{0_f}}{\epsilon_{p_z,f}^{(n)}} \\ &= -\frac{N_c}{2\pi}\sum_{n=0}^{\infty}2|q_f|B\int_{-\infty}^{\infty}\frac{dp_z}{(2\pi)}\frac{M_{0_f}}{\epsilon_{p_z,f}^{(n)}} + \frac{N_c}{2\pi}|q_f|B\int_{-\infty}^{\infty}\frac{dp_z}{(2\pi)}\frac{M_{0_f}}{\epsilon_{p_z,f}^{(0)}} \\ &= \mathcal{I}_1 + \mathcal{I}_2.\end{aligned} \tag{B2}$$

Both integrals $\mathcal{I}_1$ and $\mathcal{I}_2$ are divergent at large momentum. These integrals can be regularized using dimensional regularization scheme. In this regularization scheme, integral $\mathcal{I}_1$ can be expressed as

$$\begin{aligned}\mathcal{I}_1 &= -\frac{N_c}{2\pi}\sum_{n=0}^{\infty}2|q_f|B\int_{-\infty}^{\infty}\frac{dp_z}{(2\pi)}\frac{M_{0_f}}{\epsilon_{p_z,f}^{(n)}} \\ &= -\frac{N_c}{2\pi}\sum_{n=0}^{\infty}2|q_f|B\frac{M_{0_f}\Gamma(\epsilon/2)}{(4\pi)^{(1-\epsilon)/2}\Gamma(1/2)(x_{0_f}+n)^{\epsilon/2}},\end{aligned} \tag{B3}$$

where the dimensionless variable $x_{0_f} \equiv M_{0_f}^2/2|q_f|B$. Similarly, the integral $\mathcal{I}_2$ can be expressed as

$$\begin{aligned}\mathcal{I}_2 &= \frac{N_c}{2\pi}|q_f|B\int\frac{dp_z}{(2\pi)}\frac{M_{0_f}}{\sqrt{M_{0_f}^2+p_z^2}}\\ &= \frac{N_cM_{0_f}|q_f|B}{(2\pi)}\frac{\Gamma(\epsilon/2)}{(4\pi)^{(1-\epsilon)/2}\Gamma(1/2)x_{0_f}^{\epsilon/2}}.\end{aligned}\tag{B4}$$

Using Eqs. (B3) and (B4), vacuum part of the scalar condensate in the presence of magnetic field as given in Eq. (B2) can be recasted as

$$\begin{aligned}\mathcal{I}_1+\mathcal{I}_2 &= -\frac{N_c}{2\pi}2|q_f|BM_{0_f}\frac{\Gamma(\epsilon/2)}{(4\pi)^{(1-\epsilon)/2}\Gamma(1/2)}\left[\sum_{n=0}^{\infty}\frac{1}{(x_{0_f}+n)^{\epsilon/2}}-\frac{1}{2x_{0_f}^{\epsilon/2}}\right]\\ &= -\frac{N_c}{2\pi}2|q_f|BM_{0_f}\frac{\Gamma(\epsilon/2)}{(4\pi)^{1/2}\Gamma(1/2)}\left[\zeta(\epsilon/2,x_{0_f})-\frac{1}{2x_{0_f}^{\epsilon/2}}\right].\end{aligned}\tag{B5}$$

Expanding the right-hand side of Eq. (B5) around $\epsilon\to 0$ and keeping only the leading order terms, we get

$$\mathcal{I}_1+\mathcal{I}_2 = -\frac{N_c}{2\pi^2}|q_f|BM_{0_f}\left[-\frac{2x_{0_f}}{\epsilon}+\gamma_Ex_{0_f}+\frac{1}{2}\ln x_{0_f}+\ln\Gamma(x_{0_f})-\frac{1}{2}\ln(2\pi)\right].\tag{B6}$$

In Eq. (B5), we have used the representation of zeta function, which is given as [115]

$$\zeta(a,x)=\sum_{n=0}^{\infty}\frac{1}{(x+n)^a}.\tag{B7}$$

Also, we have used the following identities to get Eq. (B6):

$$\zeta(0,x)=\left(\frac{1}{2}-x\right),\quad \text{and,}\quad \zeta'(0,x)=\ln\Gamma(x)-\frac{1}{2}\ln(2\pi),\quad \text{where } \zeta'(0,x)=\left.\frac{d\zeta(a,x)}{da}\right|_{a=0}.\tag{B8}$$

It is clear from Eq. (B6) that the vacuum part has $1/\epsilon$ divergent part. To remove this $1/\epsilon$ divergence, we use the following integral:

$$\mathcal{I}_3=-2N_c\int\frac{d^3p}{(2\pi)^3}\frac{M_{0_f}}{\sqrt{p^2+M_{0_f}^2}}.\tag{B9}$$

Using dimensional regularization method, the integral in Eq. (B9) can be recasted as

$$\mathcal{I}_3=\frac{-2N_cM_{0_f}}{(4\pi)^{3/2}\Gamma(1/2)}\frac{\Gamma(-1+\epsilon/2)}{(2x_{0_f}|q_f|B)^{-1+\epsilon/2}}.\tag{B10}$$

Expand the right-hand side of Eq. (B10) around $\epsilon\to 0$ and keeping only the leading order terms, we get

$$\mathcal{I}_3=\frac{-N_cM_{0_f}|q_f|B}{2\pi^2}\left[-\frac{2x_{0_f}}{\epsilon}-x_{0_f}+x_{0_f}\gamma_E+x_{0_f}\ln x_{0_f}\right].\tag{B11}$$

Using Eqs. (B6) and (B11), we get

$$\mathcal{I}_1+\mathcal{I}_2-\mathcal{I}_3=-\frac{N_cM_{0_f}|q_f|B}{2\pi^2}\left[x_{0_f}(1-\ln x_{0_f})+\ln\Gamma(x_{0_f})+\frac{1}{2}\ln\left(\frac{x_{0_f}}{2\pi}\right)\right].\tag{B12}$$

Using Eqs. (B2) and (B12), we have the regularized vacuum part of the scalar condensate in the presence of magnetic field and is given as

$$\begin{aligned}\langle\bar{\psi}_f\psi_f\rangle^{\mu_5=0}_{\text{vac,B}\neq 0} &= \mathcal{I}_1+\mathcal{I}_2-\mathcal{I}_3+\mathcal{I}_3\\ &= -\frac{N_cM_{0_f}|q_f|B}{2\pi^2}\left[x_{0_f}(1-\ln x_{0_f})+\ln\Gamma(x_{0_f})+\frac{1}{2}\ln\left(\frac{x_{0_f}}{2\pi}\right)\right]-2N_c\int_{|\vec{p}|\leq\Lambda}\frac{d^3p}{(2\pi)^3}\frac{M_{0_f}}{\sqrt{p^2+M_{0_f}^2}}.\end{aligned} \tag{B13}$$

Again,

$$\begin{aligned}\mathcal{I}_1 &= \mathcal{I}_1-\mathcal{I}_3+\mathcal{I}_3\\ &= -\frac{N_c|q_f|BM_{0_f}}{2\pi^2}\left[\frac{1}{\epsilon}-\frac{\gamma_E}{2}+x_{0_f}(1-\ln x_{0_f})+\ln\Gamma(x_{0_f})-\frac{1}{2}\ln(2\pi)\right]-2N_c\int\frac{d^3p}{(2\pi)^3}\frac{M_{0_f}}{\sqrt{p^2+M_{0_f}^2}}.\end{aligned} \tag{B14}$$

Hence,

$$\begin{aligned}\mathcal{I} &\equiv -\frac{N_c|q_f|B}{(2\pi)^2}\sum_{s=\pm1}\sum_{n=0}^{\infty}\int dp_z\frac{1}{\sqrt{p_z^2+M_{0_f}^2+2n|q_f|B}}\\ &= -\frac{N_c}{2\pi^2}|q_f|B\left[\frac{1}{\epsilon}-\frac{\gamma_E}{2}+x_{0_f}(1-\ln x_{0_f})+\ln\Gamma(x_{0_f})-\frac{1}{2}\ln(2\pi)\right]-2N_c\int\frac{d^3p}{(2\pi)^3}\frac{1}{\sqrt{p^2+M_{0_f}^2}}.\end{aligned} \tag{B15}$$

Using Eq. (B15), we get

$$\begin{aligned}\frac{N_c|q_f|B}{(2\pi)^2}\sum_{s=\pm1}\sum_{n=0}^{\infty}\int dp_z\frac{1}{(p_z^2+M_{0_f}^2+2n|q_f|B)^{3/2}} &\equiv \frac{1}{M_{0_f}}\frac{\partial\mathcal{I}}{\partial M_{0_f}}\\ &= -\frac{N_c}{2\pi^2}\left[-\ln x_{0_f}+\frac{\Gamma'(x_{0_f})}{\Gamma(x_{0_f})}\right]+2N_c\int_{|\vec{p}|\leq\Lambda}\frac{d^3p}{(2\pi)^3}\frac{1}{(p^2+M_{0_f}^2)^{3/2}}.\end{aligned} \tag{B16}$$

## APPENDIX C: REGULARIZATION OF CHIRAL CONDENSATE IN A BACKGROUND MAGNETIC FIELD AND CHIRAL CHEMICAL POTENTIAL

The scalar condensate of a quark of flavor $f$ with $N_c$ color d.o.f. at finite temperature ($T$), quark chemical potential ($\mu$), chiral chemical potential ($\mu_5$), electric charge ($q_f$), and magnetic field ($B$) can be expressed as

$$\begin{aligned}\langle\bar{\psi}_f\psi_f\rangle^{\mu_5\neq0}_{B\neq0} &= -\frac{N_c|q_f|B}{(2\pi)^2}\left[\int dp_z\frac{M_f}{E^{(0)}_{p_z,f}}\left[1-f_{FD}\left(E^{(0)}_{p_z,f}-\mu\right)-f_{FD}\left(E^{(0)}_{p_z,f}+\mu\right)\right]\right.\\ &\quad\left.+\sum_{n=1}^{\infty}\sum_{s}\int dp_z\frac{M_f}{E^{(n)}_{p_z,s,f}}\left[1-f_{FD}\left(E^{(n)}_{p_z,s,f}-\mu\right)-f_{FD}\left(E^{(n)}_{p_z,s,f}+\mu\right)\right]\right]\\ &= \langle\bar{\psi}_f\psi_f\rangle^{\mu_5\neq0}_{\text{vac,B}\neq0}+\langle\bar{\psi}_f\psi_f\rangle^{\mu_5\neq0}_{\text{med,B}\neq0},\end{aligned} \tag{C1}$$

where $\langle\bar{\psi}_f\psi_f\rangle^{\mu_5\neq0}_{\text{vac,B}\neq0}$ is the $T=0$, $\mu=0$ part or the vacuum part of the scalar condensate, and $\langle\bar{\psi}_f\psi_f\rangle^{\mu_5\neq0}_{\text{med,B}\neq0}$ is the finite temperature and finite chemical potential part or the medium part of the scalar condensate in the presence of magnetic field and chiral chemical potential ($\mu_5$). It is clear from Eq. (C1) that the vacuum term is divergent at large momenta and however because of the distribution functions the medium part in Eq. (C1) is not. Hence, the vacuum term has to be regularized.

The vacuum term in the presence of magnetic field and chiral chemical potential can be expressed as

$$\begin{aligned}\langle\bar{\psi}_f\psi_f\rangle^{\mu_5\neq0}_{\mathrm{vac},B\neq0} &= -N_c\frac{|q_f|B}{(2\pi)^2}\int dp_z\frac{M_f}{\sqrt{M_f^2+(p_z-\mu_5)^2}} - N_c\frac{|q_f|B}{(2\pi)^2}\sum_{n=1}^{\infty}\sum_{s=\pm1}\int dp_z\frac{M_f}{\sqrt{M_f^2+\left(\sqrt{p_z^2+2n|q_f|B}-s\mu_5\right)^2}}\\ &= -N_c\frac{|q_f|B}{(2\pi)^2}\sum_{n=0}^{\infty}\sum_{s=\pm1}\int dp_z\frac{M_f}{\sqrt{M_f^2+\left(\sqrt{p_z^2+2n|q_f|B}-s\mu_5\right)^2}} + N_c\frac{|q_f|B}{(2\pi)^2}\int dp_z\frac{M_f}{\sqrt{M_f^2+(p_z-\mu_5)^2}}\\ &= -N_c\frac{|q_f|B}{(2\pi)^2}\sum_{n=0}^{\infty}\sum_{s=\pm1}\int dp_z\frac{1}{\pi}\int_{-\infty}^{\infty}dp_4\frac{M_f}{p_4^2+\left(M_f^2+\left(\sqrt{p_z^2+2n|q_f|B}-s\mu_5\right)^2\right)}\\ &\quad + N_c\frac{|q_f|B}{(2\pi)^2}\int dp_z\frac{1}{\pi}\int_{-\infty}^{\infty}dp_4\frac{M_f}{p_4^2+M_f^2+(p_z-\mu_5)^2}\\ &= I_1+I_2. \end{aligned} \tag{C2}$$

Using the regularization method discussed in Ref. [59], we can write the integrand of the integral $I_1$ as given in the Eq. (C2) as follows:

$$\begin{aligned}&\frac{1}{p_4^2+M_f^2+\left(\sqrt{p_z^2+2n|q_f|B}-s\mu_5\right)^2}\\ &\quad=\frac{1}{p_4^2+p_z^2+M_{0_f}^2+2n|q_f|B}-\frac{1}{p_4^2+p_z^2+M_{0_f}^2+2n|q_f|B}+\frac{1}{p_4^2+M_f^2+\left(\sqrt{p_z^2+2n|q_f|B}-s\mu_5\right)^2}\\ &\quad=\frac{1}{p_4^2+p_z^2+M_{0_f}^2+2n|q_f|B}+\frac{M_{0_f}^2-M_f^2-\mu_5^2+2s\mu_5\sqrt{p_z^2+2n|q_f|B}}{(p_4^2+p_z^2+M_{0_f}^2+2n|q_f|B)\left(p_4^2+M_f^2+\left(\sqrt{p_z^2+2n|q_f|B}-s\mu_5\right)^2\right)}. \end{aligned} \tag{C3}$$

Using Eq. (C3) twice, we can write the integrand of the integral $I_1$ in the following way:

$$\begin{aligned}\frac{1}{p_4^2+M_f^2+\left(\sqrt{p_z^2+2n|q_f|B}-s\mu_5\right)^2} &= \frac{1}{p_4^2+p_z^2+M_{0_f}^2+2n|q_f|B}+\frac{A+2s\mu_5\sqrt{p_z^2+2n|q_f|B}}{(p_4^2+p_z^2+M_{0_f}^2+2n|q_f|B)^2}\\ &\quad+\frac{\left(A+2s\mu_5\sqrt{p_z^2+2n|q_f|B}\right)^2}{(p_4^2+p_z^2+M_{0_f}^2+2n|q_f|B)^3}\\ &\quad+\frac{\left(A+2s\mu_5\sqrt{p_z^2+2n|q_f|B}\right)^3}{(p_4^2+p_z^2+M_{0_f}^2+2n|q_f|B)^3\left(p_4^2+M_f^2+\left(\sqrt{p_z^2+2n|q_f|B}-s\mu_5\right)^2\right)}, \end{aligned} \tag{C4}$$

where $A=M_{0_f}^2-M_f^2-\mu_5^2$. Performing $p_4$ integration in each term of Eq. (C4), we get

$$\frac{1}{\pi}\sum_s\int dp_4\frac{1}{p_4^2+p_z^2+M_{0_f}^2+2n|q_f|B}=\sum_s\frac{1}{\sqrt{p_z^2+M_{0_f}^2+2n|q_f|B}} \tag{C5}$$

$$\frac{1}{\pi}\sum_s \int dp_4 \frac{A+2s\mu_5\sqrt{p_z^2+2n|q_f|B}}{(p_4^2+p_z^2+M_{0_f}^2+2n|q_f|B)^2} = \sum_s \frac{1}{2}\frac{A}{(p_z^2+M_{0_f}^2+2n|q_f|B)^{3/2}} \tag{C6}$$

$$\frac{1}{\pi}\sum_s \int dp_4 \frac{\left(A+2s\mu_5\sqrt{p_z^2+2n|q_f|B}\right)^2}{(p_4^2+p_z^2+M_{0_f}^2+2n|q_f|B)^3} = \sum_s \left[\frac{3}{8}\frac{A^2}{(p_z^2+M_{0_f}^2+2n|q_f|B)^{5/2}} - \frac{3}{2}\frac{\mu_5^2 M_{0_f}^2}{(p_z^2+M_{0_f}^2+2n|q_f|B)^{5/2}} + \frac{3}{2}\frac{\mu_5^2}{(p_z^2+M_{0_f}^2+2n|q_f|B)^{3/2}}\right] \tag{C7}$$

$$\begin{aligned}
&\frac{1}{\pi}\sum_s \int dp_4 \frac{\left(A+2s\mu_5\sqrt{p_z^2+2n|q_f|B}\right)^3}{(p_4^2+p_z^2+M_{0_f}^2+2n|q_f|B)^3\left(p_4^2+M_f^2+\left(\sqrt{p_z^2+2n|q_f|B}-s\mu_5\right)^2\right)}\\
&= \frac{1}{\pi}\sum_s \int dp_4 \int_0^1 dx \frac{3(1-x)^2\left(A+2s\mu_5\sqrt{p_z^2+2n|q_f|B}\right)^3}{\left[x\left(p_4^2+M_f^2+\left(\sqrt{p_z^2+2n|q_f|B}-s\mu_5\right)^2\right)+(1-x)(p_4^2+p_z^2+M_{0_f}^2+2n|q_f|B)\right]^4}\\
&= \sum_s \frac{15}{16}\int_0^1 dx \frac{(1-x)^2\left(A+2s\mu_5\sqrt{p_z^2+2n|q_f|B}\right)^3}{\left[p_z^2+M_{0_f}^2+2n|q_f|B-x\left(A+2s\mu_5\sqrt{p_z^2+2n|q_f|B}\right)\right]^{7/2}}.
\end{aligned} \tag{C8}$$

Using Eqs. (C5)–(C8), integral $I_1$ in Eq. (C2) can be expressed as

$$\begin{aligned}
I_1 &= -N_c\frac{|q_f|B}{(2\pi)^2}\sum_{n=0}^{\infty}\sum_{s=\pm1}\int dp_z \frac{M_f}{\sqrt{M_f^2+\left(\sqrt{p_z^2+2n|q_f|B}-s\mu_5\right)^2}}\\
&= I_{1_{\mathrm{quad}}} - \frac{M_f(M_{0_f}^2-M_f^2+2\mu_5^2)}{2}I_{1_{\mathrm{log}}} + I_{1_{\mathrm{finite1}}} + I_{1_{\mathrm{finite2}}},
\end{aligned} \tag{C9}$$

where

$$I_{1_{\mathrm{quad}}} = -N_c\frac{|q_f|B}{(2\pi)^2}\sum_{n=0}^{\infty}\sum_{s=\pm1}\int dp_z \frac{M_f}{\sqrt{p_z^2+M_{0_f}^2+2n|q_f|B}}, \tag{C10}$$

$$I_{1_{\mathrm{log}}} = N_c\frac{|q_f|B}{(2\pi)^2}\sum_{n=0}^{\infty}\sum_{s=\pm1}\int dp_z \frac{1}{(p_z^2+M_{0_f}^2+2n|q_f|B)^{3/2}}, \tag{C11}$$

$$I_{1_{\mathrm{finite1}}} = -N_c\frac{|q_f|B}{(2\pi)^2}\sum_{n=0}^{\infty}\sum_{s=\pm1}\int dp_z \left(\frac{3}{8}\right)\left[\frac{M_f A^2 - 4M_f M_{0_f}^2\mu_5^2}{(p_z^2+M_{0_f}^2+2n|q_f|B)^{5/2}}\right], \tag{C12}$$

$$I_{1_{\mathrm{finite2}}} = -N_c\frac{|q_f|B}{(2\pi)^2}\left(\frac{15}{16}\right)\sum_{n=0}^{\infty}\sum_{s=\pm1}\int dp_z \int_0^1 dx \frac{(1-x)^2 M_f\left(A+2s\mu_5\sqrt{p_z^2+2n|q_f|B}\right)^3}{\left[p_z^2+M_{0_f}^2+2n|q_f|B-x\left(A+2s\mu_5\sqrt{p_z^2+2n|q_f|B}\right)\right]^{7/2}}. \tag{C13}$$

In a similar way, the integral $I_2$ in Eq. (C2) can also be written as

$$\begin{aligned}I_2 &= N_c\frac{|q_f|B}{(2\pi)^2}\int dp_z\frac{M_f}{\sqrt{M_f^2+(p_z-\mu_5)^2}}\\&= N_c\frac{|q_f|B}{(2\pi)^2}\int dp_z\frac{M_f}{\sqrt{M_f^2+(p_z-\mu_5)^2}} - N_c\frac{|q_f|B}{(2\pi)^2}\int dp_z\frac{M_f}{\sqrt{p_z^2+M_{0_f}^2}} + N_c\frac{|q_f|B}{(2\pi)^2}\int dp_z\frac{M_f}{\sqrt{p_z^2+M_{0_f}^2}}\\&= \left(\frac{1}{2}\right)N_c\frac{|q_f|B}{(2\pi)^2}\int dp_z\int_0^1 dx\frac{M_f(A+2p_z\mu_5)}{[p_z^2+M_{0_f}^2-x(A+2p_z\mu_5)]^{3/2}} + N_c\frac{|q_f|B}{(2\pi)^2}\int dp_z\frac{M_f}{\sqrt{p_z^2+M_{0_f}^2}}\\&= I_{2_{\text{finite}}}+I_{2_{\log}}.\end{aligned}\tag{C14}$$

Using Eqs. (C9) and (C14), Eq. (C2) can be recasted as

$$\langle\bar{\psi}_f\psi_f\rangle^{\mu_5\neq0}_{\text{vac,B}\neq0} = -\frac{M_f(M_{0_f}^2-M_f^2+2\mu_5^2)}{2}I_{1_{\log}}+I_{1_{\text{finite1}}}+I_{1_{\text{finite2}}}+I_{2_{\text{finite}}}+I_{1_{\text{quad}}}+I_{2_{\log}},\tag{C15}$$

where

$$I_{1_{\log}} = -\frac{N_c}{2\pi^2}\left[-\ln x_{0_f}+\frac{\Gamma'(x_{0_f})}{\Gamma(x_{0_f})}\right]+2N_c\int_{|\vec{p}|\leq\Lambda}\frac{d^3p}{(2\pi)^3}\frac{1}{(p^2+M_{0_f}^2)^{3/2}},\tag{C16}$$

and

$$I_{1_{\text{quad}}}+I_{2_{\log}} = -\frac{N_cM_f|q_f|B}{2\pi^2}\left[x_{0_f}(1-\ln x_{0_f})+\ln\Gamma(x_{0_f})+\frac{1}{2}\ln\left(\frac{x_{0_f}}{2\pi}\right)\right]-2N_c\int_{|\vec{p}|\leq\Lambda}\frac{d^3p}{(2\pi)^3}\frac{M_f}{\sqrt{p^2+M_{0_f}^2}}.\tag{C17}$$

In Eqs. (C16) and (C17), we have used Eqs. (B16) and (B13), respectively.

## APPENDIX D: CHIRAL SUSCEPTIBILITY AND ITS REGULARIZATION IN THE PRESENCE OF A BACKGROUND MAGNETIC FIELD AND CHIRAL CHEMICAL POTENTIAL

Using Eq. (C2), we get

$$\begin{aligned}\frac{\partial\langle\bar{\psi}_f\psi_f\rangle^{\mu_5\neq0}_{\text{vac,B}\neq0}}{\partial M_f} &= -\frac{N_c|q_f|B}{(2\pi)^2}\sum_{n=0}^{\infty}\sum_{s=\pm1}\int dp_z\frac{1}{\sqrt{M_f^2+\left(\sqrt{p_z^2+2n|q_f|B}-s\mu_5\right)^2}}\\&\quad+\frac{N_c|q_f|B}{(2\pi)^2}\int dp_z\frac{1}{\sqrt{M_f^2+(p_z-\mu_5)^2}}\\&\quad+\frac{N_c|q_f|B}{(2\pi)^2}\sum_{n=0}^{\infty}\sum_{s=\pm1}\int dp_z\frac{M_f^2}{\left(M_f^2+\left(\sqrt{p_z^2+2n|q_f|B}-s\mu_5\right)^2\right)^{3/2}}\\&\quad-\frac{N_c|q_f|B}{(2\pi)^2}\int dp_z\frac{M_f^2}{(M_f^2+(p_z-\mu_5)^2)^{3/2}}\\&= \mathbf{I}_1+\mathbf{I}_2+\mathbf{I}_3+\mathbf{I}_4.\end{aligned}\tag{D1}$$

Using Eq. (C9), we can write

$$\mathbf{I}_1 = -N_c \frac{|q_f|B}{(2\pi)^2} \sum_{n=0}^{\infty} \sum_{s=\pm 1} \int dp_z \frac{1}{\sqrt{M_f^2 + \left(\sqrt{p_z^2 + 2n|q_f|B} - s\mu_5\right)^2}}$$
$$= \mathbf{I}_{1,\mathrm{quad}} - \frac{(M_{0_f}^2 - M_f^2 + 2\mu_5^2)}{2} \mathbf{I}_{1,\log} + \mathbf{I}_{1,\mathrm{finite1}} + \mathbf{I}_{1,\mathrm{finite2}}, \tag{D2}$$

where

$$\mathbf{I}_{1,\mathrm{quad}} = -N_c \frac{|q_f|B}{(2\pi)^2} \sum_{n=0}^{\infty} \sum_{s=\pm 1} \int dp_z \frac{1}{\sqrt{p_z^2 + M_{0_f}^2 + 2n|q_f|B}}, \tag{D3}$$

$$\mathbf{I}_{1,\log} = N_c \frac{|q_f|B}{(2\pi)^2} \sum_{n=0}^{\infty} \sum_{s=\pm 1} \int dp_z \frac{1}{(p_z^2 + M_{0_f}^2 + 2n|q_f|B)^{3/2}}, \tag{D4}$$

$$\mathbf{I}_{1,\mathrm{finite1}} = -N_c \frac{|q_f|B}{(2\pi)^2} \sum_{n=0}^{\infty} \sum_{s=\pm 1} \int dp_z \left(\frac{3}{8}\right) \left[\frac{A^2 - 4M_{0_f}^2\mu_5^2}{(p_z^2 + M_{0_f}^2 + 2n|q_f|B)^{5/2}}\right], \tag{D5}$$

$$\mathbf{I}_{1,\mathrm{finite2}} = -N_c \frac{|q_f|B}{(2\pi)^2} \left(\frac{15}{16}\right) \sum_{n=0}^{\infty} \sum_{s=\pm 1} \int dp_z \int_0^1 dx \frac{(1-x)^2 \left(A + 2s\mu_5\sqrt{p_z^2 + 2n|q_f|B}\right)^3}{\left[p_z^2 + M_{0_f}^2 + 2n|q_f|B - x\left(A + 2s\mu_5\sqrt{p_z^2 + 2n|q_f|B}\right)\right]^{7/2}}. \tag{D6}$$

The integral $\mathbf{I}_2$ in Eq. (D1) can be expressed as

$$\mathbf{I}_2 = N_c \frac{|q_f|B}{(2\pi)^2} \int dp_z \frac{1}{\sqrt{M_f^2 + (p_z - \mu_5)^2}} = \mathbf{I}_{2,\mathrm{finite}} + \mathbf{I}_{2,\log}, \tag{D7}$$

where divergence free $\mathbf{I}_{2,\mathrm{finite}}$ is

$$\mathbf{I}_{2,\mathrm{finite}} = \left(\frac{1}{2}\right) N_c \frac{|q_f|B}{(2\pi)^2} \int dp_z \int_0^1 dx \frac{(A + 2p_z\mu_5)}{[p_z^2 + M_{0_f}^2 - x(A + 2p_z\mu_5)]^{3/2}}, \tag{D8}$$

and the divergence term $\mathbf{I}_{2,\log}$ is

$$\mathbf{I}_{2,\log} = \frac{N_c|q_f|B}{(2\pi)^2} \int dp_z \frac{1}{\sqrt{p_z^2 + M_{0_f}^2}}. \tag{D9}$$

Similarly, the integral $\mathbf{I}_3$ can be separated into a divergent term and a convergent term as

$$\mathbf{I}_3 = \frac{N_c|q_f|B}{(2\pi)^2} \sum_{n=0}^{\infty} \sum_{s=\pm 1} \int dp_z \frac{M_f^2}{\left(M_f^2 + \left(\sqrt{p_z^2 + 2n|q_f|B} - s\mu_5\right)^2\right)^{3/2}} = \mathbf{I}_{3,\mathrm{finite}} + \mathbf{I}_{3,\log}, \tag{D10}$$

where

$$\mathbf{I}_{3,\mathrm{finite}} = \frac{N_c|q_f|B}{(2\pi)^2} \sum_{n=0}^{\infty} \sum_{s=\pm 1} \int dp_z M_f^2 \left[\frac{1}{\left(M_f^2 + \left(\sqrt{p_z^2 + 2n|q_f|B} - s\mu_5\right)^2\right)^{3/2}} - \frac{1}{(M_{0_f}^2 + p_z^2 + 2n|q_f|B)^{3/2}}\right], \tag{D11}$$

and

$$\mathbf{I}_{3,\log} = \frac{N_c|q_f|B}{(2\pi)^2}\sum_{n=0}^{\infty}\sum_{s=\pm 1}\int dp_z \frac{M_f^2}{(M_{0_f}^2 + p_z^2 + 2n|q_f|B)^{3/2}}. \tag{D12}$$

It can be shown that the term $\mathbf{I}_{3,\text{finite}}$ is finite. On the other hand, the term $\mathbf{I}_{3,\log}$ is not convergent at large momenta. Using Eqs. (D2), (D7), and (D10), Eq. (D1) can be rearranged in the following way:

$$\begin{aligned}
\frac{\partial\langle\bar{\psi}_f\psi_f\rangle_{\text{vac,B}\neq 0}^{\mu_5\neq 0}}{\partial M_f} &= \mathbf{I}_{1,\text{quad}} - \frac{M_{0_f}^2 - M_f^2 + 2\mu_5^2}{2}\mathbf{I}_{1,\log} + \mathbf{I}_{1,\text{finite1}} + \mathbf{I}_{1,\text{finite2}} + \mathbf{I}_{2,\text{finite}} + \mathbf{I}_{3,\text{finite}} + \mathbf{I}_4 + \mathbf{I}_{2,\log} + \mathbf{I}_{3,\log} \\
&= -\frac{M_{0_f}^2 - M_f^2 + 2\mu_5^2}{2}\mathbf{I}_{1,\log} + \mathbf{I}_{1,\text{finite1}} + \mathbf{I}_{1,\text{finite2}} + \mathbf{I}_{2,\text{finite}} + \mathbf{I}_{3,\text{finite}} \\
&\quad + \left(\mathbf{I}_4 + \frac{N_c|q_f|B}{(2\pi)^2}\int dp_z \frac{M_f^2}{(M_{0_f}^2 + p_z^2)^{3/2}}\right) + (\mathbf{I}_{1,\text{quad}} + \mathbf{I}_{2,\log}) \\
&\quad + \left(\mathbf{I}_{3,\log} - \frac{N_c|q_f|B}{(2\pi)^2}\int dp_z \frac{M_f^2}{(M_{0_f}^2 + p_z^2)^{3/2}}\right) \\
&= -\frac{M_{0_f}^2 - M_f^2 + 2\mu_5^2}{2}\mathbf{I}_{1,\log} + \mathbf{I}_{1,\text{finite1}} + \mathbf{I}_{1,\text{finite2}} + \mathbf{I}_{2,\text{finite}} + \mathbf{I}_{3,\text{finite}} + \mathbf{I}_{\text{finite}} + \mathbf{I}_{\text{quad}} + \mathbf{I}_{\log},
\end{aligned} \tag{D13}$$

where $\mathbf{I}_{\text{finite}}$ is

$$\mathbf{I}_{\text{finite}} = \mathbf{I}_4 + \frac{N_c|q_f|B}{(2\pi)^2}\int dp_z \frac{M_f^2}{(p^2 + M_{0_f}^2)^{3/2}}, \tag{D14}$$

and

$$\begin{aligned}
\mathbf{I}_{\text{quad}} &= \mathbf{I}_{1,\text{quad}} + \mathbf{I}_{2,\log} \\
&= -\frac{N_c|q_f|B}{2\pi^2}\left[x_{0_f}(1 - \ln x_{0_f}) + \ln\Gamma(x_{0_f}) + \frac{1}{2}\ln\left(\frac{x_{0_f}}{2\pi}\right)\right] - \frac{2N_c}{(2\pi)^3}\int_{|\vec{p}|\leq\Lambda} d^3p \frac{1}{\sqrt{p^2 + M_{0_f}^2}}.
\end{aligned} \tag{D15}$$

$$\begin{aligned}
\mathbf{I}_{\log} &= \mathbf{I}_{3,\log} - \frac{N_c|q_f|B}{(2\pi)^2}\int dp_z \frac{M_f^2}{(p^2 + M_{0_f}^2)^{3/2}}, \\
&= -\frac{N_c M_f^2}{2\pi^2}\left[-\ln x_{0_f} + \frac{1}{2x_{0_f}} + \frac{\Gamma'(x_{0_f})}{\Gamma(x_{0_f})}\right] + \frac{2N_c}{(2\pi)^3}\int_{|\vec{p}|\leq\Lambda} d^3p \frac{M_f^2}{(p^2 + M_{0_f})^{3/2}},
\end{aligned} \tag{D16}$$

with

$$\begin{aligned}
\mathbf{I}_{1,\log} &= \frac{N_c|q_f|B}{(2\pi)^2}\sum_{s=\pm 1}\sum_{n=0}^{\infty}\int dp_z \frac{1}{(p_z^2 + M_{0_f}^2 + 2n|q_f|B)^{3/2}} = -\frac{N_c}{2\pi^2}\left[-\ln x_{0_f} + \frac{\Gamma'(x_{0_f})}{\Gamma(x_{0_f})}\right] \\
&\quad + 2N_c\int_{|\vec{p}|\leq\Lambda}\frac{d^3p}{(2\pi)^3}\frac{1}{(p^2 + M_{0_f}^2)^{3/2}}.
\end{aligned} \tag{D17}$$

[1] S. Jeon and V. Koch, Phys. Rev. Lett. **83**, 5435 (1999).
[2] M. Asakawa, U. W. Heinz, and B. Muller, Phys. Rev. Lett. **85**, 2072 (2000).
[3] Rafelski and B. Muller, Phys. Rev. Lett. **48**, 1066 (1982).
[4] P. Koch, B. Muller, and J. Rafelski, Phys. Rep. **142**, 167 (1986).
[5] F. Karsch and E. Laermann, Phys. Rev. D **50**, 6954 (1994).
[6] C. Bernard, T. Burch, C. DeTar, J. Osborn, S. Gottlieb, E. B. Gregory, D. Toussaint, U. M. Heller, and R. Sugar, Phys. Rev. D **71**, 034504 (2005).
[7] M. Cheng *et al.*, Phys. Rev. D **74**, 054507 (2006).
[8] Y. Aoki, Z. Fodor, S. D. Katz, and K. K. Szabó, Phys. Lett. B **643**, 46 (2006).
[9] M. Cheng *et al.*, Phys. Rev. D **75**, 034506 (2007).
[10] L. K. Wu, X. Q. Luo, and H. S. Chen, Phys. Rev. D **76**, 034505 (2007).
[11] P. Zhuang, J. Hüfner, and S. P. Klevansky, Nucl. Phys. **A576**, 525 (1994).
[12] C. Sasaki, B. Friman, and K. Redlich, Phys. Rev. D **75**, 074013 (2007).
[13] A. Smilga and J. J. M. Verbaarschot, Phys. Rev. D **54**, 1087 (1996).
[14] D. Blaschke, A. Holl, C. D. Roberts, and S. Schmidt, Phys. Rev. C **58**, 1758 (1998).
[15] P. Chakraborty, M. G. Mustafa, and M. H. Thoma, Phys. Rev. D **67**, 114004 (2003).
[16] D. E. Kharzeev, L. D. McLerran, and H. J. Warringa, Nucl. Phys. **A803**, 227 (2008).
[17] V. Skokov, A. Yu. Illarionov, and V. Toneev, Int. J. Mod. Phys. A **24**, 5925 (2009).
[18] V. Voronyuk, V. D. Toneev, W. Cassing, E. L. Bratkovskaya, V. P. Konchakovski, and S. A. Voloshin, Phys. Rev. C **83**, 054911 (2011).
[19] W.-T. Deng and X.-G. Huang, Phys. Rev. C **85**, 044907 (2012).
[20] J. Bloczynski, X.-G. Huang, X. Zhang, and J. Liao, Phys. Lett. B **718**, 1529 (2013).
[21] L. McLerran and V. Skokov, Nucl. Phys. **A929**, 184 (2014).
[22] U. Gursoy, D. Kharzeev, and K. Rajagopal, Phys. Rev. C **89**, 054905 (2014).
[23] V. Roy and S. Pu, Phys. Rev. C **92**, 064902 (2015).
[24] K. Tuchin, Phys. Rev. C **91**, 064902 (2015).
[25] I. A. Shovkovy, Lect. Notes Phys. **871**, 13 (2013).
[26] V. Gusynin, V. Miransky, and I. Shovkovy, Phys. Rev. Lett. **73**, 3499 (1994).
[27] V. Gusynin, V. Miransky, and I. Shovkovy, Phys. Lett. B **349**, 477 (1995).
[28] V. Gusynin, V. Miransky, and I. Shovkovy, Phys. Rev. D **52**, 4747 (1995).
[29] V. Gusynin, V. Miransky, and I. Shovkovy, Phys. Rev. D **52**, 4718 (1995).
[30] A. Y. Babansky, E. Gorbar, and G. Shchepanyuk, Phys. Lett. B **419**, 272 (1998).
[31] K. Klimenko, arXiv:hep-ph/9809218.
[32] D. Ebert, K. Klimenko, M. Vdovichenko, and A. Vshivtsev, Phys. Rev. D **61**, 025005 (1999).
[33] M. Vdovichenko, A. Vshivtsev, and K. Klimenko, Phys. At. Nucl. **63**, 470 (2000).
[34] V. C. Zhukovsky, K. Klimenko, and V. Khudyakov, Theor. Math. Phys. **124**, 1132 (2000).
[35] T. Inagaki, D. Kimura, and D. T. Murata, Prog. Theor. Phys. **111**, 371 (2004).
[36] T. Inagaki, D. Kimura, and D. T. Murata, Prog. Theor. Phys. Suppl. **153**, 321 (2004).
[37] S. Ghosh, S. Mandal, and S. Chakrabarty, Phys. Rev. C **75**, 015805 (2007).
[38] A. Osipov, B. Hiller, A. Blin, and J. da Providencia, Phys. Lett. B **650**, 262 (2007).
[39] A. Osipov, B. Hiller, A. Blin, and J. da Providencia, SIGMA **4**, 024 (2008).
[40] K. Klimenko and V. Zhukovsky, Phys. Lett. B **665**, 352 (2008).
[41] D. Menezes, M. Benghi Pinto, S. Avancini, A. Perez Martinez, and C. Providencia, Phys. Rev. C **79**, 035807 (2009).
[42] D. Menezes, M. Benghi Pinto, S. Avancini, and C. Providencia, Phys. Rev. C **80**, 065805 (2009).
[43] S. Fayazbakhsh and N. Sadooghi, Phys. Rev. D **83**, 025026 (2011).
[44] B. Chatterjee, H. Mishra, and A. Mishra, Phys. Rev. D **84**, 014016 (2011).
[45] S. S. Avancini, D. P. Menezes, M. B. Pinto, and C. Providencia, Phys. Rev. D **85**, 091901 (2012).
[46] G. N. Ferrari, A. F. Garcia, and M. B. Pinto, Phys. Rev. D **86**, 096005 (2012).
[47] V. Elias, D. McKeon, V. Miransky, and I. Shovkovy, Phys. Rev. D **54**, 7884 (1996).
[48] J. O. Andersen and R. Khan, Phys. Rev. D **85**, 065026 (2012).
[49] J. O. Andersen and A. Tranberg, J. High Energy Phys. 08 (2012) 002.
[50] T. D. Cohen, D. A. McGady, and E. S. Werbos, Phys. Rev. C **76**, 055201 (2007).
[51] T. D. Cohen, D. A. McGady, and E. S. Werbos, Phys. Rev. C **80**, 015203 (2009).
[52] D. E. Kharzeev, Prog. Part. Nucl. Phys. **75**, 133 (2014).
[53] M. Ruggieri, Phys. Rev. D **84**, 014011 (2011).
[54] K. Fukushima, M. Ruggieri, and R. Gatto, Phys. Rev. D **81**, 114031 (2010).
[55] J. Chao, P. Chu, and M. Huang, Phys. Rev. D **88**, 054009 (2013).
[56] L. Yu, H. Liu, and M. Huang, Phys. Rev. D **90**, 074009 (2014).
[57] L. Yu, H. Liu, and M. Huang, Phys. Rev. D **94**, 014026 (2016).
[58] Z.-F. Cui, I. C. Cloët, Y. Lu, C. D. Roberts, S. M. Schmidt, S.-S. Xu, and H.-S. Zong, Phys. Rev. D **94**, 071503 (2016).
[59] R. L. S. Farias, D. C. Duarte, G. Krein, and R. O. Ramos, Phys. Rev. D **94**, 074011 (2016).
[60] M. N. Chernodub and A. S. Nedelin, Phys. Rev. D **83**, 105008 (2011).
[61] V. V. Braguta, E.-M. Ilgenfritz, A. Y. Kotov, B. Petersson, and S. A. Skinderev, Phys. Rev. D **93**, 034509 (2016).
[62] V. V. Braguta, V. A. Goy, E. M. Ilgenfritz, A. Y. Kotov, A. V. Molochkov, M. Müller-Preussker, and B. Petersson, J. High Energy Phys. 06 (2015) 094.

[63] X. Sheng, D. H. Rischke, D. Vasak, and Q. Wang, Eur. Phys. J. A **54**, 21 (2018).
[64] X.-L. Sheng, R.-H. Fang, Q. Wang, and D. H. Rischke, Phys. Rev. D **99**, 056004 (2019).
[65] H.-Th. Elze, M. Gyulassy, and D. Vasak, Nucl. Phys **B 276**, 706 (1986).
[66] H.-Th. Elze, M. Gyulassy, and D. Vasak, Phys. Lett. B **177**, 402 (1986).
[67] U. Heinz, Phys. Rev. Lett. **51**, 351 (1983); Ann. Phys. (N.Y.) **161**, 48 (1985).
[68] E. Wigner, Phys. Rev. **40**, 749 (1932).
[69] S. R. De Groot. W. A. Van Leeuwen, and Ch. G. Van Weert, *Relativistic Kinetic Theory* (North-Holland, Amsterdam, 1980).
[70] P. Carruthers and F. Zachariasen, Rev. Mod. Phys. **55**, 245 (1983).
[71] I. Bialynicki-Birula, Acta Phys. Austriaca. Suppl. **18**, 111 (1977).
[72] N. Weickgenannt, X. Sheng, E. Speranza, Q. Wang, and D. H. Rischke, Phys. Rev. D **100**, 056018 (2019).
[73] N. Armesto, F. Dominguez, A. Kovner, and M. Lublinsky, J. High Energy Phys. 05 (2019) 025.
[74] S. Mao and D. H. Rischke, Phys. Lett. B **792**, 149 (2019).
[75] X. Sheng, R. Fang, Q. Wang, and D. H. Rischke, Phys. Rev. D **99**, 056004 (2019).
[76] J. Gao, J. Pang, and Q. Wang, Phys. Rev. D **100**, 016008 (2019).
[77] J. Gao, Z. Liang, Q. Wang, and X. Wang, Phys. Rev. D **98**, 036019 (2018).
[78] G. Prokhorov and O. Teryaev, Phys. Rev. D **97**, 076013 (2018).
[79] E. V. Gorbar, V. A. Miransky, I. A. Shovkovy, and P. O. Sukhachov, J. High Energy Phys. 08 (2017) 103.
[80] J. Gao, S. Pu, and Q. Wang, Phys. Rev. D **96**, 016002 (2017).
[81] Y. Wu, D. Hou, and H. Ren, Phys. Rev. D **96**, 096015 (2017).
[82] Y. Hidaka, S. Pu, and D.-L. Yang, Phys. Rev. D **95**, 091901 (2017).
[83] K. Hattori, Y. Hidaka, and D.-L. Yang, arXiv:1903.01653.
[84] T. Hatsuda and T. Kunihiro, Phys. Rev. Lett. **55**, 158 (1985).
[85] W. Florkowski and B. L. Friman, Acta Phys. Pol. B **25**, 49 (1994).
[86] J. Hufner, S. P. Klevansky, P. Zhuang, and H. Voss, Ann. Phys. (N.Y.) **234**, 225 (1994).
[87] S. P. Klevansky, Rev. Mod. Phys. **64**, 649 (1992).
[88] M. K. Volkov, Phys. Part. Nucl. **24**, 35 (1993).
[89] T. Hatsuda and T. Kunihiro, Phys. Rep. **247**, 221 (1994).
[90] W. Florkowski, J. Huefner, S. P. Klevansky, and L. Neise, Ann. Phys. (N.Y.) **245**, 445 (1996).
[91] W. M. Zhang and L. Wilets, Phys. Rev. C **45**, 1900 (1992).
[92] A. Abada and J. Aichelin, Phys. Rev. Lett. **74**, 3130 (1995).
[93] W. Florkowski, Phys. Rev. C **50**, 3069 (1994).
[94] R. Gatto and M. Ruggieri, Phys. Rev. D **85**, 054013 (2012).
[95] M. Ruggieri and G. X. Peng, J. Phys. G **43**, 125101 (2016).
[96] S. S. Xu, Z. F. Cui, B. Wang, Y. M. Shi, Y. C. Yang, and H. S. Zong, Phys. Rev. D **91**, 056003 (2015).
[97] B. Wang, Y. L. Wang, Z. F. Cui, and H. S. Zong, Phys. Rev. D **91**, 034017 (2015).
[98] R. L. S. Farias, G. Dallabona, G. Krein, and O. A. Battistel, Phys. Rev. C **73**, 018201 (2006).
[99] S. S. Avancini, A. Bandyopadhyay, D. C. Duarte, and R. L. S. Farias, arXiv:1907.09880.
[100] D. Vasak, M. Gyulassy, and H. T. Elze, Ann. Phys. (N.Y.) **173**, 462 (1987).
[101] R. Fang, L. Pang, Q. Wang, and X. Wang, Phys. Rev. C **94**, 024904 (2016).
[102] M. Buballa, Phys. Rep. **407**, 205 (2005); M. Frank, M. Buballa, and M. Oertel, Phys. Lett. B **562**, 221 (2003).
[103] V. Dmitrasinovic, Phys. Rev. C **53**, 1383 (1996).
[104] L. Yang and X.-J. Wen, Int. J. Mod. Phys. A **33**, 1850123 (2018).
[105] W. V. Liu and F. Wilczek, Phys. Rev. Lett. **90**, 047002 (2003); E. Gubankova, W. V. Liu, and F. Wilczek, Phys. Rev. Lett. **91**, 032001 (2003).
[106] J. Berges and K. Rajagopal, Nucl. Phys. **B538**, 215 (1999).
[107] J. Noornah and I. Shovkovy, Phys. Rev. D **76**, 105030 (2007).
[108] G. Endrodi, J. High Energy Phys. 04 (2013) 023.
[109] M. Ferreira, P. Costa, D. P. Menezes, C. Providncia, and N. N. Scoccola, Phys. Rev. D **89**, 016002 (2014).
[110] A. Abhishek and H. Mishra, Phys. Rev. D **99**, 054016 (2019).
[111] D. C. Duarte, R. L. S. Farias, and R. O. Ramos, Phys. Rev. D **99**, 016005 (2019).
[112] D. Boer and J. K. Boomsma, Phys. Rev. D **78**, 054027 (2008); J. K. Boomsma and D. Boer, Phys. Rev. D **80**, 034019 (2009).
[113] R. L. S. Farias, V. S. Timoteo, S. S. Avancini, M. B. Pinto, and G. Krein, Eur. Phys. J. A **53**, 101 (2017).
[114] I. S. Gradshteyn and I. M. Ryzhik, *Table of Integrals, Series and Products*, edited by A. Jeffrey and D. Zwillinger (Elsevier Acadmic Press Publication, San Diego, California, 2007).
[115] http://mathworld.wolfram.com/HurwitzZetaFunction.html.

Eur. Phys. J. C (2022) 82:71
https://doi.org/10.1140/epjc/s10052-022-09999-z

THE EUROPEAN PHYSICAL JOURNAL C

Check for updates

Regular Article - Theoretical Physics

# Thermoelectric transport coefficients of quark matter

**Aman Abhisek**[1,a], **Arpan Das**[2,b], **Deepak Kumar**[1,3,c], **Hiranmaya Mishra**[1,d]

[1] Theory Division, Physical Research Laboratory, Navrangpura, Ahmedabad 380 009, India
[2] Institute of Nuclear Physics Polish Academy of Sciences, 31-342 Kraków, Poland
[3] Indian Institute of Technology Gandhinagar, Gandhinagar, Gujarat 382 355, India

Received: 6 May 2021 / Accepted: 6 January 2022


**Abstract** A thermal gradient and/or a chemical potential gradient in a conducting medium can lead to an electric field, an effect known as thermoelectric effect or Seebeck effect. In the context of heavy-ion collisions, we estimate the thermoelectric transport coefficients for quark matter within the ambit of the Nambu–Jona Lasinio (NJL) model. We estimate the thermal conductivity, electrical conductivity, and the Seebeck coefficient of hot and dense quark matter. These coefficients are calculated using the relativistic Boltzmann transport equation within relaxation time approximation. The relaxation times for the quarks are estimated from the quark–quark and quark–antiquark scattering through meson exchange within the NJL model. As a comparison to the NJL model estimation of the Seebeck coefficient, we also estimate the Seebeck coefficient within a quasiparticle approach.

## 1 Introduction

Heavy-ion collision experiments conducted at particle accelerators allow us to study the properties of fundamental constituents of nature, such as quarks and gluons. Experiments at relativistic heavy ion collider (RHIC) and large hadron collider (LHC) indicate the formation of such a deconfined medium of quarks and gluons. The partonic medium such produced behaves like a strongly interacting liquid with a small value of shear viscosity ($\eta$) to entropy density ($s$) ratio ($\eta/s$), expands, cools down and undergoes a transition to the hadronic phase and finally free streams to the detector. One of the successful descriptions of the bulk evolution of such strongly interacting matter has been through relativistic hydrodynamics. Transport coefficients are important input parameters that enter in such a dissipative hydrodynamic description as well as in transport simulations that have been used to describe the evolution of such matter produced in a heavy-ion collision.

Hydrodynamic studies of the heavy-ion collisions suggest that the medium produced has a very small ratio of shear viscosity to entropy density ($\eta/s$) [1–3]. It is amongst the smallest of known materials suggesting the quark–gluon plasma (QGP) formed is the most perfect fluid. The value of this ratio estimated from experiments is also found to be close to the conjectured KSS bound on the value of $\eta/s$ [3]. Just like shear viscosity determines the response to transverse momentum gradients there are other transport coefficients such as bulk viscosity, electrical conductivity, etc. which determine the response of the system to other such perturbations. Bulk viscosity [4–9] determines the response to bulk stresses. It scales with the conformal anomaly ($\frac{\varepsilon-3P}{T^4}$) and is expected to be large near the phase transition as inferred from lattice calculations [10,11]. The effect of such a large bulk viscosity to entropy ratio have been investigated on the particle spectrum and flow coefficients [12,13]. Electrical conductivity ($\sigma_{el}$) [14–32] is also important as the heavy-ion collisions may be associated with large electromagnetic fields. The magnetic field produced in non-central collisions has been estimated to be of the order of $\sim m_\pi^2$ at RHIC energy scales [33–40]. Such magnetic fields are amongst the strongest magnetic fields produced in nature and can affect various properties of the strongly interacting medium. They may also lead to interesting CP-violating effects such as chiral magnetic effect etc [41]. In a conducting medium, the evolution of the magnetic field depends on the electrical conductivity. Electrical conductivity modifies the decay of the magnetic field substantially in comparison with the decay of the magnetic field in vacuum. Hence the estimation of the electrical conductivity of the strongly interacting medium is important regarding the decay of the magnetic field produced at the initial stage of heavy ion collision. These transport coefficients have been estimated in perturbative QCD and effective models [19,42–

[a] e-mail: aman@prl.res.in
[b] e-mail: arpan.das@ifj.edu.pl
[c] e-mail: deepakk@prl.res.in
[d] e-mail: hm@prl.res.in (corresponding author)

Published online: 24 January 2022

61]. At finite baryon densities, the other transport coefficient that is relevant is the coefficient of thermal conductivity and has been studied in [62,63] both in the hadronic matter as well as partonic matter.

In the present investigation, we focus on the thermoelectric response of the strongly interacting system produced in a heavy-ion collision. It is well known from a condensed matter system that a temperature gradient can result in the generation of an electric current. This is known as the Seebeck effect. Due to temperature gradient, there is a non zero gradient of charge density leading to the generation of an electric field. A measure of the electric field produced in a conducting medium due to a temperature gradient is the Seebeck coefficient which is defined as the ratio of an electric field to the temperature gradient in the limit of vanishing electric current. Seebeck effect has been extensively studied in condensed matter systems such as superconductors, quantum dots, high-temperature cuprates, superconductor–ferromagnetic tunnel junctions, low dimensional organic metals, etc [64–72]. Such a phenomenon could also be present in the thermal medium created in heavy-ion collisions. In condensed matter systems only a temperature gradient is required for thermoelectric effect as there is only one type of dominant charge carriers in these systems. In the strongly interacting medium produced in heavy-ion collision both positive and negative charges contribute to transport phenomena. For vanishing baryon chemical potential (quark chemical potential) with equal numbers of particles and antiparticles there is no net thermoelectric effect. Thus a finite baryon chemical potential (quark chemical potential) is required for the thermoelectric effect to be observed. The strongly interacting matter at finite baryon density can be produced in low energy heavy-ion collisions at finite, e.g. at FAIR and NICA. Along with the temperature gradient, we also consider a gradient in the baryon (quark) chemical potential to estimate the Seebeck coefficient of the partonic medium. The gradient in the chemical potential has effects similar to the temperature gradient. Using Gibbs Duhem relation for a static medium one can express gradient in the baryon (quark) chemical potential to a gradient in temperature. Effect of the chemical potential gradient significantly affects the thermoelectric coefficients as has been demonstrated in Ref. [73].

Seebeck effect in the hadronic matter has been investigated previously by some of us within the framework of the Hadron resonance gas model [73,74]. However, the Hadron resonance gas model can only describe the hadronic medium at chemical freezeout whereas one expects deconfined partonic medium at the early stages of the heavy-ion collisions. In this investigation, we estimate the thermoelectric behavior of the partonic medium within the framework of the NJL model. Seebeck coefficient has also been estimated for the partonic matter within relaxation time approximation in Ref. [75,76]. However, this has been attempted with the relaxation time estimated within perturbative QCD which may be valid for asymptotically high temperatures. Further, it ought to be mentioned that, the vacuum structure of QCD remain nontrivial near the critical temperature region with nonvanishing values for the quark–antiquark condensates associated with chiral symmetry breaking as well as Polyakov loop condensates associated with the physics of statistical confinement [77–80]. Indeed, within the ambit of the NJL model, it was shown that the temperature dependence of viscosity coefficients exhibits interesting behavior of phase transition with the shear viscosity to entropy ratio showing a minimum while the coefficient of bulk viscosity showing a maximum at the phase transition [77,78,81]. The crucial reason for this behavior was the estimation of relaxation time using medium dependent masses for the quarks as well as the exchanged mesons which reveal nontrivial dependence before and after the transition temperature. This motivates us to investigate the behavior of thermoelectric transport coefficients within the NJL model which takes into account the medium dependence of quark and meson masses. This model has been used to study different transport properties of quark matter at high temperatures [6,31,81,82] and high densities [83–90]. Apart from the NJL model we also use quasi-particle model [91–97], which provides a reasonable thermodynamic and transport behavior of the deconfined phase.

We organize the paper in the following manner. In Sect. 2, we discuss the Boltzmann equation within relaxation time approximation to have the expressions for the different thermoelectric transport coefficients in the presence of a condensate. In Sect. 3 we discuss thermodynamics and estimation of relaxation time within the two flavor NJL model. In Sect. 4 we discuss the quasiparticle approach in the absence of any quark–antiquark condensate. In Sect. 5 we present the results of different transport coefficients. Finally, we give a possible outlook of the present investigation and conclude in Sect. 6.

## 2 Boltzmann equation in relaxation time approximation and transport coefficients

Within a quasiparticle approximation, a kinetic theory treatment for the calculation of transport coefficient can be a reasonable approximation that we shall be following similar to that in Refs. [5,6,45,46,98,99]. The plasma can be described by a phase space density for each species of particle. Near equilibrium, the distribution function can be expanded about a local equilibrium distribution function for the quarks as,

$$f(\mathbf{x},\mathbf{p},t) = f^{(0)}(\mathbf{x},\mathbf{p}) + \delta f(\mathbf{x},\mathbf{p},t),$$

where the local equilibrium distribution function $f^{(0)}$ is given as

$$f^{(0)}(\mathbf{x},\mathbf{p}) = \left[\exp\left(\beta(\mathbf{x})\left(u_\nu p^\nu \mp \mu(\mathbf{x})\right)\right) + 1\right]^{-1}. \tag{1}$$

Here, $u^\mu = \gamma_u(1, \mathbf{u})$, is the flow four-velocity, where, $\gamma_u = (1 - \mathbf{u}^2)^{1/2}$; $\mu$ is the chemical potential associated with a conserved charge. Here $\mu$ denotes the quark chemical potential and $\beta = 1/T$ is the inverse of temperature. Further, $p^\mu = (E, \mathbf{p})$ is the particle four momenta, single particle energy $E = \sqrt{p^2 + M^2}$ with $p = |\mathbf{p}|$. $M$ is the mass of the particle which in general is medium dependent. The departure from the equilibrium is described by the Boltzmann equation,

$$\frac{df_a(\mathbf{x}, \mathbf{p}, t)}{dt} = \frac{\partial f_a}{\partial t} + \frac{dx^i}{dt}\frac{\partial f_a}{\partial x^i} + \frac{dp^i}{dt}\frac{\partial f_a}{\partial p^i} = C^a[f], \tag{2}$$

where we have introduced the species index '$a$' on the distribution function. The right-hand side is the collision term which we shall discuss later. The left-hand side of the Boltzmann equation involves the trajectory $\mathbf{x}(t)$ and the momentum $\mathbf{p}(t)$. This trajectory, in general, not a straight line as the particle is moving in a mean-field, which, in general, can be space time-dependent. The velocity of the particle '$a$' is given by

$$\frac{dx^i}{dt} = \frac{\partial E_a}{\partial p_a^i} = \frac{p_a^i}{E_a} = v_a^i.$$

Next, the time derivative of momentum , the force, in presence of an electric field ($\boldsymbol{\mathcal{E}}$), magnetic field ($\mathbf{B}$) and a mean field dependent mass can be written as

$$\frac{dp^i}{dt} = -\frac{\partial E_a}{\partial x^i} + q_a(\mathcal{E}^i + \varepsilon^{ijk}v_j B_k).$$

The time derivatives of $\mathbf{x}$ and $\mathbf{p}$ can be substituted on the left-hand side of the Boltzmann equation Eq. (2) and the same reduces to

$$\frac{\partial f_a}{\partial t} + v^i\frac{\partial f_a}{\partial x^i} + \frac{\partial f_a}{\partial p^i}\left(-\frac{M_a}{E_a}\frac{\partial M_a}{\partial x^i} + q_a(\mathcal{E}^i + \varepsilon^{ijk}v_j B_k)\right) = C^a[f]. \tag{3}$$

For the collision term on the right-hand side, we shall be limiting ourselves to $2 \to 2$ scatterings only. In the relaxation time approximation the collision term for species $a$, all the distribution functions are given by the equilibrium distribution function except the distribution function for particle $a$. The collision term, to first order in the deviation from the equilibrium function, will then be proportional to $\delta f_a$, given the fact that $C^a[f^{(0)}] = 0$ by the principle of local detailed balance. In that case, the collision term is given by

$$C[f] = -\frac{\delta f_a}{\tau_a}, \tag{4}$$

where, $\tau_a$, the relaxation time for particle '$a$'. In general relaxation time is a function of energy. We shall discuss more about it in the subsequent subsection where we estimate it within the NJL model. As an approximation of the collision kernel in the Boltzmann equation one can also use other collision terms, e.g. Chapmann–Enskog method apart from the relaxation time approximation [4–6,44,45,47,99]. The relaxation time approximation for the collision integral in the Boltzmann equation may not be a controlled approximation scheme. The Chapmann–Enskog method which uses a variational approach can in principle allows one to obtain solutions with arbitrary accuracy. Nonetheless, the relaxation time approximation has been used more often to evaluate transport coefficients due to its simplicity. Although Chapmann–Enskog method can be in satisfying agreement with the Green–Kubo formalism, the qualitative behavior of various transport coefficients also remains the same in the relaxation time approximation [47]. Therefore as a first step towards the estimation of the thermoelectric transport coefficient within the framework of an effective model of QCD, we stick to the relaxation time approximation. Any calculation with a more realistic collision term will be an improvement on the present results.

Returning back to the left-hand side of Eq. (3), we keep up to the first order in gradients in space-time. The left-hand side of the Boltzmann equation Eq. (3), is explicitly small because of the gradients and we, therefore, may replace $f_a$ by $f_a^{(0)}$. While the spatial derivative of the distribution function is given by,

$$\begin{aligned}\frac{\partial f_a^{(0)}}{\partial x^i} &= -f_a^{(0)}(1 - f_a^{(0)})\partial_i(\beta E_a - \beta\mu_a)\\ &= -f_a^{(0)}(1 - f_a^{(0)})\bigg(-\frac{E_a}{T^2}\partial_i T + \beta\frac{M_a}{E_a}\frac{\partial M_a}{\partial x^i}\\ &\quad - \partial_i(\beta\mu_a)\bigg),\end{aligned} \tag{5}$$

here $\mu_a = b_a\mu$, $b_a$ being the quark number, i.e. $b_a = 1$ for quarks and $b_a = -1$ for antiquarks. The momentum derivative of the equilibrium distribution function is given by,

$$\frac{\partial f_a^{(0)}}{\partial p^i} = -\frac{1}{T}f_a^{(0)}(1 - f_a^{(0)})v_a^i. \tag{6}$$

Substituting Eqs. (6) and (5) in the Boltzmann equation Eq. (3) for the static case (where the distribution function is not an explicit function of time) in the absence of magnetic field we have

$$-f_a^{(0)}(1-f_a^{(0)})\left[v_a^i\left(-\frac{1}{T^2}\partial_i T E_a - \partial_i(\beta\mu_a)\right) + q_a\beta v_a^i\mathcal{E}^i\right] = -\frac{\delta f_a}{\tau_a}. \tag{7}$$

The spatial gradients of temperature and chemical potential can be related using momentum conservation in the system and Gibbs Duhem relation. Momentum conservation in a steady-state leads to $\partial_i P = 0$ ($P$, being the pressure) [100]. Using Gibbs Duhem relation, the pressure gradient can be written as, with the enthalpy $\omega = \varepsilon + P$,

$$\partial_i P = \frac{\omega}{T}\partial_i T + T n_q \partial_i(\mu/T) \tag{8}$$

which vanishes in steady-state. $n_q$ denotes the net quark number density and $\varepsilon$ is the energy density. The above equation relates the spatial gradient of temperature to the spatial gradients in chemical potential as,

$$\partial_i \mu = \left(\mu - \frac{\omega}{n_q}\right)\frac{\partial_i T}{T}. \tag{9}$$

Using Eqs. (9) and (7), $\delta f_a$, the deviation of the distribution function is given as,

$$\delta f_a = \frac{\tau_a f_a^0(1-f_a^0)}{T}\left[q_a \mathbf{v}_a \cdot \boldsymbol{\mathcal{E}} - \left(E_a - b_a\frac{\omega}{n_q}\right)\frac{\mathbf{v}_a \cdot \nabla T}{T}\right]. \tag{10}$$

The nonequilibrium part of the distribution function gives rise to transport coefficients. The electric current is now given as,

$$\begin{aligned}\mathbf{J} &= \sum_a g_a \int \frac{d^3 p_a}{(2\pi)^3}\, q_a \mathbf{v}_a\, \delta f_a \\ &= \sum_a \frac{g_a q_a^2}{3T}\int \frac{d^3 p_a}{(2\pi)^3}\, v_a^2 \tau_a f_a^0(1-f_a^0)\,\boldsymbol{\mathcal{E}} \\ &- \sum_a \frac{g_a q_a}{3T^2}\int \frac{d^3 p_a}{(2\pi)^3}\,\tau_a\left(E_a - b_a\frac{\omega}{n_q}\right) f_a^0(1-f_a^0) v_a^2\, \nabla T.\end{aligned} \tag{11}$$

In Eq. (11) we have used $v_a^i v_a^j = \frac{1}{3}v_a^2\delta^{ij}$ as because the integrand only depends on the magnitude of momenta. Further, the sum is over all flavors including antiparticles. The degeneracy factor $g_a = 6$ corresponding to color and spin degrees of freedom. $b_a$ is the quark number i.e. $b_a = \pm 1$ for quarks and antiquarks respectively.

Next, we write down the heat current $\mathcal{I}$ associated with the conserved quark number. For a relativistic system, thermal current arises corresponding to a conserved particle number. The thermal conduction due to quarks arises when there is energy flow relative to enthalpy [100]. Therefore the heat current is defined as [100],

$$\mathcal{I}^i = \sum_a T_a^{0i} - \frac{\omega}{n_q}\sum_a b_a J_{qa}^i. \tag{12}$$

Here, $n_q$ is the net quark number density. The energy flux is given by $T^{0i}$, the spatio-temporal component of energy-momentum tensor ($T^{\mu\nu}$) [100],

$$T_a^{0i} = g_a \int \frac{d^3 p_a}{(2\pi)^3} p_a^i f_a, \tag{13}$$

while, the quark current is given $\mathbf{J}_q$ is given by

$$J_{qa}^i = g_a \int \frac{d^3 p_a}{(2\pi)^3}\frac{p_a^i}{E_a} f_a b_a. \tag{14}$$

Clearly, the contribution to the energy flux and quark current vanishes arising from the equilibrium distribution function $f_a^{(0)}$ due to symmetry consideration and it is only the nonequilibrium part $\delta f_a$ that contribute to the energy flux and quark current in Eqs. (13) and (14) respectively. Substituting the expression for $\delta f_a$ from Eq. (10) in Eq. (12), the heat current $\mathcal{I}$ is given as,

$$\begin{aligned}\mathcal{I} = \sum_a \frac{g_a}{3T}\int \frac{d^3 p_a}{(2\pi)^3} f_a^0(1-f_a^0) v_a^2 \tau_a\Bigg[q_a\left(E_a - b_a\frac{\omega}{n_q}\right)\boldsymbol{\mathcal{E}} \\ - \left(E_a - b_a\frac{\omega}{n_q}\right)^2\frac{\nabla T}{T}\Bigg]\end{aligned} \tag{15}$$

The Seebeck coefficient $S$ is defined by setting the electric current $\mathbf{J} = 0$ in Eq. (11) so that the electric field becomes proportional to the temperature gradient i.e.

$$\boldsymbol{\mathcal{E}} = S\nabla T. \tag{16}$$

Therefore the Seebeck coefficient for the quark matter in the presence of a gradient in temperature and chemical potential can be expressed as,

$$S = \frac{\sum_a \frac{g_a q_a}{3T}\int \frac{d^3 p_a}{(2\pi)^3}\tau_a v^2\left(E_a - b_a\frac{\omega}{n_q}\right) f_a^{(0)}(1-f_a^{(0)})}{T\sum_a \frac{g_a}{3T}q_a^2\int\frac{d^3 p_a}{(2\pi)^3} v^2 \tau_a f_a^{(0)}(1-f_a^{(0)})} \tag{17}$$

The denominator of the Seebeck coefficient in the above may be identified as $T\sigma_{el}$, where the electrical conductivity $\sigma_{el}$ is given by [21,101],

$$\sigma_{el} = \sum_a \frac{g_a}{3T}q_a^2\int\frac{d^3 p_a}{(2\pi)^3}\left(\frac{p_a}{E_a}\right)^2 \tau_a f_a^{(0)}(1-f_a^{(0)}) \tag{18}$$

which may be identified from Eq. (11). Let us note that, while the denominator of the Seebeck coefficient is positive definite, the numerator is not so as it is linearly dependent on the electric charge of the species as well as on the difference $(E_a - b_a\frac{\omega}{n_q})$. This makes the Seebeck coefficient not always positive definite. This is also observed in different condensed matter systems [102].

In terms of the electrical conductivity and the Seebeck coefficient, the electric current Eq. (11) can be written as

$$\mathbf{J} = \sigma_{el}\boldsymbol{\mathcal{E}} - \sigma_{el} S \nabla T. \tag{19}$$

In a similar manner, the heat current as given in Eq. (15) can be written as,

$$\boldsymbol{\mathcal{I}} = T\sigma_{el} S\boldsymbol{\mathcal{E}} - \kappa_0 \nabla T, \tag{20}$$

where, $\kappa_0$, the thermal conductivity can be written as [100]

$$\kappa_0 = \sum_a \frac{g_a}{3T^2} \int \frac{d^3 p_a}{(2\pi)^3} \tau_a \left(\frac{p_a}{E_a}\right)^2 \left(E_a - b_a \frac{\omega}{n_q}\right)^2 f_a^{(0)}(1 - f_a^{(0)}). \tag{21}$$

Using Eqs. (19) and (20), we can express the heat current ($\boldsymbol{\mathcal{I}}$) in terms of electric current ($\mathbf{J}$) in the following way,

$$\boldsymbol{\mathcal{I}} = TS\mathbf{J} - \left(\kappa_0 - T\sigma_{el} S^2\right) \nabla T. \tag{22}$$

From Eq. (22) we can identify the Peltier coefficient ($\Pi$) and thermal conductivity ($\kappa$) in the presence of nonvanishing Seebeck coefficient as,

$$\Pi = TS, \quad \kappa = \kappa_0 - T\sigma_{el} S^2. \tag{23}$$

Note that the relation between the Peltier coefficient ($\Pi$) and the Seebeck coefficient as given in Eq. (23) can be considered as the consistency relation. Also, note that the thermal conductivity in the absence of any thermoelectric effect as given in Eq. (21) matches with the expression of the thermal conductivity as reported in [100]. The Seebeck coefficient ($S$), thermal conductivity ($\kappa_0$), and the electrical conductivity ($\sigma_{el}$) depend upon, the estimation of the relaxation time as well as the quark masses that goes into the distribution functions through the single-particle energies and are medium dependent. We estimate these quantities in the Nambu–Jona–Lasinio model which is described in the next section.

Before we start the discussion of the relaxation time within the framework of the NJL model we should emphasize the key features of the formalism as discussed above. The formalism of the transport coefficients as presented in Ref. [81] was developed to incorporate the effect of a nonvanishing dynamical quark condensate. In the present manuscript, we incorporated the effect of a dynamical condensate in the formalism of thermoelectric effects following Ref. [81]. On the other hand, the formalism of thermoelectric transport coefficients as presented in Refs. [73,74] do not include the effect of any dynamical condensate. Note that the formalism to calculate transport coefficients using the Boltzmann equation is fundamentally different in the presence of a dynamical condensate. In the presence of such a condensate, there exists an additional effective force term (see Eq. (3)) which is not present otherwise [73,74]. Therefore the formalism presented here should not be considered to be the same as the formalism presented in Refs. [73,74]. Furthermore, the final expression of the Seebeck coefficient and the thermal conductivity as obtained in the present investigation exactly resembles the results as given in Refs. [73,74,81]. This is an interesting outcome despite the fact that in the present investigation we started with a Boltzmann kinetic equation which is different from the same given in Refs. [73,74]. This is because the term proportional to $\partial M/\partial x$, which also acts as an effective force term in the Boltzmann equation (see Eq. (3)), gets exactly canceled by a similar term originating from $\partial f^{(0)}/\partial x$. We should also point out that the constituent quark mass which enters into the expressions of various transport coefficients through the single particle energy also carries nontrivial temperature and chemical potential dependence due to the presence of the gap equation. Such a temperature and chemical potential dependence of the single particle energy was not present in our earlier investigations, e.g. Ref. [73,74]. Therefore even if the analytical expressions presented in this investigation look similar to the expressions presented in Ref. [73,74], the theoretical formalism and the temperature and chemical potential dependence of various thermoelectric transport coefficients are different.

## 3 Estimation of relaxation time in NJL model

We model the partonic medium using the two flavor Nambu–Jona–Lasinio (NJL) model and estimate the thermodynamic quantities, the quasi particle masses in the medium and the relaxation time. The two flavour NJL model with $u$ and $d$ quark, can be described by the following Lagrangian [103],

$$\mathcal{L} = \bar{\psi}(i\partial\!\!\!/ - m_q)\psi + G\left[(\bar{\psi}\psi)^2 + (\bar{\psi}i\gamma^5\boldsymbol{\tau}\psi)^2\right]. \tag{24}$$

Here, $\psi$ is the doublet of $u$ and $d$ quarks; $m_q$ is the current quark mass matrix which is diagonal with elements $m_u$ and $m_d$ and we take them to be same as $m_0$ assuming isospin symmetry; $\boldsymbol{\tau}$ are the Pauli matrices in the flavor space; $G$ is the scalar coupling. NJL model is a QCD inspired effective model which incorporates various aspects of the chiral symmetry of QCD. The NJL model Lagrangian as given in Eq. (24) is symmetric under the chiral symmetry group $SU(2)_V \times SU(2)_A \times U(1)_V$. The thermodynamic quantities e.g., pressure ($P$), energy density ($\varepsilon$) and the number density ($n_q$) can be obtained once we know the thermodynamic potential of the NJL model. In a grand canonical ensemble, the thermodynamic potential ($\Omega$) or equivalently the pressure ($P$) can be expressed as,

$$-P = \Omega(\beta,\mu) = \frac{(M-m_0)^2}{4G} - \frac{2N_cN_f}{(2\pi)^3\beta}\int d\mathbf{k}\Big[\log\left(1+e^{-\beta(E-\mu)}\right) + \log\left(1+e^{-\beta(E+\mu)}\right)\Big] - \frac{2N_cN_f}{(2\pi)^3}\int d\mathbf{k}\sqrt{\mathbf{k}^2+M^2}. \quad (25)$$

In the above, $N_c = 3$ is the number of colors and $N_f = 2$ is the number of flavors, $E = \sqrt{\mathbf{k}^2+M^2}$ is the single particle energy with 'constituent' quark mass M which satisfies the self consistent gap equation

$$M = m_0 + \frac{2N_cN_f}{(2\pi)^3}\int d\mathbf{k}\frac{M}{\sqrt{k^2+M^2}}(1-f^{(0)}-\bar{f}^{(0)}). \quad (26)$$

In the above equations $f^{(0)} = (1+\exp(\beta\omega_-))^{-1}$ and $\bar{f}^{(0)} = (1+\exp(\beta\omega_+))^{-1}$ are the equilibrium distribution functions for quarks and antiquarks respectively and we have written $\omega_\pm(k) = E(\mathbf{k}) \pm \mu$ with $k \equiv |\mathbf{k}|$. The energy density $\varepsilon$ is given by,

$$\varepsilon = -\frac{2N_cN_f}{(2\pi)^3}\int d\mathbf{k}E(k)(1-f^{(0)}-\bar{f}^{(0)}) + \frac{(M-m_0)^2}{4G}, \quad (27)$$

so that enthalpy $\omega = \varepsilon + P$ is also defined once the solution to the mass gap equation Eq. (26) is known. In these calculations, we have taken a three momentum cutoff $\Lambda$ for the for calculations of integrals not involving the Fermi distribution functions. The net number density of quarks $n_q$ is given as

$$n_q = \frac{2N_cN_f}{(2\pi)^3}\int d\mathbf{k}(f^{(0)}-\bar{f}^{(0)}). \quad (28)$$

This completes the discussion on the all the bulk thermodynamic quantities defined for NJL model which enters in the definitions for Seebeck coefficient, electrical conductivity and thermal conductivity.

Next we discuss the estimation of relaxation time and as mentioned earlier we consider two particle scattering processes only. For a process $a+b \to c+d$, the relaxation time for the particle $a$ i.e. $\tau_a(E_a)$ is given by [81],

$$\tau_a^{-1}(E_a) \equiv \tilde{\omega}(E_a) = \frac{1}{2E_a}\sum_b\int d\boldsymbol{\pi}_b W_{ab} f_b^{(0)}(E_b), \quad (29)$$

where, the summation is over all species other than the particle "$a$". Further, in Eq. (29), we have introduced the notation $d\boldsymbol{\pi}_i = \frac{d^3p_i}{(2\pi)^3 2E_i}$ and $W_{ab}$ is the dimensionless transition rate for the processes with $a, b$ as the initial states. $W_{ab}$ which is Lorentz invariant and a function of the Mandelstam variable ($s$) can be given by,

$$W_{ab}(s) = \frac{1}{1+\delta_{ab}}\int d\boldsymbol{\pi}_c d\boldsymbol{\pi}_d (2\pi)^4\delta(p_a+p_b-p_c-p_d) \times |\mathcal{M}|^2_{ab\to cd}(1-f_c^{(0)}(p_c))(1-f_d^{(0)}(p_d)). \quad (30)$$

In the expression of $W_{ab}$ the Pauli blocking factors have been considered. The quantity $W_{ab}$ can be related to the cross sections of various scattering processes. In the present case within the NJL model, the quark–quark, quark–antiquark and antiquark–antiquark scattering cross sections are calculated to order $1/N_c$ which occur through the $\pi$ and $\sigma$ meson exchanges in "$s$" and "$t$" channels. The meson propagators that enters into the scattering amplitude is calculated within the random phase approximation and includes their masses and the widths. The mass of the meson is estimated from the pole of the meson propagator at vanishing three momentum i.e.,

$$1 - 2G\,\mathrm{Re}\Pi_{\tilde{m}}(M_{\tilde{m}}, 0) = 0. \quad (31)$$

where $\tilde{m}$ denotes $\sigma, \pi$ for scalar and pseudoscalar channel mesons, respectively. Polarization function in the corresponding mesonic channel is expressed as $\Pi_{\tilde{m}}$. The explicit expressions for $\mathrm{Re}\Pi_{\tilde{m}}$ and the imaginary part $\mathrm{Im}\Pi_{\tilde{m}}$ is given in Ref. [81] and we do not repeat here.

While, the relaxation time is energy dependent, one can also define an energy independent mean relaxation time by taking a thermal average as,

$$\bar{\omega}_a \equiv \bar{\tau}_a^{-1} = \frac{1}{n_a}\int\frac{d^3p_a}{(2\pi)^3}f_a^{(0)}(E_a)\tilde{\omega}_a(E_a) \equiv \sum_b n_b\bar{W}_{ab}, \quad (32)$$

to get an estimate of the average relaxation time. In the above equation, the sum is over all the particles other than 'a';

$$n_a = \int\frac{d^3p_a}{(2\pi)^3}f_a^{(0)}(E_a),$$

is the number density of the species "$a$" apart from the degeneracy factor. Here, $\bar{W}_{ab}$ is the thermal-averaged transition rate given as

$$\bar{W}_{ab} = \frac{1}{n_a n_b}\int d\boldsymbol{\pi}_a d\boldsymbol{\pi}_b f(E_a)f(E_b)W_{ab}. \quad (33)$$

For the case of two flavors, there are 12 different processes but the corresponding matrix elements can be related using i-spin symmetry, charge conjugation and crossing symmetries with only two independent matrix elements. We have chosen them, as in Refs. [81,99], to be the processes $u\bar{u} \to u\bar{u}$ and $u\bar{d} \to u\bar{d}$. The explicit expressions for the matrix elements are given in Refs. [81,99]. In the meson propagators we have kept both the mass and the width of the meson resonances which are medium dependent. It is important to mention that while the matrix elements of different scattering processes are related, the thermal-averaged rates are not. This is because the thermal averaged rates involve also the thermal distribution functions for the initial states along with the Pauli blocking factors for the final states.

## 4 Quasiparticle picture of the partonic medium

In the quasiparticle description, all the quarks (anti quarks) have both the thermal mass arising due to the interaction with the constituents of the medium and the bare mass $m_0$. Therefore, in the quasiparticle picture the total effective mass of the quark flavor $i$ can be expressed as [91–97,104],

$$m_i^2 = (m_0 + m_+(T,\mu))^2 + m_+(T,\mu)^2, \tag{34}$$

with

$$2m_+^2(T,\mu) = \frac{g^2(T,\mu)T^2}{3}\left(1 + \frac{\mu^2}{\pi^2 T^2}\right). \tag{35}$$

which is related to the asymptotic form of the gauge independent hard thermal (dense) loop self energies. The temperature and the chemical potential dependent strong coupling constant up to two loop order is [105,106],

$$\alpha_S(T,\mu) = \frac{g^2(T,\mu)}{4\pi} = \frac{6\pi}{(33-2N_f)\ln\left(\frac{T}{\Lambda_T}\sqrt{1+\frac{\mu^2}{\pi^2T^2}}\right)} \times \left(1 - \frac{3(153-19N_f)}{(33-2N_f)^2}\frac{\ln\left(2\ln\frac{T}{\Lambda_T}\sqrt{1+\frac{\mu^2}{\pi^2T^2}}\right)}{\ln\left(\frac{T}{\Lambda_T}\sqrt{1+\frac{\mu^2}{\pi^2T^2}}\right)}\right), \tag{36}$$

where $\Lambda_T$ is the QCD scale parameter which we consider as $\Lambda_T = 0.35T_c$ with $T_c = 200$ MeV [106]. The effective mass of the gluon, which depends on the temperature and the chemical potential is given as [96,107],

$$m_g^2(T) = \frac{N_c}{6}g^2(T,\mu)T^2\left[1 + \frac{1}{6}\left(N_f + \frac{3}{\pi^2}\sum_f \frac{\mu_f^2}{T^2}\right)\right], \tag{37}$$

where $N_c$ and $N_f$ represents the number of color and flavors respectively. The relaxation time for the quarks and antiquarks for the massless case is given by [108],

$$\tau_{q(\bar{q})} = \frac{1}{5.1T\alpha_S^2\log\left(\frac{1}{\alpha_S}\right)\left(1+0.12(2N_f+1)\right)}. \tag{38}$$

Note that for simplicity we have used the relaxation time which is applicable for the massless case only. However, following Ref. [109] it can be argued that the effect of the massive quark is small in the estimation of the scattering cross sections and relaxation time. Therefore, we use the expressions of the relaxation time as given in Eq. (38) even for the massive quarks. To compare our results as obtained in the NJL model we consider two light flavors with bare mass $m_0 = 0.008$ GeV [96]. The relaxation time for the gluons is given by [104,108,110]

$$\tau_g = \frac{1}{22.5\alpha_s^2\ln\left(\frac{1}{\alpha_s}\right)(1+0.06n_f)}. \tag{39}$$

## 5 Results

The two flavor NJL model as given in Eq. (24) has three parameters, the four fermions coupling $G$, the three momenta cut off ($\Lambda$) to regularize the momentum integral in vacuum and the current quark mass $m_0$. These values are adjusted to fit the physical values of the pion mass ($m_\pi = 135$ MeV), the pion decay constant ($f_\pi = 94$ MeV) and the value of the quark condensate in vacuum, $\langle\bar{u}u\rangle = \langle\bar{d}d\rangle = (-241\ \text{MeV})^3$. Various combinations of $G$, $\Lambda$, $m_0$ can be used to fix the pion mass, pion decay constant, and the quark vacuum condensate. Qualitatively all these different parameterizations are equivalent. Without going into such parameter dependence we work with a single set of parameters. We have considered here the value of the parameters as $m_0 = 5.6$ MeV, $\Lambda = 587.9$ MeV and $G\Lambda^2 = 2.44$ [103]. This leads to the constituent quark mass for $u$ and $d$ type quarks, $M = 397$ MeV in vacuum ($T = 0, \mu = 0$).

To analyze the variation of different transport coefficients with temperature and quark chemical potential, we have first plotted in upper panel of Fig. 1, the constituent quark masses ($M$) as a function of temperature ($T$) for different values of the quark chemical potential ($\mu$). The constituent quark mass ($M$) results as a solution to the gap equation, Eq. (26). Constituent quark masses for $u$ and $d$ quarks are the same and they are related to the quark–antiquark condensate $\langle\bar{\psi}\psi\rangle$. In the lower panel of Fig. 1, we have plotted $dM/dT$ with temperature for different values of the chemical potential. For the range of temperature and chemical potential considered here the chiral transition is a smooth crossover. The chiral crossover temperature may be defined by the position of the peak in the variation of $dM/dT$ with temperature. For $\mu =$ 0, 100 and 200 MeV, the corresponding chiral crossover temperatures turns out to be $\sim$ 188 MeV, 180 MeV and 153 MeV

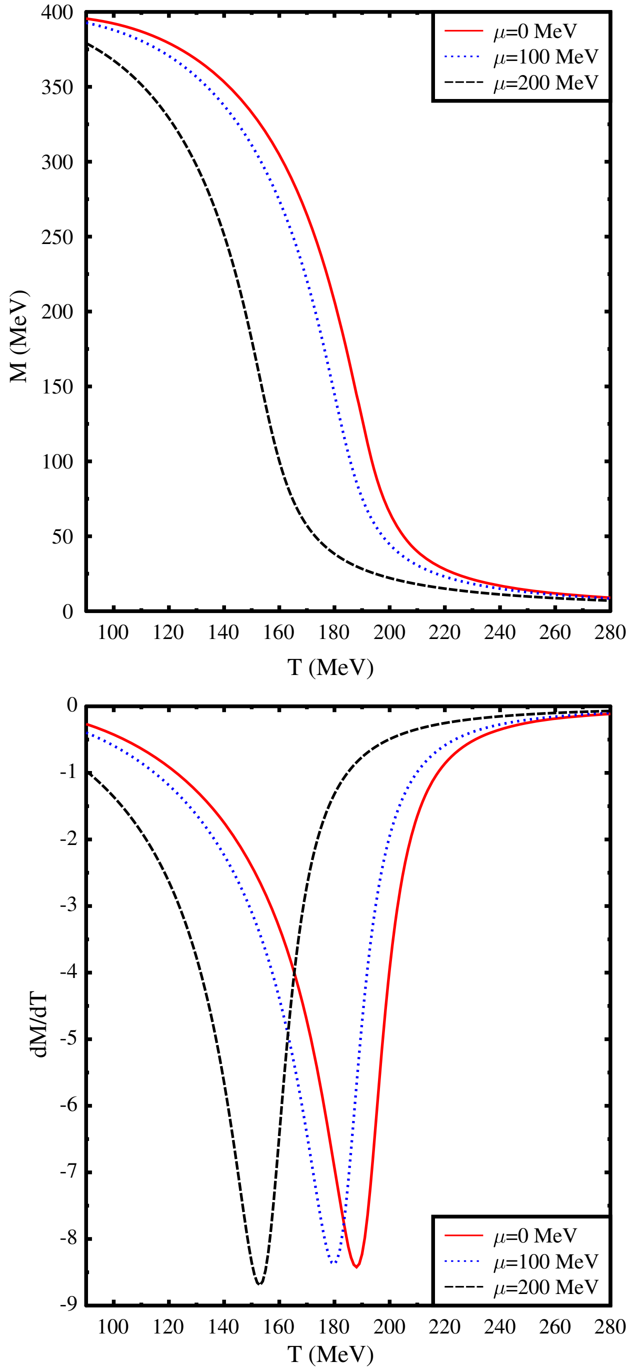


**Fig. 1** Upper panel: temperature dependence of the masses of constituent quarks ($M$) for different chemical potentials. Lower panel: variation of $dM/dT$ with temperature for different chemical potentials. The nonmonotonic variation of $dM/dT$ with a peak structure indicate the pseudo critical temperature for the chiral transition. Note that for the NJL model parameter set and the range of temperature and chemical potential considered here the chiral transition is a smooth crossover

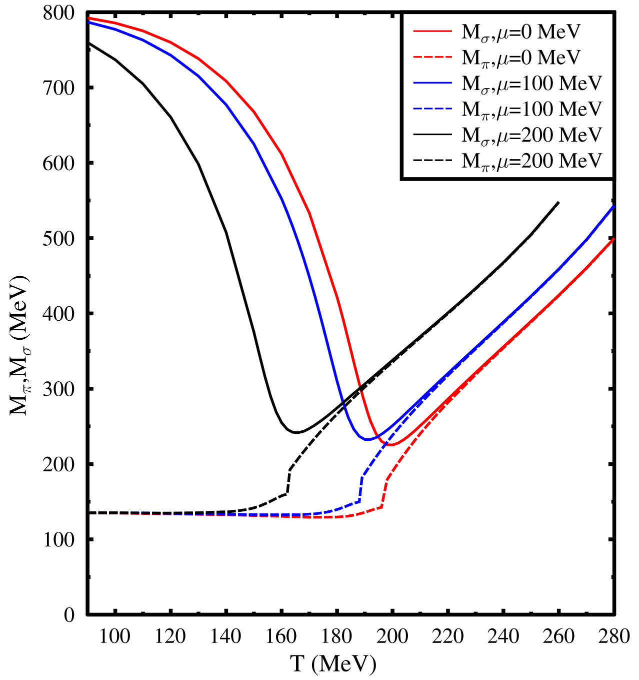


**Fig. 2** Variation of $\sigma$ and $\pi$ meson masses with temperature for different values of the chemical potentials. The solid lines correspond to $M_\sigma$ while the dashed lines correspond to pion masses, $M_\pi$

respectively. It is expected that with an increase in chemical potential the crossover temperature decreases. Note that we have considered here the values of the chemical potential which are lower than the chemical potential corresponding to the speculated critical endpoint of the quark–hadron phase transition in the QCD phase diagram.

In Fig. 2 we have plotted the meson masses $M_\pi$ and $M_\sigma$ as a function of temperature for different values of chemical potential as solutions of Eq. (31). Note that pions are pseudo-Goldstone modes, therefore in the chiral symmetry broken phase pion mass varies weakly. But $M_\sigma$ decreases rapidly near the crossover temperature. At higher temperatures, $M_\pi$ and $M_\sigma$, being chiral partners, become approximately degenerate and increase with temperature. Further one can define a characteristic temperature, the "Mott temperature" ($T_M$) where the pion mass becomes twice that of quark mass i.e. at Mott temperature $M_\pi(T_M) = 2M(T_M)$. The Mott temperatures for $\mu = 0$, 100 and 200 MeV turns out to be $\sim$ 198 MeV, 192 MeV and 166 MeV respectively. As we shall see later it is the Mott temperature that becomes relevant while estimating the relaxation times of the quarks using thermal scattering rates of the quarks through meson exchange.

In Fig. 3, we show the variation of average relaxation time as defined in Eq. (32), for quarks (solid lines) and anti-quarks(dashed lines) with temperature for different chemical potentials. Let us note that the relaxation time of given particle '$a$', as shown in Eq. (32), depends both on the scattering rates $\bar{W}_{ab}$ as well as on the number density $n_b$ of the

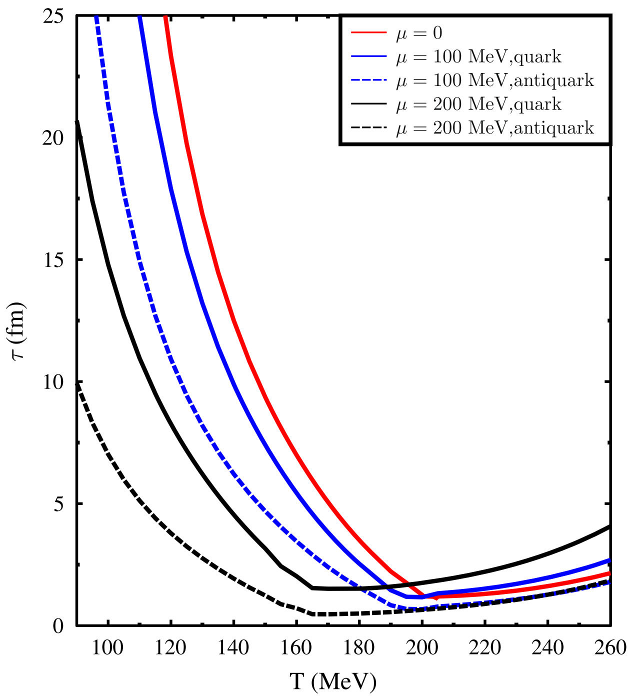


**Fig. 3** Variation of thermal averaged relaxation times for quarks and antiquarks with temperature for different chemical potentials. Solid lines correspond to the relaxation time for quarks while the dotted lines correspond to relaxation time for antiquarks. For $\mu = 0$ the thermal averaged relaxation times for the quarks and antiquarks are same. Difference between the relaxation times of quarks and antiquarks appears only at finite chemical potential

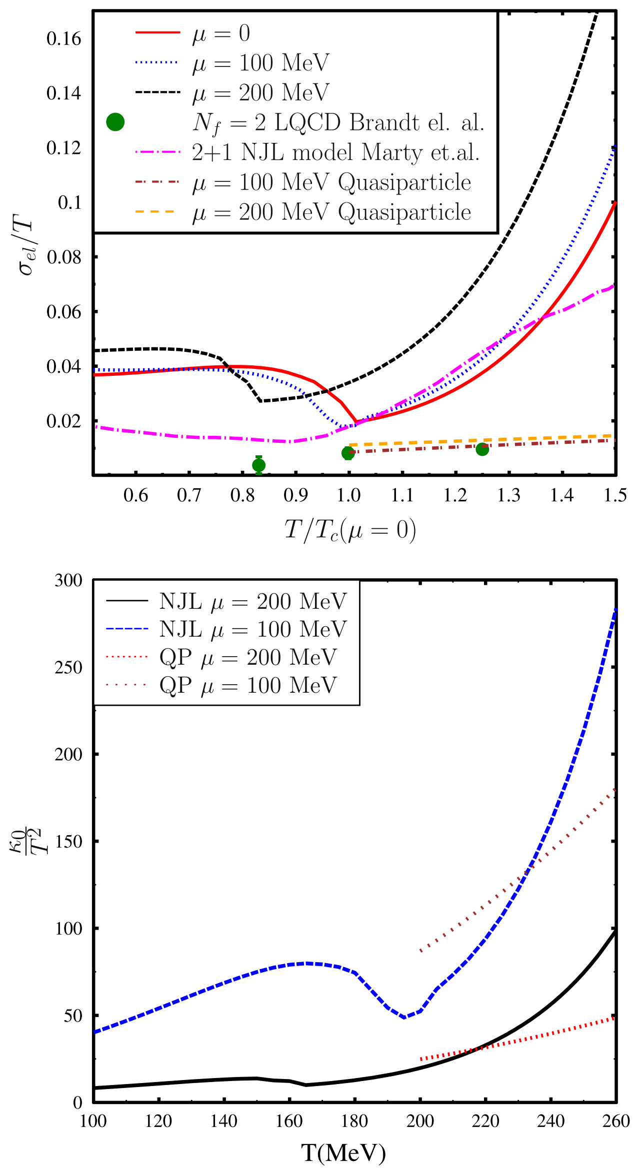


**Fig. 4** Upper panel: Variation of normalized electrical conductivity ($\sigma_{el}/T$) with temperature for different values of the chemical potential for two flavor NJL model and the quasi particle model for the partonic matter as considered here. For comparison, we also presented the two flavor Lattice QCD (LQCD) data as given in Refs. [111,112] and 2+1 flavor NJL model results as obtained in Ref. [31]. Lower panel: Variation of normalized thermal conductivity ($\kappa_0/T^2$) with temperature for different values of the chemical potential for NJL model and for the quasi particle model

particles other than '$a$' in the initial state i.e. number density of scatterers. It turns out that, for the scattering processes considered here, the process $u\bar{d} \rightarrow u\bar{d}$ [81], through charged pion exchange in the s-channel gives the largest contribution as compared to other channels. As mentioned earlier,by crossing symmetry arguments, this also means that the $ud \rightarrow ud$ scattering rate also contribute dominantly to the thermally averaged scattering rate. Let us note that, below the the Mott temperature $T_M$, the averaged scattering rate decreases mostly due to thermal distribution with large constituent quark masses apart from the suppression from the meson propagators in the scattering amplitudes arising from sigma mesons. As one approaches $T_M$ from lower temperature, the scattering rates become larger as the constituent quark mass decreases as well as the s-channel propagator develop a pole in the meson propagator for temperatures beyond $T_M$. However, at large temperature there will be a suppression due to the large meson masses which increase with temperature. This results in a maximum scattering rate at $T_M$ or a minimum in the average relaxation time as generically seen in Fig. 3.

At finite quark chemical potentials, beyond the Mott temperature, the quark–antiquark scattering still contributes dominantly to the scattering processes. However, at finite densities, there are few antiquarks as compared to quarks so that the quarks have fewer antiquarks to scatter off. This leads to a smaller cross-section giving rise to a larger relaxation time for quarks compared to $\mu = 0$ case. Due to the enhancement of quark densities at finite $\mu$, the cross-section for quark–quark scattering becomes larger resulting in a smaller relaxation time for the quarks compared to the case at vanishing chemical potential below the Mott temperature. The antiquark relaxation time, on the other hand, is always smaller compared to $\mu = 0$ case as there are more quarks to scatter off at finite chemical potential.

Some discussions on the estimation of the average relaxation time is in order here. Note that one of the initial calculations in the mid-1990s as done in Ref. [113], as well as a relatively recent calculation as done in Ref. [31], where the transport coefficients for quark–gluon plasma has been estimated within the framework of QCD-inspired effective models, do not incorporate the full field theoretical methods to estimate the relaxation time. In these studies to estimate the average scattering rates or the relaxation time, one considers "integrated cross sections", by integrating the elastic cross section over the invariant energy squared with the help of a probability function (see Ref. [31] for a detailed discussion). Such an estimation of the relaxation time does not incorporate a possible nonmonotonic variation across the transition temperature/Mott temperature. On the other hand, the formalism that we have adopted here does not consider any adhoc probability function, rather we use basic definitions of scattering cross section and the thermal average of relaxation time. Also, the estimated relaxation time as obtained here and also in Ref. [81] clearly shows a nonmonotonic variation of the relaxation time across the transition temperature/Mott temperature. Such nonmonotonic variation of the relaxation time is also reflected in the expected nonmonotonic behavior of $\eta/s$ across the transition temperature [81].

Further as a validity of the Boltzmann kinetic approach within the relaxation time approximation one may look into the value of the the mean free path $\lambda_f = v_f \tau_f$ for a given flavor $f$, here the mean velocity $v_f$ can be expressed as,

$$v_f = \frac{2N_c}{(2\pi)^3 n_f} \int d^3p \frac{|\mathbf{p}|}{E_p} f(E_p). \tag{40}$$

It can be argued that at the Mott transition temperature $\lambda_f = 1.2$ fm [81]. At the same temperature, the mass of the pion and sigma meson are of the order of 200 MeV with the corresponding Compton wavelength ($\lambda_C$) to be of the order of a Fermi. Therefore the value of the ratio $\lambda_f/\lambda_C$ is about 1.2 at the Mott transition temperature and its value increases rapidly both below and above the Mott temperature. Therefore except at the Mott transition temperature $\lambda_f$ can be significantly larger than $\lambda_C$. Thus, within the NJL model, it may not be too unreliable to use the Boltzmann equation within the relaxation time approximation except at the Mott transition temperature. Therefore we believe our analysis is not unjustified given the fact that similar approaches have been well explored by various authors also. The novelty that we are addressing is the thermoelectric properties of the QCD matter across the chiral transition scale.

In the upper panel of Fig. 4 we show the behavior of normalized electrical conductivity $\sigma_{el}/T$ with temperature for different values of chemical potential for the present case of 2 flavor NJL model as well as the quasi particle model considered here. For comparison, we also present the results as obtained using lattice QCD for two light flavors Refs. [111,112] and 2+1 flavor NJL model results as obtained in Ref. [31]. Further, for the sake of comparison, we have taken the temperature in units of $T_c$ of the corresponding models. For the 2 flavor NJL model we have taken $T_c = T_M$=198 MeV as estimated here.

As may be observed from the figure the generic behavior of relaxation time of Fig. 3 is reflected in the behavior of electrical conductivity, having a minimum at Mott transition temperature for the two flavor NJL model shown by the solid red curve in Fig. 4. Apart from this, it is also observed that $\sigma_{el}/T$ increases with chemical potential which we have shown by blue dotted ($\mu = 100$ MeV) and black dashed ($\mu = 200$ MeV) curves. This is because the contribution to the electrical conductivity arises dominantly from quarks rather than antiquarks at finite chemical potential, as the antiquark contribution gets suppressed due to the distribution function. This apart, there is an enhancement of the relaxation time at finite $\mu$ beyond the Mott transition. The dominant contribution to the scattering process is $u\bar{d} \to u\bar{d}$. As the $\bar{d}$ density decrease with $\mu$, this scattering process gets suppressed as compared to the case of $\mu = 0$ and leads to an enhancement of relaxation time at finite chemical potential. Thus both the increase of charge carriers and an increase in relaxation time with $\mu$ lead to enhancement of electrical conductivity beyond the Mott temperature. On the other hand, below the Mott temperature, although the relaxation time decrease with chemical potential, the increase in quark number density makes the coefficient of electrical conductivity increasing with chemical potential. Further, in the high-temperature range $T >> M$, one can assume the quarks and antiquarks to be massless. In this high temperature or massless limit in the two flavor NJL model $\sigma_{el}/T$ can be shown to be $\sigma_{el}/T \sim T\tau \exp(\mu/T)$ (by considering only quark contribution as they are dominant at finite $\mu$). Therefore for a temperature range higher than the Mott transition temperature predominantly due to the increasing behavior of $\tau$ with temperature $\sigma_{el}/T$ increases. Again at a very high temperature due to the factor of $\exp(\mu/T)$, $\sigma_{el}/T$ increases with chemical potential. It is clear that the order of magnitude value of the normalized electrical conductivity as obtained in the present investigation is similar to the lattice QCD (LQCD) results. However, it should be emphasized that LQCD calculations take into account the full dynamical nature of the QCD gauge fields. On the other hand, gluons are not present in the NJL model. Therefore, quantitative variation of the relaxation time and $\sigma_{el}/T$ is not expected to be the same in NJL and LQCD calculations. Further, as compared to results of Marty et al. [31] shown by magenta dot dashed curve, the 2flavor NJL model values are of similar order near the transition temperature while at high temperature ($T/T_c$>1.4) the two flvor NJL values are larger whereas the 2 + 1 flavor values flatten out.This is because of two reasons: firstly, with 2 + 1 flavors, the relaxation time decreases as there are extra channels for scatterings available that reduces the relaxation time. Further, there is a difference in the definition of relaxation time given in Ref. [31] and the present definition for the estimation of the same [81].

We have also plotted the results for the electrical conductivity estimated from the quasi particle model which remains almost constant compared to the NJL model results. The reason is , in the quasi particle models, the quasi particle masses are increasing functions of temperature and hence the thermal distribution functions get suppressed at high temperature in contrast to NJL model. Further, the magnitude of the velocity $|\mathbf{p}|/E$ also become smaller at high temperature in quasi particle model as compared to the NJL model.

Furthermore, in Ref. [114] various transport coefficients of deconfined quark matter have been studied within a different quasi particle model, namely the effective fugacity quasi-particle model. The crucial difference between the quasi particle model considered here and that in Ref. [114] lies in a different dispersion relation between the quasi particles. This is manifested in the estimation of relaxation time as well as in estimation of various transport coefficients. It should be noted that normalized electrical conductivity $\sigma_{el}/T$ as obtained in the present investigation is quantitatively as well as qualitatively different from the same as obtained in Ref. [114]. The presence of a background scalar condensate is the fundamental difference between the NJL model and the effective fugacity quasi-particle model as discussed in Ref. [114]. Further, relaxation time plays an important role in determining the variation of any transport coefficient with temperature and chemical potential. The thermal averaged relaxation time as obtained in the effective fugacity quasi-particle model as discussed in the Ref. [114] is different (quantitatively and quantitatively) from the relaxation time obtained in the NJL model as well as the quasi particle model considered here. For a more detailed analysis of the estimation of electrical conductivity in quasi particle model as considered here and that of effective fugacity quasi particle model, we refer the interested reader to Ref. [110]. The difference stems from the difference in the single particle energy dispersion relation as compared to NJL model or the quasi particle model considered here.

In the lower panel of Fig. 4 we show the variation of the normalized thermal conductivity ($\kappa_0/T^2$) with temperature both for NJL model and for the quasi particle model. For the NJL model, the ratio shows a nonmonotonic variation with temperature. The origin of such behavior again lies with the variation of relaxation time with temperature. Beyond the Mott temperature, the thermal conductivity increases sharply with temperature. This can be understood as follows. For large temperatures, when quark masses can be neglected, it can be easily shown that the enthalpy to the net quark number density ratio goes as $\omega/n_q \sim T\coth(\mu/T)$. Also note that in the expression of the thermal conductivity $(E-\frac{\omega}{n_q})^2 \sim (\frac{\omega}{n_q})^2$, due to the fact that single-particle energy $(E)$ is negligible as compared to the enthalpy per particle-$\omega/n_q$. Therefore, the variation of the normalized thermal conductivity with temperature and chemical potential will be determined by the variation of relaxation time, $\omega/n_q$, and the distribution function. It can be shown that in the high-temperature limit or the massless limit the normalized thermal conductivity, $\kappa_0/T^2$ can be approximately expressed as, $\kappa_0/T^2 \sim T\tau\exp(\mu/T)(\coth(\mu/T))^2$. Beyond the Mott transition temperature, the increasing behavior of $\tau$ essentially determines the increasing behavior of $\kappa_0/T^2$. On the other hand for $\mu << T$, $\coth(\mu/T) \sim T/\mu$ in the leading order. Therefore in the high-temperature limit, $\kappa_0/T^2$ decreases with chemical potential. For the quasi particle model, on the otherhand, the ratio $\kappa_0/T^2$ is of the same order near the transition temperature but rises slowly with temperature compared to the NJL model which again is a reflection of increasing behaviour in the masses of the quasi particle with temperature which reduces the thermal distribution functions. Similar to $\sigma_{el}/T$, the qualitative nature of the normalized thermal conductivity ($\kappa_0/T^2$) as presented here is also different from the same as obtained in the Ref. [114]. This difference is again due to different nature of the dispersion relation for the single particle energies of the quasi particles in effective fugacity quasi particle model and the NJL or the quasi particle model considered here.

We next show the behavior of the Seebeck coefficient as a function of temperature for different values of quark chemical potential in the upper panel of Fig. 5 for both in NJL model and in quasi particle model. This coefficient, which is dimensionless, decreases monotonically with temperature. The variation of the Seebeck coefficient with temperature can be understood as follows. Note that this coefficient is a ratio of two quantities each of which is proportional to the relaxation time. When we consider the relaxation time as the average relaxation time, the ratio becomes independent of the average relaxation time. Note that at finite chemical potential quark contribution to the Seebeck coefficient is dominant with respect to the antiquark contribution. Therefore, contrary to the nonmonotonic variation of $\sigma_{el}/T$ and $\kappa_0/T^2$ with temperature for NJL model, where the nonmonotonic variation has its origin stemming from the behavior of relaxation time with temperature, the variation of the Seebeck coefficient is not expected to be nonmonotonic. Further unlike other transport coefficients, the positivity of the Seebeck coefficient is not guaranteed. This is because in the expression of the Seebeck coefficient as given in Eq. (17), the integrand in the numerator has the factor which is linear in

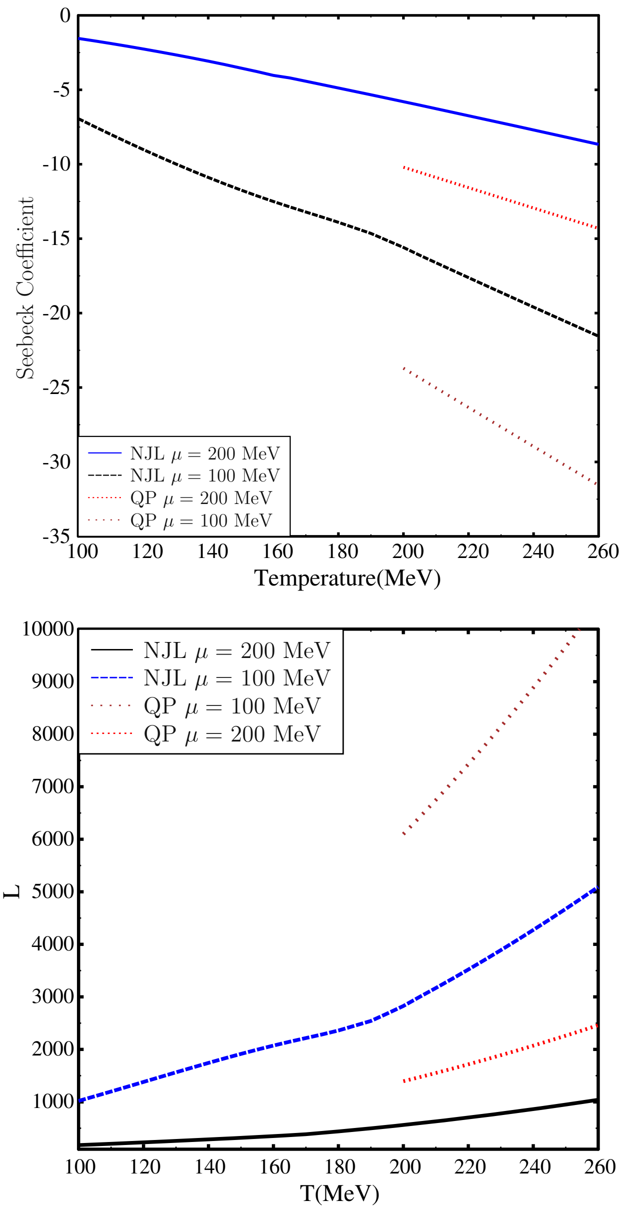


**Fig. 5** Upper panel: variation of the Seebeck coefficient with temperature for different values of the chemical potential for NJL model and for quasi particle model. Lower panel: variation of the Lorenz number, $L = \kappa_0/(\sigma_{el}T)$ with temperature for different values of the chemical potential in both NJL and quasi particle model

$(E_a - b_a\omega/n_q)$. Therefore for the quarks, this factor becomes $(E - \omega/n_q)$, and the single-particle energy $E$ is much smaller than $\omega/n_q$. Therefore the term $(E - \omega/n_q)$ is negative which makes the Seebeck coefficient negative. However it is important to note that the expression of thermal conductivity also contains a term $(E - \omega/n_q)$, but it comes as a square. Therefore positivity of the thermal conductivity is guaranteed. In the condensed matter system the Seebeck coefficient can be both positive and negative, e.g. if for electron and holes the Seebeck coefficients are opposite to each other. Further for a bipolar medium with multiple charge carriers the sign of the Seebeck coefficient depends on the range of temperature considered [102]. Similar to the case of thermal conductivity, one can do an analysis regarding the behavior of the Seebeck coefficient in the massless limit. In the massless limit, it can be shown that $S \sim -\coth(\mu/T)$. Therefore in the high-temperature limit, the leading order contribution to the Seebeck coefficient is $S \sim -T/\mu$. Hence with increasing temperature the Seebeck coefficient decreases, on the other hand with an increase in chemical potential Seebeck coefficient increases. In the simple analysis, we have assumed that the dominant contributions in the sum over species arise from quarks as the antiquark contributions are suppressed due to finite chemical potential in the thermal distribution function. A comment regarding SU(2) flavor symmetry of the NJL Lagrangian may be relevant here. The thermalisation of the medium is decided by strong interaction. Thus, the relaxation time for up and a down quarks will be same. On the other-hand, the contribution of the up quark and down quark to the Seebeck coefficient will be different as the Seebeck coefficient depend linearly on the electrical charge of the relevant species [see e.g. the numerator of the expression for Seebeck coefficient in Eq. (17)]. Thus, the contribution of the Seebeck coefficient of up quark will be twice in magnitude and opposite in sign of the down quark.

Compared to the NJL model, the behaviour of the Seebeck coefficient in the quasi particle model is qualitatively similar but quantitatively different. This can be understood from the behaviour of the electrical conductivity in the model as shown in Fig. 4. The smaller value for the electrical conductivity in quasi particle model leads to larger magnitude for the Seebeck coefficient. Further, in the quasi particle models the gluons also contribute to the enthalpy which affects the Seebeck coefficient.

In the lower panel of Fig. 5 we have plotted the ratio $L = \kappa_0/(\sigma_{el}T)$, as a function of temperature for the NJL model as well as for the quasi particle model. In condensed matter systems this ratio is a constant and is known as the Lorenz number. In the present case, however, it is observed that the ratio increase monotonically with temperature. Similar to the Seebeck coefficient, in the leading order for average relaxation time the ratio $L$, is independent of relaxation time. Further, in the high temperature limit or in the massless limit $\kappa_0/(\sigma T) \sim (\coth(\mu/T))^2$. Therefore, in the leading order for $\mu << T$, $\kappa_0/(\sigma T) \sim T^2/\mu^2$. Hence in the high temperature limit the ratio $L$ increases with temperature but decreases with quark chemical potential. In quasi particle model this ratio is higher compared to the NJL model as the electrical conductivity in the quasi particle description is smaller compared to that in NJL model. This ratio has also been estimated within the effective fugacity quasi particle model in Ref. [114] where, this ratio approach a constant at high temperature. This different behaviour has its origin in the different behaviour of the quasi particles in the effective fugacity quasi particle model as discussed earlier.

## 6 Conclusion

In the present investigation, we have estimated the Seebeck coefficient in a hot and dense partonic medium modeled by the Nambu–Jona–Lasinio model. To compare the NJL model results for the Seebeck coefficient we have also estimated the same within a quasiparticle model of the deconfined matter. We have considered thermoelectric effect arising due to temperature gradient as well as a gradient in the chemical potential. Apart from the Seebeck coefficient we have also estimated electrical conductivity, thermal conductivity, and Lorenz number associated with the Wiedemann- Franz law. Note that electrical conductivity is the response of a medium in the presence of an external electric field. $\sigma_{el}$ also decides the time evolution of a magnetic field in a conducting medium. In the context of the effect of magnetic field on the strongly interacting medium produced in non-central heavy-ion collision electrical conductivity plays a crucial role. It should be emphasized that in the presence of a magnetic field simple Ohm's law gets modified and one needs to consider the anisotropic structure of the electrical conductivity tensor. All such investigations in the presence of a magnetic field should reproduce the electrical conductivity in the absence of any magnetic field, i.e. the electrical conductivity tensor should be isotropic in the absence of any magnetic field. Therefore, the estimation of electrical conductivity without any effect of the magnetic field should serve as a baseline for the studies that include the effect of magnetic field in a conducting medium.

Although electrical conductivity and thermal conductivity always remain positive, but the Seebeck coefficient is negative for the range of temperature and chemical potential considered in this investigation. Also the variation of electrical conductivity and thermal conductivity with temperature and quark chemical potential is intimately related to the variation of the relaxation time with temperature and chemical potential. But the variation of the Seebeck coefficient and the Lorenz number are not sensitive to the variation of relaxation time with temperature and quark chemical potential.

In the presence of thermoelectric effects in a conducting medium temperature gradient can be converted into an electrical current and vice versa. Seebeck coefficient physically represents the efficiency of any conducting medium to convert a temperature gradient into an electrical current. Therefore for a nonvanishing Seebeck coefficient electrical current as well as heat current gets modified. The electrical current in the presence of Seebeck effect becomes, $\mathbf{J} = \sigma_{el}\boldsymbol{\mathcal{E}} - \sigma_{el} S \nabla T$. It is important to note that the electrical conductivity $\sigma_{el}$ is always positive due to the constructive contributions of particles and antiparticles to the electric current. Positivity of the electrical conductivity can be shown using entropy production i.e. second law of thermodynamics. By demanding that in the presence of electromagnetic field $T\partial_\mu s^\mu \geq 0$, here $s^\mu$ is the entropy current, it can be shown that the electrical conductivity is positive [115]. For a negative Seebeck coefficient in the presence of a positive temperature gradient the electric current enhances. Therefore the net electric current increases if the electric current due to the thermoelectric effect and the electric current due to the external electric field contributes constructively. On the other hand, the thermal conductivity in the presence of the thermoelectric effect gets modified. In the presence of a nonvanishing Seebeck coefficient, the net thermal conductivity which can be given as $\kappa = \kappa_0 - T\sigma_{el} S^2$ indicates that the nonvanishing value of the Seebeck coefficient reduces the thermal conductivity. It is important to note that the thermal conductivity is required to be positive for the theory to be consistent with the second law of thermodynamics, i.e., $T\partial_\mu s^\mu \geq 0$. Using the formalism of viscous hydrodynamics and viscous magnetohydrodynamics positivity of the electrical conductivity and the thermal conductivity has been shown explicitly [100,115]. But the contributions to the entropy current coming from the thermoelectric effects are not considered in these investigations. Therefore in the context of entropy production in the viscous hydrodynamics and magnetohydrodynamics, it will be interesting to study the effects of thermoelectric coefficients.

Thermoelectric coefficients could also be relevant in the context of the spin Hall effect (SHE). Spin Hall effect is an important ingredient for the generation of spin current and it is a key concept in spintronics. In the generation of spin current spin Hall effect plays an important role. In spin Hall effect an electric field induces a transverse spin current perpendicular to the direction of the electric field. Spin Hall effect has been investigated recently in a hot and dense nuclear matter in the context of heavy-ion collisions [116]. It has been argued that due to SHE, a spin current will be produced proportional to the electric field. This also means external electric field $\boldsymbol{\mathcal{E}}$ will induce a local spin polarization and the spin polarization distribution function of fermions (antifermions) in momentum space will feature a dipole distribution. Therefore there will a spin flow in the plane transverse to the direction of the electric field. Observation of spin Hall effect may open a new direction in the exploration of the many body quantum effects in hot and dense nuclear matter. However, the life-time of the electric field originated in heavy-ion collisions could be small of the order 1 fm/c. Therefore, the idea of the observation of the spin Hall effect becomes speculative. However, in the presence of nonvanishing thermoelectric coefficients any temperature gradient and/or a gradient in the chemical potential can give rise to an effective electric field which may contribute to the spin Hall effect. Therefore a detailed analysis of the thermoelectric property of the hot and dense matter produced in a heavy ion collision experiment could be relevant for spin Hall effect and needs further investigation.

**Acknowledgements** We thank Prof. Ajit M. Srivastava for suggesting and initiating discussions on the idea of thermoelectric coefficient in the context of heavy-ion collision. The authors would like to thank Prof. Jitesh R. Bhatt for useful discussions. The authors would also like to thank Sabyasachi Ghosh, Abhishek Atreya, Chowdhury Aminul Islam, Rajarshi Ray for many discussions on the topic of Seebeck coefficient during working group activities at WHEPP 2017, IISER Bhopal. The work of A.D. is supported by the Polish National Science Center Grant no. 2018/30/E/ST2/00432.

**Data Availability Statement** This manuscript has no associated data or the data will not be deposited. [Authors' comment: The plots are based on Eq. 25, Eq. 26, Eq. 31 and Eq. 32 in the paper together with the values of the parameters given. This is sufficient to generate the plots.]


Funded by SCOAP[3].

## References

1. U. Heinz, R. Snellings, Ann. Rev. Nucl. Part. Sci. **63**, 123–151 (2013)
2. P. Romatschke, U. Romatschke, Phys. Rev. Lett. **99**, 172301 (2007)
3. P. Kovtun, D.T. Son, A.O. Starinets, Phys. Rev. Lett. **94**, 111601 (2005)
4. A. Dobado, J.M. Torres-Rincon, Phys. Rev. D **86**, 074021 (2012)
5. C. Sasaki, K. Redlich, Phys. Rev. C **79**, 055207 (2009)
6. C. Sasaki, K. Redlich, Nucl. Phys. A **832**, 62–75 (2010)
7. F. Karsch, D. Kharzeev, K. Tuchin, Phys. Lett. B **663**, 217–221 (2008)
8. S.I. Finazzo, R. Rougemont, H. Marrochio, J. Noronha, JHEP **02**, 051 (2015)
9. S. Jeon, L.G. Yaffe, Phys. Rev. D **53**, 5799–5809 (1996)
10. A. Bazavov et al., Phys. Rev. D **80**, 014504 (2009)
11. A. Bazavov, P. Petreczky, PoS LATTICE2010:169, 2010
12. P. Bozek, Phys. Rev. C **81**, 034909 (2010)
13. J.B. Rose, J.F. Paquet, G.S. Denicol, M. Luzum, B. Schenke, S. Jeon, C. Gale, Nucl. Phys. A **931**, 926–930 (2014)
14. K. Tuchin, Phys. Rev. C **83**, 017901 (2011)
15. K. Tuchin, Phys. Rev. C **82**, 034904 (2010)
16. G. Inghirami, L.D. Zanna, A. Beraudo, M.H. Moghaddam, F. Becattini, M. Bleicher, Eur. Phys. J. C **76**, 659 (2016)
17. A. Das, S.S. Dave, P.S. Saumia, A.M. Srivastava, Phys. Rev. C **96**, 034902 (2017)
18. M. Greif, C. Greiner, G.S. Denicol, Phys. Rev. D **93**, 096012 (2016)
19. M. Greif, I. Bouras, C. Greiner, Z. Xu, Phys. Rev. D **90**, 094014 (2014)
20. A. Puglisi, S. Plumari, V. Greco, Phys. Lett. B **751**, 326–330 (2015)
21. A. Puglisi, S. Plumari, V. Greco, Phys. Rev. D **90**, 114009 (2014)
22. W. Cassing, O. Linnyk, T. Steinert, V. Ozvenchuk, Phys. Rev. Lett. **110**, 182301 (2013)
23. T. Steinert, W. Cassing, Phys. Rev. C **89**, 035203 (2014)
24. G. Aarts, C. Allton, A. Amato, P. Giudice, S. Hands, J.I. Skullerud, JHEP **02**, 186 (2015)
25. G. Aarts, C. Allton, J. Foley, S. Hands, S. Kim, Phys. Rev. Lett. **99**, 022002 (2007)
26. A. Amato, G. Aarts, C. Allton, P. Giudice, S. Hands, J.I. Skullerud, Phys. Rev. Lett. **111**, 172001 (2013)
27. S. Gupta, Phys. Lett. B **597**, 57–62 (2004)
28. H.T. Ding, A. Francis, O. Kaczmarek, F. Karsch, E. Laermann, W. Soeldner, Phys. Rev. D **83**, 034504 (2011)
29. O. Kaczmarek, M. Müller, PoS LATTICE2013:175 (2014)
30. S. Qin, Phys. Lett. B **742**, 358–362 (2015)
31. R. Marty, E. Bratkovskaya, W. Cassing, J. Aichelin, H. Berrehrah, Phys. Rev. C **88**, 045204 (2013)
32. D.F. Fraile, A.G. Nicola, Phys. Rev. D **73**, 045025 (2006)
33. D.E. Kharzeev, L.D. McLerran, H.J. Warringa, Nucl. Phys. A **803**, 227–253 (2008)
34. V. Skokov, AYu. Illarionov, V. Toneev, Int. J. Mod. Phys. A **24**, 5925–5932 (2009)
35. H. Li, X. Sheng, Q. Wang, Phys. Rev. C **94**, 044903 (2016)
36. G. Inghirami, M. Mace, Y. Hirono, L.D. Zanna, D.E. Kharzeev, M. Bleicher, Eur. Phys. J. C **80**, 293 (2020)
37. G. Inghirami, L.D. Zanna, A. Beraudo, M.H. Moghaddam, F. Becattini, M. Bleicher, J. Phys. Conf. Ser. **1024**, 012043 (2018)
38. M. Shokri, N. Sadooghi, Phys. Rev. D **96**, 116008 (2017)
39. M. Shokri, N. Sadooghi, JHEP **11**, 181 (2018)
40. S.M.A. Tabatabaee, N. Sadooghi, Phys. Rev. D **101**, 076022 (2020)
41. D.E. Kharzeev, K. Landsteiner, A. Schmitt, H.U. Yee, Strongly interacting matter in magnetic fields': an overview. Lect. Notes Phys. **871**, 1 (2013)
42. M. Greif, J.A. Fotakis, G.S. Denicol, C. Greiner, Phys. Rev. Lett. **120**, 242301 (2018)
43. M. Prakash, M. Prakash, R. Venugopalan, G. Welke, Phys. Rep. **227**, 321–366 (1993)
44. A. Wiranata, M. Prakash, Phys. Rev. C **85**, 054908 (2012)
45. P. Chakraborty, J.I. Kapusta, Phys. Rev. C **83**, 014906 (2011)
46. A.S. Khvorostukhin, V.D. Toneev, D.N. Voskresensky, Nucl. Phys. A **845**, 106–146 (2010)
47. S. Plumari, A. Puglisi, F. Scardina, V. Greco, Phys. Rev. C **86**, 054902 (2012)
48. M.I. Gorenstein, M. Hauer, O.N. Moroz, Phys. Rev. C **77**, 024911 (2008)
49. J. Noronha-Hostler, J. Noronha, C. Greiner, Phys. Rev. C **86**, 024913 (2012)
50. S.K. Tiwari, P.K. Srivastava, C.P. Singh, Phys. Rev. C **85**, 014908 (2012)
51. S. Ghosh, A. Lahiri, S. Majumder, R. Ray, S.K. Ghosh, Phys. Rev. C **88**, 068201 (2013)
52. R. Lang, N. Kaiser, W. Weise, Eur. Phys. J. A **51**, 127 (2015)
53. S. Ghosh, G. Krein, S. Sarkar, Phys. Rev. C **89**, 045201 (2014)
54. A. Wiranata, V. Koch, M. Prakash, X.N. Wang, J. Phys. Conf. Ser. **509**, 012049 (2014)
55. A. Wiranata, M. Prakash, P. Chakraborty, Cent. Eur. J. Phys. **10**, 1349–1351 (2012)
56. J. Noronha-Hostler, J. Noronha, C. Greiner, Phys. Rev. Lett. **103**, 172302 (2009)

57. G.P. Kadam, H. Mishra, Nucl. Phys. A **934**, 133–147 (2014)
58. G.P. Kadam, Mod. Phys. Lett. A **30**, 1550031 (2015)
59. S. Ghosh, Int. J. Mod. Phys. A **29**, 1450054 (2014)
60. J.B. Rose, J.M. Torres-Rincon, A. Schäfer, D.R. Oliinychenko, H. Petersen, Phys. Rev. C **97**, 055204 (2018)
61. C. Wesp, A. El, F. Reining, Z. Xu, I. Bouras, C. Greiner, Phys. Rev. C **84**, 054911 (2011)
62. G.S. Denicol, H. Niemi, I. Bouras, E. Molnar, Z. Xu, D.H. Rischke, C. Greiner, Phys. Rev. D **89**, 074005 (2014)
63. J.I. Kapusta, J.M. Torres-Rincon, Phys. Rev. C **86**, 054911 (2012)
64. P. Ao, arXiv:cond-mat/9505002
65. M. Matusiak, K. Rogacki, T. Wolf, Phys. Rev. B **97**, 220501 (2018)
66. C.S. Yadav, M.K. Hooda, arXiv:1704.07194
67. O. Cyr-Choinière, S. Badoux, G. Grissonnanche, B. Michon, S.A.A. Afshar, S. Fortier, D. LeBoeuf, D. Graf, J. Day, D.A. Bonn, W.N. Hardy, R. Liang, N. Doiron-Leyraud, L. Taillefer, Phys. Rev. X **7**, 031042 (2017)
68. S. Sergei, JETP Lett. **67**, 680–684 (1998)
69. M.M. Wysokinski, J. Spalek, J. Appl. Phys. **113**, 163905 (2013)
70. K.P. Wójcik, I. Weymann, Phys. Rev. B **89**, 165303 (2014)
71. K. Seo, S. Tewari, Phys. Rev. B **90**, 174503 (2014)
72. P. Dutta, A. Saha, A.M. Jayannavar, Phys. Rev. B **96**, 115404 (2017)
73. A. Das, H. Mishra, R.K. Mohapatra, Phys. Rev. D **102**, 014030 (2020)
74. J.R. Bhatt, A. Das, H. Mishra, Phys. Rev. D **99**, 014015 (2019)
75. D. Dey, B.K. Patra, arXiv:2004.03149
76. H.-X. Zhang, arXiv:2004.08767
77. P. Singha, A. Abhishek, G. Kadam, S. Ghosh, H. Mishra, J. Phys. G **46**, 015201 (2019)
78. A. Abhishek, H. Mishra, S. Ghosh, Phys. Rev. D **97**, 014005 (2018)
79. B. Singh, A. Abhishek, S.K. Das, H. Mishra, Phys. Rev. D **100**, 114019 (2019)
80. C. Ratti, M.A. Thaler, W. Weise, Phys. Rev. D **73**, 014019 (2006)
81. P. Deb, G.P. Kadam, H. Mishra, Phys. Rev. D **94**, 094002 (2016)
82. P. Rehberg, S.P. Klevansky, J. Hufner, Phys. Rev. C **53**, 410–429 (1996)
83. Y. Tsue, J. da Providencia, C. Providencia, M. Yamamura, Prog. Theor. Phys. **128**, 507–522 (2012)
84. T. Maruyama, E. Nakano, T. Tatsumi, *Horizons in World Physics, Chapter 7*, vol. 276 (Nova Science, New York, 2011)
85. D.P. Menezes, M.B. Pinto, S.S. Avancini, A.P. Martinez, C. Providencia, Phys. Rev. C **79**, 035807 (2009)
86. B. Chatterjee, H. Mishra, A. Mishra, Phys. Rev. D **84**, 014016 (2011)
87. T. Mandal, P. Jaikumar, S. Digal, arXiv:0912.1413
88. T. Mandal, P. Jaikumar, Phys. Rev. C 87045208 (2013)
89. T. Mandal, P. Jaikumar, Phys. Rev. D **94**, 074016 (2016)
90. M. Coppola, P. Allen, A.G. Grunfeld, N.N. Scoccola, Phys. Rev. D **96**, 056013 (2017)
91. M. Bluhm, QCD equation of state of hot deconfined matter at finite baryon densities: a quasi particle perspective, Ph.D. thesis, Technical University of Dresden 2008
92. A. Peshier, B. kampfer, Phys. Rev C **61**, 045203 (2000)
93. A. Peshier, B. Kampfer, G. Soff, Phys. Rev. D **66**, 094003 (2002)
94. R.A. Schneider, W. Weise, Phys. Rev. C **64**, 055201 (2001)
95. S. Koothottil, V.M. Bannur, Phys. Rev. C **102**, 015206 (2020)
96. P.K. Srivastava, S.K. Tiwari, C.P. Singh, Phys. Rev. D **82**, 014023 (2010)
97. M.V. Bannur, JHEP **09**, 046 (2007)
98. A.S. Khvorostukhin, V.D. Toneev, D.N. Voskresensky, Nucl. Phys. A **915**, 158–169 (2013)
99. P. Zhuang, J. Hufner, S.P. Klevansky, L. Neise, Phys. Rev. D **51**, 3728–3738 (1995)
100. S. Gavin, Nucl. Phys. A **435**, 826–843 (1985)
101. G.P. Kadam, H. Mishra, L. Thakur, Phys. Rev. D **98**, 114001 (2018)
102. L.Y. Zhou, Q. Zheng, L.H. Bao, W.J. Liang, Chin. Phys. Lett. **37**, 017301 (2020)
103. M. Buballa, Phys. Rep. **407**, 205–376 (2005)
104. L. Thakur, P.K. Srivastava, G.P. Kadam, M. George, H. Mishra, Phys. Rev. D **95**, 096009 (2017)
105. M.V. Bannur, Phys. Rev. C **75**, 044905 (2007)
106. L.L. Zhu, C.B. Yang, Nucl. Phys. A **831**, 49–58 (2009)
107. M.I. Gorenstein, S.N. Yang, Phys. Rev. D **52**, 5206 (1995)
108. A. Hosoya, K. Kajantie, Nucl. Phys. B **250**, 666 (1985)
109. H. Berrehrah, E. Bratkovskaya, W. Cassing, P.B. Gossiaux, J. Aichelin, M. Bleicher, Phys. Rev. C **89**, 054901 (2014)
110. A. Das, H. Mishra, R.K. Mohapatra, Phys. Rev. D **101**, 034027 (2020)
111. B.B. Brandt, A. Francis, B. Jaeger, H.B. Meyer, Phys. Rev. D **93**, 054510 (2016)
112. G. Aarts, A. Nikolaev, Eur. Phys. J. A **57**, 118 (2021)
113. P. Rehberg, S.P. Klevansky, J. Hufner, Nucl. Phys. A **608**, 356–388 (1996)
114. S. Mitra, V. Chandra, Phys. Rev. D **96**, 094003 (2017)
115. X.G. Huang, M. Huang, D.H. Rischke, A. Sedrakian, Phys. Rev. D **81**, 045015 (2010)
116. S.Y.F. Liu, Y. Yin, Phys. Rev. D **104**, 054043 (2021)

Journal of Cosmology and
Astroparticle Physics

**PAPER**

# Non-radial oscillation modes in hybrid stars: consequences of a mixed phase

Journal of Cosmology and Astroparticle Physics
An IOP and SISSA journal

# Non-radial oscillation modes in hybrid stars: consequences of a mixed phase

**Deepak Kumar,**[a,b] **Hiranmaya Mishra**[b,c] **and Tuhin Malik**[d]

[a]Indian Institute of Technology Gandhinagar,
Gandhinagar 382 355, Gujarat, India
[b]Theory Division, Physical Research Laboratory,
Navarangpura, Ahmedabad 380 009, India
[c]School of Physical Sciences, National Institute of Science Education and Research,
Jatni-752050, India
[d]CFisUC, Department of Physics, University of Coimbra,
P-3004 — 516 Coimbra, Portugal

E-mail: deepakk@prl.res.in, hiranmaya@niser.ac.in, tuhin.malik@gmail.com

Received July 19, 2022
Revised December 7, 2022
Accepted January 8, 2023
Published February 7, 2023

**Abstract.** We study the possibility of the existence of a deconfined quark matter in the core of neutron star (NS)s and its relation to non-radial oscillation modes in NSs and hybrid star (HS)s. We use relativistic mean field (RMF) models to describe the nuclear matter at low densities and zero temperature. The Nambu-Jona-Lasinio (NJL) model is used to describe the quark matter at high densities and zero temperature. A Gibbs construct is used to describe the hadron-quark phase transition (HQPT) at large densities. Within the model, as the density increases, a mixed phase (MP) appears at density about 2.5 times the nuclear matter saturation density ($\rho_0$) and ends at density about $5\rho_0$ beyond which the pure quark matter phase appears. It turns out that a stable HS of maximum mass, $M = 2.27 M_\odot$ with radius $R = 14$ km (for NL3 parameterisation of nuclear RMF model), can exist with the quark matter in the core in a MP only. HQPT in the core of maximum mass HS occurs at radial distance, $r_c = 0.27R$ where the equilibrium speed of sound shows a discontinuity. Existence of quark matter in the core enhances the non-radial oscillation frequencies in HSs compared to NSs of the same mass. This enhancement is significantly large for the $g$ modes. Such an enhancement of the $g$ modes is also seen for a density dependent Bayesian (DDB) parmeterisation of the nucleonic EOS. The non-radial oscillation frequencies depend on the vector coupling in the NJL model. The values of $g$ and $f$ mode frequencies decrease with increase the vector coupling in quark matter.

**Keywords:** neutron stars, astrophysical fluid dynamics, massive stars

**ArXiv ePrint:** 2110.00324

JCAP02(2023)015

 https://doi.org/10.1088/1475-7516/2023/02/015

## Contents



## 1 Introduction

Neutron Star (NS)s are exciting cosmic laboratories to study the behavior of matter at extreme densities. The properties of NSs not only open up many possibilities related to composition, structure and dynamics of cold matter in the observable universe but also throws light on the interaction of matter at a fundamental level [1]. Such compact stars, observed as pulsars, are believed to contain matter of densities few times nuclear saturation density ($\rho_0 \simeq 0.158$ fm$^{-3}$) in its core. To explain and understand the properties of such stars, one needs to connect different branches of physics like low energy nuclear physics, qunatum chromodynamics (QCD) under extreme conditions, general theory of relativity (GTR) etc [2–6].

The macroscopic properties of such a compact star like its mass, radius, moment of inertia, tidal deformability in a binary merging system and different modes of oscillations etc. depend crucially on its composition that affect the variation of pressure with energy density or equation of state (EOS). Indeed, recent radio, x-ray and gravitational wave observations of NSs have provided valuable insights into the EOS of dense matter [7–9]. The observations of high mass pulsars like PSR $J1614-2230$ ($M = 1.928 \pm\ 0.017 M_\odot$) [10], PSR $J0348-0432$ ($M = 2.01 \pm\ 0.04\ M_\odot$) [11] and PSR $J0740{+}6620$ ($M = 2.08 \pm\ 0.07\ M_\odot$) [12] and very recently PSR $J1810+1714$ with a mass ($M = 2.13 \pm\ 0.04\ M_\odot$) [13] have already drawn attention on nuclear interactions at high densities with questions regarding the possible presence of exotic matter in them. To constrain the nature of EOS more stringently, simultaneous measurements of NS mass and radius are essential. The precise determinations of NS radii is difficult due to inaccurate modeling the x-ray spectra emitted by the atmosphere of a NS. The high-precision x-ray space missions, such as the Neutron star Interior Composition ExploreR (NICER) have already shed some light in this direction. Of late, NICER has come up with a measurement of the radius $12.71^{+1.14}_{-1.19}$ km, for NS with mass $1.34^{+0.15}_{-0.16}$ $M_\odot$ [14], and other independent analyses show that the radius is $13.02^{+1.24}_{-1.06}$ km for an NS with mass $1.44^{+0.15}_{-0.14}$ $M_\odot$ [15]. Further, the recent measurement of the equatorial circumferential radius of the highest mass ($2.072^{+0.067}_{-0.066}$ $M_\odot$) pulsar PSR $J0740+6620$ is $12.39^{+1.30}_{-0.98}$ km [16, 17] by NICER will play an important role in this domain.

The core of the NS can, in principle, support various possible exotic phases of QCD. While perturbative QCD (pQCD) predicts deconfined quark matter at large densities, their applicability is rather limited in the sense that these conclusions are applicable only to very large baryon densities i.e. $\rho_B \geq 40\rho_0$ [18]. The most challenging region to study theoretically is, however, at intermediate densities i.e. few times nuclear matter saturation density which is actually relevant for the matter in the core of NSs. The first principle Lattice QCD (LQCD) calculation in this connection is also difficult due to the sign problem in lattice simulations at finite densities. At present such calculations are limited to low baryon densities only i.e. $\mu_B/T \leq 3.5$ [19]. On the otherhand, many effective models predict possibilities of various exotic phases of quark matter at such intermediate density region. These include pion superfluidity [20–22], various colour superconducting phases like 2-flavour colour superconductivity [23–25], colour flavour locked phase (CFL) [26], Larkin-Ovchinkov-Fulde-Ferrel (LOFF) [27, 28] phase, crystalline superconductivity phase etc. However, the signature of such phases in quark matter from the study of NSs have been rather challenging. The GW170817 [9] event explored the constraints on the EOS using tidal deformability extracted from the phase of the gravitational waveforms during the late stage of inspiral merger [29–34]. Though not conclusive, it is quite possible that one or both the merging NSs could be Hybrid Star (HS)s i.e. with a core of quark matter or a Mixed Phase (MP) core of quark and hadronic matter [35, 36]. Within the current observational status, it is difficult to distinguish between a canonical NS without a quark matter core from a HS with a core of pure quark matter or a core of quark matter in a MP with hadronic matter. This calls for exploring other observational signature to solve this "masquerade" problem [37, 38].

In this context, it has been suggested that the study of the non-radial oscillation modes of NSs can have the possibility of providing the compositional information regarding the matter in the interior of the NSs. This includes the NSs with a hyperon core [39–41], a quark core or a MP core with quark and hadronic matter [38, 42–47]. This is because the non-radial oscillations not only depend upon the EOS i.e. $p(\epsilon)$ but also on the derivatives $\frac{dp}{d\epsilon}$ and $\frac{\partial p}{\partial \epsilon}$ [48]. Since the appearance of hyperons does not involve any phase transition, their effects on the non-radial oscillation modes can be milder compared to a hadron-quark phase transition (HQPT) at finite densities whose effect can be more pronounced. The non-radial oscillation modes can be studied within the framework of GTR [49, 50]. Here, the fluid perturbation equations can be decomposed into spherical harmonics leading to two classes of oscillations depending upon the parity of the harmonics. The even parity oscillations produce spheroidal (polar) deformation while the odd parity oscillations produce toroidal deformation. The polar quasi-normal mode (QNM)s can further be classified into different kinds of modes depending upon the restoring force that acts on the fluid element when it gets displaced from its equilibrium position [51]. These oscillations couple to the gravitational waves and can be used as the diagnostic tools in studying the phase structure of the matter inside NSs. The important modes for this are the pressure ($p$) modes, fundamental ($f$) modes and gravity ($g$) modes. The frequency of the $g$ modes is lower than that of $p$ modes while the frequency of $f$ modes lie in between. These are the fluid oscillation modes to be distinguished from $w$ modes which are associated with the perturbation of space-time metric itself [52]. In the present work, we focus on $g$ and $f$ modes oscillations arising from dense matter from both neutron star matter (NSM) and hybrid star matter (HSM). For nuclear matter, the existence of such low frequency $g$ modes was shown earlier in refs. [53, 54]. The origin of $g$ mode is related to the convective stability i.e. stable stratification of the star. When a parcel of the fluid is displaced, the pressure equilibrium is restored rapidly through sound waves while compositional equilibrium, decided by the weak interaction takes a longer time causing the buoyancy force to oppose the displacement. This sets in the oscillations. The $g$ mode oscillation frequencies are related to the Brunt-Väisäla frequency ($\omega_{\rm BV}$) which depends on the difference between the equilibrium sound speed ($c_e^2$) and adiabatic or the constant composition sound speed ($c_s^2$) i.e. $\omega_{\rm BV}^2 \propto (1/c_e^2 - 1/c_s^2)$ as well as on the local metric. Such $g$ modes without any phase transition have been studied earlier for the nuclear matter, hyperonic matter, superfluidity [39, 40, 55–63].

It may be mentioned that much of the recent works on the estimation of $\omega_{\rm BV}$ are based on the parameterised form of $\beta$-equilibrated nuclear matter EOS [43, 48]. In the present work, on the otherhand, we use Relativistic Mean Field (RMF) model to estimate the $\omega_{\rm BV}$ and use it to calculate the $g$ modes oscillation frequencies. In the core of HSs with quark matter core (either in a MP or in a pure quark matter phase), the $\omega_{\rm BV}$ can become large enough inside of the star at a radial distance $r_c$ from the center where HQPT takes place and drive the $g$ mode oscillations.

It may be noted that $g$ modes oscillations have been studied earlier in the context of the HQPT [38, 42–48, 64]. In most of these investigations, the hadronic matter description is through a parameterized form of nuclear matter EOS and the quark matter description is through a bag model or an improved version of the same. In the present investigation, for the nuclear matter sector we use a RMF theory involving nucleons interacting with scalar and vector meson mean fields along with self-interactions of the mesons leading to reasonable saturation properties of nuclear matter. For the description of quark matter we use a two flavour Nambu–Jona-Lasinio (NJL) model where the parameters of the model are fixed from the physical variables like pion mass, pion decay constant and light quark condensate that encodes the physics of the chiral symmetry breaking. The phase transition from hadronic matter to quark matter can be considered either through a Maxwell construct or a Gibbs construct leading to a MP [65]. It ought to be noted that the kind of phase transition depends crucially on the surface tension [66–72] of the quark matter which, however, is poorly known. Gibbs construct is relevant for smaller value of surface tension while Maxwell construct becomes relevant for large values of surface tension [73, 74].

We organize this paper as follows. In section 2.1 we discuss salient features of RMF models describing the nuclear matter. Specifically, we consider two different RMF models — namely, the NL3 parameterized RMF with constant couplings along with nonlinear mesonic interactions and a RMF model with density dependent couplings of baryon meson interaction. Such a model has been quite successful in describing nuclear matter properties and finite nuclei [75]. Recently, using a Bayesian Inference framework in conjunction with minimal constraints on nuclear saturation properties, the maximum mass of neutron stars exceeding $2M_\odot$, and low density equation of state (EOS) calculated using chiral effective theory for pure neutron matter,the density dependent coupling parameters have been investigated [76, 77]. Such a density dependent Bayesian (DDB) model will be the other RMF model for hadronic matter that we shall use in the analysis for the HQPT. In section 2.2, we discuss the NJL model and write down the EOS for the quark matter. In section 2.3 we discuss the HQPT



JCAP02(2023)015

using Gibbs construct when there are multiple chemical potentials to describe the system. In section 3, we discuss the stellar structure equations as well as the non-radial fluid oscillations of the compact stars. We give here, in some detail, the derivation of the pulsation equations. In section 4, we discuss the estimation of the equilibrium and adiabatic speed of sound in different phases of matter. In section 5 we discuss the results of the present investigation regarding thermodynamics of the dense matter, MP construction, HS structure and the non-radial mode oscillations. Finally in section 6, we summarize the results and give an outlook for the further investigation. We use natural units here where $\hbar = c = G = 1$.

## 2 Formalism

### 2.1 Equation of state for nuclear matter

We discuss briefly the general RMF framework to construct the EOS of the NSM in Hadronic Phase (HP). In this framework, the interaction among the baryons is realized through the exchange of mesons. We confine our analysis for the NSM constituting of baryons (neutron and proton) and leptons (electron and muon). The relevant mesons for this purpose are the $\sigma$, $\omega$ and $\rho$ mesons [78–81]. The scalar $\sigma$ mesons create a strong attractive interactions, the vector $\omega$ mesons on the otherhand are responsible for the repulsive short range interactions. The neutron and proton do only differ in terms of their isospin projections. The isovector $\rho$ mesons are included to distinguish between baryons. The Lagrangian including baryons as the constituents of the nuclear matter and mesons as the carriers of the interactions is given as [82, 83]

$$\mathcal{L} = \sum_b \mathcal{L}_b + \mathcal{L}_l + \mathcal{L}_{\text{int}}, \tag{2.1}$$

where,

$$\begin{aligned}
\mathcal{L}_b &= \sum_b \bar{\Psi}_b(i\gamma_\mu\partial^\mu - q_b\gamma_\mu A^\mu - m_b + g_\sigma\sigma - g_\omega\gamma_\mu\omega^\mu - g_\rho\gamma_\mu\vec{I}_b\vec{\rho}^\mu)\Psi_b, && (2.2)\\
\mathcal{L}_l &= \bar{\psi}_l(i\gamma_\mu\partial^\mu - q_l\gamma_\mu A^\mu - m_l)\psi_l, && (2.3)\\
\mathcal{L}_{\text{int}} &= \frac{1}{2}\partial_\mu\sigma\partial^\mu\sigma - \frac{1}{2}m_\sigma^2\sigma^2 - V(\sigma) - \frac{1}{4}\Omega^{\mu\nu}\Omega_{\mu\nu} + \frac{1}{2}m_\omega^2\omega_\mu\omega^\mu, \\
&\quad -\frac{1}{4}\vec{R}^{\mu\nu}\vec{R}_{\mu\nu} + \frac{1}{2}m_\rho^2\vec{\rho}_\mu\vec{\rho}^\mu - \frac{1}{4}F^{\mu\nu}F_{\mu\nu}, && (2.4)
\end{aligned}$$

and,

$$V(\sigma) = \frac{\kappa}{3!}(g_{\sigma N}\sigma)^3 + \frac{\lambda}{4!}(g_{\sigma N}\sigma)^4. \tag{2.5}$$

Where $\Omega_{\mu\nu} = \partial_\mu\omega_\nu - \partial_\nu\omega_\mu$, $\vec{R}_{\mu\nu} = \partial_\mu\vec{\rho}_\nu - \partial_\nu\vec{\rho}_\mu$ and $F_{\mu\nu} = \partial_\mu A_\nu - \partial_\nu A_\mu$ are the mesonic and electromagnetic field strength tensors. $\vec{I}_b$ denotes the isospin operator. The $\Psi_b$ and $\psi_l$ are baryon and lepton doublets. The $\sigma$, $\omega$ and $\rho$ meson fields are denoted by $\sigma$, $\omega$ and $\rho$ and their masses are $m_\sigma$, $m_\omega$ and $m_\rho$, respectively. The parameters $m_b$ and $m_l$ denote the vacuum masses for baryons and leptons. The meson-baryon couplings $g_\sigma$, $g_\omega$ and $g_\rho$ are the scalar, vector and isovector coupling constants, respectively. In RMF approximation, one replaces the meson fields by their expectation values which then act as classical fields in which baryons move i.e. $\langle\sigma\rangle = \sigma_0$, $\langle\omega_\mu\rangle = \omega_0\delta_{\mu 0}$, $\langle\rho_\mu^a\rangle = \delta_{\mu 0}\delta_3^a\rho_3^0$. The mesonic equations of motion can be found by the Euler-Lagrange equations for the meson fields using the Lagrangian eq. (2.1)

$$m_\sigma^2\sigma_0 + V'(\sigma_0) = \sum_{i=n,p} g_\sigma n_i^s, \tag{2.6}$$

$$m_\omega^2\omega_0 = \sum_{i=n,p} g_\omega n_i, \tag{2.7}$$

$$m_\rho^2\rho_3^0 = \sum_{i=n,p} g_\rho I_{3i} n_i, \tag{2.8}$$

where, $I_{3i}$ is the third component of the isospin of a given baryon. We have taken $I_{3(n,p)} = \left(-\frac{1}{2}, \frac{1}{2}\right)$. The baryon density, $n_B$, lepton density, $n_l$, and scalar density, $n^s$, at zero temperature are given by

$$n_B = \sum_{i=n,p} \frac{\gamma k_{Fi}^3}{6\pi^2} \equiv \sum_{i=n,p} n_i, \tag{2.9}$$

$$n_l = \frac{k_{Fl}^3}{3\pi^2}, \tag{2.10}$$

and

$$n^s = \frac{\gamma}{(2\pi)^3} \sum_{i=n,p} \int_0^{k_{Fi}} \frac{m^*}{E(k)} d^3k \equiv \sum_{i=n,p} n_i^s, \tag{2.11}$$

where, $E(k) = \sqrt{m^{*2} + k^2}$ being the single particle energy for nucleons with a medium dependent mass given as

$$m^* = m_b - g_\sigma\sigma_0. \tag{2.12}$$

Further, $k_{Fi} = \sqrt{\tilde{\mu}_i^2 - m^{*2}}$ is the Fermi momenta of the nucleons defined through an effective baryonic chemical potential, $\tilde{\mu}_i$ given as

$$\tilde{\mu}_i = \mu_i - g_\omega\omega_0 - g_\rho I_{3i}\rho_3^0. \tag{2.13}$$

Similarly, $k_{Fl}$ is the leptonic Fermi momenta i.e. $k_{Fl} = \sqrt{\mu_l^2 - m_l^2}$. Further $\gamma = 2$ correspond to the spin degeneracy factor for nucleons and leptons and $\mu_l$ denotes the chemical potential for leptons.

The total energy density, $\epsilon_{\mathrm{HP}}$, within the RMF model is given by

$$\begin{aligned}\epsilon_{\mathrm{HP}} = &\frac{m^{*4}}{\pi^2} \sum_{i=n,p} H(k_{Fi}/m^*) + \sum_{l=e,\mu} \frac{m_l^4}{\pi^2} H(k_{Fl}/m_l) \\ &+ \frac{1}{2}m_\sigma^2\sigma_0^2 + V(\sigma_0) + \frac{1}{2}m_\omega^2\omega_0^2 + \frac{1}{2}m_\rho^2\rho_3^{02}.\end{aligned} \tag{2.14}$$

The pressure, $p_{\mathrm{HP}}$, can be found using the thermodynamic relation as

$$p_{\mathrm{HP}} = \sum_{i=n,p,l} \mu_i n_i - \epsilon_{\mathrm{HP}}. \tag{2.15}$$

In eq. (2.14) we have introduced the function $H(z)$ which is given as

$$H(z) = \frac{1}{8}\left[z\sqrt{1+z^2}(1+2z^2) - \sinh^{-1} z\right]. \tag{2.16}$$

**Table 1**. The nucleon masses ($m_b$), $\sigma$ meson mass ($m_\sigma$), $\omega$ meson mass ($m_\omega$), $\rho$ meson mass ($m_\rho$) and couplings $g_\sigma$, $g_\omega$, $g_\rho$, $\kappa$, $\lambda$ in NL3 parameterisation [84].

| Parameters | Values |
|---|---|
| $m_b$ (MeV) | 939 |
| $m_\sigma$ (MeV) | 508.194 |
| $m_\omega$ (MeV) | 782.501 |
| $m_\rho$ (MeV) | 763.000 |
| $g_\sigma^2$ | 104.387 |
| $g_\omega^2$ | 165.585 |
| $g_\rho^2$ | 79.6 |
| $\kappa$ (fm$^{-1}$) | 3.86 |
| $\lambda$ | -0.0159 |

**Table 2**. The nucleon masses ($m_b$), meson masses, $m_i$ ($i = \sigma, \omega, \rho$) and coupling constants $g_{i0}$, $a_i$ ($i = \sigma, \omega, \rho$) and the saturation nuclear density $n_0$ in DDB model [76, 77].

| Parameters | Values |
|---|---|
| $m_b$ (MeV) | 939 |
| $m_\sigma$ (MeV) | 508.194 |
| $m_\omega$ (MeV) | 782.501 |
| $m_\rho$ (MeV) | 763.000 |
| $a_\sigma$ | 0.071 |
| $a_\omega$ | 0.046 |
| $a_\rho$ | 0.666 |
| $g_{\sigma 0}$ | 9.690 |
| $g_{\omega 0}$ | 11.756 |
| $g_{\rho 0}$ | 8.281 |
| $n_0$ (fm$^{-3}$) | 0.147 |

In the present investigation, we consider two different parameterisation for the nucleonic EOS — (i) the NL3 parameterisation of RMF model as discussed in ref. [84]. The corresponding parameters are listed in table 1. The other parameterisation of the RMF model is DDB [76, 77] consistent with the phenomenology of the saturation properties of nuclear matter as well as the gravitational wave data regarding tidal deformation [9]. In case of DDB, the couplings are density dependent and defined as

$$g_\sigma = g_{\sigma 0}\ e^{-(x^{a_\sigma}-1)}, \tag{2.17}$$
$$g_\omega = g_{\omega 0}\ e^{-(x^{a_\omega}-1)}, \tag{2.18}$$
$$g_\rho = g_{\rho 0}\ e^{-a_\rho(x-1)}, \tag{2.19}$$

where, $x = n_{\rm B}/n_0$. The DDB parameters $g_{i0}$, $a_i$, ($i = \sigma,\ \omega,\ \rho$) and $n_0$ are given in table 2. In DDB parameterisation, the cubic and quartic terms in eq. (2.1) are taken to be zero so that $V(\sigma) = 0$. We mention here that these parameter set lies within the 90 percent confidence inference (CI) of the $R_{1.4}$ of NS with mass 1.4M$_\odot$ as analysed in refs. [76, 77]

Due to the density dependent couplings, the effective baryon chemical potential as in eq. (2.13) gets redefined as

$$\tilde{\mu}_i = \mu_i - g_\omega \omega_0 - g_\rho I_{3i}\rho_3^0 - \Sigma^r, \tag{2.20}$$

where, $\Sigma^r$ is the "rearrangement term" which is given as [75]

$$\Sigma^r = \sum_{i=n,p}\left\{-\frac{\partial g_\sigma}{\partial n_{\rm B}}\sigma_0 n_i^s + \frac{\partial g_\omega}{\partial n_{\rm B}}\omega_0 n_i + \frac{\partial g_\rho}{\partial n_{\rm B}}\rho_3^0 I_{3i} n_i\right\}. \tag{2.21}$$

The NSs are globally charge neutral as well as the matter inside the core is under $\beta$-equilibrium. So the chemical potentials and the number densities of the constituents of NSM are related by the following equations,

$$\mu_i = \mu_B + q_i\mu_E, \tag{2.22}$$
$$\sum_{i=n,p,l} n_i q_i = 0, \tag{2.23}$$



JCAP02(2023)015

where, $\mu_B$ and $\mu_E$ are the baryon and electric chemical potentials and $q_i$ is the charge of the $i^{\rm th}$ particle.

### 2.2 Equation of state for quark matter

We note down here, for the sake of completeness, the salient features of the thermodynamics of NJL model with two flavours that we use to describe the EOS of the quark matter. The Lagrangian of the model with four point interactions is given by

$$\begin{aligned}\mathcal{L} = \bar{\psi}_q(i\gamma^\mu\partial_\mu - m_q)\psi_q + G_s\left[(\bar{\psi}_q\psi_q)^2 + (\bar{\psi}_q i\gamma^5\tau\psi_q)^2\right] \\ +G_v\left[(\bar{\psi}_q\gamma^\mu\psi_q)^2 + (\bar{\psi}_q i\gamma^\mu\gamma^5\tau\psi_q)^2\right].\end{aligned} \tag{2.24}$$

Here, $\psi_q$ is the doublet of $u$ and $d$ quarks. We have also taken here a current quark mass, $m_q$ which is that we have taken as same for $u$ and $d$ quarks. The second term describes the four point interactions in the scalar and pseudo-scalar channel. The third term is a phenomenological vector interaction giving rise to repulsive interaction for $G_v > 0$ which can make the EOS stiffer. Except for the explicit symmetry breaking term proportional to current quark mass, the Lagrangian is chirally symmetric. Using the standard method of thermal field theory one can write down the thermodynamic potential $\Omega$ within a mean field approximation at a given temperature, $(T = \beta^{-1})$ and quark chemical potential, $(\mu_q = \mu_B/3)$ [85] as

$$\begin{aligned}\Omega(M,T,\mu) = -2N_c\sum_{i=u,d}\int\frac{d\mathbf{k}}{(2\pi)^3}\times\Big\{E_k + \frac{1}{\beta}\log\left(1+\exp\left(-\beta(E_k-\tilde{\mu}_i)\right)\right) \\ +\frac{1}{\beta}\log\left(1+\exp\left(-\beta(E_k+\tilde{\mu}_i)\right)\right)\Big\} + G_s\rho_s^2 - G_v\rho_v^2.\end{aligned} \tag{2.25}$$

Where, $N_c = 3$ is the colour degrees of freedom and $E_k = \sqrt{\mathbf{k}^2 + M^2}$ is the on shell single particle energy of the quark with constituent quark mass $M$ and $\tilde{\mu}_i$ being an effective quark chemical potential in the presence of the vector interaction. The constituent quark mass, $M$, satisfies the mass gap equation

$$M = m_q - 2G_s\rho_s, \tag{2.26}$$

and the effective quark chemical potential satisfies

$$\tilde{\mu}_i = \mu_i - 2G_v\rho_v. \tag{2.27}$$

Here, we focus our attention to $T = 0$ which is applicable to the cold NSs. Using the relation $\lim_{\beta\to\infty}\frac{1}{\beta}\log\left(e^{-\beta x}+1\right) = -x\Theta(-x)$, the thermal factors in eq. (2.25) go over into step functions and the mean field thermodynamic potential eq. (2.25) becomes in the limit $T \to 0$

$$\Omega(M,0,\mu) = -2N_c\sum_{i=u,d}\int\frac{d\mathbf{k}}{(2\pi)^3}\Big\{E_k + (\tilde{\mu}_i - E_k)\ \Theta\left(\tilde{\mu}_i - E_k\right)\Big\} + G_s\rho_s^2 - G_v\rho_v^2. \tag{2.28}$$

The scalar density, $\rho_s$, and vector density, $\rho_v$, are given as

$$\begin{aligned}\rho_s &= -2N_c\sum_{i=u,d}\int\frac{d\mathbf{k}}{(2\pi)^3}\frac{M}{E_k}\Big(1-\Theta\left(\tilde{\mu}_i - E_k\right)\Big) \\ &= -\frac{N_cM^3}{\pi^2}\sum_{i=u,d}\Big[G(\Lambda/M) - G(k_{Fi}/M)\Big],\end{aligned} \tag{2.29}$$

and

$$\rho_v = 2N_c \sum_{i=u,d} \int \frac{d\mathbf{k}}{(2\pi)^3} \Theta\left(\tilde{\mu}_i - E_k\right) = 2N_c \sum_{i=u,d} \frac{k_{Fi}^3}{6\pi^2}. \tag{2.30}$$

In eq. (2.29), we have introduced the function $G(z)$ which is defined as

$$G(z) = \frac{1}{2}\left[z\sqrt{1+z^2} - \tanh^{-1}\left(\frac{z}{\sqrt{1+z^2}}\right)\right]. \tag{2.31}$$

The difference of the vacuum energy densities between the non-perturbative vacuum (characterized by the constituent quark mass, $M$) and energy density of the perturbative vacuum (characterized by current quark mass, $m_q$) is the bag constant, $B$, i.e.

$$B = \Omega(M, T=0, \mu=0) - \Omega(m_q, T=0, \mu=0). \tag{2.32}$$

This bag constant is to be subtracted from eq. (2.28) so that the thermodynamic potential vanishes at vanishing temperature and density. The pressure, $p_{\rm NJL}$, i.e. the negative of the thermodynamic potential of the quark matter in NJL model is given as

$$p_{\rm NJL} = p_{\rm vac} + p_{\rm med} + B, \tag{2.33}$$

where the vacuum, $p_{\rm vac}$, and the medium, $p_{\rm med}$, contributions to the pressure are given by

$$p_{\rm vac} = \frac{4N_c}{(2\pi)^3} \int_{|k|\leq\Lambda} d\mathbf{k}\sqrt{\mathbf{k}^2 + M^2} \equiv \frac{2N_c}{\pi^2} M^4 \; H(\Lambda/M), \tag{2.34}$$

and,

$$\begin{aligned} p_{\rm med} &= \frac{2N_c}{(2\pi)^3} \sum_{i=u,d} \int_0^{k_{Fi}} d\mathbf{k}\left[\sqrt{\mathbf{k}^2+M^2} - \tilde{\mu}_i\right] + G_s\rho_s^2 - G_v\rho_v^2 \\ &= \frac{N_c}{\pi^2} \sum_{i=u,d} M^4\left[H(k_{Fi}/M) - \tilde{\mu}_i\rho_i\right] + G_s\rho_s^2 - G_v\rho_v^2, \end{aligned} \tag{2.35}$$

where, $k_{Fi} = \Theta(\tilde{\mu}_i - M)\sqrt{\tilde{\mu}_i^2 - M^2}$ is the fermi-momenta of $i = u, d$ quark and $\Lambda$ is the three momentum cut-off. The function $H(z)$ is already defined in eq. (2.16). From the thermodynamic relation, the energy density, $\epsilon_{\rm NJL}$, is given as

$$\epsilon_{\rm NJL} = \sum_{i=u,d} \mu_i\rho_i - p_{\rm NJL}. \tag{2.36}$$

where, $\rho_i = \frac{\gamma k_{Fi}^3}{6\pi^2}$, $(i = u, d, e)$ with the degeneracy factor $\gamma = 6$ for quarks and $\gamma = 2$ for electron. NSM is charge neutral as well as $\beta$-equilibrated. So the chemical potentials of the $u$ and $d$ quarks can be expressed in terms of quark chemical potential, $\mu_q$, and electric chemical potential, $\mu_E$, as $\mu_i = \mu_q + q_i\mu_E$ $(i = u, d)$. $q_i$'s are the electric charges of $u$ and $d$ quarks. The condition of charge neutrality is

$$\frac{2}{3}\rho_u - \frac{1}{3}\rho_d - \rho_e = 0. \tag{2.37}$$



JCAP02(2023)015

Since the typical electric charge chemical potential is of the order of MeV, one can neglect the electron mass so that $k_{Fe} = |\mu_e|$. The total pressure and the energy density for the charge neutral quark matter are then given by

$$p_{\mathrm{QP}} = p_{\mathrm{NJL}} + p_e, \tag{2.38}$$

$$\epsilon_{\mathrm{QP}} = \epsilon_{\mathrm{NJL}} + \epsilon_e, \tag{2.39}$$

where, $\epsilon_e \simeq \frac{\mu_e^4}{4\pi^2}$ and $p_e \simeq \epsilon_e/3$.

We may note that NJL model has four parameters − namely, the current quark mass, $m_q$, the three momentum cutoff, $\Lambda$, and the two coupling constants, $G_s$ and $G_v$. The values of the parameters are usually chosen by fitting the pion decay constant, $f_\pi = 92.4\,\mathrm{MeV}$, the chiral condensate, $\langle -\bar{\psi}_q\psi_q\rangle_u = \langle -\bar{\psi}_q\psi_q\rangle_u = (240.8\,\mathrm{MeV})^3$ and the pion mass, $m_\pi = 135\,\mathrm{MeV}$. This fixes $m_q = 5.6\,\mathrm{MeV}$, $G_s\Lambda^2 = 2.44$ and $\Lambda = 587.9\,\mathrm{MeV}$. As mentioned $G_v$ is not fitted from any other physical constraint and we take it as a free parameter. We shall show our results for the two values of $G_v$ namely $G_v = 0$ and $G_v = 0.2G_s$. With this parameterisation, the constituent quark mass, $M$, comes 400 MeV, the critical chemical potential, $\mu_c$ for the chiral transition turns out to be $\mu_c = 1168\,\mathrm{MeV}$ for the vector coupling constant $G_v = 0$ in NJL model.

### 2.3 Hadron-quark phase transition and mixed phase

The baryon number density or the quark chemical potential at which the hadronic-quark phase transition occurs is not known precisely from the first principle calculations in QCD but it is expected from various model calculations to occur at a density which is few times the nuclear matter saturation density. In the context of NSs, two types of phase transitions can be possible depending upon the surface tension [66–72] of the quark matter. If the surface tension is large then there will be sharp interface and one can have a Maxwell construct for the phase transition. On the otherhand, if the surface tension is small we can have a Gibbs construct for the phase transition, where there is a MP of nuclear and quark matter. It ought to be mentioned, however, the estimated values of the surface tension for quark matter vary over a wide range and is very much model dependent. As the value of the surface tension is not precisely known yet both the scenarios, (Maxwell and Gibbs) are plausible. We adopt here the Gibbs construct for the HQPT as nicely outlined in ref. [86]. In this case, one can achieve the charge neutrality with a positively charged hadronic matter mixed with a negatively charged quark matter in necessary amount leading to a global charge neutrality where the pressures of the both phases are the functions of two independent chemical potentials $\mu_B$ and $\mu_E$. The Gibbs condition for the equilibrium at the zero temperature between the two phases for such a two component system is given by [65]

$$p_{\mathrm{HP}}(\mu_B, \mu_E) = p_{\mathrm{QP}}(\mu_B, \mu_E) = p_{\mathrm{MP}}(\mu_B, \mu_E), \tag{2.40}$$

where, the pressure for HP, $p_{\mathrm{HP}}$, is given in eq. (2.15) and the pressure for the Quark Phase (QP), $p_{\mathrm{QP}}$, is written down in eq. (2.38). In figure 1 we illustrate this calculation, where the pressure is plotted as a function of baryon chemical potential, $\mu_B(= \mu_n)$, and the electric chemical potential, $-\mu_E(= \mu_e)$. The green surface denotes the pressure in the HP estimated from the RMF model using NL3 parameters. The purple surface denotes the pressure in the QP estimated in NJL model. The two surfaces intersect along the curve $AB$ satisfying the global charge neutrality condition,

$$\chi\ \rho_c^{\mathrm{QP}} + (1-\chi)\ \rho_c^{\mathrm{HP}} = 0, \tag{2.41}$$

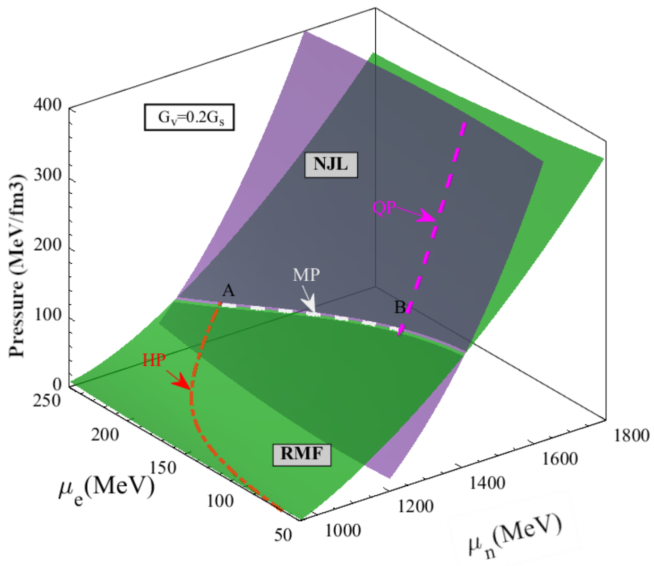


**Figure 1**. Pressure is plotted as a function of $\mu_n(\mu_B)$ and $\mu_e(-\mu_E)$ for HP and QP. The green surface is for HP and the purple surface is for the QP. The two surfaces intersect along the curve $AB$. The along the dashed portion on this line, the electrical charge neutrality is maintained. Along the red dashed line and magenta dashed line charge neutrality is maintained in HP and QP respectively. The quark matter fraction $\chi$ increases monotonically from $\chi = 0$ to $\chi = 1$ along the curve $AB$. We have considered here the NL3 parameterisation of RMF for the description of HP matter.

where, $\rho_c^{\rm HP}$ and $\rho_c^{\rm QP}$ denote the total charge densities in HP and QP respectively and $\chi$ defines the volume fraction of the quark matter in MP defined as,

$$\chi = \frac{V_{\rm QP}}{V_{\rm QP} + V_{\rm HP}}. \tag{2.42}$$

Explicitly, for a given $\mu_B$, we calculate the electric charge chemical potential $\mu_E$ such that the pressure in both the phases are equal satisfying the Gibbs condition eq. (2.40). This gives the intersection line ($AB$) of the two surfaces as shown in figure 1. Further imposing the global charge neutrality condition eq. (2.41) one obtains the volume fraction $\chi$ occupied by the quark matter in MP. Thus along the line $AB$ in figure 1, the volume fraction occupied by quark matter increases monotonically from $\chi = 0$ to $\chi = 1$. This gives the pressure for the charge neutral matter in MP. Below $\chi < 0$, EOS corresponds to the charge neutral hadronic matter EOS shown as the red dash curve while for $\chi > 1$ EOS corresponds to the charge neutral quark matter EOS shown as the purple dash curve in figure 1. With the present parametrisation of the RMF model for hadronic matter and NJL model for the quark matter, MP starts at $(\mu_B, \mu_e, p) = (1423\text{MeV}, 289.26\text{MeV}, 144.56\text{MeV/fm}^3)$ and ends at $(\mu_B, \mu_e, p) = (1597\text{MeV}, 102.40\text{MeV}, 266.23\text{MeV/fm}^3)$. This corresponds to the starting of MP at baryon density $\rho_B = 2.75\rho_0$ and ending of MP at baryon density $\rho_B = 5.72\rho_0$. For NJL model we have taken here $G_v = 0.2G_s$. For $G_v = 0$, MP starts little earlier i.e. $\rho_B = 2.36\rho_0$ and ends at $\rho_B = 5.22\rho_0$. After MP, as baryon density increases the matter is in pure charge neutral QP. We can find the energy density in the MP as follows,

$$\epsilon_{\rm MP} = \chi\epsilon_{\rm QP} + (1-\chi)\epsilon_{\rm HP}. \tag{2.43}$$



JCAP02(2023)015

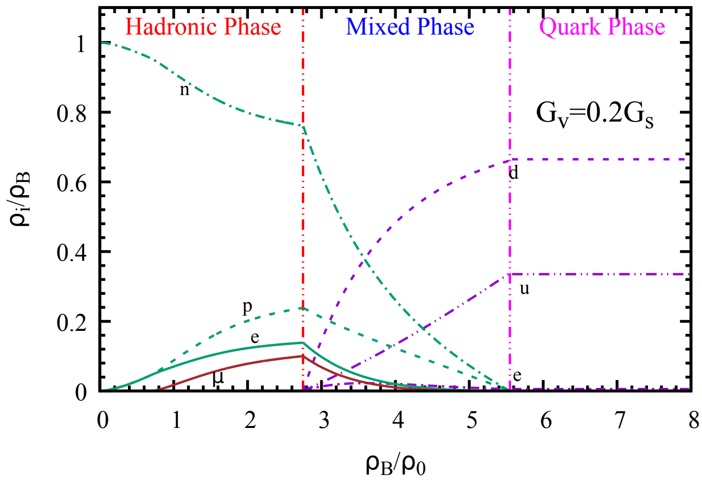


**Figure 2**. The particle fractions normalized with respect to baryon density for the charge neutral matter are plotted as a function of the baryon number density. The plot is for $G_v = 0.2G_s$. At $\rho_B = 2.75\rho_0$ the quark matter starts appearing and at $\rho_B = 5.72\ \rho_0$ the hadronic matter melts completely to the quark matter. The HP is described by RMF model with NL3 parameterisation.

We display the particle content as a function of density for the charge neutral matter for $G_v = 0.2G_s$ in figure 2. In the HP, the neutron density dominates with a small fraction of proton and a small fraction of electron is also appeared to get the charge neutral HP. At $\rho_B \sim 2.76\rho_0$, the MP starts and the nucleon fraction decreases while quark fraction start increasing. Finally, at densities $\rho_B \sim 5.56\rho_0$ and above, the pure QP takes over with d-quark densities roughly becoming twice that of the u-quarks to maintain the global charge neutrality.

Similar to eq. (2.43) the baryon number density in MP

$$\rho^B_{\mathrm{MP}} = \chi\rho^B_{\mathrm{QP}} + (1-\chi)\rho^B_{\mathrm{HP}}. \tag{2.44}$$

In MP region, nuclear matter fraction decreases while quark matter fraction increases with increasing $\rho_B$. As $\rho_B$ increases further the nuclear matter melts completely to quark matter which occurs for densities beyond $\rho_B = 5.72\rho_0$.

MP construction using DDB parameterisation of the hadronic EOS is also similar except that the MP starts at $(\mu_B, \mu_e, p, \rho_B) = (1416.5\ \mathrm{MeV}, 204.58\ \mathrm{MeV}, 181.76\ \mathrm{MeV/fm^3},\ 3.93\rho_0)$ and ends at $(\mu_B, \mu_e, p, \rho_B) = (1504\ \mathrm{MeV},\ 108.42\ \mathrm{MeV},\ 245.51\ \mathrm{MeV/fm^3},\ 6.98\rho_0)$ beyond which we find QP as the stable phase.

## 3 Non-radial fluid oscillation modes of compact stars

In this section, we outline the equations governing the oscillation modes of the fluid comprising NSM. The most general metric for a spherically symmetric space-time is given by

$$\begin{aligned} ds^2 &= g_{\alpha\beta}dx^\alpha dx^\beta \\ &= e^{2\nu}dt^2 - e^{2\lambda}dr^2 - r^2(d\theta^2 + \sin^2\theta d\phi^2), \end{aligned} \tag{3.1}$$

where, $\nu$ and $\lambda$ are the metric functions. It is convenient to define the mass function, $m(r)$ in the favour of $\lambda$ as

$$e^{2\lambda} = \left(1 - \frac{2m}{r}\right)^{-1}. \tag{3.2}$$

Starting from the line element eq. (3.1) one can obtain the equations governing the structure of spherical compact objects, the Tolman-Oppenheimer-Volkoff (TOV) equations, as

$$\frac{dp}{dr} = -\left(\epsilon + p\right)\frac{d\nu}{dr}, \tag{3.3}$$

$$\frac{dm}{dr} = 4\pi r^2 \epsilon, \tag{3.4}$$

$$\frac{d\nu}{dr} = \frac{m + 4\pi r^3 p}{r(r-2m)}. \tag{3.5}$$

In the above set of equations $\epsilon$, $p$ are the energy density and the pressure respectively. $m(r)$ is the mass of the compact star enclosed within a radius $r$. To solve these equations, one has to supplement these equations with an equation relating pressure and energy density i.e. an EOS. Further, one has to set the boundary conditions at the center and surface as

$$m(0) = 0 \qquad \text{and} \qquad p(0) = p_c, \tag{3.6}$$

$$p(R) = 0, \tag{3.7}$$

$$e^{2\nu(R)} = 1 - \frac{2M}{R}, \tag{3.8}$$

where, the total mass of the compact object is given by $M = m(R)$,[1] $R$ being it's radius which is defined as the radial distance where the pressure vanishes while integrating out eqs. (3.3), (3.4) and (3.5) from the center to the surface of the star. One can solve these equations along with a boundary conditions eqs. (3.6), (3.7) and (3.8) for a set of central densities $\epsilon_c$ or corresponding pressure $p_c$ to obtain the mass-radius, $(M-R)$ curve.

For the sake of completeness, we give below a succinct derivation of pulsating equations in the context of NS within a relativistic setting [53, 87]. The Einstein field equation that relates the curvature of space time to the energy momentum tensor is given as

$$R_{\alpha\beta} - \frac{1}{2}g_{\alpha\beta}R = 8\pi T_{\alpha\beta}, \tag{3.9}$$

with $T_{\alpha\beta}$ being the stress energy tensor, which for a perfect fluid is given by

$$T^{\mu\nu} = (p+\epsilon)u^\mu u^\nu - p g^{\mu\nu}, \tag{3.10}$$

with $p$ and $\epsilon$ being the pressure and energy density respectively and $u^\mu$ is the four-velocity. Taking (covariant) divergence of the Einstein equation, eq. (3.9), the left hand side of eq. (3.9) vanishes using Bianchi identity leading to covariant conservation equation of the energy momentum tensor i.e. $T^{\mu\nu}_{;\mu} = 0$. With $T^{\mu\nu}$ given in eq. (3.10), this reduces to

$$(p+\epsilon)u^\mu u_{\nu;\mu} = \partial_\nu p - u_\nu u^\mu \partial_\mu p \tag{3.11}$$

which is the relativistic Euler equation [87]. Next, to derive the equation of motion, we use the conservation of baryon number. This is similar to using continuity equation in non-relativistic case which follows from mass conservation. The baryon number conservation equation is given by

$$\frac{dn}{d\tau} = -n u^\mu_{;\mu}, \tag{3.12}$$

where, $n$ is the baryon number density.

[1]In this section, $M$ denotes the mass of the compact stars to be distinguished from the constituent quark mass defined in section 2.2.



JCAP02(2023)015

We shall derive the equations in spherical coordinates and the perturbations will be expanded in terms of vector spherical harmonics. The position $(t, r, \theta, \phi)$ of a fluid element in space time as a function of proper time $\tau$ is given by the position four-vector $\xi(\tau)$ as

$$\xi(\tau) = \begin{pmatrix} \xi^t \\ \xi^r \\ \xi^\theta \\ \xi^\phi \end{pmatrix}. \tag{3.13}$$

Consider a fluid element located at $\xi_0$ as its equilibrium position is displaced to $\xi(\xi_0, \tau) = \xi_0 + \zeta(\xi_0, \tau)$. This results perturbation in pressure $p$, in energy density $\epsilon$ and in baryon number density $n$ as

$$p = p_0 + \delta p, \tag{3.14}$$
$$\epsilon = \epsilon_0 + \delta\epsilon, \tag{3.15}$$
$$n = n_0 + \delta n, \tag{3.16}$$

where, the subscript '0' refers to the corresponding quantities in equilibrium. To derive the equations of motion for the perturbation, one has to linearize the Euler equation, eq. (3.11) in the perturbation. For this we need the four velocities of the fluid elements $u^\mu = \frac{d\xi^\mu}{d\tau} = \frac{d\zeta^\mu}{d\tau}$. Further, we shall confine ourselves to performing the analysis for spherical harmonic component with the azimuthal index $m = 0$. For the displacement vector $\zeta^\mu$ we take the ansatz

$$\begin{pmatrix} \zeta^t \\ \zeta^r \\ \zeta^\theta \\ \zeta^\phi \end{pmatrix} = \begin{pmatrix} t \\ \dfrac{e^{-\lambda} Q(r,t)}{r^2} P_l(\cos\theta) \\ -\dfrac{Z(r,t)}{r^2} \partial_\theta P_l(\cos\theta) \\ 0 \end{pmatrix}, \tag{3.17}$$

where, $Q(r, t)$ and $Z(r, t)$ are the perturbing functions. We choose a harmonic time dependence for the perturbation i.e. $\propto e^{i\omega t}$ with frequency $\omega$. Further, we do not consider here toroidal deformations. From the normalisation condition for the velocity $u_\mu u^\mu = 1$, and keeping up to linear terms in the perturbation, we have $u^t = d\zeta^t/d\tau = e^{-\nu}$. The other components of the four-velocity are given as

$$\begin{pmatrix} u^t \\ u^r \\ u^\theta \\ u^\phi \end{pmatrix} = \begin{pmatrix} e^{-\nu} \\ e^{-\nu}\dot{\zeta}^r \\ e^{-\nu}\dot{\zeta}^\theta \\ 0 \end{pmatrix}, \tag{3.18}$$

where, the dot on the perturbed coordinate denotes the derivative with respect to time '$t$'. Similarly, the contravarient velocity components are given using the metric given in eq. (3.1) and eq. (3.18) as

$$\begin{pmatrix} u_t \\ u_r \\ u_\theta \\ u_\phi \end{pmatrix} = \begin{pmatrix} e^{\nu} \\ -e^{2\lambda-\nu}\dot{\zeta}^r \\ -r^2 e^{-\nu}\dot{\zeta}^\theta \\ 0 \end{pmatrix}. \tag{3.19}$$

Now we simplify the Euler equation i.e. eq. (3.11) by substituting the expressions for pressure, energy density and the fluid four-velocity and linearize in terms of the perturbing



JCAP02(2023)015

functions. The $\nu = t$ component of the Euler equation, eq. (3.11), reduces to

$$(p_0 + \epsilon_0)\nu'(r) = -p_0'(r), \tag{3.20}$$

where, the superscript 'prime' corresponds to derivative with respect to '$r$'. To obtain eq. (3.20), we have used in the l.h.s. of eq. (3.11), with $\nu = t$, $u^\mu u_{t;\mu} = \nu'\dot{\zeta}^r$ and in r.h.s. we have used the fact that $p_0$ is isotropic so that $\dot{p}_0 - u_t u^\mu \partial_\mu p \sim -\dot{\zeta}^r p_0'(r)$. Let us recognise that the eq. (3.20) is essentially a part of the TOV equations (eq. (3.3)) relating pressure gradient and the metric function gradient. Next, the $\nu = r$ component of the Euler equation, eq. (3.11), reduces to

$$\omega^2(\epsilon_0 + p_0)e^{2(\lambda-\nu)}\zeta^r - (\delta\epsilon + \delta p)\nu'(r) - \frac{d}{dr}(\delta p) = 0. \tag{3.21}$$

Similarly, the $\nu = \theta$ component of the Euler equation, eq. (3.11), by using $u^\mu u_{\theta;\mu} = u^t\partial_t u_\theta = -e^{-2\nu}r^2\ddot{\zeta}^\theta$, is given as

$$\omega^2(\epsilon_0 + p_0)e^{-2\nu}r^2\zeta^\theta - \partial_\theta \delta p = 0. \tag{3.22}$$

Having written down the Euler equation to linear order in the perturbation, let us next consider the baryon number conservation equation i.e. eq. (3.12). With the velocity components given in eqs. (3.18), (3.19) and eq. (3.17) for the perturbation,the number conservation equation, eq. (3.12) can be written in terms of the radial and azimuthal perturbing functions $Q(r)$ and $Z(r)$ as

$$\frac{dn}{d\tau} = -\frac{n}{r^2}\left[e^{-(\lambda+\nu)}\frac{\partial^2 Q(r,t)}{\partial r\partial t} + e^{-\nu}l(l+1)\dot{Z}\right]P_l(\cos\theta). \tag{3.23}$$

We might note here that, since the proper time derivative is taken along the world line of the fluid parcel, we can write $\frac{dn}{d\tau} = \frac{d\Delta n}{d\tau}$, where, $\Delta n$ is the Lagrangian perturbation. Further, using the relation $\partial/\partial t = e^{-\nu}\partial/\partial\tau$, we can integrate eq. (3.23) over $d\tau$ to obtain the Lagrangian perturbation in number density $\Delta n$ in terms of the perturbing functions $Q$ and $Z$ as

$$\frac{\Delta n}{n_0} = -\frac{1}{r^2}\left[e^{-\lambda}Q' + l(l+1)Z\right]P_l(\cos\theta). \tag{3.24}$$

To write down the equations in terms of the perturbing functions $Q(r)$ and $Z(r)$, we need to express the energy density perturbation $\delta\epsilon$ and pressure perturbation $\delta p$ occurring in eqs. (3.20), (3.21) in terms of the functions $Q(r)$ and $Z(r)$. The strategy is to use the Euler equation eq. (3.11) to write $\delta\epsilon$ in terms of $\delta n$ and use definition of bulk modulus ($\kappa = n\frac{\Delta p}{\Delta n}$) to write $\delta p$ in terms of $\delta n$. One can then use the baryon number conservation equation eq. (3.23) to write $\delta\epsilon$ and $\delta p$ in terms of the perturbing functions.

Thus, using the Euler equation eq. (3.11) to eliminate $u^\mu_{;\mu}$ in the baryon number conservation eq. (3.12), we have

$$\frac{dn}{d\tau} = \frac{n}{p+\epsilon}\frac{\partial\epsilon}{\partial\tau}, \tag{3.25}$$

which leads to

$$\Delta\epsilon \simeq \frac{\epsilon_0 + p_0}{n_0}\Delta n. \tag{3.26}$$

Further, using the relation between the Lagrangian perturbation and the Eulerian perturbation i.e. $\Delta\epsilon = \delta\epsilon + \zeta^r\frac{d\epsilon_0}{dr}$ and using eq. (3.24), we have

$$\delta\epsilon = -\left[\frac{\epsilon_0 + p_0}{r^2}\left\{e^{-\lambda}Q' + l(l+1)Z\right\} + \frac{e^{-\lambda}}{r^2}Q\frac{d\epsilon_0}{dr}\right]P_l(\cos\theta). \tag{3.27}$$



JCAP02(2023)015

Next, let us find out the relation between $\delta p$ and $\Delta n$. The Eulerian variation $\delta p$ and the Lagrangian variation $\Delta p$ are related as

$$\delta p = \Delta p - \zeta^r \frac{dp_0}{dr}. \tag{3.28}$$

Thus, using eq. (3.17) and eq. (3.24), we have

$$\delta p = -\left[\frac{\kappa}{r^2}(e^{-\lambda}Q' + l(l+1)Z) + \frac{e^{-\lambda}}{r^2}\frac{dp_0}{dr}Q\right] P_l(\cos\theta). \tag{3.29}$$

Further, $\Delta p$ is related to $\Delta n$, through bulk modulus $\kappa$ i.e.

$$\kappa = n\frac{\Delta p}{\Delta n}.$$

In the relativistic Cowling approximation, the metric perturbations are neglected. This will mean the energy and pressure perturbations should also vanish. In the relativistic Cowling approximation, the energy density perturbation $\delta\epsilon$ is set to zero but pressure perturbation is not set to zero. As shown in ref. [53], such an approximation leads to qualitatively correct result which we shall also follow. Setting $\delta\epsilon = 0$ in eq. (3.21), and using eq. (3.29), we have

$$\nu'\delta p + \frac{d\delta p}{dr} = -\nu'\kappa X - \frac{d(\kappa X)}{dr} - \nu'(p_0+\epsilon_0)l(l+1)\frac{Z}{r^2} + (p_0+\epsilon_0)Q\frac{d}{dr}\left(\frac{e^{-\lambda}\nu'}{r^2}\right), \tag{3.30}$$

where, we have defined for the sake of brevity $X = (e^{-\lambda}Q' + l(l+1)Z)/r^2$.Using this, the radial Euler equation, eq. (3.21) becomes

$$\omega^2(\epsilon_0+p_0)e^{\lambda-2\nu}\frac{Q}{r^2} + \frac{d\,[\kappa X]}{dr} + \nu'\kappa X + \nu'(\epsilon_0+p_0)l(l+1)\frac{Z}{r^2} - (\epsilon_0+p_0)\frac{d}{dr}\left(\frac{e^{-\lambda}\nu'}{r^2}\right) = 0. \tag{3.31}$$

Similarly, the azimuthal component of the Euler equation eq. (3.22) becomes

$$\omega^2(p_0+\epsilon_0)e^{-2\nu}Z - \kappa X - p_0'\frac{e^{-\lambda}Q}{r^2} = 0. \tag{3.32}$$

It can be shown that the eq. (3.31) through a rearrangement of terms is identical to that obtained earlier by McDermott et al. [53] with an appropriate change of factor 2 in the metric functions $\nu(r)$ and $\lambda(r)$. Few more comments here may be in order. In literature, sometimes the adiabatic index $\gamma$ is used instead of $\kappa$ and is defined as [42]

$$\gamma = \left(\frac{\partial \ln p_0}{\partial \ln n_0}\right)_s = \frac{n_0\Delta p}{p_0\Delta n} \tag{3.33}$$

so that $\kappa = \gamma p_0$. Further, the same can be related to adiabatic speed of sound as follows. By using the definition of Jacobian and standard thermodynamic relation

$$\left(\frac{\partial \ln p_0}{\partial \ln n_0}\right)_s = \frac{n_0^2}{p_0\chi_{\mu\mu}} \tag{3.34}$$



JCAP02(2023)015

in the zero temperature limit. The adiabatic speed of sound at zero temperature is defined as [88]

$$c_s^2 = \left(\frac{\partial p_0}{\partial \epsilon_0}\right)_s = \frac{n}{\mu \chi_{\mu\mu}}$$

so that

$$\gamma = \frac{p_0 + \epsilon_0}{p_0} c_s^2. \tag{3.35}$$

Let us note that eq. (3.31) is a second order differential equation for the perturbing function $Q(r)$. We now use eq. (3.32) to write down two coupled first order equation for the perturbing functions. Using eq. (3.32) and eq. (3.35), we have the equation for perturbation as

$$Q' - \frac{1}{c_s^2}\left[\omega^2 r^2 e^{\lambda - 2\nu} Z + \nu' Q\right] + l(l+1)e^{\lambda} Z = 0. \tag{3.36}$$

Next one can calculate the combination $d[eq.\ (3.32)]/dr + [eq.\ (3.31)]$ and substitute eq. (3.32) again which leads to the first order differential equation for $Z'$ as

$$Z' - 2\nu' Z + e^{\lambda}\frac{Q}{r^2} - \nu'\left(\frac{1}{c_e^2} - \frac{1}{c_s^2}\right)\left(Z + \nu' e^{-\lambda+2\nu}\frac{Q}{\omega^2 r^2}\right) = 0. \tag{3.37}$$

In the above equation $c_e^2 = \frac{dp_0}{d\epsilon_0} = \frac{p_0'}{\epsilon_0'}$ is the equilibrium speed of sound. It may be noted that eq. (3.40) can be rewritten as

$$\omega^2 e^{\lambda}\frac{Q}{r^2} + \omega^2 Z' + A_- e^{\lambda}\omega^2 Z - A_+ e^{2\nu}\frac{p_0'}{p_0 + \rho_0}\frac{q}{r^2} = 0, \tag{3.38}$$

where, $A_+ = e^{-\lambda}(\epsilon_0'/(p_0 + \epsilon_0) + \nu'/c_s^2)$ and $A_- = A_+ - 2\nu' e^{-\lambda}$. It is reassuring to see that the eq. (3.36) and eq. (3.38) are identical to the corresponding equations eq. (3b) and eq. (4a) given in ref. [53]. The gravity mode ($g$ mode) oscillation frequencies are closely related to the Brunt-Väisäla frequency, $\omega_{BV}$ [53]. The relativistic generalisation of $\omega_{BV}$ is given by

$$\omega_{BV}^2 = \nu'^2 e^{2\nu}\left(1 - \frac{2m}{r}\right)\left(\frac{1}{c_e^2} - \frac{1}{c_s^2}\right). \tag{3.39}$$

This also reduces to the expression for the $\omega_{BV}$ in Newtonian limit [54].

The equation for the perturbation function $Z(r)$ can be rewritten in terms of the Brunt-Väisäla frequencies as

$$Z' - 2\nu' Z + e^{\lambda}\frac{Q}{r^2} - \frac{\omega_{BV}^2 e^{-2\nu}}{\nu'\left(1 - \frac{2m}{r}\right)}\left(Z + \nu' e^{-\lambda+2\nu}\frac{Q}{\omega^2 r^2}\right) = 0. \tag{3.40}$$

The two coupled first order differential equations for the perturbing functions $Q(r,t)$ and $Z(r,t)$, eqs. (3.36), (3.40), are to be solved with appropriate boundary conditions at the center and the surface. Near the center of the compact stars the behavior of the functions $Q(r)$ and $Z(r)$ are given by [42]

$$Q(r) = Cr^{l+1} \qquad \text{and} \qquad Z(r) = -Cr^l/l \tag{3.41}$$

where, $C$ is an arbitrary constant and $l$ is the order of the oscillation. The other boundary condition is the vanishing of the Lagrangian perturbation pressure, i.e. $\Delta p = 0$ at the stellar



JCAP02(2023)015

surface. Using equations eqs. (3.28), (3.29) and (3.36), we have the Lagrangian perturbation pressure $\Delta p$ given as

$$\Delta p = -\frac{(p_0 + \epsilon_0)}{r^2}\left[\omega^2 r^2 e^{\lambda-2\nu} Z + \nu' Q\right] e^{-\lambda}. \tag{3.42}$$

Thus the vanishing of $\Delta p$ at the surface of the star ($r = R$) leads to the boundary condition [89]

$$\omega^2 r^2 e^{\lambda-2\nu} Z + \nu' Q\Big|_{r=R} = 0. \tag{3.43}$$

Further, in case one considers stellar models with a discontinuity in the energy density, one has to supplement additional condition at the surface of discontinuity demanding $\Delta p$ to be continuous i.e. $\Delta p(r = r_{c-}) = \Delta p(r = r_{c+})$. Where, $r_c$ is the radial distance of the surface of energy density discontinuity from the center. This leads to [42, 89]

$$Q_+ = Q_-, \tag{3.44}$$

$$Z_+ = \frac{e^{2\nu}}{\omega^2 r_c}\left\{\frac{\epsilon_{0-} + p_0}{\epsilon_{0+} + p_0}\left(\omega^2 r_c^2 e^{-2\nu} Z_- + e^{-\lambda}\nu' Q_-\right) - e^{-\lambda}\nu' Q_+\right\}, \tag{3.45}$$

where, the $-(+)$ subscript corresponds to the quantities before(after) the surface of discontinuity. In case of a Maxwell construct for phase transition, there is a discontinuity in energy density while in Gibbs construct of phase transition the energy density is continuous at the phase boundary as considered here.

With these boundary conditions the problem becomes an eigen-value problem for '$\omega$'. To calculate the eigen frequencies $\omega$, we proceed as follows. For a given central density $\epsilon_c$, we first solve the TOV equations eqs. (3.3)–(3.5) to get the profile of the unperturbed metric functions $\lambda(r)$, $\nu(r)$ and also the mass $M$ and the radius $R$ of the spherical star. For a given $\omega$, we solve the pulsating equations eqs. (3.36) and (3.40) to determine the fluid perturbing functions $Q(r)$ and $Z(r)$ as a function of $r$. To solve these equations, we take the initial values for $Q$ and $Z$ consistent with eq. (3.41). Specifically we took $C$ of the order 1. The solutions of $Q$ and $Z$ are independent of this choice. We then calculate l.h.s. of eq. (3.43). The value of $\omega$ is then varied such that the boundary condition, eq. (3.43), is satisfied. This gives the frequency, $\omega$ as function of mass and radius. It may be noted that there can be multiple solutions of $\omega$ satisfying the pulsating equations and the boundary conditions corresponding to different initial trail values for $\omega$. These different solutions for $\omega$ correspond to frequencies of different modes of oscillations of the compact star.

## 4 Equilibrium and adiabatic sound speeds

In this section we discuss both equilibrium and adiabatic sound speeds which are needed to solve the pulsating equations eqs. (3.36) and (3.40). We present the expressions of both sound speeds for matter in HP, QP and MP. The equilibrium speed of sound is given by

$$c_e^2 = \frac{dp}{d\epsilon} = \frac{dp/dr}{d\epsilon/dr}, \tag{4.1}$$

where, $p$ and $\epsilon$ are the total pressure and energy density. The equilibrium sound speed in NS can be evaluated numerically as a function of radial distance from the center of the star while keeping the NSM in $\beta$-equilibrium. Using the above definition (4.1), we find the equilibrium speed of sound in HP, QP and MP.

The characteristic time scale of the QNM is about $10^{-3}$ sec which is much smaller than the $\beta$-equilibrium time scale. Therefore, during the oscillations the composition of the matter can be assumed to be constant. Such adiabatic approximation means the adiabatic speed of sound corresponds to the constant composition i.e.

$$c_s^2 = \left(\frac{\partial p}{\partial \epsilon}\right)_{y_i} = \frac{(\partial p/\partial n_B)_{y_i}}{(\partial p/\partial n_B)_{y_i}}, \tag{4.2}$$

where, $y_i = (n_i/n_B)$'s are the fractions of the constituents of the matter which need to be held fixed while taking the derivatives. Once the derivatives are taken, we apply the $\beta$-equilibrium condition and get the adiabatic speed of sound in different phases. In the following subsections we present the analytical expressions for the adiabatic speeds of sound in HP, QP and MP.

### 4.1 Speed of sound in hadronic phase

In the following we estimate the adiabatic speed of sound of hadronic matter within the RMF model as

$$c_{s,\mathrm{HP}}^2 = \frac{\left(\frac{\partial p_{\mathrm{HP}}}{\partial n_B}\right)_{y_i}}{\left(\frac{\partial \epsilon_{\mathrm{HP}}}{\partial n_B}\right)_{y_i}}. \tag{4.3}$$

The total energy density and total pressure of matter in HP are given in eqs. (2.14) and (2.15). Using these equations we find the partial derivative of pressure and energy density with respect to baryon number density at constant composition (fixed $y_i$) as

$$\left(\frac{\partial p_{\mathrm{HP}}}{\partial n_B}\right)_{y_i} = \sum_{i=n,p,l}\left[\mu_i y_i + \left(\frac{\partial \mu_i}{\partial n_B}\right)_{y_i} n_B\right] - \left(\frac{\partial \epsilon_{\mathrm{HP}}}{\partial n_B}\right)_{y_i}, \tag{4.4}$$

and,

$$\begin{aligned}\left(\frac{\partial \epsilon_{\mathrm{HP}}}{\partial n_B}\right)_{y_i} =& \frac{1}{2\pi^2}\sum_{i=n,p,e,\mu}\left[E_{Fi}k_{Fi}^2\left(\frac{\partial k_{Fi}}{\partial n_B}\right)_{y_i} + m^*\left(E_{Fi}k_{Fi} - m^{*2}\log x_i\right)\left(\frac{\partial m^*}{\partial n_B}\right)_{y_i}\right] \\ &+ (m_\sigma^2\sigma_0 + V'(\sigma_0))\left(\frac{\partial \sigma_0}{\partial n_B}\right)_{y_i} + m_\omega^2\omega_0\left(\frac{\partial \omega_0}{\partial n_B}\right)_{y_i} + m_\rho^2\rho_3^0\left(\frac{\partial \rho_3^0}{\partial n_B}\right)_{y_i}. \end{aligned} \tag{4.5}$$

Here, $x_i = \dfrac{E_{Fi} + k_{Fi}}{m^*}$. The derivatives of the meson fields at constant composition, using eqs. (2.6)–(2.8) are given as

$$\left(\frac{\partial \sigma_0}{\partial n_B}\right)_{y_i} = \frac{g_\sigma(a_p + a_n)}{m_\sigma^2 + V''(\sigma_0) - g_\sigma(b_p + b_n)}, \tag{4.6}$$

$$\left(\frac{\partial \omega_0}{\partial n_B}\right)_{y_i} = \frac{g_\omega(y_p + y_n)}{m_\omega^2}, \tag{4.7}$$

$$\left(\frac{\partial \rho_3^0}{\partial n_B}\right)_{y_i} = \frac{g_\rho(y_p - y_n)}{2m_\rho^2}, \tag{4.8}$$



JCAP02(2023)015

where, $V''(\sigma_0)$ is the second derivative of eq. (2.5) with respect to $\sigma_0$. The quantities $a_i$ and $b_i$, $(i = n, p)$ are given by

$$a_i = \frac{m^* y_i}{E_{Fi}}, \tag{4.9}$$

$$b_i = \frac{g_\sigma}{2\pi^2}\left[3m^{*2}\log x_i - E_{Fi}k_{Fi} - \frac{2m^{*2}k_{Fi}}{E_{Fi}}\right]. \tag{4.10}$$

Eqs. (4.4) and (4.5) lead, inturn, to the derivatives of the medium dependent mass ($m^*$) and the chemical potential ($\mu_i$) with respect to baryon number density at constant composition is given as

$$\left(\frac{\partial m^*}{\partial n_B}\right)_{y_i} = -g_\sigma\left(\frac{\partial \sigma_0}{\partial n_B}\right)_{y_i}, \tag{4.11}$$

$$\left(\frac{\partial \mu_i}{\partial n_B}\right)_{y_i} = \left(\frac{\partial \tilde{\mu}_i}{\partial n_B}\right)_{y_i} + g_\omega\left(\frac{\partial \omega_0}{\partial n_B}\right)_{y_i} + g_\rho I_{3i}\left(\frac{\partial \rho_{30}}{\partial n_B}\right)_{y_i}, \tag{4.12}$$

where, $\tilde{\mu}_i = \sqrt{k_{Fi}^2 + m^{*2}}$. Further, we have on direct evaluation, using $n_B = \sum_{i=n,p}\frac{k_{Fi}^3}{3\pi^2}$,

$$\left(\frac{\partial k_{Fi}}{\partial n_B}\right)_{y_i} = \frac{k_{Fi}}{3n_B}. \tag{4.13}$$

Thus the partial derivatives of pressure, eq. (4.4) and energy density eq. (4.5) gets completely defined. This gives the adiabatic speed of sound in hadronic matter in the RMF model.

Similarly, one can determine the sound speeds in DDB model. The expressions of the partial derivatives of pressure and energy density in DDB model are similar to eq. (4.4) and eq. (4.5) except that there are additional terms due to the density dependent couplings. Here we give the expressions with the incorporation of corresponding changes arising from the density dependent couplings. The derivatives of the meson fields in DDB model is given as follows

$$\left(\frac{\partial \sigma_0}{\partial n_B}\right)_{y_i} = \frac{1}{m_\sigma^2 - g_\sigma(b_p + b_n)}\left(g_\sigma(a'_p + a'_n) + \left(\frac{\partial g_\sigma}{\partial n_B}\right)_{y_i}(n_p^s + n_n^s)\right), \tag{4.14}$$

$$\left(\frac{\partial \omega_0}{\partial n_B}\right)_{y_i} = \frac{1}{m_\omega^2}\left(g_\omega(y_p + y_n) + \left(\frac{\partial g_\omega}{\partial n_B}\right)_{y_i}(n_p + n_n)\right), \tag{4.15}$$

$$\left(\frac{\partial \rho_3^0}{\partial n_B}\right)_{y_i} = \frac{1}{2m_\rho^2}\left(g_\rho(y_p - y_n) + \left(\frac{\partial g_\rho}{\partial n_B}\right)_{y_i}(n_p - n_n)\right), \tag{4.16}$$

where, with $a_i$ and $b_i$ as given in eqs. (4.9) and (4.10),

$$a'_i = a_i + \frac{b_i\sigma_0}{g_\sigma}\left(\frac{\partial g_\sigma}{\partial n_B}\right)_{y_i}, \tag{4.17}$$

and, the derivatives of the density dependent couplings are given as

$$\left(\frac{\partial g_\sigma}{\partial n_B}\right)_{y_i} = -\frac{g_\sigma a_\sigma}{\rho_0}x^{a_\sigma - 1}, \tag{4.18}$$

$$\left(\frac{\partial g_\omega}{\partial n_B}\right)_{y_i} = -\frac{g_\omega a_\omega}{\rho_0}x^{a_\omega - 1}, \tag{4.19}$$

$$\left(\frac{\partial g_\rho}{\partial n_B}\right)_{y_i} = -\frac{g_\rho a_\rho}{\rho_0}. \tag{4.20}$$



JCAP02(2023)015

The derivatives of the medium dependent mass and the effective chemical potential at constant composition is defined as

$$\left(\frac{\partial m^*}{\partial n_B}\right)_{y_i} = -g_\sigma \left(\frac{\partial \sigma_0}{\partial n_B}\right)_{y_i} - \left(\frac{\partial g_\sigma}{\partial n_B}\right)_{y_i} \sigma_0, \tag{4.21}$$

and,

$$\begin{aligned}\left(\frac{\partial \mu_i}{\partial n_B}\right)_{y_i} = &\left(\frac{\partial \mu_i^*}{\partial n_B}\right)_{y_i} + \left(\frac{\partial g_\omega}{\partial n_B}\right)_{y_i} \omega_0 + g_\omega \left(\frac{\partial \omega_0}{\partial n_B}\right)_{y_i} \\ &+ \left(\frac{\partial g_\rho}{\partial n_B}\right)_{y_i} I_{3i}\rho_3^0 + g_\rho I_{3i} \left(\frac{\partial \rho_3^0}{\partial n_B}\right)_{y_i} + \left(\frac{\partial \Sigma^r}{\partial n_B}\right)_{y_i}.\end{aligned} \tag{4.22}$$

The last term on the r.h.s. above is due to the extra 're-arrangement term' in the effective baryon chemical potential, $\tilde{\mu}_i$, given in eq. (2.21) and can be written as

$$\begin{aligned}\left(\frac{\partial \Sigma^r}{\partial n_B}\right)_{y_i} = \sum_{i=p,n} \Bigg[ &-\sigma_0 n_i^s \left(\frac{\partial^2 g_\sigma}{\partial n_B^2}\right)_{y_i} - \sigma_0 \left(\frac{\partial n_i^s}{\partial n_B}\right)_{y_i} \left(\frac{\partial g_\sigma}{\partial n_B}\right)_{y_i} - \left(\frac{\partial \sigma_0}{\partial n_B}\right)_{y_i} n_i^s \left(\frac{\partial g_\sigma}{\partial n_B}\right)_{y_i} \\ &+\omega_0 n_i \left(\frac{\partial^2 g_\omega}{\partial n_B^2}\right)_{y_i} + \omega_0 \left(\frac{\partial n_i}{\partial n_B}\right)_{y_i} \left(\frac{\partial g_\omega}{\partial n_B}\right)_{y_i} + \left(\frac{\partial \omega_0}{\partial n_B}\right)_{y_i} n_i \left(\frac{\partial g_\omega}{\partial n_B}\right)_{y_i} \\ &+ \rho_3^0 I_{3i} n_i \left(\frac{\partial^2 g_\rho}{\partial n_B^2}\right)_{y_i} + \rho_3^0 I_{3i} \left(\frac{\partial n_i}{\partial n_B}\right)_{y_i} \left(\frac{\partial g_\rho}{\partial n_B}\right)_{y_i} + \left(\frac{\partial \rho_3^0}{\partial n_B}\right)_{y_i} I_{3i} n_i \left(\frac{\partial g_\rho}{\partial n_B}\right)_{y_i} \Bigg].\end{aligned} \tag{4.23}$$

In the above, using eqs. (4.18)–(4.20) the second derivatives of the couplings are directly given as

$$\left(\frac{\partial^2 g_\sigma}{\partial n_B^2}\right)_{y_i} = -\left(\frac{\partial g_\sigma}{\partial n_B}\right)_{y_i} \frac{a_\sigma x^{a_\sigma} - a_\sigma + 1}{x\ \rho_0}, \tag{4.24}$$

$$\left(\frac{\partial^2 g_\omega}{\partial n_B^2}\right)_{y_i} = -\left(\frac{\partial g_\omega}{\partial n_B}\right)_{y_i} \frac{a_\omega x^{a_\omega} - a_\omega + 1}{x\ \rho_0}, \tag{4.25}$$

$$\left(\frac{\partial^2 g_\rho}{\partial n_B^2}\right)_{y_i} = -\left(\frac{\partial g_\rho}{\partial n_B}\right)_{y_i} \frac{a_\rho}{\rho_0}. \tag{4.26}$$

Finally the derivative of the scalar condensate in eq. (4.23) is given by, using eq. (2.11)

$$\left(\frac{\partial n_i^s}{\partial n_B}\right)_{y_i} = a_i' + b_i \left(\frac{\partial \sigma_0}{\partial n_B}\right)_{y_i}. \tag{4.27}$$

Thus, the speed of sound in DDB is found using eqs. (4.4)–(4.5) with the relevant derivatives in the DDB model defined in eqs. (4.14)–(4.27).

### 4.2 Speed of sound in quark phase

In an identical manner one can estimate the adiabatic speed of sound in QP by taking the partial derivatives of total pressure and total energy density which are collected in eqs. (2.38) and (2.39). In this subsection we present the analytic expression for the adiabatic speed of sound for the quark matter in NJL model. The partial derivatives of the pressure with respect to baryon number density using the eq. (2.33) is given by

$$\left(\frac{\partial p_{\rm NJL}}{\partial n_q}\right)_{y_i} = \left(\frac{\partial p_{\rm vac}}{\partial n_q}\right)_{y_i} + \left(\frac{\partial p_{\rm med}}{\partial n_q}\right)_{y_i}, \tag{4.28}$$

where,

$$\left(\frac{\partial p_{\rm vac}}{\partial n_q}\right)_{y_i} = -\frac{N_c M^4}{\pi^2}\sum_{i=u,d}\left[H(z_\Lambda)\frac{4}{M}\left(\frac{\partial M}{\partial n_q}\right)_{y_i} + H'(z_\Lambda)\left(\frac{\partial z_\Lambda}{\partial n_q}\right)_{y_i}\right], \tag{4.29}$$

and,

$$\begin{aligned}\left(\frac{\partial p_{\rm med}}{\partial n_q}\right)_{y_i} &= \frac{N_c M^4}{\pi^2}\sum_{i=u,d}\left[H(z_i)\frac{4}{M}\left(\frac{\partial M}{\partial n_q}\right)_{y_i} + H'(z_i)\left(\frac{\partial z_i}{\partial n_q}\right)_{y_i}\right] \\ &\quad -\frac{N_c}{3}\sum_{i=u,d}\left[y_i\tilde{\mu}_i + n_i\left(\frac{\partial \tilde{\mu}_i}{\partial n_q}\right)_{y_i}\right] - 2g_v n_q + 2g_s\rho_s\left(\frac{\partial \rho_s}{\partial n_q}\right)_{y_i}. \end{aligned} \tag{4.30}$$

The partial derivative of the energy density using eq. (2.36) with respect to the baryon number density is given as

$$\left(\frac{\partial \epsilon_{\rm NJL}}{\partial n_q}\right)_{y_i} = \sum_{i=u,d}\left[y_i\mu_i + n_i\left(\frac{\partial \mu_i}{\partial n_q}\right)_{y_i}\right] - \left(\frac{\partial p_{\rm NJL}}{\partial n_q}\right)_{y_i}, \tag{4.31}$$

where, $z_i = k_{Fi}/M$ and $z_\Lambda = \Lambda/M$. The function $H(z)$ is given in eq. (2.16) and $H'(z)$ is its derivative with respect to $z$. The derivative of the constituent mass is given by

$$\left(\frac{\partial M}{\partial n_q}\right)_{y_i} = -\frac{\frac{2N_c g_s}{\pi^2}M^2(B_u+B_d)}{1+\frac{2N_c g_s}{\pi^2}M^2(A_u+A_d)} \tag{4.32}$$

where

$$A_i = 3G(z_i) - 3G(z_\Lambda) - G'(z_i)z_i + G'(z_\Lambda)z_\Lambda \tag{4.33}$$

$$B_i = G'(z_i)\frac{\partial k_{Fi}}{\partial n_q} \tag{4.34}$$

Here $i = u, d$. The function $G(z)$ is given in eq. (2.31) and $G'(z)$ is its derivative with respect to $z$. Using these relations we can find the adiabatic speed of sound of quark matter in QP as

$$c^2_{s,\rm QP} = \frac{\left(\frac{\partial p_{\rm QP}}{\partial n_q}\right)_{y_i}}{\left(\frac{\partial \epsilon_{\rm QP}}{\partial n_q}\right)_{y_i}}. \tag{4.35}$$

### 4.3 Speed of sound in mixed phase

Once we have the expressions for the different sound speeds in HP and QP then it is state forward to get the sound speeds in MP by using the quark matter fraction $\chi$ as given in eq. (2.42) in MP. In case of equilibrium sound speed, the total pressure and the total energy

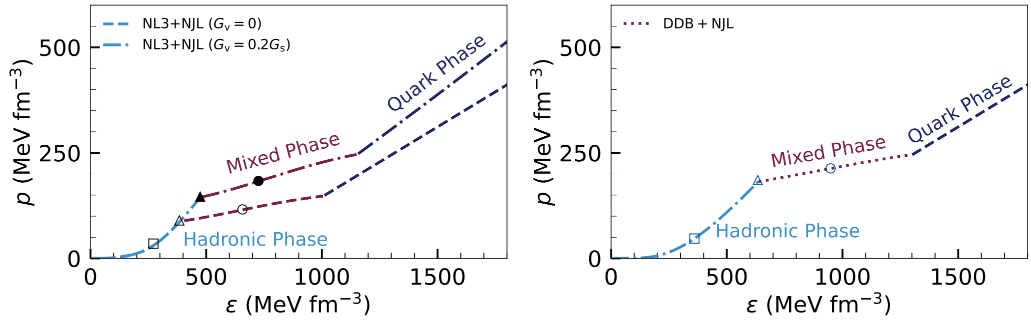


**Figure 3**. The EOSs of the charge neutral matter including the MP for both nuclear models in HP and the NJL model in QP. The left figure corresponds to the EOS with the NL3 parameterized hadronic matter while the right figure corresponds to the DDB parameterized hadronic matter. At high density, the NJL model is considered for the quark matter EOS with different vector couplings. In left figure, the EOSs correspond to the vector couplings $G_v = 0$ (upper curve) and $G_v = 0.2G_s$ (lower curve) in quark sector. In the right figure, the quark matter EOS corresponds to the vector coupling $G_v = 0$. In both the figures, the sky blue curve refers to the HP and the dark blue curve refers to the QP while the red curve corresponds to the MP. The open square corresponds to the central energy density of a NS of mass $1.4M_\odot$. The triangles denote the starting of the MP and correspond to NSs of mass $2.17M_\odot$ ($G_v = 0$) and $2.50M_\odot (G_v = 0.2G_s)$ for NL3+NJL and $2.18M_\odot$ ($G_v = 0$) for the DDB+NJL. The circles indicate the central pressure and energy density of the maximum mass stars which are $2.27M_\odot (G_v = 0)$ and $2.55M_\odot (G_v = 0.2G_s)$ for NL3+NJL and $2.20M_\odot (G_v = 0)$ for the DDB+NJL HSs. The pure quark matter phase is not achieved prior to the maximum mass in all the cases.

density of the MP is calculated by using the eqs. (2.40) and (2.43). We take the numerical derivative of pressure with respect to energy density and get the equilibrium sound speed in MP. To estimate the adiabatic sound speed in MP we take the corresponding quantities in HP and QP and hence $c^2_{s,\mathrm{MP}}$ is given as [48]

$$\frac{1}{c^2_{s,\mathrm{MP}}} = \frac{\chi}{c^2_{s,\mathrm{HP}}} + \frac{1-\chi}{c^2_{s,\mathrm{QP}}} \tag{4.36}$$

## 5 Results and discussion

In this section, we present the structural properties and non-radial oscillations of NSs and HSs. We consider two RMF models, one with NL3 [84] parameterized and other is DDB [76, 77] for nucleonic matter EOS (see section 2.1) and a two flavour NJL model for the quark matter EOS (see section 2.2) with parameters, $(G_s\Lambda^2, \Lambda, m) = (2.24, 587.6\mathrm{MeV}, 5.6\mathrm{MeV})$ [85]. The MP is calculated using Gibbs construction, as outlined in section 2.3.

### 5.1 Equation of state and properties of neutron/hybrid star

In figure 3 we display the EOS with a Gibbs construct for the HQPT with the NJL EOS describing the QP. The left figure corresponds to the HP described by RMF with NL3 parametrisation while in right figure the HP is described by RMF with DDB parametrisation for the couplings. We note here that for the QP, the vector interaction induces additional repulsion among quarks and makes the EOS stiffer which is reflected in the left figure for the two values of $G_v$. As may be seen from eq. (2.27); the effective chemical potential decreases for non vanishing and positive $G_v$. This results in a chiral transition occurring at a

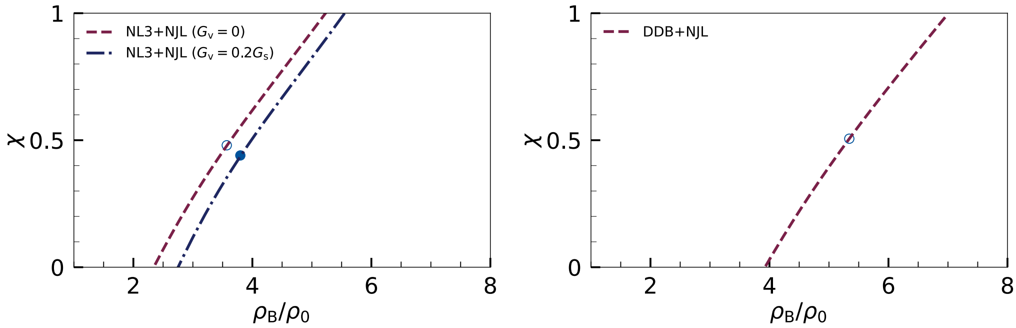


**Figure 4**. In the left figure, the quark fraction as a function of baryon density for the NL3 parameterized EOSs in HP and NJL model in QP while in the right figure, the quark fraction as a function of baryon density for the DDB parameterized EOS in HP and NJL model in QP as shown in figure 3. In the left figure, the open (dark) circle indicates the central density of the maximum mass star i.e. $\rho_{B,\max} \simeq 3.5\rho_0(3.8\rho_0)$ corresponding to $M_{\max} = 2.27M_\odot(2.55M_\odot)$ for $G_v = 0$ ($G_v = 0.2G_s$). In the right figure, the open circle indicates the central density of the maximum mass star i.e. $\rho_{B,\max} \simeq 5.5\rho_0$.
.

higher chemical potentials as $G_v$ increases along with a corresponding higher critical energy density. As a matter of fact, with DDB EOS, we get a HQPT for $G_v = 0$ for stable NS/HS configuration. For $G_v = 0.2G_s$, the corresponding critical energy density is much too high to have a stable star with a quark matter core. Therefore, in all the results that follow, we consider only $G_v = 0$ for describing HSs when the corresponding HP is described by DDB EOS. In the left of figure 3, we have plotted the MP EOS for two different vector couplings for the NJL model description while RMF with NL3 parametrisation for the HP. In the case of $G_v = 0$, the MP starts at baryon density $\rho_B \sim 2.36\rho_0$ with corresponding energy density being about 400 MeV/fm$^3$ and ends at densities $\rho_B \sim 5.22\rho_0$ with the corresponding energy density being about 1000 MeV/fm$^3$. As mentioned, increasing $G_v$ results in a stiffer EOS with the higher $G_v$ corresponding to a larger critical energy density at which the mixed phase starts to occur. In figure 3 (right), we show the EOS where the nuclear matter is described by the DDB model and the quark matter is described by the NJL model with $G_v = 0$. In this case, the MP starts at baryon density $\rho_B \sim 3.93\rho_0$ density and ends at $\rho_B \sim 6.98\rho_0$. The open and filled circles in the EOSs denote the central energy densities of the maximum mass stars for the corresponding EOSs in figure 3. These circles lie in MP region indicating no pure quark matter core is realized within the present modelling of EOS. It can also be seen in figure 4, where we plot the quark matter fraction $\chi$ as a function of density for different $G_v$s and nuclear matter EOSs. The open (filled) circle in figure 3(left) corresponds to the maximum mass star denotes $\chi = 0.482$ (0.438) which means 48.2% (43.8%) of quark matter fraction present in the core of HS of NL3+NJL type with $G_v = 0$ ($0.2G_s$). On the otherhand, in figure 3 (right) the open circle correspond to the maximum mass star has $\chi = 0.506$ i.e. 50.6% of quark matter present in the core of HS of DDB+NJL in a MP. It is further observed that for the HSs considered here, there is no pure quark matter core. Quark matter is only realised in a MP in the HSs within the models considered here for the EOSs.

In figure 5 (left) we show the variation of the squared sound speeds, $c_e^2$ and $c_s^2$ with the normalised baryon density $\rho_B/\rho_0$. On the left, we show this behaviour for the HSM described by RMF with NL3 parametrisation and NJL model. On the right the same is shown for the HSM described by RMF with DDB parametrisation and NJL model. As the density increases

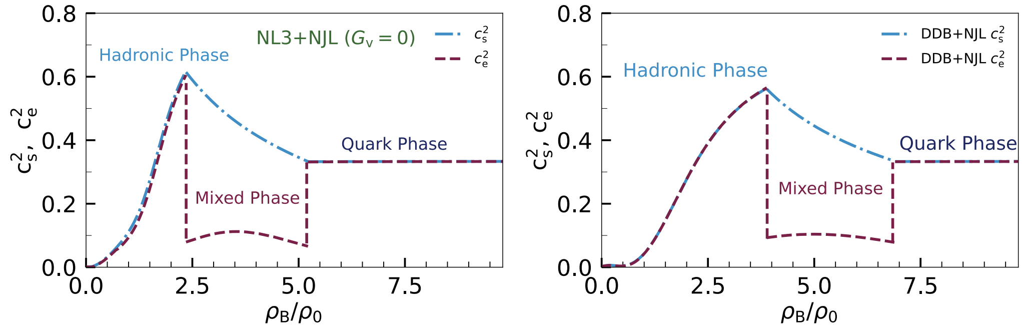


**Figure 5**. The variation of the square of sound speeds, ($c_e^2$ and $c_s^2$) as a function of baryon number density for the charge neutral matter. The brown dashed (blue dot-dashed) curve corresponds to the equilibrium (adiabatic) sound speed in the different phases like HP, QP and MP for the hybrid EOSs described by NL3+NJL in the left figure and DDB+NJL in the right figure. The vector coupling strength in NJL model is $G_v = 0$ in the case of the both hybrid models.

in the HP, the squared speeds of both the sounds increase monotonically for either cases. The maximum value of the square of speeds of sound are 0.608 in NL3+NJL model and 0.564 in DDB+NJL at the critical density after which the MP starts. In either case, the square of two sound speeds behave very differently in the MP. The square of equilibrium sound speed $c_e^2$ decreases discontinuously at the onset of MP to a value 0.08 (0.09) beyond which it shows a continuous behaviour till the end of MP where it again discontinuously increases from 0.06 (0.08) to 0.33 (0.33) for NL3+NJL (DDB+NJL) case. The square of the adiabatic sound speed $c_s^2$, on the otherhand does not show similar discontinuous behaviour. It has an important consequence for the $g$ modes as we shall see later. While the difference between the squared sound speeds is small in HP, at the onset of MP, this difference become large leading to large Brunt-Väisäla frequency giving rise to an enhancement of $g$ mode frequency. We may note here that the difference between the two squared sound speeds turns out to be vanishing for the present case of two flavor NJL model. This is similar to the case of bag model EOS [38]. For massless two flavors, the charge neutrality and $\beta$-equilibrium condition renders the electron density to be constant which makes the difference between the two squared sound speeds to be vanishing. On the otherhand, this need not be the same for 3 quark flavors as the electron chemical potential $\mu_e \sim m_s^2/(4\mu_q)$ leading to electron density depending on quark mass and quark chemical potential leading to a non-vanishing value for the difference between the two speeds of sound.

Apart from enhancing the $g$ mode frequency, the existence of the sudden rise of equilibrium sound speed has also important consequence regarding the mass and radius relation in NS. One actually needs a rise in speed of sound in a narrow region of densities, for an explanation of the compact stars to have large mass and small radius [90]. To achieve this possibility, a quarkyonic phase [90] or a vector condensate phase along with pion superfluidity [91] have been proposed recently. On the other hand, such a steep rise in the speed of sound can also arise in a MP construct within the model for hadronic matter and quark matter as used here.

In figure 6, we show the mass-radius relations for our models. For pure nucleonic matter the maximum mass turns out to be $2.77M_\odot$ ($2.35M_\odot$) and radius turns out to be 13.26 km (11.87 km) when the nuclear matter is describes in NL3 (DDB). If one uses MP EOS the maximum mass reduces to $2.27M_\odot$ for $G_v = 0$ with the corresponding radius $R = 14.39$ km and to $2.55M_\odot$ for $G_v = 0.2G_s$ with the radius being $R = 14.17$km in NL3+NJL case while



JCAP02(2023)015

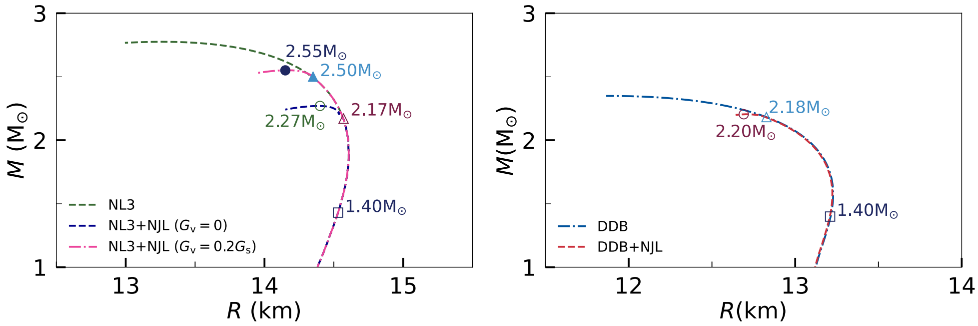


**Figure 6**. The mass-radius curves are plotted for the compact stars described by the models NL3, NL3+NJL in the left figure and DDB and DDB+NJL in the right figure for the different values of the vector couplings, $G_v$ in the NJL model. In case of DDB and DDB+NJL model, the vector coupling is taken zero i.e. $G_v = 0$. The circles denote the maximum mass HSs having quark matter inside their cores for different values of vector interaction in NJL model. While the triangles represents the maximum mass NSs having hadronic matter inside the core. In the left figure, the maximum mass of HSs described by NL3+NJL hybrid model are $2.27M_\odot$ where $G_v = 0$ and $2.55M_\odot$ where $G_v = 0.2G_s$. In the right figure, the maximum mass HS described by DDB+NJL is $2.20M_\odot$.

the same decreases to $2.20M_\odot$ with corresponding radius 12.71 km. This is essentially due to the fact that the quark matter EOS is softer compared to the nuclear matter EOS. The central energy densities for the maximum mass HSs are $\epsilon_c^{\max} = 656\,\mathrm{MeV/fm^3}$ ($G_v = 0$) and $\epsilon_c^{\max} = 738\,\mathrm{MeV/fm^3}$ ($G_v = 0.2G_s$) in NL3+NJL case while $\epsilon_c^{\max} = 948\,\mathrm{MeV/fm^3}$ ($G_v = 0$) in DDB+NJL. As central energy density is increased further, HSs become unstable i.e. $dM/d\epsilon < 0$. Thus, within the present models, we do not find stable HSs with the pure quark matter core. The quark matter, if it is present in the core, is always in MP. As $G_v$ increases in NL3+NJL case, the MP starts at higher energy density and hence larger fraction of hadronic matter contributes to the total mass of the star as we have seen in figure 4 (left). This leads to an increase of the maximum mass of HS. With increasing $G_v$ further we might expect NSs without any quark matter in the core. The radius $R_{1.4}$ for the canonical mass of $1.4M_\odot$ NSs turns out to be 14.52 km in NL3+NJL case while same turns out to be 13.21 km in DDB+NJL case. It may be noted that the x-ray pulse analysis of NICER data from PSR $J0030 + 0451$ by Miller et al. found $R = 13.02^{+1.14}_{-1.19}$ km for $M = 1.44 \pm 0.15M_\odot$ [15]. Such a star will not have a quark core within these present models for the EOS of dense matter. Such a conclusion, however, should be taken with caution as this is very much dependent upon the EOSs both in hadronic and quark phase. In particular, more exotic phases of quark matter could also be possible including various color superconducting phases, various inhomogeneous phases for dense quark matter which have not been considered here.

In figure 7, we show the energy density and pressure profiles i.e. energy density and pressure as the functions of the radial distance from the center of the maximum mass HSs described in the present models. In the left we show for the NL3+NJL model while in the right we show for the DDB+NJL model. As mentioned earlier, the cores of the such stars are in the MP with about the 50% of quark matter and 50% of nuclear matter (see figure 4). The radius of the MP core is about 3.8 km (2.7 km) with the total radius of 14.17 km (12.71 km) for the HS described in NL3+NJL (DDB+NJL). We have taken here the vector coupling $G_v = 0.2G_s$ in NL3+NJL model and $G_v = 0$ in DDB+NJL model. For $G_v = 0$, in NL3+NJL, the MP core radius slightly larger i.e. 4.2 km while the star's radius being about 14.39 km.

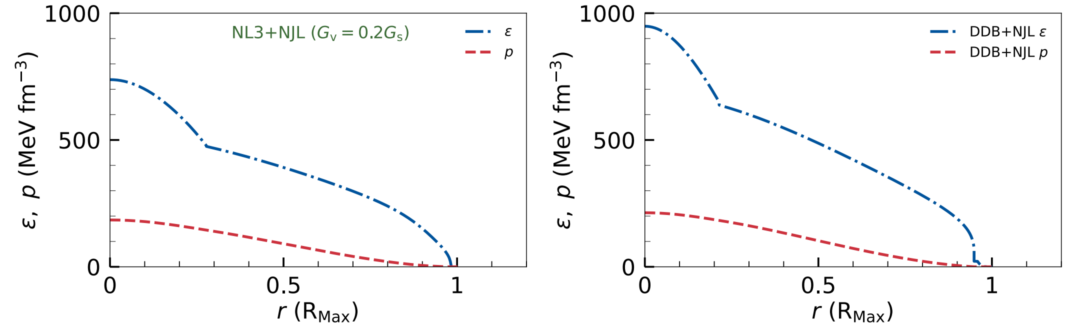


**Figure 7**. The energy density, $\epsilon$ (blue dot-dashed) and pressure, $p$ (red dashed) profiles as a function of radial distance from the center of the maximum mass HSs described by the hybrid models NL3+NJL (left) and DDB+NJL (right). In case of NL3+NJL hybrid model, the vector coupling is none-zero i.e. $G_v = 0.2G_s$ while in case of DDB+NJL hybrid model, the vector coupling is zero i.e. $G_v = 0$. The transition from MP to HP happens at $\rho_B = 2.75\rho_0$ ($\rho_B = 3.95\rho_0$) corresponding with the radial distance $r_c = 0.27R_{\rm Max}$ ($r_c = 0.21R_{\rm Max}$) in the NL3+NJL (DDB+NJL) model.

At $r = r_c$, the critical radial distance, where the matter goes from a MP to HP or vice-versa, the energy density becomes non-differentiable while pressure shows smooth behavior as may be observed in figure 7.

The variation of the squared sound speeds $c_e^2$ and $c_s^2$ are shown in figure 8 as a function of radial distance from the center of the stars for both HS as well as NS. In figure 8 (left) we show the profiles of both $c_e^2$ and $c_s^2$ for the maximum mass stars described in NL3 and NL3+NJL models while in figure 8 (right) we display the same for the maximum mass stars described in DDB and DDB+NJL models. In both the cases, we have taken here $G_v = 0$. The HQPT in HSs is reflected in the variation of the square of the equilibrium sound speed, $c_e^2$ which changes abruptly from $c_e^2 = 0.08$ to $c_e^2 = 0.608$ in NL3+NJL model and from $c_e^2 = 0.06$ to $c_e^2 = 0.564$ for the DDB+NJL model at the critical radius $r_c$ where the transition from a MP to a HP takes place. Such an abrupt change in $c_e^2$ while a smooth behaviour of $c_s^2$ makes the Brunt-Väisäla frequency, ($\omega_{\rm BV}^2 \sim (c_e^{-2} - c_s^{-2})$), becoming significant at the boundary of the MP core in the HSs. As may be observed from eq. (3.37) or eq. (3.40), a nonvanishing $\omega_{BV}$ will affect the fluid perturbation functions $Z(r)$ and $Q(r)$ and hence will have its effect on the oscillation frequency $\omega$. In particular this leads to an enhancement of g-mode frequencies for the HSs. We discuss more of this in subsection 5.3.

In figure 9 (left), we show the profile of Brunt-Väisäla frequency, $\omega_{\rm BV}$, in the stars of maximum masses described in NL3 and NL3+NJL while in figure 9 (right), we show the same described in DDB and DDB+NJL where the vector coupling $G_v = 0$ in NJL model. The steep rise of $\omega_{\rm BV}$ at the onset of MP may be noted. The Brunt-Väisäla frequency, $\omega_{\rm BV}$, depends on the both the speeds of sound, see eq. (3.39). In the core of maximum mass HS, the variation of the both sound speeds are different which is reflected in the $\omega_{\rm BV}$ profile. The onset of muons is shown by a little kink in the figure with a slight increase in $\omega_{\rm BV}$.

### 5.2 Tidal deformability

The tidal distortion of neutron stars in a binary system links the EOS to the gravitational wave emissions during the inspiral [92]. Next we discuss the results for the tidal deformability with the equation of state considered here. In figure 10 (left) shows the dimensionless tidal deformability parameters $\Lambda_1$ and $\Lambda_2$ of the NSs involved in the Binary Neutron Star (BNS)



JCAP02(2023)015

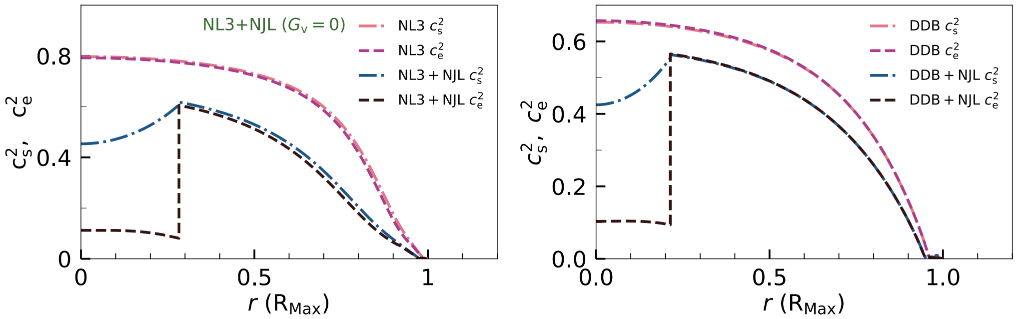


**Figure 8**. The equilibrium $c_e^2$ and the adiabatic $c_s^2$ sound speeds profiles inside the maximum mass stars as a function of radial distance from the center of the stars. In the left figure, the $c_e^2$ and $c_s^2$ profiles is shown as a function of the radial distance in the stars described by the NL3 and NL3+NJL models while in the right figure same in the stars described by the DDB and DDB+NJL models. The black dashed (darkblue dot-dashed) curve correspond to the $c_e^2$ ($c_s^2$) profile for the HS described by NL3+NJL (DDB+NJL) model while brown dashed (magenta dot-dashed) curve corresponds to the $c_e^2(c_s^2)$ profile in the NS described by NL3(DDB) model. The discontinuity in the profile of $c_s^2$ in the case of HSs at $r_c = 0.27R_{\rm Max}$ ($r_c = 0.21R_{\rm Max}$) shows the appearance of quark matter in the hybrid model NL3+NJL(DDB+NJL).

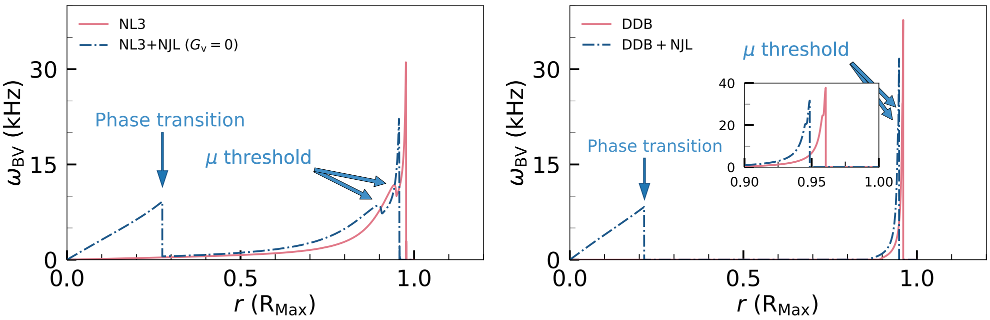


**Figure 9**. The Brunt-Väisäla frequency ($\omega_{\rm BV}$) profile in the maximum mass stars as a function of the radial distance from the center of the star. In the left figure, the $\omega_{\rm BV}$ profile is plotted as a function of radial distance in the stars described by the NL3 and NL3+NJL model while in the right we plot same in the stars described by the DDB and DDB+NJL models. Red solid (blue dot-dashed) curve shows the $\omega_{\rm BV}$ profile in the NS (HS where the vector coupling is considered to be zero i.e. $G_v = 0$). The little kink in the profiles near the surface of the stars shows the threshold for the appearance of muons in the all the models.

with masses $m_1$ and $m_2$, respectively, for the hadronic EOSs DDB, NL3 and corresponding mixed phase EOS with NJL model DDB+NJL, NL3+NJL. In the GW170817 event, the chirp mass, $\mathcal{M}_{\rm chirp} = (m_1 m_2)^{3/5}(m_1 + m_2)^{-1/5}$, was measured as $1.186 M_\odot$ [9] and these curves were calculated based on the masses involve in the BNS merger by varying $m_1$ in the observed range $1.365 < m_1 < 1.60$. We may note here that the quark matter core occurs for NSs of masses at around $2M_\odot$. Thus the tidal deformability $\Lambda_1$ and $\Lambda_2$ as shown in the figure 10 (left) will correspond to hadronic phase only. We also show the constraint imposed on $\Lambda_1 - \Lambda_2$ plane from GW170817 event in the same plot. Based on a marginalized posterior for the tidal deformability of the two binary components of GW170817, the gray solid (dot-dashed) line represents the 90%(50%) confidence interval (CI) for the tidal deformability of these two components. There are magenta solid (blue dashed) lines representing 90%(50%) confidence

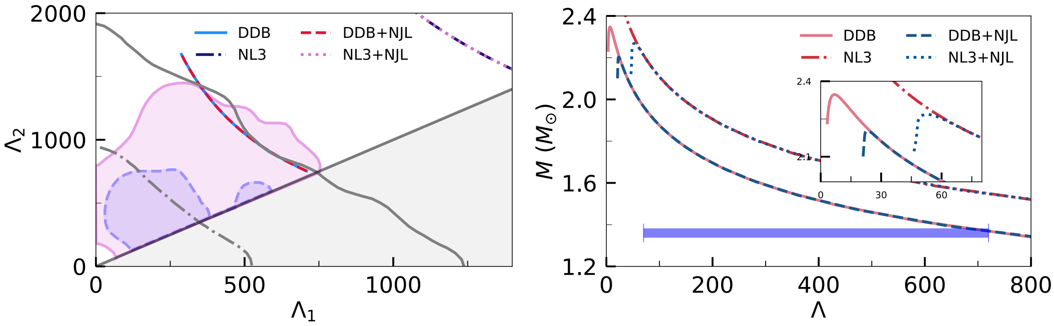


**Figure 10**. Based on the hadronic NL3, DDB and their hybrid EOS with NJL quark matter model for a mixed phase. (left) we show the dimensionless tidal deformability parameters $\Lambda_1$ and $\Lambda_2$ of the GW170817 binary neutron star merger, for the fixed measured chirp mass of $\mathcal{M}_{\rm chirp} = 1.186 M_\odot$. A gray solid (dot-dashed) line indicates a 90%(50%) confidence interval for the tidal deformability of GW170817's two binary components based on their marginalized posteriors. In this figure, magenta solid (blue dashed) lines represent 90%(50%) confidence intervals for the constraints from GW170817 : marginalized posterior using a parameterized EOS and a maximum mass requirement of $1.97 M_\odot$. (right) The dimensionless tidal deformability as a function of the NS mass. The tidal deformability constraint of a $1.36 M_\odot$ star is represented by the blue bar in the right panel.

intervals for the constraints from GW170817: marginalized posterior using a parameterized EOS with a maximum mass requirement of at least $1.97 M_\odot$. In this regard, GW170817 and its electromagnetic counterpart disfavour NL3 parameterisation of the RMF model. The DDB, however, is less stiff than NL3, so it satisfies those constraints well. The stiffness of the EOS may be attributed to either its symmetric nuclear part or its density-dependent symmetry energy. While NL3 and DDB exhibit similar symmetric nuclear matter (SNM), DDB has a softer symmetry energy than NL3. For the models NL3 and DDB, the nuclear matter incompressibility $K_0$ is 271 MeV, and 269 MeV and the slope of the symmetry energy $L_0$ is 118 MeV, 32 MeV, at saturation density respectively. Figure 10 (right) shows the dimensionless tidal deformability as a function of NS mass of the EOS models adopted here. The blue horizontal bar indicates the 90% CI obtained for the tidal deformability of a $1.36 M_\odot$ or the combined tidal deformability in the BNS for $q = m_1/m_2 = 1$ [9]. It is clear that the NL3 is outside of the 90% CI constraint whereas DDB is within the acceptable range. As discussed above the NSs masses below $2.18 M_\odot$ and $2.17 M_\odot$ correspond to the only hadronic phase EOSs for DDB and NL3 mixed phases EOSs, respectively. It can be seen from the figure that the tidal deformability $\Lambda$ bifurcate from the same NS masses for those EOSs.

### 5.3 Oscillation modes in hybrid stars

We next show, here, the results for $f$ and $g$ modes for NSs and HSs in different models presented in this study. We shall focus our attention to the quadruple mode ($l = 2$) only. It may be expected from the coupled eqs. (3.36) and (3.40) for the fluid perturbation functions $Q(r)$ and $Z(r)$ the two sound speeds $c_s^2$ and $c_e^2$ play an important role in the determination of different solutions for these functions and hence on the frequencies of the oscillation modes. The typical frequency of $g$ modes lies in the range from few 100 Hz up to 1 kHz while that of $f$ modes lies in the range $1-3$ kHz. As mentioned in section 3, we solve eqs. (3.36) and (3.40) in a variational method to determine the oscillation frequencies. As this is computed using a variational method, the final solutions depend upon the initial guesses for the frequencies.

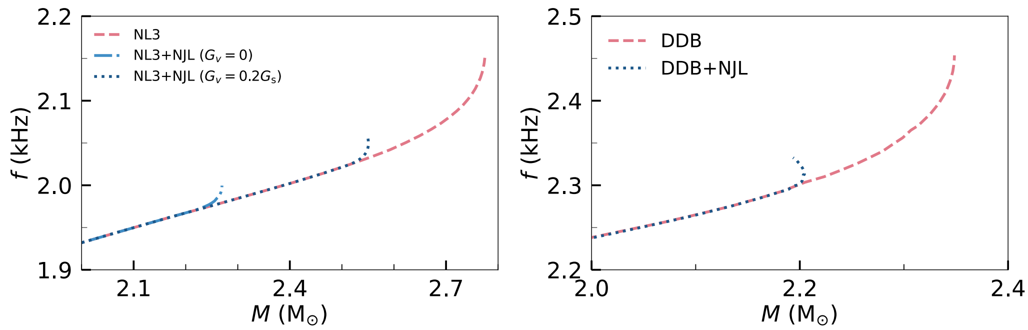


**Figure 11**. The oscillation frequencies of $f$ mode $f = \omega/2\pi$ in kHz as a function of the star's masses which are described by NL3 and NL3+NJL models in the left figure and same as a function of the star's masses which are described by DDB and DDB+NJL models in the right figure. The magenta dashed curve corresponds to NSs i.e. without any quark matter core. (left) The blue dot-dashed (blue dotted) curves correspond to the $f$ mode frequencies of the HSs which are described by NL3+NJL hybrid model for $G_v = 0 (G_v = 0.2G_s)$. (right) The blue dotted curve corresponds to the $f$ mode frequencies of the HSs which are described by DDB+NJL hybrid model for $G_v = 0$. The appearance of the quark matter in the core enhances the oscillation frequencies.

To get a solution of the $f$ mode, we give the initial guess for the frequency ($f = \omega/2\pi$) of the order of few kHz. On the other hand, to look for a $g$ mode we give the initial guess for the same in the range of few hundred Hz. In figure 11, we show the $f$ mode frequencies as a function of mass of compact stars for the both NS and HS described by NL3 and NL3+NJL models in the left figure while same as described by DDB and DDB+NJL model in the right figure. In the left figure, the blue curves refer to the $f$ mode frequencies for HSs with $G_v = 0$ (blue dotted) and with $G_v = 0.2G_s$ (blue dot-dashed) while the magenta curve refers to the $f$ mode frequencies for NSs described by NL3+NJL and NL3, respectively. In the right figure, we show same as the left figure but for the DDB+NJL and DDB model, respectively where the vector coupling is zero i.e. $G_v = 0$. We may observe here that there is a mild rise in the frequencies for the $f$ modes for stars with a quark matter core. Such a rise of non-radial oscillation frequencies due to the quark matter core was also observed in refs. [38, 48]. However for $f$ modes, the rise due to the quark matter in the core, is very small. *Eg.* for a HS star, described by NL3+NJL where $G_v = 0$, of mass $M = 2.27M_\odot$, the $f$ mode frequency becomes 2 kHz from a value of 1.97 kHz of a NS of same mass.

In figure 12, we plot the $g$ mode frequencies as a function of the mass of the compact stars for the both NS and HS described by NL3 and NL3+NJL models in the left figure while same as described by DDB and DDB+NJL model in the right figure. For NSs, the compact stars without any quark matter core, the $g$ mode frequencies lie in the range of $(322 - 341)$ Hz $(139 - 148)$ Hz for the stars of masses larger than 2 $M_\odot$ described by NL3 (DDB) model. On the otherhand, in the presence of quark matter in MP, the frequencies rise sharply to about 589 Hz ($G_v = 0$) and 589 Hz ($G_v = 0.2G_s$) in the case of NL3+NJL model while same rises sharply to about 303 Hz ($G_v = 0$) in the case of DDB+NJL. Let us note that at the onset of the MP in case of NSs, $c_e^2$ decreases abruptly. This is due to the fact that the electron chemical potential falls at the onset of MP. This is due to the fact that the charge neutral nuclear matter undergoes a phase transition to one component of HP which is positively charged and the other component of QP which is negatively charged. This sudden change in the lepton number density at MP threshold leads to sudden drop of $c_e^2$ as shown in

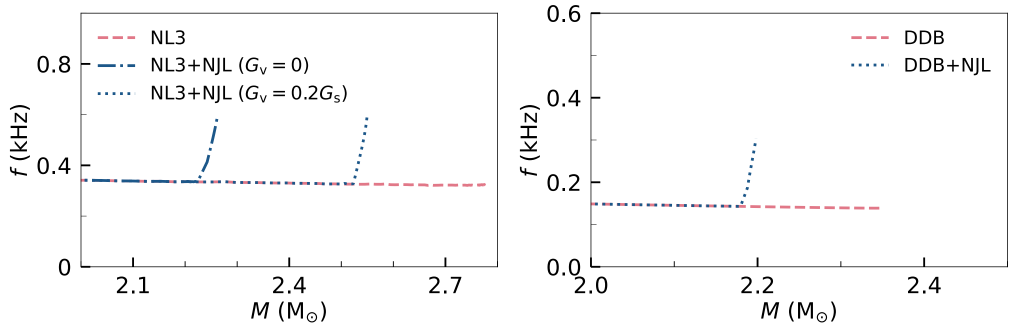


**Figure 12**. The oscillation frequencies of $g$ mode $f = \omega/2\pi$ in kHz as a function of the star's masses which are described by NL3 and NL3+NJL models in the left figure and same as a function of the star's masses which are described by DDB and DDB+NJL models in the right figure. The magenta dashed curve corresponds to NSs i.e. without any quark matter core. (left) The blue dot-dashed (blue dotted) curves correspond to the $g$ mode frequencies of the HSs which are described by NL3+NJL hybrid model for $G_v = 0 (G_v = 0.2G_s)$. (right) The blue dotted curve corresponds to the $g$ mode frequencies of the HSs which are described by DDB+NJL hybrid model for $G_v = 0$. The appearance of the quark matter in the core enhances the oscillation frequencies.

figure 8. This leads to an abrupt rise of the $\omega_{\rm BV}$ which enhances the $g$ mode frequency. As $G_v$ increases the MP core decreases and hence its contribution to the $g$ mode enhancement also decreases.

We note that the $g$ modes that we obtained for NSs or HSs are driven by the Brunt-Väisäla frequency which quantifies the mismatch between the mechanical and chemical equilibrium rates of a displaced fluid parcel and is expressed by the local equilibrium and adiabatic speeds of sound. Such core $g$ mode solutions in sub-kHz frequency range can also arise due to a sharp discontinuity in energy density in a first order phase transition [93, 94]. Such low frequency $g$ modes due to quark-hadron discontinuity has also been shown to be a feature of HSs that distinguish hadronic stars or strange quark stars based on non-radial oscillation modes [43]. On the otherhand non-radial oscillation modes with a MP of quark-hadron matter was explored by Sotani et al. [42]. It was shown here that including finite size effects in the mixed phase it is possible to distinguish between the existence or absence of density discontinuity in NS interior from gravitational waves of the $f$ mode [42]. In an interesting later work of Ranea-Sandoval et al. explored different non-radial oscillation modes ($f$, $p$ and $g$ modes) with an interpolating function relating hadron and quark phases unlike a Gibbs construct as has been attempted here [45]. We might note that for the phase transition considered here with NJL model, a Gibbs construct is consistent as the recent calculation using effective models like linear sigma model [68]; Polyakov quark meson model [70] as well as NJL model [69] suggest a lower value of surface tension $\sim 5-20{\rm MeV/fm}^2$ justifying the use of a Gibbs construct.

Next, we discuss the solution of the perturbing functions $Q(r)$ and $Z(r)$. In figure 13, we have plotted the functions $Q(r)$ and $Z(r)$ as a function of radial distance from the center for both $g$ and $f$ modes. Let us first discuss the solutions of perturbing functions $Q(r)$ and $Z(r)$ for NSs. The angular function $Z(r)$ is plotted as a solid red line ($\rm Z_f$) for $f$ mode and as a solid blue line ($\rm Z_g$) for $g$ mode. For $f$ modes, $Z(r)$ decreases monotonically starting from a vanishing value at $r = 0$ consistent with the initial condition given in eq. (3.41). As may be clear from eq. (3.40), for vanishing $\omega_{\rm BV}$, $Z'(r)$ is negative and therefore $Z(r)$ decreases as

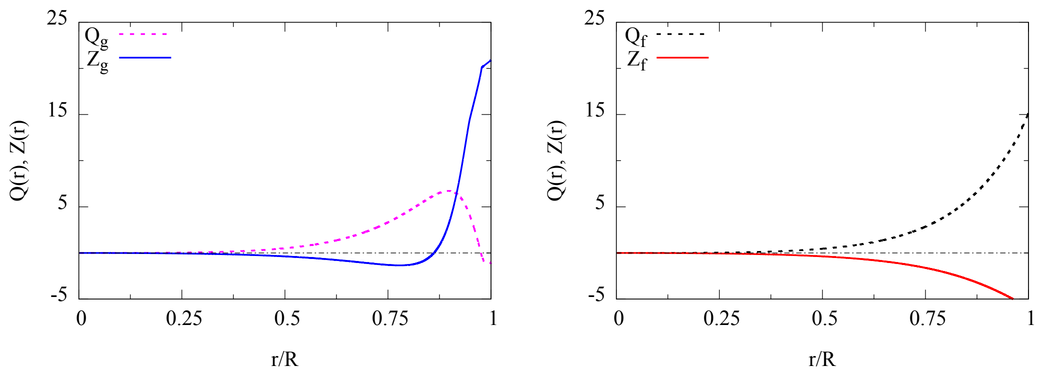


**Figure 13**. The solutions of the fluid perturbation functions $Q(r)$ and $Z(r)$ as a function of the radial distance for the maximum mass ($M = 2.77M_\odot$) neutron star obtained from the NL3 parameterized EOS. The solid (dashed) line corresponds to the angular function, $Z(r)$ (radial function, $Q(r)$). Both perturbing functions for $f$ modes ($\mathrm{Q_f}$ and $\mathrm{Z_f}$) show monotonic behavior while for $g$ modes these function do not and have nodes near the surface of the NS.

$r$ increases. When the Brünt-Väisala frequency, $\omega_{\mathrm{BV}}$ becomes significant, the forth term in eq. (3.40) starts to become important. However, if $\omega$ is large (as in the case with $f$ modes) the contribution of the second term in the parenthesis of eq. (3.40) is suppressed so that $Z(r)$ decreases monotonically as seen (red solid line) in figure 13. On the otherhand, for the $g$ mode with the lower $\omega$, the second term in the parenthesis becomes dominant. This makes the forth term in eq. (3.40) negative and significant near the surface as $\omega_{\mathrm{BV}}$ becomes significant here. It turns out that the overall sign of $Z'(r)$ becomes positive near the surface resulting eventually in the change of sign of $Z(r)$ as shown (blue solid line) in figure 13. Thus the $f$ mode shows no node for $Z(r)$, the $g$ mode solution shows a node. We have taken through out $l = 2$. The dashed lines show the behaviour of the perturbing function $Q(r)$ as $\mathrm{Q_f}$ and $\mathrm{Q_g}$ for $f$ and $g$ modes respectively. Both these functions start from vanishing values and start to increase with $r$. $Q(r)$ for $f$ mode ($\mathrm{Q_f}$) increases monotonically while $Q(r)$ for $g$ mode ($\mathrm{Q_g}$) starts to decrease when $Z(r)$ changes sign and eventually become negative near the surface consistent with the boundary condition given in eq. (3.43). Thus similar to $Z(r)$, $Q(r)$ also does not show any node for $f$ modes while the solutions of the $Q(r)$ for the $g$ modes, ($\mathrm{Q_g}$) has a node near the surface.

We, next, display the perturbing functions $Q(r)$ and $Z(r)$ for HSs in figure 14. On the left, we show the functions $Q(r)$ and $Z(r)$ for $g$ modes while on the right display the same functions associated with the $f$ modes. Let us first discuss the $g$ mode perturbing functions. We first observe that the Brunt-Väisäla frequency, $\omega_{\mathrm{BV}}$ is significant near the center as well as at the surface as may be seen in figure 9 in contrast to the hadronic matter (relevant for NSs) for which it becomes significant only near the surface. Therefore there are additional nodes for $\mathrm{Z_g}$ in case of HSs as compared to NSs. This is also reflected in the behaviour of the functions $Q(r)$ and $Z(r)$ as shown in the left figure. As was the case with NS, for $g$ mode the dominating contribution arises from the second term of the parenthesis of equation eq. (3.40). The quantity in the parenthesis has a canceling effect on the other two terms in the eq. (3.40). This leads to a slight oscillatory behaviour for the functions $Z(r)$ depending upon whether $Z'(r)$ is positive or negative up to $r_c$. Beyond it, $\omega_{\mathrm{BV}}$ becomes significant only near the surface and the behaviour of $Z(r)$ and $Q(r)$ are similar to that of NS. In the right figure, we have shown the same functions for the $f$ mode. The behaviour of these functions $Q(r)$ and $Z(r)$ associated to the f-modes are essentially similar to NSs.

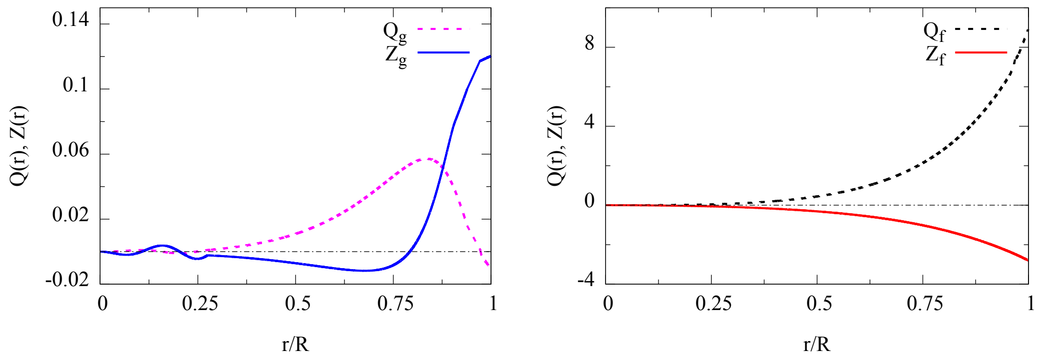


**Figure 14**. The solutions for the fluid perturbation functions $Q(r)$ and $Z(r)$, for the hybrid star of mass $M = 2.27M_\odot$ as a function of radial distance. The NL3 parameterized EOS is taken for hadronic matter while NJL model is taken for the quark matter EOS and Gibbs construction to find the mixed EOS. The left figure shows the perturbing functions associated with the $g$-modes while the right figure shows the same functions corresponding to $f$ modes. The oscillatory behavior of $Z_g(r)$ near the core may be noted in the contrast to the figure 13.

## 6 Summary and conclusion

Let us summarize the salient features of the present investigation. We have looked into possible distinct features of HSs with a quark matter in the core and a NS without a quark matter in the core. This is investigated by looking into non-radial oscillations of compact stars. The EOS for HS is constructed using a RMF theory for nuclear matter and NJL model for quark matter. Gibbs criterion for MP is used to construct MP with two chemical potentials ($\mu_B$ and $\mu_E$) imposing global charge neutrality condition. It is observed that the core of HSs can accommodate a mixture of nucleonic and quark matter, the pure quark matter phase being never achieved. In comparison to a NS without quark matter, the inclusion of MP of matter softens EOS, resulting in lower values for the maximum masses and bigger corresponding radii. Determining the composition of NS through observables it is necessary to break the degeneracy between normal and hybrid star. To this end, we looked into non-radial oscillation modes of such compact stars for this purpose. Unlike M-R curves for which EOS is sufficient, the analysis of oscillation modes requires the speed of sound of the charge neutral matter. Using a MP structure, it is observed that the equilibrium speed of sound shoots up at the transition between MP and HP in such a construct. It may be noted that such a steep rise in the velocity of sound in a narrow region of density as one comes from the core towards the surface was also seen in a quarkyonic to hadronic matter transition [90] as well as in an EOS with $\omega$ condensate and fluctuations in pion condensate [91]. Such a steep rise in velocity in sound speed is generated naturally here through MP construct. This EOS is used to determine the frequencies of non-radial oscillations in NS within a relativistic Cowling approximation that neglects the fluctuation of the space time metric and results in a much simpler equation to solve and analyze. While this is not strictly consistent with the fully relativistic treatment, the impact of such simplified approximation is not severe, typically affecting the $g$ modes at the $5 - 10\%$ level while $f$ modes are more sensitive to Cowling approximation [87]. Within the RMF model for nuclear matter, we estimated the $f$ and $g$ modes frequencies. The $g$ mode solution for NS arises due to $\omega_{\rm BV}$ when become significant towards the surface of NS. On the otherhand for HSs the $\omega_{\rm BV}$ become significant

JCAP02(2023)015

near the core where the HQPT occurs. Due to the quark matter core both the $\omega_{\mathrm{BV}}$ and $g$ mode frequency get enhanced as compared to a normal NS.

We have focused our attention in the present investigation to non-radial oscillation modes corresponding to the quadruple fundamental modes and the gravity modes. In the presence of quark matter in a mixed phase with charge neutral nuclear matter, both these modes are enhanced with the effect being more for the $g$ modes as compared to the high frequency $f$ modes. The $g$ modes that we have considered here are driven by nonvanishing Brunt-Väisäla frequency resulting from a chemical stratification and depends upon the compositional characteristics rather than a density discontinuity. This enhancement is due to the sharp drop of the equilibrium speed of sound at the on onset of the MP and is a distinct feature of HS as compared to a NS. In the context of gravitational wave from BNS merger, it is known that $g$ modes can couple to tidal forces and can draw energy and angular momentum from the binary to the NS and cause an associated phase shift in gravitational wave signal [95]. With distinct enhancement of this mode for HS as compared to NS, one might expect a distinguishing signal from GW observations. However, the resulting phase shifts for NSs and HSs turns out to be similar order due to the longer merger times for the NSs [48]. Such conclusions are of course limited by the uncertainties arising from the value of tidal coupling. When these uncertainties are reduced through improved theoretical estimations, the high frequency $g$ modes of HS can possibly be distinguished from those of NSs. The detection of $g$ modes in BNS mergers by current detectors is challenging. Nonetheless, one hopes that with the third generation detectors like Einstein telescope or Cosmic explorer, one can possibly have direct detection of these modes and have conclusive signatures regarding the composition of the NS interior.

One of the novel feature of the present investigation has been the use of hadronic EOS modeled through RMF models with their parameters determined from the nuclear matter properties at saturation density with the NL3 parameterisation as well DDB parameterisation.

Unlike meta models [48], mean field model EOS are derived from a microscopic model described in terms of nucleons and mesons and quite successful in describing various properties of finite nuclei as well as NSs. The derivation for $\omega_{\mathrm{BV}}$ as described here is rather general and can be used for any mean field model for nuclear/hyperonic matter. Similarly for quark matter NJL model is used which captures the important features of chiral symmetry breaking in strong interactions. It may be noted that these models can be extended to include strange quark matter. The calculational method developed here can be applied to the various other sophisticated models like 3 flavour NJL model, quark-meson model or Polyakov loop extension of such model describing the quark matter.

We have given in some detail the derivation of the relativistic pulsating equations involving Brunt-Väisäla frequency in which such a MP EOS as derived here. In addition we have discussed the behavior of the fluid perturbing functions in some details both with and without the HQPT which adds an understanding of the enhancement of oscillation frequencies for HSs. In future we would like to include the effects of the strange quarks in quark matter sector and correspondingly hyperons in the hadronic sector. It will also be interesting and important to include the effects of strong magnetic field for the structure of NSs [92] and its effect on the non-radial oscillation modes. We have focused our attention for NSM which is at zero temperature and vanishing a neutrino chemical potential. However, to study the proto-neutron stars we should take into account the thermal effects on the oscillations including the effects of neutrino trapping on the phase structure of matter. This will be relevant for the studying the oscillation modes from merging NS and detecting in future experimental facilities like advanced LIGO/Virgo and Einstein telescope.

## Acknowledgments

The authors gratefully acknowledge discussions with P. Jaikumar, Bharat Kumar and their useful suggestions.

## References

[1] L. Rezzolla, P. Pizzochero, D.I. Jones, N. Rea and I. Vidaña, eds., *The Physics and Astrophysics of Neutron Stars*, vol. 457, Springer (2018), [DOI] [INSPIRE].

[2] P. Haensel, A.Y. Potekhin and D.G. Yakovlev, *Neutron stars 1: Equation of state and structure*, vol. 326, Springer, New York, U.S.A. (2007), [DOI] [INSPIRE].

[3] J.M. Lattimer, *The nuclear equation of state and neutron star masses*, Ann. Rev. Nucl. Part. Sci. **62** (2012) 485 [arXiv:1305.3510] [INSPIRE].

[4] J.M. Lattimer and M. Prakash, *The Equation of State of Hot, Dense Matter and Neutron Stars*, Phys. Rept. **621** (2016) 127 [arXiv:1512.07820] [INSPIRE].

[5] M. Oertel, M. Hempel, T. Klähn and S. Typel, *Equations of state for supernovae and compact stars*, Rev. Mod. Phys. **89** (2017) 015007 [arXiv:1610.03361] [INSPIRE].

[6] G. Baym, T. Hatsuda, T. Kojo, P.D. Powell, Y. Song and T. Takatsuka, *From hadrons to quarks in neutron stars: a review*, Rept. Prog. Phys. **81** (2018) 056902 [arXiv:1707.04966] [INSPIRE].

[7] A.L. Watts et al., *Colloquium: Measuring the neutron star equation of state using x-ray timing*, Rev. Mod. Phys. **88** (2016) 021001 [arXiv:1602.01081] [INSPIRE].

[8] F. Özel and P. Freire, *Masses, Radii, and the Equation of State of Neutron Stars*, Ann. Rev. Astron. Astrophys. **54** (2016) 401 [arXiv:1603.02698] [INSPIRE].

[9] LIGO Scientific and Virgo collaborations, *GW170817: Measurements of neutron star radii and equation of state*, Phys. Rev. Lett. **121** (2018) 161101 [arXiv:1805.11581] [INSPIRE].

[10] E. Fonseca et al., *The NANOGrav Nine-year Data Set: Mass and Geometric Measurements of Binary Millisecond Pulsars*, Astrophys. J. **832** (2016) 167 [arXiv:1603.00545] [INSPIRE].

[11] J. Antoniadis et al., *A Massive Pulsar in a Compact Relativistic Binary*, Science **340** (2013) 6131 [arXiv:1304.6875] [INSPIRE].

[12] E. Fonseca et al., *Refined Mass and Geometric Measurements of the High-mass PSR J0740+6620*, Astrophys. J. Lett. **915** (2021) L12 [arXiv:2104.00880] [INSPIRE].

[13] R.W. Romani, D. Kandel, A.V. Filippenko, T.G. Brink and W. Zheng, *PSR J1810+1744: Companion Darkening and a Precise High Neutron Star Mass*, Astrophys. J. Lett. **908** (2021) L46 [arXiv:2101.09822] [INSPIRE].

[14] T.E. Riley et al., *A NICER View of PSR J0030+0451: Millisecond Pulsar Parameter Estimation*, Astrophys. J. Lett. **887** (2019) L21 [arXiv:1912.05702] [INSPIRE].

[15] M.C. Miller et al., *PSR J0030+0451 Mass and Radius from NICER Data and Implications for the Properties of Neutron Star Matter*, Astrophys. J. Lett. **887** (2019) L24 [arXiv:1912.05705] [INSPIRE].

[16] T.E. Riley et al., *A NICER View of the Massive Pulsar PSR J0740+6620 Informed by Radio Timing and XMM-Newton Spectroscopy*, Astrophys. J. Lett. **918** (2021) L27 [arXiv:2105.06980] [INSPIRE].

[17] M.C. Miller et al., *The Radius of PSR J0740+6620 from NICER and XMM-Newton Data*, Astrophys. J. Lett. **918** (2021) L28 [arXiv:2105.06979] [INSPIRE].



JCAP02(2023)015

[18] T. Gorda, A. Kurkela, P. Romatschke, M. Säppi and A. Vuorinen, *Next-to-Next-to-Next-to-Leading Order Pressure of Cold Quark Matter: Leading Logarithm*, Phys. Rev. Lett. **121** (2018) 202701 [arXiv:1807.04120] [INSPIRE].

[19] S. Borsányi et al., *Lattice QCD equation of state at finite chemical potential from an alternative expansion scheme*, Phys. Rev. Lett. **126** (2021) 232001 [arXiv:2102.06660] [INSPIRE].

[20] D.T. Son and M.A. Stephanov, *QCD at finite isospin density*, Phys. Rev. Lett. **86** (2001) 592 [hep-ph/0005225] [INSPIRE].

[21] D. Ebert and K.G. Klimenko, *Pion condensation in electrically neutral cold matter with finite baryon density*, Eur. Phys. J. C **46** (2006) 771 [hep-ph/0510222] [INSPIRE].

[22] A. Barducci, R. Casalbuoni, G. Pettini and L. Ravagli, *A calculation of the QCD phase diagram at finite temperature, and baryon and isospin chemical potentials*, Phys. Rev. D **69** (2004) 096004 [hep-ph/0402104] [INSPIRE].

[23] M.G. Alford, K. Rajagopal and F. Wilczek, *QCD at finite baryon density: Nucleon droplets and color superconductivity*, Phys. Lett. B **422** (1998) 247 [hep-ph/9711395] [INSPIRE].

[24] A. Mishra and H. Mishra, *Chiral symmetry breaking, color superconductivity and color neutral quark matter: A variational approach*, Phys. Rev. D **69** (2004) 014014 [hep-ph/0306105] [INSPIRE].

[25] A. Abhishek and H. Mishra, *Chiral Symmetry Breaking, Color Superconductivity, and Equation of State for Magnetized Strange Quark Matter*, Springer Proc. Phys. **261** (2021) 593 [INSPIRE].

[26] M.G. Alford, K. Rajagopal and F. Wilczek, *Color flavor locking and chiral symmetry breaking in high density QCD*, Nucl. Phys. B **537** (1999) 443 [hep-ph/9804403] [INSPIRE].

[27] M. Mannarelli, K. Rajagopal and R. Sharma, *Testing the Ginzburg-Landau approximation for three-flavor crystalline color superconductivity*, Phys. Rev. D **73** (2006) 114012 [hep-ph/0603076] [INSPIRE].

[28] K. Rajagopal and R. Sharma, *The Crystallography of Three-Flavor Quark Matter*, Phys. Rev. D **74** (2006) 094019 [hep-ph/0605316] [INSPIRE].

[29] D. Radice, A. Perego, F. Zappa and S. Bernuzzi, *GW170817: Joint Constraint on the Neutron Star Equation of State from Multimessenger Observations*, Astrophys. J. Lett. **852** (2018) L29 [arXiv:1711.03647] [INSPIRE].

[30] T. Malik et al., *GW170817: constraining the nuclear matter equation of state from the neutron star tidal deformability*, Phys. Rev. C **98** (2018) 035804 [arXiv:1805.11963] [INSPIRE].

[31] C.-M. Li, Y. Yan, J.-J. Geng, Y.-F. Huang and H.-S. Zong, *Constraints on the hybrid equation of state with a crossover hadron-quark phase transition in the light of GW170817*, Phys. Rev. D **98** (2018) 083013 [arXiv:1808.02601] [INSPIRE].

[32] J. Hu, S. Bao, Y. Zhang, K. Nakazato, K. Sumiyoshi and H. Shen, *Effects of symmetry energy on the radius and tidal deformability of neutron stars in the relativistic mean-field model*, PTEP **2020** (2020) 043D01 [arXiv:2002.00562] [INSPIRE].

[33] S. De, D. Finstad, J.M. Lattimer, D.A. Brown, E. Berger and C.M. Biwer, *Tidal Deformabilities and Radii of Neutron Stars from the Observation of GW170817*, Phys. Rev. Lett. **121** (2018) 091102 [arXiv:1804.08583] [*Erratum ibid.* **121** (2018) 259902] [INSPIRE].

[34] K. Chatziioannou, C.-J. Haster and A. Zimmerman, *Measuring the neutron star tidal deformability with equation-of-state-independent relations and gravitational waves*, Phys. Rev. D **97** (2018) 104036 [arXiv:1804.03221] [INSPIRE].

[35] V. Paschalidis, K. Yagi, D. Alvarez-Castillo, D.B. Blaschke and A. Sedrakian, *Implications from GW170817 and I-Love-Q relations for relativistic hybrid stars*, Phys. Rev. D **97** (2018) 084038 [arXiv:1712.00451] [INSPIRE].

[36] R. Nandi and P. Char, *Hybrid stars in the light of GW170817*, *Astrophys. J.* **857** (2018) 12 [arXiv:1712.08094] [INSPIRE].

[37] M. Alford, M. Braby, M.W. Paris and S. Reddy, *Hybrid stars that masquerade as neutron stars*, *Astrophys. J.* **629** (2005) 969 [nucl-th/0411016] [INSPIRE].

[38] W. Wei, M. Salinas, T. Klähn, P. Jaikumar and M. Barry, *Lifting the Veil on Quark Matter in Compact Stars with Core g-mode Oscillations*, *Astrophys. J.* **904** (2020) 187 [arXiv:1811.11377] [INSPIRE].

[39] V.A. Dommes and M.E. Gusakov, *Oscillations of superfluid hyperon stars: decoupling scheme and g-modes*, *Mon. Not. Roy. Astron. Soc.* **455** (2016) 2852 [arXiv:1512.04900] [INSPIRE].

[40] H. Yu and N.N. Weinberg, *Resonant tidal excitation of superfluid neutron stars in coalescing binaries*, *Mon. Not. Roy. Astron. Soc.* **464** (2017) 2622 [arXiv:1610.00745] [INSPIRE].

[41] B.K. Pradhan and D. Chatterjee, *Effect of hyperons on f-mode oscillations in Neutron Stars*, *Phys. Rev. C* **103** (2021) 035810 [arXiv:2011.02204] [INSPIRE].

[42] H. Sotani, N. Yasutake, T. Maruyama and T. Tatsumi, *Signatures of hadron-quark mixed phase in gravitational waves*, *Phys. Rev. D* **83** (2011) 024014 [arXiv:1012.4042] [INSPIRE].

[43] C.V. Flores and G. Lugones, *Discriminating hadronic and quark stars through gravitational waves of fluid pulsation modes*, *Class. Quant. Grav.* **31** (2014) 155002 [arXiv:1310.0554] [INSPIRE].

[44] A. Brillante and I.N. Mishustin, *Radial oscillations of neutral and charged hybrid stars*, *EPL* **105** (2014) 39001 [arXiv:1401.7915] [INSPIRE].

[45] I.F. Ranea-Sandoval, O.M. Guilera, M. Mariani and M.G. Orsaria, *Oscillation modes of hybrid stars within the relativistic Cowling approximation*, *JCAP* **12** (2018) 031 [arXiv:1807.02166] [INSPIRE].

[46] M.C. Rodriguez, I.F. Ranea-Sandoval, M. Mariani, M.G. Orsaria, G. Malfatti and O.M. Guilera, *Hybrid stars with sequential phase transitions: the emergence of the $g_2$ mode*, *JCAP* **02** (2021) 009 [arXiv:2009.03769] [INSPIRE].

[47] S.Y. Lau and K. Yagi, *Probing hybrid stars with gravitational waves via interfacial modes*, *Phys. Rev. D* **103** (2021) 063015 [arXiv:2012.13000] [INSPIRE].

[48] P. Jaikumar, A. Semposki, M. Prakash and C. Constantinou, *g-mode oscillations in hybrid stars: A tale of two sounds*, *Phys. Rev. D* **103** (2021) 123009 [arXiv:2101.06349] [INSPIRE].

[49] K.S. Thorne and A. Campolattaro, *Non-Radial Pulsation of General-Relativistic Stellar Models. I. Analytic Analysis for $L \geq 2$*, *Astrophys. J.* **149** (1967) 591.

[50] S.L. Detweiler and L. Lindblom, *On the nonradial pulsations of general relativistic stellar models*, *Astrophys. J.* **292** (1985) 12 [INSPIRE].

[51] K.D. Kokkotas and B.G. Schmidt, *Quasinormal modes of stars and black holes*, *Living Rev. Rel.* **2** (1999) 2 [gr-qc/9909058] [INSPIRE].

[52] N. Andersson and K.D. Kokkotas, *Towards gravitational wave asteroseismology*, *Mon. Not. Roy. Astron. Soc.* **299** (1998) 1059 [gr-qc/9711088] [INSPIRE].

[53] P.N. McDermott, H.M. van Horn and J.F. Scholl, *Nonradial g-mode oscillations of warm neutron stars*, *Astrophys. J.* **268** (1983) 837.

[54] A. Reisenegger and P. Goldreich, *Excitation of neutron star normal modes during binary inspiral*, *Astrophys. J.* **426** (1994) 688.

[55] U. Lee and T.E. Strohmayer, *Nonradial oscillations of rotating neutron stars: The effects of the Coriolis force*, Tech. Rep. PRINT-96-027 (1996) [INSPIRE].

[56] R. Prix and M.L.E. Rieutord, *Adiabatic oscillations of non-rotating superfluid neutron stars*, *Astron. Astrophys.* **393** (2002) 949 [astro-ph/0204520] [INSPIRE].

[57] N. Andersson and G.L. Comer, *On the dynamics of superfluid neutron star cores*, *Mon. Not. Roy. Astron. Soc.* **328** (2001) 1129 [astro-ph/0101193] [INSPIRE].

[58] M.E. Gusakov and E.M. Kantor, *Thermal g-modes and unexpected convection in superfluid neutron stars*, *Phys. Rev. D* **88** (2013) 101302 [INSPIRE].

[59] L. Gualtieri, E.M. Kantor, M.E. Gusakov and A.I. Chugunov, *Quasinormal modes of superfluid neutron stars*, *Phys. Rev. D* **90** (2014) 024010 [arXiv:1404.7512] [INSPIRE].

[60] E.M. Kantor and M.E. Gusakov, *Composition temperature-dependent g-modes in superfluid neutron stars*, *Mon. Not. Roy. Astron. Soc.* **442** (2014) 90 [arXiv:1404.6768] [INSPIRE].

[61] A. Passamonti, N. Andersson and W.C.G. Ho, *Buoyancy and g-modes in young superfluid neutron stars*, *Mon. Not. Roy. Astron. Soc.* **455** (2016) 1489 [arXiv:1504.07470] [INSPIRE].

[62] H. Yu and N.N. Weinberg, *Dynamical tides in coalescing superfluid neutron star binaries with hyperon cores and their detectability with third generation gravitational-wave detectors*, *Mon. Not. Roy. Astron. Soc.* **470** (2017) 350 [arXiv:1705.04700] [INSPIRE].

[63] P.B. Rau and I. Wasserman, *Compressional modes in two-superfluid neutron stars with leptonic buoyancy*, *Mon. Not. Roy. Astron. Soc.* **481** (2018) 4427 [arXiv:1802.08741] [INSPIRE].

[64] C. Constantinou, S. Han, P. Jaikumar and M. Prakash, *g modes of neutron stars with hadron-to-quark crossover transitions*, *Phys. Rev. D* **104** (2021) 123032 [arXiv:2109.14091] [INSPIRE].

[65] N.K. Glendenning, *First order phase transitions with more than one conserved charge: Consequences for neutron stars*, *Phys. Rev. D* **46** (1992) 1274 [INSPIRE].

[66] M.G. Alford, K. Rajagopal, S. Reddy and F. Wilczek, *The minimal CFL nuclear interface*, *Phys. Rev. D* **64** (2001) 074017 [hep-ph/0105009] [INSPIRE].

[67] D.N. Voskresensky, M. Yasuhira and T. Tatsumi, *Charge screening at first order phase transitions and hadron quark mixed phase*, *Nucl. Phys. A* **723** (2003) 291 [nucl-th/0208067] [INSPIRE].

[68] L.F. Palhares and E.S. Fraga, *Droplets in the cold and dense linear sigma model with quarks*, *Phys. Rev. D* **82** (2010) 125018 [arXiv:1006.2357] [INSPIRE].

[69] M.B. Pinto, V. Koch and J. Randrup, *The Surface Tension of Quark Matter in a Geometrical Approach*, *Phys. Rev. C* **86** (2012) 025203 [arXiv:1207.5186] [INSPIRE].

[70] B.W. Mintz, R. Stiele, R.O. Ramos and J. Schaffner-Bielich, *Phase diagram and surface tension in the three-flavor Polyakov-quark-meson model*, *Phys. Rev. D* **87** (2013) 036004 [arXiv:1212.1184] [INSPIRE].

[71] G. Lugones, A.G. Grunfeld and M. Al Ajmi, *Surface tension and curvature energy of quark matter in the Nambu-Jona-Lasinio model*, *Phys. Rev. C* **88** (2013) 045803 [arXiv:1308.1452] [INSPIRE].

[72] N. Yasutake, R. Lastowiecki, S. Benic, D. Blaschke, T. Maruyama and T. Tatsumi, *Finite-size effects at the hadron-quark transition and heavy hybrid stars*, *Phys. Rev. C* **89** (2014) 065803 [arXiv:1403.7492] [INSPIRE].

[73] D.N. Voskresensky, M. Yasuhira and T. Tatsumi, *Charge screening at first order phase transitions*, *Phys. Lett. B* **541** (2002) 93 [nucl-th/0109009] [INSPIRE].

[74] T. Maruyama, S. Chiba, H.-J. Schulze and T. Tatsumi, *Hadron-quark mixed phase in hyperon stars*, *Phys. Rev. D* **76** (2007) 123015 [arXiv:0708.3277] [INSPIRE].

[75] S. Typel and H.H. Wolter, *Relativistic mean field calculations with density dependent meson nucleon coupling*, *Nucl. Phys. A* **656** (1999) 331 [INSPIRE].

[76] T. Malik and C. Providência, *Bayesian inference of signatures of hyperons inside neutron stars*, *Phys. Rev. D* **106** (2022) 063024 [arXiv:2205.15843] [INSPIRE].



JCAP02(2023)015

[77] T. Malik, M. Ferreira, B.K. Agrawal and C. Providência, *Relativistic Description of Dense Matter Equation of State and Compatibility with Neutron Star Observables: A Bayesian Approach*, *Astrophys. J.* **930** (2022) 17 [arXiv:2201.12552] [INSPIRE].

[78] J.D. Walecka, *A theory of highly condensed matter*, *Annals Phys.* **83** (1974) 491 [INSPIRE].

[79] J. Boguta and A.R. Bodmer, *Relativistic Calculation of Nuclear Matter and the Nuclear Surface*, *Nucl. Phys. A* **292** (1977) 413 [INSPIRE].

[80] J. Boguta and H. Stoecker, *Systematics of Nuclear Matter Properties in a Nonlinear Relativistic Field Theory*, *Phys. Lett. B* **120** (1983) 289 [INSPIRE].

[81] B.D. Serot and J.D. Walecka, *Recent progress in quantum hadrodynamics*, *Int. J. Mod. Phys. E* **6** (1997) 515 [nucl-th/9701058] [INSPIRE].

[82] A. Mishra, P.K. Panda and W. Greiner, *Vacuum polarization effects in hyperon rich dense matter: A nonperturbative treatment*, *J. Phys. G* **28** (2002) 67 [nucl-th/0101006] [INSPIRE].

[83] L. Tolos, M. Centelles and A. Ramos, *The Equation of State for the Nucleonic and Hyperonic Core of Neutron Stars*, *Publ. Astron. Soc. Austral.* **34** (2017) e065 [arXiv:1708.08681] [INSPIRE].

[84] L. Tolos, M. Centelles and A. Ramos, *Equation of State for Nucleonic and Hyperonic Neutron Stars with Mass and Radius Constraints*, *Astrophys. J.* **834** (2017) 3 [arXiv:1610.00919] [INSPIRE].

[85] M. Buballa, *NJL model analysis of quark matter at large density*, *Phys. Rept.* **407** (2005) 205 [hep-ph/0402234] [INSPIRE].

[86] K. Schertler, S. Leupold and J. Schaffner-Bielich, *Neutron stars and quark phases in the NJL model*, *Phys. Rev. C* **60** (1999) 025801 [astro-ph/9901152] [INSPIRE].

[87] P. Gregorian, *Nonradial neutron star oscillations*, MSc Thesis, Universiteit Utrecht, Institute for theoretical physics, (November 2014). https://studenttheses.uu.nl/handle/20.500.12932/19369.

[88] M. Albright and J.I. Kapusta, *Quasiparticle Theory of Transport Coefficients for Hadronic Matter at Finite Temperature and Baryon Density*, *Phys. Rev. C* **93** (2016) 014903 [arXiv:1508.02696] [INSPIRE].

[89] H. Sotani, K. Tominaga and K.-i. Maeda, *Density discontinuity of a neutron star and gravitational waves*, *Phys. Rev. D* **65** (2002) 024010 [gr-qc/0108060] [INSPIRE].

[90] L. McLerran and S. Reddy, *Quarkyonic Matter and Neutron Stars*, *Phys. Rev. Lett.* **122** (2019) 122701 [arXiv:1811.12503] [INSPIRE].

[91] R.D. Pisarski, *Remarks on nuclear matter: How an $\omega_0$ condensate can spike the speed of sound, and a model of $Z(3)$ baryons*, *Phys. Rev. D* **103** (2021) L071504 [arXiv:2101.05813] [INSPIRE].

[92] N.K. Patra, T. Malik, D. Sen, T.K. Jha and H. Mishra, *An Equation of State for Magnetized Neutron Star Matter and Tidal Deformation in Neutron Star Mergers*, *Astrophys. J.* **900** (2020) 49 [INSPIRE].

[93] G. Miniutti, J.A. Pons, E. Berti, L. Gualtieri and V. Ferrari, *Non-radial oscillation modes as a probe of density discontinuities in neutron stars*, *Mon. Not. Roy. Astron. Soc.* **338** (2003) 389 [astro-ph/0206142] [INSPIRE].

[94] C.J. Krüger, W.C.G. Ho and N. Andersson, *Seismology of adolescent neutron stars: Accounting for thermal effects and crust elasticity*, *Phys. Rev. D* **92** (2015) 063009 [arXiv:1402.5656] [INSPIRE].

[95] D. Lai, *Resonant oscillations and tidal heating in coalescing binary neutron stars*, *Mon. Not. Roy. Astron. Soc.* **270** (1994) 611 [astro-ph/9404062] [INSPIRE].

# Robust universal relations in neutron star asteroseismology

Deepak Kumar [1,2] Tuhin Malik [3] Hiranmaya Mishra [1] and Constança Providência [3]

[1] *Theory Division, Physical Research Laboratory, Navarangpura, Ahmedabad 380 009, India*
[2] *Indian Institute of Technology Gandhinagar, Gandhinagar 382 355, Gujarat, India* *
[3] *CFisUC, Department of Physics, University of Coimbra, PT 3004-516 Coimbra, Portugal*†

(Dated: May 16, 2023)

The non-radial oscillations of the neutron stars (NSs) have been suggested as an useful tool to probe the composition of neutron star matter (NSM). With this scope in mind, we consider a large number of equations of states (EOSs) that are consistent with nuclear matter properties and pure neutron matter EOS based on a chiral effective field theory (CFT) calculation for the low densities and perturbative QCD EOS at very high densities. This ensemble of EOSs is also consistent with astronomical observations, gravitational waves in GW170817, mass and radius measurements from Neutron star Interior Composition ExploreR (NICER). Apart from verifying the robustness of universal relations (URs) among the quadrupolar $f$ modes frequencies, masses and radii with such a large number of EOSs, we find a strong correlation between the $f$ mode frequencies and the radii of NSs. Such a correlation is very useful in accurately determining the radius from a measurement of $f$ mode frequencies in near future. We also show that the quadrupolar $f$ mode frequencies of NS of masses 2.0 $M_\odot$ and above lie in the range 1.68-2.16 kHz in this ensemble of physically realistic EOSs. A NS of mass $2M_\odot$ with a low $f$ mode frequency may indicate the existence of non-nucleonic degrees of freedom.

*Introduction.* The neutron star (NS) observations in the multi-messenger astronomy have piqued a lot of interest in the field of nuclear astrophysics and strong interaction physics. The recent radio, x-rays and gravitational waves (GWs) observations in the context of NSs have provided interesting insights into the properties of matter at high density. The core of such compact objects is believed to contain matter at few times nuclear saturation density, $\rho_0$ ($\rho_0 \approx 0.16$ fm$^{-3}$) [1–4] and provides an unique window to get an insight into the behavior of matter at these extreme densities. On the theoretical side, no controlled reliable calculations are there that can be applicable to matter densities relevant for the NS cores. The lattice quantum chromodynamics (lQCD) simulations are challenging at these densities due to sign problem in montecarlo simulations. On the otherhand, the analytical calculations like chiral effective field theory (CFT) is valid only at very low densities while perturbative quantum chromodynamics (pQCD) is reliable at extremely high densities. In recent approaches, the equation of state (EOS)s between these two limits have been explored by connecting these limiting cases using a piecewise polytropic interpolation, speed of sound interpolation or spectral interpolation [5–11].

The NS properties such as mass, radius and quadrupole deformation of merging NSs can constrain the uncertainty in EOS. The discovery of the massive NS with masses of the order of $2M_\odot$ which requires EOS to be stiff while the fact that EOS is soft with non-nucleonic degrees of freedom at high density, already puts a constraint on the EOS at the intermediate densities. The observations of GWs from binary neutron star (BNS) inspiral by Advanced LIGO and Advanced Virgo GWs observatories have opened a new window in the field of multi-messenger astronomy and nuclear physics. The inspiral phase of NS-NS merger leads to tidal deformation ($\Lambda$), which is strongly sensitive to the compactness. Since $\Lambda$ is related to the EOS of the neutron star matter (NSM), this measurement acts as another constraint on the EOS. On the other hand, recovering the nuclear matter properties from the EOS of $\beta$-equilibriated matter is rather non trivial. This further requires the knowledge of the composition (for $eg$ proton fraction) of matter at high densities [12–15].

In the context of GWs, the non-radial oscillations of NS are particularly interesting as they can carry information of the internal composition of the stellar matter. These oscillations in the presence of perturbations (electromagnetic or gravitational) can emit GWs at the characteristic frequencies of its quasi-normal mode (QNM). The frequencies of QNM depend on the internal structure of NS and it may be an another probe to get an insight regarding the composition of NSM also known as asteroseismology. Different QNMs are distinguished by the restoring forces that act on the fluid element when it gets displaced from its equilibrium position. The important fluid modes related to GWs emission include fundamental ($f$) modes, pressure ($p$) modes and gravity ($g$) modes driven by the pressure and buoyancy respectively. The frequency of $p$ modes is higher than that of $g$ modes while the frequency of $f$ modes lies in between. The focus of the present investigation is on the quadrupolar $f$ modes that are correlated with the tidal deformability during the inspiral phase of NS merger [16] and have the strongest tidal coupling among all the oscillation modes. More importantly, these modes lie within the sensitivity range of the current as well as upcoming generation of the GWs detector networks [17]. In this context, QNMs have been studied with various EOS models and some universal/quasi-universal behaviors for the frequency and damping time which are insensitive to the EOS models [18–25]. This needs to be explored further regarding the robustness of these relations for a large number of EOSs consistent with recent observational constraints.

In this letter we propose two major points of interest. Firstly we estimate, within the Cowling approximation, the $f$ mode oscillation frequencies for NSs using a large number of EOSs and demonstrate that observation of $f$ mode frequencies, apart from causality $c_s^2 \leq 1$ and maximum mass constraints, further restrict the EOSs. Secondly we verify the robustness of few universal relation (UR) among the quadrupolar $f$ mode frequencies, masses and radii studied earlier with limited EOSs. It has been earlier found that these URs between NS properties are strongly violated by hybrid EOSs [26–28] and certain exotic phases [29]. We consider here a large number of EOSs and show that some of them are almost insensitive to the EOSs.

*Setup* - An ensemble of EOSs that we consider here are constructed by stitching together EOSs valid for different segments in baryon densities. For the outer crust the Bethe-Pethick-Sutherland (BPS) EOS is chosen [30]. Outer crust and the core are joined using a polytropic form $p(\varepsilon) = a_1 + a_2\varepsilon^{\gamma}$ in order to construct the inner crust, where the parameters $a_1$ and $a_2$ are determined in such a way that the EOS for the inner crust matches with the outer crust at one end ($\rho = 10^{-4}$ fm$^{-3}$) and with the core at the other end ($\rho = 0.04$ fm$^{-3}$). The polytropic index $\gamma$ is taken to be $4/3$ [31]. It is important to note that the differences in NSs radii between this treatment of the inner crust EOS and the unified inner crust description including the pasta phases have been found to be less than 0.5 km, as discussed in [32]. The core EOSs are considered within the two different approaches: (i) a nucleonic $\beta-$ equilibritated EOS based on a relativistic description of hadrons through their density-dependent coupling with mesons constrained by the existing observational, theoretical and experimental data through Bayesian analysis (DDB), obtained in [32], which satisfies pure neutron matter (PNM) constraints at low densities obtained from next-to-next-to-next-to leading order (N$^3$LO) calculations in the CFT [33, 34]. (ii) a hybrid set of EOSs which consists of the DDB EOS at low density ($\leq 2\rho_0$) and the deconfined quark matter at very high densities ($\geq 40\rho_0$) while the region ($2\rho_0$-$40\rho_0$) is interpolated by piecewise polytropes (DDB-Hyb). For the deconfined quark matter, we employ NNLO pQCD results of Refs. [6, 35] which can be cast in a simple fitting function for the pressure as a function of chemical potential ($\mu$) given as

$$P_{pQCD}(\mu) = \frac{\mu^4}{108\pi^2}\left(c_1 - \frac{d_1 X^{-\nu_1}}{(\mu/GeV) - d_2 X^{-\nu_2}}\right) \quad (1)$$

where the parameters are $c_1 = 0.9008$, $d_1 = 0.5034$, $d_2 = 1.452$, $\nu_1 = 0.3553$ and $\nu_2 = 0.9101$ [36]. Here $X$ is a dimensionless renormalization scale parameter, $X = 3\bar{\Lambda}/\mu$ which is allowed to vary $X \in [1, 4]$. We use this pQCD EOS for densities beyond $\rho \simeq 40\rho_0$ which corresponds to $\mu_{\rm pQCD} = 2.6$ GeV [36]. Between the region of the validity of pQCD and DDB i.e. $\mu_{\rm DDB} \leq \mu \leq \mu_{\rm pQCD}$, where $\mu_{\rm DDB}$ is the chemical potential of DDB EOS at $\rho = 2\rho_0$, we divide the interval into two segments, ($\mu_{\rm DDB}$-$\mu_c$) and ($\mu_c$-$\mu_{\rm pQCD}$), and assume EOS has a polytropic form in each segment i.e. $P_i(\rho_i) = \kappa_i\rho_i^{\gamma_i}$ for the $i$-th segment [35]. The segments can be connected to each other by requiring that pressure and energy density are continuous at $\mu_c$ as well as pressure shoud be an increasing function of energy density and EOS must be subluminal. We also ensure that there is no jump in baryon number density. This corresponds to assuming no first order phase transition between hadronic matter and quark matter. If one wishes to include a first order phase transition, an extra term to the number density at $\mu_c$ can be added [35].

To obtain EOS of the core, we proceed as follows. Below $\rho = 2\rho_0$ till the inner crust, we use a soft (stiff) DDB EOS as obtained in Ref. [32] within 90% CI. The corresponding value of chemical potential at $\rho = 2\rho_0$ is $\mu_{\rm DDB} = 1.036$ $(1.097)$ GeV for a soft (stiff) DDB EOS. We interpolate the region from $\mu = \mu_{\rm DDB}$ to $\mu = \mu_c$ and from $\mu = \mu_c$ to $\mu = \mu_{\rm pQCD}$ with a piecewise polytrope. We select all those EOSs which (i) match with pQCD at $\mu = \mu_{\rm pQCD}$ (i.e. $X \in [1, 4]$) (ii) have pressure as an increasing function of energy density, and (iii) are subluminal. We refer this EOS as DDB-Hyb. The chemical potential $\mu_c$ is here chosen in such a way that it satisfies pQCD at $\mu = \mu_{\rm pQCD}$. We take $\mu_c \in [1.04, 2.2]$ GeV and the corrosponding pressure $P_c \in [20, 1260]$ MeV.fm$^{-3}$. For an ensemble of DDB-Hyb EOSs we choose $\mu_c, P_c$ randomly in the prescribe domain by Latin-Hypercube-Sampling method [37] for an uniform distribution. For a given $\mu_c, P_c$ and $P_{\rm DDB}$, the parameters of the first polytrope, $(\kappa_1, \gamma_1)$ get determined. Similarly for a given $\mu_c, P_c$ and $P_2$ (where $P_2$ is the pQCD pressure for a given value of $X$ at $\mu = \mu_{\rm pQCD}$), the parameters of the second polytrope $(\kappa_2, \gamma_2)$ get determined. The domains for pressure ($P_c$) and chemical potential ($\mu_c$) become $P_c \in [45, 1255]$ MeV·fm$^{-3}$ and $\mu_c \in [1.07, 2.09]$ GeV after constrained by pQCD. These domains further squeeze to $P_c \in [53, 680]$ MeV.fm$^{-3}$ and $\mu_c \in [1.15, 1.88]$ GeV after putting constraint of $M_{\rm max} \geq 2M_\odot$ and so we find 0.38 million EOSs out of 54 million sampled EOSs satisfying these constraints. It may be mentioned here that for an interpolation between ($\mu_{\rm DDB}$-$\mu_{\rm pQCD}$), we have used two polytropes. There have been different interpolation functions like spectral decomposition [38, 39] and speed of sound method [9, 11, 40].

*Pulsating equations* - To estimate the specific oscillation frequency of NSs, let us discuss the non-radial oscillation of a spherically symmetric NS characterized by the background space-time metric where the line element is given by

$$ds^2 = -e^{2\Phi}dt^2 + e^{2\Lambda}dr^2 + r^2\left(d\theta^2 + \sin^2\theta d\phi^2\right). \quad (2)$$

We shall consider the pulsating equations within the Cowling approximation so that our study is limited to the modes related to fluid perturbations and neglect the metric perturbations. The Lagrangian fluid displacement vector is given by

$$\xi^i = \left(e^{-\Lambda}W, \ -V\partial_\theta, \ -V\sin^{-2}\theta\partial_\phi\right) r^{-2}Y_{lm} \quad (3)$$

Where $W(r,t)$ and $V(r,t)$ are the perturbation functions and $Y_{lm}$ are the spherical harmonic function. The perturbation equations that describe oscillations can be obtained by the perturbed Einstein field equations $\delta G_{\alpha\beta} = 8\pi\delta T_{\alpha\beta}$ with $G_{\alpha\beta} = R_{\alpha\beta} - \frac{1}{2}g_{\alpha\beta}R$ being the Einstein tensor. Linearizing these equations in the perturbation, while choosing a harmonic time dependence for the perturbation i.e. $W(r,t) \propto W(r)e^{i\omega t}$ and $V(r,t) \propto V(r)e^{i\omega t}$ with frequency $\omega$, the differential equations further fluid perturbation functions can be obtained as

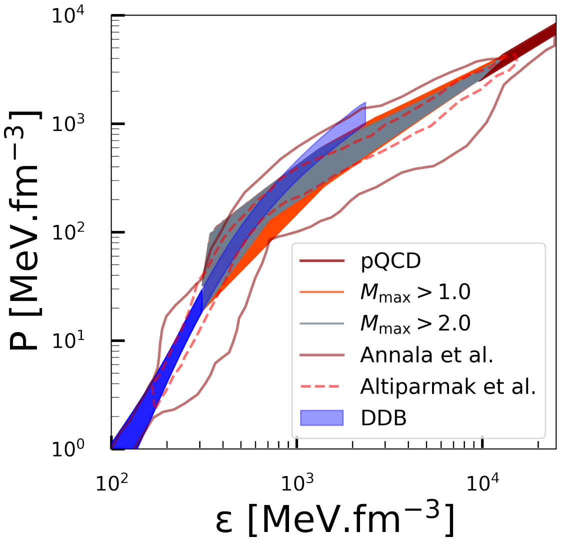


FIG. 1. We show pressure and energy density regions in MeV.fm$^{-3}$ of our sampled EOSs (DDB and DDB-Hyb). We consider nucleonic $\beta$-equilibrated EOS of the 90% CIs for DDB (lightblue) as a full range and (darkblue) upto $2\rho_0$ [32] and at very high density $\sim 40\rho_0$ the NNLO pQCD (dark red). In the intermediate region, EOS is evolved in thermodynamically consistent way with two polytropic segments (see text for details).

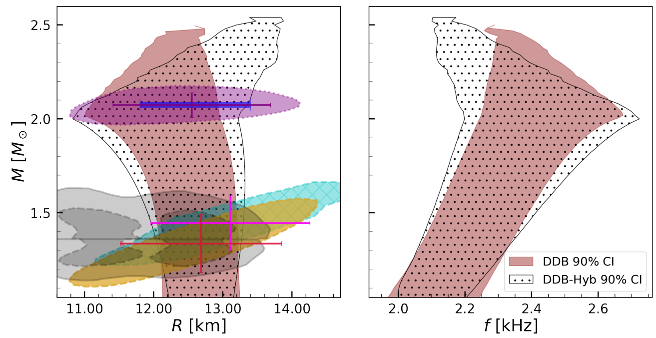


FIG. 2. We plot NS mass ($M$)-radii ($R$) and $f$ mode frequency-mass ($M$) region obtained from the 90% CI for the conditional probabilities $P(R|M)$ (left) and $P(f|M)$ (right) for DDB-Hyb (black dotted) and DDB (dark red). The blue horizontal bar on the left panel indicates the 90% CI radius for a $2.08M_\odot$ star determined in [42] combining observational data from GW170817 and NICER as well as nuclear saturation properties. The top and bottom gray regions indicate, respectively, the 90% (solid) and 50% (dashed) CI of the LIGO/Virgo analysis for each binary component from the GW170817 event [43]. The $1\sigma$ (68%) credible zone of the 2-D posterior distribution in mass-radii domain from millisecond pulsar PSR J0030+0451 (cyan and yellow) [44, 45] as well as PSR J0740 + 6620 (violet) [42, 46] are shown for the NICER x-rays data. The horizontal (radius) and vertical (mass) error bars reflect the $1\sigma$ credible interval derived for the same NICER data's 1-D marginalized posterior distribution.

[24, 41]

$$W' = \frac{d\epsilon}{dP}\left(\omega^2 r^2 e^{\Lambda-2\Phi}V + W\Phi'\right) - l(l+1)e^{\Lambda}V, \quad (4)$$

$$V' = 2V\Phi' - \frac{1}{r^2}We^{\Lambda}, \quad (5)$$

here, the 'prime' denotes the total derivative with respect to $r$. These equations are solved with appropriate boundary conditions at the stellar center $r = 0$ and at the surface $r = R$. The $W$ and $V$ in the vicinity of the stellar center are taken as $W(r) \sim Cr^{l+1}$ and $V(r) \sim -Cr^l/l$, where $C$ is an arbitrary constant. The other boundary condition that needs to be fullfilled is that the Lagrangian perturbation to the pressure must vanish at the stellar surface. This leads to [24, 41]

$$\omega^2 r^2 e^{\Lambda-2\Phi}V + W\Phi'\big|_{r=R} = 0 \quad (6)$$

This apart in the case of density discontinuity these equations have to be supplemented by an extra junction condition at the surface of discontinuity. We shall not consider here density discontinuity. With these boundary conditions, the problem becomes an eigenvalue problem for the parameter $\omega$ which can be estimated numerically. We shall confine ourselves to $l = 2$ quadrupolar modes.

*Results* - We now proceed to analyze the ensembles of EOSs that are consistent with nuclear matter properties or PNM EOS based on theoretically robust CFT at low densities and pQCD at very high densities. As mentioned earlier, we started with 54 million EOSs. We discarded those EOS which do not match the two end points or are superluminal (square of speed of sound $c_s^2 > 1$) as well as the condition of positive speed of sound. This leaves us with an ensemble of 0.38 million DDB-Hyb EOSs. This ensemble of EOSs is represented in Fig. 1 by the orange band. We next enforce the $M_{\max} \geq 2.0M_\odot$ constraint resulting from solving the Tolman-Oppenheimer-Volkoff (TOV) equations with this ensemble. This constraint further reduces the number of EOSs to 55,000 which are displayed in Fig. 1 as the gray band, named here after DDB-Hyb set. The polytrope indices $\gamma_1$ and $\gamma_2$ are seen to vary over an intervals $\gamma_1 \in [1.67, 13.76]$ and $\gamma_2 \in [1.0, 1.51]$. The tight constraint on $\gamma_2$ has its origin on the matching to the pQCD pressure. In Fig. 1, the light blue band is the $\beta$-equilibrated nuclear matter $\approx$ 10K EOSs (DDB 90% CI) while the dark red band corresponds to pQCD EOS. For comparison, we also plot the domain of EOSs obtained in Ref. [10] (red solid curve) compatible with recent NICER and GWs observations. The red dashed lines refers to the dense PDF ($\geq 0.08$) obtained in Ref. [11] with continuous sound speed and consistent not only with nuclear theory and pQCD, but also with astronomical observations. It is to be noted that both of DDB and DDB-Hyb sets are compatible with them.

In Fig.2, we plot NS mass-radii and $f$ mode frequency-mass regions obtained for 90% CI for the conditional probabilities $P(R|M)$ (left) and $P(f|M)$ (right) from the mass-radius clouds arising from the ensembles of EOSs of DDB-Hyb (black dotted) and DDB (dark red). The blue horizontal bar on the left panel indicates the 90% CI radius for a $2.08M_\odot$ star determined in Ref. [42] combining observational data from GW170817 and NICER as well as nuclear data. The top and bottom gray regions indicate, the 90% (solid) and 50% (dashed) CI of the LIGO/Virgo analysis for each binary component from the GW170817 event [43] respectively. The $1\sigma$ (68%) credible zone of the 2-D posterior distribution in mass-radii domain from millisecond pulsar PSR J0030+0451 (cyan and yellow) [44, 45] as well as PSR J0740 + 6620 (violet) [42, 46] are shown for the NICER x-rays data. The horizontal (radius) and vertical (mass) error bars reflect the $1\sigma$ credible interval derived for the same NICER data's 1-D marginalized posterior distribution. The mass-radius domain for the DDB-Hyb set sweeps a wider range than the DDB set, restricted to nucleonic degrees of freedom. The DDB-Hyb set constrained by pQCD at high density leads to larger radii for high mass NS. We conclude that the present observational constraints either obtained from GW170817 or NICER cannot rule out the existence of exotic degrees of freedom. In the right panel, we see that the 90% CI for $P(f|M)$ $f$ mode frequency $f \in [1.95, 2.7]$ kHz for both the DDB and DDB-Hyb sets. The range is smaller for low NS mass and as the mass increases the 90% CI for $f$ mode frequency increases. The $f$ mode frequency of a NS above $2M_\odot$ mass is in the range (2.1-2.7) kHz and (2.3-2.65) kHz for the DDB-Hyb and DDB sets, respectively. As mentioned in the earlier sections, the solutions for $f$ mode obtained in this work are within the Cowling approximation (neglecting perturbations of the background metric). It was shown that the Cowling approximation can overestimate the quadrupolar $f$ mode frequency of NSs by up to 30 to 10 % for NS masses in the range (1.0-2.5) $M_\odot$ compared to the frequency obtained in the linearized general relativistic (GR) formalism [21, 47, 48]. The accurate measurement of $f$ modes may further constrain EOS to a narrower range. Besides, a star of $2M_\odot$ with a low $f$ mode frequency may indicate an existence of non-nucleonic degrees of freedom.

In Fig. 3, we have studied two known URs involving the $f$ mode frequency with global properties of NS, often studied in literature with a limited EOSs. In particular, we have named UR1 for the $f$ mode frequency as a function of square root of the average star density $\sqrt{M/R^3}$, and UR2a for the $\omega M$ versus the compactness $M/R$, where $\omega = 2\pi f$. We have verified their robustness with our EOS sets, DDB-Hyb and DDB. We have also obtained a new and direct relation between the $f$ modes frequency, $f$ and radius, $R$ with the help of the existing strong correlation between them. In the left panel of the figure we show UR1:

$$f = a\sqrt{(M/R^3)} + b. \tag{7}$$

It has been shown in Refs. [19, 49] that the average density can be well parameterized via the $f$ mode frequency. The following values of $a$ and $b$ have been obtained: $a = 22.27 \pm 0.023$ $(26.76 \pm 0.01)$ kHz.km, $b = 1.520 \pm 0.001$ $(1.348 \pm 0.001)$ kHz for DDB-Hyb (DDB). The maximum relative percentage error obtained for UR1 within 90% CI is 6.0%(4.5%) for DDB-Hyb (DDB). In fact, the UR1 depends on EOS, therefore the dispersion, is obtained with a 90%CI. We can note that these uncertainties will remain for the entire valid domain of EOSs even if one solves full the linearized GR equations. For example, at 0.4 km$^{-1}$ mass density the frequency can vary by 400 Hz.

In Andersson & Kokkotas (Benhar et al) the authors have obtained the following parameters $a = 35.9(33.0)\mathrm{kHz.km}$ and $b = 0.78$ $(0.79)$ kHz [19, 21, 49], the difference between both works being the EOS considered in the study. In those studies the linearized GR equations were solved, and, as expected, lower frequencies have been determined. In Ref. [47], the oscillations of non-rotating and fast rotating NSs have been explored with a different set of EOSs based on microscopic theories within the Cowling approximation. The values of the coefficients of the UR1 obtained were $a = 25.32$ kHz.km and $b = 1.562$ kHz, which are at the 90% CI upper limit of the relations we have obtained.

In center panel of the Fig. 3 we display UR2a:

$$\omega M = a\left(\frac{M}{R}\right) + b \tag{8}$$

obtained for both DDB-Hyb and DDB sets, with $a = 0.6474 \pm 4.6 \times 10^{-5}$ $(a = 0.6549 \pm 2.6 \times 10^{-5})$ and $b = -0.0085 \pm 1.05 \times 10^{-5}$ $(b = -0.0103 \pm 6.18 \times 10^{-6})$ for DDB-Hyb (DDB) set. Both the coefficients are in dimensionless. The maximum relative percentage error obtained for UR2a within 90% CI is 3.78% (2.20%) for DDB-Hyb (DDB) set. The values of the slope and intercept for UR2a are also compatible with the ones obtained in Ref. [50] within Cowling approximation with a few nucleonic and hyperonic EOSs as $a = 0.65765$ and $b = 0.0127866$, respectively. We have also obtained a relation as UR2b for $\omega R$ as $\omega R = a\left(\frac{M}{R}\right)^2 + b\left(\frac{M}{R}\right) + c$. The coefficients are found to be $a = -3.0369 \pm 0.0013(-3.1844 \pm 0.0020)$, $b = 1.5829 \pm 0.0005(1.6288 \pm 0.0008)$ and $c = 0.4095 \pm 5 \times 10^{-5}(0.4087 \pm 7 \times 10^{-5})$ for DDB-Hyb (DDB) set, all the coefficients are dimensionless. In this case the maximum relative percentage error is 2.6% (1.6%) in the set DDB-Hyb (DDB). Compared with UR1, the relative maximum uncertainty is smaller for UR2a and UR2b for both DDB-Hyb and DDB sets. Using these relations we predict $f$ mode frequencies for the PSR J0740+6620. For this pulsar, the mass and radius are determined as $2.08 \pm 0.7$ $M_\odot$ and $12.35 \pm 0.75$ km in [42] combining observational data from GW170817 and NICER as well as nuclear data. The corresponding mean values of $f$ mode frequency is calculated as 2.35 kHz and 2.36 kHz for UR2a and UR2b, respectively, with a $\sim 1 - 4\%$ intrinsic error in the URs and additional $\sim 10 - 12\%$ error due to uncertainty present in mass and radius.

We have identified a strong linear correlation between the $f$ mode frequency and NS radius $R$ and we are naming it as UR3. The values $r \in [0.98, 0.99]$ of the Pearson correlation coefficient were obtained between $f$ and $R$ for NS with a mass $M \in [1.6, 2.4]$ with our two sets of EOSs. These results can also be traced back from UR1 by keeping fixed NS mass while noting that the correlation is stronger only for the NS of larger mass. In the right panel of Fig. 3, we plot the linear relations between $f$ and $R$. The values of slope

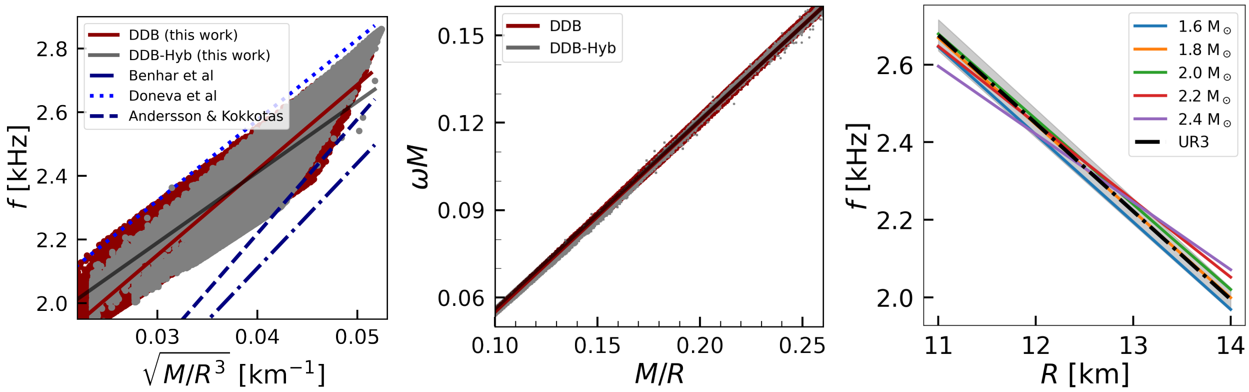


FIG. 3. We plot URs obtained with our sets of EOSs, namely DDB-Hyb and DDB. UR1 (left): The frequency of the $f$ mode is plotted as a function of the square root of the average density, UR2a (center): The universality among $\omega M$ and $M/R$ and UR3 (right) the universal linear relations among $f$ mode frequency and radii of NS with masses ranged from 1.6 to 2.4 $M_\odot$ in a step of 0.2$M_\odot$.

$m \in [-0.2256, -0.2233, -0.2196, -0.1984, -0.1748]$ and intercept are $c \in [5.1271, 5.1256, 5.0952, 4.8305, 4.5191]$ for NS mass $M \in [1.6, 1.8, 2.0, 2.2, 2.4]$. We also plot a marginalized UR3 obtained with NS masses in the range of 1.6 to 2.4 $M_\odot$ with a slope, ($m = -0.227$) and an intercept, ($c = 5.173$). This gives $\approx 1.5\%$ relative residual within 90% CI. We expect that the correlation is also present if the full GR solutions are considered. Taking this correction factor into account, the new relation (UR3) will be very useful for the upcoming future detection in order to constrain NS radius of massive NS precisely. For example, in order to measure a radius of a NS with $\sim 0.2$ km uncertainty, the $f$ mode frequency needs to be measured within $\sim 2\%$ uncertainty.

*Summary and conclusion -* The QNMs are related with the viscous properties of matter. In the future, precise measurements of them can put constraints on EOS of dense matter. We have studied the $f$ mode frequency among the QNMs, which is in the sensitivity band of the future gravitational waves networks [17]. We have calculated the $f$ mode frequency within the Cowling approximation with a nucleonic set of 14,000 EOSs (DDB set), obtained in Ref. [32] based on the relativistic mean field (RMF) theory, constrained by existing observational, theoretical and experimental data through Bayesian analysis. We have also generated an ensemble of EOSs using DDB below twice saturation density ($\rho \leq 2\rho_0$) and pQCD at high densities ($\rho \geq \rho_0$) as in Ref.[9]. Piecewise polytropes have been used to interpolate region from $2\rho_0$ to $40\rho_0$. Implementing the constraints of causality and maximum mass $M_{\rm max} \geq 2.0 M_\odot$ a set of 55000 DDB-Hyb typed EOSs has obtained. The mass-radius cloud that we obtain from the ensembles of these EOSs is consistent with the GW170817 joint probability distribution as well as the recent NICER observations of mass and radius. We have analyzed the robustness of a few previously known universal relations and confirmed their disperson with our large number of EOSs. We also found a novel strong correlation between the $f$ mode frequency, ($f$) and the radius, ($R$) for a NS of mass in the range (1.6-2.4) $M_\odot$. These new direct relations between $f$ and $R$ will allow an accurate determination of radius of NS using future $f$ mode detection.

We show that the quadrupolar $f$ mode frequencies obtained in Cowling approximation of NS of masses 2.0$M_\odot$ and above lie in the range (2.1-2.7) kHz and (2.3-2.65) kHz for DDB-Hyb and DDB sets, respectively. We use these URs to predict the $f$ mode frequencies of the NICER observations and obtain ~2.35 (1.88) kHz in Cowling approximation (renormalized to full GR solutions) for the PSR J0740+6620 which interestingly lies within the sensitivity band of the future gravitational wave detector networks [17] for the detection of gravitational waves. It was shown that a two solar mass star with a low $f$ mode frequency may indicate the existence of non-nucleonic degrees of freedom. In the future, a detailed investigation of how this frequency is correlated with the individual component of the EOS or different particle compositions in NS core will be carried out.

*Acknowledgments-* The authors acknowledge the Laboratory for Advanced Computing at the University of Coimbra for providing HPC resources for this research results reported within this paper, URL: https://www.uc.pt/lca. T.M and C.P would like to thank national funds from FCT (Fundação para a Ciência e a Tecnologia, I.P, Portugal) under Projects No. UID/FIS/04564/2019, No. UIDP/04564/2020, No. UIDB/-04564/2020, and No. POCI-01-0145-FEDER-029912 with financial support from Science, Technology, and Innovation, in its FEDER component, and by the FCT/MCTES budget through national funds (OE).

* deepakk@prl.res.in
† tuhin.malik@uc.pt

[1] N. K. Glendenning, *Compact Stars* (1996).
[2] P. Haensel, A. Y. Potekhin, and D. G. Yakovlev, *Neutron Stars 1 : Equation of State and Structure*, Vol. 326 (2007).
[3] L. Rezzolla, P. Pizzochero, D. I. Jones, N. Rea, and I. Vidaña, eds., *The Physics and Astrophysics of Neutron Stars*, Vol. 457

(Springer, 2018).
[4] J. Schaffner-Bielich, *Compact Star Physics* (Cambridge University Press, 2020).
[5] L. Lindblom and N. M. Indik, Phys. Rev. D **86**, 084003 (2012), arXiv:1207.3744 [astro-ph.HE].
[6] A. Kurkela, E. S. Fraga, J. Schaffner-Bielich, and A. Vuorinen, Astrophys. J. **789**, 127 (2014), arXiv:1402.6618 [astro-ph.HE].
[7] E. R. Most, L. R. Weih, L. Rezzolla, and J. Schaffner-Bielich, Phys. Rev. Lett. **120**, 261103 (2018), arXiv:1803.00549 [gr-qc].
[8] E. Lope Oter, A. Windisch, F. J. Llanes-Estrada, and M. Alford, J. Phys. G **46**, 084001 (2019), arXiv:1901.05271 [gr-qc].
[9] E. Annala, T. Gorda, A. Kurkela, J. Nättilä, and A. Vuorinen, Nature Phys. **16**, 907 (2020), arXiv:1903.09121 [astro-ph.HE].
[10] E. Annala, T. Gorda, E. Katerini, A. Kurkela, J. Nättilä, V. Paschalidis, and A. Vuorinen, (2021), arXiv:2105.05132 [astro-ph.HE].
[11] S. Altiparmak, C. Ecker, and L. Rezzolla, (2022), arXiv:2203.14974 [astro-ph.HE].
[12] P. B. de Tovar, M. Ferreira, and C. Providência, Phys. Rev. D **104**, 123036 (2021), arXiv:2112.05551 [nucl-th].
[13] S. M. A. Imam, N. K. Patra, C. Mondal, T. Malik, and B. K. Agrawal, (2021), arXiv:2110.15776 [nucl-th].
[14] C. Mondal and F. Gulminelli, (2021), arXiv:2111.04520 [nucl-th].
[15] R. Essick, I. Tews, P. Landry, and A. Schwenk, Phys. Rev. Lett. **127**, 192701 (2021).
[16] C. Chirenti, P. R. Silveira, and O. D. Aguiar, Int. J. Mod. Phys. Conf. Ser. **18**, 48 (2012), arXiv:1205.2001 [gr-qc].
[17] G. Pratten, P. Schmidt, and T. Hinderer, Nature Commun. **11**, 2553 (2020), arXiv:1905.00817 [gr-qc].
[18] N. Andersson and K. D. Kokkotas, Phys. Rev. Lett. **77**, 4134 (1996), arXiv:gr-qc/9610035.
[19] N. Andersson and K. D. Kokkotas, Mon. Not. Roy. Astron. Soc. **299**, 1059 (1998), arXiv:gr-qc/9711088.
[20] O. Benhar, E. Berti, and V. Ferrari, Mon. Not. Roy. Astron. Soc. **310**, 797 (1999), arXiv:gr-qc/9901037.
[21] O. Benhar, V. Ferrari, and L. Gualtieri, Phys. Rev. D **70**, 124015 (2004), arXiv:astro-ph/0407529.
[22] L. K. Tsui and P. T. Leung, Mon. Not. Roy. Astron. Soc. **357**, 1029 (2005), arXiv:gr-qc/0412024.
[23] T. K. Chan, Y. H. Sham, P. T. Leung, and L. M. Lin, Phys. Rev. D **90**, 124023 (2014), arXiv:1408.3789 [gr-qc].
[24] H. Sotani, Phys. Rev. D **103**, 123015 (2021), arXiv:2105.13212 [astro-ph.HE].
[25] H. Sotani and B. Kumar, Phys. Rev. D **104**, 123002 (2021), arXiv:2109.08145 [gr-qc].
[26] S. Y. Lau, P. T. Leung, and L. M. Lin, Phys. Rev. D **99**, 023018 (2019), arXiv:1808.08107 [astro-ph.HE].
[27] D. Bandyopadhyay, S. A. Bhat, P. Char, and D. Chatterjee, Eur. Phys. J. A **54**, 26 (2018), arXiv:1712.01715 [astro-ph.HE].
[28] S. Han and A. W. Steiner, Phys. Rev. D **99**, 083014 (2019), arXiv:1810.10967 [nucl-th].
[29] P. von Doetinchem *et al.*, JCAP **08**, 035 (2020), arXiv:2002.04163 [astro-ph.HE].
[30] G. Baym, C. Pethick, and P. Sutherland, Astrophys. J. **170**, 299 (1971).
[31] J. Carriere, C. J. Horowitz, and J. Piekarewicz, Astrophys. J. **593**, 463 (2003), arXiv:nucl-th/0211015.
[32] T. Malik, M. Ferreira, B. K. Agrawal, and C. Providência, (2022), arXiv:2201.12552 [nucl-th].
[33] I. Tews, T. Krüger, K. Hebeler, and A. Schwenk, Phys. Rev. Lett. **110**, 032504 (2013), arXiv:1206.0025 [nucl-th].
[34] K. Hebeler, J. M. Lattimer, C. J. Pethick, and A. Schwenk, Astrophys. J. **773**, 11 (2013), arXiv:1303.4662 [astro-ph.SR].
[35] A. Kurkela, P. Romatschke, and A. Vuorinen, Phys. Rev. D **81**, 105021 (2010), arXiv:0912.1856 [hep-ph].
[36] E. S. Fraga, A. Kurkela, and A. Vuorinen, Astrophys. J. Lett. **781**, L25 (2014), arXiv:1311.5154 [nucl-th].
[37] A. Florian, Probabilistic Engineering Mechanics **7**, 123 (1992).
[38] L. Lindblom, Phys. Rev. D **82**, 103011 (2010), arXiv:1009.0738 [astro-ph.HE].
[39] L. Lindblom, Phys. Rev. D **97**, 123019 (2018), arXiv:1804.04072 [astro-ph.HE].
[40] E. Annala, T. Gorda, A. Kurkela, J. Nättilä, and A. Vuorinen, Nature Phys. **16**, 907 (2020), arXiv:1903.09121 [astro-ph.HE].
[41] D. Kumar, H. Mishra, and T. Malik, (2021), arXiv:2110.00324 [hep-ph].
[42] M. C. Miller *et al.*, Astrophys. J. Lett. **918**, L28 (2021), arXiv:2105.06979 [astro-ph.HE].
[43] B. P. Abbott *et al.* (LIGO Scientific, Virgo), Phys. Rev. X **9**, 011001 (2019), arXiv:1805.11579 [gr-qc].
[44] T. E. Riley *et al.*, Astrophys. J. Lett. **887**, L21 (2019), arXiv:1912.05702 [astro-ph.HE].
[45] M. C. Miller *et al.*, Astrophys. J. Lett. **887**, L24 (2019), arXiv:1912.05705 [astro-ph.HE].
[46] T. E. Riley *et al.*, Astrophys. J. Lett. **918**, L27 (2021), arXiv:2105.06980 [astro-ph.HE].
[47] D. D. Doneva, E. Gaertig, K. D. Kokkotas, and C. Krüger, Phys. Rev. D **88**, 044052 (2013), arXiv:1305.7197 [astro-ph.SR].
[48] B. K. Pradhan, D. Chatterjee, M. Lanoye, and P. Jaikumar, (2022), arXiv:2203.03141 [astro-ph.HE].
[49] K. D. Kokkotas, T. A. Apostolatos, and N. Andersson, Mon. Not. Roy. Astron. Soc. **320**, 307 (2001), arXiv:gr-qc/9901072.
[50] B. K. Pradhan and D. Chatterjee, Phys. Rev. C **103**, 035810 (2021), arXiv:2011.02204 [astro-ph.HE].